UNIVERSITY OF ZÜRICH

Script - Lecture PHY 432

Physics with Muons: From Atomic Physics to Solid State Physics

Alex Amato

February 2022

Contents

Forwords

The first version of this lecture notes was composed in December 2017 and Januar 2018. Though I have presented the topics my way, the script is in some parts based on the previous notes composed by Elvezio Morenzoni (see `https://www.psi.ch/lmu/lectures`). Also, I took profit of many valuable inputs and available documents authored by my colleagues at the Laboratory for Muon Spin Spectroscopy of the Paul Scherrer Institute. Among them, I would like to specially thank Hubertus Luetkens, Thomas Prokscha, Andreas Suter, Rustem Khasanov, Robert Scheuermann and Stefan Holenstein. I would like to thank also Daniel Andreica (Cluj-Napoca University) for discussions about the concept and finally Klara Mihov (Humboldt-Universität zu Berlin) for useful inputs about, and a critical reading of, the first version of the script.

Alex Amato

Literature

Books

- A. Yaouanc, P. Dalmas de Réotier
  Muon Spin Rotation, Relaxation and Resonance
  Oxford University Press, 2011

- E. Karlsson
  Solid State Phenomena, As Seen by Muons, Protons, and Excited Nuclei
  Clarendon, Oxford, 1995

- S.L. Lee, S.H. Kilcoyne, R. Cywinski (eds.)
  Muon Science: Muons in Physics; Chemistry and Materials
  IOP Publishing, Bristol and Philadelphia, 1999

- A. Schenck
  Muon Spin Rotation Spectroscopy
  Adam Hilger, Bristol, 1985

Introductory articles

- S.J. Blundell
  Spin-Polarized Muons in Condensed Matter Physics
  Contemporary Physics 40, 175-192 (1999)

- P. Bakule, E. Morenzoni
  Generation and Application of Slow Polarized Muons
  Contemporary Physics 45, 203-225 (2004)

- A. Amato and D. Andreica
  Muon Spin Rotation
  in: Encyclopedia of Condensed Matter Physics, ed. by F. Bassani *et al.*, Elsevier, Oxford (2005) Pages 41-49

- A. Amato
  Muon Spin Rotation (μSR): Applications in Magnetism

in: Encyclopedia of Materials: Science and Technology (Second Edition) 2001, Pages 5888-5892

Reviews articles: applications

- P. Dalmas de Réotier and A. Yaouanc
  Muon Spin Rotation and relaxation in Magnetic Materials
  J. Phys. Condens. Matter 9, 9113-9166 (1997)

- A. Schenck and F.N. Gygax
  Magnetic Materials Studied by Muon Spin Rotation Spectroscopy
  in: *Handbook of Magnetic Materials*, edited by K.H.J. Buschow, Vol. 9, Pages 57-302
  Elsevier, Amsterdam, 1995

- B.D. Patterson
  Muonium States in Semiconductors
  Rev. Mod. Phys. 60, 69-159 (1988)

- A. Amato
  Heavy-Fermion Systems Studied by μSR Techniques
  Rev. Mod. Phys., 69, 1119-1179 (1997)

- V. Storchak, N. Prokovev
  Quantum Diffusion of Muons and Muonium Atoms in Solids
  Rev. Mod. Physics, 70, 929 (1998)

- J. Sonier, J. Brewer, R. Kiefl
  μSR Studies of Vortex State in Type-II Superconductors
  Rev. Mod. Physics, 72, 769 (2000)

- E. Roduner
  The Positive Muon as a Probe in Free Radical Chemistry
  Lecture Notes in Chemistry No. 49
  Springer Verlag, Berlin, 1988

1. Introduction: the Muon

1.1. The muon: an elementary particle

The muon (μ) is one of the few an elementary particles, possessing a unit electric charge and a spin 1/2. It is a *charged lepton*, that is an elementary particle which does not participate in the strong interaction. Note that the muon particle has a negative charge, whereas the antimuon (μ^+) has a positive charge. In the following we will simply speak about negative and positive muons.
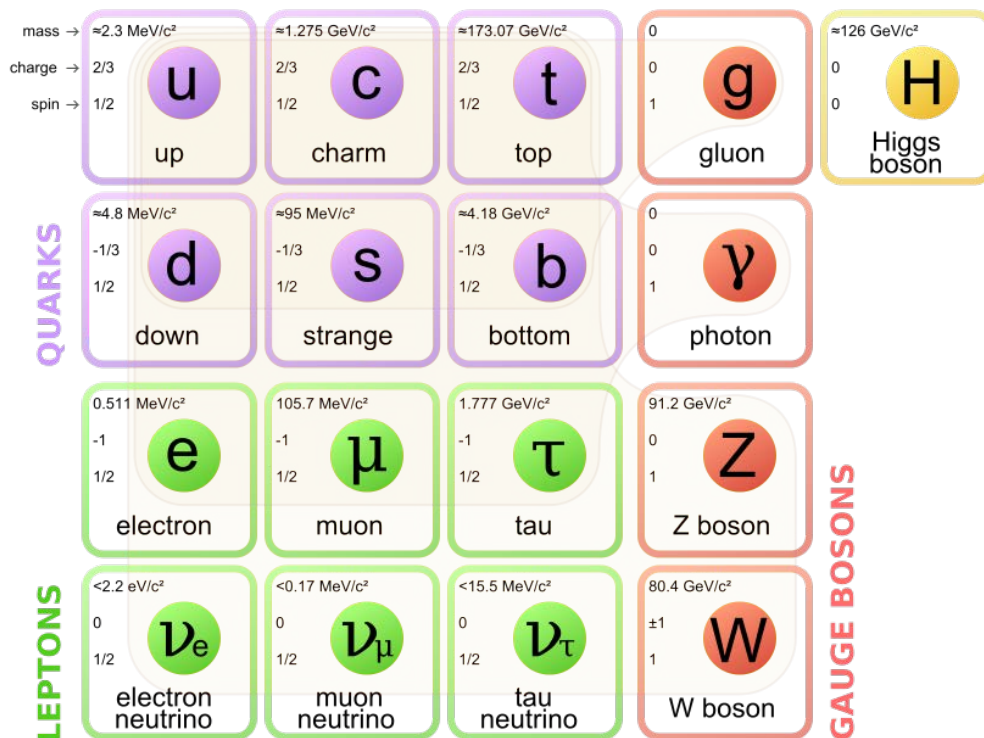
Figure 1.1.: *Standard model of elementary particles: the 12 fundamental fermions (half-integer spin 1/2) and 4 fundamental bosons (integer spin). Brown loops indicate which bosons (red) couple to which fermions (purple and green). Note that the gauge boson Graviton is still a hypothetical elementary particle (i.e. not shown) that mediates the force of gravitation in the framework of quantum field theory. Note also that the term elementary particle just indicate that the substructure of this particle is unknown, thus it is unknown whether it is composed of other particles. (Taken from* https://en.wikipedia.org/wiki/Elementary_particle.*)*

1.2. Muon discovery

1785 Charles Augustin de Coulomb found that electroscopes can spontaneously discharge by the action of the air and not by defective insulation.

1850 In 1850, Italian physicist Cano Matteucci and later British physicist William Crookes in 1879 showed that the rate of spontaneous discharge decreased at lower atmospheric pressures.

1896 Becquerel discovered natural radioactivity. The discovery of radioactivity triggered interest about the origin of the spontaneous electrical discharge observed earlier in the air. The obvious hypothesis was that the discharge was caused by the radioactive materials on Earth, though this was difficult to prove.

1899 Elster and Geitel found that surrounding a gold leaf electroscope with a thick metal box would decrease its spontaneous discharge. From this observation, they concluded that the discharge was due to highly penetrating ionizing agents outside of the container.

1909-1910 Theodor Wulf performed experiments with precise electrometers, which detected natural radiation sources on the ground. Wulf took his electroscope to the top of the Eiffel tower. Actually he wanted to test whether the radiation was coming from the Earth. He found that the intensity of radiation *decreases at nearly 300 m [altitude to] not even to half of its ground value*, but the results were not really conclusive.

1910 Albert Gockel (Uni. Fribourg) arranged the first balloon flights with the purpose of studying the properties of penetrating radiation.[1] Albert Gockel, measured the levels of ionizing radiation up to a height of 3000 meters. He concluded that the ionization did not decrease with height and consequently could not have a purely terrestrial origin. He also introduced the term "kosmische Strahlung" (cosmic radiation).

1907-1911 Domenico Pacini observed that ionization underwater was significantly lower than on the sea surface. For these measurements he immersed an electroscope 3 m deep in the sea at Livorno. This demonstrates that part of the ionization itself must be due to sources other than the radioactivity of the Earth. Pacini concluded that "...*sizable cause of ionization exists in the atmosphere, originating from penetrating radiation, independent of the direct action of radioactive substances in the ground*" [1].

---

[1]See for example
http://www.sps.ch/artikel/geschichte-der-physik/albert-gockel-from-atmospheric-electricity-to-cosmic-radiation-5/

Figure 1.2.: *Domenico Pacini.*
Taken from `https://commons.wikimedia.org/wiki/File:APacini_measurement.jpg`

1911-1912 Victor Hess makes measurements from balloons up to an altitude of 5.2 km. He measures an increasing charge with increasing altitude.

Figure 1.3.: *Victor F. Hess, center, departing from Vienna about 1911.*

1913 The results by Hess were confirmed by the young Werner Kolhörster during different flights up to 9.2 km.

1924-1926 Millikan first questioned the existence of cosmic rays after flight above Texas up to 15 km (the results were blured by the latitude geomagnetic effect, see below). "*We conclude, therefore, that there exists no such penetrating radiation as we have assumed*" [2].

By using unmanned balloons to perform experiments at even higher altitude, Millikan

completely changed his mind and coins the expression 'cosmic rays'. "... *all this constitutes pretty unambiguous evidence that the high altitude rays do not originate in our atmosphere, very certainly not in the lower nine-tenhs of it, and justify the designation 'cosmic rays'* " [3].

Backed by US media, Millikan moved to take the glory of the discovery, which triggered an angry answer by Hess [4]: "...*The recent determination by Millikan and his colleagues of the high penetrating power of high-altitude radiation has been an occasion for American scientific journals such as 'Science' and 'Scientific Monthly' to propose to name the name 'Millikan Rays'. As his work is merely a confirmation and extension of the results obtained by Gockel, myself and Kolhörster from 1910 to 1913 using balloon borne measurements of the rays, this appellation should be rejected as it is misleading and unjustified....*

1927 The geomagnetic effect on the cosmic rays was discovered by J. Clay [5]. As the interstellar charged particles that approach at the level of the equator have to travel in a direction perpendicular to the earth magnetic field, they are deflected away through the Lorentz force and only very energetic particles reach the earth. Near the poles, incoming particles have a higher probability that their trajectory is along the magnetic lines and therefore will not sense the Lorentz force.
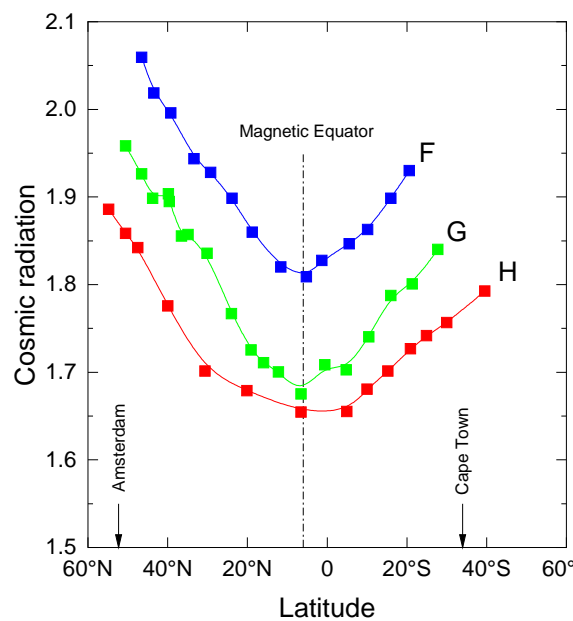
Figure 1.4.: *Change of cosmic radiation as a function of the latitude (adapted from Ref. [5]) obtained during an expedition from Amsterdam to Batavia (nowadays Jakarta). Note that no unit was specified in the original publication. The curve F corresponds to the bare measurements of an electrometer and the curve G are measurements performed with 8 cm iron shielding. Also along this curve the measurements obtained by J.A. Prins [6] for the north hemisphere are reported. The curve H reports the points obtained by H. Hoerlin et al. [7].*
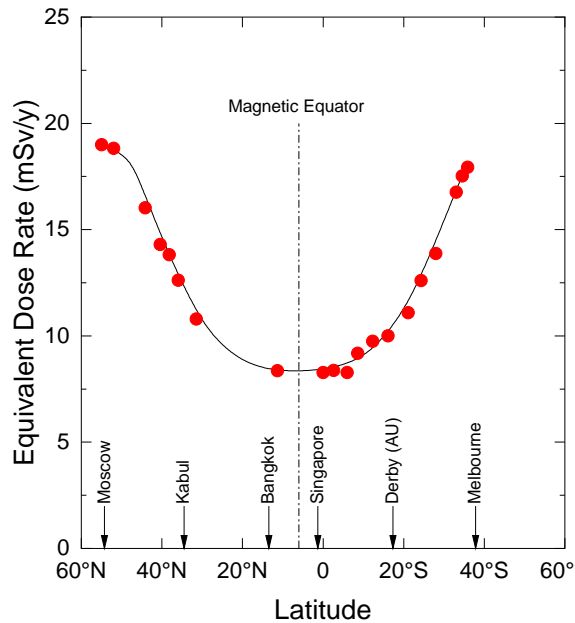
Figure 1.5.: *Same experiment performed during an aircraft flight in 1988 from Melbourne to Frankfurt [8]. Note that the radiation does not disappear near the magnetic equator, as the geomagnetic effect has a larger impact on the part of the cosmic ray with relatively low energy, i.e. the plasma coming from the sun.*

1933 First muon picture (but not correctly identified) in a Wilson cloud chamber by Kunze [9].
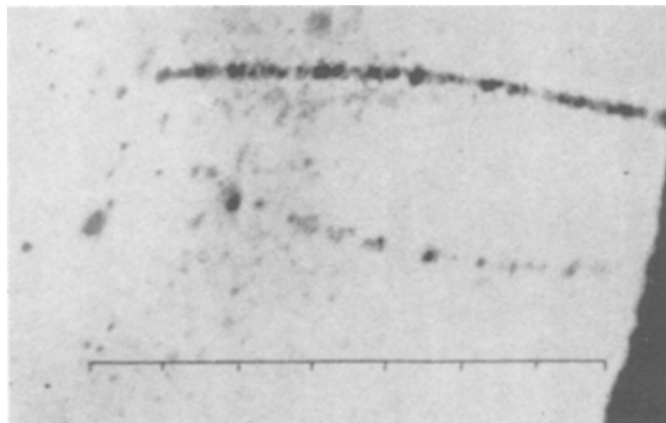
Fig. 5.
Doppelspur als Resultat einer vermutlichen Kernexplosion.
7-fache Vergrößerung. Untere Spur ⇌ Elektron von 37 000 000 V.
Natur der oberen positiven Korpuskel nicht sicher bekannt.

Figure 1.6.: *First observation of a muon (not identified) [9]. The original figure caption is also reported.*

1936 V. Hess receives the Nobel Prize for the discovery of cosmic radiation.

1936-1937 Discovery of the muon by C. Anderson and S. Neddermeyer using a cloud chamber to an altitude of 4300 m on Pike's Peak [10]. The gave it the name 'mesotron'. The muon however was first misinterpreted as the so-called H. Yukawa's particle [11] mediating the nuclear force (residual strong interaction between hadrons).

1941 B. Rossi and D.B. Hall [12] determine the muon life time to be $\tau_\mu = (2.4 \pm 0.3) \times 10^{-6}$ s.

1945-1947 Conversi *et al.* [13] measure the lifetime of positive and negative muons. The lifetime is too long for strongly interacting particles. It turns out that the Yukawa's particle is actually the pion.

1946 Discovery of the pion by C.F. Powell *et al.* [14] studying the cosmic rays using specialized photographic emulsions at high-altitude. **The pion**, which proved to be the Yukawa's particle, **primary decays into a muon and a muon neutrino** (see Section 1.3.1).

1946 T.D. Lee and C.N. Yang [15] predicted that any process governed by the weak interaction should lead to a violation of parity. The Nobel Prize in Physics 1957 was awarded jointly to them.
Between Christmas of 1946 and New Year's, National Bureau of Standards (NBS) scientists led by Columbia Prof. C.S. Wu. [16] confirmed that the emission of beta particles is asymmetric for cobalt-60 nuclei oriented with a strong magnetic field.

1957 R. Garwin *et al.* [17] measure **the parity violation in weak decay of the muon** [18]. This work was followed by the one of Friedman *et al.* few months later [17].
Garwin *et al.* made the following remark: *It seems possible that polarized positive and negative muons will become a powerful tool for exploring magnetic fields in nuclei [...], atoms, and interatomic regions*, hence predicting the later us of muons by solid state physicists.

1.3. The pion: the parent particle

1.3.1. Pion properties

The generic name pion is for any of the particles π^-, π^+ and π^0. The pion is classified as a meson as it consists of a quark and an antiquark (u and d quark). As proposed by Hideki Yukawa [11], the exchange of virtual pions provides an explanation for the residual strong force between nucleons. Pions are produced in high energy accelerators in collisions between hadrons (see Section 1.3.2). Pions are also produced in nature when high energy cosmic rays enter in the Earth's atmosphere.

Table 1.1.: *Main properties of the pion.*

	π^+	π^-	π^0
Lifetime (s)	$26.033 \pm 0.005 \times 10^{-9}$	$26.033 \pm 0.005 \times 10^{-9}$	$8.4 \pm 0.6 \times 10^{-17}$
Spin I_π	0	0	0
Mass (MeV/c^2)	139.57018 ± 0.00035	139.57018 ± 0.00035	134.9766 ± 0.0006
Decay	$\to \mu^+ + \nu_\mu$	$\to \mu^- + \bar{\nu}_\mu$	$\to \gamma + \gamma$

1.3.2. Pion production reactions

Pions are not produced in radioactive decay, but are produced through high energy collisions between hadrons. These collisions happen either in natural processes, for example when high energy cosmic ray protons interact with matter in the Earth's atmosphere, or in high energy accelerators.

The production of pions occurs through the collision of nucleons with sufficient energy involved, *i.e.* with an available energy in the center of mass exceeding the rest pion mass (see Table 1.1). The reactions to produce a single positive pion are:

$$p + p \to p + n + \pi^+$$
$$p + n \to n + n + \pi^+$$
$$p + n \to d + \pi^+ \tag{1.1}$$
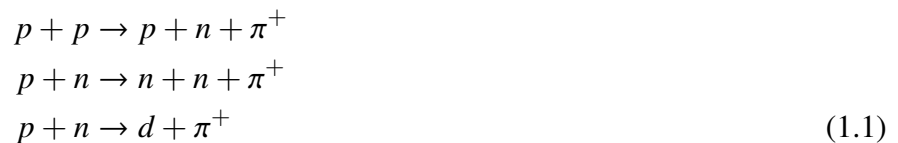
Even though the neutral pion mass is 135 MeV/c^2 (see Table 1.1) an incoming proton with 135 MeV of kinetic energy will not be able to create a neutral pion in a collision with a proton of the target. This is due to the conservation of momentum.

The simplest way to figure the necessary energy the incoming proton needs to create a neutral pion is to calculate in the **center of mass frame** (see exercise). In this frame the least possible

kinetic energy must be just enough to create the neutral pion with the final state particles at rest. One finds that the necessary velocity of the proton (in the center mass frame) must be 0.36c. We need to know the energy necessary in the "lab" frame, *i.e.* that in which one of the protons is initially at rest. Using the relativistic addition of velocities formula, we obtain 0.64c. This implies the incoming proton has a kinetic energy around 280 MeV.

Thus to create a pion of rest energy 135 MeV, it is necessary to give the incoming proton at least 280 MeV of kinetic energy. This is called the "threshold energy" for pion production. The "inefficiency" arises because momentum is also conserved, so there is still considerable kinetic energy in the final particles. As shown on Fig. 1.7 the optimum energy for pion production is above 500 MeV (corresponding to the maximum of the cross section). This defines the energy of an accelerator needed to produced pion (and muon) beams.
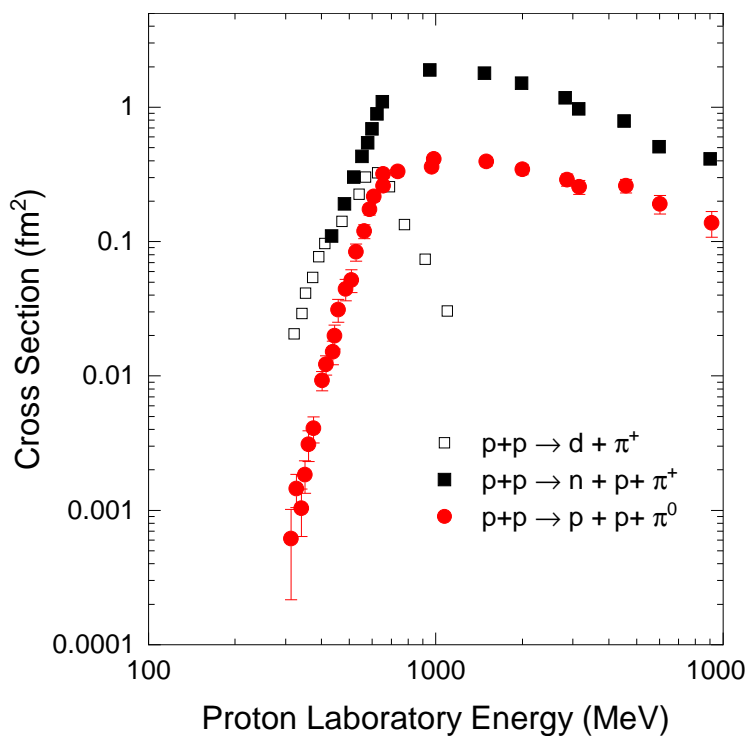
Figure 1.7.: *Energy dependence of the cross section[2] for pion production in some nucleon-proton reactions (adapted from Ref. [19]).*

In a laboratory, one measures often double differential scattering cross-sections, which are determined by measuring the produced particles at a given energy at a particular angular position. From the double differential scattering cross-section one obtains the total cross section by integrating over the energy of the produced particles and over the solid angle.

---

[2]The cross section can be considered as the effective area for the collision, *i.e.* it is often used to mean the probability that two particles will collide and react. The natural unit of the cross section is of course m^2, but the cross section is often given in barn, with 1 b $= 10^{-28}$ m$^2 = 100$ fm^2.
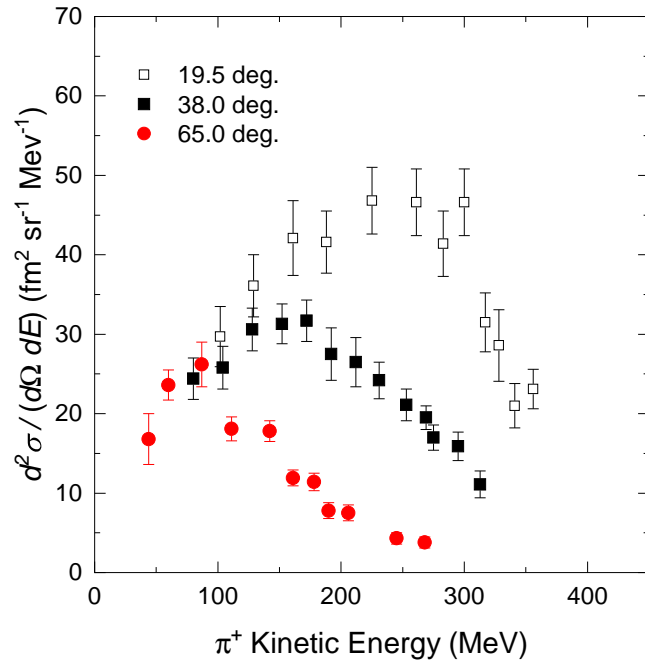
Figure 1.8.: *Double differential production cross section as a function of the positive pion energy.*

For a maximum number of single pions the incident proton beams should have energies in the range 500 MeV to 1000 MeV. At higher energies, it is possible to have reactions producing a pair of pions. However, the "threshold energy" is here of the orther of 600 MeV with the cross section reaching a saturation above 1.5 GeV.

1.3.3. The pion decay

In this Section we will concentrate on the decay of the positive pion.

As seen in Table 1.1, the pion life-time is about 26 ns and the primary decay mode, with a branching fraction of 0.999877, is a leptonic decay into a muon and a muon neutrino:

$$\pi^+ \rightarrow \mu^+ + \nu_\mu \tag{1.2}$$

Figure 1.9.: *Schematic of a pion decay. The black arrows represent the flying paths and the colored arrows represents the particle spins.*

Two points are important in this decay process.

1. It is a two-body decay, then the conservation of momentum and energy leads to important features. Hence, the muon and neutrino fly in opposite directions in the reference frame of the pion. Also the decay products have definite energies. The muon has always the energy 4.1 MeV ($\rightarrow$ Exercises) in the reference frame of the pion (assuming that the neutrino has a mass $M_\nu = 0$).

2. The pion has a spin $I_\pi = 0$. The total spin is conserved during the decay. As only left-handed neutrinos are produced in nature, this has as consequence that the muon has a spin $S = 1/2$ and is 100% polarized.

The decay proceeds by the weak interaction[3]. During the decay a parity violation occurs: this is evidenced by the fact that no neutrino with helicity +1 exist and therefore the parity operation of the pion decay (see Fig. 1.9) does not exist.
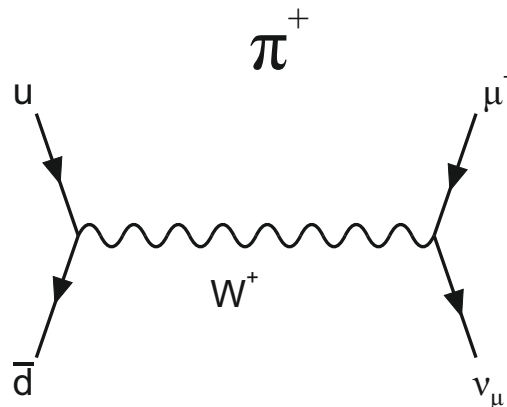
Figure 1.10.: *Feynman diagram of the pion decay. The pion is composed by the u and $\bar{d}$ quarks.*

---

[3]The weak interaction involves the exchange of the intermediate vector bosons, the W and the Z (in this case a boson W^+). It has a range of about 10^{-18} meter which is about 0.1% of the diameter of a proton. We will not treat the weak interaction, which goes beyond the scope of the lecture. A discussion of the weak interaction can be found in Ref. [20] and on Ref. [21] for the muon decay (pages 29 to 36).

1.4. Muon properties

Table 1.2 provides the main muon properties which will be important to perform muon-spin spectroscopy experiments. We can identify several crucial points:

Table 1.2.: *Main properties of the muon.*

Lifetime (s)	$2.1969811(22) \times 10^{-6}$
Charge	$+e$ (or $-e$ for the μ^-)
Spin I_μ	$1/2$
Magnetic Moment	$m_\mu = 4.836 \times 10^{-3}\ \mu_B$ ($1\ \mu_B = 9.274009994(57) \times 10^{-24}$ J/T)
	$3.18 \times \mu_p$
	$8.9 \times \mu_N$
Gyromagnetic ratio γ_μ	$2\pi \times 135.538817$ MHz/T
Mass	$105.6583745(24)$ MeV/c^2
	$206.768 \times M_e$
	$0.1124 \times M_p$
Principal decay	$\rightarrow e^+ + \nu_e + \bar{\nu}_\mu$

- The muon is a *purely magnetic* probe.
  Classically the electric quadrupole moment of an entity of charge e and charge density ρ is given by

$$Q = \int (3z^2 - r^2)\rho(r)\ d^3r \ . \tag{1.3}$$

For a spherical distribution of charge, $\langle x^2 \rangle = \langle y^2 \rangle = \langle z^2 \rangle = 1/3 \times \langle r^2 \rangle$, and the quadrupole moment vanishes.[4]

---

[4]In the quantum mechanics, the approach can be made by noting that

$$Q = \int (3z^2 - r^2)\rho(r)\ d^3r = \int r^2(3\cos^2\theta - 1)\rho(r)\ d^3r = \sqrt{\frac{16\pi}{5}} \int r^2\ Y_2^0\ \rho(r)\ d^3r = Q_{20}\ , \tag{1.4}$$

where Y_2^0 is the spherical function with $\ell = 2$ and $m = 0$.
In the quantum mechanics the quadrupole moment is defined as the expectation value of the quadrupolar tensor Q_{20} in the substate $|I, M = I\rangle$ [so-called spectroscopic quadrupole moment $Q_s(I)$].
At this point it is useful to use the Wigner-Eckart Theorem, where:

$$\langle J\,M|T_{(k)}^q|J'\,M'\rangle = \frac{\langle J'\,M'\,k\,q|J\,M\rangle\langle J\|T_{(k)}\|J'\rangle}{\sqrt{2J+1}}\ , \tag{1.5}$$

where $T_{(k)}^q$ is the q-th component of the spherical tensor operator $T_{(k)}$ of rank k (in our case $k = 2$), $\langle J'M'kq|JM\rangle$ is the "Clebsch-Gordan" coefficient for coupling J' with k to get J, and $K = \langle J \| T_{(k)} \| J'\rangle$ is a value that is called the "reduced matrix element". This means that the matrix element of a tensor operator can be factored into a part which is independent of the tensor itself, but involves the projection quantum numbers ("Clebsch-Gordan" coefficient), and a part not involving the projection quantum numbers ("reduced matrix element").

- The muon magnetic moment (or in other words the gyromagnetic ratio) is large making the muon a very sensitive magnetic probe.

- The muon life time is short but still easily accessible with modern detector and timing techniques.

- The decay into a positron and neutrinos represents a branching fraction of basically 100%. Other possible decays involve either a positron and a gamma ($\rightarrow e^+ + \nu_e + \bar{\nu}_\mu + \gamma$) or 2 positrons and an electron ($\rightarrow e^+ + \nu_e + \bar{\nu}_\mu + e^+ + e^-$).

We have therefore:

$$
\begin{aligned}
Q_s(I) &= \langle I, M = I | Q_{20} | I, M = I \rangle \\
&= \langle I, M = I \, 2 \, 0 | I, M = I \rangle \times \frac{\langle I \| Q_2 \| I \rangle}{\sqrt{2J+1}} \quad,
\end{aligned}
\tag{1.6}
$$

where

$$
\langle I, M = I \, 2 \, 0 | I, M = I \rangle = \sqrt{\frac{I(2I-1)}{(2I+3)(I+1)}}
\tag{1.7}
$$

is the appropriate Clebsch-Gordan coefficient. Therefore, for either $I = 0$ and $I = 1/2$ (for example the muon) the quadrupolar interaction vanishes.

1.5. The muon decay

1.5.1. Generalities

As said, muons is an unstable particle and decays with a mean lifetime of $\tau_\mu \simeq 2.197\ \mu$s as follows

$$\mu^+ \rightarrow e^+ + \nu_e + \bar{\nu}_\mu$$
$$\mu^- \rightarrow e^- + \bar{\nu}_e + \nu_\mu \ . \tag{1.8}$$

As this is a three-body decay, the kinetic energy of the emerging positron[5] may take values varying continuously from zero up to a maximum value $E_{e^+,\ \max}$.

The case of zero kinetic energy represents the situation where the neutrino and antineutrino emerge antiparallel and carry away all the available kinetic energy. On the other hand side, the kinetic energy of the positron is maximum when the neutrino and antineutrino travel together in the direction opposed to the one of the positron.

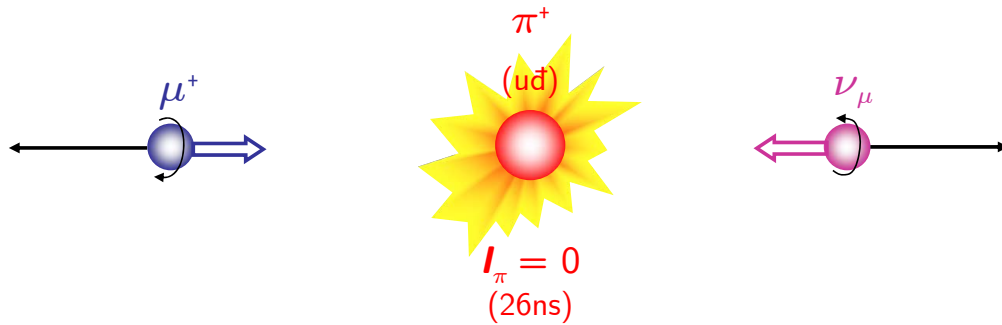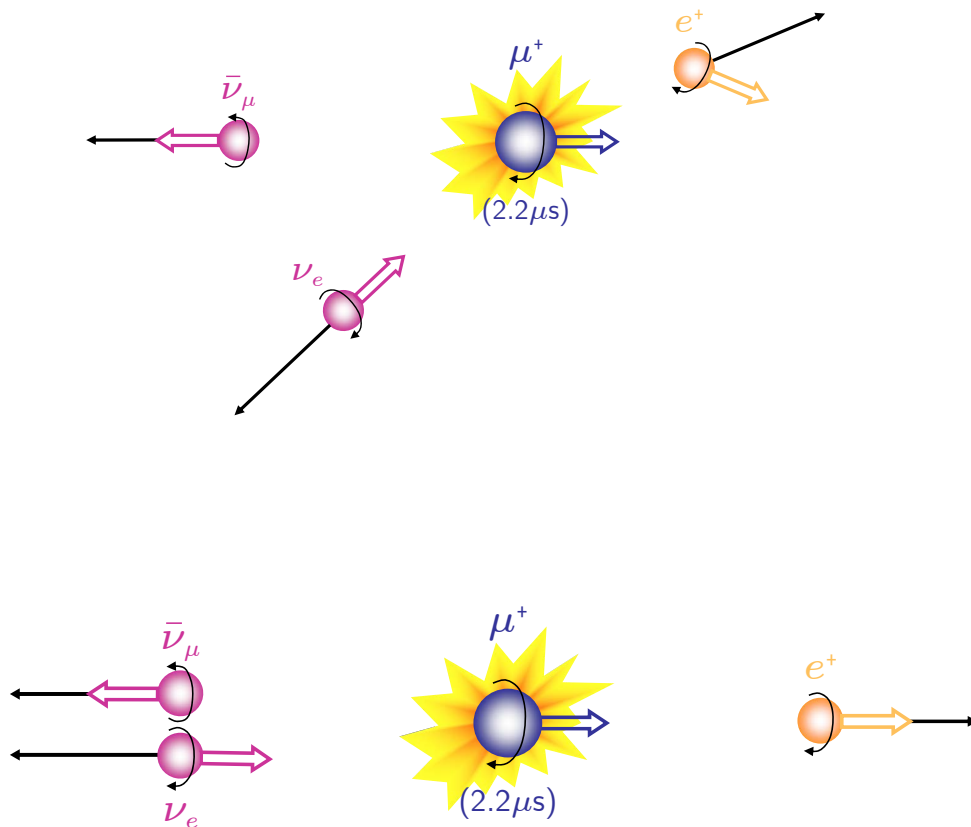**Figure 1.11.:** *Upper panel: Schematic of a positive muon decay. The black arrows represent the flying paths and the colored arrows represents the particle spins. The lower panel represents the situation of a decay producing a positron of maximum energy.*

---

[5]We concentrate the discussion on the positive muons, but the considerations are analog for the negative ones.

The maximum and mean positron energies resulting from the three body decay are given by (see Exercices):

$$E_{e^+, \text{max}} = \frac{M_\mu^2 + M_e^2}{2M_\mu^2} \, c^2 = 52.82 \text{ MeV} \quad \text{and} \tag{1.9}$$

$$\bar{E}_{e^+} = 36.9 \text{ MeV} \quad . \tag{1.10}$$

1.5.2. Differential positron emission

The quantitative treatment of the muon decay is based on the weak interaction and we are interested by the differential positron emission probability per unit of time as function of the energy and solid angle, which is given by [22]

$$d\Gamma = W(\varepsilon, \theta) \, d\varepsilon \, d\Omega = \frac{1}{4\pi\tau_\mu} 2\varepsilon^2 (3 - 2\varepsilon) \left[1 + \frac{2\varepsilon - 1}{3 - 2\varepsilon} \cos\theta \right] d\varepsilon \, d\Omega \quad , \tag{1.11}$$

where we have $\varepsilon = E_{e^+} / E_{e^+, \text{max}}$, and $d\Omega = \sin\theta \, d\theta \, d\phi$ is the solid angle (with here θ is the polar angle and ϕ is the azimuthal one). We see that $d\Gamma$ is independent of ϕ.

The important point in Eq. 1.11 is the energy dependent asymmetry term

$$a(\varepsilon) = \frac{2\varepsilon - 1}{3 - 2\varepsilon} \quad , \tag{1.12}$$

which is a direct consequence that the muon decay is governed by the weak interaction. Therefore the positrons are emitted asymmetrically around the muons. As we will see in Section 3 this asymmetric positron emission is the key feature at the base of the μSR technique.

With this definition, we can rewrite the Eq. 1.11

$$\begin{aligned} d\Gamma = W(\varepsilon, \theta) \, d\varepsilon \, d\Omega &= \frac{1}{4\pi\tau_\mu} 2\varepsilon^2 (3 - 2\varepsilon) \left[1 + a(\varepsilon) \cos\theta \right] d\varepsilon \, d\Omega \\ &= \frac{1}{4\pi\tau_\mu} E(\varepsilon) \left[1 + a(\varepsilon) \cos\theta \right] d\varepsilon \, d\Omega \quad . \end{aligned} \tag{1.13}$$

We can understand this asymmetry term, by considering the situation for positrons emitted with kinetic energies of the order of $E_{e^+, \text{max}}$. Those positrons can be considered as ultra-relativistic antiparticles (recall that the mass of the positron is 0.511 MeV/c^2) for which the Dirac theory tells us that these antiparticles behave as antineutrinos with helicity $h = 1$, *i.e.* with a spin pointing in the propagation direction (see Fig. 1.11). Therefore, we see that for high energy positron, in order to conserve the spin during the muon decay process, the positron emission direction will be preferentially along the muon spin direction (*i.e.* asymmetric). We see that for $\varepsilon \to 1$ then $a(\varepsilon) \to 1$, *i.e.* we have a maximum asymmetry. On the other hand side, the asymmetry disappears for $\varepsilon = 1/2$ and becomes even negative for lower positron energies.

We can see first that if we integrate Eq. 1.11 over the energy and the solid angle (*i.e.* the angles θ and ϕ) we get the total decay rate

$$\Gamma = \int_0^{2\pi} \int_0^{\pi} \int_0^1 W(\varepsilon, \theta) \, d\varepsilon \, \sin(\theta) \, d\theta \, d\phi = \frac{1}{\tau_\mu} \ , \qquad (1.14)$$

as we should.

We can now look at the rate as a function of the energy, *i.e.* the energy spectrum of the positrons independent of the emission angle. This is of course obtained from Eq. 1.11 by integrating over the angles θ and ϕ (see Fig. 1.12)

$$d\Gamma = W(\varepsilon) \, d\varepsilon = \frac{1}{\tau_\mu} 2\varepsilon^2 (3 - 2\varepsilon) d\varepsilon = \frac{1}{\tau_\mu} E(\varepsilon) d\varepsilon \ . \qquad (1.15)$$
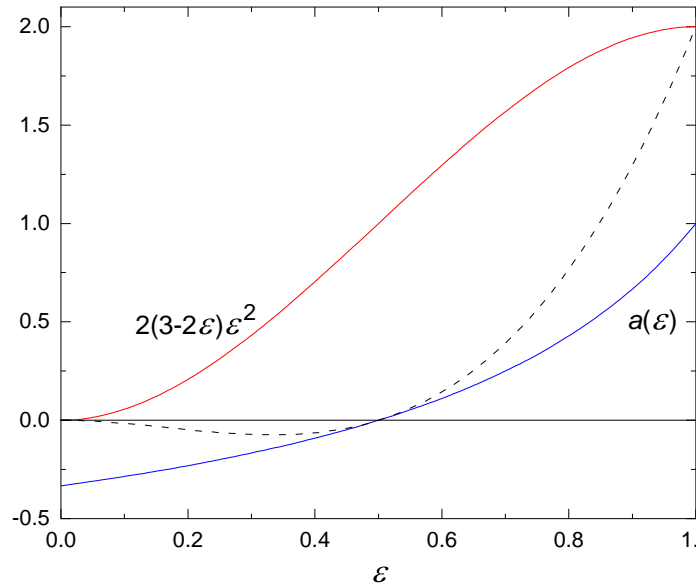
Figure 1.12.: *Normalized energy spectrum of the emitted positrons (red curve). Normalized energy dependence of the asymmetry positron emission (blue curve). Dashed line: weighted positron emission asymmetry $E(\varepsilon)a(\varepsilon)$. Note that for negative muons $a(\varepsilon)$ has the opposite sign.*

Since both the number of positrons and their decay asymmetry rise with energy, the asymmetry of the total angular distribution is mainly due to the high energy positrons.

If we integrate over all the energies (*i.e.* the ideal case where all the positrons are detected with similar efficiency), the average asymmetry is obtained with

$$\bar{A} = \int_0^1 a(\varepsilon) E(\varepsilon) \, d\varepsilon = \frac{1}{3} \ , \qquad (1.16)$$

and we can write the angular distribution

$$d\Gamma = W(\theta)\,d\Omega = \frac{1}{4\pi\tau_\mu}\left(1 + \frac{1}{3}\cos\theta\right)d\Omega \ . \qquad (1.17)$$
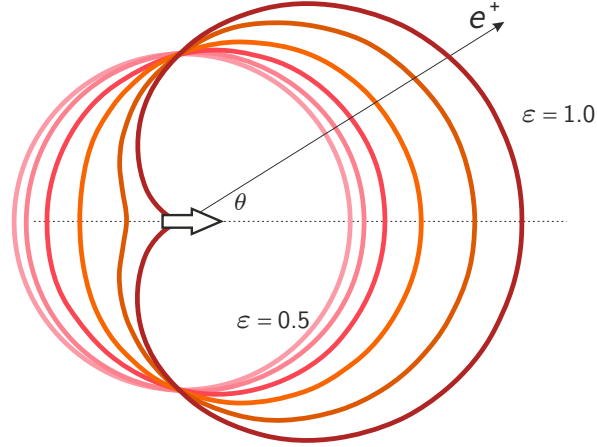
Figure 1.13.: *Sketch of the anisotropic rate of positron emission as a function of the angle with the direction of the muon spin at decay time (cardioid curves). Energies between $\varepsilon = 0.5$ and $\varepsilon = 1.0$ are shown. For lower positron energies, the asymmetric rate becomes negative (see Fig 1.12).*

1.5.3. Decay of a muon ensemble

μSR experiments are based on the observation of the decay of an ensemble of say N_0. As said, the decay is monitored through the observation of the emitted positrons. The number of positrons $N_{e^+}(t)$ which are emitted at time t is of course related to the number of muons decaying in the interval dt at time t. By looking at the full solid angle around the muons (assumed all located at the same place), we have:

$$N_{e^+}(t) = -\frac{dN_\mu}{dt} = \Gamma N_\mu(t) = \frac{1}{\tau_\mu}N_\mu(t) = \frac{1}{\tau_\mu}N_{\mu,0}\,e^{-\frac{t}{\tau_\mu}} \ . \qquad (1.18)$$

$N_{e^+}(t)$ can be associated to the time evolution of the total activity during the "radioactive" decay of the implanted muons.[6]

If we know restrict ourselves to one direction of space, sustaining a solid angle $d\Omega$, we have (see Eq. 1.13):

$$N_{e^+}(t) = N_\mu(t)d\Gamma = \frac{N_{\mu,0}}{4\pi\tau_\mu}\,e^{-\frac{t}{\tau_\mu}}\,E(\varepsilon)\left[1 + a(\varepsilon)\cos\theta\right]d\varepsilon\,d\Omega \ . \qquad (1.19)$$

---

[6]This should not be mixed with the total number of remaining muons which is $N_\mu(t)$.

We have here assumed that the muon ensemble is and remains completely polarized, *i.e.* $|\mathbf{P}(t)| = 1$. This is of course not the case in real life and the time evolution of $\mathbf{P}(t)$ is precisely what the μSR technique is tracking (see Section 3). To obtain the real number of positrons observed by a detector, we have also to consider its energy efficiency and the solid angle $\Delta\Omega$ that it covers. A reduced energy efficiency will both reduce the number and the asymmetry of the observed positrons ($a(\varepsilon)$ and $E(\varepsilon)$ will be reduced), whereas a large solid angle will decrease the asymmetry (reducing $\bar{A}$, see Section 3) but will increase the number of the observed positrons by increasing the ratio $\Delta\Omega/(4\pi)$.

1.6. Muon magnetic moment and spin precession

1.6.1. Muon magnetic moment

Muons, as electrons and different elementary particles, have an intrinsic magnetic moment related to their spin (*i.e.* their intrinsic angular momentum)

The magnetic moment of the muon is

$$\mathbf{m}_\mu = \gamma_\mu \mathbf{I}_\mu = g_\mu \frac{e}{2M_\mu} \mathbf{I}_\mu \qquad (1.20)$$

The gyromagnetic ratio γ_μ is the ratio of its magnetic moment ($\mathbf{m}_\mu$) to its spin ($\mathbf{I}_\mu$) and is given as

$$\gamma_\mu = g_\mu \frac{e}{2M_\mu} \quad . \qquad (1.21)$$

The *g*-factor (which can be considered as the quantum mechanical correction with respect to the classical case) for the muon is predicted to be $g_\mu = 2$ by the Dirac equation, which describes spin-1/2 massive particles. In reality the present admitted value is $g_\mu = 2.0023318418$.[7] By taking into account the value of the spin ($\frac{1}{2}\hbar$) we obtain for the muon magnetic moment

$$m_\mu = g_\mu \frac{e}{2M_\mu} \frac{1}{2}\hbar = 4.490448 \times 10^{-26} \text{ J T}^{-1} \text{ or Am}^2 \text{ which is better expressed as}$$
$$= 8.890597 \times \mu_N$$
$$= g_\mu^* \times \mu_N \qquad (1.22)$$

Here $\mu_N = e\hbar/(2M_p)$ represents the magnetic moment of a Dirac particle possessing the mass and charge of the proton. It is the natural magnetic moment unit for particles like hadrons.[8] Note that the *g*-factor g_μ is defined by calculating the magnetic moment with the real mass of the muon M_μ, whereas g_μ^* gives the value of the muon magnetic moment in μ_N. This is quite often mixed-up in literature (and probably in this script...).

The muon magnetic moment value is large (actually larger than the values observed for the nuclei) and therefore makes the muon a very sensitive probe to magnetic fields (in other words the interaction between a field and the moment will be large; se Eq. 1.27 in the next section).

---

[7]The very slight difference between the real value of g_μ and 2 (difference of the order of 0.1%) tells us that indeed the muon is an elementary particle. This difference is called the anomalous magnetic dipole moment and its value is important in precision tests of the QED theory (quantum electrodynamics) and for looking at effects beyond the Standard Model.

[8]Note that even though μ_N is expressed with the charge and mass of the proton, the real magnetic moment of the proton is much larger ($m_p = 2.792847 \times \mu_N$) reflecting the fact that the proton is not an elementary particle but is composed by 3 quarks.

1.6.2. Muon spin precession

When a magnetic field is sensed by the muon, its spin (or in other words, its magnetic moment) will precess due to the Larmor precession. We can understand the Larmor precession of the muon spin either classically or from a quantum mechanics point of view.

1.6.2.1. Classical view

Classically, a magnetic field $\mathbf{B}_\mu$[9] will create a torque on the magnetic moment of the muon

$$\boldsymbol{\tau} = \mathbf{m}_\mu \times \mathbf{B}_\mu = \gamma_\mu \, \mathbf{I}_\mu \times \mathbf{B}_\mu \ , \tag{1.23}$$

where as we have seen γ_μ is the gyromagnetic ratio of the muon, *i.e.* the ratio of its magnetic moment ($\mathbf{m}_\mu$) to its spin ($\mathbf{I}_\mu$). The torque can be expressed as the rate of change of the muon spin

$$\boldsymbol{\tau} = \frac{d\mathbf{I}_\mu}{dt} \ , \tag{1.24}$$

and therefore

$$\tau = \frac{\Delta I_\mu}{\Delta t} = \frac{I_\mu \sin\theta \Delta\phi}{\Delta t} = \gamma_\mu I_\mu B_\mu \sin\theta \ , \tag{1.25}$$

and by taking the derivative form we get the Larmor precession angular velocity

$$\omega_{\mathrm{L}} = \gamma_\mu B_\mu \ . \tag{1.26}$$
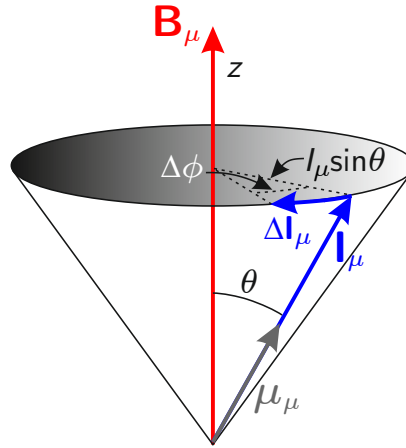
Figure 1.14.: *Classical view of the Larmor precession.*

---

[9]Per convention we will try to always call $\mathbf{B}_\mu$ the magnetic field sensed by the muon

1.6.2.2. Quantum mechanics view

For the quantum mechanics treatment we start from the Hamiltonian describing the interaction of the spin with the field

$$\mathcal{H} = -\mathbf{m}_\mu \cdot \mathbf{B}_\mu = -\gamma\, \mathbf{B}_\mu \cdot \mathbf{I}_\mu = -\gamma\, \left(B_x I_{\mu,x} + B_y I_{\mu,y} + B_z I_{\mu,z} \right)\ . \tag{1.27}$$

For example, if the field is along the z-axis we have the Hamiltonian

$$\mathcal{H} = -\gamma\, B_z I_{\mu,z}\ . \tag{1.28}$$

When looking at the time evolution of the spin state, we have to use the unitary operator[10]

$$\mathcal{U}(t,0) = \exp\left(-\frac{i\mathcal{H}t}{\hbar}\right)\ , \tag{1.29}$$

which represents, when acting on a spin, a rotation by an angle $\gamma B_\mu t$ about the z-axis (given by the direction of the field). This can be seen when considering a muon spin pointing at $t = 0$ along the direction given by the angles (θ, ϕ). Considering the quantization axis given by the field we can write[11]

$$\Psi(\mathbf{r},0) = \cos\frac{\theta}{2}|+\rangle + \sin\frac{\theta}{2}e^{i\phi}|-\rangle\ . \tag{1.30}$$

The eigenvalues of the Hamiltonian acting on the states $|+\rangle$ and $|-\rangle$ are $-\gamma_\mu B_\mu \hbar/2$ and $\gamma_\mu B_\mu \hbar/2$, respectively.
We can write therefore

$$\begin{aligned}
\Psi(\mathbf{r},t) &= \mathcal{U}(t,0)\Psi(\mathbf{r},0) \\
&= e^{-i\mathcal{H}t/\hbar}\left(\cos\frac{\theta}{2}|+\rangle + \sin\frac{\theta}{2}e^{i\phi}|-\rangle\right) \\
&= \cos\frac{\theta}{2}e^{+i\gamma_\mu B_\mu t/2}|+\rangle + \sin\frac{\theta}{2}e^{i\phi}e^{-i\gamma_\mu B_\mu t/2}|-\rangle \\
&= e^{+i\gamma_\mu B_\mu t/2}\left(\cos\frac{\theta}{2}|+\rangle + \sin\frac{\theta}{2}e^{i(\phi-\gamma_\mu B_\mu t)}|-\rangle\right)
\end{aligned} \tag{1.31}$$

Comparing with the state at time $t = 0$ (and recalling that an overall phase is not relevant in quantum mechanics), we see that the new spin state corresponds to change of the azimuthal angle of $\gamma_\mu B_\mu t$, corresponding to a Larmor angle velocity of

$$\omega_{\mathrm{L}} = \gamma_\mu B_\mu\ , \tag{1.32}$$

as in the classical case.

As already seen, the value of the muon magnetic moment, and therefore of the gyromagnetic ratio, is large. This leads to large Larmor frequencies of the muon of $\nu_\mu = 135.538817$ MHz/T (see Table 1.2).

---

[10]See the nonrelativistic time-dependent Schrödinger equation

$$i\hbar\frac{\partial}{\partial t}\Psi(\mathbf{r},t) = \mathcal{H}\Psi(\mathbf{r},t)$$

[11]Remember that the muon is a spin 1/2 particle. General superposition state → see Bloch sphere.

1.7. Atmospheric muons

Most muons observed at the surface of the Earth are produced by primary cosmic rays in the upper atmosphere. They are the most numerous energetic particles arriving at sea level, with a flux of about 1 muon per square centimeter per minute. This can be compared to a solar neutrino flux of about 5×10^6 cm^{-2}s^{-1}.

The mean energy of muons reaching sea level is about 4 GeV. Muons, being charged particles, interact with matter by ionizing it. The loss of energy by muons passing through the atmosphere is proportional to the amount of matter they traverse. The medium is usually characterized by its density (g/cm^3) times the distance traveled in centimeters. This is sometimes called the "interaction length" and is measured in g/cm^2. The energy loss for muons is about 2 MeV per g/cm^2 (see Fig. 2.5). The interaction depth of the atmosphere is about 1000 g/cm^2, so muons lose about 2 GeV in passing through the atmosphere (see Exercises for a slightly better approximation of the interaction length). With the sea level mean energy of muons detected at the surface equal to 4 GeV, this suggests an original muon energy in the neighborhood of 6 GeV.

Most muons are thought to be created at altitudes of about 15000 meters and travel with other particles to the Earth in conical showers within about 1 degree of the trajectory of the primary particle which creates them. Measurement of muon flux at different altitudes is a useful example of relativistic time dilation. With an energy of 4 GeV, the time dilation factor is $\gamma = 38.8$.
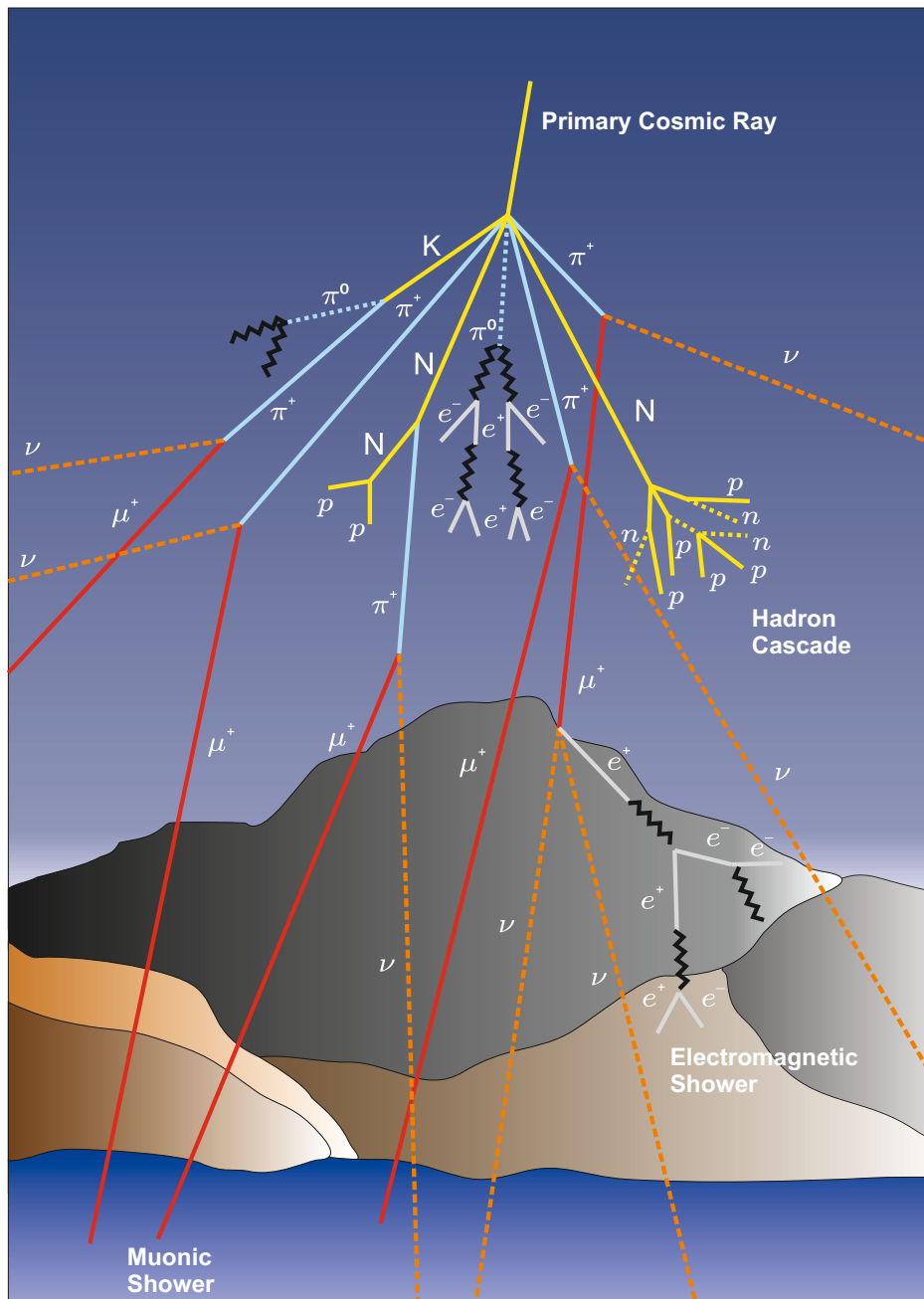
Figure 1.15.: *Schematic view of the particle shower produced by cosmic rays. Particles: K kaons, N heavy nuclei, π pions, μ muons, e electrons/positrons, p protons, n neutrons and ν neutrinos.*
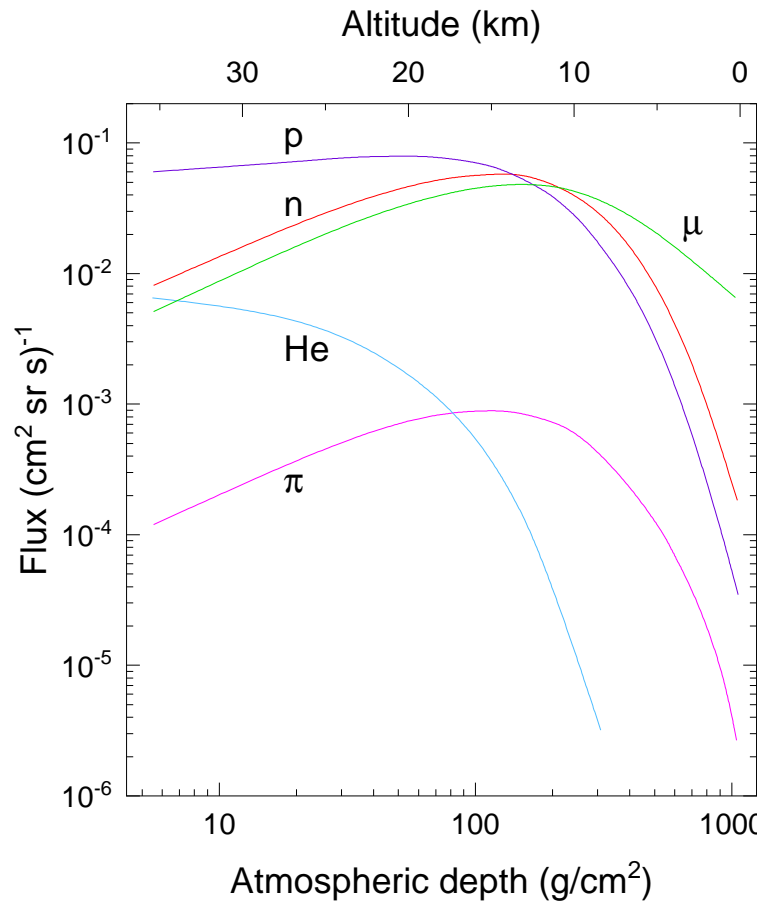
Figure 1.16.: *Typical flux for different particles reaching the Earth. Though often called 'cosmic', some particles are created in the high atmosphere.*

Even though atmospheric muons cannot be used to performed muon-spin spectroscopy experiments, they can be used to make radiography from large massive objects. Some projects in Japan were dedicated to the observation of the magma inside of a spent volcano. Another very recent and very much publicized example is the discovery of a large cavity in the Cheops's (Khufu's) pyramid [23]. In this experiment huge muon detectors were installed at the base of the pyramid. Absorption measurements were performed. In such measurements, a variation of muon counts would reveal a change in the pyramid density, in other word an excess of muons would reveal the presence of a cavity in the pyramid.
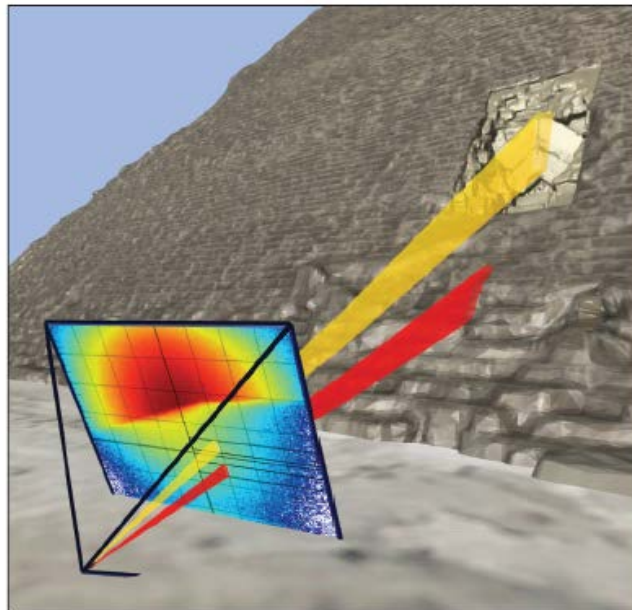
Figure 1.17.: *Sketch of the muon detector. On the two cones excess of muons were observed (see also Fig. 1.18 and 1.19).*
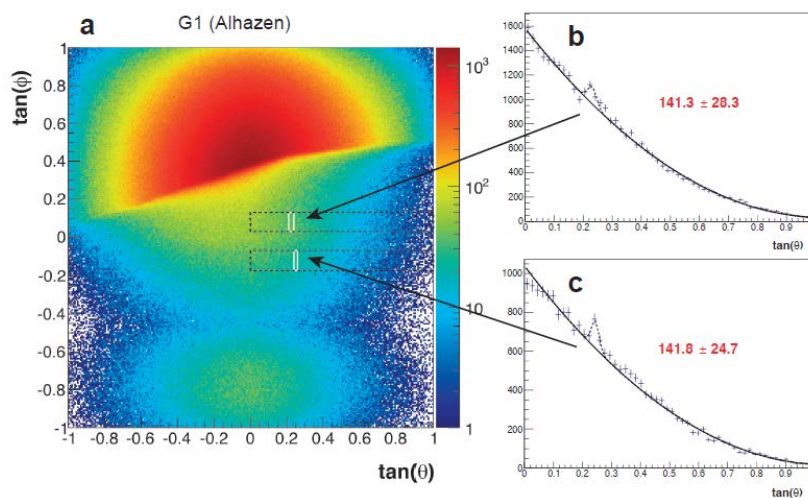
Figure 1.18.: *Two regions with excess of muons were observed. The lower one represents the known Grand Gallery. The upper one represents an unknown cavity (see also Fig. 1.19).*
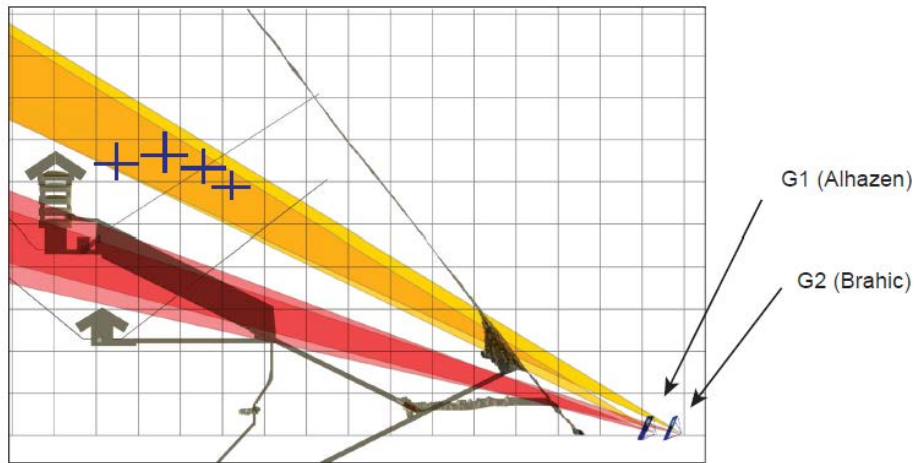
Figure 1.19.: *Schematic of the position of the unknown cavity.*

Recently, TEPCO (Tokyo Electric Power Company) has begun to investigated its damaged nuclear reactor in Fukushima using cosmic rays. Here a combination of absorption and scattering experiments are being followed.
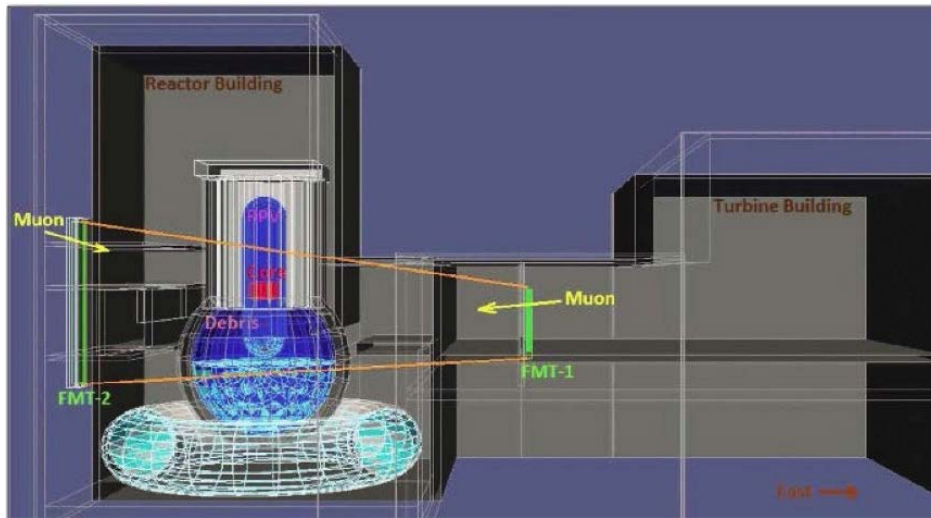
Figure 1.20.: *Schematic of one Fukushima reactor with muon detectors.*
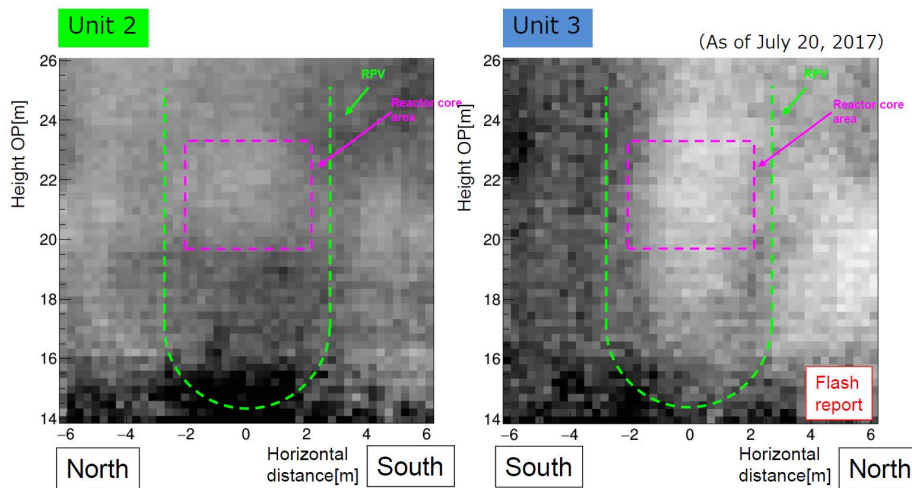
Figure 1.21.: *Comparisons between measurements performed for the Reactors 2 and 3. Whereas indications are present that fuel is located in the Reactor Pressure Vessel (RPV) for the unit 2, no indication of spent fuel is so far observed for the unit 3.*

1.8. "Man-made" muons

The muons created in the high atmosphere have too high energy and are too few to be reasonably used for condensed matter experiments. Therefore, muon spin-spectroscopy experiments are solely possible using high-energy accelerators where polarized muon beams of high intensity are available.

In the next Sections we will first describe different types of accelerators to produce pions, the parent particle of the muon. We will then see different muon beams characterized by different energies. Note that the production description of the so-called Low-Energy Muons (with energies of the order keV) will be presented in the Section 7.
Here, in addition to the high-energy and surface muon beams, we will also look at the typical devices located on a beamline which will transport the beam to the experiment.

1.8.1. Pion production: 3 different possible accelerators

In addition to the pions produced in the atmosphere, linear accelerators (linacs), cyclotrons, and synchrotrons are three ways to accelerate protons to eventually produce pions.

As their name suggests, linacs accelerate particles in a straight line. The particles travel in a pipe-shaped vacuum chamber. Electrodes inside the pipe are spaced so that a driving radio frequency can be timed to energize them as particles are in the gap between electrodes, and thereby accelerate them as they travel from one gap to another.
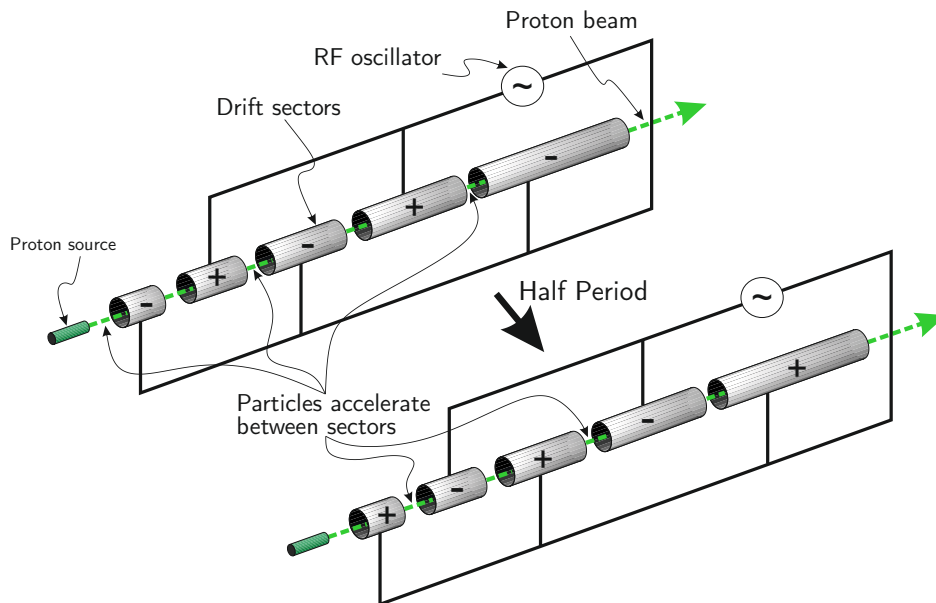
Figure 1.22.: *Schematic of a linear accelerator.*

Cyclotrons accelerate particles along a spiral path and are held in that path by a static electromagnetic field perpendicular to the spiral path. The protons are injected into the center of

the cyclotron into a vacuum chamber between two hollow metal electrodes (because of the resemblance of this semicircular structure with the capital D, the electrodes have been called "dees"). An alternating RF voltage is applied to one dee and then the other. The timing of the RF voltage is switched between dees, accelerating the particles and increasing the diameter of their circular path with every revolution, turning it into a spiral. The RF frequency is of the order of tens of MHz and therefore finally leading to quasi-continuous muon beams (see below).

A cyclotron can accelerate protons to energies no greater than 25 MeV. This limitation is imposed by the relativistic increase in the proton mass as its speed approaches that of light. As the mass increases, the orbital frequency decreases, and the particles cross the gap at times when the electric field decelerates them. To overcome this limitation, a technique is to strengthen the magnetic field near the periphery of the dees, hence keeping the angular velocity $\omega_c = eB/\gamma M$ constant[12]. Cyclotrons operated in this way are called *isochronous*. Such isochronus cyclotrons can produce beams with energy up to about 1 GeV. The limitation is due to the magnetic field limitation (saturation field of about 2 T). Another technique is to effectively change the frequency of the RF voltage (reducing the frequency when the mass of the proton increases with energy at large radius). Cyclotrons operated in this way are called *synchrocyclotron*. However the disadvantage of a synchrocyclotron is the production of a pulsed beam with relatively low intensity.
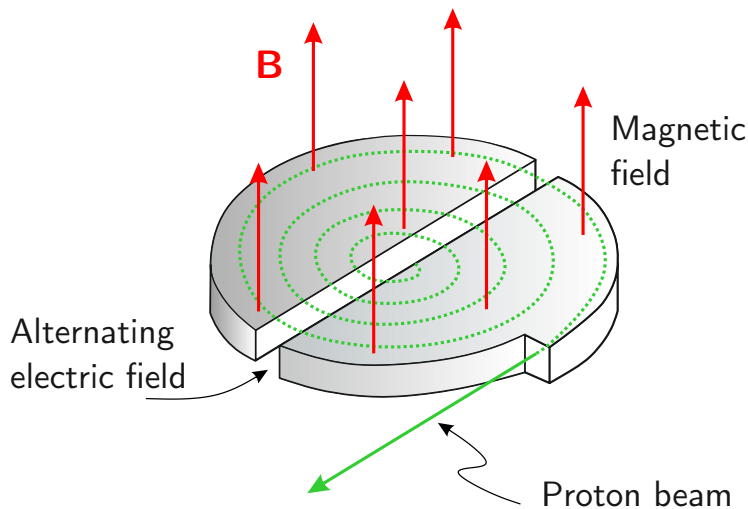
Figure 1.23.: *Cyclotron: operation principle.*
(Adapted from `http://hyperphysics.phy-astr.gsu.edu/hbase/magnetic/cyclot.html`*).*

Finally, synchrotrons, like cyclotrons, are cyclic accelerators and send particles into a closed-loop path. Acceleration is achieved by the application of radio frequency electric fields at RF cavities along the circumference of the ring. Unlike cyclotrons, the synchrotron's loop is not a spiral and therefore the magnetic fields bending the proton trajectory must be increased synchronously with the acceleration in order to keep the particles on the constant radius path. The path can be a circle, oval or a polygon with rounded corners. Synchrotrons

---

[12]In the classical limit the principle of a cyclotron is expressed by equating the centrifugal force to the Lorentz force, *i.e.*: $evB = Mv^2/r$, and therefore $\omega_c = v/r = eB/M$.

produce pulsed proton beams which can reach very high energy (up to TeV). The typical pulse frequency is 50 Hz. Due to the closed-path shape, a synchrotron needs an injection accelerator (usually a linac system).

1.8.2. Pion production: for example at the Paul Scherrer Institute

At the Paul Scherrer Institute (PSI, Villigen, Switzerland), protons are first extracted from a source made up of hydrogen atoms and then accelerated in three steps.
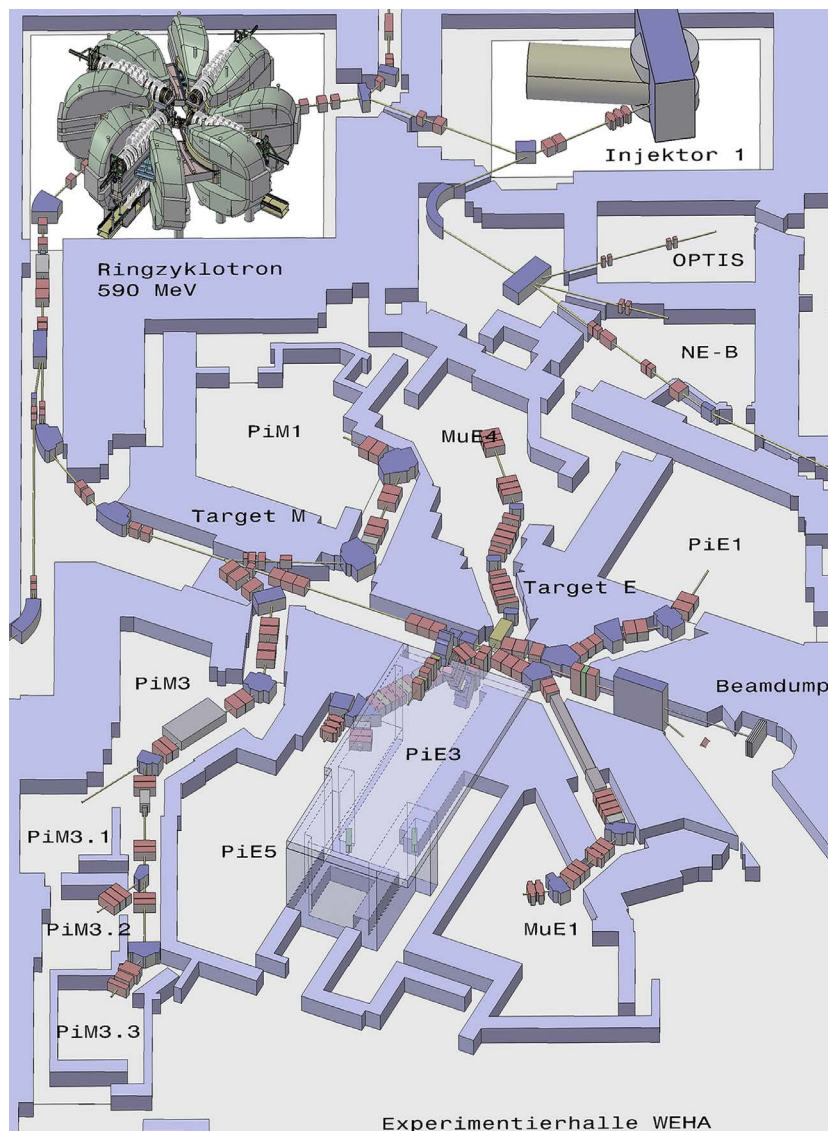
Figure 1.24.: *Sketch of the High Energy Proton Accelerator (HIPA) at PSI (Courtesy PSI).*

- A Cockcroft-Walton accelerator, which actually also contains the proton source, is used as the first stage from which protons are fed into Injector II (both not shown on Fig. 1.24).

Figure 1.25.: *PSI Cockcroft-Walton accelerator.*

- The Injector II is a first pre-accelerator, actually a small ring cyclotron. It accelerates protons to a speed of approximately 37% of the speed of light (72 MeV) before feeding them to the center of the large ring cyclotron.

- The core of this facility is the large ring isochronus cyclotron with a diameter of approximately 15 meters, in which protons are accelerated to their terminal speed of almost 80% of the speed of light over 186 revolutions (equivalent to a kinetic energy of 590 MeV).
  As mentioned above, in a cyclotron the protons are accelerated in stages, with the electrical fields building up every time particles pass through an accelerator cavity and giving them an additional impulse. At PSI, several accelerator cavities of this kind are positioned between the magnets in the path of the beam. The principle components of the large PSI ring cyclotron are eight sector magnets and four accelerator cavities.
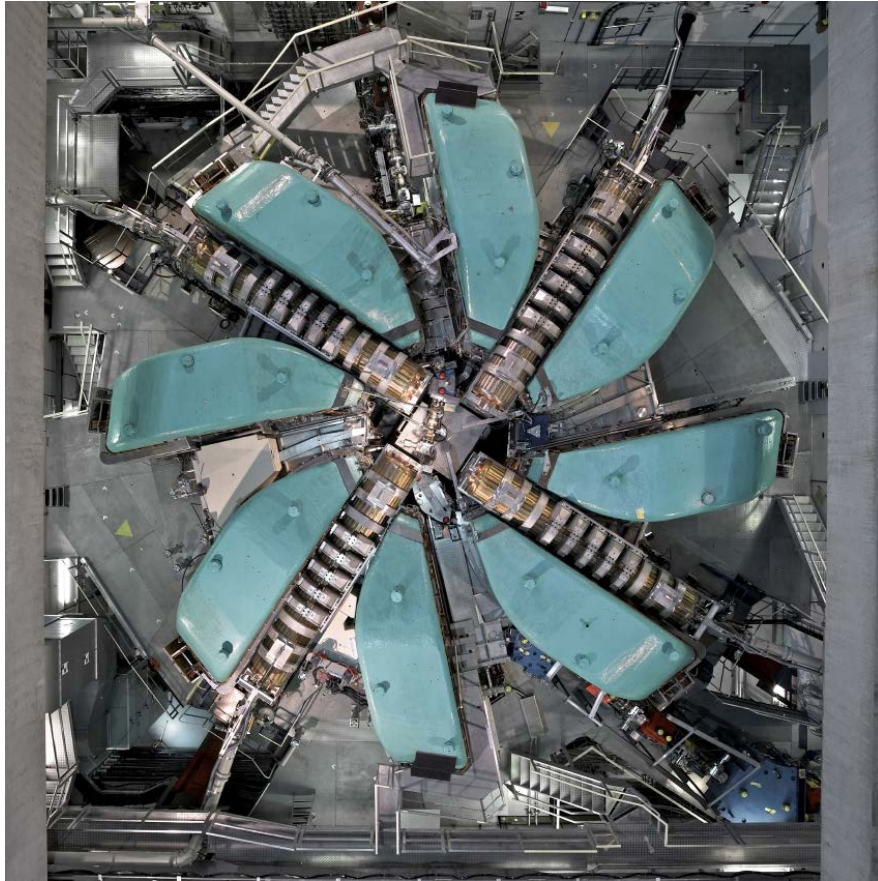
Figure 1.26.: *The PSI 590 MeV cyclotron.*

After the acceleration, the proton are transported in the so-called proton-channel toward two graphite production targets into which the pions are produced:

- The first target is rather thin with a thickness of 5 mm. It is called the target M: ("Mince" – in French),

- The second one is rather thick and is available in two versions with a thickness of either 4 or 6 cm. It is called the target E: '('Epaisse" – in French). Figures 1.27 and Figures 1.28 represent the target E and the proton beam trajectory.
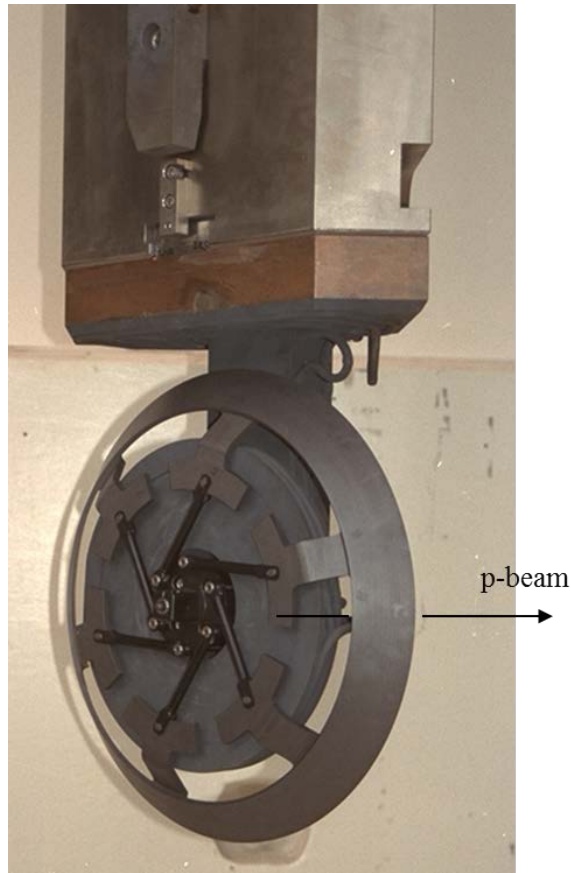
Figure 1.27.: *Photograph of the PSI E graphite target.*
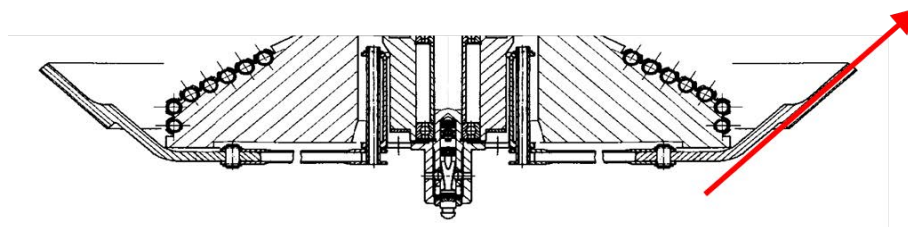
Figure 1.28.: *Schematic of the PSI E target (top-view). The red arrow indicates the direction of the proton beam. After the target, the beam is transported to the neutron spallation source SINQ or to the beam dump.*

Rough estimate of the number of pions produced in the E target:

- PSI cyclotron current: $I = 2200\,\mu\text{A} = 1.373 \times 10^{16}$ protons/s
  (as $+e = 1.602 \times 10^{-19}$ C).

- The cross section is roughly $2\,\text{fm}^2 = 2 \times 10^{-30}\,\text{m}^2$ (see Fig. 1.7).

- The number of mole of graphite per cm^3 is given by $n = \rho/(4A)$, where $\rho = 2.23\ \text{g/cm}^3$ is the graphite density and $A = 12$ is the mass number of carbon. The

factor 4 arises as 4 C atoms are in the unit cell.

The number of carbon atoms per cm^3 is given by $n_C = n\,4\,N_{Av}$, where N_{Av} is the Avogadro number. Here again the factor 4 arises as 4 carbon atoms are in the unit cell.

- Assuming a constant cross section σ of the reaction proton-nucleon through the target, the total cross section as seen by a proton will be $\sigma_{tot} = n_C\,V\,\sigma = n_C\,S_{tot}\,d\,\sigma$, where $V = S_{tot}\,d$ is the volume of the target (with S_{tot} the surface of the target and d the length of the target, say 4 cm). For one proton, the probability to have a collision with a nucleon is $\sigma_{tot}/S_{tot} = n_C\,\sigma\,d$.

- Therefore the number of pions produced will be $I\,n_C\,\sigma\,d \simeq 1.2 \times 10^{14}$ pions/s over the entire 4π solid angle.

1.8.3. Muon beams for condensed matter

1.8.3.1. "High-energy" muons

For some experiments, one needs muons with a high energy (*i.e.* bigger than the 4.1 MeV that they have in the pion reference frame). This can be necessary if the sample is placed in a container with thick walls (for example in the case of a liquid or for a sample place inside a clamp pressure cell). The solution to obtain high-energy muons is to first extract high energy pions from the production target. These pions are first selected by a bending magnet (where pion of a given momentum will have the correct trajectory) and are transported to a long superconducting solenoid ("decay muon channel") where the pions decay in flight.
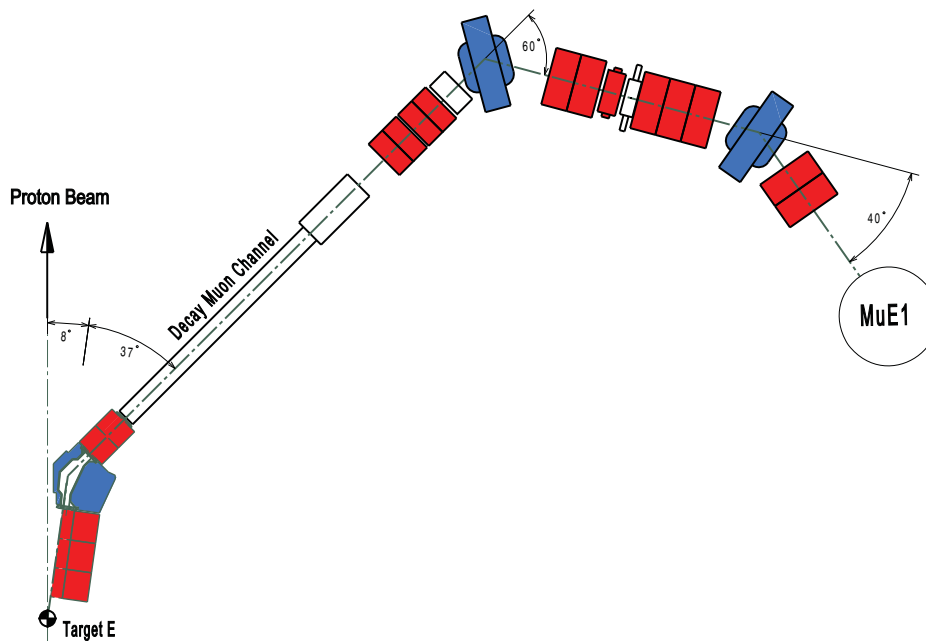
Figure 1.29.: *Schematic view of the μE1 high energy beamline at PSI (courtesy PSI).*

Depending on the muon direction emission, resulting muons beams with different polarization can be obtained.

In practice, two extreme conditions are used:

1. The muon is emitted in the direction of the pion momentum, *i.e.* "forward" direction. The momenta $\mathbf{p}_\mu^0$ (corresponding to the muon momentum in the pion reference frame) and $\mathbf{p}_\pi$ are additive and the final muon momentum $\mathbf{p}_\mu$ is greater than than the one of the pion. The muon has a spin pointing in the opposite direction of its propagation.
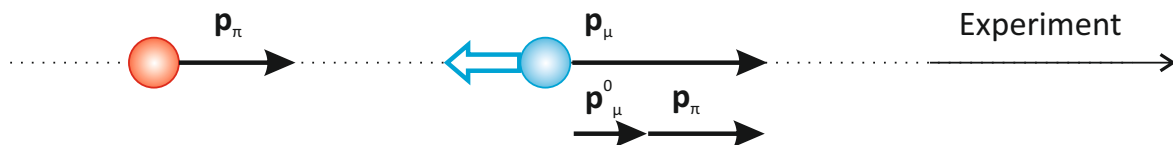
Figure 1.30.: *Schematic view of the creation of "forward" muons in the muon decay channel.*

2. The muon is emitted in the direction of the pion momentum, *i.e.* "backward" direction. The momenta $\mathbf{p}_\mu^0$ (corresponding to the muon momentum in the pion reference frame) and $\mathbf{p}_\pi$ are pointing in opposite directions and the final muon momentum $\mathbf{p}_\mu$ is smaller than than the one of the pion. The muon has a spin pointing in the direction of its propagation.
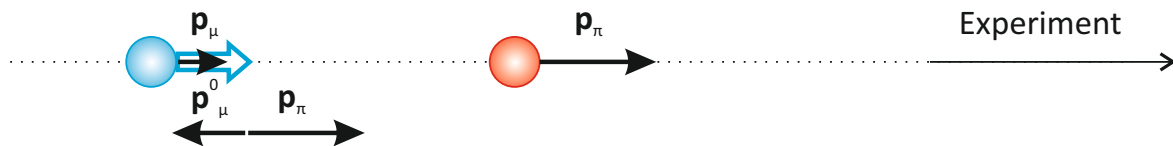
Figure 1.31.: *Schematic view of the creation of "backward" muons in the muon decay channel.*

The choice between these two extreme cases is performed by tuning the first bending magnet (momentum selection) after the decay channel (magnet ASK81 shown in Fig. 1.29).
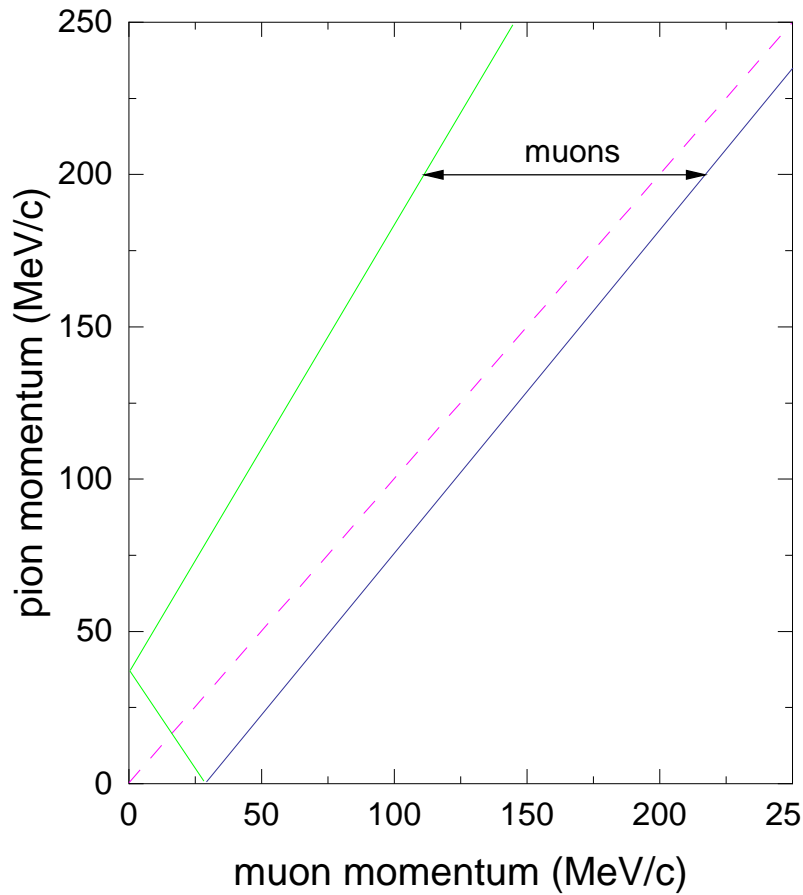
Figure 1.32.: *Decay kinematics of the pion decay. The red curve would correspond to muons with a momentum equal to the one of the pions. The allowed region is located in-between the "forward" muons (light blue) and the "backward" muons (dark blue).*
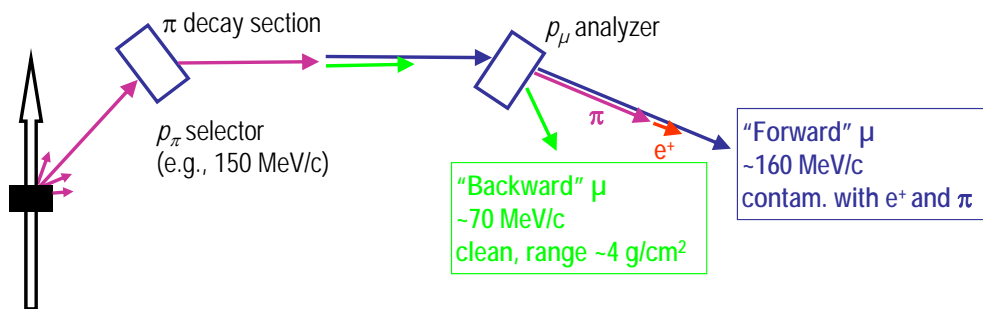
Figure 1.33.: *Principle of a high energy beamline (as μE1 at PSI). In practice "backward" muon beams are used which are less energetics but are much less contaminated by other particles. For high-pressure experiments, one usually use momentum up to 110 MeV/c.*

1.8.3.2. "Surface" muons

The large majority of the muon beamlines around the world are so-called "surface" or "Arizona" beam (recalling the pioneer works of Pifer *et al.* from the University of Arizona [24]). The fundamental difference with a high-energy beam is that here muons are extracted from the production target. These muons arise from pion decaying at rest still inside, but near the surface, of the production target.[13] As already seen, the muons arising from pions decaying at rest are 100% polarized, ideally monochromatic and have a low momentum of 29.8 MeV/c and have a range width in matter of the order of 130 mg/cm^2 (see Section 2.2.1). Hence the paramount advantage of this type of beam is the possibility to use relatively thin samples.

Another advantage is that they are rather easy to be manipulated, as for example concerning their polarization or their detection.
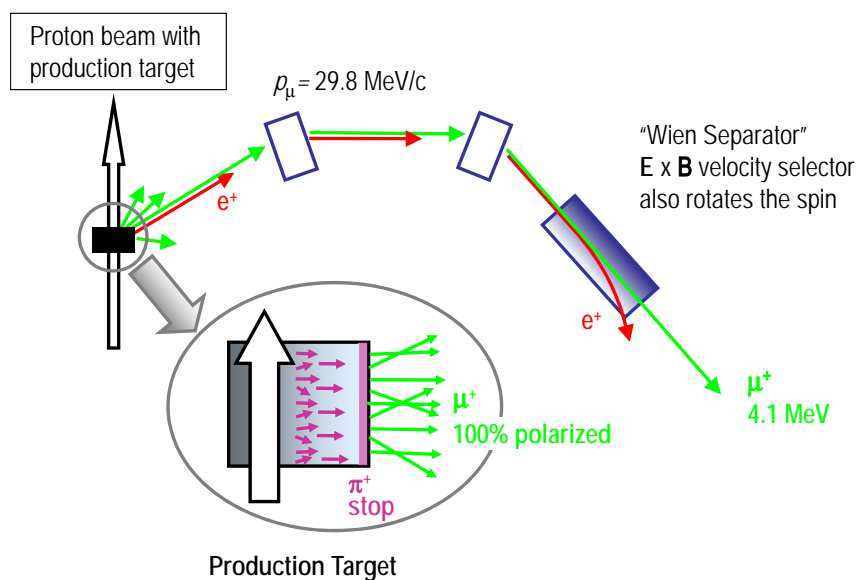
Figure 1.34.: *Principle of a surface muon beamline (as πE3 or πM3 at PSI).*

---

[13]Pions decaying deep inside the target will produce muons which will not have enough energy to escape the target (see Section 2).

Figure 1.35.: *Picture of the surface muon beamline πM3 at PSI.*

1.8.3.3. Few words about a typical beamline and beam optics

The beam optics can be defined as the whole process of guiding a charged particle beam from A to B. This is usually done with magnets. The point A is usually the source and B the experiment.

As seen in Section 1.3.3, after a pion decay, the muon has a well defined spin polarization with respect to its velocity. However, the velocity direction is changed (through bending magnets) in a beamline. One can therefore ask himself how come the polarization is maintained during the muon transport?

As seen above (Section 1.8.1), the muon cyclotron angular velocity ω_c (describing the change of the trajectory in field) is given by:

$$\omega_c = \frac{eB}{M} \quad . \tag{1.33}$$

On the other hand the Larmor angular velocity ω_L is given by (see Sections 1.6.2 and 3.3.2):

$$\omega_L = \gamma_\mu B = g_\mu \frac{e}{2M_\mu} B \simeq \frac{eB}{M_\mu} \quad . \tag{1.34}$$

This results to the fact that the cyclotron frequency is identical to the Larmor frequency and therefore a bending of the muon trajectory by a magnetic field will be accompanied by a spin direction rotation such that the muon-spin direction will always stay exactly opposite to the muon momentum. This is of paramount importance when transporting the muons from the production target to the experimental area.

Two types of magnets are used for the transport: bending magnets (dipoles) and focusing magnets (quadrupoles).
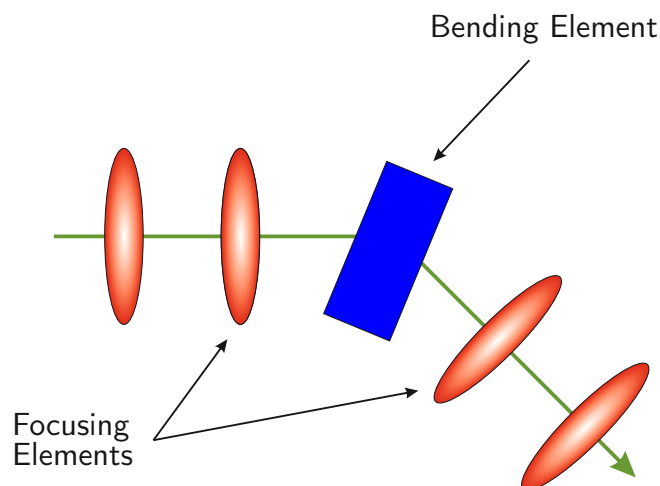
Figure 1.36.: *Schematic view of the typical elements on a beamline.*

Dipole magnets   A dipole magnet provides a constant field **B**. The field lines in a magnet run from North to South pole (see Fig. 1.37).
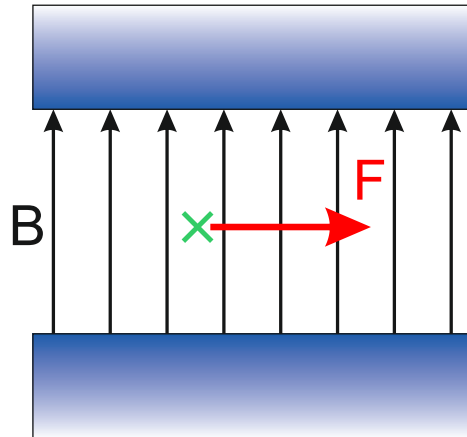
Figure 1.37.: *Schematic view of the field in a dipole magnet. The force acting on muons flying into the paper is shown.*

Recall the Lorentz Force on a particle:

$$F = Ma = e\left|(\mathbf{E} + \mathbf{v} \times \mathbf{B})\right| = \frac{Mv^2}{r} \quad, \tag{1.35}$$

where $M = \gamma M_0$ is the relativistic mass and r is the bending radius. In the absence of an electrical field and considering that **B** and **v** are perpendicular (particles flying into the page at the point × in Fig. 1.37), one obtains

$$\frac{1}{r} = \frac{e\,B}{p} \quad. \tag{1.36}$$

And numerically:

$$\frac{1}{r}[\mathrm{m}^{-1}] = 0.2998\frac{B\,[\mathrm{T}]}{p\,[\mathrm{GeV/c}]} \quad. \tag{1.37}$$

Therefore, for a given bending radius (given by the geometry of the beamline), by tuning the field one tunes the momentum of the particle flying with the correct trajectory. Therefore the first bending magnet along a beamline will select the momentum of the beam.[14]

---

[14]Keep in mind that here solely the momentum is selected and that different particles (with obviously different velocities) can possess the same momentum. To "clean" the beam a Wien filter is required (see below).
  A sector mass spectrometer uses the same principle but, prior to the bending by the main field, a velocity selection is performed by the combined action of perpendicular electric and magnetic fields *i.e.* this corresponds to the Wien filter that we apply here after the bending.

Quadrupole magnets To focus the beam, so-called "quadrupole magnets" are used. They consist of groups of four magnets designed is such a way that the lowest significant terms in the field equations are quadrupole. They produce a magnetic field whose magnitude grows as a function of the distance from beam center axis.

Figure 1.38.: *Typical quadrupole magnet.*
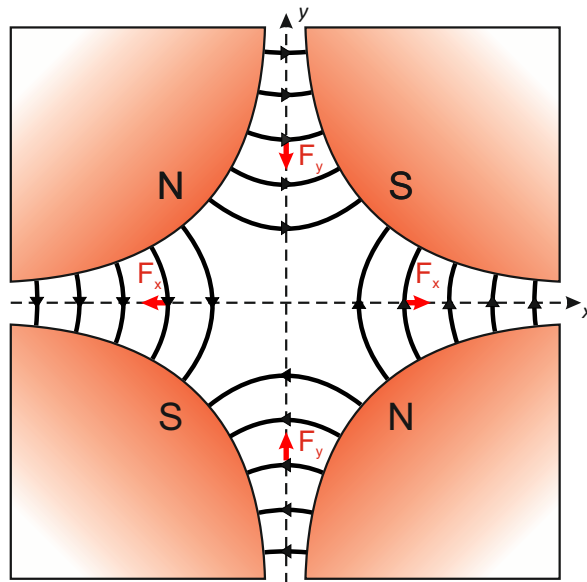
Figure 1.39.: *Schematic of the magnetic fields in a quadrupole magnets (orange lines). The pole shoes have the shape of hyperbolas. The forces are represented for muons flying into the paper.*

Between the pole shoes, we do not have any electrical currents and one can write using the

Maxwell equations:

$$\nabla \cdot \mathbf{B} = 0 \tag{1.38}$$

$$\nabla \times \mathbf{B} = 0 \tag{1.39}$$

From the first equation, there exists a vector potential $\mathbf{A}$, such that $\mathbf{B} = \nabla \times \mathbf{A}$ and from the second one, there exists a scalar potential $\mathbf{B} = -\nabla\Phi$. By taking the long cylinder approximation, the component of the field along the beam is vanishing, *i.e.* $B_z = 0$ and $\mathbf{A} = (0,0,A)$. One can therefore write that:

$$B_x = \frac{\partial A}{\partial y} = -\frac{\partial \Phi}{\partial x} \tag{1.40}$$

$$B_y = -\frac{\partial A}{\partial x} = -\frac{\partial \Phi}{\partial y} \tag{1.41}$$

One can show that a magnetic field $\mathbf{B} = (B_x, B_y, B_z)$ with B_z constant (in our case equal to zero) and B_x, B_y given by

$$B_y + i\, B_x = C_n (x + i\, y)^{n-1} \quad, \tag{1.42}$$

(where C_n is a complex constant) satisfies Eqs 1.38 and 1.39.[15]

Fields of the form given by Eq. 1.42 are known as "multipole" fields, with the index n indicating the order of the multipole.[16]

One can use the principle of superposition and add a set of multipole fields to obtain a general magnetic field:

$$B_y + i\, B_x = \sum_{n=1}^{\infty} C_n (x + i\, y)^{n-1} \quad. \tag{1.43}$$

The coefficients C_n characterize the strength and orientation of each multipole component. Using the polar coordinates ($x = r\cos\theta$ and $y = r\sin\theta$), we have

$$B_y + i\, B_x = \sum_{n=1}^{\infty} C_n r^{n-1} e^{i(n-1)\theta} \quad. \tag{1.44}$$

We see that the strength of the field in a pure multipole of the order n varies as r^{n-1} with distance from the magnetic axis[17]. If we express the field in the polar components ($B_x = B_r \cos\theta - B_\theta \sin\theta$ and $B_y = B_r \sin\theta + B_\theta \cos\theta$) we have

$$B_\theta + i\, B_r = \sum_{n=1}^{\infty} C_n r^{n-1} e^{in\theta} \quad. \tag{1.45}$$

---

[15]This is seen by applying the differential operator $\partial/\partial x + i\partial/\partial y$ to each side of the Eq. 1.42.

[16]$n = 1$ is a dipole field , $n = 2$ is a quadrupole field, $n = 3$ is a sextupole field and so on.

[17]A "pure" multipole represents the case where only one value of either b_n or a_n is different from zero, whereas all the other coeeficient are equal to zero.

Therefore, for a pure multipole of order n, rotation of the magnet through π/n around the z axis simply changes the sign of the field as actually shown on Fig. 1.39 ($n = 2$) and Fig 1.37 ($n = 1$).

The constants C_n have units which depend on the order of the multipole. For a dipole, the unit of C_1 (dipole) is tesla (T); for a quadrupole, the unit of C_2 is T/m; for a sextupole, the unit of C_3 is T/m^2, and so on. But, the multipole components are usually given in dimensionless units. In that case, a reference field, B_0, and a reference radius, R_0 are given. They can be chosen arbitrarily, but must be specified if the C_n coefficients need to be fully interpreted.

By writing the constant C_n as

$$C_n = \frac{B_0}{R_0^{n-1}}(b_n + i\, a_n) \ , \tag{1.46}$$

then Eq. 1.43 can be expressed as

$$B_y + i\, B_x = B_0 \sum_{n=1}^{\infty} (b_n + i\, a_n) \left(\frac{x + i\, y}{R_0}\right)^{n-1} \ . \tag{1.47}$$

One can see that the coefficient a_n and b_n will determine the orientation of the field. As a convention, a pure multipole is called a "normal" multipole if $b_n \neq 0$ and $a_n = 0$, whereas if $a_n \neq 0$ and $b_n = 0$ it is called a "skew" multipole. These coefficient are related to the derivatives of the field:

$$\frac{\partial^{n-1} B_y}{\partial x^{n-1}} = (n-1)! \frac{B_0}{R_0^{n-1}} b_n \ \ \text{and} \tag{1.48}$$

$$\frac{\partial^{n-1} B_x}{\partial y^{n-1}} = (n-1)! \frac{B_0}{R_0^{n-1}} a_n \ . \tag{1.49}$$
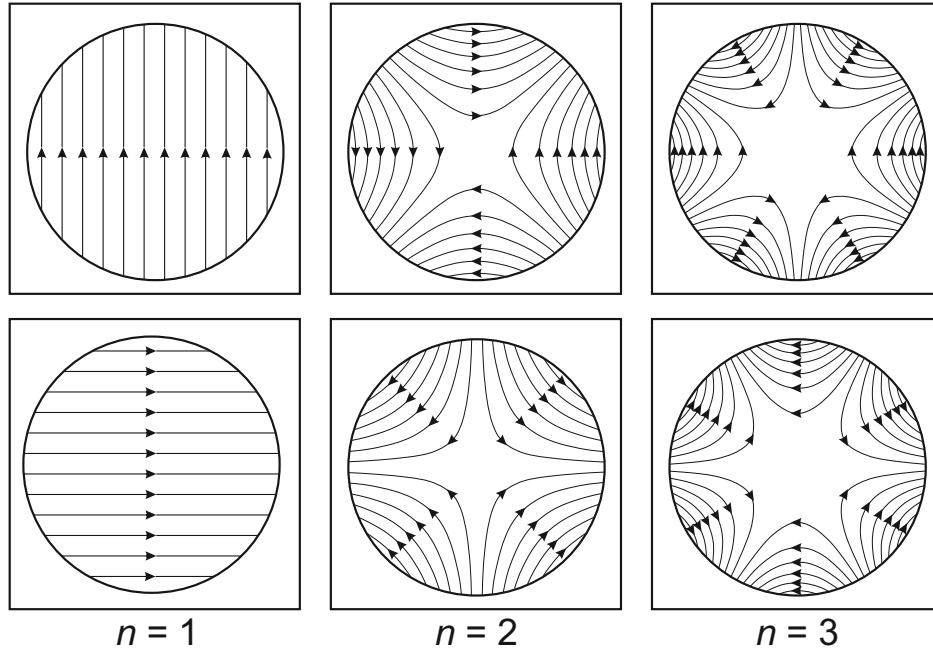
Figure 1.40.: *"Pure" multipole fields. Top: dipole. Middle: quadrupole. Bottom: sextupole. Fields on the left are "normal"; those on the right are "skew".*

We see that the fields shown on Fig 1.37 and Fig. 1.39 correspond to "pure" dipole and quadrupole (in these case "normal" fields), respectively.

The field for the quadrupole is given by

$$B_x = gy \tag{1.50}$$
$$B_y = gx \quad \text{with} \tag{1.51}$$
$$g = \frac{\partial B_y}{\partial x} = \frac{\partial B_x}{\partial y} = \frac{B_0}{R_0} b_2 \quad . \tag{1.52}$$

In the air space of the quadrupole we have

$$\mathbf{B} = -\nabla \Phi \quad \text{with} \quad \Phi(x, y) = -g \, xy \quad . \tag{1.53}$$

The equipotential lines are the hyperbolas $xy = const$. The field lines are perpendicular to them.

As shown from the force vectors represented on Fig. 1.39, a single quadrupole will focus the beam in one direction (in this case the direction y) whereas defocussing the beam in the other. At this point we could ask ourselves how an overall focusing in both direction can be achieved. This is performed by creating a so-called FODO lattice, consisting of a focusing (say in the y direction) F quadrupole, a drift space O, a defocussing (in the y direction) D quadrupole and again a space O, which is called a quadrupole doublet (see Exercises).[18]

---

[18]Note that the FODO is used as a general name for a focusing lattice and that the magnet arrangement can be more complicated.

We can calculate the focal length of a quadrupole (see Fig. 1.41). If L denotes the length of the quadrupole, the deflection angle for a particle flying in the beam direction at a distance $y = R$ from the central axis is given by (using Eqs. 1.50 and 1.36 and considering the thin lens approximation):

$$\alpha \simeq \frac{L}{r} = \frac{eB_x}{p}L \simeq \frac{egR}{p}L \quad . \tag{1.54}$$
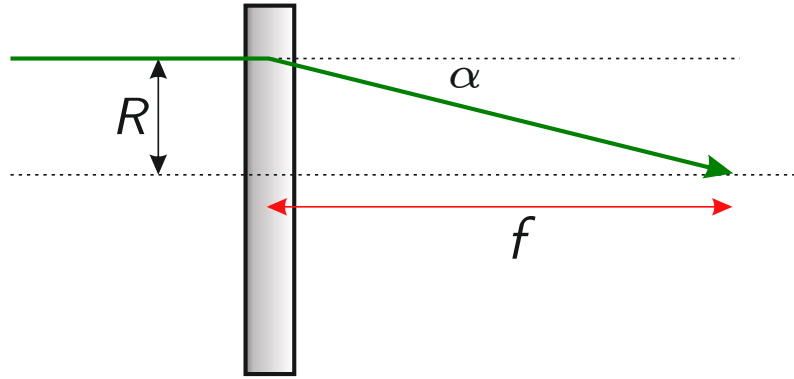
Figure 1.41.: *Schematic of the focal length of a focusing quadrupole.*

The focal length f is therefore:

$$\alpha \simeq \frac{R}{f} \rightarrow \frac{1}{f} = \frac{eg}{p}L = kL \quad , \tag{1.55}$$

where we have defined the quadrupole strength $k = eg/p$ which normalizes the field gradient to the momentum of the particle (in analogy to the bending strength $1/r$ defined in Eq. 1.36). And numerically we have:

$$k \, [\text{m}^{-2}] = 0.2998 \frac{g \, [\text{T/m}]}{p \, [\text{GeV/c}]} \quad . \tag{1.56}$$

Separator (Wien filter) and spin rotator As seen above, the momentum selection performed by the first bending magnet does not differentiate between different types of particle having the same momentum. This task is performed downstream by a "separator" or better say a "Wien filter".

A Wien filter is a device where perpendicular electric and magnetic fields are applied. It can be used as a velocity filter for charged particles.[19] The particles with the right speed will not be affected by the fields (*i.e.* will sense a Lorentz force equal to zero) while other particles will be deflected. It is named after Wilhelm Wien.

---

[19]In addition to muon beams, Wien filters can be used for electron microscope or in accelerator mass spectrometry.
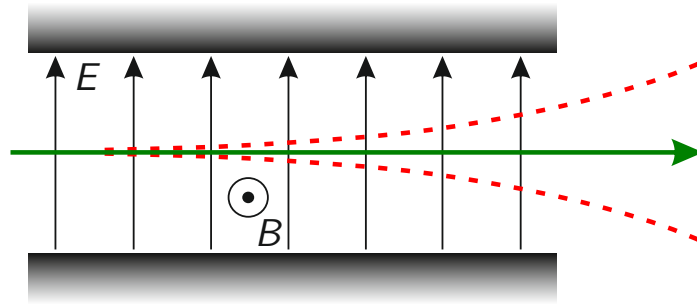
Figure 1.42.: *Schematic of a Wien filter. The particles following the green trajectory will have the chosen velocity. The one with a lower (higher) velocity will be deflected on the top (bottom) of the figure.*

The total Lorentz force on a particle with charge e is given by:

$$\mathbf{F} = e\mathbf{E} + e\mathbf{v} \times \mathbf{B} \tag{1.57}$$

Here, the vectors $\mathbf{v}$, $\mathbf{E}$ and $\mathbf{B}$ are orthogonal and therefore the "electrical" part and the "magnetic" part of the Lorentz force are pointing into opposite directions. Therefore the central trajectory will be followed by particles having the velocity

$$v = \frac{E}{B} \ , \tag{1.58}$$

meaning that any combination of electric and magnetic fields will allow charged particles with only velocity through.[20]

Although the trajectory of the muons having the chosen velocity is not altered with the correct ratio between the electrical and magnetic fields, the magnetic field applied will change the orientation of the muon spin compared to the trajectory following Eq. 1.34. For a beam of surface muons, the angle introduced by the Wien filter (used as a separator) is typically of the order of 5-10°. This small spin rotation results in a polarization loss of the order of 1%.

A Wien filter can be used for surface-muon beams (see Section 1.8.3.2) and low-energy-muon beams (see Section 7). However, it cannot be used for high-energy muon beams as a separation between muons and positrons would be ineffective with reasonable fields. For a surface muon beam, the electrodes creating the electrical field have a gap of typically 0.2 m and one applies a voltage difference of about 80 kV.

For some μSR experiments, it could be very convenient to apply at the sample position a magnetic field perpendicular to the muon spin direction (see Section 3.5.2). For high-energy muon beams, the magnetic field is applied transverse to the muon momentum direction at the sample position. This solution cannot be adopted for the other beams, as the magnetic

---

[20]Note that here we sticked with the classical case. In the reality for muons with a high momentum, a static electrical field will also be seen as a magnetic field and corrections to the given formula will be necessary.

field would dramatically influence the beam trajectory due to the reduced velocity.[21]   For these beams, the solution is to rotate the muon spin to 90°(or close to this value) with respect to the momentum direction prior to send the muon into the sample. This can be achieved by a Wien filter (used here as a "spin-rotator") but using much higher magnetic field (and consequently much higher electrical field to select the correct trajectory) resulting to a much higher spin rotation than the one achieved in separator mode.[22]

A typical "spin-rotator" (*i.e.* a Wien filter used to rotate the muon-spin) has a length of say about 3 m and can rotate the spin by typically 45 to 65°. For a complete 90°rotation a FODO (quadrupole doublet) is usually introduce in-between two Wien-filters to increase the overall transmission. The typical voltage used for the electrical field are of the order of 500 kV difference and, as the muon beam is in vacuum, requires special technology for the feedthroughs.

Figure 1.43.: *Typical spin rotators installed in the πE3 beamline of the Paul Scherrer Institute.*

---

[21]Note that even for high-energy muon beams the influence on the muon trajectory of the applied magnetic field at the sample site is not negligible and precise sample and detector position corrections have to be applied. These corrections will depend on the applied value of the magnetic field and on the value of the muon momentum.

[22]The use of a spin-rotator is not possible in high-energy beams due to the large velocity of the particles.

2. Implanting Muons in Matter

2.1. Energy loss of particles in matter

The stopping power of particles in matter occurs by radiative and collision processes with probabilities given by their interaction cross sections. What one observes is a statistical average of the two processes occurring as the particle slows down.

One defines the "Energy Loss" (or stopping power) which is given by

$$-\frac{dE}{d\ell} \tag{2.1}$$

where E is the charged particle kinetic energy. The SI units of stopping power are J/m, but as usual in particle physics the energy is normally given in eV. The higher the stopping power, the shorter the range into the material the particle can penetrate. The negative sign expresses the loss of energy. As the energy loss is proportional to the material density, one often scales it to the density ρ:

$$-\frac{dE}{d\ell}\frac{1}{\rho} = -\frac{dE}{dx} \quad , \tag{2.2}$$

with $x = \ell\rho$ (with the units [g/cm^2]) and therefore the energy loss is often expressed in eV cm^2/g.

After a relatively well-defined distance, called the "range",[1] the particles will come at rest having lost all their kinetic energy. At the end of the range, the energy loss can no more be considered as continuous and the individual encounters are important. For electrons, this can lead to a significant statistical variation in path length, but for muons or protons (and other heavy particles) with kinetic energies of several MeV or more, one observes path length variations of only a few percent or less, for identical monoenergetic particles. The statistical variation of the path lengths is called the "straggling".

They are many different types of interactions and the dominating processes will depend on the particle type and on their energy.

Photon: The main energy losses processes are:

---

[1]Note that the range is often given with the units g/cm^2 which corresponds to the distance range (or mean penetration depth) normalized to the material density *i.e.* L/ρ.

- The photoelectric effect, which is the emission of electrons resulting from the transfer of energy from the light to an electron. This is a low-energy phenomenon.

- Compton scattering (that is the inelastic scattering of a photon by a charged particle, usually an electron).

- Thomson scattering (which can be seen as the low-energy limit of the Compton scattering) is the elastic scattering of electromagnetic radiation by a free charged particle.

- And finally the pair production which is the creation of an elementary particle and its antiparticle from the neutral photon. This can be seen as a high-energy phenomenon.

Charged particles: The main mechanisms are: Bremsstrahlung, Cherenkov effect radiation, ionization and excitation.

- The Bremsstrahlung is the radiation produced by the deceleration of a charged particle deflected by the field of a target charged particle. The energy loss of a charged particle emitting Bremsstrahlung is proportional to

$$\frac{Z^2 E}{M^2} \ .$$
(2.3)

This proportionality is the reason that light particles such as electrons can intensively emit Bremsstrahlung. On the other hand, muons will generate Bremsstrahlung with a probability more than four orders of magnitude lower. Actually, for all particles other than electrons or positrons, Bremsstrahlung is negligible at energies below 1 TeV (see also Fig 2.4).

- The Cherenkov effect is the radiation emitted when a charged particle travels in a medium faster than the speed of light in that medium (*i.e.* at a speed higher than c/n (where n is the refraction index which as typical values around 1.5 in liquids or solids). The Cherenkov effect is similar to the 'supersonic boom' of a plane flying faster than the speed of sound. The electric field of the 'slowly' flying charged particle will polarize the medium by disrupting the local electromagnetic field. After the particle has passed, the medium relaxes to its original unpolarized state. This change of polarization in the medium represents an electromagnetic perturbation that will propagate at the speed of light in the medium. Therefore, far away from the particle's trajectory, the perturbations will arrive randomly and annihilate each other. On the other hand if the particle travels at a speed faster than the speed of light in the medium, then the small electromagnetic perturbations caused by the polarization and depolarization of the medium propagate less rapidly than the particle and will form together one wavefront. This wave will propagate in a direction given by the speed of the particle and the speed of light in the medium.

The energy loss contributions due to Cherenkov radiation are small (of the order of 1% to the usual energy loss.

- For the muons we are interested for (having a speed of the order of $0.3c$), the main channel of energy loss is the transfer of energy to electrons leading to ionization or excitation of electrons on upper shells.[2] The number of these collisions is large in dense materials and the cross section of these collisions is large ($\sigma \sim 10 \times 10^{-13}$ m^2) but of course the energy loss is very small per collision.

  If the energy of the particles is large compared with the ionization energies, the energy loss in each 'collision' with an electron will be only a small fraction of the particle's energy. As the number of electrons in matter is so large, we can treat the loss of energy as continuous.

Hadrons: As seen with the collision of the proton with a nucleus which produces pions, here an additional mechanism is inelastic nuclear interactions, which can produce (as seen) pions, kaons, protons, neutrons or fragment of nucleus.

The history of the energy loss calculation is first marked by the works of Bohr in 1913 and 1915 [25, 26]. In 1930, the quantum mechanical version (first non-relativistic, then relativistic) was proposed by Bethe [27]. The Bethe's formulation is based using quantum mechanical perturbation theory.

2.1.1. Energy loss by ionization: classical approach

We first derive the classical formula for the interaction particle/electron. This represents the Bohr formulation of the interaction.

---

[2]Note that in general, the elastic collisions between muons and nucleus can be safely neglected as (in the classical limit) the maximum energy transfer in an elastic collision is given by:

$$
\begin{aligned}
\Delta E_{\max} &= \frac{1}{2} M v^2 \left(\frac{4 M M_{\mathrm{N}}}{(M + M_{\mathrm{N}})^2} \right) \\
&= \frac{2 M_{\mathrm{N}} v^2}{1 + 2 \frac{M_{\mathrm{N}}}{M} + \frac{M_{\mathrm{N}}^2}{M^2}} \quad ,
\end{aligned}
\tag{2.4}
$$

where M is the mass of the incoming particle and M_{N} is the nucleus mass. It is therefore negligible for $M_{\mathrm{N}} \gg M_\mu$.
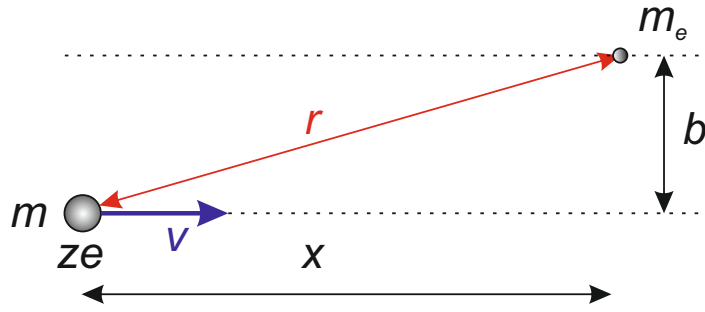
Figure 2.1.: *Model for calculating the energy lost by a charged particle in a collision with an electron. The parameter b is called the impact parameter.*

The momentum transfered to the electron (supposed at rest prior the interaction) is equal to

$$\Delta p = \int_{-\infty}^{\infty} F_{\text{Coul}} dt \quad . \tag{2.5}$$

For the Coulomb force, we only have to consider the transversal component, as the contribution from the longitudinal part will cancel out.

$$F_{\text{Coul}}^{\perp} = F_{\text{Coul}} \frac{b}{r} = F_{\text{Coul}} \frac{b}{\sqrt{b^2 + x^2}} = \frac{kze^2}{b^2 + x^2} \frac{b}{\sqrt{b^2 + x^2}} \tag{2.6}$$

where k is the Coulomb constant (value dependent on the units chosen) and ze is the charge of the flying particle. Therefore

$$\Delta p = \int_{-\infty}^{\infty} \frac{kze^2}{b^2 + x^2} \frac{b}{\sqrt{b^2 + x^2}} \frac{dx}{v} \quad , \tag{2.7}$$

where v is the velocity and we get

$$\Delta p = \frac{2kze^2}{vb} \quad , \tag{2.8}$$

and therefore the energy transfer in one encounter is

$$\Delta E(b) = \frac{\Delta p^2}{2M_e} = \frac{2k^2 z^2 e^4}{M_e v^2 b^2} \quad . \tag{2.9}$$
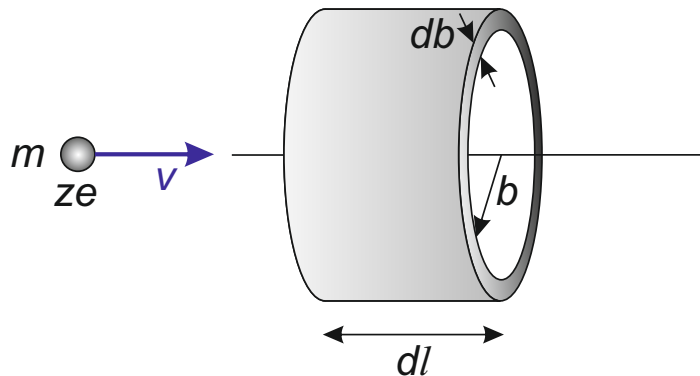
Figure 2.2.: *In path length dℓ, the charged particle collides with the electrons with impact parameters in db.*

To find how many encounters occur, we consider a cylindrical volume of thickness db and length $d\ell$ (see Fig. 2.2). There are

$$\frac{ZN_A}{A}\rho\, 2\pi\, db\, d\ell \tag{2.10}$$

electrons in this volume, where Z is the atomic number, A the atomic weight, N_A the Avogadro's number, and ρ the mass density. The total energy lost to these electrons is then

$$\Delta E = \frac{2k^2 z^2 e^4 Z N_A}{M_e v^2 A b^2}\rho\, 2\pi b\, db\, d\ell \quad . \tag{2.11}$$

We have to remember that Eq. 2.11 is for the volume dV of thickness db and therefore we have to integrate from a minimum to a maximum value of b. Hence, we have now to identify the maximum and minimum value of the impact parameter b.

For one encounter, the maximum energy transfer is $\Delta E_{\max} = 2M_e v^2$ (consider Eq. 2.4 with $M_N = M_e \ll M$). These collisions are usually called "hard" collisions. In some of the hard collisions the atomic electron acquires such a large energy that it causes secondary ionisation. We have

$$\Delta E_{\max} = 2M_e v^2 = \Delta E(b_{\min}) = \frac{2k^2 z^2 e^4}{M_e v^2 b_{\min}^2} \quad \text{and so} \tag{2.12}$$

$$b_{\min} = \frac{kze^2}{M_e v^2} \quad . \tag{2.13}$$

The minimum value of the energy transfer correspond to the so-called "mean excitation energy", *i.e.* $\Delta E_{\min} = I$. These collisions are usually called "soft" collisions. The value of I is not something that can be easily calculated and usually it has to be determined experimentally. It can be approximate (for $Z > 1$) by

$$I = 16\,\text{eV} \times Z^{0.9} \quad , \tag{2.14}$$

and for $Z > 20$ by

$$I = 10\,\text{eV} \times Z \quad . \tag{2.15}$$
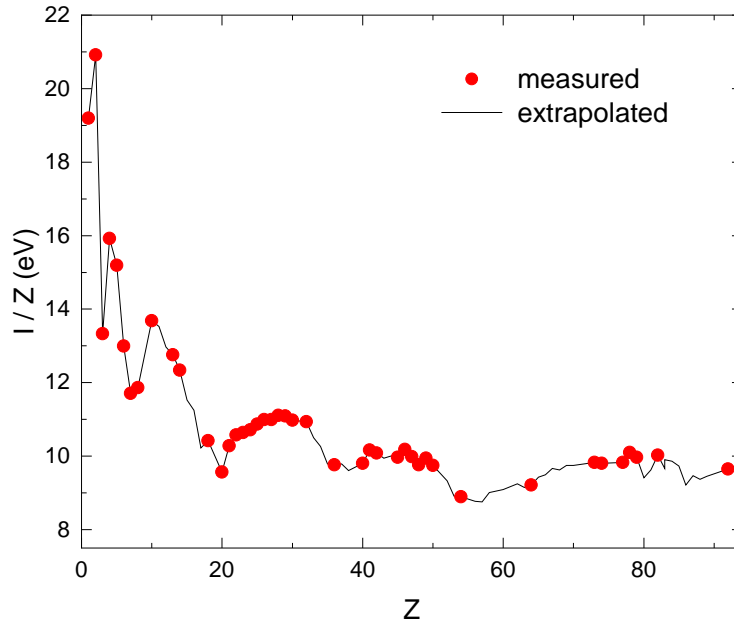
Figure 2.3.: *Mean potential energy determined experimentally (data from Ref. [?]).*

We can write therefore

$$\Delta E_{\min} = I = \Delta E(b_{\max}) = \frac{2k^2z^2e^4}{M_ev^2b_{\max}^2} \quad \text{and so} \tag{2.16}$$

$$b_{\max} = \frac{kze^2}{v}\sqrt{\frac{2}{M_eI}} \quad . \tag{2.17}$$

We recall that $dx = \rho\, d\ell$ and we have (introducing a negative sign to take into account the loss of energy for the incoming particle)

$$-\frac{dE}{dx} = \int\limits_{b_{\min}}^{b_{\max}} \frac{2k^2z^2e^4ZN_A}{M_ev^2Ab}\, 2\pi\, db = \frac{4\pi k^2z^2e^4ZN_A}{M_ev^2A}\frac{1}{2}\ln\left(\frac{2M_ev^2}{I}\right) \tag{2.18}$$

$$= \frac{4\pi k^2z^2e^4ZN_A}{M_e\beta^2c^2A}\frac{1}{2}\ln\left(\frac{2M_e\beta^2c^2}{I}\right) \quad , \tag{2.19}$$

(where we have introduced $\beta = v/c$) which represents the Bohr classical derivation of the Bethe formula.

In cgs units we have $k = 1$ and the energy loss is as said expressed in eV cm^2/g.

2.1.2. Energy loss: Bethe formula

As said, Bethe performed the full quantum mechanical derivation, and obtained:

$$-\frac{dE}{dx} = \frac{4\pi k^2z^2e^4ZN_A}{M_e\beta^2c^2A}\left(\frac{1}{2}\ln\frac{2M_e\beta^2c^2\gamma^2T_{\max}}{I^2} - \beta^2 - \frac{\delta(\beta\gamma)}{2}\right) \quad . \tag{2.20}$$

The term $T_{\max}$ represents the maximum kinetic energy transfer onto one electron calculated relativistically and is given by:

$$T_{\max} = \frac{2M_e c^2 \beta^2 \gamma^2}{1 + 2\gamma \frac{M_e}{M} + \frac{M_e^2}{M^2}} \quad , \tag{2.21}$$

where $\gamma = (1 - \beta^2)^{-1/2}$ is the Lorentz factor.
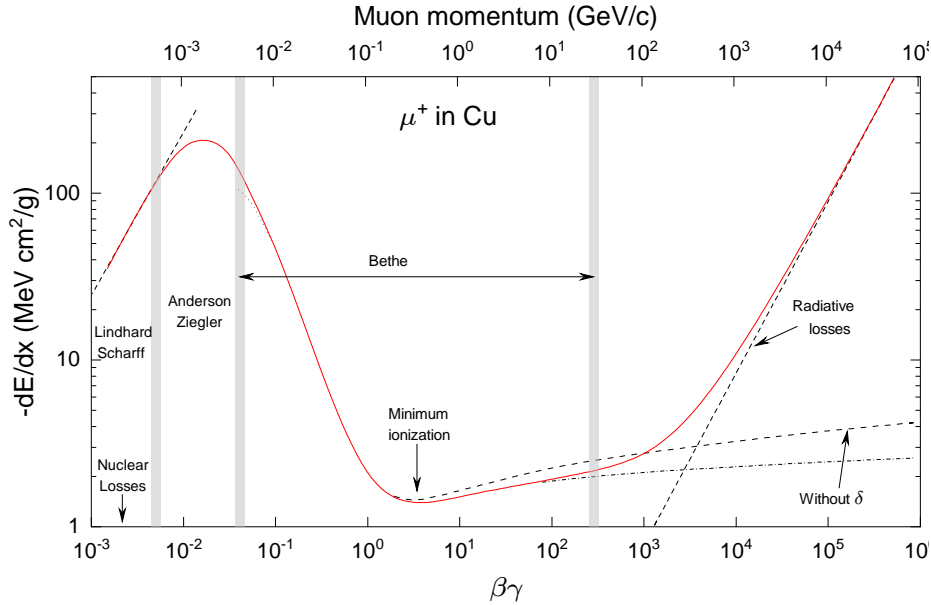
Figure 2.4.: *Stopping power $-dE/dx$ for positive muons in copper as a function of $\beta\gamma = p/(mc)$ over nine orders of magnitude. The validity range of the Bethe formula is indicated (adapted from Ref. [28]). There are two regions where the Bethe formula is no more valid. First at high velocity, the radiation effects are the result of Bremsstrahlung which becomes important here in reason of the kinetic energy (see Eq. 2.3). On the other side at low velocity, one observes a linear increase of the stopping power. For these low energies, a positively charged particle can pick-up an electron and therefore its effective charge, and therefore the stopping power, will be reduced. By increasing the velocity, this effect will decrease as the probability to pick-up an electron will decrease. Alternatively, if the flying particle is an ion with electrons, these will be stripped with a probability which grows with velocity [29].*

They are few important points concerning this formula:

- In the range where the Bethe formula is valid, we have three different regions :

  1. At low energies a $(1/\beta)^2$ (kinematic factor) drop to a minimum at about $\beta\gamma \sim 3 - 4$.
     Particles at this point are called minimum ionising particles ("MIP").
     For low energies and when the mass of the incoming particle is bigger than the electron one, we have $\gamma M_e \ll M$ and therefore

     $$T_{\max} \simeq 2M_e c^2 \beta^2 \gamma^2 \quad . \tag{2.22}$$

Introducing that in the Bethe formula we see that (assuming $\gamma \simeq 1$) the Bethe result corresponds to the classical result except a factor of 2.[3]

By looking at the Fig 2.4, we see that a muon at the MIP point looses about 13 MeV/cm in copper (density 8.96 g/cm³).

2. At higher energies a logarithmic rise follows, which is due to relativistic effects. It reflects the relativistic increase of the transversal component of the electrical field (Lorentz transformation of the field). This leads to larger collision distances and therefore to more collisions.

3. At very high energies a plateau is reached. This is due to the density effect. In high density material, the electric field will be partially shielded due to the polarization. Therefore, we have effectively some cuts of the long range contributions. These are of course more relevant at high γ (see the previous point).

- An important point is that the stopping power dE/dx is marginally dependent of the target material (actually only the factor Z/A depends on the material, which is constant over a large range of materials).
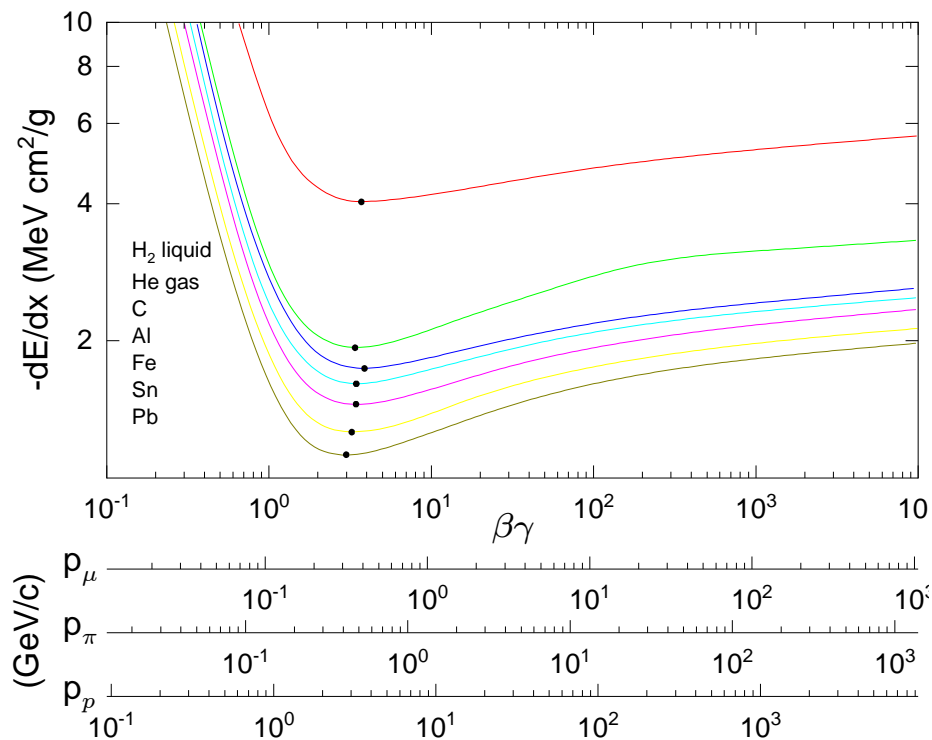
Figure 2.5.: *Stopping power $-dE/dx$ in liquid hydrogen, heluim gas, carbon, aluminum, iron, tin and lead. Except in hydrogen, particles of the same velocity have similar energy loss in different materials (adapted from Ref. [28]).*

---

[3]This factor arises from the fact that the classical limit does not describe correctly the very far collisions and that the binding of the electrons cannot be neglected.

- The Bethe equation does *not* depend on the mass of the incoming particle. This means that it is an universal curve as a function of $\beta\gamma$ for particles with the same charge. However the stopping power "split up" for different particle masses if taken (or measured) as a function of the incoming momentum or energy.
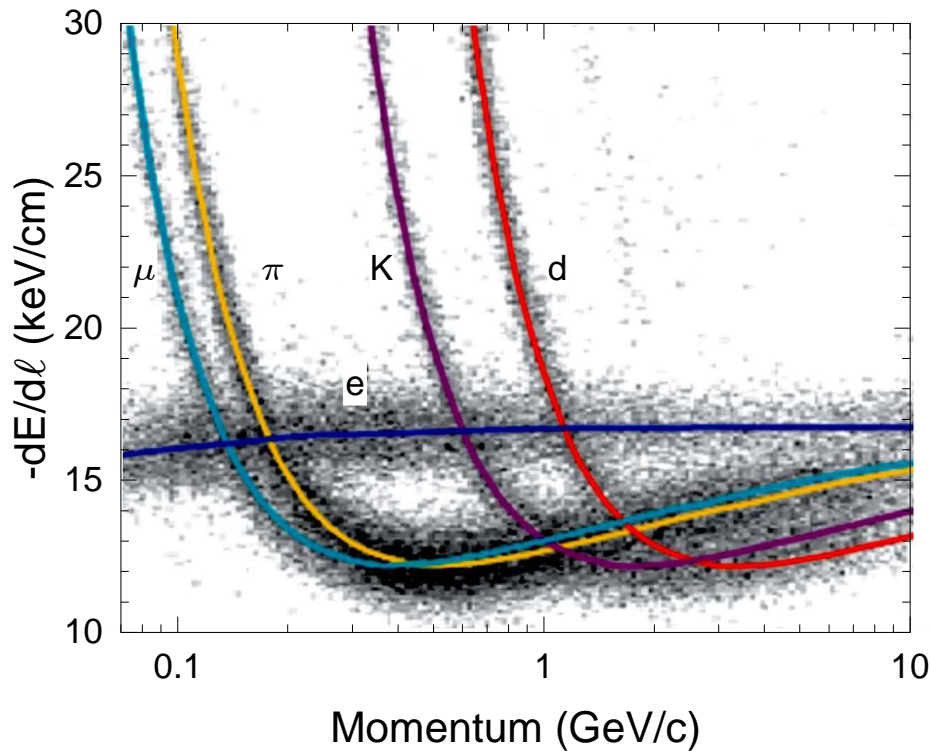
Figure 2.6.: *Stopping power $-dE/d\ell = -dE/dx\ \rho$ in a mixture of argon (80%) at 8.5 bar reported as a function of the particle impulse. The electron stopping power does not follow the Bethe formula (Bremsstrahlung dominant). Adapted from Manfred Krammer [30].*

- The energy loss is a statistical process. Hence the number of collisions and energy loss varies from particle to particle. Also the distribution of stopping depth is usually asymmetric. This reflects the fact that collisions with a small energy transfer are more probable than those with a large energy transfer. A result of the asymmetric distribution is that the mean energy loss is larger than the most probable energy loss.
The energy loss as function of the penetration depth is called the "Bragg Curve" (or Bragg peak). The fact that the energy loss is maximum just before the particle comes to a complete stop is used in particle therapy of cancer, to concentrate the effect of ion beams on the tumor while minimizing the effect on the surrounding healthy tissue.

This property is used for so-called proton therapy, for example at the Paul Scherrer Institute.
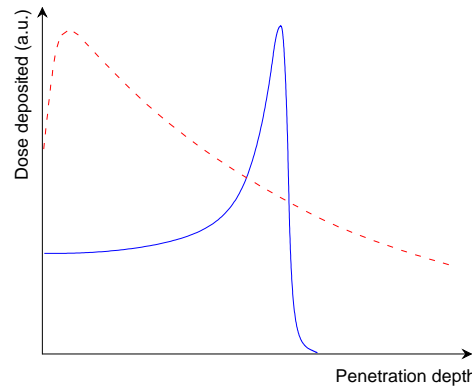
Figure 2.7.: *Schematic of the stopping power for photons (red) and protons (blue) as a function of the penetration depth.*

Figure 2.8.: *Proton therapy treatments at PSI use an in-house built supercon-ductor accelerator, a compact cyclotron, called COMET. It was especially de-veloped for medical applications by the company ACCEL (now part of Varian Medical Systems) and brought into service in 2007. It delivers a beam energy of 250 MeV, which can be reduced when needed for patient treatments (see* `https://www.psi.ch/protontherapy/center-for-proton-therapy-cpt`*).*

2.2. Range and thermalization time

2.2.1. Range of muons

The range R (in g/cm^2) is given by the integration

$$R = \int\limits_{E_{\text{kin}}}^{0} \frac{1}{dE/dx} dE$$

$$= \int\limits_{E_{\text{tot}}}^{Mc^2} \frac{1}{dE/dx} dE \quad . \tag{2.23}$$

We can also define the range in length units (say cm) for a given material as

$$R_\ell = \frac{R}{\rho}$$

$$= \frac{1}{\rho} \int\limits_{E_{\text{tot}}}^{Mc^2} \frac{1}{dE/dx} dE \quad . \tag{2.24}$$

Within its validity range, the integration should be performed with the Bethe-Bloch formula, which is a hard task due to the logarithmic term. Often one considers some approximations for the different ranges. For example for a muon having an initial impulse $p = \gamma M v = \beta \gamma M c$, one often uses:

$$-\frac{dE}{dx} = \begin{cases} a \dfrac{\ln(\beta)}{\beta^2}, & \text{for } \beta\gamma = \dfrac{p}{Mc} \ll 1 \\[2ex] b \dfrac{1}{\beta^2}, & \text{for } \beta\gamma = \dfrac{p}{Mc} \lesssim 1 \\[2ex] c, & \text{for } \beta\gamma = \dfrac{p}{Mc} \simeq 3-4 \\[2ex] c + d\ln(\beta), & \text{for } \beta\gamma = \dfrac{p}{Mc} \gg 1 \end{cases} \tag{2.25}$$

We have seen that for high energy beamlines we use backward muons with high impulse (see Fig. 1.32). For these impulses we can use the second condition and therefore:

$$-\frac{dE}{dx} = b \frac{1}{\beta^2} \quad , \tag{2.26}$$

with $b \simeq 1.3$ MeV/(g/cm^2). We therefore have (see Exercises for details)

$$
\begin{aligned}
R &= \int_{E_{\text{tot}}}^{Mc^2} \frac{1}{dE/dx} dE \\
&= \int_{E_{\text{tot}}}^{Mc^2} -\frac{\beta^2}{b} dE \\
&= \ldots \\
&= \frac{1}{b} \frac{(\gamma - 1)^2}{\gamma} Mc^2 \; .
\end{aligned}
\tag{2.27}
$$

For a muon with an impulse $p = 110$ MeV/c (that is a total energy of about 152.5 MeV and $\gamma \simeq 1.444$) one gets a range of $R \simeq 11.1$ g/cm^2. For copper ($\rho_{\text{Cu}} = 8.96$ g/cm^3) this represent a penetration of the muon to $R_\ell = \frac{R}{\rho_{\text{Cu}}} \simeq 1.24$ cm.

For the lower impulse (as the one present in surface muon beams), the above formula underestimates the true range by a fair amount. This is the consequence of having neglected the logarithmic term in the stopping power.

For surface muon beams with a momentum of the order of $p \simeq 30$ MeV/c^2 and a typical momentum bite of $\Delta p / p \simeq 0.03$, the range R is of the order of 130 mg/cm^2 and the straggling ΔR is about 13% of R.
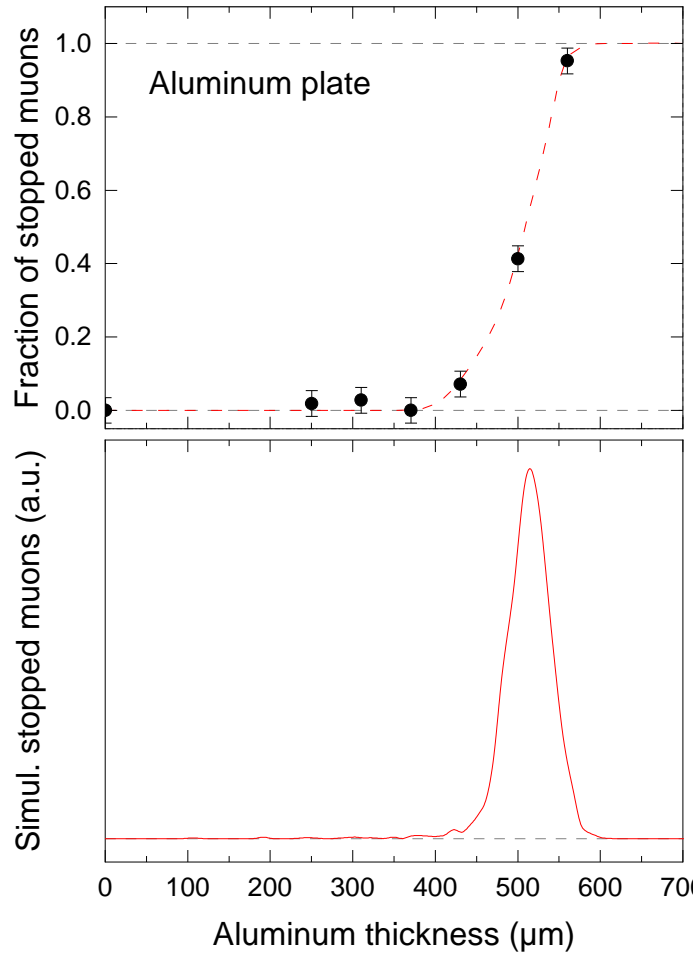
Figure 2.9.: *Fraction of the muon beam stopped as a function of the aluminum sample thickness. The measurements were performed at the GPS instrument at PSI using surface muons. For thin samples, the muons are flying through the sample. The full beam is typically stopped by an aluminum sample with a thickness of about $L = 0.50 \pm 0.05$ mm, which corresponds to a range of $R = L\rho \simeq 135$ mg/cm^2.*

Analog to what we saw for the proton therapy, the muons will present a Bragg peak (see Fig. 2.7). We can roughly determine the shape of the Bragg curve, by starting from Eq. 2.26. The loss of kinetic energy will be

$$-\frac{dE}{dx} \simeq -\frac{d}{dx}\left(\frac{1}{2}M\beta^2(x)c^2\right) \ , \tag{2.28}$$

neglecting the relativistic character. Therefore

$$-\frac{d}{dx}\left(\frac{1}{2}M\beta^2(x)c^2\right) = \frac{b}{\beta^2(x)}$$

$$-Mc^2\beta(x)\frac{d\beta}{dx} = \frac{b}{\beta^2(x)}$$

$$-\beta^3(x)\,d\beta = \frac{b}{Mc^2}dx$$

$$\beta^4(x) - \beta_0^4 = -\frac{4b}{Mc^2}x$$

$$\beta^2(x) = \beta_0^2\sqrt{1 - \frac{4b}{Mc^2\beta_0^4}x}$$

$$\beta^2(x) = \beta_0^2\sqrt{1 - \frac{x}{R}} \quad . \tag{2.29}$$

Using now this dependence of $\beta(x)$, we can rewrite Eq. 2.26 as

$$-\frac{dE}{dx}(x) = \frac{b}{\beta_0^2\sqrt{1 - \frac{x}{R}}} \quad . \tag{2.30}$$
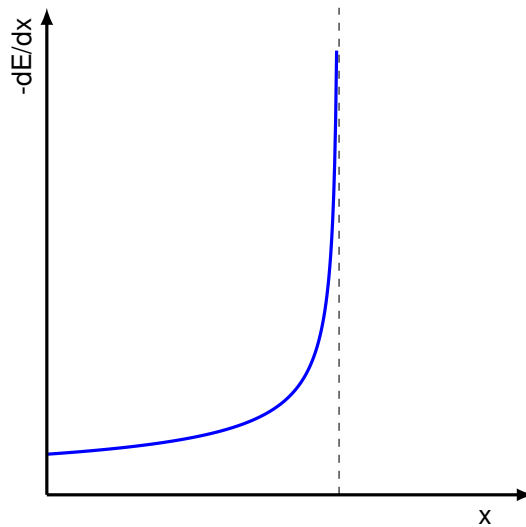
Figure 2.10.: *Rough estimate of the Bragg curve obtained with Eq. 2.30. The real maximum occurs before the full range is reached (see text and Fig. 2.7).*

This is of course a rough estimation as the stopping power will not follow Eq. 2.26 for all the velocities. Overall, the Bragg curve is much less peaked than predicted by Eq. 2.30 and its maximum occurs before the full range is reached.

2.2.2. Thermalization time

The thermalization time is given by:

$$t_{th} = \int\limits_{E_{in}}^{0} dt = \int\limits_{E_{in}}^{0} \frac{d\ell}{v} = \int\limits_{E_{in}}^{0} \frac{1}{v\dfrac{dE}{d\ell}} dE$$

$$= \int\limits_{E_{in}}^{0} \frac{1}{v\rho\dfrac{dE}{dx}} \, dE \quad . \tag{2.31}$$

We see that this time is proportional to the inverse of the density and is of the order of ~ 10 ps for usual solids.

2.3. "Free" muon vs muonium

After its deceleration, the positive muon actually represent a charged impurity which will be generally located at an interstitial position in the crystal lattice. In a metal, its charge will change the local charge density of the conduction electrons.
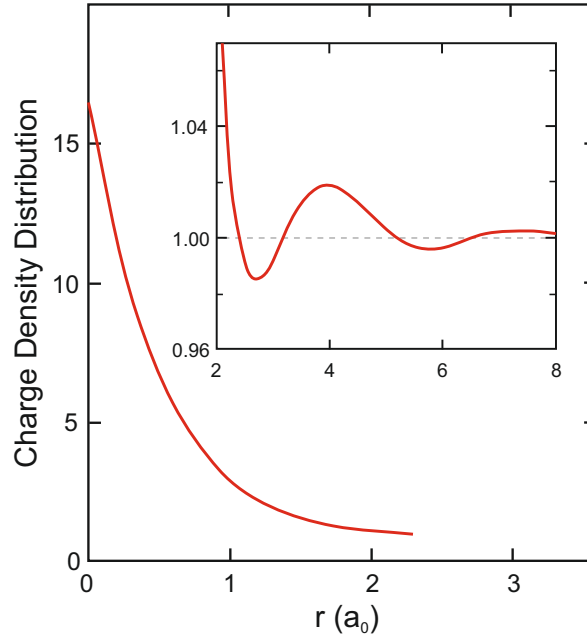
Figure 2.11.: *Typical normalized electron charge-density distribution around the positive muon (adapted from [31]). The red curve corresponds to the normalized charge density $n(r)/n_0$ (see text). The exact form will depend on the density of the conduction electrons with obviously $n(r = 0)/n_0$ increasing strongly for large values of r_s.*

One can define the unperturbed electron density as n_0 writing

$$n_0 = \frac{1}{\frac{4}{3}\pi(r_s a_0)^3} \quad , \tag{2.32}$$

where a_0 is the Bohr radius and r_s is conventionally being referred to as the electron density parameter. So $r_s a_0$ represents the radius of a sphere containing one electron.
The unperturbed electron density is obtained by taking typically $r_s = 2$ giving

$$n_0(r_s) = \frac{1}{\frac{4}{3}\pi(2a_0)^3} \quad . \tag{2.33}$$

The Fig. 2.11 shows us that in the presence of the muon we have quite an increase at the muon site ($r = 0$) with

$$n(r = 0) \simeq 16 \times n_0 = \frac{16}{\frac{4}{3}\pi(2a_0)^3} \quad . \tag{2.34}$$

We note that the electron density for muonium corresponds to the situation with $r_s = 1$ (the Bohr radius for the muonium is almost identical to the one for hydrogen; see Section 8.1) and therefore the electron density at the muon site in a metal is only twice the one in muonium as

$$n_{e,\mathrm{Mu}} = \frac{1}{\frac{4}{3}\pi a_0^3} \simeq \frac{1}{2} \, n(r = 0) \quad . \tag{2.35}$$

In spite of this, muonium is not observed in metal. The collective screening of the muon Coulomb potential will impede the formation of a bound state muon-electron. Even if the state is shortly formed, it will be extremely short lived and will be destroyed by the scattering of the bound electron with the conduction electrons.

Therefore the positive muon implanted into a metal will behave as a "free" muon (so-called diamagnetic state).

A very important point is that the involved slowing-down processes are only electrostatic, and therefore, the muon polarization will not be affected.

(a) *CeRu$_2$Si$_2$*   **(b)** *CeB$_6$*   **(c)** *UPd$_2$Al$_3$*
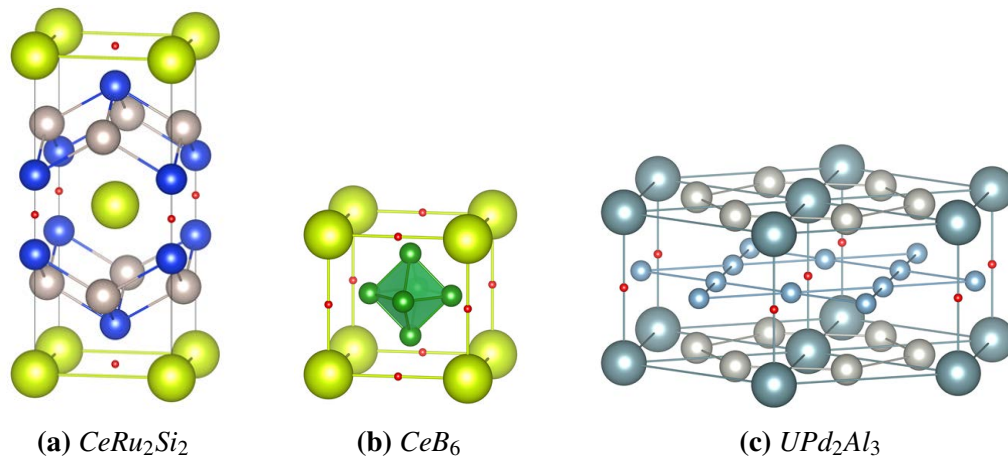
Figure 2.12.: *Examples of muon stopping sites (red spheres) determined experimentally for different systems. For each system, the sites are crystallographically equivalent.*

The story is different in materials where the free-electron density is low as insulators, semiconductors, molecular systems, liquids or gases. In these system the muon can pick-up an electron and form muonium (see Section 8). Actually a limit on the electron density to observe muonium in a material was given by Estreicher and Meier [32] with $n \sim 3 \times 10^{22}$ cm^{-1}. In these materials, when the kinetic energy of the implanted muons has dropped to several tens of keV, *i.e.* when the muon velocity becomes comparable to the orbital velocity of electrons of the medium, then the positive muon can pick-up an electron to form a muonium. Generally, the muon will be stripped of this electron but can bind again with another one. The muon undergoes a rapid series of several hundred electron pickup and stripping cycles, loosing energy at each cycle. If the last step before a complete thermalization leaves intact the muonium, then one speaks of "prompt" formation. On the other side if the muon thermalizes as a bare particle and subsequently pick-up an electron, the formation is called "delayed".

3. μSR Technique

3.1. Introduction

The expression μSR is the acronym for Muon Spin Rotation/Relaxation/Resonance and underlines the analogy with NMR (Nuclear Magnetic Resonance) and ESR (Electron Spin Resonance, often called EPR, *i.e.* Electron Paramagnetic Resonance).[1] There are, however, important differences. The μSR technique does not require specific target nuclei as NMR, and is therefore universally applicable as muons can be implanted in any kind of materials. Also, whereas NMR and ESR rely upon a thermal equilibrium spin polarization (and therefore require usually both high magnetic fields and low temperatures) with μSR it is possible to perform measurements without applying a magnetic field (so called zero field μSR, ZF) allowing one to investigate magnetic systems without perturbation.[2] The method is based on the observation of the time evolution of the muon spin polarization $\mathbf{P}(t)$ of an ensemble of muons implanted in a sample. Since a few millions of muons are recorded in a typical experiment, the average $\langle \mathbf{I}_\mu(t) \rangle$ over all the muon spin vectors has to be considered. Therefore, the polarization vector can be written as

$$\mathbf{P}(t) = \frac{\langle \mathbf{I}_\mu(t) \rangle}{|\mathbf{I}_\mu(0)|} \quad , \tag{3.1}$$

which could also be written with the Pauli matrices as (see Eqs. A.65 to A.67)

$$\mathbf{P}(t) = \langle \boldsymbol{\sigma}(t) \rangle \quad . \tag{3.2}$$

The muon spin polarization contains the physical information about the interaction of the muon magnetic moment with its local environment. Due to the anisotropic decay positron emission, with a higher probability to be emitted along the spin direction of the muon, the precession and/or depolarization of $\mathbf{P}(t)$ can be deduced. The muon acts as a local very sensitive magnetic probe being able to determine the value, direction, distribution and/or dynamics of the internal magnetic fields present at its localization site inside the material.

μSR is not a scattering technique and therefore magnetic structures can not be easily obtained as by neutron diffraction. However with μSR it is possible to determine magnetic, non-magnetic, and superconducting fractions in a straightforward way. In magnetic systems for example, magnetic volume can be obtained independently of the determination of the

---

[1] In the first μSR Newsletter in 1974 Jess Brewer wrote:"μSR stands for Muon Spin Relaxation, Rotation, Resonance, Research or what have you".

[2] Note that NQR (Nuclear Quadrupole Resonance) is also a zero field technique, but for magnetic investigations less direct than zero field μSR.

magnetic moment in magnetic systems. In systems where it is formed, the Muonium acts as a Hydrogen isotope (for example in chemical reactions) or as impurity in semiconductors and dielectrics providing valuable information about the electronic environment.

3.2. The μSR signal

During a so-called "time-differential" μSR measurement[3] (hereafter just called μSR measurement), one wants to gain access to the time evolution of the muon polarization of an ensemble of muons implanted into a material to be investigated, through the anisotropic emission of positrons (see Section 1.5). This muon ensemble is not implanted at once into the sample, but either one-by-one (at "continuous-wave" beams, see Section 3.4.1) or by bunches (at pulsed beams, see Section 3.4.2). The discussion here is limited to the continuous beam case but is basically identical for a pulsed beam. Measuring one-by-one the decay of individual muons is identical as the measurement of an muon ensemble implanted at once. The only "difficulty" is to determine the exact implantation time for each muon (*i.e.* the time t_0 for each muon). So in addition to the positron detectors, a first muon detector is needed to provide the arrival time of the muon.

---

[3]Sometimes called Δt-μSR
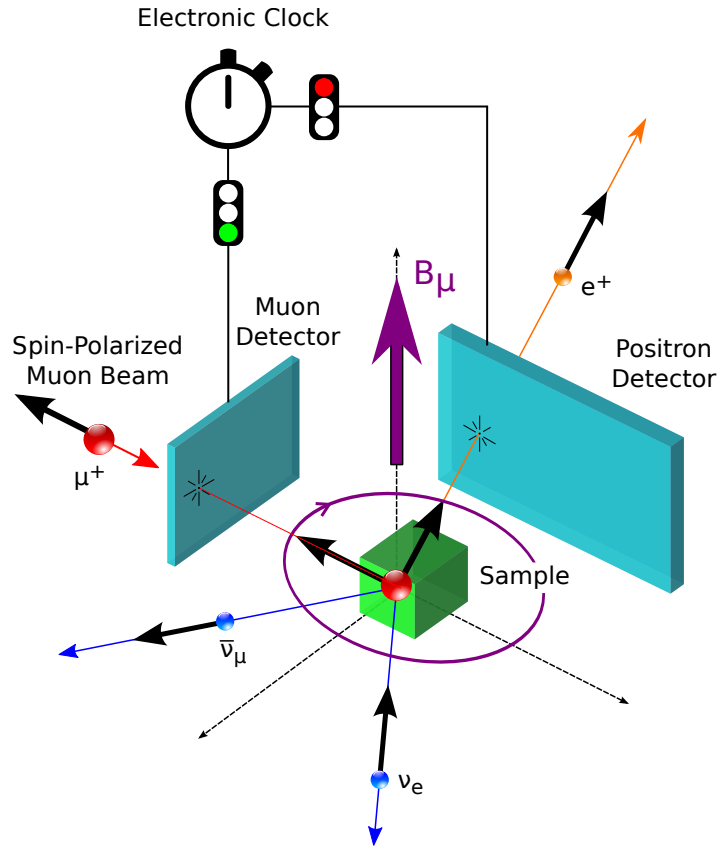
Figure 3.1.: *Sketch of a time-differential μSR measurement. The polarized muon is coming from the upper-left part of the figure and is first detected by a (thin) Muon Detector. The arrival signal starts a very precise electronic clock and will define the time t_0 (remember that the implantation time is extremely fast, see Section 2.2.2). In the sample, the muon will possibly sense a magnetic field (of internal or external origin) and its spin will begin to precess with the Larmor frequency. When the muon decays, a positron will be emitted with more probabilities along the direction of the muon spin at decay time. The decay will be recorded by a (thick) Positron Detector, which will also determine the positron flying path (note that in reality many positron detectors are located around the sample). The positron detector signal is sent to stop the clock, which has therefore measured the time t between the muon implantation and its decay [drawing: courtesy of Andreas Suter (PSI)].*

The number of positrons detected as a function of time by a positron detector having a solid angle $\Delta\Omega$ is

$$N(t) = B + \frac{N_{\mu,0}\,\Delta\Omega\,\epsilon}{4\pi\tau_\mu}\,e^{-\frac{t}{\tau_\mu}}\left[1 + A_0\,\mathbf{P}(t)\cdot\hat{\mathbf{n}}\right]$$

$$= B + N_0\,e^{-\frac{t}{\tau_\mu}}\left[1 + A_0\,\mathbf{P}(t)\cdot\hat{\mathbf{n}}\right]\ . \tag{3.3}$$

We see that compared to Eq. 1.19, we have introduced some new terms and/or notation:

Background B: This term takes into account the inevitable time-independent background due to uncorrelated events. In a continuous beam, it is usually lower that $0.01 \times N_0$.

The "initial" value N_0: We have written that the starting intensity $N_0 = N_{\mu,0} \Delta\Omega\epsilon / (4\pi\tau_\mu)$, where the parameter $\epsilon \lesssim 1$ reflects the fact that the energy efficiency of the detector is not perfect.[4]

The asymmetry term A_0: Even though we have integrated over the energies, we generally have that $A_0 < \bar{A}$ (see Eq. 1.16). This is due to two reasons:

1. Here again we have the energy efficiency of the detector which is not perfect. If high energy positrons are not always detected, this will play quite a role for the value of A_0 as they contribute the most to an high asymmetry.

2. The solid angle of the detector $\Delta\Omega$ is finite. This will reduce the asymmetry measured by this detector.[5]

In real measurements the experimental asymmetry parameter is of the order of 0.25 to 0.3.

The time dependent muon polarization $\mathbf{P}(t)$: This is what will be interesting for us. In Eq. 1.19, we have actually assumed that the polarization was time independent. We see of course that if $\mathbf{P}$ is time dependent, the angle θ will become time dependent and we will have $\cos\theta(t) = \mathbf{P}(t) \cdot \hat{\mathbf{n}}$, where $\hat{\mathbf{n}}$ defines the direction of the positron detector.[6]

We see that Eq. 3.3 contains parameters just given by the geometry of the measurements and the muon lifetime. These are normally corrected for and the **μSR signal** for say a detector i is defined as the measured quantity

$$
\boxed{\begin{aligned}
A(t) &= A_0\, \mathbf{P}(t) \cdot \hat{\mathbf{n}}_i \quad \text{or just,} \\
A(t) &= A_0\, P_i(t) \ ,
\end{aligned}}
\tag{3.5}
$$

where $P_i(t)$ is the norm projection of the muon polarization along the direction of the detec-

---

[4] $\epsilon = \int\limits_0^1 E(\varepsilon) f(\varepsilon)\, d\varepsilon$, where $f(\varepsilon)$ is the efficiency of the detector as a function of the energy.

[5] It can be shown that the effect of the solid angle can be written as

$$
A_{0,\Delta\Omega} = \frac{\bar{A} \int\limits_{\theta-\Delta\theta/2}^{\theta+\Delta\theta/2} \cos\theta'\, d\theta'}{\Delta\theta\, \cos\theta} \ ,
\tag{3.4}
$$

where θ is the observation direction (*i.e.* the angle between $\mathbf{P}$ and $\hat{\mathbf{n}}$) and $\Delta\theta$ defines the solid angle range of the detector.

[6] Note that we always assume that $|\mathbf{P}(0)| = 1$. If this is not the case the factor will be integrated into the asymmetry A_0.

tor i, that is

$$\mathbf{P}(t) \cdot \hat{\mathbf{n}}_i = P_i(t) = \frac{\langle \mathbf{I}_\mu(t) \cdot \hat{\mathbf{n}}_i \rangle}{|\mathbf{I}_\mu(0)|} \quad , \tag{3.6}$$

where $\mathbf{I}_\mu$ is the muon spin and the brakets $\langle ... \rangle$ represents the average over the muon ensemble. The time evolution of the polarization contains all the physics of the interaction between the muon (and its spin) with the material to be investigated. The task of a physicist using the μSR technique will be to extract relevant information from the observed time evolution of the muon polarization. As we will see, this will consist in modeling $\mathbf{P}(t)$ for a given problem.

In the literature, the μSR signal (sometimes normalized to A_0) is often also called "asymmetry signal" or "polarization signal" or "relaxation signal" or "depolarization signal", etc.
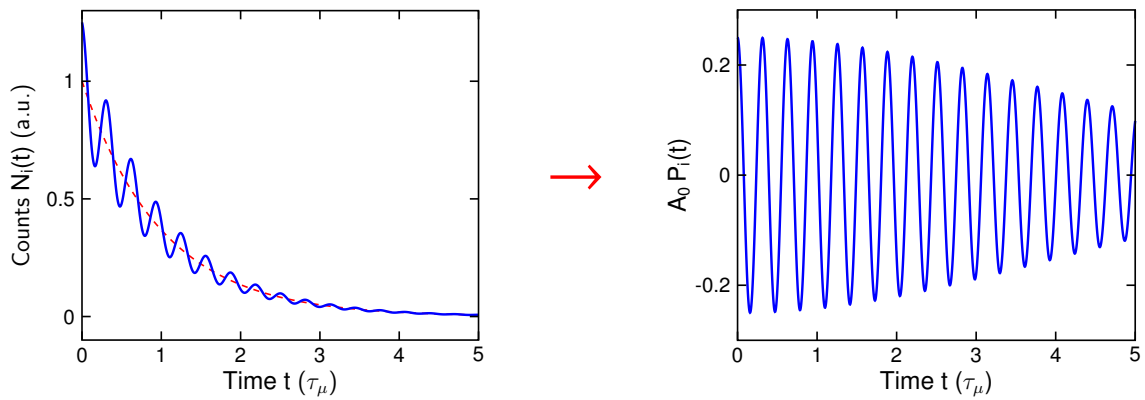
Figure 3.2.: *μSR signal for a given detector, say in the $\hat{\mathbf{n}}_i$ direction: i) (left panel) on first builds a histogram containing the number muon-positron events recorded as a function of their time difference measured by the clock (see Figure 3.1). One muon decay produces of course at the most only one event (if the positron is indeed detected by the considered positron detector) at a given time difference. Hence the histogram is obtained by observing typically 10^6 muon decays; ii) (right panel) Subsequently, one removes the background signal and corrects for the radioactive exponential decay and for the normalization.*
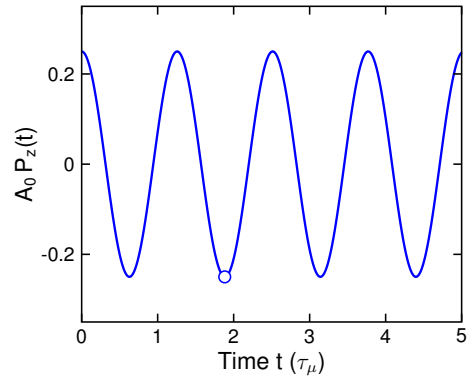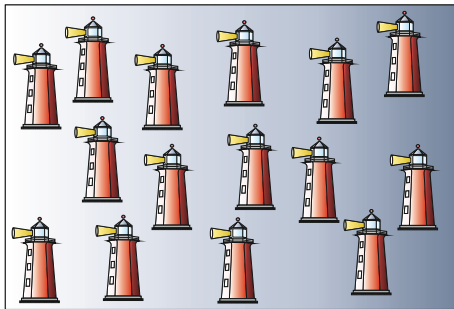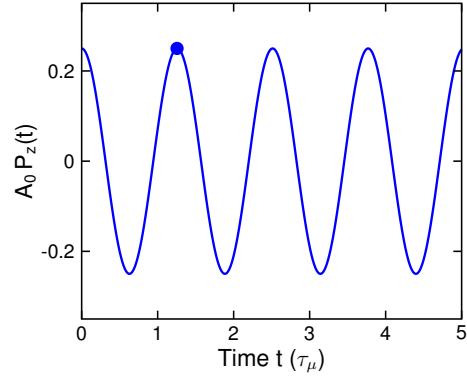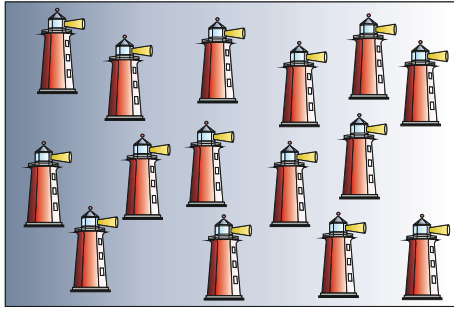
Figure 3.3.: *A simple illustration of the μSR signal. Imagine that the muon spins are lighthouses with lenses (that would be their spin) rotating at a given frequency (that would be the Larmor frequency) and all in phase. When one of the muon decay, its lighthouse will send a flash of light (that would be the positron) in the direction of the lens. Imagine that the positron detector is located on the right-hand side of the lighthouses. When the lenses face the detector (upper row) and some muons decay, the μSR signal will have a maximum amplitude as some lighthouses will send light in the direction of the detector (solid symbol). After a time corresponding to 1/2 of the oscillation period, when the lenses face the opposite direction with respect to the detector (lower row) and some muons decay, the μSR signal will have a minimum amplitude as some lighthouses will send light in the direction opposite to the detector (open symbol). Figures adapted from Hubertus Luetkens (PSI).*

3.3. Key features of the μSR technique

In the following, we will look at some of the key features of the μSR technique. We will first look at the capability of the technique to differentiate between different fraction of the sample having different ground states. We will also look at the sensitivity of the technique to measure very weak magnetic phenomena.

3.3.1. Local probe - volume sensitivity

The muon is considered as a local probe. It provides (mainly magnetic) information about the surrounding of its interstitial stopping site. In this sense it can be compared to other local probe techniques as NMR or Mössbauer. Probably the main difference is that for NMR or Mössbauer, the "probes" are directly ions composing the crystallographic lattice. This is of advantage as one a priori knows where the probes are located, but these techniques are limited to specific nuclei. On the other hand-side, the μSR technique, even though having always the problem to determine where the muon localizes, has the adavantage that in can be used in any kind of materials.

The local probe feature makes μSR a perfectly complementary technique to scattering techniques like neutron diffraction, where the wave character of the neutron is used to determine crystallographic and magnetic structures. For magnetic materials, the neutron diffraction technique is also often used to determine the temperature dependence of the order parameter (*i.e.* of the ordered magnetic moment μ_{ord}), however this determination is done by assuming that 100% of the investigated sample volume (V) is magnetic. Indeed the magnetic intensity measured by neutron scattering (looking at Bragg peaks) is proportional to $V\mu_{\mathrm{ord}}^2$ and both quantities cannot be disentangled. If for example only part of the volume is magnetic, the oberved intensity (if associated to the entire volume) will lead to an underestimation of the magnetic moment value. The same is true for so-called bulk techniques as for example magnetization measurements, where the observed magnetization is associated with the entire volume.

The situation is different for μSR. Let assume that your sample has at a given temperature two volume fractions: a paramagnetic one V_{par} and a magnetic one V_{mag}. The muons stopping in these two volumes will present different magnetic responses, *i.e.* different muon-spin polarization behavior. Therefore the muon ensemble will be split and the μSR signal will have two components[7]

$$A(t) = A_{0,\mathrm{par}}\, P_{\mathrm{par}}(t) + A_{0,\mathrm{mag}}\, P_{\mathrm{mag}}(t) \ , \tag{3.7}$$

which can usually been easily distinguished. From the asymmetry, one obtains readily the

---

[7]We forget here the index of the detector for clarity.

volume occupied by the paramagnetic and magnetic parts of the sample

$$\begin{aligned} \frac{A_{0,\text{par}}}{A_0} &= \frac{V_{\text{par}}}{V_{\text{tot}}} \\ \frac{A_{0,\text{mag}}}{A_0} &= \frac{V_{\text{mag}}}{V_{\text{tot}}} \quad . \end{aligned} \tag{3.8}$$

Information about the value of the ordered moment in the magnetic volume is obtained by studying the polarization $P_{\text{mag}}(t)$, will present spontaneous one (or more) Larmor frequency due to the internal field sensed by the muon in the magnetic volume. As we will see, the value of the frequency is related to the value of the ordered moment. Therefore

$$\begin{aligned} A_{0,\text{mag}} &\Longleftrightarrow V_{\text{mag}} \\ P_{\text{mag}}(t) &\Longleftrightarrow \mu_{\text{ord}} \quad . \end{aligned} \tag{3.9}$$

Note that we have limited the discussion here to the question about magnetic and non-magnetic volumes, but it can be extended to other types of ground state. For example μSR can test whether the superconducting state is bulk (which is not a trivial task to do with thermodynamic or transport properties) or, for example filamentary.
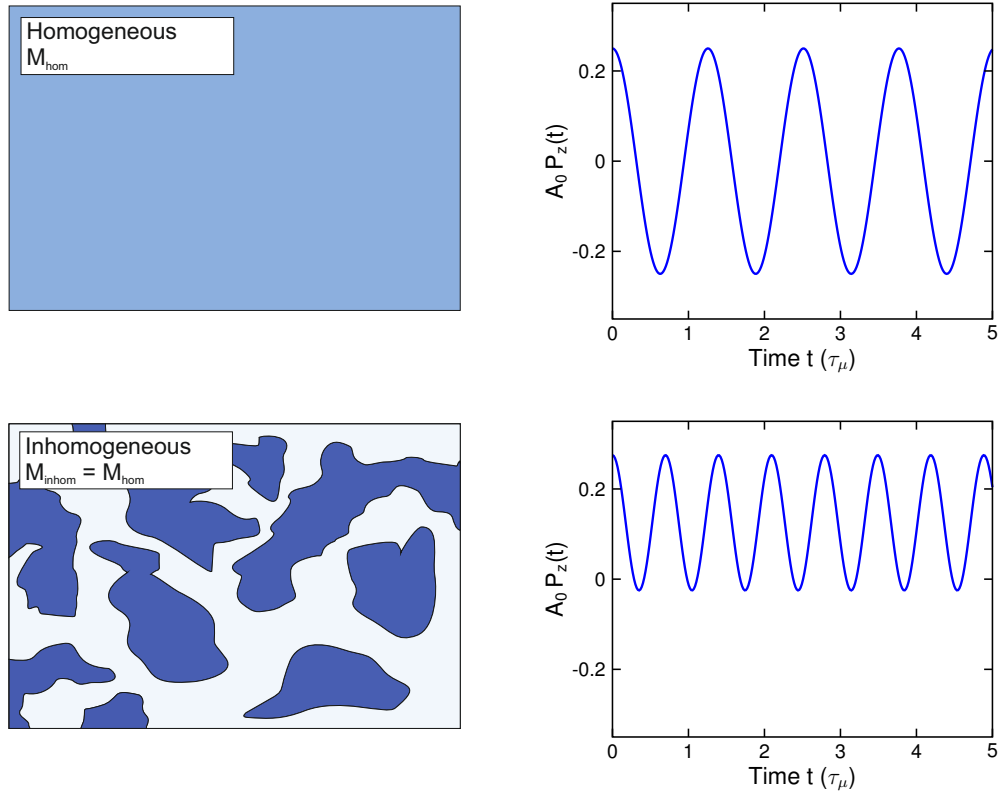
Figure 3.4.: *Schematics of the µSR capability to distinguished between magnetically homogeneous and inhomogeneous samples. Assume that two samples exhibit similar values of the magnetization even though one of the sample is magnetically homogeneous (i.e. full volume magnetic, top left sketch) and the other one is magnetically inhomogeneous (i.e. part of the volume magnetic and part paramagnetic, bottom left sketch). Obviously, in order to have similar magnetizations, the magnetic state of the homogeneous sample should be "stronger" than the the one of the inhomogeneous one (as the paramagnetic part will not contribute to the magnetization).*
The muons stopping in the homogeneous sample will sense a same weak magnetic environment and will therefore constitute one muon ensemble. Their spin will precess around the internal field (Larmor frequency) and the µSR typical signal will be as shown on the top right part of the figure.
The muons stopping in the inhomogeneous sample will sense either a strong magnetic environment or a paramagnetic environment. Therefore these muons will be divided into two muon ensembles. One muon ensemble will present a fast spin frequency and the other one will not sense an internal field and the spin of these muons will remain fixed. The respective amplitudes (asymmetries) of these two signals will represent the volume fractions occupied by the two states. Note that the same argument applies if instead of magnetization one speaks about the neutron diffraction magnetic Bragg peak intensities.
Adapted from an idea of Hubertus Luetkens (PSI).

3.3.2. Larmor frequency - magnetic field sensitivity

We have seen in Section 1.6.2 that if a magnetic field is present at the muon site, its spin will precess around the field with an angular velocity

$$\omega_L = \gamma_\mu B_\mu = g_\mu \frac{e}{2M_\mu} B_\mu \quad . \tag{3.10}$$

We look now at the minimum field value that the muon can detect. In typical μSR experiments, the time window of the μSR signal extend to about five muon lifetimes, so say 10 μs. If we consider that we need to see half of a spin precession period to determine the field, we say that the minimum frequency will be $\nu_{min} = 1/T = 0.05$ MHz, corresponding to a minimum field of

$$B_{\mu,min} = \frac{\omega_{L,min}}{\gamma_\mu} = \frac{\nu_{min} 2\pi}{\gamma_\mu} \simeq 3.7 \times 10^{-4} \text{ T} \quad . \tag{3.11}$$

We can now ask ourselves what is the minimum value for an ordered (*i.e.* static) magnetic moment that we can detect. We can obtain a rough estimation by considering that in magnetic systems the internal field sensed by the muon has basically two origins: i) the so called contact hyperfine field due to the polarization of the conduction electrons which have a non-zero probability ($|\Psi(\mathbf{r}_\mu)|^2$) to be at the muon stopping site ($\mathbf{r}_\mu$); ii) the dipolar field created by the surrounding ordered magnetic moments (which is actually the sum of the contributions from all individual moments $\mathbf{m}_i$). We have therefore the internal field at the muon site:

$$\mathbf{B}_\mu = \boxed{\mathbf{B}_c} + \boxed{\mathbf{B}_{dip}} \tag{3.12}$$

- Contact field $\propto e|\Psi(\mathbf{r}_\mu)|^2$

- Dipolar contribution

$$\mathbf{B}_{dip} = \frac{\mu_0}{4\pi} \sum_j \frac{1}{r_j^3} \Big[\frac{(3\mathbf{m}_j \cdot \mathbf{r}_j)}{r_j^2} \mathbf{r}_j - \mathbf{m}_j \Big]$$

$$B_{dip} \simeq \frac{\mu_0}{4\pi} \frac{m}{r^3}$$

The first contribution is not easy to compute, and we concentrate on the dipolar part. Assuming that each ordered moment has a value of $m = 1\,\mu_B$ and that the typical distance between the muon stopping site and an ordered moment is $r = 1$ Å, we obtain $B_{dip} \simeq 1$ T.

Therefore, μSR is capable to detect static moments of the order of 0.001 μ_B, *i.e.* of the order of the nuclear magneton. Hence, even nuclear moments are detectable by μSR.[8]

---

[8]Remember that a Bohr magneton is given as $\mu_B = e\hbar/(2m_e) = 1837 \times \mu_N$, due to the ratio between the proton and electron masses.

3.3.3. Typical time window

As seen the μSR signal time window is typically 10 μs. However, μSR is able detect quite a large dynamical range concerning the magnetic fluctuation and relaxation phenomena. As we will see in Section 4.3, the presence of magnetic fluctuations will result into a muon ensemble depolarization, with a depolarization rate λ of the order of

$$\lambda \propto \gamma_\mu^2 \left\langle B_\mu^2 \right\rangle \nu_c \quad , \tag{3.13}$$

where $\left\langle B_\mu^2 \right\rangle$ is the second moment of the field distribution seen by the muon and ν_c is the characteristic fluctuation frequency of the magnetic field.
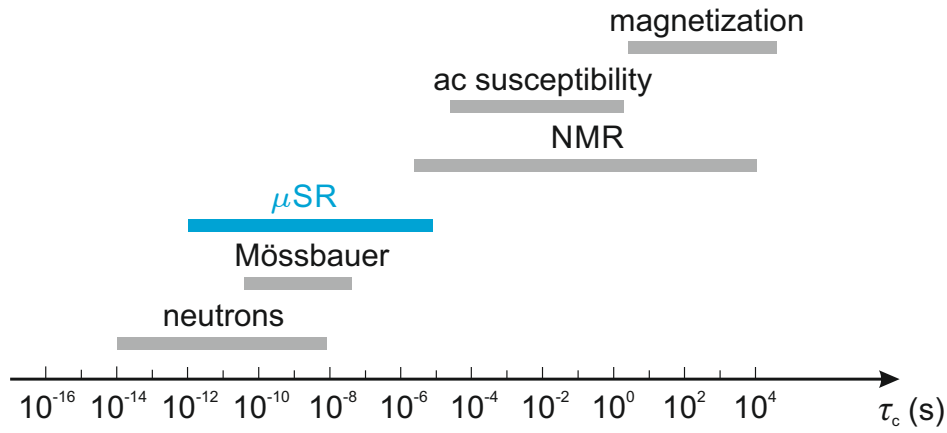
Figure 3.5.: *Comparison of dynamical ranges accessible to different techniques. $\tau_c = 1/\nu_c$ is the characteristic fluctuation time associated with the magnetic fluctuations.*

We see that μSR bridges the gap between NMR and neutron techniques.

3.3.4. Other important features

We list here few other features of the muon probe:

- As said in Section 1.4, the muon is a purely magnetic probe and is free of quadrupolar effects. This considerably simplify the interpretation of the data.

- In addition to its magnetic sensitivity, μSR is also sensitive to random magnetism like for example the so-called "spin glasses". Whereas neutron diffraction needs a well defined magnetic structure in order to observe Bragg magnetic peaks, μSR can detect field distributions.

- Connected to previous point, μSR can detect also extremely short range ordered structures, where neutron scattering is not sensitive.

- As seen, the muon beam is polarized (around 100% for surface muons) and therefore μSR measurements can be performed in zero-field. In addition this polarization is independent of the sample temperature. Therefore, at the opposite of NMR, one here does not require a field which could disturb the system. The polarization in NMR can be calculated to be (see Exercises)

$$P_{z,\,\mathrm{N}} = \frac{\gamma_{\mathrm{N}} \hbar \, (I + 1)}{3 k_{\mathrm{B}} T} B \quad , \tag{3.14}$$

where γ_{N} and I are the gyromagnetic ratio and spin of the nucleus used for NMR.

Taking the ^{63}Cu nucleus [$I = 3/2$ and $\gamma_{\mathrm{N}} = 71.118 \times 10^6$ rad/(s·T)], we obtain a polarization of the order of $4.5 \times 10^{-4} \cdot B/T$, *i.e.* much smaller than in μSR.

In addition, no special isotope is needed for μSR and we do not have restriction in the choice of materials to be studied.

- We have seen that in insulator, the muon will form a bound state called muonium (Mu=$\mu^+ e^-$). This state can be used as a hydrogen isotope for spectroscopy, impurity studies, radical chemistry and reaction kinetics.

3.4. Experimental setup

The experimental setup for a μSR experiment can be divided in few parts:

- The muon beamline transporting the muons from the production target to the experiment (see Section 1.8.3.3 for details). This beamline can incorporate a Wien filter which can be used as filter of spin rotator.

- A detector system (or spectrometer) and its associated electronics, which will detect the incoming muon (in a cw beam) and the produced positrons. The detector system can also accommodate so-called "veto" detectors which will have the task to reject bad events. The spectrometer is the heart of the setup.

- For some experiments, the presence of an external field is desired. This field can serve as calibration purpose or be used to perform so-called Knight-shift experiments (*i.e.* the local susceptibility) or flux line lattices in superconducting materials. The magnet used is either a conventional one (Helmholtz copper coils producing field up to about 1 T) or a superconducting one (with fields up to about 10 T).

- A sample environment. This is usually a cryostat to cool the sample to typically 1.5 K or even lower temperatures using a dilution fridge (down to 0.008 K). For some experiments, oven are used with temperatures reaching 1000 K. Note that as the kinetic muon energy is rather low (at least in surface beams or low-energy muon beams), the cryostat require special design. For example, no thick wall can be used and they are replaced by very thin windows (usually titanium with a thickness of 0.01 mm). For so-called low-energy muons, the full cryogenic is performed without window, with the sample directly exposed to the beam.

In the following Sections, we will shortly describe the typical spectrometer arrangement for a continuous and pulsed beam.

3.4.1. At a "continuous-wave" (cw) beam

As seen, a cw beam is created by a cyclotron (see Section 1.8.1). Actually a cyclotron has a microstructure given by the frequency of the electrical field switching. At PSI, this frequency is 50 MHz, that means that the pion production target will receive bunches of protons every 20 ns. However, due to the finite lifetime of the pion (26 ns), the muon rate at the production target (and even more at the end of the beamline) will be practically continuous (see Fig. 3.6).

This means that the arrival time of the muon at the experiment is unknown (following a Poisson distribution) and that a thin muon detector (M) is necessary just in front of the sample. After the detection of the M-event (that is after the muon implantation), the decay positron will be expected in the positron detectors (P) and the time difference is measured. The detec-

Table 3.1.: *Main µSR setup differences between cw and pulsed beams.*

	cw beam	pulsed beam
Muon rate	limited to avoid pile-up events $\sim 4 \times 10^4$ events/s (time window of $10\,\mu s$)	limited by the muon source and detector granularity $\sim 1 \times 10^5$ events/s
Time resolution	only limited by detectors and electronics down to 50 ps	limited by the muon pulse width about 100 ns
Beam size	can be strongly limited by the use of active veto counters down to few mm^2 no loss of rate	no use of veto possible. flypass method reducing drastically the rate
Sample mass	down to 10 mg	between 0.5 and 1 g
Background B	$\sim 1\%$ time window only up to $10\,\mu s$	essentially background free standard time window $20\,\mu s$
Detector setup	necessity of muon counter, large positron detectors	no need of muon counter, large number (up to 600) positron detectors to cope with the high instantaneous rate

tion of individual *M-P* events leads to a very high time resolution of the spectrometer, only limited by the quality of the detectors and electronics.
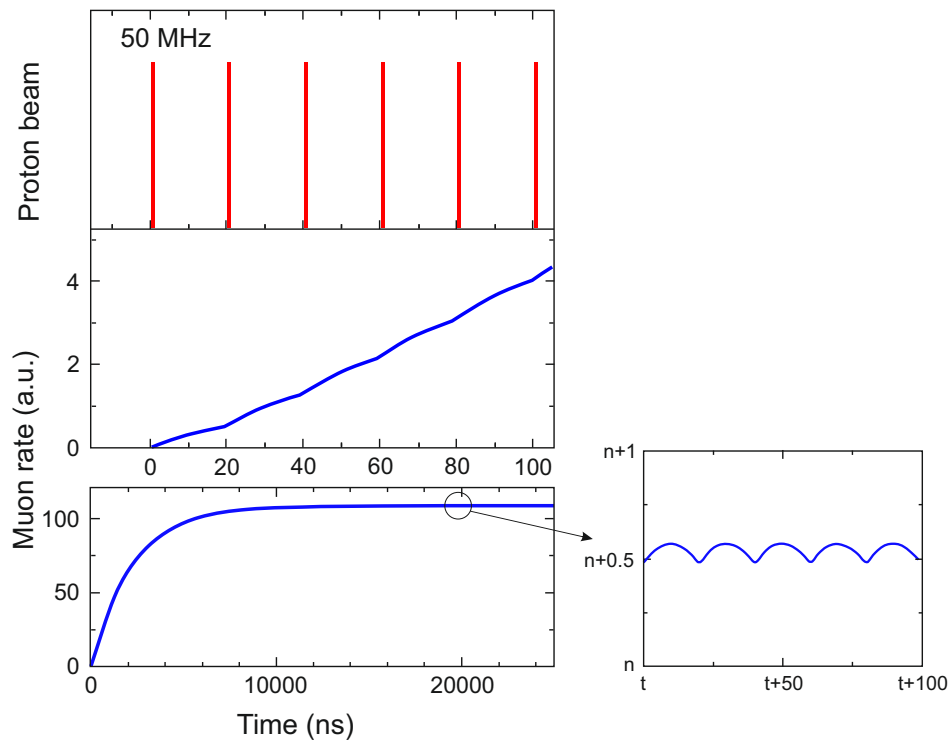
Figure 3.6.: *Time evolution of the muon rate after that the proton beam has been switched ON at time t = 0. After about 20 μs the muon rate is stable and the beam proton time structure of 50 MHz is almost completely washed out. Adapted from an idea of Thomas Prokscha (PSI).*
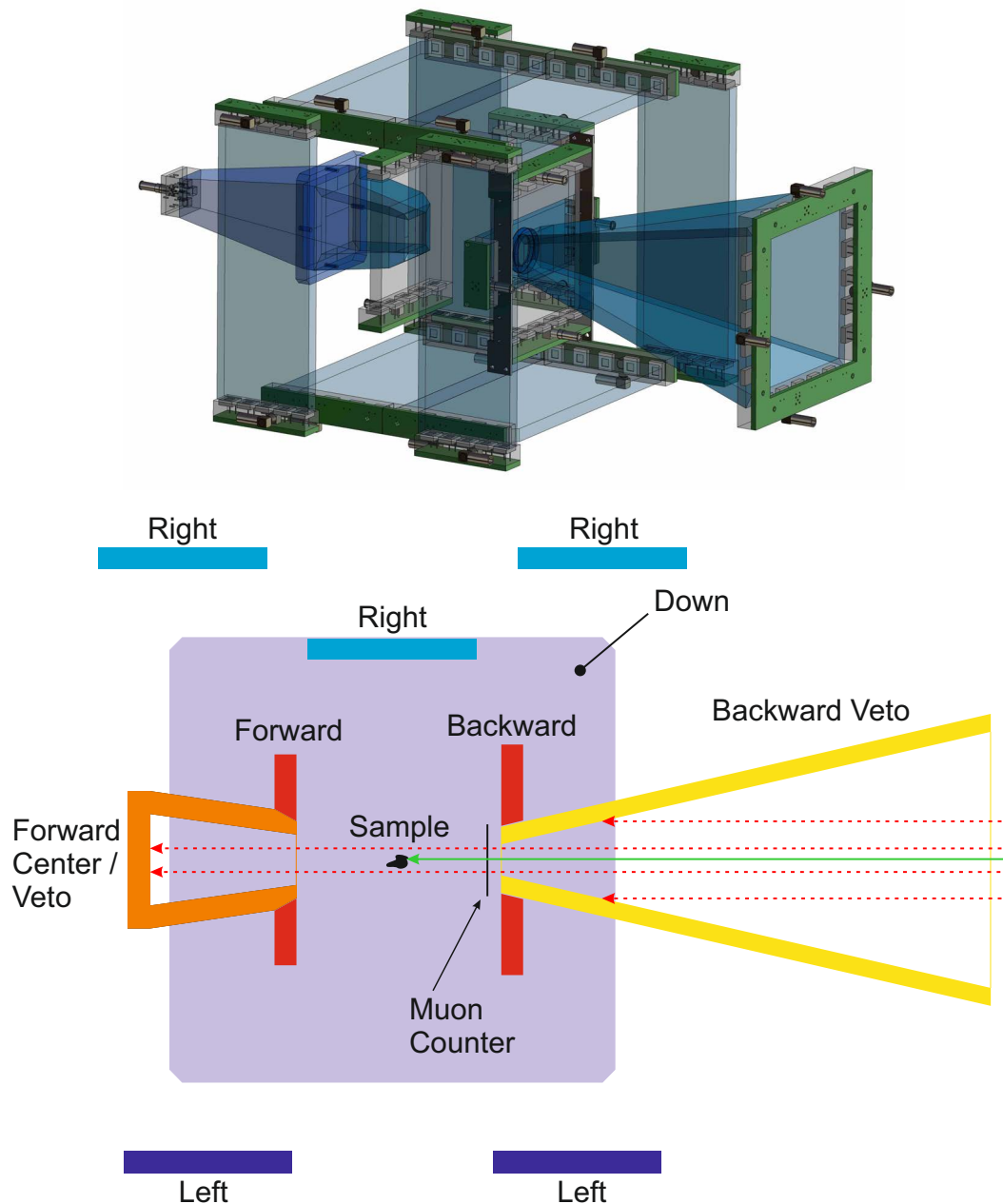
Figure 3.7.: *Schematic view of a typical μSR detector setup at a continuous beamline (Instrument GPS at PSI [33]). Top: 3D-view of the muon and positron detectors where the SiPM-readout is visible. Bottom: Cross-section at the sample level (top view). The muons are entering the spectrometer from the right-hand side, i.e. parallel to the axis of the Backward veto pyramid. The lateral dimension of the Down detector is 10 cm.*

Figure 3.7 shows a typical detector setup. We note few points:

- The positron detectors cover a large fraction of the total solid angle around the sample.

- The granularity of these detectors is very low. As the instantaneous positron rate is rather low, a detector and its associated electronics can easily cope with the rate.

- The presence of different veto detectors (the "pyramids" Backward Veto and Forward Center). Hence a good muon event (M) is defined by the logic

$$M_{\text{good}} = M_{\text{counter}} \cap \overline{(B_{\text{veto}} \cup F_{\text{center}})} \ , \tag{3.15}$$

and therefore only the muons stopping into the sample will produce a signal for the clock (green event on Fig 3.7; the red events do not fulfill the logic condition). This allows one to measure extremely small samples, of the order of 10 mg, at a cw beam. A veto system is not possible at a pulsed beam as we will see in the next Section.

In a cw beam, in order to be sure to correlate one M-event with a P event, the experiment electronics will only allow one muon at a time in the sample in a defined time-window (data gate), *i.e.* if a 2nd muon (or a 2nd positron) arrives prior the end of the data gate then all the concerns events are discarded. Therefore, at a cw beam one often reduces the rate of the incoming muons to avoid pile-up events. On the other hand, as seen, the detection of individual M-P events leads to a very high time resolution of the spectrometer, which is not accessible at pulsed beam.
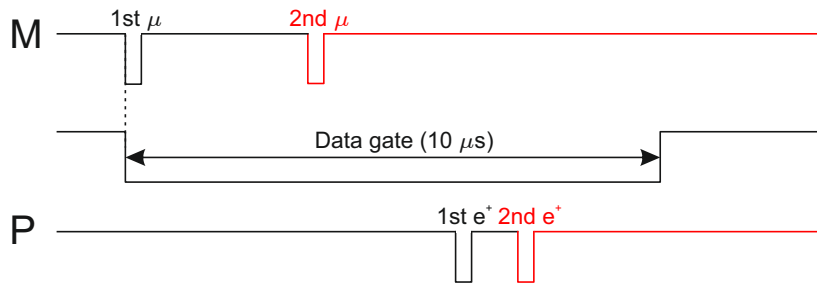
Figure 3.8.: *Timing diagram of a μSR measurement at a cw beam. Here we assume that all the muon events have passed the logic condition defined above. The first muon will start the clock and the data gate. In this data gate only one positron has to be detected. If a 2nd muon or a 2nd positron is detected then the full set of events is rejected. Note that the 1st muon is actually a "good muon" only if there was no other muon event in the past for at least the length of the data gate.*

As the incoming muons are Poisson distributed, *i.e.*

$$f_{\text{Poisson}}(k, \lambda) = \frac{\lambda^k \, e^{-\lambda}}{k!} \ , \tag{3.16}$$

where λ represents the expected number of muons within a given time (*i.e.* the rate of the incoming muons) and k is the number of "unwanted" muon events (we always consider that we have a first muon event which defines the data gate). As we do not want any "unwanted" muon events within twice the data gate Δt (see caption Fig. 3.8), we have $k = 0$ and $\lambda = 2\Delta t R_\mu$, where R_μ is the total good muon rate. Therefore the accepted muon rate as a function of the total good muon rate will be

$$R_{\mu,\text{acc}} = R_\mu \times f_{\text{Poisson}}(0, \lambda) = R_\mu \times e^{-2 \, \Delta t \, R_\mu} \ . \tag{3.17}$$
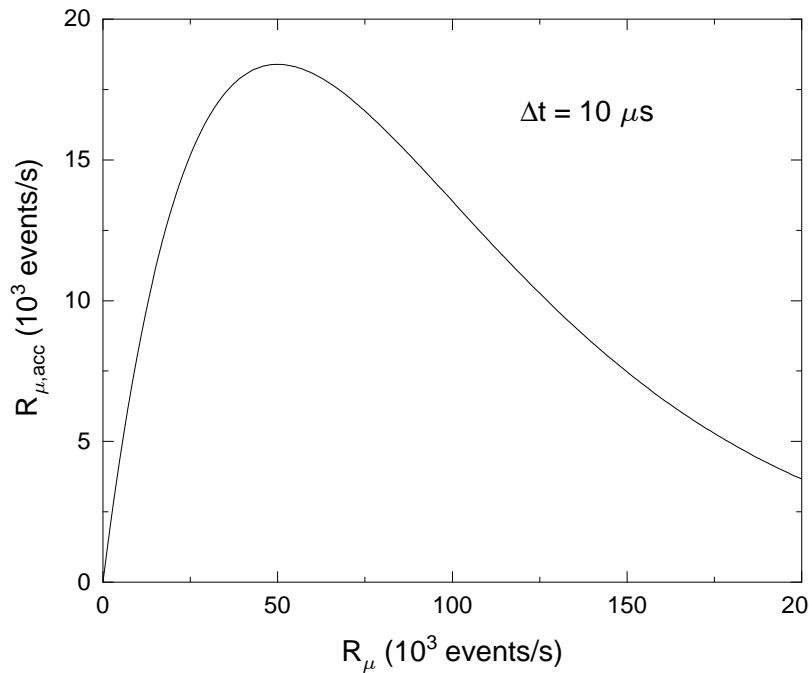
Figure 3.9.: *Accepted rate as a function of the incoming rate for a data gate of 10 μs (see also Fig. 3.8). In reality, the rate is even kept lower to avoid a too high background (parameter B in Eq. 3.3).*

3.4.2. At a pulsed beam

A pulsed muon beam is created by a synchrotron (see Section 1.8.1). The pulsed structure of the accelerator is typically 100 ns, with a repetition rate of 50 Hz. After the production target, the muon beam created will conserve this structure with a rather asymmetric shape of the pulse due to the pion lifetime.

This means that the muons will arrive grouped (with 100 ns) at the sample and an individual detection of the muons is not possible. This pulse structure has the advantage that a muon detector is not required and the implantation time is given by this pulse. This means that all the decay positrons of a pulse are measured at once. This permit high rates as pile-up events are not a problem. On the other side, this high rate requires a high granularity (segmentation) of the detectors to reduce to a minimum the loss of positron signals due to double hits.

A big disadvantage of a pulsed machine is that the time resolution is given by the pulse width, whereas at a continuous beam line the time resolution is determined by the muon counter which is typically much better than 1 ns (down to 50 ps). A pulsed beam has in principle a lower background than a continuous beam as "contamination" from the beam is present after the pulse. A pulsed muon beam also allows an exploitation of a pulsed environment using for example external stimuli (laser, etc).
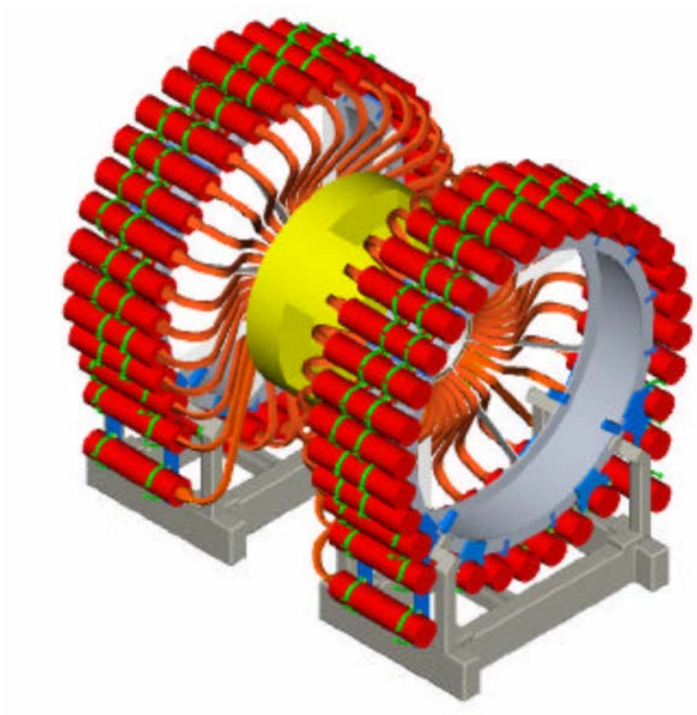
Figure 3.10.: *Schematic view of a μSR instrument at a pulsed beam. The red cylinders are photomultipliers connected to positron detectors (here 64 in total, "MUSR" instrument at ISIS). The diameter of the frame where the photomultipliers are mounted is more than one meter. Newer instruments can have up to 600 detectors.*

3.4.3. Muon-on-request setup

At PSI, the so-called Muon On REquest (MORE) electrostatic kicker device allows only one muon at the time in the apparatus. This reduces the background, while keeping the excellent time resolution of the continuous beam.

3.5. The different measurement geometries

Depending on the type of information that we want to extract from the μSR measurements, different geometries can be adopted. In the following, we will briefly introduce these geometries.

3.5.1. ZF & LF geometry

The zero-field technique (often called ZF) is the most important technique to investigate magnetic systems. As its name indicates, measurements are performed in zero-field environment and the goal is to measure effects on the muon polarization produced by the internal field of the sample.[9] ZF experiments with surface muons are usually performed with the muon spin pointing antiparallel to the muon beam direction, corresponding to the "natural" spin direction.[10]
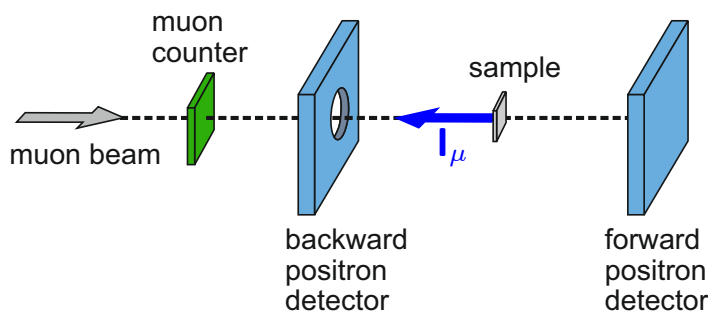
Figure 3.11.: *Zero-field (ZF) μSR geometry. In reality, the detectors are located about 2 cm away from the sample. The denomination of the detectors refers to the beam direction. Adapted from P. Dalmas de Réotier and A. Yaouanc [34].*

As we will see, static and fluctuating internal magnetic fields can have an effect on the muon polarization and therefore can be detected in ZF experiments. In order to differentiate between static and fluctuating internal magnetic fields, so-called longitudinal-field experiments are performed where the externally applied magnetic field is along the initial muon spin direction.

---

[9]Note that the muon gyromagnetic ratio is so large that a special dynamical compensation of the earth and surrounding field is needed to perform ZF experiments in ideal conditions. The compensation is usually better than 2×10^{-6} T.

[10]Note that ZF experiments can also be performed by rotating the spin by 90°with a spin rotator. In this case the Up and Down detectors are used.
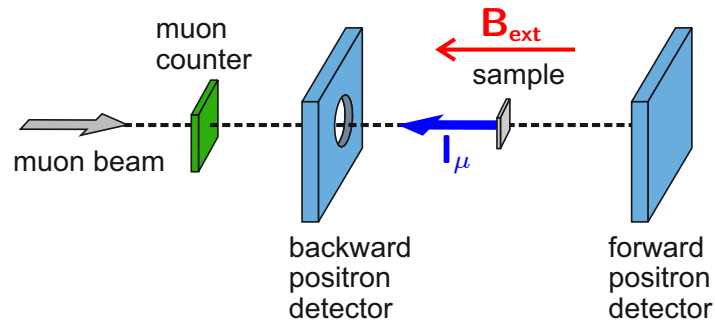
Figure 3.12.: *Longitudinal-field (LF) μSR geometry. The externally applied magnetic field is along the initial muon spin direction. Adapted from P. Dalmas de Réotier and A. Yaouanc [34].*

By convention and following the literature, we will adopt for the z-axis the direction of the initial muon polarization (initial quantization axis). With the Backward and Forward detectors, we will therefore measure $P_z(t)$.
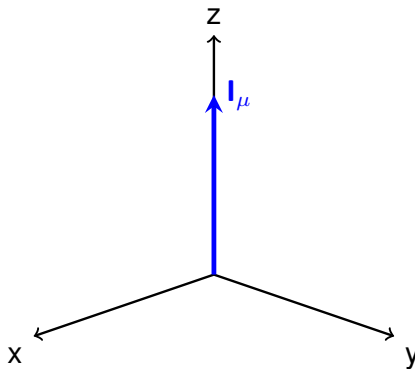
Figure 3.13.: *Definition of the axes in the laboratory frame for ZF and LF experiments [(x, y, z) is the usual orthogonal reference frame].*

Figure 3.14 exhibits basics examples of a μSR signal recorded in the Backward detector during a ZF experiment. If the sample is in the paramagnetic state, no static field of electronic origin is seen by the muon and therefore its spin will not show an evolution in time.[11] On the other hand, if a measurement is performed on a magnetic sample, the muon polarization will change as a function of time due to the Larmor precession around the local field (see our analogy with lighthouses in Fig. 3.3).

---

[11]We will later see that the nuclear moments will produce a slight change of the polarization.
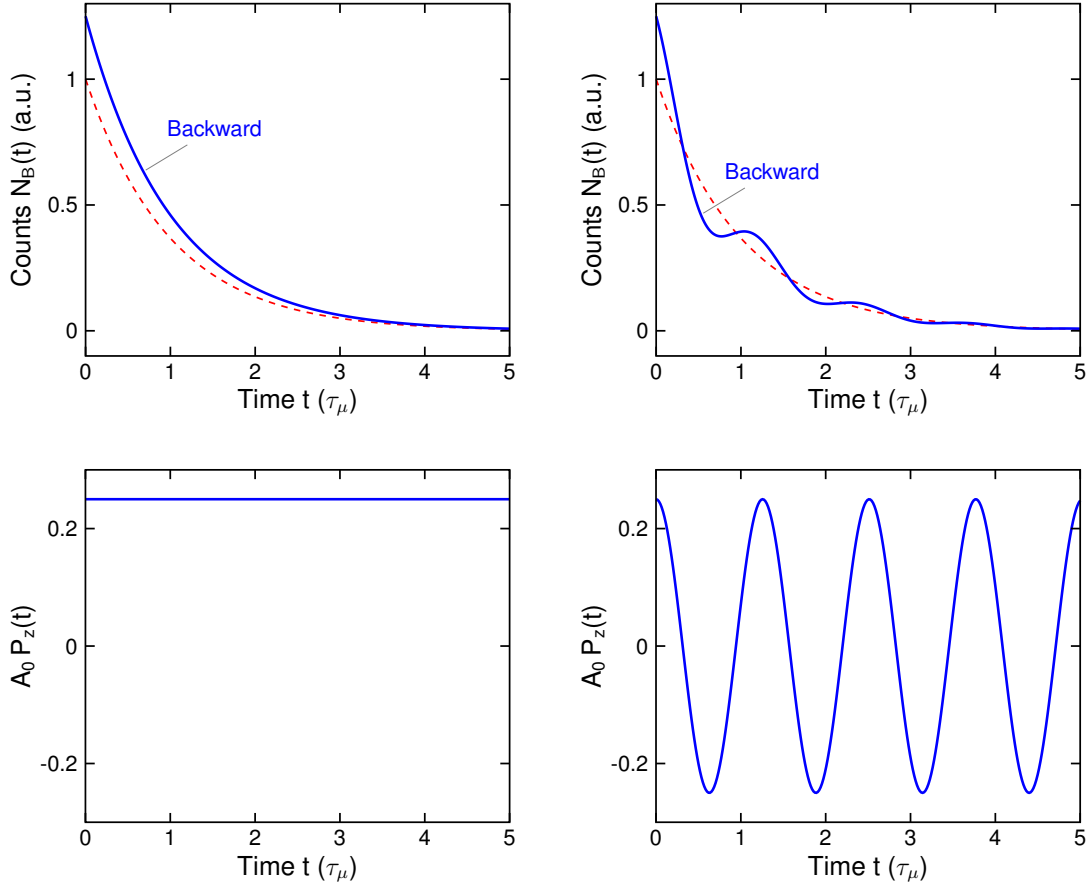
Figure 3.14.: *The top panels display schematics of the signals obtained in the Backward detector for paramagnetic (left) and magnetic (right) samples. In the paramagnetic sample, no internal field is present and the muon polarization will remain fixed, resulting in a constant μSR signal (bottom left). For a magnetic sample, the muon spin precesses around the local field and a Larmor frequency is observed, resulting in an oscillation in the μSR signal. The μSR signal in the Forward detector will have the opposite sign as* $\mathbf{P}(t) \cdot \hat{\mathbf{n}}_F = -\mathbf{P}(t) \cdot \hat{\mathbf{n}}_B$.

As clear from the caption of Fig. 3.14, the opposite detectors Forward and Backward actually contain the same information. Therefore, the μSR signal can be obtained either by considering the individuals detectors or it can be directly obtain by combining the raw signals of the two opposite detectors. Recalling Eq. 3.3, we have (by forgetting the background)

$$N_B(t) = N_0 \, e^{-\frac{t}{\tau_\mu}} \left[1 + A_0 \, \mathbf{P}(t) \cdot \hat{\mathbf{n}}_B \right] \text{ and}$$

$$N_F(t) = N_0 \, e^{-\frac{t}{\tau_\mu}} \left[1 + A_0 \, \mathbf{P}(t) \cdot \hat{\mathbf{n}}_F \right]$$

$$= N_0 \, e^{-\frac{t}{\tau_\mu}} \left[1 - A_0 \, \mathbf{P}(t) \cdot \hat{\mathbf{n}}_B \right] \ .$$

From these two equations describing the raw counts in the detectors, we can directly extract the μSR signal

$$A(t) = A_0\, P(t) = \frac{N_\mathrm{B}(t) - N_\mathrm{F}(t)}{N_\mathrm{B}(t) + N_\mathrm{F}(t)} \quad . \tag{3.18}$$

As the efficiency and solid angle of the detectors are not identical, one introduce one additional parameter (called α, see Exercises) in Eq. 3.18.

3.5.2. TF geometry

The so-called transverse-field geometry (TF) refers to experiments where an *external* magnetic field is applied. This configuration is used in several situations. Some examples are:

Magnetism:
To determine the magnetic transition temperature ("weak TF" measurements).
To test the homogeneity of the sample.
To determine the Knight shift, *i.e.* the local susceptibility at the muon site. From these measurements also the muon stopping site can be deduced.

Superconductivity:
To obtain the absolute value and temperature dependence of the London penetration depth.
To determine the coherence length of the superconducting state.
To study the vortex structure and vortex dynamics of the so-called Abrikosov state.
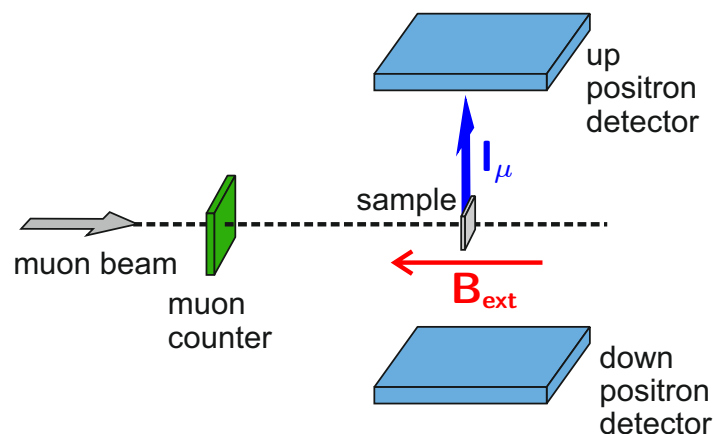
Figure 3.15.: *Transverse-field (TF) μSR geometry. The externally applied magnetic field is along the muon beam (surface beam) to avoid a beam bending through the Lorentz force. The initial muon spin direction is (ideally) 90° with respect to the beam direction (rotation by a spin rotator up-stream).[12]Adapted from P. Dalmas de Réotier and A. Yaouanc [34].*

---

[12]As seen in Section 1.8.3.3, for a high energy beam no spin-rotator can be used.

Here also, by convention and following the literature, we will adopt for the z-axis the direction of the applied magnetic field (quantization axis). With the Up and Down detectors, we will therefore measure $P_x(t)$.
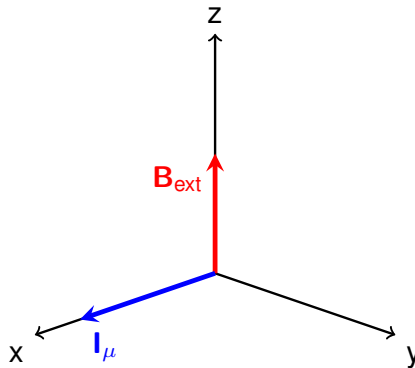
Figure 3.16.: *Definition of the axes in the laboratory frame for TF experiments [(x, y, z) is the usual orthogonal reference frame].*
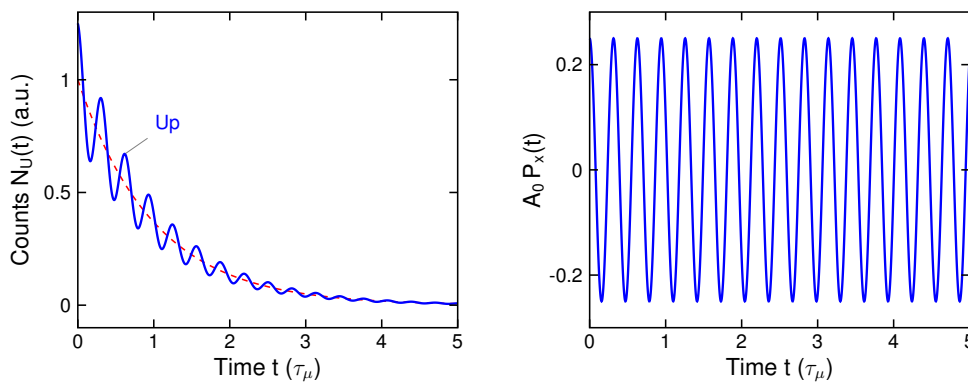
Figure 3.17.: *Schematics of the signal obtained in the Up detector. The field seen by the muon is a combination of the externally applied field and of the internal fields. Here again, the μSR signal in the Down detector will have the opposite sign as $\mathbf{P}(t) \cdot \hat{\mathbf{n}}_D = -\mathbf{P}(t) \cdot \hat{\mathbf{n}}_U$.*

4. Depolarization Functions

In this Chapter we will look at the muon polarization function in different cases. We will differentiate between the situation when the internal field seen by the muon is static (*i.e.* constant over time $t \gtrsim 5 - 20 \times \tau_\mu$), and the one where the local field experienced by the muon is fluctuating. In the last Section, we will discuss the situation when an external transverse field is applied.

4.1. Depolarization function for static internal fields (ZF geometry)

We look first at the characteristic μSR signal, when a muon ensemble experienced an internal field forming an angle θ with respect to the initial polarization.
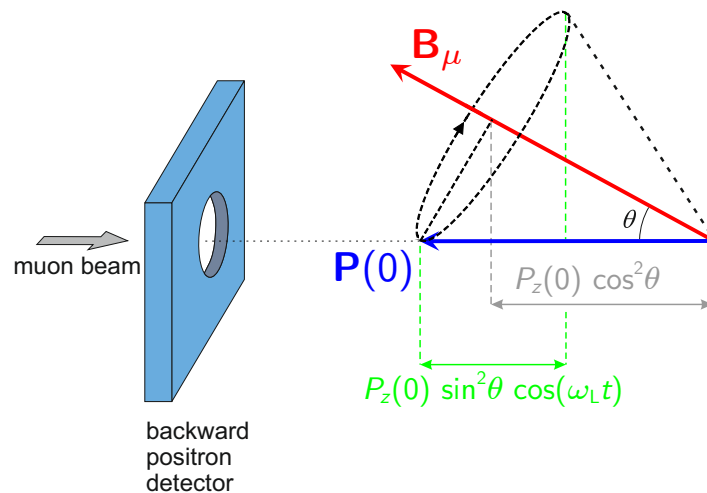
Figure 4.1.: *Muon ensemble experiencing an internal field forming an angle θ with respect to the initial polarization.*

When a muon ensemble sense an internal field forming an angle θ with respect to the initial polarization (assumed antiparallel to the muon beam $\rightarrow$ surface beam), then the polarization will start to precess about the internal field. The time polarization along the z-axis (defined

in ZF, as seen, as the inital polarization direction) will be

$$P_z(t) = \cos^2\theta + \sin^2\theta \, \cos(\omega_\mathrm{L}t)$$
$$= \cos^2\theta + \sin^2\theta \, \cos(\gamma_\mu B_\mu t) \ , \tag{4.1}$$

where we have assumed that $P_z(0) = 1$. We see that $P_z(t)$ does not depend on the azimuthal angle ϕ. To be complete, we give also the time evolution for $P_x(t)$ and $P_y(t)$ (still assuming that $P_z(0) = 1$)

$$P_x(t) = \frac{1}{2}\sin 2\theta \sin\phi[1 - \cos(\gamma_\mu B_\mu t)] - \sin\theta\cos\phi\sin(\gamma_\mu B_\mu t)$$
$$P_y(t) = \frac{1}{2}\sin 2\theta \cos\phi[1 - \cos(\gamma_\mu B_\mu t)] + \sin\theta\sin\phi\sin(\gamma_\mu B_\mu t) \ . \tag{4.2}$$

To obtain Eq. 4.1, the initial polarization vector $\mathbf{P}(0)$ has first to be decomposed in the magnetic field frame. The time evolution $\mathbf{P}(t)$ is obtained in the magnetic field frame and then projected back to the vector $\hat{\mathbf{n}}$ defining the direction of the detectors. Hence the first projection gives:

$$\mathbf{P}(t) = [\mathbf{P}(0)\cdot\hat{\mathbf{b}}]\hat{\mathbf{b}} + \left(\mathbf{P}(0) - [\mathbf{P}(0)\cdot\hat{\mathbf{b}}]\hat{\mathbf{b}}\right)\cos(\gamma_\mu B_\mu t) + [\mathbf{P}(0)\times\hat{\mathbf{b}}]\sin(\gamma_\mu B_\mu t) \ , \tag{4.3}$$

where the $\hat{\mathbf{b}} = \mathbf{B}_\mu/B_\mu$ defines the direction of the field. The second projection is obtained by doing the scalar product $\mathbf{P}(t)\cdot\hat{\mathbf{n}}$.

By making use of Eq. 4.1, we immediately see that for a single crystal one can determine the direction of the internal fields by studying the amplitude of the oscillating signal when rotating the sample compare to the beam direction.

In reality, in many cases the muon ensemble will not see an unique value and direction for $\mathbf{B}_\mu$ but rather a distribution of fields $f(\mathbf{B})$, and one will get

$$P_z(t) = \int f(\mathbf{B})\Big[\ \cos^2\theta\ +\ \sin^2\theta\cos(\gamma_\mu Bt)\ \Big]d\mathbf{B} \tag{4.4}$$

- Non-oscillating part
- Oscillating part

4.1.1. The simple case: single value of field

4.1.1.1. Single-crystal case

The most easiest case is the one where the muon ensemble senses a field in a given direction θ. This is the ideal situation in a single crystal. For this situation, we have a muon polarization given by Eq. 4.1, *i.e.*

$$P_z(t) = \cos^2\theta + \sin^2\theta\,\cos(\gamma_\mu B_\mu t) \ . \tag{4.5}$$

For example if

- $\theta = \pi/2$: we have of course
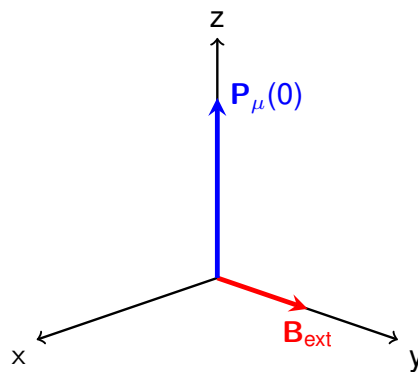
$$P_z(t) = \cos(\gamma_\mu B_\mu t) \ . \tag{4.6}$$
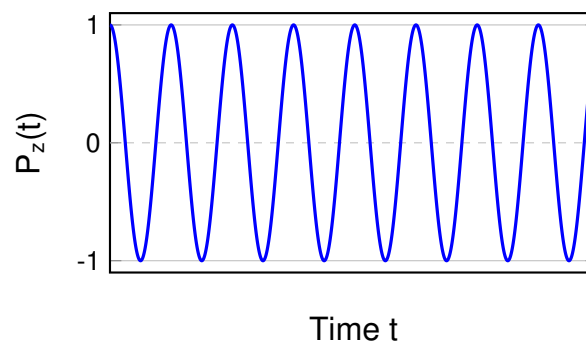
Figure 4.2.: *Time evolution of the muon polarization in a magnetic ideal single crystal. For $\theta = \pi/2$ no non-oscillating part is present in the μSR signal [which is $A_0P(t)$] when looking at the z direction defined by the $\mathbf{P}(0)$ direction.*

- $\theta \neq \pi/2$: we have
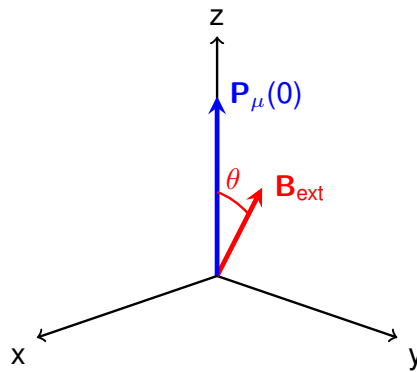
$$P_z(t) = \cos^2\theta + \sin^2\theta \ \cos(\gamma_\mu B_\mu t) \ \ . \tag{4.7}$$
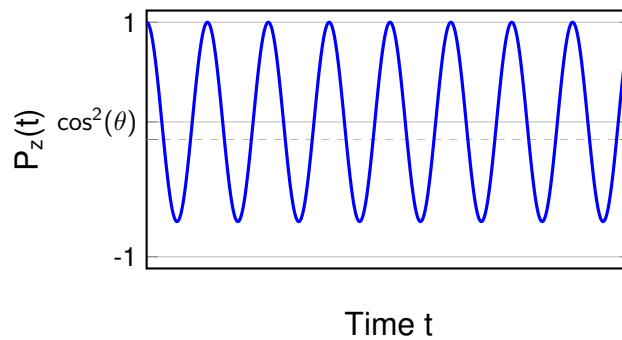
Figure 4.3.: *Time evolution of the muon polarization in a magnetic ideal single crystal. For $\theta \neq \pi/2$ a non-oscillating part is present in the μSR signal [which is $A_0 P(t)$] and the amplitude of the oscillation is reduced. The spin precesses on a cone around the field.*

- And if $\theta = 0$ the muon spin will not precess and the μSR signal will remain a constant

$$P_z(t) = P(0) \ \ . \tag{4.8}$$

Hence, by performing experiments for different sample orientation (*i.e.* turning the sample with respect to the beam) one can determine the direction of the field at the muon site (in addition to the field strength which is provided by the Larmor frequency).

Some examples   An example is given by the measurements performed on the heavy fermion compound UGe_2 [35], which is a remarkable system exhibiting under pressure a coexistence between ferromagnetism and superconductivity.[1] In this system (orthorhombic structure *Cmmm*), one determine the presence of two muon stopping sites (2*b* and 4*i* sites), *i.e.* we have two muon ensembles. From the μSR measurements performed at ambient pressure, one clearly determine that for both sites, the internal fields are directed along the *a* crystallographic axis.
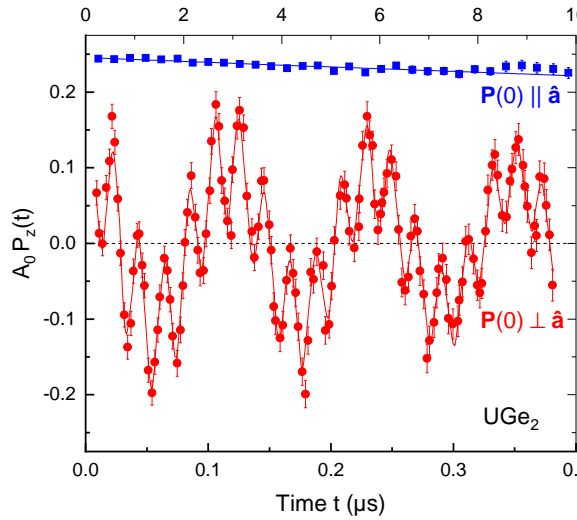
Figure 4.4.: *μSR signal measured well into the ferromagnetic state of UGe_2 ($T_C \simeq 50$ K). When the initial muon polarization is along the a-axis, no precession are seen (blue curve). This is the situation with $\theta = 0$. When the initial muon polarization is perpendicular to the a-axis, nice spontaneous frequencies are seen, with a signal oscillating around 0. This is the situation with $\theta = \pi/2$. The observed signal correspond to two frequencies attributed to the two muon ensembles (two stopping sites).*

Another example is the spin-chain antiferromagnet system Li_2CuO_2 [36]. Here, one has even three stopping sites. In the magnetic state, no precession are seen when the initial muon polarization is along the *a*-axis (not shown), whereas nice precessions (around 0) are detected when $\mathbf{P}(0) \perp \hat{\mathbf{a}}$ (see Fig. 4.5).

---

[1]Usually for normal BCS superconductor, as the Cooper pairs are formed by $|+\rangle$ and $|-\rangle$ spin states, the magnetic field tend to destroy the superconducting state.
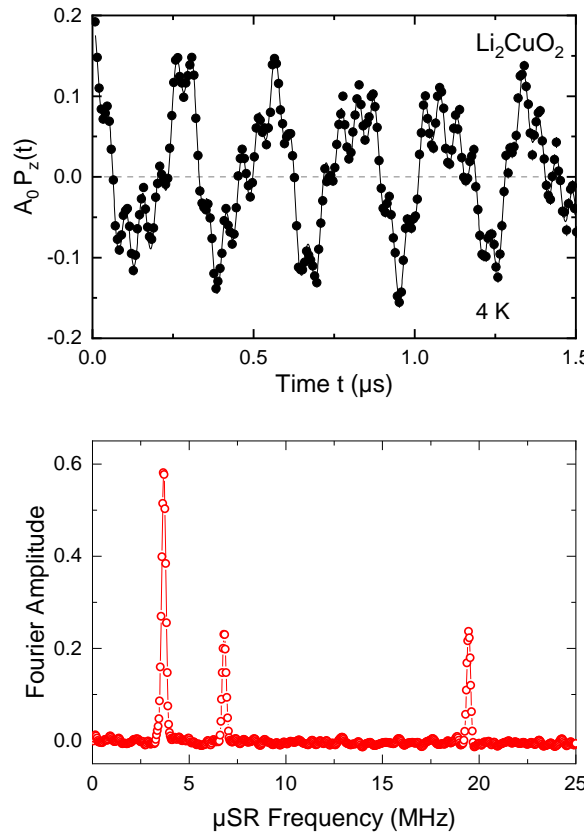
Figure 4.5.: *μSR signal (here called "Asymmetry") measured in the antiferromagnetic state of Li_2CuO_2. When the initial muon polarization is along the a-axis, no precession are seen (not shown). When the initial muon polarization is perpendicular to the a-axis, three spontaneous frequencies are seen, with a signal oscillating around 0. The observed signal correspond to frequencies attributed to the three muon ensembles (three stopping sites). The right-hand side panel shows the Fast Fourier Transform of the μSR signal.*

4.1.1.2. Polycrystal case

A polycrystalline sample is composed by a multitude of crystallites aligned randomly (corresponding to a powder). Therefore the initial muon polarization will point randomly with respect to the crystallographic axes of the crystallites. For a magnetic system, the muon ensemble will therefore see a constant value of the internal field B_μ, but $\mathbf{B}_\mu$ will have a random direction isotropically distributed, *i.e.* pointing on a sphere with respect to $\mathbf{P}(0)$.
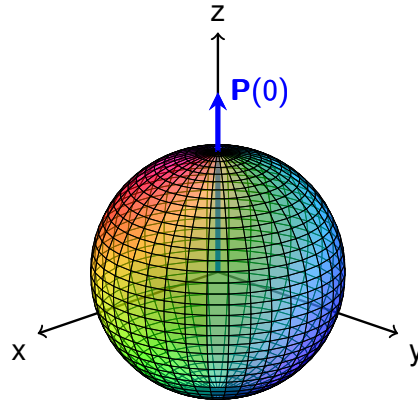
In a polycrystalline sample, the vector of the internal field will have an arbitrary direction with respect to the muon polarization.
Its probability distribution function can be written in polar coordinates

$$f(\mathbf{B})d\mathbf{B} = f(\mathbf{B})B^2 \sin(\theta)\,d\theta\,d\phi\,dB \quad . \tag{4.9}$$

As $f(\mathbf{B})$ is isotropic, if we integrate over the angles, we get (see Exercises)

$$f(\mathbf{B})d\mathbf{B} = \frac{f(|\mathbf{B}|)}{4\pi} \sin(\theta)\,d\theta\,d\phi\,dB \quad . \tag{4.10}$$

As the distribution $f(|\mathbf{B}|)$ is a δ-function (see Fig. 4.7), by pluging $f(\mathbf{B})$ in the Eq. 4.4 we finally get (see Exercises)

$$P_z(t) = \frac{1}{3} + \frac{2}{3}\cos(\gamma_\mu B_\mu t) \quad . \tag{4.11}$$

The 1/3 and 2/3 components can be qualitatively understood by considering that the local field is random in all directions, *i.e.* about 1/3 is parallel or antiparallel to the initial muon spin direction and about 2/3 is perpendicular.

The physicist has therefore to keep in mind that if a non-oscillating 1/3-term is observed, this does not (always) indicate the direction of the internal field (*i.e.* a situation where $\cos^2\theta = 1/3$) but more probably this reflects the presence of differents crystallites in his sample. Note that so far we have assumed that all the muons see the same value of the field (though in different directions).

An important point is that if the frequency is too high compared to the time resolution of the instrument, the 2/3-term will be lost and one remain with a 1/3-term non-oscillating in the magnetic phase. This is often the case in pulsed muon sources where the time-resolution is of the order of 100 ns and therefore frequencies higher than 10 MHz will be completely lost. In cw sources like PSI, this problem is very much reduced as the resolution can be as good as 50 ps.
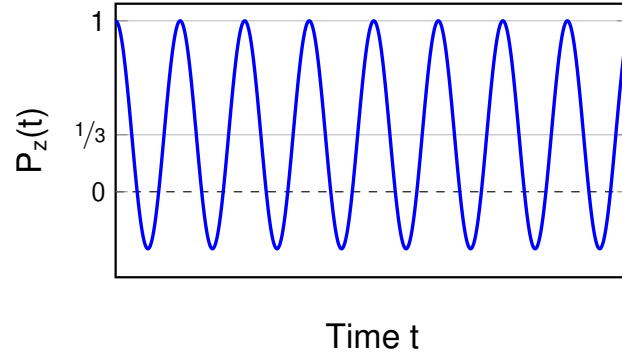
Figure 4.6.: *Time evolution of the muon polarization in an ideal polycrystalline magnetic system. Note the non-oscillating part at 1/3.*

Note that so far we have assumed that all the muons see the very same value of the field (though in different directions). This is of course the ideal case and in real life the magnetic structure will always carry some disorder producing a distribution of the fields around a mean value $\langle B_\mu \rangle$. If we assume that the distribution is Gaussian, we have

$$f(|\mathbf{B}|) = \frac{1}{\sqrt{2\pi \langle \Delta B^2 \rangle}} \exp\left[-\frac{(B - \langle B_\mu \rangle)^2}{2\langle \Delta B^2 \rangle}\right] \ , \tag{4.12}$$

where $\langle \Delta B^2 \rangle$ is the second moment (variance) of the distribution

$$\begin{aligned}
\langle \Delta B^2 \rangle &= \langle (B - \langle B_\mu \rangle)^2 \rangle \\
&= \langle B^2 \rangle - \langle B_\mu \rangle^2 \\
&= \int (B - \langle B_\mu \rangle)^2 f(|\mathbf{B}|) dB \ .
\end{aligned} \tag{4.13}$$
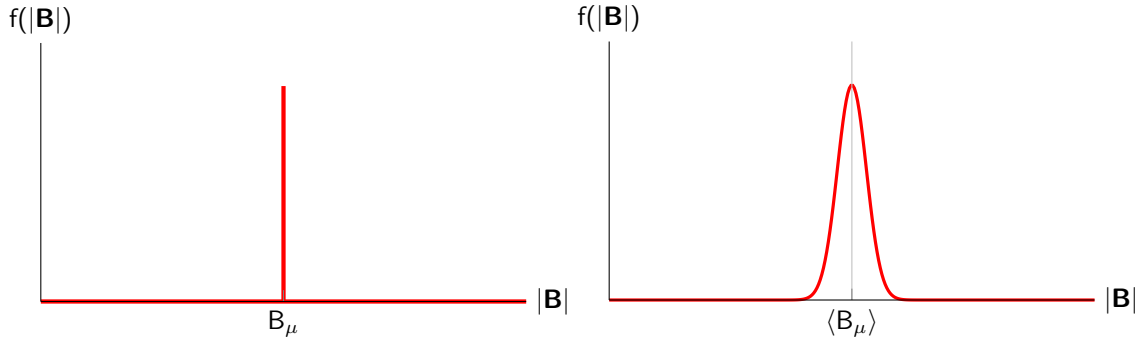
Figure 4.7.: *Left: ideal field distribution for the field value in a polycrystalline sample. Right: more real distribution with a width determined by the intrinsic disorder (Gaussian distribution, see Eq. 4.12).*

Using Eq. 4.10, we introduce the Gaussian field distribution (Eq. 4.12) into the equation for the time dependence of the polarization (Eq. 4.4) and integrate. We get

$$
\begin{aligned}
P_z(t) &= \frac{1}{3} + \frac{2}{3}\cos(\gamma_\mu \langle B_\mu \rangle t)\ \exp\left[-\frac{1}{2}\gamma_\mu^2 \langle \Delta B^2 \rangle t^2\right] \\
&= \frac{1}{3} + \frac{2}{3}\cos(\gamma_\mu \langle B_\mu \rangle t)\ \exp\left[-\frac{\sigma^2 t^2}{2}\right]\ ,
\end{aligned}
\tag{4.14}
$$

where we have defined the depolarization rate $\sigma = \sqrt{\gamma_\mu^2 \langle \Delta B^2 \rangle}$.
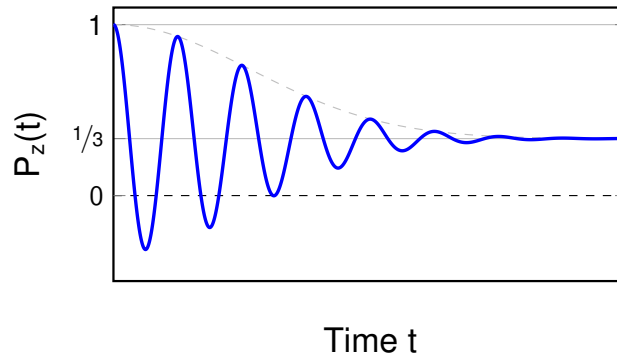
Figure 4.8.: *Time evolution of the muon polarization in a realistic polycrystalline magnetic system. A Gaussian field distribution causes a Gaussian depolarization (envelope). By measuring the depolarization rate σ, one directly determines the second moment $\langle \Delta B^2 \rangle$ of the Gaussian distribution.*

As shown on Fig. 4.8, one can determine the depolarization rate (by fitting Eq. 4.14 to the data and therefore obtain directly the second moment of the field distribution.

Some examples The large majority of the measurements performed on magnetic systems are done on polycrystal and the literature is full of examples of system showing the so-called 1/3-term (or tail). We present here only few examples.

MnP is a quite interesting system showing at room pressure a ferromagnetic state at high temperature and a helical state at low temperatures. Under pressures the magnetic state is changed and one also observed superconductivity. This system has been extensively studied by μSR [37] using polycrystalline samples. Figure 4.9 exhibits a typical μSR spectra in the ferromagnetic state.
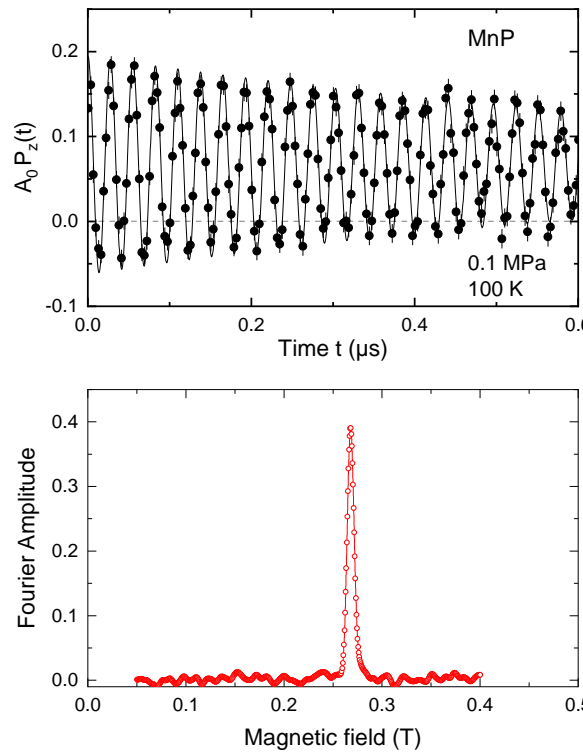
Figure 4.9.: *μSR signal recorded in a polycrystalline sample of MnP in the ferromagnetic state. Note the spontaneous oscillation around 1/3 of the total signal. Note also the very weak depolarization (though the time window shown is rather short) indicating a rather high quality sample. This is of course also evidenced by the very sharp width of the signal in the FFT.*

Another example is furnished by the iron-based high-T_c superconductors discovered in 2008 by the group of Hideo Hosono [38]. In these systems, superconductivity and magnetism compete. μSR has been instrumental in determining the magnetic properties as the ordered moment is small ~ 0.3 μ_B (but still quite large for μSR). The so-called "1111" family shows magnetism in the absence of doping [39].
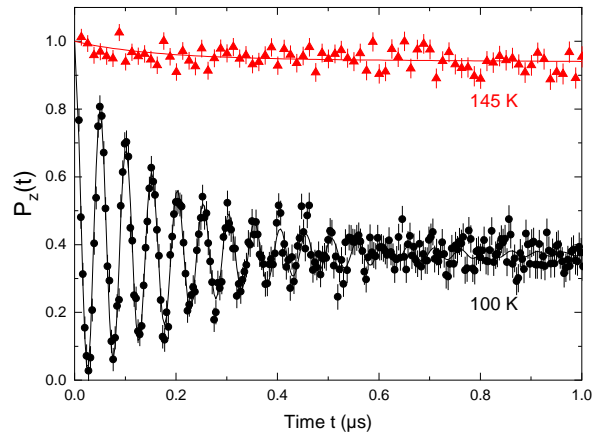
Figure 4.10.: *μSR signals recorded in a polycrystalline sample of LaFeAsO in the paramagnetic state (145 K) and in the antiferromagnetic state (100 K). Note the spontaneous oscillation around 1/3 of the total signal. Note also the strong depolarization reflecting a quite disordered magnetic structure.*

(a) *μSR*
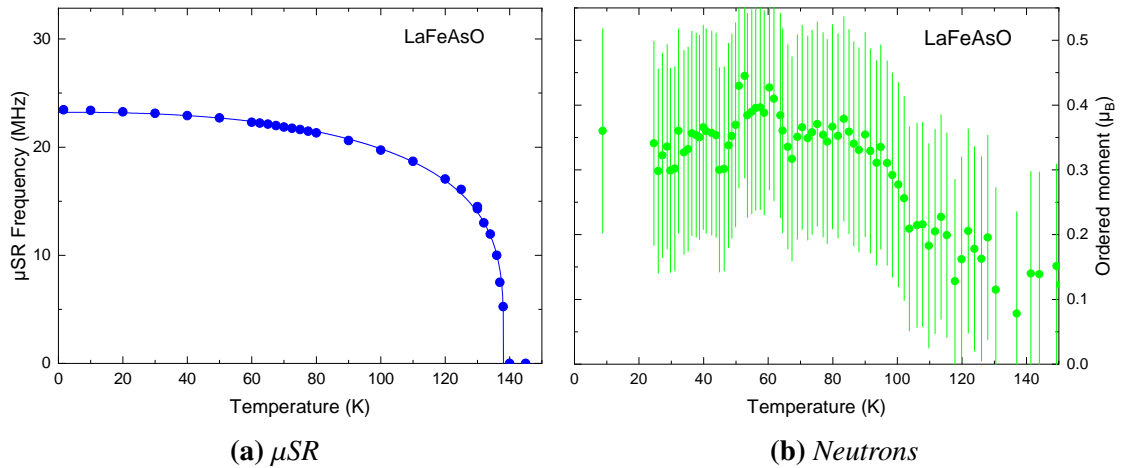
(b) *Neutrons*

Figure 4.11.: *Temperature dependence of the frequency (μSR) and of the ordered magnetic moment extracted from the Bragg peak intensity obtained from neutron scattering experiments. Note the precision of the μSR points. Note also that here also the neutron data are shown by assuming that the full volume is magnetic (which is indeed the case here).*

4.1.2. Randomly oriented fields

In this Section, we will see the effect on the muon polarization if the surrounding is randomly oriented. This disorder will create for each crystallographic direction a field distribution at the muon site which will be centered around 0. We will differentiate between the case where this field distribution is Gaussian and Lorentzian.[2]

4.1.2.1. Gaussian distribution

A Gaussian distribution of fields along each Cartesian directions is obtained in the case of a dense arrangement of randomly oriented moments (for example nuclear moments, which on the μSR time scale can be considered as static) and is justified by the central limit theorem.[3]
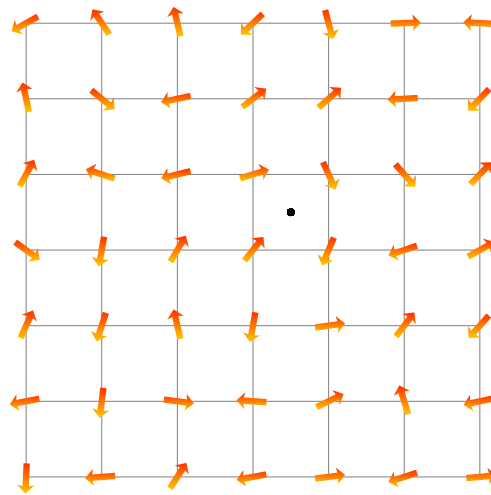
Figure 4.12.: *Muon stopping (black dot) at an interstitial site for which the surrounding presents randomly oriented magnetic moments.*

For each Cartesian direction a Gaussian field distribution occurs with

$$f(B_\alpha) = \frac{1}{\sqrt{2\pi\langle\Delta B^2\rangle}} \exp\left[-\frac{B_\alpha^2}{2\langle\Delta B_\alpha^2\rangle}\right] \; , \tag{4.15}$$

with $\alpha = x, y, z$ and $\langle\Delta B_\alpha^2\rangle$ is the second moment of the field distribution along one Cartesian direction. We assume that along the three directions we have the same width of the distribution.

---

[2]Note that this situation is different from the one that we encountered in Section 4.1.1.2, where we had only a slight variation of the field around its mean value, which was considered $\langle B_\mu\rangle \gg 0$. For a generalization, see Section 4.1.3.

[3]The Central Limit Theorem specifies that the sampling distribution of the sample mean is, approximately, normally distributed, regardless of the distribution of the underlying random sample.

As we have that $\langle B_\alpha \rangle = 0$, we can write

$$\langle \Delta B_\alpha^2 \rangle = \langle (B_\alpha - \langle B_\alpha \rangle)^2 \rangle$$
$$= \langle B_\alpha^2 \rangle \ . \tag{4.16}$$

f(B$_\alpha$)

B$_\alpha$
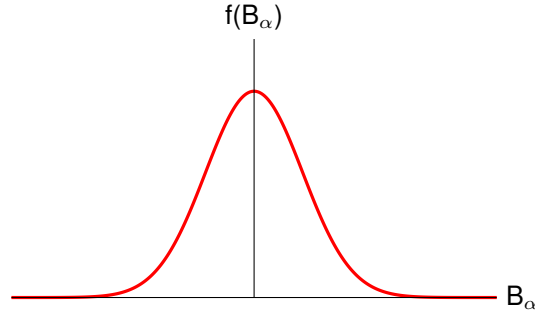
Figure 4.13.: *Distribution of the field along one Cartesian direction.*

Here again we have

$$f(\mathbf{B}) = \frac{f(|\mathbf{B}|)}{4\pi B^2} \ , \tag{4.17}$$

as $f(\mathbf{B})$ is isotropic. The distribution function for the absolute value of the field is given by the Maxwell distribution[4]

$$f(|\mathbf{B}|) = \frac{1}{\sqrt{(2\pi\langle B_\alpha^2 \rangle)^3}} 4\pi B^2 \exp\left[-\frac{B^2}{2\langle B_\alpha^2 \rangle}\right] \ . \tag{4.18}$$

We note that the Maxwell distribution is obtained by considering that the three field components are uncorrelated, *i.e.* that we can choose them independently. In other words

$$f(\mathbf{B}) = f(B_x)f(B_y)f(B_z) \ . \tag{4.19}$$

f(|**B**|)

|**B**|
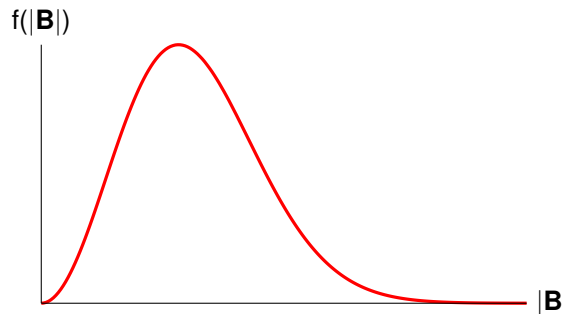
Figure 4.14.: *Maxwell distribution of the field value |**B**| for Gaussian distributed B_x, B_y and B_z. The maximum occurs at $B_{Max,max} = \sqrt{2\langle B_\alpha^2 \rangle}$.*

---

[4]The Maxwell (or Maxwell-Boltzmann) distribution describes for example the speed of molecules in a gas.
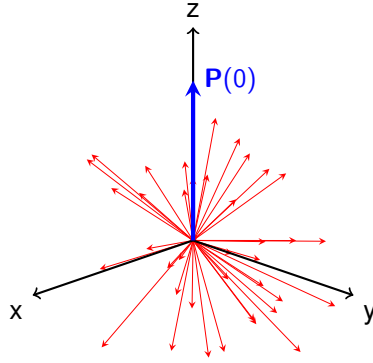
Figure 4.15.: *Schematic view of the fields sensed by the muon ensemble.*

Here again, we use Eq. 4.10 and introduce the Maxwell field distribution (Eq. 4.18) into the equation for the time dependence of the polarization (Eq. 4.4) and integrate. We get

$$
\begin{aligned}
P_z^{\text{GKT}}(t) &= \frac{1}{3} + \frac{2}{3}(1 - \gamma_\mu^2 \langle B_\alpha^2 \rangle t^2) \exp\left[-\frac{1}{2}\gamma_\mu^2 \langle B_\alpha^2 \rangle t^2\right] \\
&= \frac{1}{3} + \frac{2}{3}(1 - \sigma^2 t^2) \exp\left[-\frac{\sigma^2 t^2}{2}\right] ,
\end{aligned}
\tag{4.20}
$$

where here again we have defined

$$
\sigma^2 = \gamma_\mu^2 \langle B_\alpha^2 \rangle \ . \tag{4.21}
$$

This is the very well know Gaussian "Kubo-Toyabe" function [40].

Here again, the 1/3 and 2/3 components can be qualitatively understood by considering that the local field is random in all directions, *i.e.* about 1/3 is parallel or antiparallel to the initial muon spin direction and about 2/3 is perpendicular.
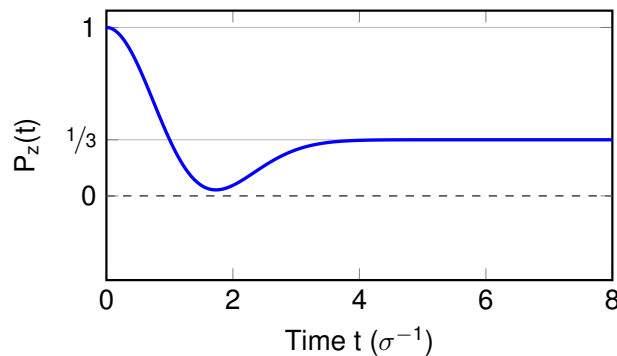
Figure 4.16.: *Time evolution of the muon polarization in a system where the (dense) magnetic moments are randomly oriented. The Maxwell field distribution produces the so-called Gaussian Kubo-Toyabe function. The minimum occurs at $t = \sqrt{3}/\sigma$.*

For very short times ("st") or very slow depolarization rate, the Gaussian Kubo-Toyabe function approaches a Gaussian function with $P_z^{\text{GKT}}(t) \simeq \exp(-\sigma_{\text{st}}^2 t^2/2)$ (see Exercises), where $\sigma_{\text{st}}^2 = 2\sigma^2$. The fact that at short time the Gaussian depolarizarization rate is $\sqrt{2}\sigma$ is due to the fact that in ZF the second moments for field directions perpendicular to the initial muon polarization (thus x and y) contribute to the muon depolarization, that is $\sigma_{\text{st}}^2 = \gamma_\mu^2(\langle B_x^2 \rangle + \langle B_y^2 \rangle) = 2\sigma^2$ or $\sigma_{\text{st}} = \sqrt{2}\sigma$. Note that when a field is present [either ZF case in a magnetic state (see Section 4.1.1.2 and Eq. 4.14) or in TF measurements (see Section 4.2 and Eq. 4.32), the solely the second moment along the field direction contributes to the muon depolarization.

We can understand the form of the Kubo-Toyabe function by looking at Fig. 4.17. There we show the time dependence of the muon-spin polarization for different chosen values of field (each polarization curve following Eq. 4.11). If these field values value are chosen to follow the Maxwell distribution, the curves initially do roughly the same thing (*i.e.* fall from 1 to a minimum value and then increase), but after a short time they become out of phase with respect to each other. Hence their average is expected to fall from unity to a minimum and then recover to one-third.
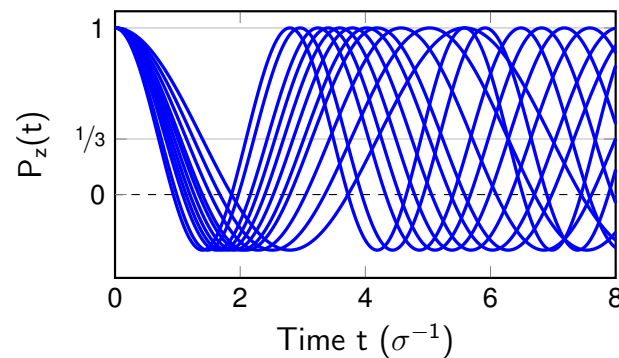
Figure 4.17.: *Time evolution of the muon-spin polarization for Eq. 4.11 with different values of the magnitude of the local field. Adapted from Stephen Blundell [41].*

Some examples   As said, the nuclear moments (magnetic moments of the nuclei) are weak and (when no external field is applied) can be considered static on the μSR time window. In the paramagnetic state of systems, the electronic moments are fluctuating much too fast to have an effect on the μSR signal and the muon spin will solely sense the field distribution created by the nucleus moments. As these are randomly oriented, they will create a weak Kubo-Toyabe depolarization of the muon ensemble (small second moment) and the minimum of the function will not always be visible in the data.

The literature is full of example, but we show here only very few. An example is given by the compound $CeCu_5Au$ which orders magnetically below 2.3 K. This system is close parent to the heavy-fermion system $CeCu_6$. Above the ordering temperature, the ZF μSR data show a very weak Kubo-Toyabe depolarization.
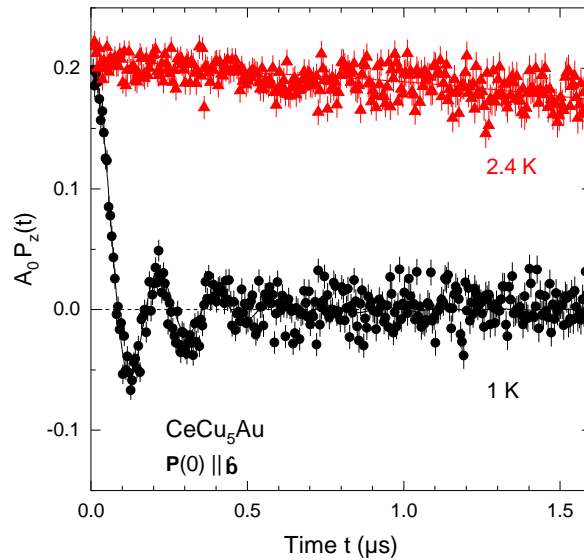
Figure 4.18.: *μSR signal in the compound CeCu$_5$Au [42]. The lower curve is measured in the magnetic state and represents a spontaneous precession due to the internal field create by the electronic moments. The upper curve is measured in the paramagnetic state and the depolarization is due to the nucleus moments. This curve is fitted by a Kubo-Toyabe function with a very small σ parameter.*

The system MnSi is characterized by a so-called non-centrosymmetric crystallographic structure. Below about 30 K, the systems exhibits a helical magnetic state. This systems has attracted quite a lot of interest due to the occurrence of skyrmions in the magnetic phase in the presence of an external field. In the paramagnetic phase a rather strong Kubo-Toyabe depolarization of the muon ensemble is visible in the ZF μSR data.
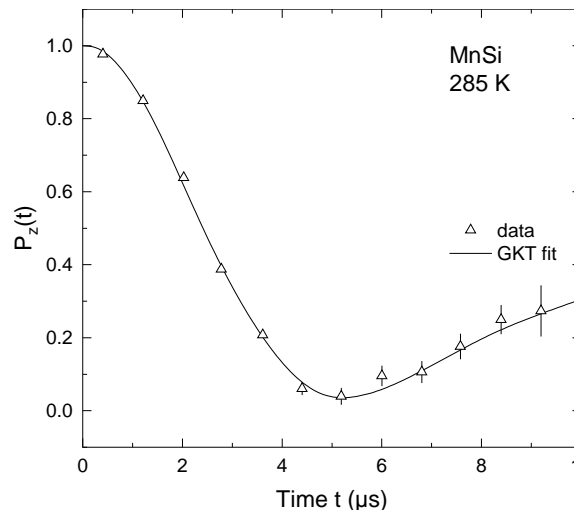
Figure 4.19.: *μSR signal in the compound MnSi. The stronger depolarization compared to the system CeCu$_5$Au (even though the time scale is different) can arise either from the fact that the ^{55}Mn nuclei has a larger magnetic moment compared to the ones of the Cu nuclei (^{63}Cu and ^{65}Cu) or from the position of the muon close to the Mn nuclei.*

4.1.2.2. Lorentzian distribution

A Lorentzian distribution of fields along each Cartesian directions is obtained in the case of a dilute arrangement of randomly oriented moments, for example static electronic moments due to magnetic impurities.
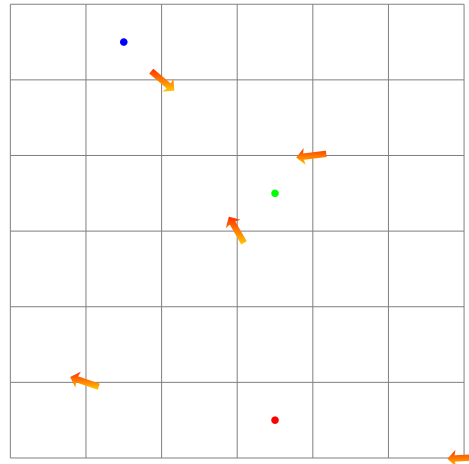
Figure 4.20.: *Diluted static magnetic moments in a lattice. Muons stopping at different interstitial sites (e.g. dots) will sense different fields.*

For each Cartesian direction a Lorentzian field distribution occurs with

$$f(B_\alpha) = \frac{1}{\pi} \cdot \frac{\Lambda}{\Lambda^2 + B_\alpha^2} \quad , \tag{4.22}$$

with $\alpha = x, y, z$ and Λ is the half-width at half-maximum (HWHM) of the field distribution along one Cartesian direction. We assume that along the three directions we have the same width of the distribution.
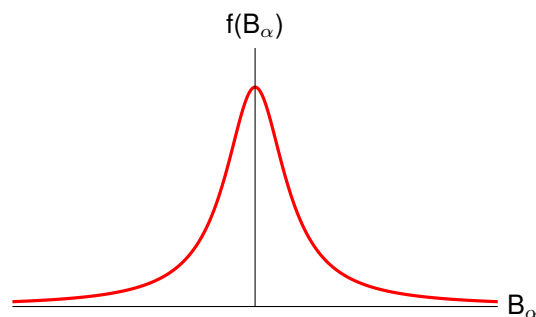
Figure 4.21.: *Lorentzian distribution of the field along one Cartesian direction.*

One can show (not demonstrated, see [34] and [43] for example) that the distribution function for the absolute value of the field is given by a squared-Lorentzian distribution

$$f(|\mathbf{B}|) = \frac{1}{\pi^2} \cdot \frac{\Lambda}{(\Lambda^2 + B^2)^2} \cdot 4\pi B^2 \quad . \tag{4.23}$$
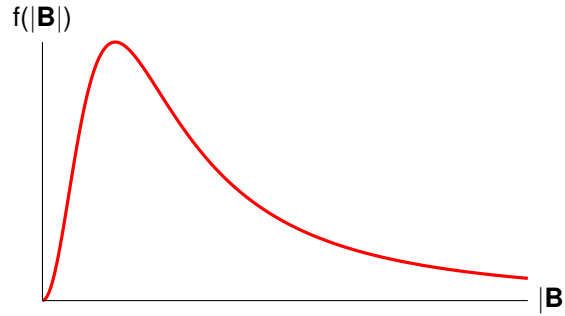
Figure 4.22.: *Squared Lorentzian distribution of the field value $|\mathbf{B}|$ for Lorentzian distributed B_x, B_y and B_z. The maximum occurs at $B_{SQL,max} = \Lambda$.*

Using the distribution given by Eq. 4.23 and plugging it into Eq. 4.4, one gets

$$P_z^{\text{LKT}}(t) = \frac{1}{3} + \frac{2}{3}(1 - at)\, e^{-at} \quad , \tag{4.24}$$

where $a = \gamma_\mu \Lambda$. This depolarization function is called the Lorentz Kubo-Toyabe function.

Here again, the 1/3 and 2/3 components can be qualitatively understood by considering that the local field is random in all directions, *i.e.* about 1/3 is parallel or antiparallel to the initial muon spin direction and about 2/3 is perpendicular.
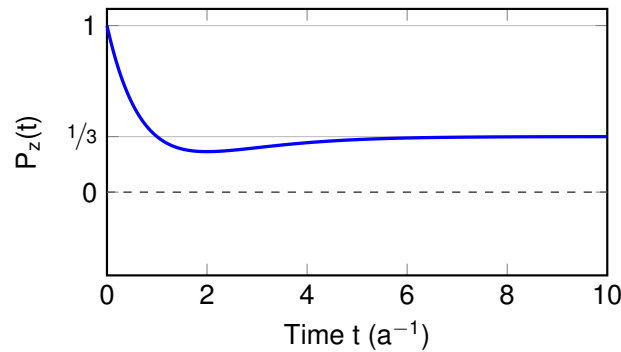
Figure 4.23.: *Time evolution of the muon polarization in a system where the diluted magnetic moments are randomly oriented. The squared-Lorentzian field distribution produces the so-called Lorentzian Kubo-Toyabe function. For very short times, the function approaches an exponential function (see text). The minimum occurs at $2/a$. The Lorentzian KT has a shallower dip than the Gaussian KT because there is a wider range of fields leading to faster damping.*

For very short times or very slow depolarization rate, the Lorentzian Kubo-Toyabe function approaches an exponential decaying function with $P_z^{\mathrm{LKT}}(t) \simeq \exp(-4at/3)$ (see Exercises).

4.1.2.3. "In between"

Sometimes a more generic depolarization function is given, which would reflect a field distribution between Gaussian and Lorentzian

$$P_z^{\mathrm{gen.KT}}(t) = \frac{1}{3} + \frac{2}{3}(1 - (\lambda t)^\beta) \exp\left(-\frac{(\lambda t)^\beta}{\beta}\right) \ , \tag{4.25}$$

where if $\beta = 1$ we find Eq. 4.24 and if $\beta = 2$ we get Eq. 4.20.

4.1.3. Generalization

The situations leading to Eqs. 4.14 and 4.20 differ only by the fact that for Eq. 4.14 one admits that the internal field is much stronger than the broadening (*i.e.* $\langle B_\mu \rangle \gg \sqrt{\langle \Delta B^2 \rangle} = \sigma^2 / \gamma_\mu^2$, taken along the field direction), whereas for the Kubo-Toyabe the broadening is around zero ($\langle B_\alpha \rangle = 0$ for $\alpha = x, y, z$). Therefore one can ask himself what would be the situation if $\langle B_\mu \rangle \simeq \sqrt{\langle \Delta B^2 \rangle}$. The situation has been investigated by Kornilov *et al.* [44] who found a generalized formula, assuming a Gaussian broadening,

$$P_z^{\text{Kor.G}}(t) = \frac{1}{3} + \frac{2}{3}\left(\cos(\gamma_\mu \langle B_\mu \rangle t) - \frac{\sigma^2 t}{\gamma_\mu \langle B_\mu \rangle} \sin(\gamma_\mu \langle B_\mu \rangle t)\right)\exp\left[-\frac{\sigma^2 t^2}{2}\right] \ . \qquad (4.26)$$

One sees that

- for $\langle B_\mu \rangle \gg \sigma^2 / \gamma_\mu^2$ the second term in the braket will disappear and Eq. 4.26 converges to Eq. 4.14.

- if $\langle B_\mu \rangle \to 0$ then Eq. 4.26 converges to Eq. 4.20.

- in addition, we have that Eq. 4.26 converges to Eq. 4.11 if $\sigma \to 0$, as we expect.

Corresponding conclusions can be obtained by assuming a Lorentzian broadening

$$P_z^{\text{Kor.L}}(t) = \frac{1}{3} + \frac{2}{3}\left(\cos(\gamma_\mu \langle B_\mu \rangle t) - \frac{a}{\gamma_\mu \langle B_\mu \rangle} \sin(\gamma_\mu \langle B_\mu \rangle t)\right)\exp(-at) \ . \qquad (4.27)$$

4.2. Depolarization function for applied external fields (TF geometry)

As said, when an external field is applied to the sample in the paramagnetic regime (TF geometry) we are probing the time evolution of the $P_x(t)$ component of the muon polarization (z-direction defined by the external field). In addition, we will admit that the external field is applied perpendicular to the initial muon polarization (*i.e.* $\theta = 90°$).

With this in mind, we can basically make usage of the Eq. 4.4 and write

$$P_x(t) = \int f(\mathbf{B}) \cos(\gamma_\mu B t) d\mathbf{B} \qquad (4.28)$$
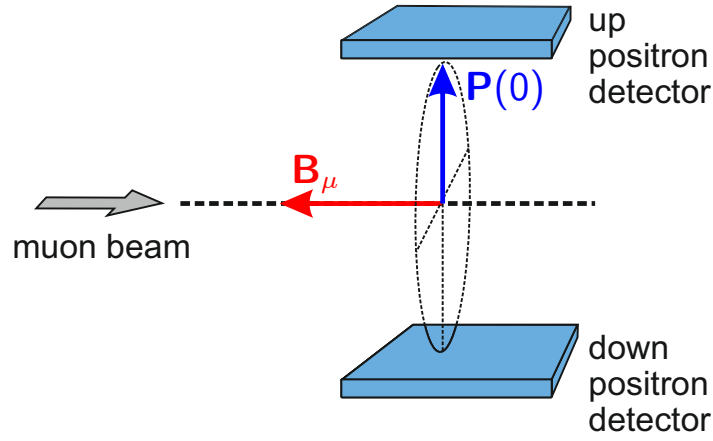
Figure 4.24.: *Schematic of the TF geometry.*

Usually, the applied field can always be considered as much higher than an internal field broadening. Therefore the field sensed by the muons will always be almost exactly along the z-axis. If we consider again a Gaussian distribution. We get

$$f(\mathbf{B}) = f(B_x)f(B_y)f(B_z)$$
$$= \frac{1}{\sqrt{2\pi\langle\Delta B_x^2\rangle}}e^{-\frac{B_x^2}{2\langle\Delta B_x^2\rangle}} \cdot \frac{1}{\sqrt{2\pi\langle\Delta B_y^2\rangle}}e^{-\frac{B_y^2}{2\langle\Delta B_y^2\rangle}} \cdot \frac{1}{\sqrt{2\pi\langle\Delta B_z^2\rangle}}e^{-\frac{(B_z-B_{\text{ext}})^2}{2\langle\Delta B_z^2\rangle}} \quad , \qquad (4.29)$$

and as the field sensed by the muons is almost exactly along the z-axis, only the field distribution along the applied field comes into play and we can write

$$P_x^{GTF}(t) = \frac{\gamma_\mu}{\sqrt{2\pi}\sigma} \int e^{-\frac{\gamma_\mu^2(B_z-B_{\text{ext}})^2}{2\sigma^2}} \cos(\gamma_\mu B_z t) dB_z \cdot \underbrace{\frac{\gamma_\mu}{\sqrt{2\pi}\sigma} \int e^{-\frac{\gamma_\mu^2 B_x^2}{2\sigma^2}} dB_x}_{1} \cdot \underbrace{\frac{\gamma_\mu}{\sqrt{2\pi}\sigma} \int e^{-\frac{\gamma_\mu^2 B_y^2}{2\sigma^2}} dB_y}_{1} \quad ,$$
$$(4.30)$$

where here again we have defined $\sigma = \sqrt{\gamma_\mu^2\langle\Delta B_\alpha{}^2\rangle}$.

Therefore, $P_x^{GTF}(t)$ can be obtained by performing the change of variable $B_z - B_{\text{ext}} \rightarrow x$, and we have

$$
\begin{aligned}
P_x^{GTF}(t) &= \frac{\gamma_\mu}{\sqrt{2\pi}\sigma} \int e^{-\frac{\gamma_\mu^2(B_z-B_{\text{ext}})^2}{2\sigma^2}} \cos(\gamma_\mu B_z t) dB_z \\
&= \frac{\gamma_\mu}{\sqrt{2\pi}\sigma} \int e^{-\frac{\gamma_\mu^2 x^2}{2\sigma^2}} \cos[\gamma_\mu(x + B_{\text{ext}})t] dx \\
&= \frac{\gamma_\mu}{\sqrt{2\pi}\sigma} \left[\int e^{-\frac{\gamma_\mu^2 x^2}{2\sigma^2}} \cos(\gamma_\mu x t) dx \right] \cos(\gamma_\mu B_{\text{ext}} t) - \\
&\quad - \frac{\gamma_\mu}{\sqrt{2\pi}\sigma} \left[\int e^{-\frac{\gamma_\mu^2 x^2}{2\sigma^2}} \sin(\gamma_\mu x t) dx \right] \sin(\gamma_\mu B_{\text{ext}} t) \\
&= \frac{\gamma_\mu}{\sqrt{2\pi}\sigma} \left[\int e^{-\frac{\gamma_\mu^2 x^2}{2\sigma^2}} \cos(\gamma_\mu x t) dx \right] \cos(\gamma_\mu B_{\text{ext}} t) \ .
\end{aligned}
\tag{4.31}
$$

This high transverse-field expression (actually an approximation) is quite general and actually does not depend on the precise form of the field distribution, though the last step requires that $f(x) = f(-x)$. We note that the overall depolarization of $P_x^{GTF}(t)$ (*i.e.* the part in the square brackets in the Eq. 4.31) is actually the cosine Fourier transform of the field distribution along the direction of the externally applied magnetic field. We can therefore write the time evolution of the polarization for a Gaussian broadening as

$$
\boxed{
\begin{aligned}
P_x^{GTF}(t) &= \cos(\gamma_\mu B_{\text{ext}} t) \ \exp\left[-\frac{1}{2}\gamma_\mu^2 \langle \Delta B_z^2 \rangle t^2\right] \\
&= \cos(\gamma_\mu B_{\text{ext}} t) \ \exp\left[-\frac{\sigma^2 t^2}{2}\right] \ .
\end{aligned}
}
\tag{4.32}
$$

The difference with Eq. 4.14 is that here the full initial muon polarization rotates about the field sensed by the muon as we have imposed in the TF geometry that $\theta = 90°$.

An important point, that we will use later, is that the depolarization rate σ that one can determine in TF experiments is a direct measure of the second moment of the field distribution seen by the muon.

Similarly for a Lorentzian broadening one obtains

$$
\boxed{
P_x^{LTF}(t) = \cos(\gamma_\mu B_{\text{ext}} t) \ \exp(-at) \ ,
}
\tag{4.33}
$$

where also here a/γ_μ is the HWHM of the Lorentzian distribution along the direction (z) of the applied field.

By writing Eqs. 4.32 and 4.33, we have assumed that the average value of the field seen by the muon is the external field B_{ext}. In reality different contributions will modify the field seen by the muon with respect to B_{ext}. For example the shape of the sample will play a role through the demagnetization factor. In addition, the Knight-shift will modify the field sensed by the muon through the polarization of the conduction electrons (producing a contact

hyperfine contribution) and through the polarization of possible local moments (which will create a dipolar field at the muon site). Also, when determining the penetration depth of a superconductor by μSR (see Section 6) the field probed by the muon will be modified by the so-called vortex-lattice.

4.3. Dynamical effects

So far we have limited ourselves to the case where the field seen by the muon is static (at least during the measurement time-window). This is the usual situation in a magnetic sample where the magnetic moments are static. In this Section, we will see the effect of dynamical fields at the muon site.[5] We will see that fluctuations can have quite an impact on the observed depolarization of the μSR signal.

4.3.1. Stochastic processes

The interpretation that the local field at the muon site is static is usually rarely valid, and the μSR technique is rather sensitive to dynamical effects. One usually considers that the dynamical effects are stationary *stochastic* processes, that is that their properties do not change with the origin of time and that they are random.

An important class of these stochastic processes are the *Markovian* ones, for which the fluctuation probability (in our case of the local field) does not depend on the state of the system in the past but only on the present state, *i.e.* these are memoryless processes. We will use the hypothesis that the processes are Markovian and that they are in addition Gaussian. This means that if we define a process as a collection of random variables indexed by time (for example in our case the components x, y and z of our local field $\mathbf{B}_\mu$), every finite collection of those random variables has a multivariate normal distribution. For these Gaussian-Markovian processes one can show that the field-autocorrelation function (*i.e.* the correlation between field values taken at different time) can be written as (Doob theorem)

$$\langle B_\alpha(t')B_\alpha(t'+t)\rangle = \langle B_\alpha(0)B_\alpha(t)\rangle = \langle B_\alpha(0)^2\rangle \exp(-t/\tau_c) \ , \qquad (4.34)$$

where $\alpha = x$, y and z and where we have to perform the ensemble average. Here τ_c is called the field correlation time.

4.3.2. The strong collision approximation

In the absence of an external field, a complete mathematical description is obtained by the strong collision approximation. It is assumed that the local field changes orientation and magnitude with a single fluctuation rate ν. The process is called *collision* or *fluctuation*. After a fluctuation, occurring after an average time of $\tau = 1/\nu$, the field is randomly chosen from a probability distribution $f(\mathbf{B})$, without any correlation to the field before the fluctuation.

---

[5]The fluctuations can be due to real fluctuations of the internal field, or to "muon diffusion" which occurs at high temperature, where the muon diffuses from site to site in a static magnetic environment.
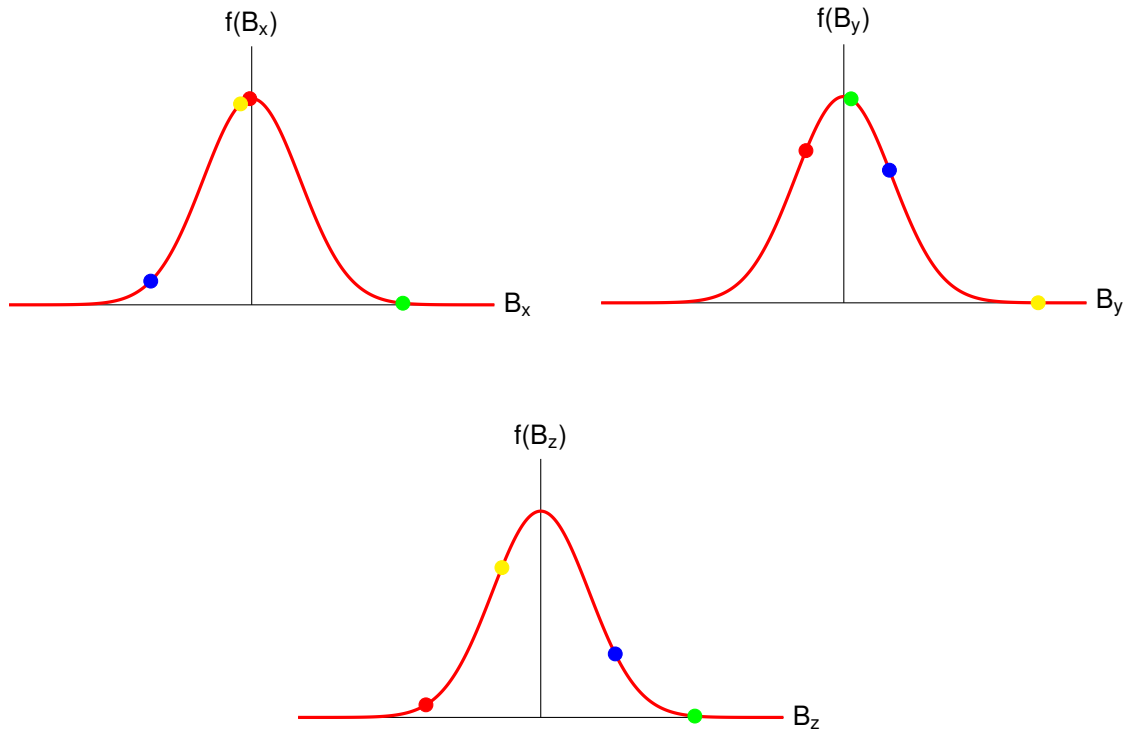
Figure 4.25.: *Schematic of the strong collision model. After each fluctuation (represented by the different color points), the muon sees another field randomly choosen from the "snap-shot" field distribution (here assumed Gaussian).*

The numbers of fluctuations is given by the following diagram, where each row represents a time dt:
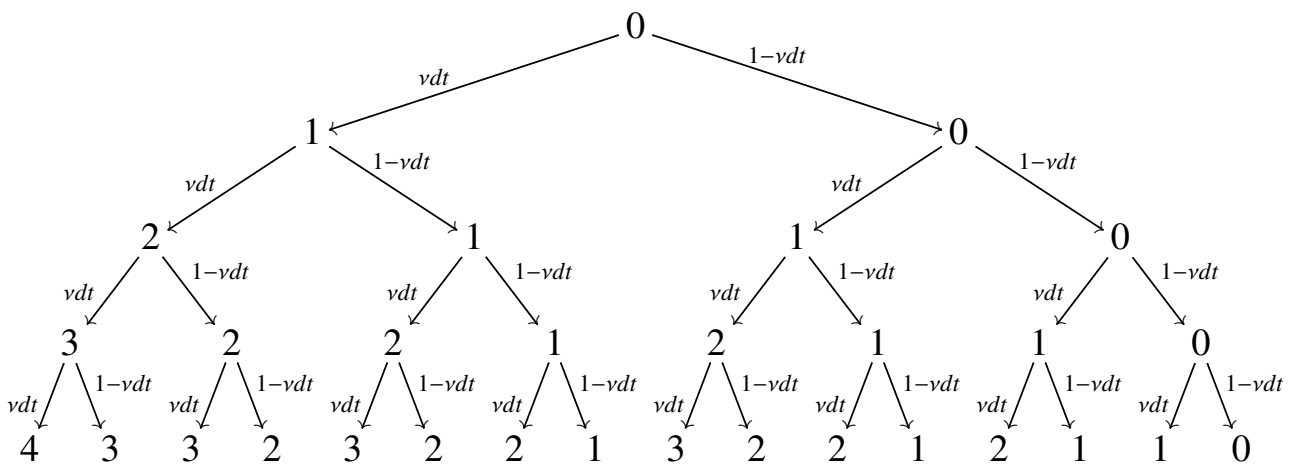
We can first look at the fraction of muons seeing a given number of fluctuations at a time $t = n\,dt$.

- The muon fraction with 0 fluctuation is given by

$$p_0(t) = (1 - v\, dt)(1 - v\, dt)(1 - v\, dt)... = (1 - v\, dt)^n = \left(1 - \frac{v\, t}{n}\right)^n$$

hence, for $n \to \infty$

$$p_0(t) = e^{-v t} \tag{4.35}$$

- For 1 fluctuation, the fraction is the probability for a muon to have 0 fluctuation up to a time t_1, times the probability to have a fluctuation at that time, times the probability not having an additional fluctuation up to the time t (one of course has to vary the time t_1 from 0 to t, which will corresponds to different paths of the diagram.)

$$p_1(t) = \int_0^t \underbrace{e^{-v t_1}}_{0 \text{ Fluc. for } 0 \to t_1} \times \overbrace{v\, dt_1}^{\text{Fluc. prob. between } t_1 \text{ and } t_1 + dt_1} \times \underbrace{e^{-v (t - t_1)}}_{0 \text{ Fluc. for } t_1 \to t}$$

$$= e^{-v t} v \int_0^t dt_1 \quad \text{hence,}$$

$$p_1(t) = e^{-v t} v\, t \tag{4.36}$$

- For 2 fluctuations, the fraction is the probability for a muon to have 1 fluctuation up to a time t_2 (and we know that it is $p_1(t_2)$), times the probability to have a fluctuation at that time, times the probability not having an additional fluctuation up to the time t (one of course has to vary the time t_2 from 0 to t). Hence

$$p_2(t) = \int_0^t \underbrace{p_1(t_2)}_{1 \text{ Fluc. for } 0 \to t_2} \times \overbrace{v\, dt_2}^{\text{Fluc. prob. between } t_2 \text{ and } t_2 + dt_2} \times \underbrace{e^{-v (t - t_2)}}_{0 \text{ Fluc. for } t_2 \to t}$$

$$= e^{-v t} v^2 \int_0^t t_2\, dt_2 \quad \text{hence,}$$

$$p_2(t) = e^{-v t} \frac{v^2 t^2}{2} \tag{4.37}$$

- And therefore:

$$p_n(t) = \int_0^t p_{n-1}(t_n)\, v\, dt_n\, e^{-v (t - t_n)}$$

$$p_n(t) = e^{-v t} \frac{v^n t^n}{n!} \tag{4.38}$$

- Let see whether the sum of all these fractions gives 1:

$$p(t) = \sum_{n=0}^{\infty} e^{-v t} \frac{v^n t^n}{n!} = e^{-v t} \sum_{n=0}^{\infty} \frac{v^n t^n}{n!} = e^{-v t} e^{+v t}$$

$$p(t) = 1 \tag{4.39}$$

4.3.2.1. The muon depolarization

For the static field distribution we will assume a Gaussian distribution along each Cartesian directions $f(B_{\mu,\alpha})$ (Eq. 4.15) in zero field leading to the Kubo-Toyabe function $P_z^{\text{GKT}}(t)$ (Eq. 4.20).

It is clear that the muon depolarization function in the dynamical case $[P_{\text{dyn}}(t,\nu)]$ will be the sum of the muon depolarization functions corresponding to all configurations of fluctuations number $[g_n(t)]$.

$$P_{\text{dyn}}(t,\nu) = \sum_{n=0}^{\infty} g_n(t) \tag{4.40}$$

- Let see first the situation for no fluctuation. The depolarization function is given by the GKT function times the probability that a muon does not see a fluctuation:

$$g_0(t) = e^{-\nu t} P_z^{\text{GKT}}(t) \tag{4.41}$$

- for one collision we will have a GKT function until time t_1 and a new GKT function with same depolarization rate but starting at time t_1 (note that the "snapshot" field distribution before and after the fluctuation is the same)

$$g_1(t) = \int_0^t \underbrace{P_z^{\text{GKT}}(t_1)\, e^{-\nu t_1}}_{0 \text{ Fluc. for } 0 \to t_1} \times \quad \overbrace{\nu\, dt_1}^{\text{Fluc. prob. between } t_1 \text{ and } t_1 + dt_1} \times \underbrace{P_z^{\text{GKT}}(t-t_1) e^{-\nu\,(t-t_1)}}_{0 \text{ Fluc. for } t_1 \to t}$$

$$g_1(t) = \nu \int_0^t g_0(t_1)\, g_0(t-t_1)\, dt_1 = e^{-\nu t} \nu \int_0^t P_z^{\text{GKT}}(t_1)\, P_z^{\text{GKT}}(t-t_1)\, dt_1 \tag{4.42}$$

- For 2 fluctuations, we we will have the depolarization function $g_1(t)$, that we have just calculated and corresponding to 1 fluctuation until time t_2, and a new GKT function with same depolarization rate but starting at time t_2

$$g_2(t) = \int_0^t \underbrace{g_1(t_2)}_{1 \text{ Fluc. for } 0 \to t_2} \times \quad \overbrace{\nu\, dt_2}^{\text{Fluc. prob. between } t_2 \text{ and } t_2 + dt_2} \times \underbrace{P_z^{\text{GKT}}(t-t_2) e^{-\nu\,(t-t_2)}}_{0 \text{ Fluc. for } t_2 \to t}$$

$$g_2(t) = \nu \int_0^t g_1(t_2)\, g_0(t-t_2)\, dt_2 \tag{4.43}$$

- We have the recursive relation

$$g_n(t) = \nu \int_0^t g_{n-1}(t_n)\, g_0(t-t_n)\, dt_n \tag{4.44}$$

We can therefore write [6]

$$P_{z,\,\mathrm{dyn}}^{\mathrm{GKT}}(t, \nu) = \sum_{n=0}^{\infty} g_n(t)$$

$$= e^{-\nu t} P_z^{\mathrm{GKT}}(t) + \nu \int_0^t g_0(t_1)\, g_0(t - t_1)\, dt_1 + \nu \int_0^t g_1(t_2)\, g_0(t - t_2)\, dt_2 + \ldots$$

$$+ \nu \int_0^t g_{n-1}(t_n)\, g_0(t - t_n)\, dt_n + \ldots \quad \text{or explicitly}$$

$$= e^{-\nu t} \Bigg[P_z^{\mathrm{GKT}}(t) + \nu \int_0^t P_z^{\mathrm{GKT}}(t_1)\, P_z^{\mathrm{GKT}}(t - t_1)\, dt_1 +$$

$$+ \nu^2 \int_0^t \int_0^{t_2} P_z^{\mathrm{GKT}}(t_1)\, P_z^{\mathrm{GKT}}(t_2 - t_1)\, P_z^{\mathrm{GKT}}(t - t_2)\, dt_1\, dt_2 + \ldots \Bigg] .$$

$$(4.46)$$

Approximations for some limiting cases For sufficiently fast fluctuations (*i.e.* when $\nu \gtrsim 3\sigma$ in the case of a Gaussian static distribution) one can approximate the depolarization by

$$P_{z,\,\mathrm{dyn}}^{\mathrm{GKT}}(t, \sigma, \nu) \simeq \exp\left[-2 \frac{\sigma^2}{\nu^2} \left[\exp(-\nu t) - 1 + \nu t \right] \right]. \tag{4.47}$$

This equation is actually the Abragam formula in zero-field[7].

In the quasi-static limit ($\nu \ll \sigma$) one has the limit

$$P_{z,\,\mathrm{dyn}}^{\mathrm{GKT}}(t, \sigma, \nu) \simeq \frac{1}{3} \exp\left(-\frac{2}{3}\nu t\right) + \frac{2}{3}(1 - \sigma^2 t^2) \exp\left(-\frac{\sigma^2 t^2}{2}\right). \tag{4.48}$$

The $2/3$-factor in front of ν reflects the fact that only the transverse components of $\mathbf{B}_\mu$ induce a depolarization. Fluctuations along the z-axis (initial direction of the polarization in zero-field geometry) will not lead to a depolarization.

---

[6]We should keep in mind that we have here worked with a static depolarization function $P_z^{\mathrm{GKT}}(t)$ corresponding to a Gaussian field distribution. But we stress that the strong collision model can be applied with any type of static depolarization function. In such a case the GKT-function in the above equations has to be replaced by the corresponding static depolarization function, say $P_{z,\,\mathrm{static}}(t)$, and one gets

$$P_{z,\,\mathrm{dyn}}(t, \nu) = e^{-\nu t} \Bigg[P_{z,\,\mathrm{static}}(t) + \nu \int_0^t P_{z,\,\mathrm{static}}(t_1)\, P_{z,\,\mathrm{static}}(t - t_1)\, dt_1 +$$

$$(4.45)$$

$$+ \nu^2 \int_0^t \int_0^{t_2} P_{z,\,\mathrm{static}}(t_1)\, P_{z,\,\mathrm{static}}(t_2 - t_1)\, P_{z,\,\mathrm{static}}(t - t_2)\, dt_1\, dt_2 + \ldots \Bigg] .$$

[7]In transverse field, the factor 2 disappears as only the component along the external field is important for the depolarization. Note that for extremely fast fluctuations, the situation is again different.

The extreme motional narrowing limit is

$$P_{z,\,\text{dyn}}^{\text{GKT}}(t,\sigma,\nu) \simeq \exp\!\left[-\frac{2\sigma^2}{\nu}t\right].\qquad(4.49)$$

This equation justifies the fact that in the paramagnetic regime no sign of depolarization due to the electronic moments can be observed in the μSR signal.

To see this point we consider first that in solids the electron moments fluctuation rate in the paramagnetic state is typically about $\nu = 10^{12} - 10^{16}$ s^{-1}. A value for the second moment can be estimate starting from the observed depolarization rate value due to the nuclear moments which is of the order of typically $\sigma_N \simeq 0.3 \ \mu$s^{-1}, leading to a loss of polarization of about 18% after one muon lifetime (Eq. 4.20). As the electron has a magnetic moment about 1000 larger than a typical nuclei, and assuming a fluctuation rate of 10^{14} s^{-1}, one obtains a depolarization rate due to the fluctuating moments of $2\sigma_e^2/\nu \simeq 1.8 \times 10^{-3} \ \mu$s^{-1}, leading to a loss of polarization of only about 0.4% after one muon lifetime (Eq. 4.49).

Examples
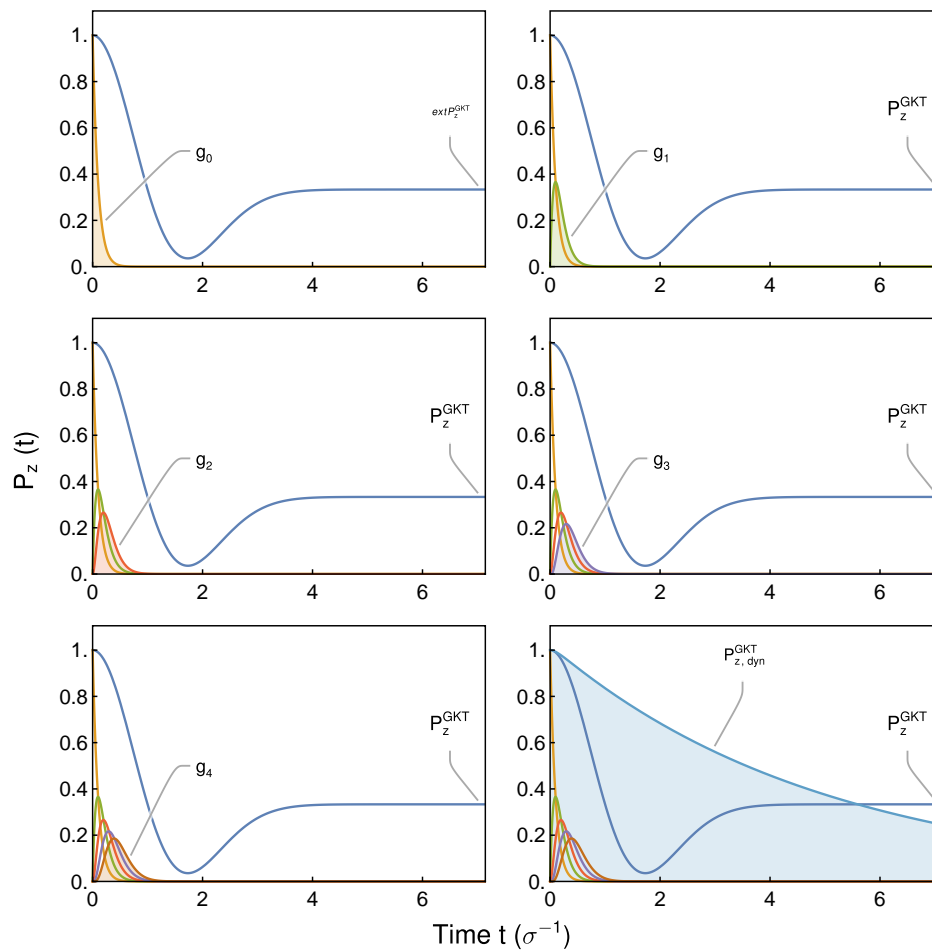
Figure 4.26.: *Polarization as a function of time. Case for $\nu = 10 \times \sigma$. The time axis is given in $1/\sigma$. The graphs show the static GKT function with g_0, g_1, g_2, g_3, g_4 and the curve obtained with the Eq. 4.47. Note the overall decreases of the depolarization due to the motional narrowing.*
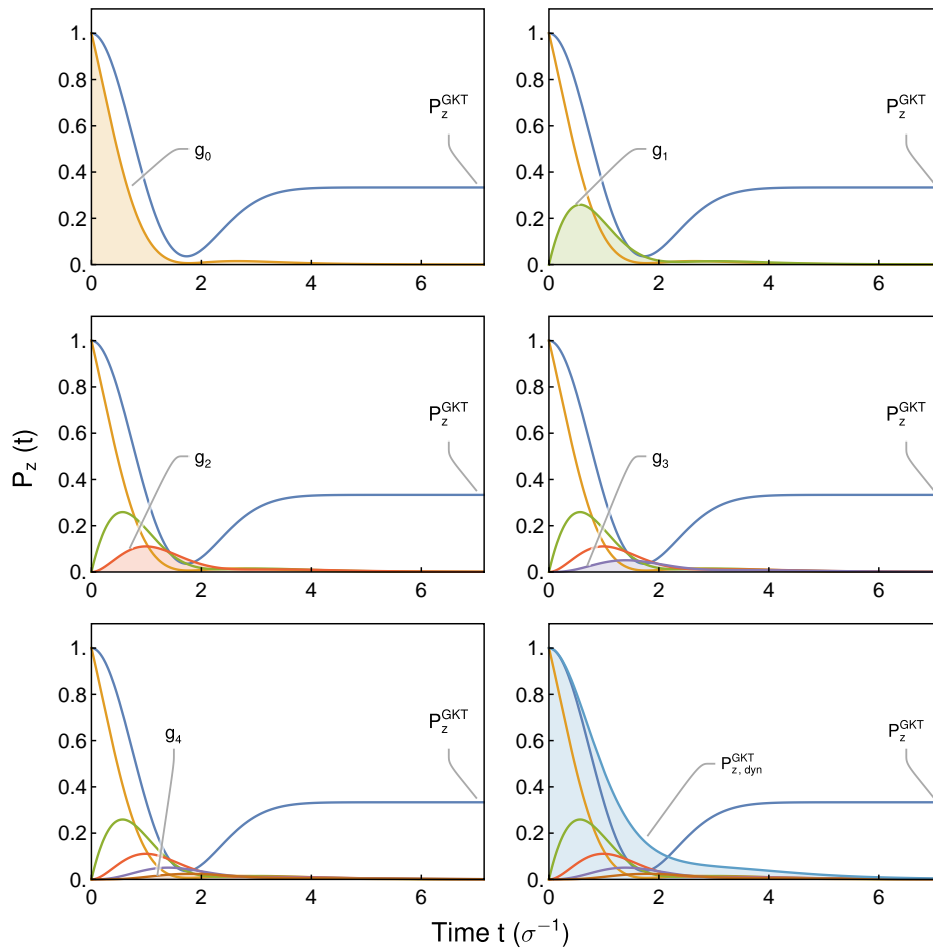
Figure 4.27.: *Polarization as a function of time. Case for $\nu = \sigma$. The time axis is given in $1/\sigma$. The graphs show the static GKT function with g_0, g_1, g_2, g_3, g_4 and the sum representing $P_{z,\,dyn}^{GKT}$.*
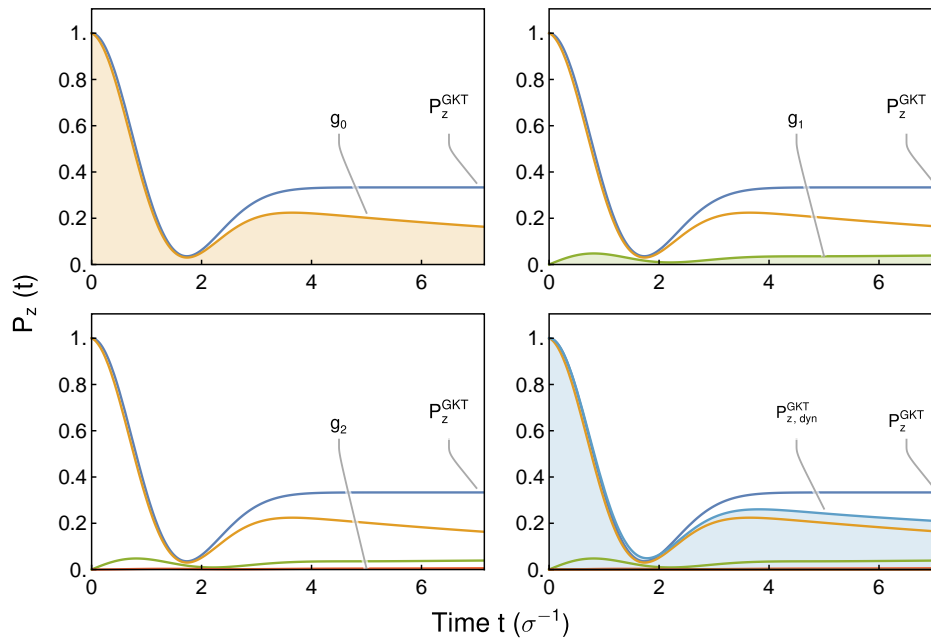
Figure 4.28.: *Polarization as a function of time. Case for $\nu = 0.1 \times \sigma$. The time axis is given in $1/\sigma$. The graphs show the static GKT function with g_0, g_1, g_2 and the sum representing $P^{GKT}_{z,\,dyn}$. Note that the functions g_3 and g_4 are practically not contributing as the probability to have more than two fluctuations is negligible. Note also that basically only the tail of the static GKT function is affected (see also Eq. 4.48).*

Fluctuation time or correlation time? In Section 4.3.1 we introduced the notion of correlation time and in Section 4.3.2 the one of fluctuation time. We can at this point ask ourselves about the difference between these two concepts. We first intuitively note that the parameter which will play a role on the depolarization of the muon-spin ensemble is actually the correlation time τ_c, as solely large variations of the field seen by the muon will affect its polarization. So, at this point we can ask ourselves why we are using the term (and parameter) of fluctuations in discussing the strongly collision approximation in this Section dealing with the Strong Collision Approximation. The answer is located in the definition of the strong collision model, which assumes that the local field changes orientation and magnitude after a single fluctuation, and that the field after the fluctuation has no correlation to the field before the fluctuation. Therefore, it is obvious that we have here the situation where $\tau = \tau_c$.

As an example, we can calculate the autocorrelation function for a typical time evolution of the field. Mathematically, the autocorrelation corresponding to a delay time t is calculated by

- finding the value of the signal at a time t',

- finding the value of the signal at a time $t' + t$,

- multiplying those two values together,

- repeating the process for all possible times t' and then

- computing the average of all those products.

The process can be repeated for other values of t, resulting in an autocorrelation as a function of the delay time t. Mathematically, assuming a stationary process, this corresponds to

$$\langle B_\alpha(0)B_\alpha(t)\rangle = \langle B_\alpha(t')B_\alpha(t'+t)\rangle = \frac{1}{t_{\max}-t_{\min}}\int_{t_{\min}}^{t_{\max}} B_\alpha(t')B_\alpha(t'+t)dt' \quad . \tag{4.50}$$

As an example, we show on Fig. 4.29 simulated data of a Gaussian distributed field component B_α (mean value 0 and standard deviation 1 in arbitrary field units) assuming a fluctuation time of $\tau = 0.1$ (in arbitrary time units), *i.e.* corresponding to a fluctuation rate of $\nu = 1/\tau = 10$ (in arbitrary frequency units). We see that the time between the fluctuation is not constant but that its average is τ.
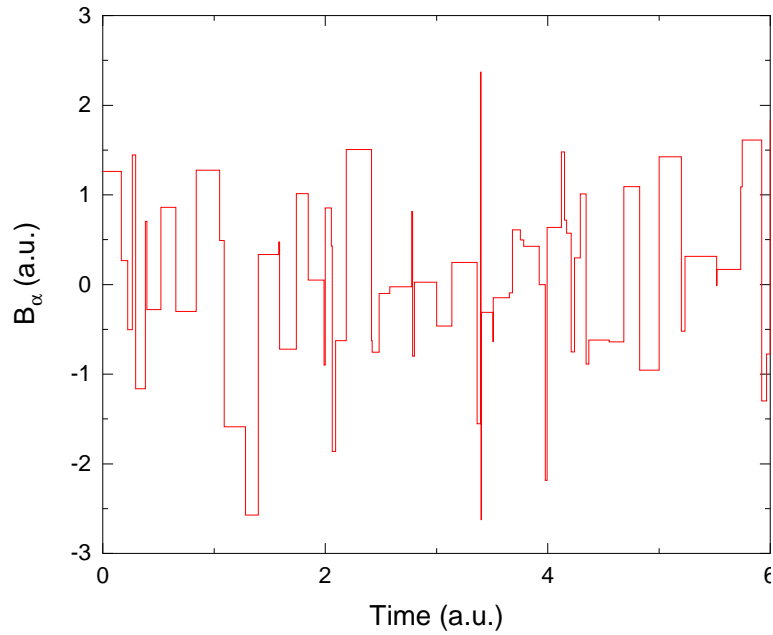
Figure 4.29.: *Simulated data with a fluctuation time of $\tau = 0.1$ (in arbitrary time units) and a Gaussian distributed field B_α (having mean value 0 and standard deviation 1, in arbitrary field units).*
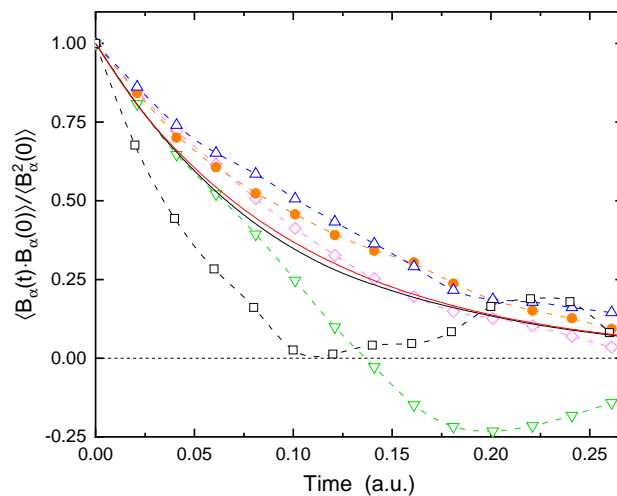
Figure 4.30.: *Calculation of the autocorrelation function for the data set shown on Fig. 4.29. The different curves with symbols are examples of integration using a time range $(t_{max} - t_{min}) = 3$. Note the difference between the curves arising from the short integration range compare to τ (only 30 fluctuations in average. The black solid line represents an integration with $(t_{max} - t_{min}) = 30$. Note that the curve is now close to the exponential decay represented by the solid red curve $\exp(-t/\tau_c)$ (see Eq. 4.34) with as expected $\tau_c = \tau = 0.1$.*

The exponential decay of the autocorrelation function can actually also be understood by looking at our diagram on page 123 and concentrating on the branch without decay (on the right-hand side). All the other processes will provide in average a vanishing contribution to the autocorrelation function as the fields before and after the fluctuations are uncorrelated. We see that we retrieve our exponential decay governed by $\exp(-t/\tau_c)$ with $\tau_c = \tau$.

The situation at the opposite of the strong collision model is often described as the weak collision model. This model describes a situation where the field remains correlated after a fluctuation process. This means that the fluctuations *do not* anymore map the static field distribution into itself. In other words this is a situation where $\tau \ll \tau_c$. Though we will not consider this model here, we just note that, as previously said, the fundamental parameter affecting the μSR depolarization rate is the correlation time τ_c.

4.3.3. Testing for the dynamical character with a longitudinal external field (LF)

In the previous Section, we have seen that for a magnet at high temperature (in the paramagnetic phase), the electronic spin moments are fluctuating too fast to be picked-up by the μSR technique ("motional narrowing"). On the other side, below the magnetic transition (ferro or antiferromagnetic) the moments can be considered as static leading to precessions in the μSR signal. However, when approaching the transition from above, the magnetic fluctuations will slow down and the muon spin will be able to sense the fluctuating field and a depolarization is observed. As we have seen with Eq. 4.49, this depolarization is exponential. However, we have seen that also a Lorentzian *static* field distribution lead to an exponential decay of the muon polarization (at least for early times or slow depolarization; See Eq. 4.24).

Let see this with an example. Admit that we measure a μSR signal with an exponential relaxation of $\lambda = 0.3 \ \mu s^{-1}$. This depolarization can be due either to:

- a field distribution which is **Lorentzian without field fluctuations** (see Section 4.1.2.2). In this case we have

$$\lambda = \frac{4a}{3} \ ,$$

  as the early time depolarization of the Lorentzian Kubo-toyabe is (as seen) $P_z^{\text{LKT}}(t) \simeq \exp(-4at/3)$. In this case the HWHM value of the field distribution is $a/\gamma_\mu = 3\lambda/(4\gamma_\mu) \simeq 2.6 \times 10^{-4}$ T.

- a field distribution which is **Gaussian with field fluctuations** (see Section 4.3.2.1). In this case we have (see Eq. 4.49)

$$\lambda = 2\frac{\Delta^2}{\nu} \ ,$$

  If we assume a fluctuation rate of $\nu = 10^9 \ s^{-1}$ (which is already rather slow), we have a standard deviation for the Gaussian distribution $\sqrt{\langle B_\alpha^2 \rangle} = \sqrt{\lambda\nu/2}/\gamma_\mu \simeq 1.4 \times 10^{-2}$ T.

Therefore, the Gaussian distribution is about 55 times broader than the Lorentzian one, but the muon ensemble undergoes the same polarization due to the "motional narrowing".
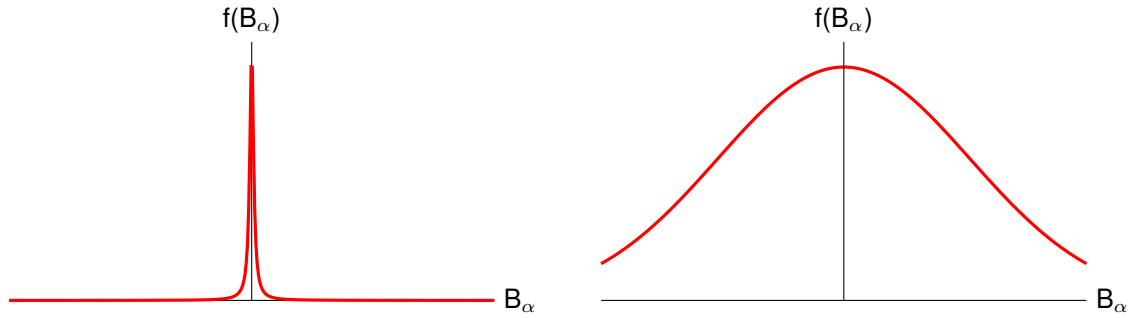
Figure 4.31.: *Left: Lorentzian distribution of the field producing, in a static case, a muon depolarization of say λ. Right: Gaussian field distribution producing the same muon spin depolarization λ. The muon ensemble will sense a much narrower field distribution due to the "motional narrowing". The HWHM for the left panel and the standard deviation for the right panel are taken from the above given example.*
Note that, whereas the x-scales are the same, the y-scale of the right panel is adjusted (expanded) for visibility. The integrals of both curves are equal to 1.

Therefore, we can ask ourselves how one could differentiate between fluctuating and static field distributions. The answer is provided by the application of a magnetic field along the initial muon polarization, *i.e.* a so-called "longitudinal field" (LF, see Fig. 3.12). As presented on Fig. 4.32, we see that if the value of the external field is quite larger than the ones of the internal fields, the muon will see a resulting field which will possess a reduced angle with respect to the initial polarization direction (*i.e.* θ small). Recalling our main formula given by Eq. 4.4, we see that the static part of $P_z(t)$ will increase. Also, for large external fields, the field distribution will be narrowly distributed around the value of the external field, meaning that the depolarization will be reduced. We will have a "decoupling" of the muon spin with respect to the static internal fields. On the other side, the oscillating part will be reduced while still showing indication of a precession around the external field.

For an external field (LF) which is about 10 times larger than the internal field characteristic width (either HWHM or standard deviation for Lorentzian or Gaussian distributions, respectively), the muon polarization will essentially be time independent. This effect will not be present if large internal fields are fluctuating. Taking the example above, we see that a field of about 25×10^{-4} T would be able to decouple the muon spin from the static internal fields, but this very same field would have basically no effect on the depolarization in the fluctuating case.

Therefore, LF measurements are used to distinguish between static and dynamic contributions to the depolarization.
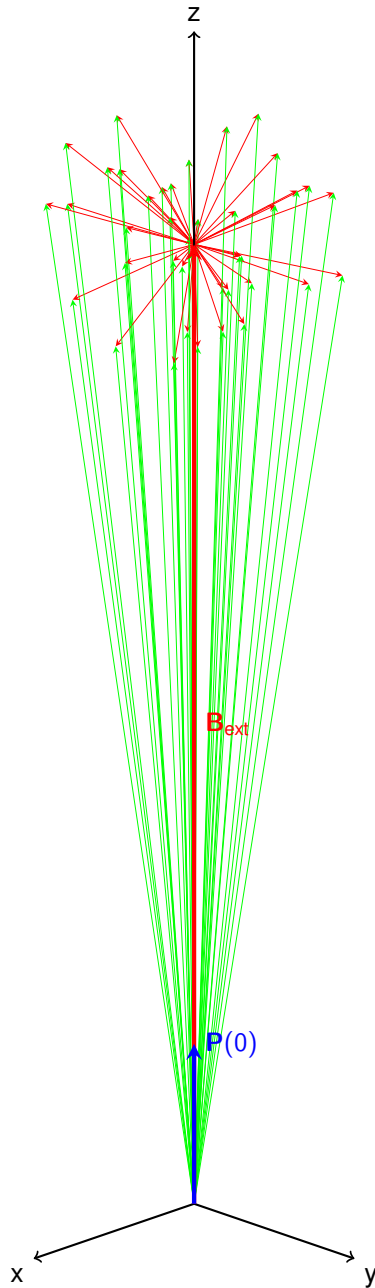
Figure 4.32.: *Schematic view of the fields in the LF configuration (static case). The muon ensemble will sense the combination of the external field (**B**$_{ext}$ applied along the initial muon polarization **P**(0), thick red vector) and of the internal fields (thin red vector) which are randomly oriented at the muon site. The resulting fields are the green thin vectors.*

4.3.3.1. LF external field and static field distribution

If we take first the situation of a static Gaussian field distribution is present at the muon site (see Section 4.1.2.1), then the addition of the external field along the *z*-axis will modify the

field distribution along the z-axis to

$$f(B_z) = \frac{1}{\sqrt{2\pi\langle\Delta B^2\rangle}} \exp\left[-\frac{(B_z - B_{\text{ext}})^2}{2\langle\Delta B_\alpha^2\rangle}\right] \, , \tag{4.51}$$

whereas the ones along x and y-axis will not be modified.

By introducing the field distributions in the main formula Eq. 4.4 and integrating, one gets

$$P_z^{\text{long.GKT}} = 1 - \frac{2\sigma^2}{(\gamma_\mu B_{\text{ext}})^2} \cdot \left[1 - e^{-\frac{\sigma^2 t^2}{2}} \cos(\gamma_\mu B_{\text{ext}} t)\right] + \frac{2\sigma^4}{(\gamma_\mu B_{\text{ext}})^3} \int_0^t e^{-\frac{\sigma^2 t'^2}{2}} \sin(\gamma_\mu B_{\text{ext}} t')dt' \, . \tag{4.52}$$
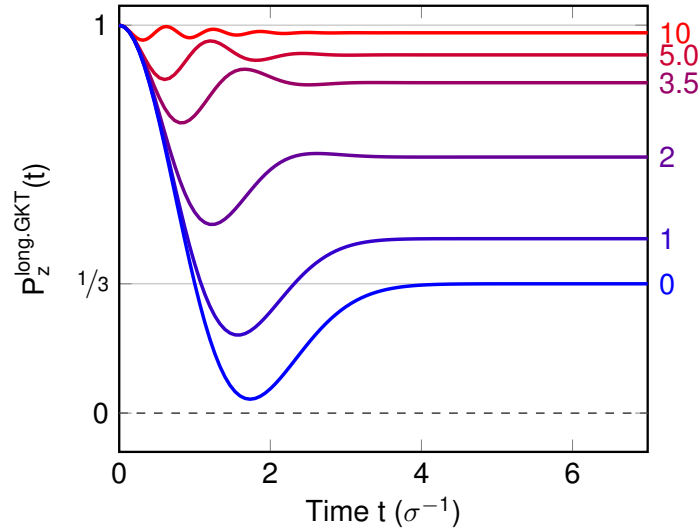
Figure 4.33.: *Effect of an external field* **B**$_{ext}$ *on the shape of the longitudinal polarisation function for a Maxwell distribution of the field modulus (isotropic Guassian distribution). The numbers close to each full line are B$_{ext}$ in units of the standard deviation σ/γ_μ.*
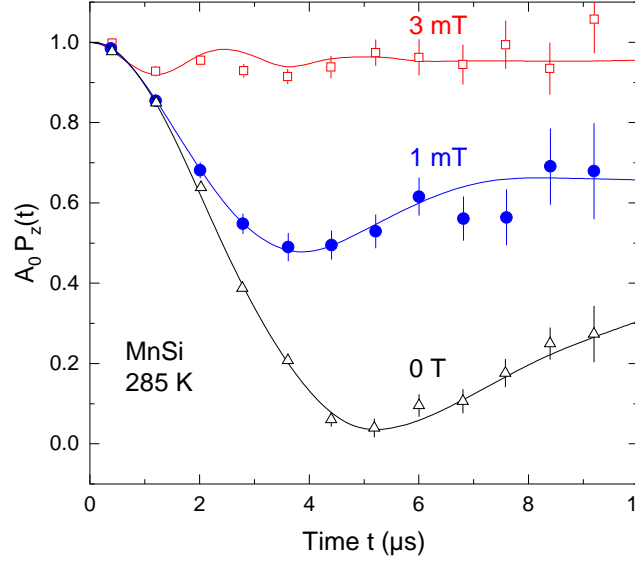
Figure 4.34.: *Example of a Gaussian Kubo-Toyabe depolarization with a longitudinal field-decoupling: Muon spin relaxation in the paramagnetic phase of MnSi [45]. The local field is produced in this case mainly by the Mn nuclear moments. The electronic Mn moments fluctuate very fast and do not contribute to the muon spin depolarization (i.e. $\nu \gg 1$).*

Similarly, if a Lorentzian field distribution is present at the muon site (see Section 4.1.2.2), then the addition of the external field along the z-axis will modify the field distribution along the z-axis to

$$f(B_z) = \frac{1}{\pi} \cdot \frac{\Lambda}{\Lambda + (B_z - B_{\text{ext}})^2} \quad , \tag{4.53}$$

and we finally get the polarization function

$$P_z^{\text{long.LKT}} = 1 - \frac{a}{\gamma_\mu B_{\text{ext}}} \cdot j_1(\gamma_\mu B_{\text{ext}} t)\, e^{-at} - \left(\frac{a}{\gamma_\mu B_{\text{ext}}}\right)^2 \cdot \left[j_0(\gamma_\mu B_{\text{ext}} t)\, e^{-at} - 1\right] -$$

$$- \left[1 + \left(\frac{a}{\gamma_\mu B_{\text{ext}}}\right)^2\right] \cdot a \int_0^t j_0(\gamma_\mu B_{\text{ext}} t')\, e^{-at'}\, dt' \quad , \tag{4.54}$$

where, as before $a/\gamma_\mu = \Lambda$, and j_0 and j_1 are spherical Bessel functions.
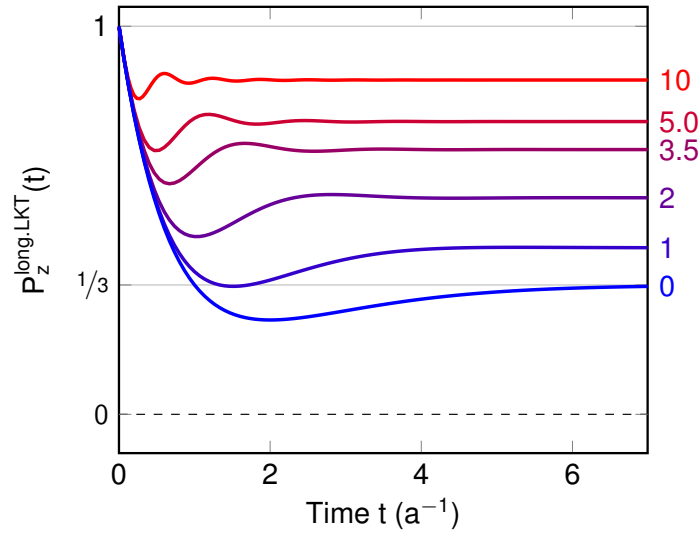
Figure 4.35.: *Effect of an external field $\mathbf{B}_{ext}$ on the shape of the longitudinal polarisation function for a squared-Lorentzian distribution of the field modulus. The numbers close to each full line are B_{ext} in units of the HWHM $\Lambda = a/\gamma_\mu$.*
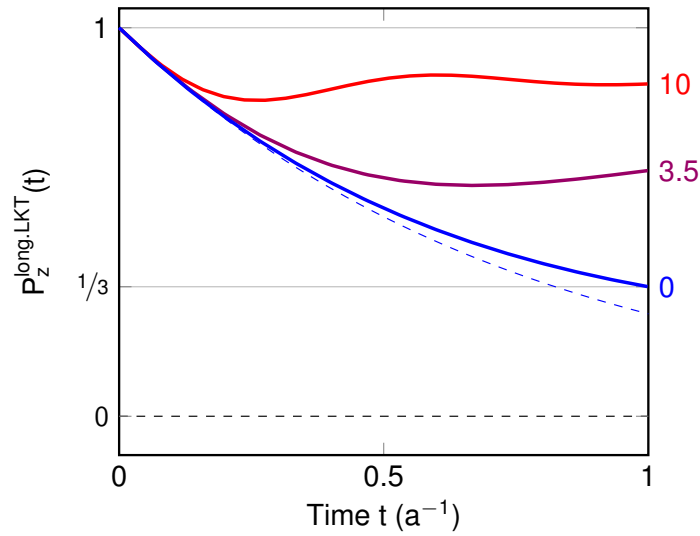
Figure 4.36.: *Effect of an external field $\mathbf{B}_{ext}$ on the shape of the longitudinal polarisation function for a squared-Lorentzian distribution of the field modulus shown for early times. The numbers close to each full line are B_{ext} in units of the HWHM a/γ_μ. The dashed line represents an exponential depolarization $P_z^{LKT}(t) \simeq \exp(-4at/3)$ which is the early time development of the static P_z^{LGT} function (see Section 4.1.2.2).*
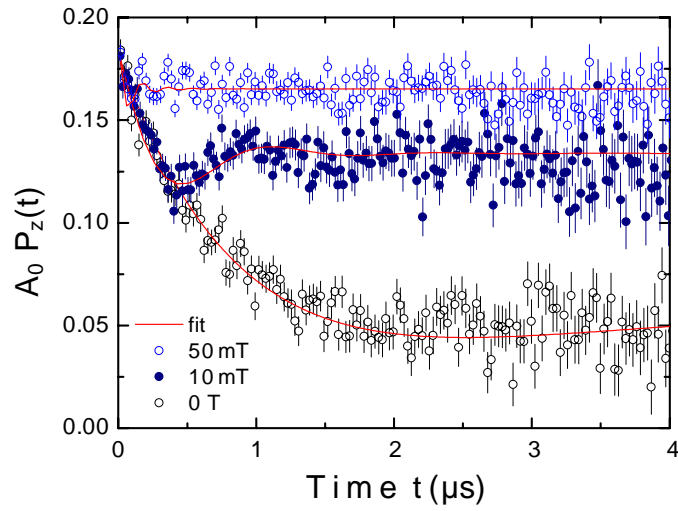
Figure 4.37.: *Example of a Lorentzian Kubo-Toyabe depolarization with a longitudinal field-decoupling: Muon spin relaxation in the paramagnetic phase of LaFeAsO (parent coumpound of the so-called iron-based supercon-ductors) [46]. The depolarization is mainly due to ferromagnetic impurities.*

4.3.3.2. LF external field and dynamical effects

We investigate now the effect of dynamics when an external longitudinal field is applied to the system. The application of this LF field creates Zeeman levels for the muon spin with an energy difference $2|\Delta E|$ (see Fig. 4.38). The spin $|+\rangle$ configuration is the most favorable and will have its energy lowered by

$$\Delta E = -\langle \mathbf{m}_\mu \cdot \mathbf{B}_{\text{ext}} \rangle = -\gamma_\mu \langle \mathbf{I}_\mu \cdot \mathbf{B}_{\text{ext}} \rangle = -\gamma_\mu \hbar \frac{1}{2} B_{\text{ext}} \quad , \qquad (4.55)$$

and the spin $|-\rangle$ will have its energy raised by the same amount. The difference is therefore

$$2|\Delta E| = 2\gamma_\mu \hbar \frac{1}{2} B_{\text{ext}} = \hbar \gamma_\mu B_{\text{ext}} = \hbar \omega_{\text{L}} \quad . \qquad (4.56)$$

We see that the Zeeman splitting correspond to the Larmor angular velocity (see also Section 1.6.2.2).
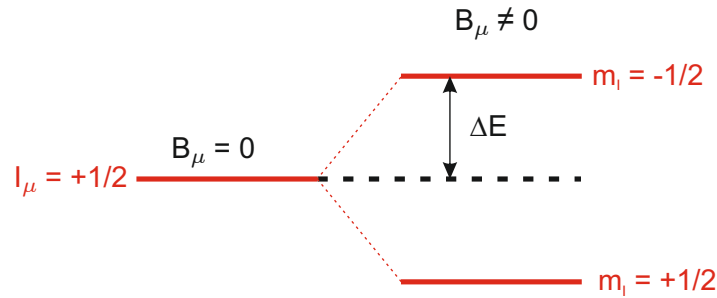
Figure 4.38.: *Splitting of the muon energy levels $|+\rangle$ and $|-\rangle$ when a LF field is applied.*

In the previous Section, we have seen that if the internal field distribution (which is on top of the external field) is static and weaker than the external field, the muon polarization is essentially quenched (*i.e.* no depolarization), with a gradually disappearing oscillating amplitude corresponding to the fact that the total field is not exactly parallel to the external one. Therefore, we see that a time-dependent perturbation of the internal field (*i.e.* a fluctuation process) is needed to observe a depolarization. This kind of depolarization is called "spin-lattice" depolarization (or relaxation) as we need an exchange of energy between the spin-bath and the muon spin.[8]

Basically, two conditions are needed:

1. The fluctuating field must have a component transverse to the external field and

2. the fluctuation process must supply energy to the muon corresponding to the Zeeman splitting, such that the muon spin can flip.

---

[8]Note that the situation is different than the previous cases, where only the "adiabatic" or dephasing part of the depolarization was considered. This was due either to the absence of Zeeman splitting (ZF) case in Section 4.3.2.1 or to the assumption of a static internal field distribution in Section 4.3.3.1.

We can understand the first condition by seeing that longitudinal fluctuations (*i.e.* changing only slightly the field seen by the muon, as the external field is much higher than the internal one) only slightly modulate the Zeeman splitting (as the spin eigenstates are not function of the field strength) but do not induce transitions between the levels.

The second condition will be discussed later in this Section.

Let assume now that we apply a longitudinal field applied to a system which presents without field an isotropic Gaussian field distribution, but in which also magnetic fluctuations are present. The corresponding static depolarization case is described by the complicated equation for $P_z^{\text{long.GKT}}$ (Eq. 4.52) that we just introduced in the previous Section. The task now would be to use this depolarization function $P_z^{\text{long.GKT}}$ in the strong collision model approximation (see Section 4.3.2 and Eq. 4.45). We see that this is a formidable task and actually no analytical formula is obtained. Fortunately for us an approximate analytical solution has been by provided by A. Keren [47] from perturbation theory and is written as

$$P_{z,\,\text{dyn}}^{\text{long.GKT}}(t, \sigma, \nu, \omega_\mu) = \exp\left[-\Gamma(t)\,t\right] \quad, \tag{4.57}$$

with

$$\Gamma(t)\,t = 2\sigma^2 \frac{\left\{\left(\omega_\mu^2 + \nu^2\right)\nu t + \left(\omega_\mu^2 - \nu^2\right)\left[1 - e^{-\nu t}\cos(\omega_\mu t)\right] - 2\nu\omega_\mu e^{-\nu t}\sin(\omega_\mu t)\right\}}{\left(\omega_\mu^2 + \nu^2\right)^2} \quad, \tag{4.58}$$

where $\omega_\mu = \gamma_\mu B_{\text{ext}}$.

We can now examine the behavior of Eq. 4.57 in three different limits:

- In zero applied field we have $\omega_\mu = 0$ and we see that the depolarization function simplifies to

$$P_{z,\,\text{dyn}}^{\text{long.GKT}}(t, \sigma, \nu, \omega_\mu = 0) = \exp\left[-2\frac{\sigma^2}{\nu^2}\left[\exp(-\nu t) - 1 + \nu t\right]\right] \quad, \tag{4.59}$$

  which is as expected equivalent to the Abragam formula (Eq. 4.47) obtained above.

- In the fast fluctuation limit (or extreme narrowing limit) where $\nu \gg 1$, one finds

$$P_{z,\,\text{dyn}}^{\text{long.GKT}}(t, \sigma, \nu, \omega) = \exp\left[-\frac{2\sigma^2\nu}{\omega_\mu^2 + \nu^2}t\right] \quad. \tag{4.60}$$

  The depolarization has an exponential shape and here again by setting the external field to zero one obtains the Equation 4.49 already obtained above.

By looking at the Eq. 4.60, we can see that we can express the depolarization rate in this limit as a function of the Fourier transform $J(\omega)$ of the autocorrelation function, often referred to as the spectral density, as we have (remembering that $\tau_c = \tau = 1/\nu$)

$$J(\omega) = \langle B_\alpha^2(0)\rangle \int\limits_{-\infty}^{\infty} e^{-|t'|/\tau_c}e^{-i\omega t'}\,dt' \propto \frac{1/\tau_c}{\omega^2 + 1/\tau_c^2} = \frac{\nu}{\omega^2 + \nu^2} \quad. \tag{4.61}$$
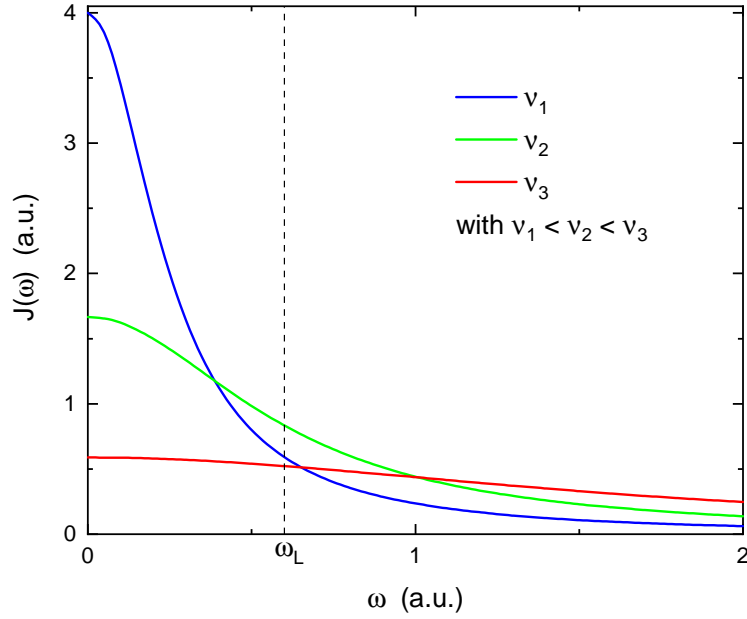
Figure 4.39.: *Spectral density functions for different values of the fluctuation rate $\nu = 1/\tau$ with here $\nu_1 < \nu_2 < \nu_3$. A particular value of the Larmor angular velocity ω_L is chosen and we see that $J(\omega_L)$ is maximum for a particular value of the fluctuation rate (see text).*

We see therefore that for fast fluctuations, the depolarization rate samples the spectral density of the autocorrelation function at the value of the Larmor angular velocity ω_μ.[9] We first note that in view of the muon gyromagnetic ratio, the angular velocity is about 85.1×10^6 rad/s for a typical applied field of 0.1 Tesla, and this value is much smaller that the typical fluctuation rates in solids ranging between $\nu = 10^{13} - 10^9$ s^{-1}.

Therefore, usually the depolarization rate arising from fluctuations shows little dependence on the applied field. This situation would correspond to the flat slopes, just above $\omega = 0$, observed for the curves with large ν values displayed on Figure 4.39. Hence, this situation is in sharp contrast with the one reported with static internal fields, where a strong dependence of the depolarization is observed with modest values of the applied LF field (see for example Eq. 4.52).

---

[9]This corresponds to the second conditions that we listed above.
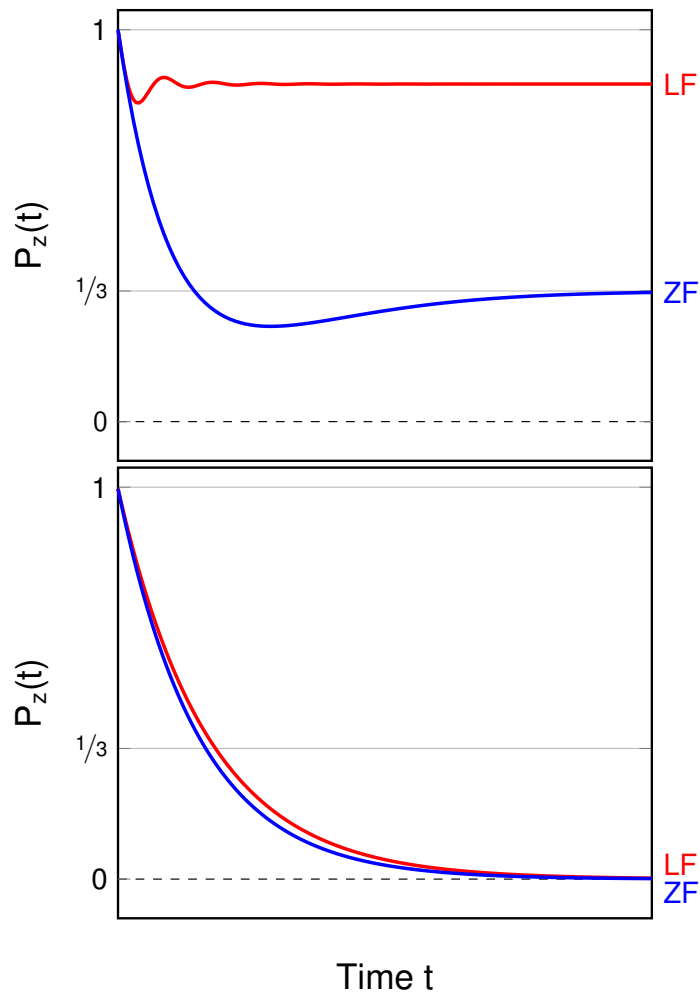
Figure 4.40.: *Schematic comparison of the effect of a LF field on two early-time exponential like depolarization function. Top panel: here the ZF depolarization is due to a static Lorentzian field distribution due to dilute magnetic moments (see Eq. 4.24). The quenching of the depolarization occurs with low values of the LF field. Bottom panel: here the ZF depolarization is due to the presence of fluctuations acting on a instantaneous Gaussian field distribution a static Lorentzian field distribution (see Eq. 4.49). As the fluctuations are fast, the application of a LF field has only a very small effect on the depolarization ($\nu \gg \omega_L$).*
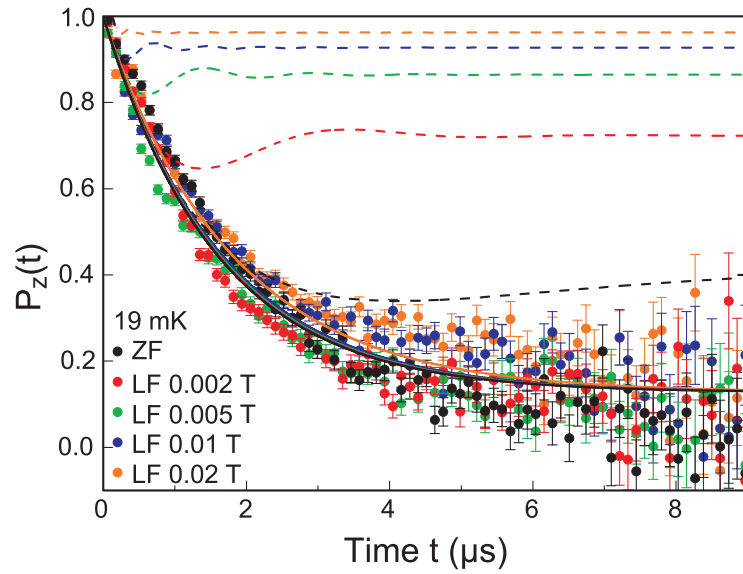
Figure 4.41.: *Very convincing example of the occurrence of fluctuations acting on the muon-spin depolarization rate. The measurements are performed on the system $Ca_{10}Cr_7O_{28}$. This system is a so-called spin liquid (SL). A SL state is a lattice of magnetic ions whose ground state has no static magnetism and, in fact, the magnetic moments fluctuate coherently down to the lowest temperatures. Spin-liquid behavior can be due when competition (known as frustration) between interactions suppresses the long-range magnetic order.*
The data shown were obtained in longitudinal field at 19 mK. The zero-field data set is modeled by both a LKT function (static hypothesis, see Eq. 4.24, dashed black line) and a function exhibiting fast dynamics (see Eq. 4.49, solid black line). Using the fitted parameters, the corresponding static (dashed lines) and dynamic (solid lines) depolarization functions are simulated for various longitudinal fields (using respectively the Eqs. 4.54 and 4.60). Clearly, the dynamic scenario is in much better agreement with the data. The colour code of the simulations corresponds to the colour code of the data. Taken from Ref. [48]

We note that information on the fluctuation rate can be obtained either by dramatically increasing the LF field (nowadays field up to 10 Tesla are available) or when approaching a magnetic transition upon cooling the temperature. At this point one observes a slowing-down of the fluctuations, which become usually observable in the μSR time window [corresponding to a narrow spectral density $J(\omega)$].

In the best case (*i.e.* if ν is not too large), they are two ways to determine possibly the fluctuation rate ν:

- Measurement as a function of field are performed at a given temperature in the paramagnetic phase (ν is constant and assumed not too fast). As a function of field, the depolarization will follow the spectral density $J(\omega)$ and its field dependence can be fitted using Eq. 4.60.

- Measurements as a function of temperature are performed at a fixed applied field. For a given applied field B_{ext} corresponding to a Larmor angular velocity (or Zeeman splitting) $\omega_{\text{L}} = \gamma_\mu B_{\text{ext}}$ the muon depolarization can be small if the power spectrum of the fluctuation is too narrow (corresponding to slow fluctuations) or too broad (corresponding to fast fluctuations). A maximum is reached when the fluctuation rate matches the Larmor angular velocity:

$$\omega_{\text{L}} = \nu = \frac{1}{\tau} \quad . \tag{4.62}$$
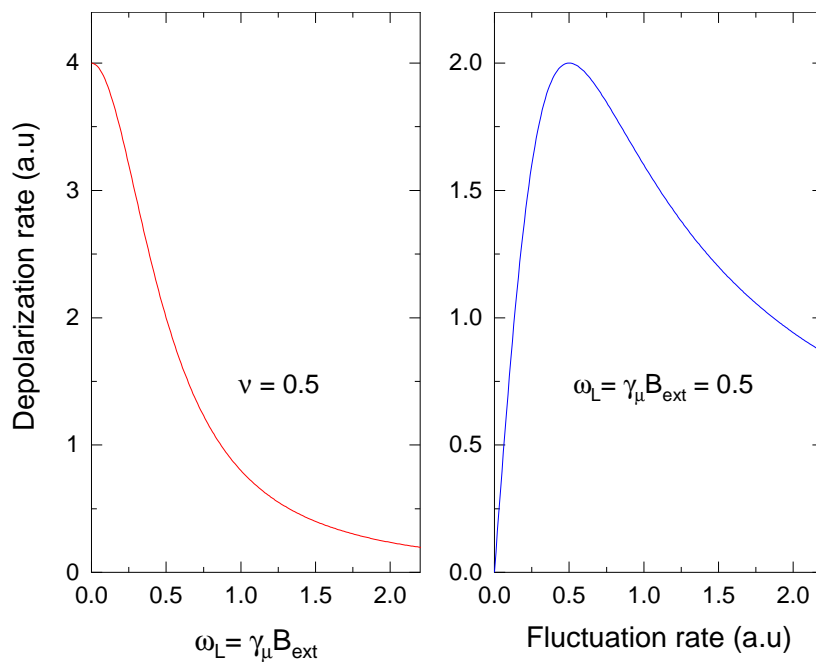
Figure 4.42.: *Dependence of the depolarization rate as a function: (left panel) of the applied LF field with a constant fluctuation rate (this situation is obtained by performing measurements at a given temperature). This is actually a mapping of the spectral density function; (right panel) of the fluctuation rate with a constant applied LF field (situation may occur by performing measurements as a function of the temperature). Note the maximum when $\nu = \omega_L$.*
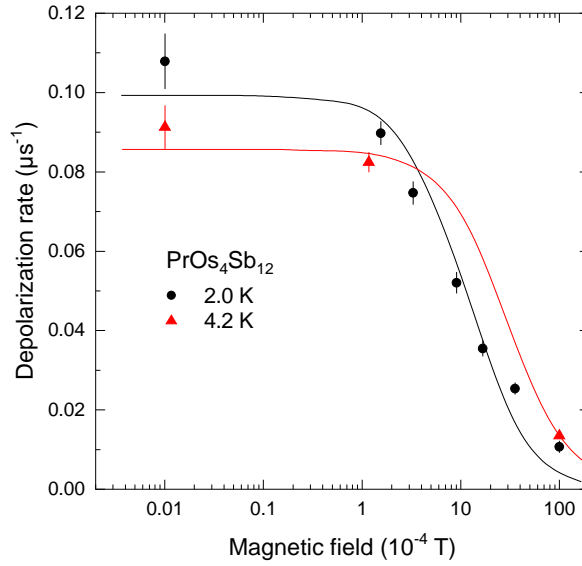
Figure 4.43.: *Example of LF measurements to determine the fluctuation rate on the filled-skutterudite system PrOs$_4$Sb$_{12}$. Here, the parameter Λ represents the depolarization rate. This system is superconductor below 1.8 K, but also shows very slow fluctuation just above T_c. The lines represent fits of the Eq. 4.60 on the data providing a very slow fluctuation time of, for example, $\tau = 0.51\,\mu s$ at 2.0 K. Taken from Ref. [49].*
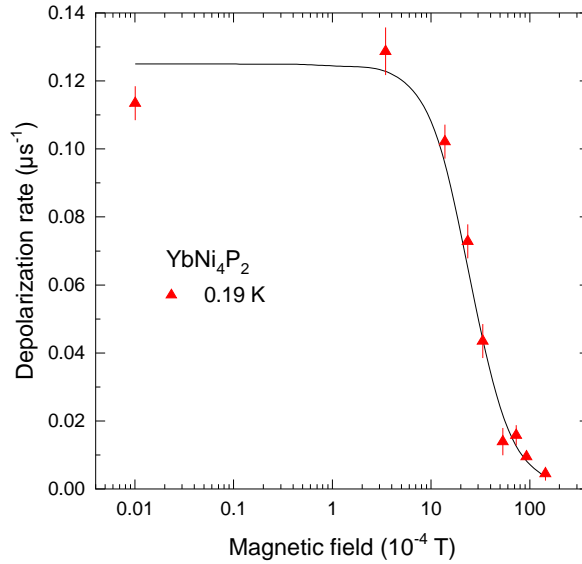
Figure 4.44.: *Another example of LF measurements to determine the fluctuation rate on the ferromagnetic system YbNi$_4$P$_2$. This system has a ferromagnetic transition at 140 mK. It also shows very slow fluctuation just above T_C. Here, the parameter λ_L represents the depolarization rate which is marked to be equal to $1/T_1$ (see text). The line in the main panel represents a fit using Eq. 4.60 providing a very slow fluctuation time of $\tau = 0.6\,\mu s$ at 190 mK. Taken from Ref. [50].*

The maximum of the depolarization rate as a function of temperature, which occurs when the fluctuation rate matches the Larmor angular velocity is often referred as T_1 minimum in the literature (where $1/T_1$ is associated to the spin-lattice relaxation in the wording used by NMR). By looking at the right panel of Fig. 4.42, we see that in the slow fluctuation regime the depolarization rate is *proportional* to the fluctuation rate, but it becomes *inversely proportional* to it in the fast fluctuation regime. This decrease of the depolarization with increasing fluctuation rate may appear counter-intuitive, but it reflects the fact that the muon spins cannot respond if the fluctuations become much faster than the Larmor angular velocity.

4.3.4. Dynamical effects in TF external field

For completeness, we just mention the main formula considering the presence of dynamics in a TF experiment. One finds that the in the fast fluctuation limit ($\nu \gg 1$) the TF and LF depolarization function have the same decay rate. This is different that the situation without fluctuation, where one observes a factor of 2 difference (see the paragraph on page 113 treating the early time behavior of the Kubo-Toyabe formula and the Eq. 4.32). Also for slow fluctuation, this factor of 2 persists. This reflects the fact that in these limits only the "adiabatic" or dephasing part of the depolarization was considered and in ZF the second moments for field directions perpendicular to the initial muon polarization contribute to the muon depolarization, whereas in TF only the second moment for direction of the external field plays a role. On the other hand for fast fluctuations in addition to the "adiabatic" part, another process which destroys the muon spin polarization is the transition between the Zeeman levels which exists also in TF experiments. However, the efficiency of this process in TF is half of that that we have in LF, as when a spin flip occurs this corresponds in TF to a loss of polarization from +1 to 0, whereas the polarization changes from +1 to -1 in LF.

Hence the contribution to the depolarization arising from dynamical effects in TF can be written as

$$\lambda = \gamma_\mu^2 \left[\frac{\langle B_z^2 \rangle}{\nu} + \frac{\nu \left(\langle B_x^2 \rangle + \langle B_y^2 \rangle \right)}{2(\omega_\mu^2 + \nu^2)} \right] \quad , \tag{4.63}$$

where the first term on the right-hand side is due to the "adiabatic" part (dephasing effects) and the second represents the spin-flip processes. For rapid fluctuations ($\nu \gg 1$), we see that we can write

$$\lambda = \frac{\gamma_\mu^2}{\nu} \left[\langle B_z^2 \rangle + \frac{\langle B_x^2 \rangle + \langle B_y^2 \rangle}{2} \right] \quad , \tag{4.64}$$

and by assuming an isotropic internal field distribution $\gamma_\mu^2 \langle B_\alpha^2 \rangle = \sigma^2$ we obtain

$$\lambda = \frac{2\sigma^2}{\nu} \quad , \tag{4.65}$$

which is the same depolarization rate as in the LF case when $\nu \gg 1$ (see limit of Eq. 4.60).

5. Studying magnetism with the μSR technique

5.1. Local magnetic fields in magnetic materials

In this Section, we will first look at the interaction muon-electron in order to deduce the main contributions acting on the local field sensed by the muon in a magnetic material.

5.1.1. The interaction muon - electron

We assume first a muon located at the origin in interaction with a single electron. This interaction is most generally described by the Dirac equation in the low energy limit and making use of a nonrelativistic approach. If the muon is static, we can write the Hamiltonian of the muon-electron ensemble as[1]

$$\hat{\mathcal{H}} = \frac{1}{2M_e}(\mathbf{p} + e\mathbf{A})^2 + g_e\mu_B\mathbf{S}\cdot(\nabla\times\mathbf{A}) + V(r) \ , \qquad (5.1)$$

where the first term on the right-hand side (kinetic energy term) is obtained considering the canonical momentum (see Eq. A.87), V represents the potential energy and $\mathbf{A}$ is the magnetic vector potential with $\mathbf{B} = \nabla\times\mathbf{A}$, where $\mathbf{B}$ is the field due to the muon magnetic moment $\mathbf{m}_\mu$. The spin of the electron is defined as $\mathbf{S}$ and is given in without units (*i.e.* the $\hbar$ is integrate

---

[1]Remember that the moment of the electron is pointing in opposite direction to the spin or to the angular momentum.

into the Bohr magneton μ_B). The magnetic vector potential can be written as[2]

$$\mathbf{A} = \frac{\mu_0}{4\pi}\frac{\mathbf{m}_\mu \times \mathbf{r}}{r^3} = \frac{\mu_0}{4\pi}\nabla \times \left(\frac{\mathbf{m}_\mu}{r}\right) \ . \tag{5.2}$$

By omitting the term quadratic in $\mathbf{m}_\mu$, one can rewrite the Hamiltonian as

$$\begin{aligned} \hat{\mathcal{H}} &= \hat{\mathcal{H}}_0 + \hat{\mathcal{H}}' \\ &= \hat{\mathcal{H}}_0 + \frac{e}{2M_e}(\mathbf{p}\cdot\mathbf{A} + \mathbf{A}\cdot\mathbf{p}) + g_e\mu_B\mathbf{S}\cdot(\nabla\times\mathbf{A}) \end{aligned} \tag{5.3}$$

where $\hat{\mathcal{H}}_0 = \mathbf{p}^2/2M_e + V(r)$ contains the non-interesting terms which do not couple with $\mathbf{m}_\mu$. Taking into account the singularity of the interaction at $r = 0$, we finally get (see Exercises)

$$\boxed{\hat{\mathcal{H}}' = \frac{\mu_0}{4\pi}2g_\mu^*\mu_B\mu_N\mathbf{I}_\mu \cdot \left[\frac{\mathbf{L}}{r^3} + \left(\frac{3\mathbf{r}(\mathbf{S}\cdot\mathbf{r})}{r^5} - \frac{\mathbf{S}}{r^3}\right) + \frac{8\pi}{3}\mathbf{S}\,\delta(\mathbf{r})\right]} \tag{5.4}$$

The first term represents the coupling of the muon with the angular momentum of the electron. The term in curly brackets represents the dipole-dipole interaction everywhere but not at the origin (muon site). Finally, the last term takes care of the case when the electron as a non-zero probability density at the muon site, *i.e.* represents the contact term due to the electron spin density at the muon site.

Even though Eq. 5.4 represents the interaction with a single electron, it show us the main interactions that we will have to deal with, when studying the muon in a solid where a multitude of electron are near the muon, represented by an electronic wave function ψ_e.[3]

5.1.2. Dipolar and contact contributions

The Hamiltonian given by Eq. 5.4 looks like a Zeeman interaction of the muon-spin $\mathbf{I}_\mu$ with some effective fields.

---

[2]This formula is obtained by using the 4th Maxwell equation without electrical field and the vector identity

$$\begin{aligned} \nabla\times\mathbf{B} &= \nabla\times(\nabla\times\mathbf{A}) \\ &= \nabla(\nabla\cdot\mathbf{A}) - \nabla^2\mathbf{A} \\ &= \mu_0\mathbf{J} \ . \end{aligned}$$

Choosing the Coulomb gauge ($\nabla\cdot\mathbf{A} = 0$) we finally have

$$\nabla^2\mathbf{A} = -\mu_0\mathbf{J} \ ,$$

which is the Poisson equation for each of the components of $\mathbf{A}$. The solution is

$$\mathbf{A}(\mathbf{r}) = \frac{\mu_0}{4\pi}\int\frac{\mathbf{J}(\mathbf{r}')}{|\mathbf{r}-\mathbf{r}'|}d\mathbf{r}' \ ,$$

and by integrating over a hypothetical loop of current producing the moment we get Eq. 5.2 for 'large' values of r.

[3]We could also see the application to solid by considering a *mean field approximation* and replace all electronic operators by their expectation values (*i.e.* $\mathbf{S} \to \langle\mathbf{S}\rangle$).

5.1.2.1. Orbital field

The first part of the Hamiltonian can be written as

$$
\begin{aligned}
\hat{\mathcal{H}}'_{\text{orb}} &= -\mathbf{m}_\mu \cdot (-1) \frac{\mu_0}{4\pi} 2\mu_{\text{B}} \frac{\mathbf{L}}{r^3} \\
&= -\mathbf{m}_\mu \cdot \mathbf{B}_{\text{orb}} \quad .
\end{aligned}
\tag{5.5}
$$

We have used that $\mathbf{m}_\mu = g_\mu^* \mu_{\text{N}} \mathbf{I}_\mu$. The distance between the electron and the muon is r. We have defined

$$
\boxed{\mathbf{B}_{\text{orb}} = -\frac{\mu_0}{4\pi} 2\mu_{\text{B}} \frac{\mathbf{L}}{r^3} \quad .}
\tag{5.6}
$$

$\mathbf{B}_{\text{orb}}$ is the hypothetical field created by an electron orbiting around the muon at distances r with angular momentum $\mathbf{L}$. Such a situation has not been observed yet and we will safely discard this contribution.

5.1.2.2. Dipolar field

Let us now consider the case where we have electrons with a negligible probability density at the muon site. These electrons could be located on orbitals of atoms of the lattice and can be considered as localized. Therefore these electrons do not orbit around the muon and the first term of Eq. 5.4 vanishes. Similarly the last term, the contact term, will not contribute as it is proportional to $\delta(\mathbf{r})$. The interaction will therefore be limited to

$$
\hat{\mathcal{H}}'_{\text{dip}} = \frac{\mu_0}{4\pi} 2g_\mu^* \mu_{\text{B}} \mu_{\text{N}} \mathbf{I}_\mu \sum_j \left(\frac{3\mathbf{r}_j(\mathbf{S}_j \cdot \mathbf{r}_j)}{r_j^5} - \frac{\mathbf{S}_j}{r_j^3} \right) \quad ,
\tag{5.7}
$$

which is also often written as

$$
\begin{aligned}
\hat{\mathcal{H}}'_{\text{dip}} &= -\mathbf{m}_\mu \cdot \frac{\mu_0}{4\pi} \sum_j \left(\frac{3\mathbf{r}_j(\mathbf{m}_{e,j} \cdot \mathbf{r}_j)}{r_j^5} - \frac{\mathbf{m}_{e,j}}{r_j^3} \right) \\
&= -\mathbf{m}_\mu \cdot \mathbf{B}_{\text{dip}}(\mathbf{r}_\mu)
\end{aligned}
\tag{5.8}
$$

We have used here that $\mathbf{m}_e \simeq -2\mu_{\text{B}}\mathbf{S}$ and we have defined

$$
\boxed{\mathbf{B}_{\text{dip}}(\mathbf{r}_\mu) = \frac{\mu_0}{4\pi} \sum_j \left(\frac{3\mathbf{r}_j(\mathbf{m}_{e,j} \cdot \mathbf{r}_j)}{r_j^5} - \frac{\mathbf{m}_{e,j}}{r_j^3} \right) \quad .}
\tag{5.9}
$$

We note few points:

- The dipolar field seen by the muon at a given site linearly scales with the value of the electronic moment.

- The dipolar field value and direction are strongly dependent on the muon stopping site with respect to the electronic moments.
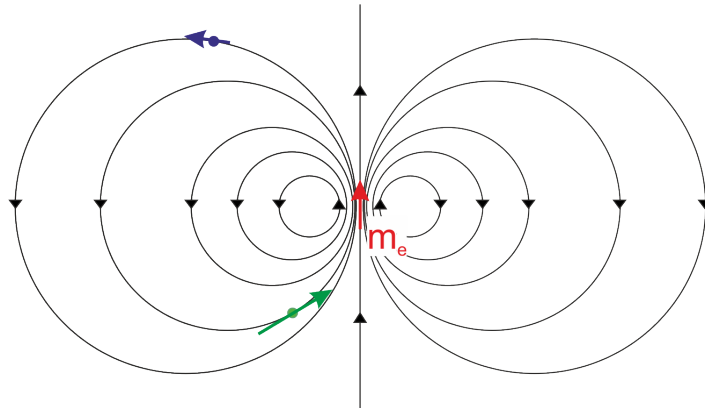
Figure 5.1.: *Comparison of the direction and value (sketched) for muon sites around a single electronic moment.*

- As the dipolar field is anisotropic, the direction of the field at the muon site is not necessarily parallel to the direction of the electronic moments (for example in the case of a ferromagnet)
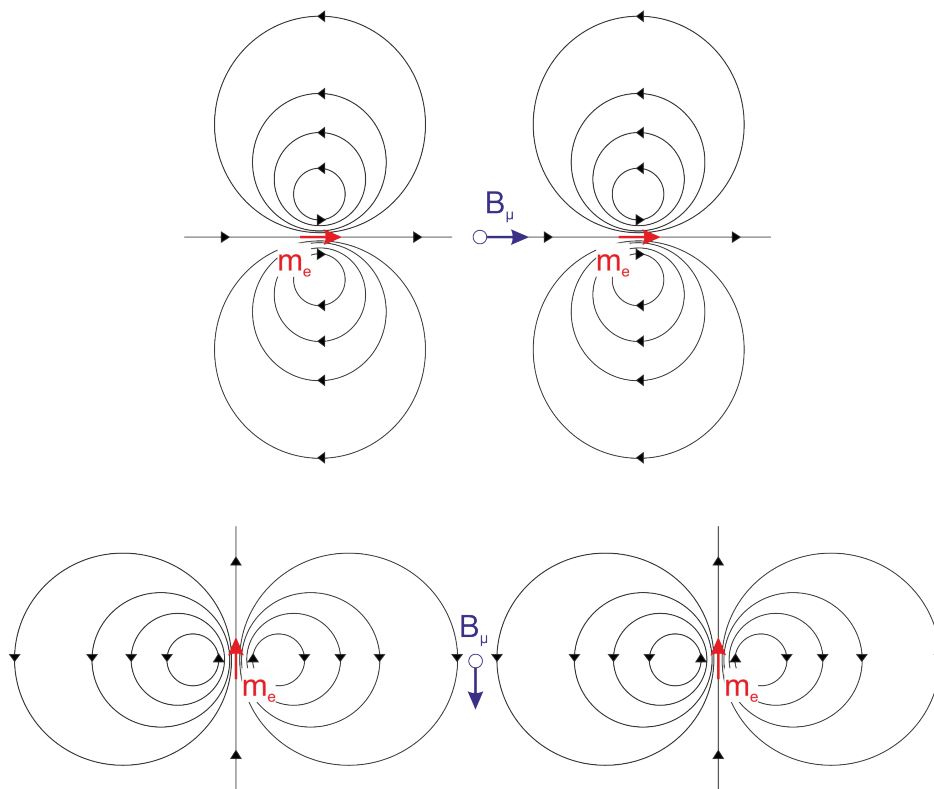
Figure 5.2.: *Comparison of the direction of the field seen by the muon in between two moments with different orientation. Note the different orientation of the field seen by the muon with respect to the orientation of the electronic moments in the lower figure.*

- For muons stopping at crystallographic equivalent sites, the direction and value of the field seen by the muons is dependent of the magnetic structure and is often not unique. In other words, crystallographic equivalent sites can be magnetically inequivalent.
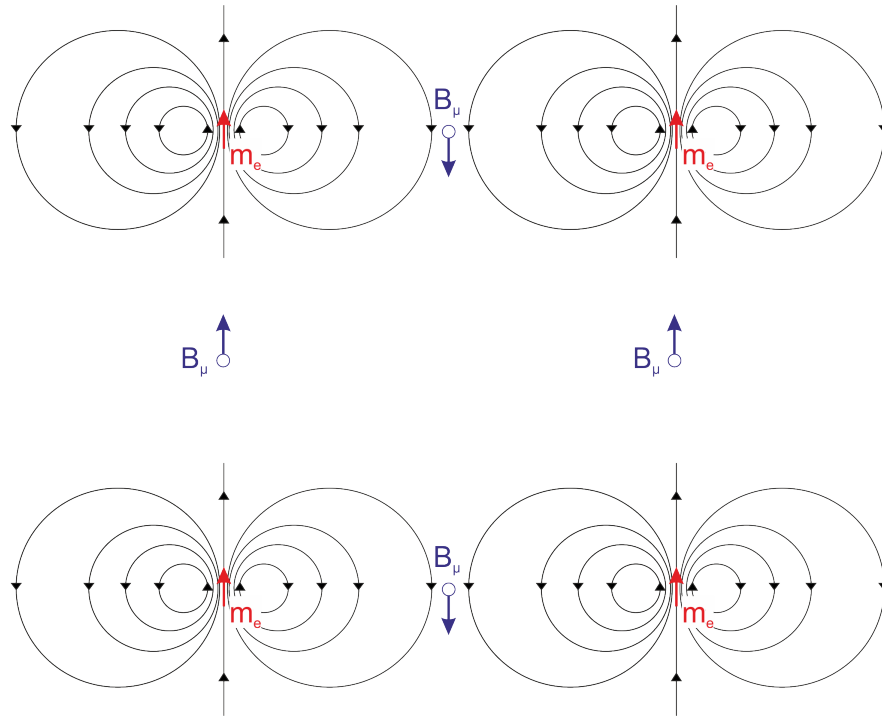
Figure 5.3.: *Simple squared arrangement of ferromagnetically aligned moments. Assume that the muons stop at equivalent muon sites located between two moments. Note the different direction of the field for the equivalent muon sites.*

5.1.2.3. Contact field

Finally the last term of the right-hand side of Eq. 5.4 can be written as

$$\hat{\mathcal{H}}'_{\text{cont}} = -\frac{2\mu_0}{3}\mathbf{m}_\mu \cdot (-1)2\mu_B \mathbf{S}\,\delta(\mathbf{r}) \tag{5.10}$$

$$= -\frac{2\mu_0}{3}\mathbf{m}_\mu \cdot \mathbf{m}_e\,\delta(\mathbf{r})\ . \tag{5.11}$$

As the electron wave function can be written as the tensor product of a position state vector and a spin state vector (a spinor) we can write

$$\Psi(\mathbf{r}, s_z) = \psi(\mathbf{r})\,\chi\ , \tag{5.12}$$

and calculate the matrix elements of the contact term

$$\langle n = 1, \ell = 0, m_S, m_I\,|\,-\frac{2\mu_0}{3}\mathbf{m}_\mu \cdot \mathbf{m}_e\,\delta(\mathbf{r})\,|\,n = 1, \ell = 0, m_S, m_I\rangle\ , \tag{5.13}$$

where we take into account the quantum numbers [*i.e.* n is the principal quantum number giving the electron shell, ℓ is the orbital angular momentum quantum number of the electron (as $\ell = 0$ then $m_\ell = 0$), m_S is the electron spin quantum number and m_I is the muon spin quantum number]. We can write the matrix elements either by keeping the moments or the spins

$$-A'\langle m_S, m_I \mid \mathbf{m}_\mu \cdot \mathbf{m}_e \mid m_S, m_I \rangle = A\langle m_S, m_I \mid \mathbf{I}_\mu \cdot \mathbf{S} \mid m_S, m_I \rangle \ . \tag{5.14}$$

Usually the notation with the spins is adopted and we have

$$A = \frac{2\mu_0}{3} g_e \mu_B g_\mu^* \mu_N \underbrace{\langle n=1, \ell=0 \mid \delta(\mathbf{r}) \mid n=1, \ell=0 \rangle}_{|\psi_{1s}(0)|^2} \ . \tag{5.15}$$

We can therefore rewrite the Hamiltonian in an effective spin (or moment) Hamiltonian as

$$\begin{aligned} \hat{\mathcal{H}}'_{\text{cont}} &= -A'\mathbf{m}_\mu \cdot \mathbf{m}_e \ \text{ or} \\ &= A\,\mathbf{I}_\mu \cdot \mathbf{S} \ . \end{aligned} \tag{5.16}$$

As again the Hamiltonian given by Eq. 5.4 looks like a Zeeman interaction of the muon-spin $\mathbf{I}_\mu$ with some effective fields, we can define here the contact field as

$$\boxed{\mathbf{B}_{\text{cont}} = -\frac{2\mu_0}{3}\,|\psi_{1s}(0)|^2\,g_e\mu_B\mathbf{S} = \frac{2\mu_0}{3}\,|\psi_{1s}(0)|^2\,\mathbf{m}_e \ .} \tag{5.17}$$

Note that as the density of the conduction electrons is enhanced locally at the muon site in order to screen the muon charge (see Section 2.3), the bare contact field is often multiplied by an enhancement factor to account for this perturbation. In this case we just write the probability density for a spherical electron cloud at the muon site by $\eta(0)\,|\psi_{1s}(0)|^2$

In summary, we can say that the dipole and contact fields arise respectively from the localized and the conduction electrons. Hence for s and p electron metals, the dipole field basically vanishes and solely the contact field will be present. On the other hand in systems with unpaired d and f electrons, where those can be considered localized at the ion sites[4], the dipole field is dominant. However, these local electronic moments can also interact with the conduction electrons through the Ruderman-Kittel-Kasuya-Yosida (RKKY) interaction which may strongly enhance the contact term.

5.1.3. Demagnetizing field and Lorentz sphere

We have now determined some contributions of the local field at the muon site for a magnet. We try now to write the equations to compute this local field.

The dipole field is actually expressed as a sum of the contributions of local magnetic moments over the *whole* sample. Even though the dipole field decreases as $1/r^3$ for a moment at a distance r from the muon, the number of moments will increase with r^2. Therefore the

---

[4]This is basically verified by determining the magnetic form factor by neutrons.

sum is expected to have a logarithmic divergence. However, Lorentz has shown that to evaluate $\mathbf{B}_\mu$ we proceed as follow: the muon is imagined to be surrounded by a spherical cavity whose radius R is taken sufficiently large that the matrix lying outside it may be treated as a continuous medium as far as the muon is concerned. This cavity is called the Lorentz sphere. The problem is to calculate the dipole field inside the sphere by restricting the lattice sum and to consider the rest as a continuous medium.
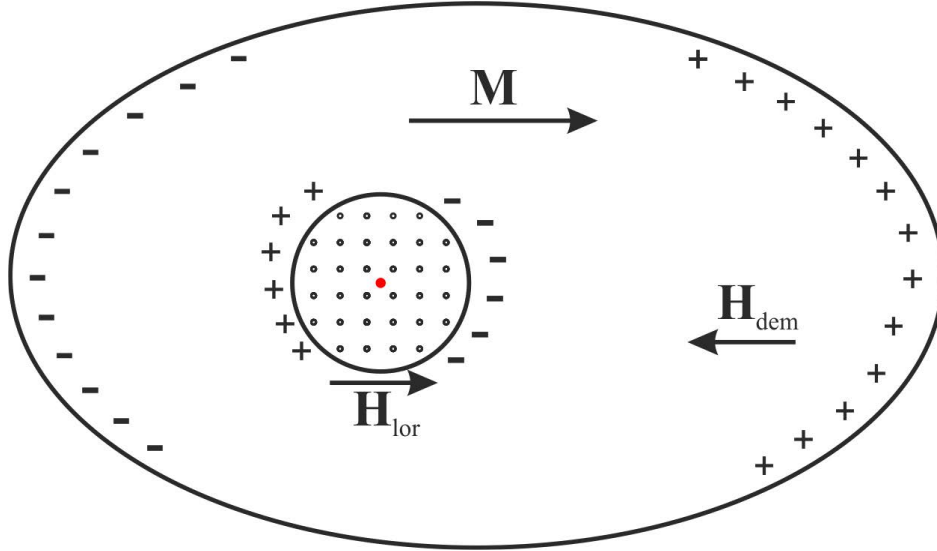
Figure 5.4.: *Schematic representation of the contributions to the local field seen by the muon. We assume a ferromagnetic sample (with a single domain) with a magnetization* **M**. *This magnetization will be accompanied by a demagnetizing field* $\mathbf{H}_{dem}$ *which will have an intensity that will depend on the shape of the sample. In addition, within the Lorentz sphere (which can be thought as a cavity) a so-called "Lorentz-field" is present which can be understood as arising from the "magnetic charges" at the surface of the sphere. The dipolar field created by the moments inside the Lorentz sphere is calculated by performing the sum of the contributions of the individual atoms in the Lorentz sphere (muon: red point at the center of the sphere).*

As seen in Annex A.4, a ferromagnetic sample (with only one domain) having a magnetization **M** will be accompanied by a demagnetizing field

$$\mathbf{H}_{\text{dem}} = -\tilde{N}\,\mathbf{M}\ .\tag{5.18}$$

In addition, inside the Lorentz sphere one will have also a field created by the surface "magnetic charges"

$$\mathbf{H}_{\text{Lor}} = \frac{1}{3}\,\mathbf{M}\ ,\tag{5.19}$$

which will be aligned to the magnetization. The factor $1/3$ arises from the shape of the Lorentz cavity (*i.e.* a sphere).

Inside the Lorentz sphere, the dipole field is calculated by performing the direct sum

$$\mathbf{B}'_{\text{dip}}(\mathbf{r}_\mu) = \frac{\mu_0}{4\pi} \sum_{\text{Lor}} \left(\frac{3\mathbf{r}_j(\mathbf{m}_{e,j} \cdot \mathbf{r}_j)}{r_j^5} - \frac{\mathbf{m}_{e,j}}{r_j^3} \right) \ , \tag{5.20}$$

where the sum is done only on the local moments inside the Lorentz sphere.

Therefore the total field at the muon site for a ferromagnet will be

$$\mathbf{B}_\mu = \mathbf{B}'_{\text{dip}} + \mathbf{B}_{\text{cont}} + \mu_0 \mathbf{H}_{\text{Lor}} + \mu_0 \mathbf{H}_{\text{dem}} \ . \tag{5.21}$$

Note that if the ferromagnetic is not single-domain (the sample is not magnetized), then total magnetization will be zero and $\mathbf{H}_{\text{dem}}$ also. However, if the Lorentz sphere is located in a domain, then $\mathbf{H}_{\text{Lor}}$ will not vanish and the field at the muon site will be

$$\mathbf{B}_\mu = \mathbf{B}'_{\text{dip}} + \mathbf{B}_{\text{cont}} + \mu_0 \mathbf{H}_{\text{Lor}} \ . \tag{5.22}$$

In the case of an antiferromagnet, the total magnetization vanishes. Therefore we will have $\mathbf{H}_{\text{dem}} = \mathbf{H}_{\text{Lor}} = 0$ (also around the Lorentz sphere the magnetization is zero) and the field at the muon site is given as

$$\mathbf{B}_\mu = \mathbf{B}'_{\text{dip}} + \mathbf{B}_{\text{cont}} \ . \tag{5.23}$$

5.2. Examples of magnetic states studied by μSR

The literature is nowadays full of examples of μSR studies dedicated to the magnetic properties of systems, and an interested student will have no difficulty to find a large variety of (review) articles online. The following examples have been chosen to illustrate some special aspects that may appear when performing μSR studies on magnetic materials.

- *Possibility to measure on different type of material: Example in organic system*
  The search for purely organic molecular ferromagnets containing only light elements (carbon, hydrogen, oxygen and nitrogen) is a subject of strong interest. Many organic radicals exist which have unpaired spins, but few are stable enough to be assembled into crystalline structures. Moreover, even when that is possible aligning these spins ferromagnetically is usually impossible. Ferromagnets are rather rare even among the elements and are exclusively found in the *d* or *f*-series. Therefore it is remarkable that ferromagnetism can be found in certain nitronyl nitroxide molecular crystals which possess only *s*- and *p*-electrons (nitronyl nitroxides contain only the elements C, H, N, and O and are therefore fully organic). The first such material to be found, the so-called β crystal phase of para-nitrophenyl nitronyl nitroxide (p-NPNN, $C_{13}H_{16}N_3O_4$), was reported to have a Curie temperature $T_C \simeq 0.6$ K.
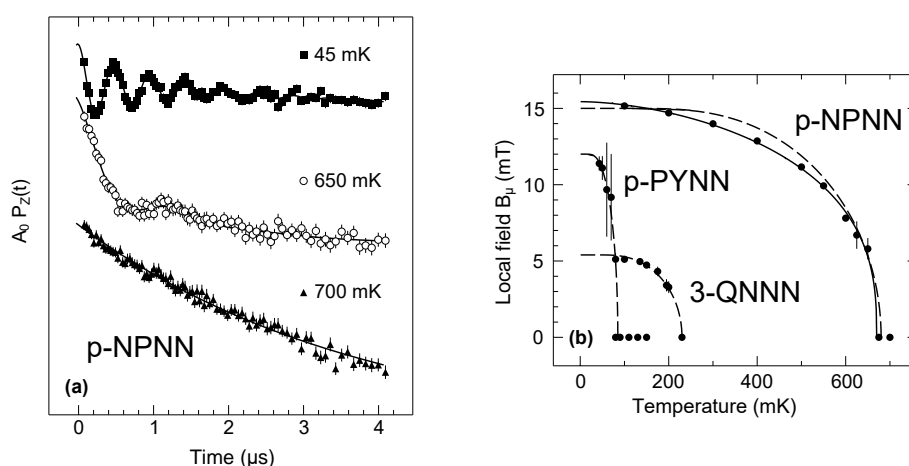
Figure 5.5.: *Magnetic phase transition in organic compounds. Left-hand side panel: some zero-field spectra recorded for p-NPNN. The solid lines result from fits. Right-hand side panel: temperature dependence of the spontaneous μSR frequency in p-NPNN, p-PYNN and 3-QNNN. Taken from Ref. [51].*

The first direct evidence of spontaneous magnetic order in p-NPNN was from μSR measurements [52]. The order was later confirmed by neutron diffraction. The observation of a clear oscillating signal at low temperature is a clear evidence of the existence of long-range static magnetism.

- *Iron-based superconductors: Low moments and subtle features*
  Iron-based superconductors are nowadays considered as the second class of high-T_c superconductors beside the cuprates. This new type of superconductors is based on

conducting layers of iron and a pnictide (typically arsenic and phosphorus). Similarly to the cuprate family, the properties of iron based superconductors change dramatically with doping. The parent compounds are metals (unlike the cuprates) but are ordered antiferromagnetically (like the cuprates). As for cuprates, the superconducting state emerges upon either hole or electron doping.

As said in Section 4.1.1.2, μSR has been instrumental in determining the magnetic properties as the ordered moment is small. The so-called "1111" family shows Fe-magnetism in the absence of doping with a rather low moment, which can be esily detected by μSR (see Fig. 4.11).
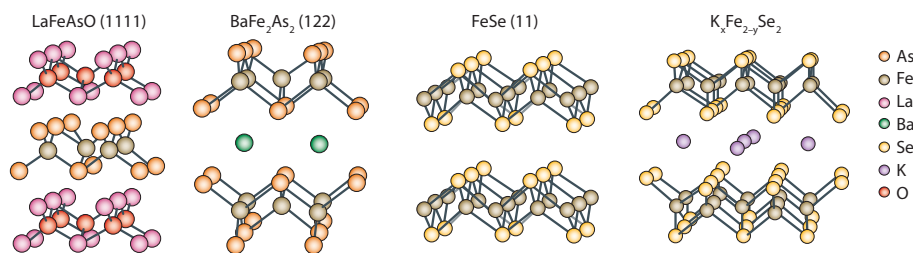
Figure 5.6.: *Crystal structure of LaFeAsO (1111), BaFe$_2$As$_2$ (122), FeSe (11) and K$_x$Fe$_{2-y}$Se$_2$ (adapted from Ref. [53]).*

Interesting insight can be obtained by μSR with the 1111 systems REFeAsO (where RE is a rare-earth). Whereas in the LaFeAsO system solely the iron-magnetism is detected (as La does not have a $4f$ electron), the REFeAsO systems present at low temperature a second magnetic transition $T_{N,RE}$ much below the magnetic ordering of the iron $T_{N,Fe}$. With the exception of the Ce-based system, all the REFeAsO compounds present a similar temperature dependence of the spontaneous μSR frequency reflecting the magnetization of the Fe-sublattice.
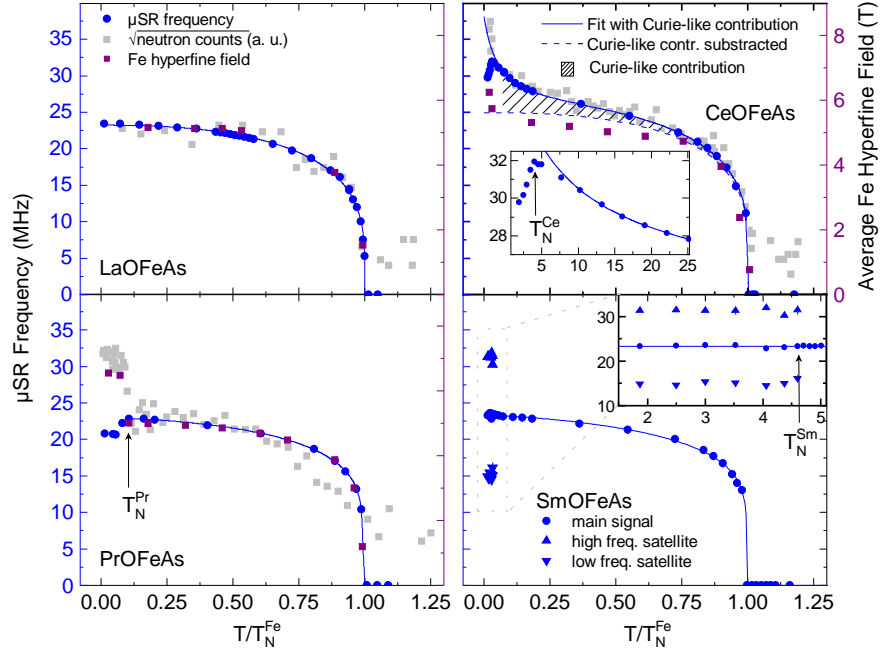
Figure 5.7.: *Main μSR frequency as a function of reduced temperature $T/T_{N,Fe}$ together with the average magnetic hyperfine field at the Fe site from Mössbauer spectroscopy and the square root of the magnetic Bragg-peak intensity of available neutron scattering. The error bars of the μSR frequency are smaller than the data points. Note: i) the different temperature dependence of the μSR frequency for the Ce-based system; and ii) the RE magnetism at low temperatures (with the exception of course of the La-based system).*

The temperature dependence of the Ce-based system below $T/T_{N,Fe}$ reflects the magnetization of the Ce-moments created by the field of the Fe-sublattice, *i.e.* for the Ce-moments, the field from the irons will act as an "external" field. In turn, the induced Ce-moments in the field of the Fe-sublattice will couple with the muon-spin (via dipolar and contact field) and will change the μSR frequency. We can therefore write the temperature dependence of the μSR frequency for CeFeAsO for $T_{N,RE} < T < T_{N,Fe}$ as

$$f_\mu(T) = f_0\Big[1 - \Big(\frac{T}{T_{N,Fe}}\Big)^\alpha\Big]^\gamma \times \Big[1 + \frac{\tilde{C}}{T-\Theta}\Big] \tag{5.24}$$

Fe-sublattice $f_0(T)$

Curie-like Ce magnetization

where $\tilde{C}$ describes the coupling constant of the Ce moments with the muon spin. This model describes the data reasonably well for temperatures between 10 K and up to $T_{N,Fe} = 137\,\text{K}$.
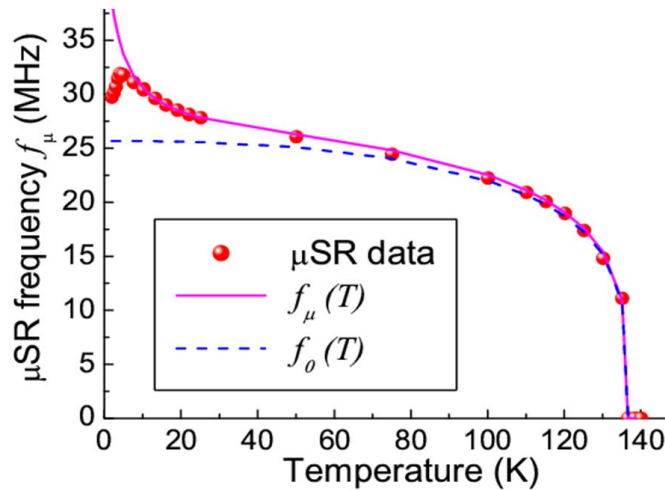
Figure 5.8.: *Main µSR frequency as a function of temperature in CeFeAsO. The continuous line is a fit using the model above. The dashed line represents $f_0(T)$. We see that the obtained $f_0(T)$ is close to the data Mössbauer measurements, which measures the Fe hyperfine field.*

We note few additional points:

– The Ce-ions magnetization contributes to the same magnetic Bragg peak recorded by neutron diffraction. Therefore, the neutron data cannot disentangle between Fe and Ce contributions. A similar approach as the one done for µSR could be possible.

– The obtained temperature evolution of $f_0(T)$ is similar to the Fe hyperfine field as obtained by Mössbauer measurements. The confirms a posteriori the validity of the approach.

– The susceptibility if proportional to the square of the "effective Bohr magneton number" $p = g(JLS)[J(J+1)]\,1/2$, where $g(JLS)$ is the Landé factor.
The Cerium, which has solely one $4f$ electron, has $S = 1/2$, $L = \sum l_z = 3$ and $J = |L - S| = 5/2$, resulting to

$$g(JLS) = \frac{3}{2} + \frac{1}{2}\left[\frac{S(S+1) - L(L+1)}{J(J+1)}\right] = \frac{6}{7} \quad . \tag{5.25}$$

The same calculation for Samarium gives 2/7 meaning that the Sm moments are about 10 times less induced compared to the Ce-moments. Probably, due to this feature, one observes very similar µSR spectra in the Sm and La compounds. Why the Pr compound has also a similar response is not completely clear but probably lies in the crystal-electric-field splitting of the multiplet.

- *UPd$_2$Al$_3$ – Local fields cancellation*
  The so-called heavy-fermion systems have attracted quite a lot of attention due to the possibility of unconventional superconducting states, with a close vicinity of magnetism and superconductivity.

  Thermodynamic measurements of the hexagonal heavy-fermion system UPd$_2$Al$_3$ suggest the coexistence at low temperature of superconductivity and long-range magnetism. This system undergoes an antiferromagnetic transition at $T_N = 14$ K followed by a superconducting transition at $T_c = 2$ K.

  Zero-field muon spin rotation were intended to probe into the different phases. Figure 5.9 exhibits the behavior of the μSR signal recorded at 80 mK, which is best fitted by an exponential decay with $\lambda = 0.42\ \mu s^{-1}$. This value is temperature independent between 0.08. K and 2.5 K. Most interesting is the absence of any spontaneous muon-spin precession frequency below T_N. Neutron scattering data indicate an antiferromagnetic structure with propagation vector $\mathbf{k} = (0, 0, 1/2)$ and magnetic moments of U lying in the basal plane.

  Therefore, the non-observation of spontaneous muon-spin precession frequencies in such a simple magnetic structure suggests that all muons are stopped at a highly symmetric site, where the dipolar fields arising from the ordered $5f$-moments cancel.
  The only interstitial candidate site of the proper symmetry is the b site (Wyckoff notation, see Fig. 5.9). Below T_N , part of the depolarization arises from the random local fields due to the sizable nuclear magnetic moment of the ^{27}Al-nuclei (see Section 4.1.2.1). For the b site, the calculated value of the depolarization rate is 0.175 μs^{-1} which leads to a much smaller time decay of the muon asymmetry than the observed one. Such a difference, as well as the observation of an exponential relaxation, suggest that a large part of the depolarization rate arises from distortions of the magnetic sublattices producing an additional distribution of internal fields with zero mean at the muon site.
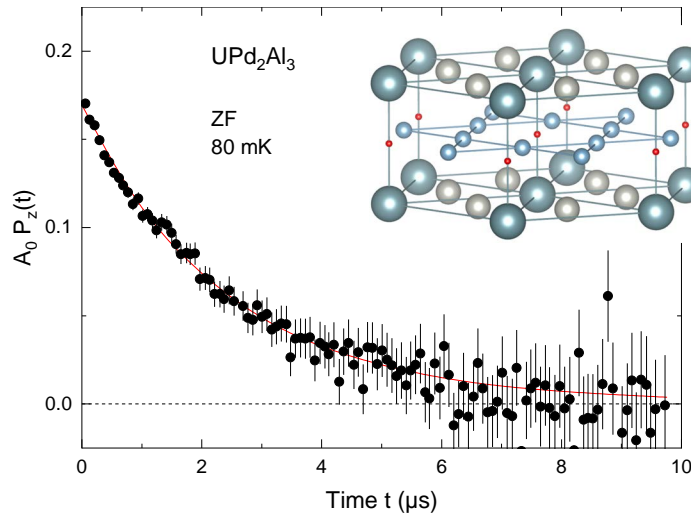
Figure 5.9.: *μSR signal recorded at 80 mK in UPd$_2$Al$_3$. The muon site (see text) is shown by the small red spheres. The large sphere represents the U-ions and the Pd-ions are located on the same plane. The Al-ions are located on the same plans as the muon (adapted from Ref. [54]).*

At this point, one could ask the question of the contact field contribution. Equation 5.17 provides us with the contribution of a single electronic moment. In a compound, the sum over the surrounding moments has to be performed.[5] Therefore for an antiferromagnet with the muon sitting at a high-symmetry site, there is a large probability that this vector sum is zero, and that as the dipolar field, also the contact field cancels.

The example of elemental iron given later provides a case where the dipolar field averages out, whereas the contact contribution is still present.

---

[5]The exact number of moments to take into account is a not trivial question...

- *UPt₃ - different time scales*

  The low-temperature normal-state properties of the hexagonal heavy-fermion material UPt$_3$ are exemplary of a strongly renormalized Fermi-liquid system with a quasiparticle mass of the order of 200 times the free electron value. UPt$_3$ appears to be the heavy-fermion compound for which the most indications for unconventional superconductivity have been reported (for a review see Ref. [55]). Careful measurements on high-quality crystals reveal the presence of a double superconducting transition (at about 0.5 K) in zero external field. In addition, peculiar magnetic properties are observed, such as the occurrence of so-called small-moment antiferromagnetic order (SMAF) which is found below $T_{N,SMAF} \simeq 6$ K [56]. The ordered phase, which is characterized by an unusually small magnetic moment ($\mu_s = 0.02$ μ_B/U) was solely observed by neutron diffraction and magnetic x-ray scattering. Thermodynamic and transport property studies, as well as microscopic studies (NMR and μSR), could not reliably detect the SMAF order.

  Besides the SMAF order, conventional antiferromagnetism (*i.e.* with rather large moments) can be induced upon substituting small amounts of Pd or Au for Pt, or when U is replaced by small amounts of Th. For both pseudo-binary systems U$_{1-x}$Th$_x$Pt$_3$ and U(Pt$_{1-x}$Pd$_x$)$_3$ the so-called large-moment antiferromagnetism (LMAF) can be induced in the concentration range of about $0.01 \leq x \leq 0.1$, with a maximum for the Néel temperature of $T_{N,max,LMAF} \simeq 6$ K at about 5 at.% Th or Pt. Although the LMAF state is characterized by magnetic moments at least one order of magnitude stronger that those observed in the SMAF phase, the magnetic structure is identical for both phases. Moreover, the transition temperature of the SMAF phase and the highest transition temperature of the LMAF phase appear strikingly equal, pointing to a close relationship between these phases.
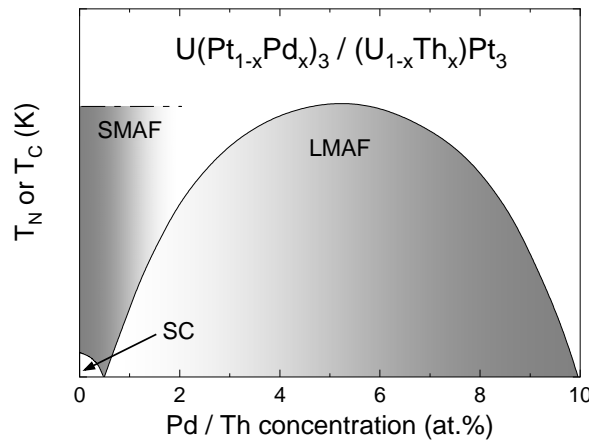
Figure 5.10.: *Schematic magnetic and superconducting phase diagram for U$_{1-x}$Th$_x$Pt$_3$ and U(Pt$_{1-x}$Pd$_x$)$_3$ alloys. Whereas the SMAF state, occurring below $T_{N,SMAF} \simeq 6$ K, is only observed by neutron diffraction and magnetic x-ray scattering, the LMAF and the superconducting (SC) states are detected by different techniques.*

μSR studies performed on high-quality UPt$_3$ crystals, as well as NMR studies, lead to

the conclusion that this state does not involve static moments but rather possesses moments which fluctuate at a rate larger than 100 MHz, yet slower than the nearly instantaneous scales of neutron and x-ray scattering. For μSR experiments, this conclusion was inferred from the absence of any anomaly of the muon depolarization rate when cooling the sample into the SMAF phase. The alternative explanation for the absence of a SMAF signature in the μSR signal, invoking the cancellation of the internal fields at the muon stopping site in the SMAF phase (see example above for UPd_2Al_3), could be safely discarded since it does not hold for the Pt site and is therefore incompatible with the NMR results. The μSR results, indicating the dynamic nature of the SMAF phase, were obtained not only on pure UPt_3 samples, but also on samples with low (*i.e.* $x \leq 0.005$) Pd concentration. μSR studies on a $U(Pt_{0.99}Pd_{0.01})_3$ sample [57], which according to neutron scattering studies should exhibit both magnetic phases, could only detect the LMAF phase (see Fig. 5.11). Therefore, the $T_{N,SMAF}$ should be considered as a crossover temperature signaling a slowing down of magnetic fluctuations rather than being regarded as a true phase transition temperature.

For $T > T_{N,LMAF}$, the muon spin depolarization of the $U(Pt_{1-x}Pd_x)_3$ samples is found to result from the Gaussian distribution of static, randomly oriented, magnetic fields due to ^{195}Pt nuclei. As expected, the form of the depolarization function is given by the Kubo-Toyabe function (see Eq. 4.20). Since there is no zero-field μSR signature for the SMAF state, the Kubo-Toyabe function works equally well in the paramagnetic phase and in the anomalous SMAF region. On the other hand, the signature of the LMAF phase is characterized by the occurrence of a two-component function in the μSR signal: one showing a oscillatory behavior (see Eq. 4.11) and the other one showing a Lorentz Kubo-Toyabe behavior (see Eq. 4.24). These two components are indicative of two magnetically inequivalent muon stopping sites. Whereas one site presents a finite local field B_μ, the second site is characterized by an isotropic Lorentzian distribution of local fields with an average zero value producing a Kubo-Lorentzian polarization decay.
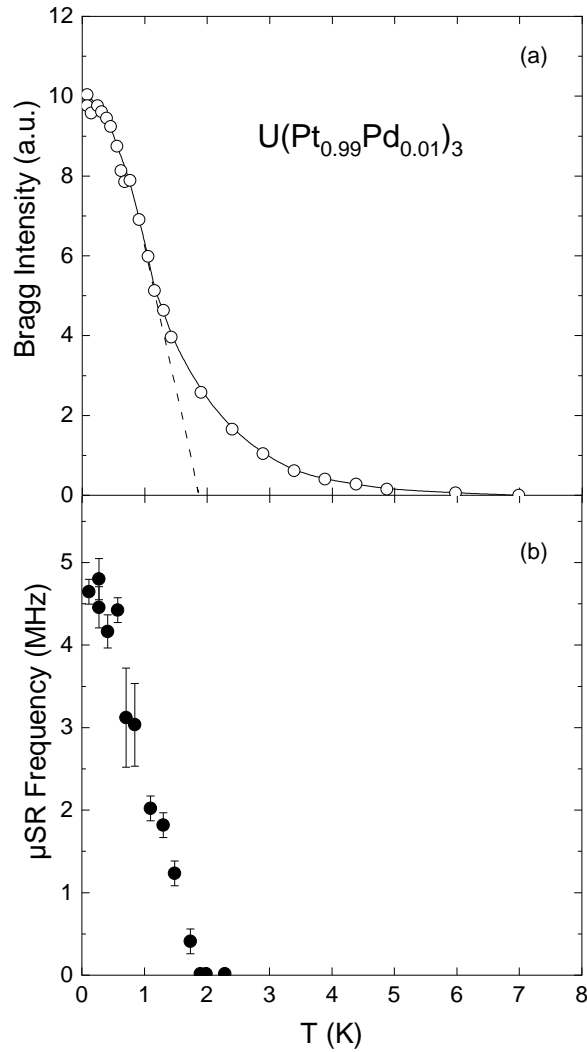
Figure 5.11.: *Temperature variation of the magnetic intensity measured at the magnetic Bragg peak* **k** $= (0.5, 0, 1)$ *for an annealed U(Pt$_{0.99}$Pd$_{0.01}$)$_3$ sample. The sharp increase in the intensity near 1.9 K indicates a crossover from SMAF to LMAF. (b) Spontaneous µSR-frequency obtained on the same sample. Note the absence of magnetic signal above $T_{N,LMAF} \simeq 1.9$ K.*
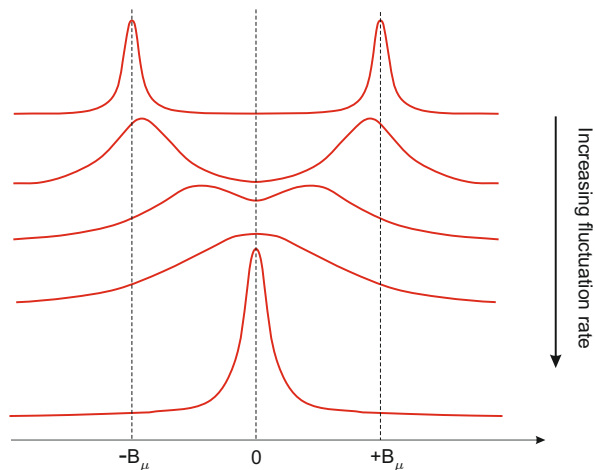
Figure 5.12.: *Sketch of the field distribution seen by the muon ensemble in the case of a fluctuating magnetic environment. For slow fluctuations ($\tau \gg \gamma_\mu B_\mu / (2\pi)$), some muons will see one field configuration and others will see the other (top curve). When increasing the fluctuation rate (i.e. decreasing the fluctuation time) the muons will see an average field and a field distribution which will decrease in width (lower curve). If the field fluctuates between two values symmetric around zero, no oscillations will be registered in the μSR signal for fast fluctuations.*

- *Elemental iron (Fe BCC) – averaging out the dipolar field*
  As an additional example, we provide the results obtained in elemental Fe. Iron crystallizes at room temperature in a BCC structure. The muon is located at the tetrahedral site located in-between 4 Fe-ions [corresponding to the site(0.50,0.25,0.0)]. There are 12 symmetry equivalent muon sites in the crystallographic unit cell. These muon sites become magnetically inequivalent when the iron magnetic order sets in. The order is ferromagnetic (*i.e.* propagation vector $\mathbf{k} = (0, 0, 0)$) with the moments pointing in say the *c*-axis (we consider here only one domain). One can show that the tetrahedral muon sites have either the tetrahedral axis parallel ($T_\parallel$, 4 sites) or perpendicular ($T_\perp$, 8 sites) to the domain magnetization. Interestingly, one can show that the dipolar fields are all align along the magnetization and that

$$B_{\mathrm{dip},\mathrm{T}_\parallel} = -2B_{\mathrm{dip},\mathrm{T}_\perp} \quad . \tag{5.26}$$
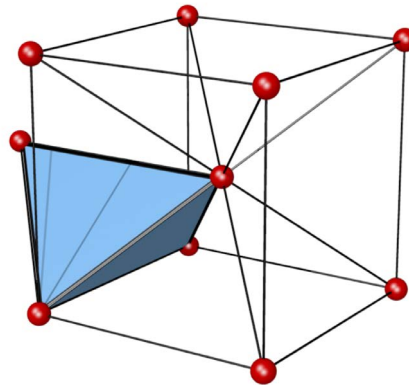
Figure 5.13.: *BCC structure of iron. The muon is located at the center of the tetrahedron.*

In iron, it is believed that the muon diffuses at all temperatures sufficiently fast that B_{dip} averages out to zero. Therefore the local field at the muon site is the sum of $\mathbf{B}_{\mathrm{cont}}$ and $\mu_0\mathbf{H}_{\mathrm{Lor}}$. Knowing the Lorentz contribution, the contact field can be extracted (see Fig. 5.14). The contact field is not strictly proportional to $\mathbf{M}$ which could arise either from a spin density at the muon site is not simply linearly proportional to the magnetization or to thermal volume expansion.
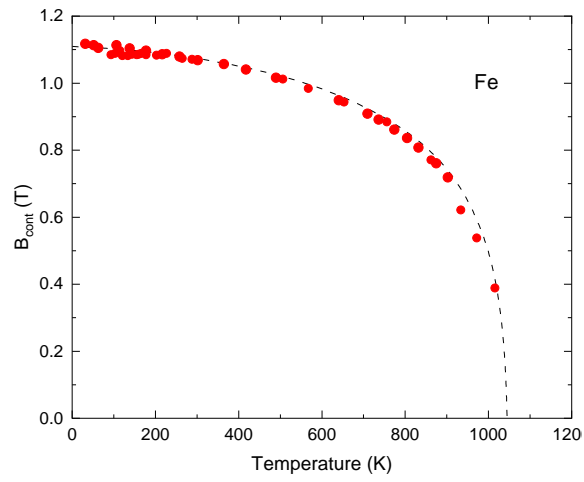
Figure 5.14.: $B_{cont}(T)$ *compared with normalized* $M(T)$ *for iron (dashed line). Adapted from Ref. [34].*

5.3. Special cases magnetic states

5.3.1. Incommensurate vs commensurate magnetic structure

5.3.1.1. The simple case

When the magnetic structure is commensurate to the crystallographic structure, the number of magnetically inequivalent muon sites (which can result from inequivalent or even equivalent crystallographic sites) will be finite. The resulting field distribution $f(B_\mu)$ obtained from the μSR signal will show well defined peaks.

Some materials exhibit so-called "incommensurate magnetic structures" in which the magnetic moments are ordered, but with a periodicity that is not commensurate with that of the crystal structure. In the case of localized moments, the ordered moment function

$$\mathbf{m}(\mathbf{R}_{lj}) = \sum_{\mathbf{k}} \mathbf{m_k} \exp(-2\pi\, i\, \mathbf{k} \cdot \mathbf{R}_l) \quad , \qquad (5.27)$$

(where l defines the unit cell which origin is at $\mathbf{R}_l$ and the position of the moment is $\mathbf{R}_{lj} = \mathbf{R}_l + \mathbf{r}_j$) has Fourier components with irrational indices with respect to the reciprocal lattice of the crystal. Incommensurate magnetic structures may be linear, but occur as quite complicated, like helical structures etc. as well. Especially, in rare-earth compounds very complicated magnetic phase diagrams have been found.

The muon site is located at a crystallographic site and therefore if the magnetic structure is incommensurate, each muon will sense another field and the field distribution $f(B_\mu)$ will appear as continued between a minimum and a maximum cutoff field and therefore completely different from the commensurate case. With neutron scattering, such distinction can sometimes be difficult as it depends on the magnetic Bragg peak position.

In the following, we will derive the time evolution of the muon polarization $P_z(t)$ for a muon ensemble seeing a modulation of the internal field which is incommensurate with the crystallographic structure.

We assume that the internal field point along the x direction and that the initial muon polarization is along z.

In the simplest model, the value of the field at the muon-site is given by

$$B_\mu = B_{\max} \sin(2\pi\, k\, r_\mu) \qquad (5.28)$$

where k represents the value of the propagation vector $\mathbf{k}$ of the magnetic structure and the muon position is $\mathbf{r}_\mu$ (here we assume that $\mathbf{k}$ and $\mathbf{r}_\mu$ are parallel).

We have to find the probability distribution function $f(B_\mu)$.

We make first the change of variable $u = 2\pi\, k\, r_\mu$ and concentrate on a full period, $i.e.$ u from 0 to 2π. The number of states in an interval dB_μ must be equal to number of states in an

interval du. Considering that for a given value of B_μ we have two choices (see Fig. 5.15) of u, we can write

$$f(B_\mu)\, dB_\mu = 2\, f(u)\, du \quad . \tag{5.29}$$
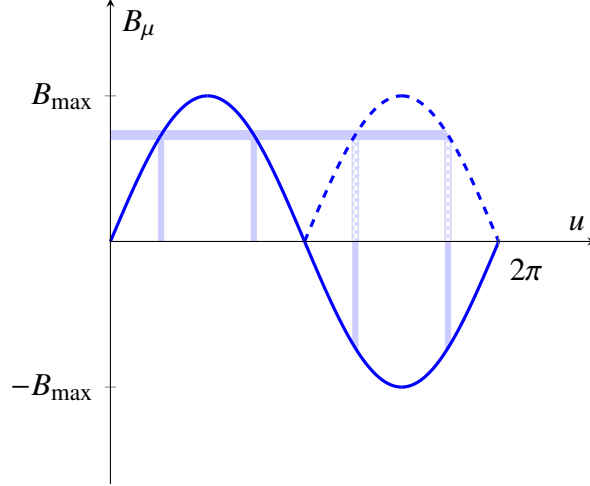
Figure 5.15.: *Evolution of the field seen by the muon as a function of the variable u (see text).*

In addition for a muon, the value of the Larmor frequency will only depend on the absolute value of B_μ, which will introduce an additional factor of two in the above equation, *i.e.*:

$$f(|B_\mu|)\, dB_\mu = 4\, f(u)\, du \quad . \tag{5.30}$$

The probability distribution function for u is a constant (the muon can be everywhere along the wave, as the vector **k** is incommensurate to the lattice). For normalization reasons, we have

$$f(u) = \frac{1}{2\pi} \quad . \tag{5.31}$$

Therefore we can write

$$f(|B_\mu|) = \frac{4}{2\pi}\frac{du}{dB_\mu} = \frac{2}{\pi}\frac{d\left(\arcsin\left(\frac{B_\mu}{B_{\max}}\right)\right)}{dB_\mu} = \frac{2}{\pi\sqrt{B_{\max}^2 - B_\mu^2}} \quad . \tag{5.32}$$
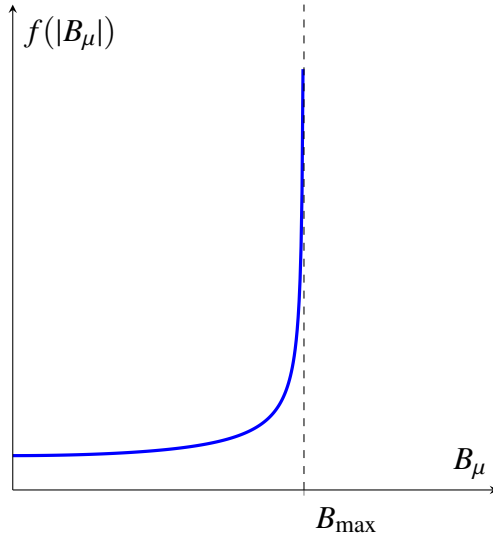
We use this probability distribution function in our polarization formula (Eq. 4.4), taking into account that $\theta = 90°$:

$$P_z(t) = \int f(|B_\mu|) \, \cos(\gamma_\mu B_\mu t) dB_\mu \tag{5.33}$$

and we find that

$$P_z(t) = J_0(\gamma_\mu B_{\max} t) \quad, \tag{5.34}$$

where J_0 is the zeroth-order Bessel function of the first kind.
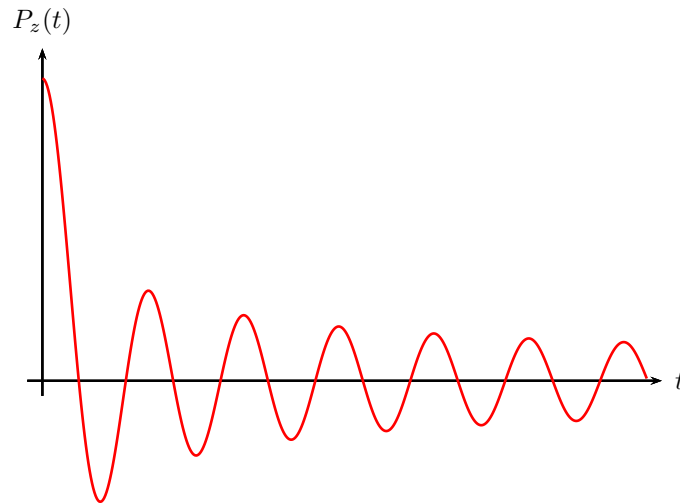
Figure 5.16.: *Time evolution of the μSR signal in presence of an incommensurate magnetic lattice (see text).*

We note that when the time t is large relative to $1/(\gamma_\mu B_{\max})$, we can use the following

asymptotic expansion

$$J_0(x \to \infty) = \sqrt{\frac{2}{\pi \, x}} \cos\left(x - \frac{\pi}{4}\right) \;, \tag{5.35}$$

and one gets the large time expansion

$$J_0(\gamma_\mu B_{\max} \, t) \simeq \sqrt{\frac{2}{\pi \, \gamma_\mu B_{\max} \, t}} \cos\left(\gamma_\mu B_{\max} \, t - \frac{\pi}{4}\right) \;. \tag{5.36}$$

This large time expansion already matches the actual polarization function for $\gamma_\mu B_{\max} \, t \gtrsim 1$. Hence, if only the large time region is fitted by a simple cosine function, a negative phase shift is obtained. This example shows that the phase parameter (which significance is easily neglected by the μSR users) can reveal some subtle information.

Also, recalling that the Bessel function fulfills

$$J_0(x) = \sum_{k=0}^{\infty} \frac{(-1)^k}{k!^2} \left(\frac{x}{2}\right)^{2k} \;, \tag{5.37}$$

the short time expansion is given by

$$J_0(\gamma_\mu B_{\max} \, t) \simeq 1 - \frac{(\gamma_\mu B_{\max})^2}{4} \, t^2 \;. \tag{5.38}$$

For short time, the damping is strong and controlled by the cutoff field $B_{\max}$ of the field distribution and not by the second moment as usual.
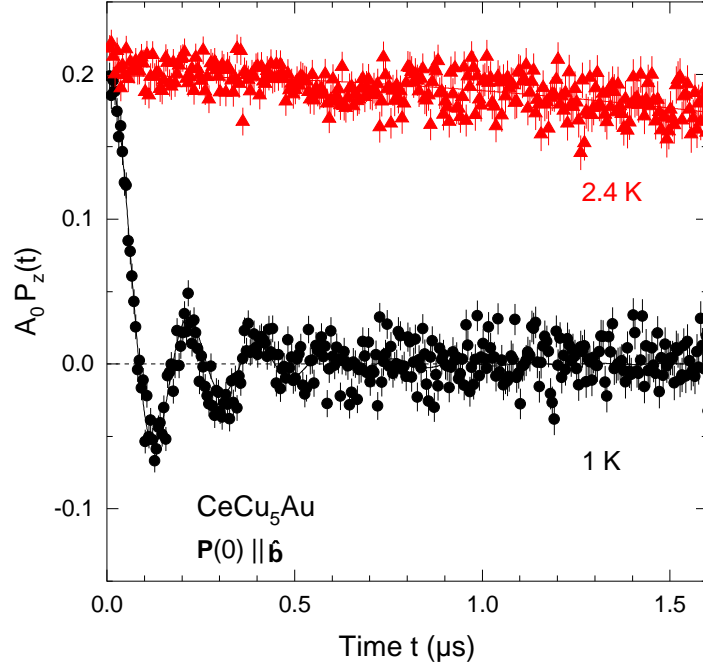
Figure 5.17.: *Example of μSR signal presenting a Bessel function. The data are taken on the system CeCu₅Au, which present a magnetic ground state below 2.2 K. The data were taken on a single crystal and therefore no "1/3" term is present. Above T_N, the μSR signal reflects the field distribution create by the ^{63}Cu and ^{65}Cu nuclear moments. Below T_N the observation of a Bessel function indicates the presence of a incommensurate magnetic structure (see Ref. [42] for details).*

5.3.1.2. The slightly more difficult case

Finally, for completeness, we note that Eq. 5.28 is actually a rather drastic simplification, where one assumes that the field is pointing to a fixed direction of space. If this situation can actually occur in special cases where the muon sits at a highly symmetric site, it is not valid for non symmetric sites and for helical incommensurate structure. In both cases, the direction of the field at the muon site will not be constant (see for example Refs. [58], [34] and [59]). It was shown that such incommensurate magnetic structures lead to a field distribution given by

$$f(B_\mu) = \frac{2}{\pi} \frac{B}{\sqrt{B^2 - B^2_{\min}} \sqrt{B^2_{\max} - B}} \quad , \tag{5.39}$$

and is characterized by two peaks due to the minimum and maximum cutoff field values. This is due to the fact that the values of $\mathbf{B}_\mu$ are located on the path of an ellipse for which the semimajor and semiminor axis values are $B_{\max}$ and $B_{\min}$. The oscillatory part of the muon polarization function associated with this field distribution cannot be obtained analytically.

One often approximates the field distribution with a shifted Overhauser distribution

$$f_{\text{approx}}(B_\mu) \simeq \frac{1}{\pi} \frac{1}{\sqrt{\Delta B^2 - (B - B_{\text{av}})^2}} \quad , \tag{5.40}$$

where $\Delta B = (B_{\text{max}} - B_{\text{min}})/2$ and $B_{\text{av}} = (B_{\text{max}} + B_{\text{min}})/2$. The upper panel of Fig. 5.18 shows the difference between the exact and approximated field distribution, which is symmetrical with respect to the singularities, *i.e.* some weight is transfered from the upper cutoff to the lower cutoff field. The lower panel of Fig. 5.18 shows the oscillatory part of the muon polarization function obtained for both field distributions. For the exact field distribution a numerical calculation was performed, whereas for the approximated field distribution the muon polarization function can be obtained analytically and is given by

$$P_{z,\text{approx}}(t) = J_0(\gamma_\mu \Delta B\, t)\, \cos(\gamma_\mu B_{\text{av}}\, t) \,, \tag{5.41}$$

where as before J_0 is a Bessel function of the first kind. We see that the approximate function $P_{z,\text{approx}}(t)$ catches the essential features of the polarization function calculated with the exact field distribution and constitutes a good approximation.
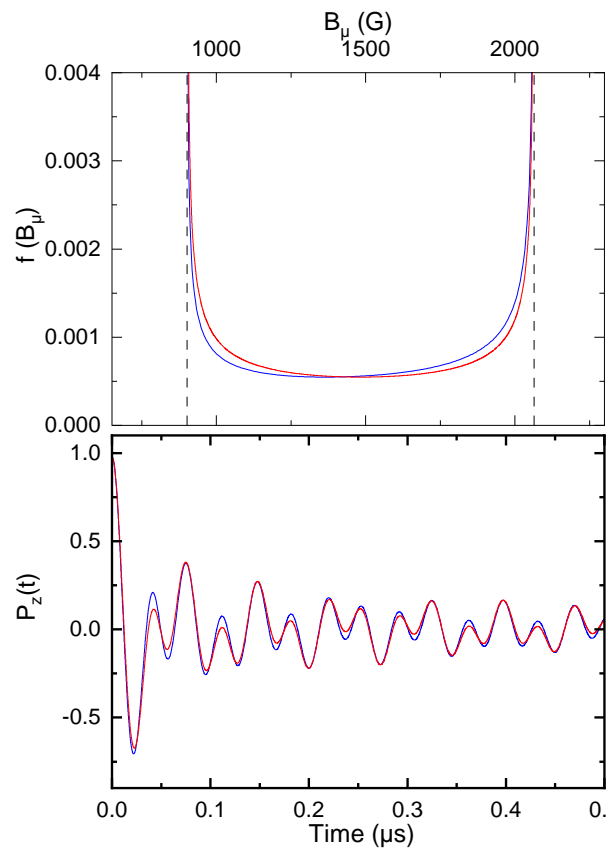
Figure 5.18.: *Upper panel: exact (blue line/symbols) and approximated (red line: see Eq. 5.40) field distribution at the muon site for an incommensurate helical structure. Lower panel: muon polarization function deduced from the field distributions shown on the upper panel (see also text). The field values correspond to the example of the helical structure of MnSi (see Ref. [60] and Fig. 5.19)*
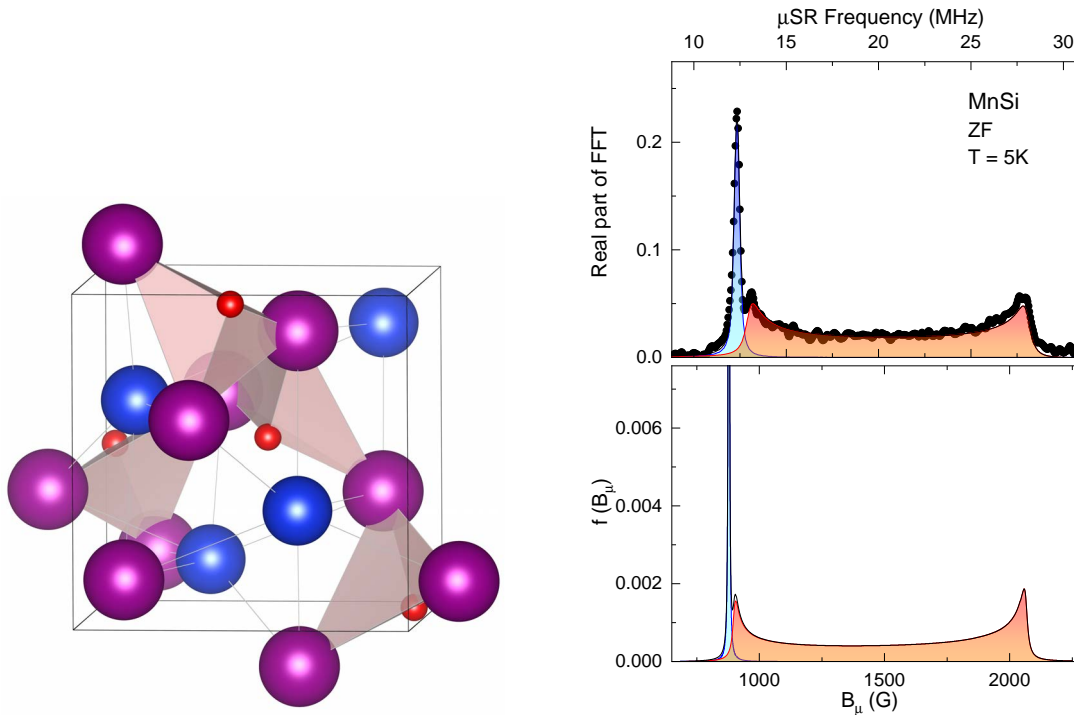
Figure 5.19.: *Left: Crystallographic structure of MnSi. The Mn-ions are in magenta and the Si-ions in blue. The muon is located at the (x, x, x) position with $x = 0.532$ (red). Four crystallographically equivalent muon sites are present in the unit cell at: (x, x, x), $(1/2 - x, \bar{x}, 1/2 + x)$, $(1/2 + x, 1/2 - x, \bar{x})$ and $(\bar{x}, 1/2 + x, 1/2 - x)$. Right: i) upper part: Fourier transform of the µSR signal recorded in ZF mode. Due to the helical magnetic structure with* **k** *along the [111]-axis, three of the four crystallographic muon sites produce a field distribution as given by Eq. 5.39 and the last muon site [the one at (x, x, x)] gives a narrow field distribution; ii) lower part: calculated field distribution with the muon site at (0.532,0.532,0.532).*

5.3.2. Study of spin glasses

We have seen in Section 4.1.2.2 that a Lorentzian distribution of fields along each Cartesian directions is obtained in the case of a dilute arrangement of randomly oriented magnetic moments, for example static electronic moments due to magnetic impurities. Such compounds are called *spin glasses*. The suffix 'glass' refers to the analogy between the magnetic disorder in a spin glass and the spatial disorder in a conventional glass, which possesses numerous metastable states at low energy. When a given type of liquid (as for example a silica compound) is cooled quickly, it is possible that it will be blocked in a metastable state (not the ground state) at a temperature called T_g. This blocking arises from the abrupt lack of thermal vibration. Below the transition, the viscosity becomes so large (increasing by up to 10 orders of magnitude) so that the liquid does not flow anymore and 'appears' as a solid.[6] The situation is similar for spin glasses, whose energy 'landscape' is composed by numerous metastable states at low energy. For temperature below T_g, a spin glass presents an amorphous magnetic state, or quenched disorder, but here the disorder is magnetic and not structural as in a usual glass.

We have seen without demonstration (for a discussion see Ref. [61]) that below T_g (*i.e.* when the magnetic moments become blocked) the field distribution along the Cartesian directions for a spin glass is given by Eq. 4.22, leading to a depolarization of the μSR signal following a Lorentz Kubo-Toyabe function (Eq. 4.24). We can now ask ourselves what is impact of the spin fluctuations present above T_g for a spin glass on the μSR signal. The first guess is simply to plug the static Lorentz Kubo-Toyabe function (Eq. 4.24) into the Eq. 4.45, *i.e.* to calculate via the strong-collision approximation. As shown by Uemura *et al.* [62], this approach corresponding to an order of the operations

$$\text{spatial averaging} \;\rightarrow\; \text{static} \;\rightarrow\; \text{dynamic}$$

is not correct, and that rather an order

$$\text{static} \;\rightarrow\; \text{dynamic} \;\rightarrow\; \text{spatial averaging}$$

has to be adopted.

We first discuss the spatial averaging. The situation for a spin glass, where the magnetic moments are diluted and randomly oriented, is rather different from the one of a dense arrangement of randomly oriented moments (see Section 4.1.2.1). In a dense arrangement of moments, the only difference from one muon site to another will be that the orientation of the moments will be different. Considering now a fluctuation of these dense moments, the variable range of the field modulation sensed by the muons is identical from site to site. In other words, for all the muon sites the dynamic variable range of the field components will be identical for all sites and given by Eq. 4.15, *i.e.*,[7]

$$f^{\text{G}}(B_\alpha) = \frac{\gamma_\mu}{\sqrt{2\pi\sigma^2}} \exp\left[-\frac{\gamma_\mu^2 B_\alpha^2}{2\sigma^2}\right] \;. \tag{5.42}$$

---

[6]We note here that an answer to the simple question: *Why is glass rigid?* is presently not clear. Many theories exist but are not universally accepted.

[7]We stress here with the index 'G' the Gaussian character of the dynamic variable range. Note that we have used here the relation $\sigma^2 = \gamma_\mu^2 \langle B_\alpha^2 \rangle$ (Eq. 4.21).

For a spin glass with diluted moments, the situation will be rather in the sense that the dynamic variable range of the field components for each sites will strongly depend on the magnetic environment of the muon site. Considering again the Figure 4.20 representing the schematic situation for a spin glass, we can see that the dynamic variable range of the field components for the green muon site will be more broader that for the red one.
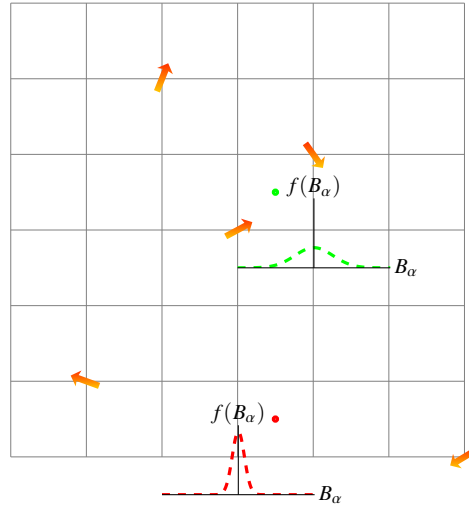
Figure 5.20.: *Schematic situation of a spin glass where two crystallographically equivalent muon sites are shown. As the green muon site has here a more dense magnetic environment, this leads to a broader dynamic variable range of the field components than for the red stopping site.*

Assuming that the dynamic variable range of the field components for each type of sites is also here Gaussian, *i.e.* given by the same Equation 5.42 as above, we can calculate the probability $\rho(\sigma)$ to find a site charaterized by a dynamic variable range of the field components with a second moment $\langle \Delta B_\alpha^2 \rangle = \sigma^2 / \gamma_\mu^2$. Indeed, as we have discussed above, when the magnetic moments become blocked in a spin glass (below T_g) the field distribution along the Cartesian directions is given by Eq. 4.22, *i.e.* a Lorentzian field distribution,[8]

$$f^{\,\mathrm{L}}(B_\alpha) = \frac{\gamma_\mu}{\pi} \cdot \frac{a}{a^2 + \gamma_\mu^2 B_\alpha^2} \quad , \tag{5.43}$$

Therefore, $\rho(\sigma)$ must fulfill the condition

$$f^{\,\mathrm{L}}(B_\alpha) = \int_0^\infty f^{\,\mathrm{G}}(B_\alpha)\rho(\sigma)d\sigma \quad , \tag{5.44}$$

and one can rather easily verify that the probability function $\rho(\sigma)$ is given as

$$\rho(\sigma) = \sqrt{\frac{2}{\pi}} \cdot \frac{a}{\sigma^2} \exp\left(-\frac{a^2}{2\sigma^2}\right) \quad . \tag{5.45}$$

---

[8]We also here stress with the index 'L' the Lorentzian character of the static field distribution.
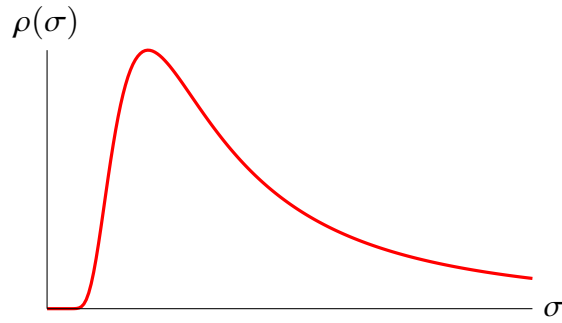
Figure 5.21.: *Probability distribution $\rho(\sigma)$. The maximum occurs at $\sigma = a/\sqrt{2}$.*

Let us now come back to the depolarization above T_g created by the fluctuations of the diluted moments. We have seen that we must apply the path

$$\text{static} \;\rightarrow\; \text{dynamic} \;\rightarrow\; \text{spatial averaging}$$

That is, we have first to consider one type of muon sites and apply the strong collision model (Eq. 4.45). But we have seen that for a Gaussian dynamic range the solution of this problem is given by the depolarization function $P_{z,\,\text{dyn}}^{\text{GKT}}$ (see Eq. 4.46). We have now the dynamic depolarization function and we have now to apply the spatial averaging, and we get the spin glass depolarization function

$$P_{z,\,\text{dyn}}^{\text{SG}} = \int\limits_0^\infty P_{z,\,\text{dyn}}^{\text{GKT}}\, \rho(\sigma)d\sigma \;\;. \tag{5.46}$$

We have seen that for fast fluctuations the depolarization function $P_{z,\,\text{dyn}}^{\text{GKT}}$ has an exponential character (see Eq. 4.49), and by inserting this limit in the Eq. 5.46, one gets

$$P_{z,\,\text{dyn}}^{\text{SG}} = \int\limits_0^\infty \exp\left(-\frac{2\sigma^2}{\nu}t\right)\rho(\sigma)d\sigma$$

$$= \exp\left[-\left(\frac{4a^2}{\nu}t\right)^{1/2}\right] \;\;, \tag{5.47}$$

which is usually called "root-exponential".

To conclude with this short introduction to the study of spin glasses with μSR, we note that, so far, in Section 4.3 and in the present Section we always have considered a unique correlation time for the field-autocorrelation function. This assumption seems reasonnable for systems with a homogeneous magnetic environment, but is most probably nor more correct in the case of spin glasses, where the magnetic moments are diluted. Allowing also a

distribution of τ_c we should write for fast fluctuations[9]

$$P_{z,\,\mathrm{dyn}}^{\mathrm{SG}} = \int\limits_0^\infty \int\limits_0^\infty \exp\left(-2\sigma^2\tau t\right)\rho(\sigma,\tau)d\sigma d\tau \ . \tag{5.48}$$

The exact form of the distribution of correlation time is a very hard problem, but we can keep in mind here that broad distributions of τ_c lead to stretched exponential muon depolarization functions, *i.e.*

$$P_{z,\,\mathrm{dyn}}^{\mathrm{SG}} = \exp\left[-(\lambda t)^\beta\right] \ , \tag{5.49}$$

with a β exponent smaller than 1/2 (see for example Ref. [63] and [64]).

---

[9]Remember that for the Strong Collision Approximation $\tau_c = \tau = 1/\nu$.

5.4. Determining magnetic volume fractions

With a so called weak transverse field experiment (wTF), it is possible to determine the fraction of a magnetic phase and the transition temperature.

The amplitude of the muon signal precessing at a frequency corresponding to the applied field B_{ext} reflects the volume fraction of the sample, which is paramagnetic or not ordered magnetically.[10] Muons stopping in the magnetically ordered regions will experience a broader field distribution, which leads to a rapid decay of the muon-spin asymmetry at early times. Therefore, the amplitude of the muon signal precessing at a frequency corresponding to B_{ext} will start to decrease at the magnetic transition and reach a level determined by the non-magnetic phase (which can also include some background signal).

The magnetic volume fraction is the given by

$$\frac{V_{\text{magn}}(T)}{V_{\text{tot}}} = 1 - \frac{A_{0,\text{wTF}}(T)}{A_0} \quad , \tag{5.50}$$

where A_0 is the total asymmetry of the μSR signal corresponding to the sample, and

$$A_{\text{wTF}}(t,T) = A_{0,\text{wTF}}(T)G(t)\cos(\gamma_\mu B_{\text{ext}}t + \phi) \quad , \tag{5.51}$$

where $G(t)$ into account some field broadening.

We note that also from ZF data it is possible to determine the magnetic volume fraction. However, one needs to know the depolarization function appropriate for the physical situation. However, the wTF measurements are extremely fast and straightforward.

Here again, the literature is full of examples of wTF μSR measurements and we show only very few selected and new examples:

- RENiO$_3$ (RE=rare-earth element) is an archetypal Mott insulator system.[11] When tuned by chemical substitution it exhibits a quantum phase transition (QPT) between an antiferromagnetic Mott insulating state and a paramagnetic metallic state. Because novel physics often appears near a Mott QPT, the details of this transition, such as whether it is first or second order, are important. It was shown [65] by μSR that the QPT in RENiO$_3$ is first order: the magnetically ordered volume fraction decreases to zero at the QPT, resulting in a broad region of intrinsic phase separation, while the ordered magnetic moment retains its full value until it is suddenly destroyed at the QPT.

---

[10]Actually the precession does not exactly occurs at B_{ext}, but with a value of field slightly modified by the Knight-shift. For low fields, this difference can be safely neglected.

[11]Mott insulators are a class of materials that should conduct electricity under conventional band theories, but are actually insulators. This can occur for given concentration of electrons and when the Coulomb repulsion between the electrons is strong, which are not considered in conventional band theory.
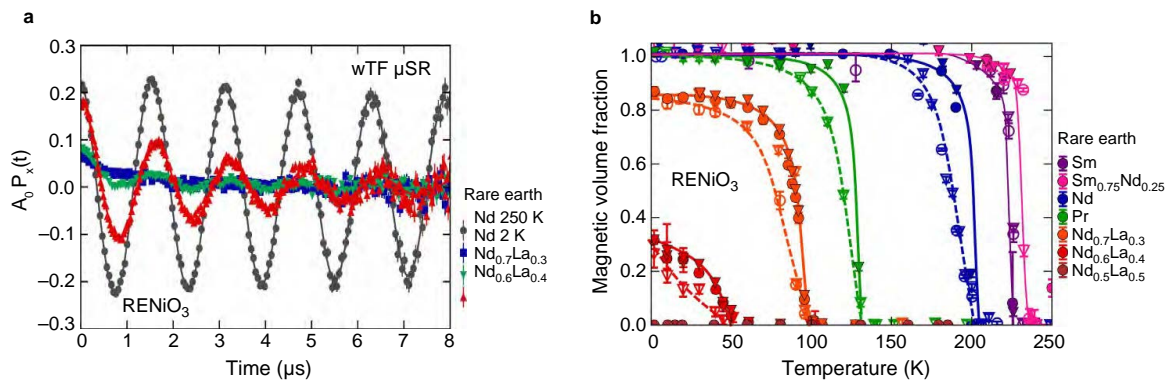
Figure 5.22.: *wTF time spectra for three compounds of RENiO$_3$ near the quantum phase transition (QPT) at 2 K, with one spectrum measured at higher temperature (250 K) shown for comparison (taken from Ref. [65]).*

- Mn-doped GaAs is a ferromagnetic semiconductor studied because of its possible application for spintronics devices. The high sensitivity of its physical properties to preparation conditions and heat treatments have generated a view in the research community that ferromagnetism in (Ga,Mn)As may be associated with unavoidable and intrinsic strong spatial inhomogeneity. LEM μSR wTF probed magnetism and demonstrated that (Ga, Mn)As shows a sharp onset of ferromagnetic order, developing homogeneously in the full volume fraction, in both insulating and metallic films.
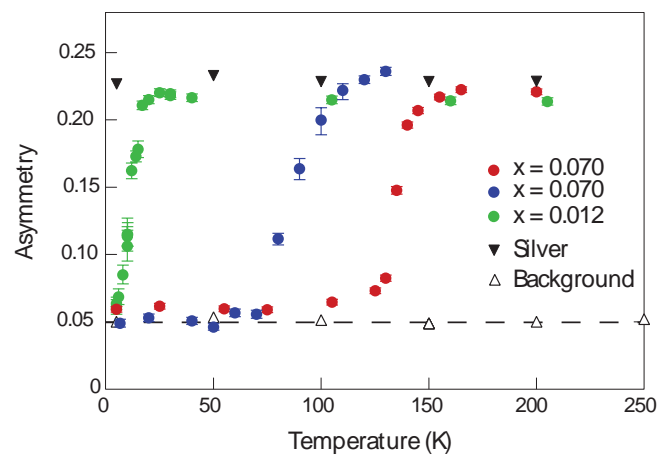
Figure 5.23.: *Muon precession asymmetry, representing muons in para- or non-magnetic environments, observed in (GA,Mn)As in a wTF of 100 G (taken from [66]).*

- The heavy-fermion compound URu$_2$Si$_2$ exhibits two successive phase transitions at 17.5 and 1.4 K. Whereas, the transition at 1.4 K signals the occurrence of unconventional superconductivity, the phase transition at 17.5 K still remains mysterious. A controversy appeared when comparing different microscopic measurements performed under external pressure. On one side, neutron scattering measurements suggested that

the 17.5 K was magnetic and that the magnetic Bragg-scattering intensity was significantly enlarged with pressure. This was interpreted as an increase of the staggered moment up to 0.25 μ_B/U at about 1 GPa. On the other side, NMR and μSR measurements suggested that at zero pressure the 17.5 K transition is not magnetic. Under pressure the transition becomes magnetic and solely the magnetic volume fraction is affected, but that the staggered moment remains essentially constant.
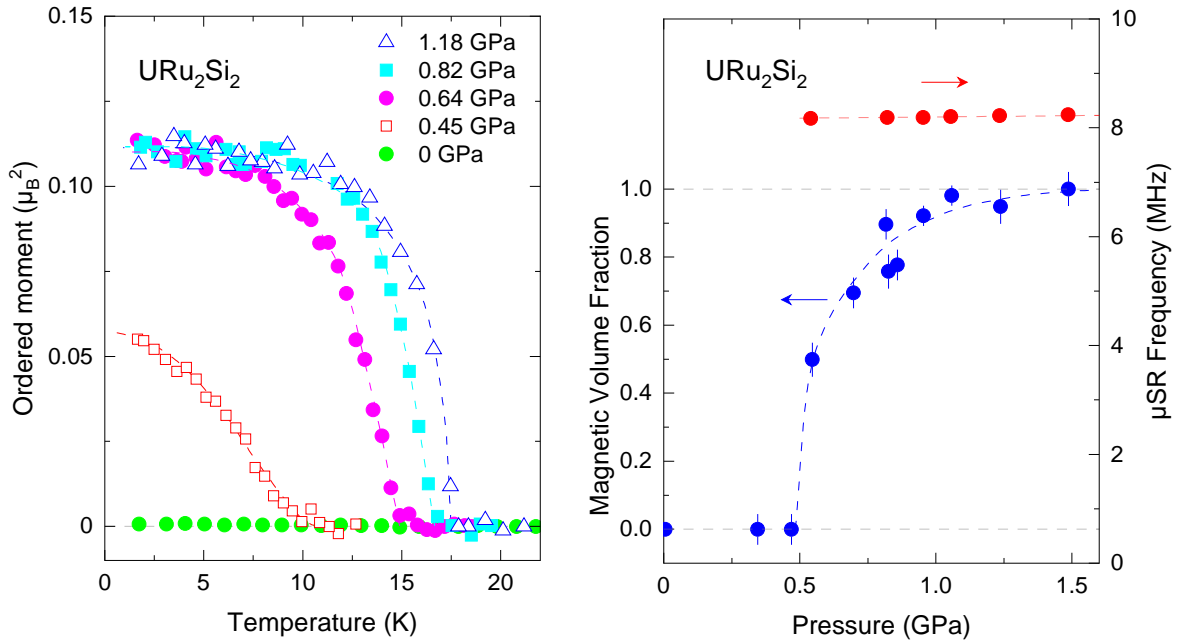
Figure 5.24.: *Comparison of neutron scattering and μSR data taken under pressure on URu$_2$Si$_2$. Note that the value of the moment extracted from the neutron data is obtained by assuming a full magnetic volume fraction, i.e. $V_{magn} = V_{tot}$ (the Bragg-peak intensity is proportional to $V_{magn}m^2$). From the μSR data (right panel) the magnetic volume fraction and the pressure dependence of the ordered moment (i.e. proportional to the μSR frequency) can be obtained separately.*

5.5. Studying the magnetic response in the paramagnetic or diamagnetic states: the Knight shift

We consider here the case of a sample which is not magnetic, *i.e.* the sample in a paramagnetic state or is a diamagnet. When we apply a magnetic field to the sample a magnetic polarization proportional to B_{ext} is induced.[12] One can measure by TF μSR the magnetic response of the system and define the normalized scalar product

$$K_{\text{exp}} = \frac{\mathbf{B}_{\text{ext}} \cdot (\mathbf{B}_\mu - \mathbf{B}_{\text{ext}})}{B_{\text{ext}}^2} \quad . \tag{5.52}$$
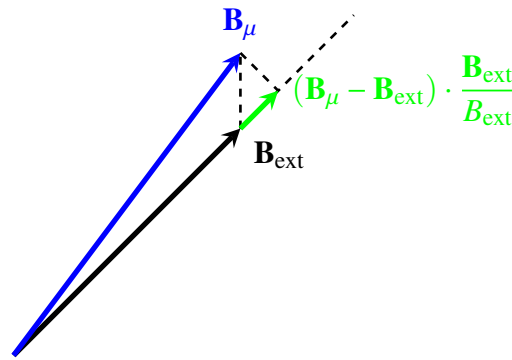
Figure 5.25.: *The parameter K_{exp}, which measures the muon frequency shift, corresponds to the vector difference between the field seen by the muon and the external field projected to the external field direction and normalized to the value of the external field.*

K_{exp} is usually in the few tens of parts per million range for a diamagnet and at most a few percent for a paramagnet.

Similar to Eq. 5.21, we can write[13]

$$\mathbf{B}_\mu = \mathbf{B}_{\text{ext}} + \mathbf{B}'_{\text{dip}} + \mathbf{B}_{\text{cont}} + \mu_0 \mathbf{H}_{\text{Lor}} + \mu_0 \mathbf{H}_{\text{dem}} \quad . \tag{5.53}$$

As the Lorentz and the demagnetizing field do not contain microscopic information, one defines the so-called muon Knight shift as

---

[12]The proportionality is valid if the field intensity is not too large (see Brillouin function).

[13]The Lorentz field is here present, as the sample has a magnetization created by the external field.

$$K_\mu = \frac{\mathbf{B}_{\mathrm{ext}} \cdot \left[(\mathbf{B}_\mu - \mathbf{B}_{\mathrm{Lor}} - \mathbf{B}_{\mathrm{dem}}) - \mathbf{B}_{\mathrm{ext}} \right]}{B_{\mathrm{ext}}^2}$$

$$= K_{\mathrm{exp}} - \frac{\mathbf{B}_{\mathrm{ext}} \cdot (\mathbf{B}_{\mathrm{Lor}} + \mathbf{B}_{\mathrm{dem}})}{B_{\mathrm{ext}}^2} \quad . \tag{5.54}$$

If we assume the sample to be an ellipsoid, with one of its principal axis oriented along the laboratory z axis that we take as the direction of the external field, we have

$$K_\mu = K_{\mathrm{exp}} - \left(\frac{1}{3} - N_{zz} \right) \chi_0 \quad , \tag{5.55}$$

where χ_0 is the bulk susceptibility of the sample along the z-direction. We therefore see (and it is what we will assume below) that if the sample is a sphere, the demagnetizing factor will be $N_{zz} = 1/3$ and we will have a cancellation of the demagnetizing field with the Lorentz field. Note that if this is not the case, a careful estimation of the demagnetizing factor has to be done, as $\mathbf{B}_{\mathrm{dem}}$ is usually a dominant contribution to the field sensed by the muon.

5.5.1. Knight shift (contact term): Studying the paramagnetism of the conduction electrons

The magnetic properties of simple metallic systems are determined essentially by the conduction electrons. The magnetic response and susceptibility is determined by the Pauli paramagnetism (related to the spin of the conduction electrons) and Landau diamagnetism (related to the orbital moment of the conduction electrons).

The local spin susceptibility can be probed by NMR or μSR via Knight-shift measurements.

In systems without localized electronic moments the shift is determined by the contact interaction between μ^+ spin and spin of the conduction electrons (in the presence of localized moments, *e.g.* rare earth, additional dipolar and the enhancement of the contact terms have to be considered, see below). We assume also that the sample considered is a sphere. With our assumptions:

$$\mathbf{B}_\mu = \mathbf{B}_{\mathrm{ext}} + \mathbf{B}_{\mathrm{cont}} \quad . \tag{5.56}$$

The Knight-shift is therefore K_μ and can be written as:

$$K_\mu = K_{\mathrm{cont}}$$

$$= \frac{\mathbf{B}_{\mathrm{ext}} \cdot \mathbf{B}_{\mathrm{cont}}}{B_{\mathrm{ext}}^2}$$

$$= \frac{B_{\mathrm{cont}}}{B_{\mathrm{ext}}} \quad . \tag{5.57}$$

As explained above, we take the projection of the internal contribution to the direction of the external field.

It is proportional to the density of conduction electrons at the muon site (which gives the strength of the contact interaction, see Section 5.1.2.3) and to the Pauli susceptibility (which reflects how much the conduction electrons are polarized by an external magnetic field).

5.5.1.1. Pauli susceptibility

In a free electron gas, the density of states is:

$$D(E) = \frac{3}{2} \frac{n}{E_{\mathrm{F}}^{3/2}} \sqrt{E} \quad, \tag{5.58}$$

where n is the electron density and E_{F} is the Fermi energy.

Without external field, spin up and spin down states are equally populated. If a field B_{ext} is applied, the band with magnetic moments parallel to B_{ext} will be lowered by $\mu_{\mathrm{B}} B_{\mathrm{ext}}$ and the band with antiparallel moment will be raised by the same amount. Since both bands are filled up to E_{F}, there is an overweight of electrons with magnetic moment parallel to B_{ext}. As a consequence the metal develops a weak spin polarization.

Electron density for both states:[14]

$$n_+ = \frac{1}{2} \int D(E + \mu_{\mathrm{B}} B_{\mathrm{ext}}) f(E) dE$$
$$n_- = \frac{1}{2} \int D(E - \mu_{\mathrm{B}} B_{\mathrm{ext}}) f(E) dE \quad. \tag{5.59}$$

$f(E)$ is the Fermi (-Dirac) distribution:

$$f(E) = \frac{1}{e^{(E - E_{\mathrm{F}})/k_{\mathrm{B}} T} + 1} \tag{5.60}$$

with the Fermi level E_{F}.[15]

For small B_{ext} the density of levels can be expanded and we have:

$$D(E \pm \mu_{\mathrm{B}} B_{\mathrm{ext}}) = D(E) \pm \mu_{\mathrm{B}} B_{\mathrm{ext}} D'(E) \tag{5.62}$$

---

[14]Note that here n_+ and n_- are describing the magnetic moment direction.

[15]Note that in the Fermi distribution we have actually to consider the chemical potential μ (*i.e.* the increase of the Helmholtz free energy when adding an electron) instead of the Fermi energy. At $T = 0$, both quantities are identical but at $T > 0$ we have (see for example Ref. [67])

$$\mu = E_{\mathrm{F}} \left[1 - \frac{\pi^2}{12} \left(\frac{k_{\mathrm{B}} T}{E_{\mathrm{F}}} \right)^2 + O \left(\frac{k_{\mathrm{B}} T}{E_{\mathrm{F}}} \right)^4 \right] \quad. \tag{5.61}$$

For typical electronic densities, $k_{\mathrm{B}} T / \mu \simeq 0.01$.

Therefore, the magnetization becomes:

$$M = \mu_B(n_+ - n_-)$$

$$\simeq \mu_B^2 \, B_{\text{ext}} \int\limits_0^\infty \frac{dD}{dE} f(E) dE$$

$$= \mu_B^2 \, B_{\text{ext}} \left[\underbrace{D(E)f(E)\Big|_0^\infty}_{D(0)=0, f(\infty)=0} - \int\limits_0^\infty \underbrace{\frac{df}{dE}}_{\simeq -\delta(E-E_F)} D(E) dE \right]$$

$$\simeq \mu_B^2 \, B_{\text{ext}} \, D(E_F) \tag{5.63}$$

Hence:

$$M \simeq \frac{3}{2} \frac{n\mu_B^2}{E_F} \, B_{\text{ext}} \tag{5.64}$$

The Pauli susceptibility is:

$$\chi_P = \frac{M}{H_{\text{ext}}} = \frac{\mu_0 M}{B_{\text{ext}}} = \mu_0 \frac{3}{2} \frac{n\mu_B^2}{E_F} \tag{5.65}$$

The magnetization of the conduction electrons can be rewritten as:

$$M = -n g_e \mu_B \, \langle S_z \rangle = \chi_P \, \frac{B_{\text{ext}}}{\mu_0}$$

$$\Rightarrow \langle S_z \rangle = -\frac{B_{\text{ext}}}{\mu_0 \, n \, g_e \, \mu_B} \chi_P \tag{5.66}$$

the average spin polarization $\langle S_z \rangle$ can be written in terms of the average contact field B_{cont}. At the muon site (say $\mathbf{r}_\mu$), the contact field produced by an electron will be (see Eq. 5.17) :

$$\mathbf{B}_{\text{cont}}(\mathbf{r}_\mu) = \frac{2}{3} \, \mu_0 \mathbf{M}(\mathbf{r}_\mu) \tag{5.67}$$

The factor 2/3 arises due to the demagnetization field assumed to be the one of a sphere. Assuming $\hat{\mathbf{z}}$ to be the quantization axis, we have also:

$$M_z(\mathbf{r}_\mu = 0) \simeq -g_e \, \mu_B \, \langle S_z \rangle \, |\psi(0)|^2 \tag{5.68}$$

and therefore:

$$B_{\text{cont}} = -\frac{2}{3}\mu_0 \, g_e \, \mu_B \, \langle S_z \rangle \, |\psi(0)|^2 \tag{5.69}$$

With Eq. 5.66, one gets:

$$B_{\text{cont}} = -\frac{2}{3} \, \mu_0 \, g_e \, \mu_B \, |\psi(0)|^2 \left(-\frac{B_{\text{ext}}}{\mu_0 \, n \, g_e \, \mu_B} \chi_P \right)$$

$$= \frac{2}{3} \, \chi_P \, \frac{|\psi(0)|^2 B_{\text{ext}}}{n} \tag{5.70}$$

and finally the muon Knight shift due to the conduction electrons can be written as:

$$
\begin{aligned}
K_\mu &= K_{\text{cont}} \\
&= \frac{B_{\text{cont}}}{B_{\text{ext}}} \\
&= \frac{2}{3} \chi_{\text{P}} \frac{|\psi(0)|^2}{n}
\end{aligned}
\tag{5.71}
$$

Up to a factor 2/3, K_{cont} is equal to the Pauli susceptibility multiplied with the enhancement factor $|\psi(0)|^2/n$, which gives the ratio of the electron density at the muon site (in the μSR measurements) or at the nuclear site (in the case of NMR measurements) to the density of electrons in the free electron gas.

$|\psi(0)|^2/n$ is called "spin density enhancement factor".

The actual value of $|\psi(0)|^2$ depend on the structure of the electronic cloud around the muon, screening its positive charge. Its value has to be derived of the electronic structure. Therefore its experimental determination can be a valuable check for any electronic band calculations. In addition, quite some theoretical work is dedicated to the screening of hydrogen (*i.e.* proton) in metal. As the muon can be considered as a light isotope of the proton, it was used to test such theories [68].

We note that another contribution to the Knight shift should have been considered which is the contribution of Landau diamagnetism (orbital magnetism) from the conduction electrons at the Fermi surface. Typically it amounts to a few parts per million and can be safely discarded.
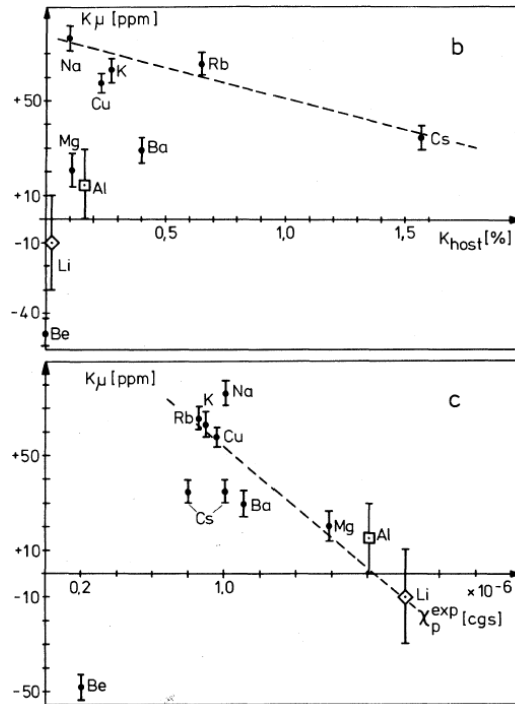
Figure 5.26.: *Top: Knight-shift at muon site (K_μ determined by TF-μSR) as a function of the Knight-shift at the nuclear (lattice) site (K_{host} determined by NMR) plotted for various metals. Bottom: Muon Knight-shift as a function of the Pauli electron spin susceptibility (taken from Ref. [68]).*

5.5.2. Knight shift in materials with local moments

For d and f electron compounds, the dipole contribution to K_μ is important. We will also see in a second step that the local moments can enhance the contact term.

5.5.2.1. The dipole field contribution

By looking first at the dipole contribution, we can write, in analogy to the contact term seen in the previous Section, that

$$K'_{\text{dip}} = \frac{\mathbf{B}_{\text{ext}} \cdot \mathbf{B}'_{\text{dip}}}{B^2_{\text{ext}}} \quad , \tag{5.72}$$

where K'_{dip} accounts for the shift from the field arising from dipoles inside the Lorentz.

The response of the f or d local moments is described by their susceptibility tensor, χ_{fd}. The susceptibility contribution of the local is usually (at least at low temperatures) much higher than the Pauli susceptibility. Using the tensor χ_{fd}, we can write the value of the moments polarized by the external field[16]

$$\mathbf{m}_e = \frac{v_0}{\mu_0} \chi_{fd} \mathbf{B}_{\text{ext}} \tag{5.73}$$

where v_0 is the volume per magnetic ion. For example, if we assume that the external field is in the z-direction (lab. frame) we have

$$m_e^\beta = \frac{v_0}{\mu_0} \chi_{fd}^{\beta z} B_{\text{ext}} \quad . \tag{5.74}$$

We note also that we can write the components of the dipole field in Eq. 5.20 in terms of a tensor or (assuming again that the external field is in the z-direction)

$$B'^\alpha_{\text{dip}} = \frac{\mu_0}{4\pi v_0} \sum_{\text{Lor}} \sum_\beta D^{\alpha\beta}_{\mathbf{r}_j} m^\beta_{e,j} \quad , \tag{5.75}$$

where $\mathbf{D}_{\mathbf{r}_j}$ is the dipole field tensor for one particular moment, such that

$$D^{\alpha\beta}_{\mathbf{r}_j} = v_0 \left(\frac{3 r_j^\alpha r_j^\beta}{r_j^5} - \frac{\delta_{\alpha,\beta}}{r_j^3} \right) \quad . \tag{5.76}$$

An important point to see is that the dipole field tensor is traceless. and that $D^{\alpha\beta}_{\mathbf{r}_j} = D^{\beta\alpha}_{\mathbf{r}_j}$. In the case of an applied TF, all the local moments will have the same value given by the Eq. 5.73 and the moment vector can be removed from the sum in Eq. 5.75 so that

$$\begin{aligned} \mathbf{B}'_{\text{dip}} &= \frac{\mu_0}{4\pi v_0} \left(\sum_{\text{Lor}} \mathbf{D}_{\mathbf{r}_j} \right) \mathbf{m}_e \\ &= \frac{\mu_0}{v_0} \left(\frac{1}{4\pi} \sum_{\text{Lor}} \mathbf{D}_{\mathbf{r}_j} \right) \frac{v_0}{\mu_0} \chi_{fd} \mathbf{B}_{\text{ext}} \\ &= \mathcal{D}_{\mathbf{r}_\mu} \chi_{fd} \mathbf{B}_{\text{ext}} \quad , \end{aligned} \tag{5.77}$$

---

[16]Remember that the magnetization represents the volume density of the magnetic moments.

where we have defined the total dipolar tensor $\mathcal{D}_{\mathbf{r}_\mu}$ which will depend on the muon stopping site and the position of the magnetic moments in the Lorentz sphere. Therefore, this tensor can be easily calculated for a known crystallographic structure by assuming a muon site.[17]

5.5.2.2. The enhanced contact field contribution

As said, the localised magnetic density contributes to the muon Knight-shift in a second way through the Ruderman-Kittel-Kasuya-Yosida (RKKY) interaction. The RKKY field arises from the indirect exchange interaction between the muon and the magnetic moments of the localized electrons mediated by the conduction electrons. In the RKKY interaction, the conduction electron magnetic moments are coupled to the localized electron magnetic moment through the exchange interaction. In turn, these electrons are coupled to the muon spin via the contact interaction. The exact strength of the RKKY interaction depends on the electronic density of states at the Fermi level, the volume enclosed by the Fermi surface, the exchange interaction between the spins (moments) of the localized and conduction electrons, and the electronic density at the muon site. Therefore, whereas it contains valuable information, its *ab initio* estimation is difficult. In its simplest form, this interaction will produce an enhanced contact field

$$
\begin{aligned}
\mathbf{B}_{\text{cont,fd}} &= \frac{\mu_0}{v_0} \, \mathcal{A}_{\mathbf{r}_\mu} \, \mathbf{m}_e \\
&= \mathcal{A}_{\mathbf{r}_\mu} \, \chi_{fd} \, \mathbf{B}_{\text{ext}} \quad,
\end{aligned}
\tag{5.78}
$$

where $\mathcal{A}_{\mathbf{r}_\mu}$ is the enhanced contact tensor. Since the contact coupling is normally independent of the direction of $\mathbf{B}_{\text{ext}}$, we can write $\mathcal{A}_{\mathbf{r}_\mu} = A_{\text{cont,fd},\mathbf{r}_\mu} \cdot \mathcal{E}$, where $\mathcal{E} = \left(\mathcal{E}^{\alpha\beta}\right) = \left(\delta^{\alpha\beta}\right)$ is the unit tensor. Itself, $A_{\text{cont,fd},\mathbf{r}_\mu}$ is given by

$$
A_{\text{cont,fd},\mathbf{r}_\mu} \propto \mathcal{J} \sum_{\text{nn}} \frac{2k_{\text{F}}r_j \cos(2k_{\text{F}}r_j) - \sin(2k_{\text{F}}r_j)}{(2k_{\text{F}}r_j)^4} \quad,
\tag{5.79}
$$

where the sum is done on the nearest neighbor ions, k_{F} is the Fermi wave number and $\mathcal{J}$ is the exchange energy between the localized moment and the conduction electrons.

Here also we can write the Knight-shift

$$
K_{\text{cont,fd}} = \frac{\mathbf{B}_{\text{ext}} \cdot \mathbf{B}_{\text{cont,fd}}}{B_{\text{ext}}^2} \quad,
\tag{5.80}
$$

---

[17]Note that in order to use Eq. 5.77, all vectors and tensors have to be expressed in the same reference frame (if this is not the case, the Euler angles have to be used to transform the quantities).

5.5.2.3. The total Knight shift

Wrapping up and using Eqs. 5.71, 5.72 and 5.80, we can write the total Knight shift for systems with local moments as

$$
\begin{aligned}
K_\mu &= K_\text{cont} + K'_\text{dip} + K_\text{cont,fd} \\
&= \frac{\mathbf{B}_\text{ext} \cdot \mathbf{B}_\text{cont}}{B_\text{ext}^2} + \frac{\mathbf{B}_\text{ext} \cdot \mathbf{B}'_\text{dip}}{B_\text{ext}^2} + \frac{\mathbf{B}_\text{ext} \cdot \mathbf{B}_\text{cont,fd}}{B_\text{ext}^2} \\
&= \frac{2}{3} \chi_\text{P} \frac{|\psi(0)|^2}{n} + \frac{\mathbf{B}_\text{ext} \cdot \mathcal{D}_{\mathbf{r}_\mu} \chi_{fd} \mathbf{B}_\text{ext}}{B_\text{ext}^2} + \frac{\mathbf{B}_\text{ext} \cdot \mathcal{A}_{\mathbf{r}_\mu} \chi_{fd} \mathbf{B}_\text{ext}}{B_\text{ext}^2} \quad .
\end{aligned}
\tag{5.81}
$$

We can note few point here:

1. At low temperature, the susceptibility due to the local moments (which varies with $1/T$) is much stronger than the Pauli susceptibility and the the first term on the right-hand side of Eq. 5.81 (K_cont), can be safely neglected.

2. K'_dip and $K_\text{cont,fd}$ are both dependent on the same susceptibility tensor and will follow a similar temperature dependence.

3. As the Pauli susceptibility χ_P and the enhanced contact tensor $\mathcal{A}_{\mathbf{r}_\mu}$ are isotropic, the entire angular dependence of the Knight-shift is contained in the dipolar tensor $\mathcal{D}_{\mathbf{r}_\mu}$ and the susceptibility tensor χ_{fd} (the angular dependence of the susceptibility is usually determined by bulk magnetization measurements).

4. The temperature dependence is entirely contained in the susceptibility tensor χ_{fd}.

5.5.3. Determining the muon-stopping site

Using what we just saw in the previous Section, we can now see how we can determine experimentally the muon site in systems possessing localized moments.

The task is to determine the diagonal components of the total dipolar tensor $\mathcal{D}_{\mathbf{r}_\mu}$ and to compare them with calculate values. Of course this method requires single crystals, which are not always available.

One way to do it, is to measure as a function of the temperature the Knight-shift along the principal direction of the crystal [say (a, b, c)], where the susceptibility tensor is diagonal. One will get:[18]

$$\begin{cases} K_\mu^a(T) & = \left(\mathcal{D}_{\mathbf{r}_\mu}^{aa} + A_{\text{cont,fd},\mathbf{r}_\mu}\right) \chi_a(T) \\ K_\mu^b(T) & = \left(\mathcal{D}_{\mathbf{r}_\mu}^{bb} + A_{\text{cont,fd},\mathbf{r}_\mu}\right) \chi_b(T) \\ K_\mu^c(T) & = \left(\mathcal{D}_{\mathbf{r}_\mu}^{cc} + A_{\text{cont,fd},\mathbf{r}_\mu}\right) \chi_c(T) \end{cases} \qquad (5.82)$$

Therefore, if the susceptibility along the principal direction of the crystal is know, by measuring as a function of the temperature the Knight-shift along these direction and by taking into account that the dipolar tensor is traceless (3 measurements + 1 condition), then the diagonal components of $\mathcal{D}_{\mathbf{r}_\mu}$ can be obtained and compared to calculate values for high symmetry interstitial sites.
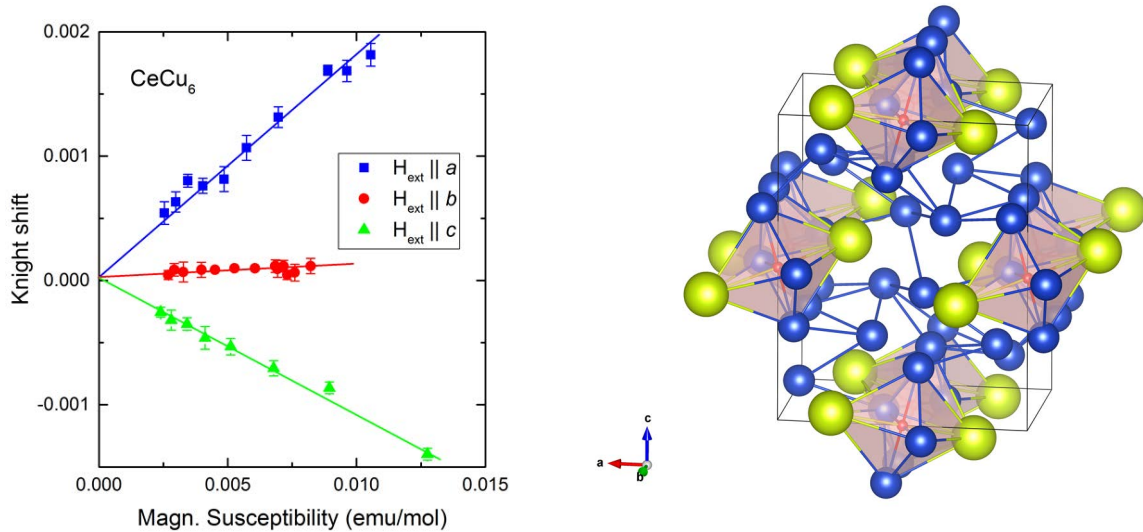
Figure 5.27.: *Left: muon Knight-shift plotted versus the magnetic suscep-tibility (Clogston-Jaccarino plot) for the principal direction in CeCu$_6$ (or-thorhombic structure) with the temperature as an implicit parameter. From the slopes the main components of the dipolar tensor can be obtained and com-pared to calculation. Right: It is found that the muon sits between two Ce-ions (Ce: yellow spheres, muon: small red spheres). Adapted from Ref. [69].*

---

[18]Care should be taken to always express the tensors and the field direction in the same reference frame.
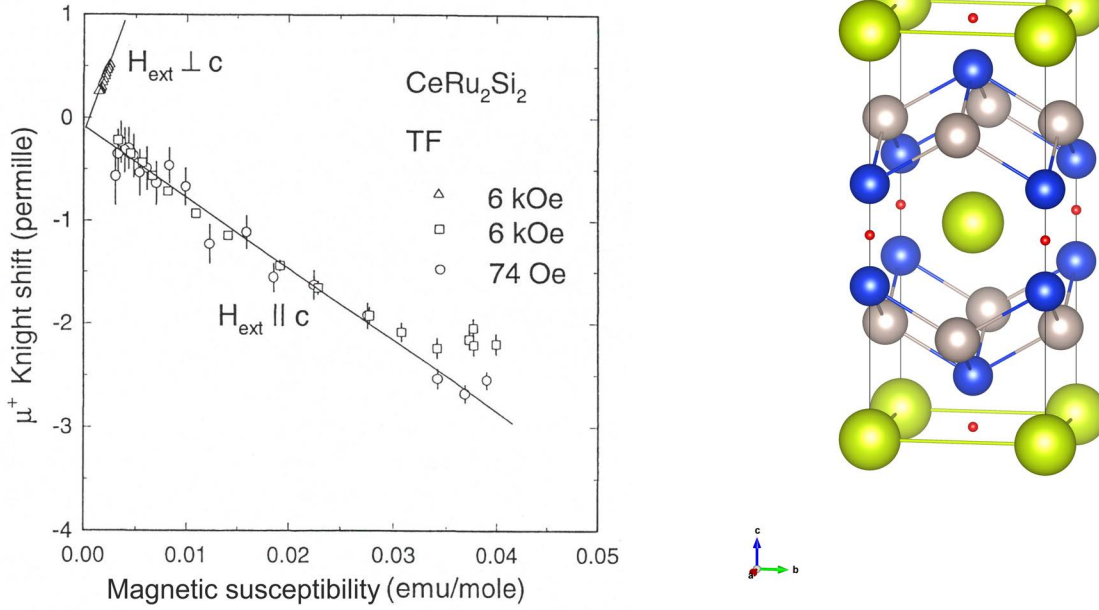
Figure 5.28.: *Left: muon Knight-shift plotted versus the magnetic suscep-
tibility for the principal direction in CeRu$_2$Si$_2$ with the temperature as an
implicit parameter. Only two measurements are necessary as the system is
tetragonal. From the slopes the main components of the dipolar tensor can be
obtained and compared to calculation. Right: It is found that the muon sits
between the 4 Ce-ions in the basal plane (Ce: yellow spheres, muon: small
red spheres). Adapted from Ref. [69].*

Another route to determine the dipolar tensor is to perform angular dependence at a given
temperature, *i.e.* the sample is turned with respect to the applied field after each measure-
ment.

In the reference frame of the rotation axis and plane, one can express the external field as
$\mathbf{B}_{\text{ext}} = B_{\text{ext}}(\sin\theta\cos\phi, \sin\theta\sin\phi, \cos\theta)$, where θ and ϕ are the polar and azimuth angles of
the field in the reference frame. Generally, the angular dependence of the component of $\mathbf{B}'_{\text{dip}}$
along the direction of the external field is obtained by projecting the dipolar field and can be
expressed as [70]

$$
\begin{aligned}
B'_{\text{dip},\parallel} = {} & \tfrac{1}{3}\big(\mathcal{D}^{xx}_{\mathbf{r}_\mu}\chi_x + \mathcal{D}^{yy}_{\mathbf{r}_\mu}\chi_y + \mathcal{D}^{zz}_{\mathbf{r}_\mu}\chi_z\big)B_{\text{ext}} \\
& + \tfrac{2}{3}\big[\mathcal{D}^{zz}_{\mathbf{r}_\mu}\chi_z - \tfrac{1}{2}\big(\mathcal{D}^{xx}_{\mathbf{r}_\mu}\chi_x + \mathcal{D}^{yy}_{\mathbf{r}_\mu}\chi_y\big)\big]P_2^0(\cos\theta)B_{\text{ext}} \\
& - \tfrac{1}{3}\mathcal{D}^{xz}_{\mathbf{r}_\mu}(\chi_x + \chi_z)\,P_2^1(\cos\theta)\cos\phi\,B_{\text{ext}} \\
& - \tfrac{1}{3}\mathcal{D}^{yz}_{\mathbf{r}_\mu}(\chi_y + \chi_z)\,P_2^1(\cos\theta)\sin\phi\,B_{\text{ext}} \\
& + \tfrac{1}{6}\big(\mathcal{D}^{xx}_{\mathbf{r}_\mu}\chi_x - \mathcal{D}^{yy}_{\mathbf{r}_\mu}\chi_y\big)P_2^2(\cos\theta)\cos2\phi\,B_{\text{ext}} \\
& + \tfrac{1}{6}\mathcal{D}^{xy}_{\mathbf{r}_\mu}(\chi_x + \chi_y)\,P_2^2(\cos\theta)\sin2\phi\,B_{\text{ext}}\ ,
\end{aligned}
\tag{5.83}
$$

where the terms P_l^m represent the associated Legendre polynomials. Again, the tensors and the external field vector have to be expressed in the same frame. The P_l^m that we use are

$$
\begin{aligned}
P_2^0(\cos\theta) &= \tfrac{1}{2}(3\cos^2\theta - 1) \\
P_2^1(\cos\theta) &= -3\cos\theta\sin\theta \\
P_2^2(\cos\theta) &= 3\sin^2\theta
\end{aligned}
\tag{5.84}
$$

Equation 5.83 will be more simpler in real systems taking into account the symmetry of the system.

For example, if we come back to the example of UPd_2Al_3 (see Fig 5.9) and we assume, as discussed on Page 164, that the muon occupies solely the b site $(0, 0, 1/2)$ (Wyckoff notation) of the hexagonal structure with space group $P6/mmm$, then we have[19]

$$
\mathcal{D}_{\mathbf{r}_\mu}^{xx} = \mathcal{D}_{\mathbf{r}_\mu}^{yy} = -\frac{1}{2}\mathcal{D}_{\mathbf{r}_\mu}^{zz} \;,
\tag{5.85}
$$

as the b-site is axially symmetric with respect to z. Also, due to the hexagonal symmetry, we can write for the susceptibility tensor $\chi_x = \chi_y = \chi_\perp$ and $\chi_z = \chi_\parallel$. If we perform TF measurements and rotate around the field around the x axis (*i.e.* the field is actually in the $y - z$ plane with $\phi = \pi/2$) then Eq. 5.83 becomes

$$
B'_{\text{dip},\parallel} = B_{\text{ext}}\mathcal{D}_{\mathbf{r}_\mu}^{zz}\left[\cos^2\theta\left(\chi_\parallel + \frac{1}{2}\chi_\perp\right) - \frac{1}{2}\chi_\perp\right]
\tag{5.86}
$$

and by dividing with B_{ext} one gets K'_{dip} which contains all the angular dependence of the Knight shift. Figure 5.29 shows the row muon frequency data, which, when corrected by the demagnetizing and Lorentz field, provide us with the angular dependence of K'_{dip}. By fitting Eq. 5.86 to the data, one obtains $\mathcal{D}_{\mathbf{r}_\mu}^{zz}$ which can be compared to the computed value and one finds an excellent agreement with the muon at site b.

---

[19]Here we assume that our sample is so oriented that $a = x$, $a^* = y$ and $c = z$.

Figure 5.29.: *Angular dependence of the muon precession frequency measured for a single crystal sample of the hexagonal compound UPd$_2$Al$_3$ in a transverse field of 0.38 T at 37 K. The field is rotated in the a* − c (or y − z) plane and θ denotes the angle between the field and the c axis. The solid line is the result of a fit (adapted from Ref. [69]).*

We take as another system CeB$_6$ which crystallizes in the simple cubic structure *Pm3m* (see Fig. 5.30). The muon locates at the *d*-site (1/2,0,0) [multiplicity of 3; other sites (0,1/2,0) and (0,0,1/2)]. These sites may become magnetically inequivalent when applying an external field and performing Knight-shift measurements as they have the following related dipolar tensors:

$$
\mathcal{D}_{(\frac{1}{2},0,0)} = \begin{pmatrix} \mathcal{D} & 0 & 0 \\ 0 & -\frac{1}{2}\mathcal{D} & 0 \\ 0 & 0 & -\frac{1}{2}\mathcal{D} \end{pmatrix}
$$

$$
\mathcal{D}_{(0,\frac{1}{2},0)} = \begin{pmatrix} -\frac{1}{2}\mathcal{D} & 0 & 0 \\ 0 & \mathcal{D} & 0 \\ 0 & 0 & -\frac{1}{2}\mathcal{D} \end{pmatrix}
$$

$$
\mathcal{D}_{(0,0,\frac{1}{2})} = \begin{pmatrix} -\frac{1}{2}\mathcal{D} & 0 & 0 \\ 0 & -\frac{1}{2}\mathcal{D} & 0 \\ 0 & 0 & \mathcal{D} \end{pmatrix}
\tag{5.87}
$$

Taking into account that we have a cubic system (*i.e.* $\chi_x = \chi_y = \chi_z$), we see that if we apply along the [001]-axis (*z*-direction) the sites (1/2,0,0) and (0,1/2,0) will have the same $\mathbf{B}'_{\text{dip}}$, which will have half of the value and the opposite direction compared to the one felt by the muon at the (0,0,1/2) site. This will be true when rotating the external field around the [1$\bar{1}$10] axis (see Fig. 5.30). When the field is directed along the [111] axis [*i.e.* corresponding to the magic angle $\theta_m = \arccos(1/\sqrt{3}) \approx 54.7°$] then all the sites are also magnetically equivalent and only one μSR frequency is observed. Note that for this angle the dipolar contribution is actually zero.
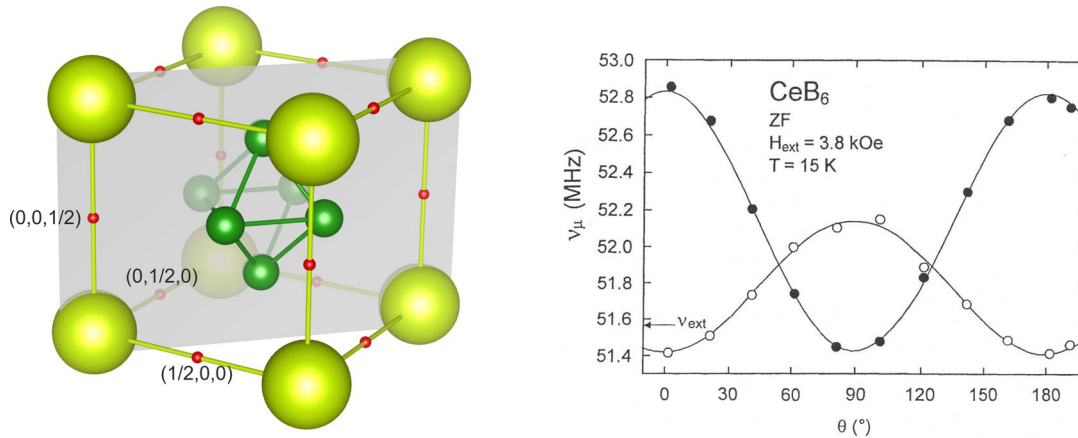
Figure 5.30.: *Left panel: Cubic struture of CeB_6. The cerium atoms are at the position (0,0,0) and at the equivalent positions. The muon site is located in-between two cerium atoms (small red spheres). Right panel: Angular dependence of the observed muon precession frequency measured for a single crystal sample of the cubic compound CeB_6 in a transverse field of 0.38 T at 15 K. The field is rotated around the $[1\bar{1}10]$ axis (i.e. the field is located in the gray plane on the left panel) and θ denotes the angle between the field and the [001] axis. The two signals have an amplitude (asymmetry) ratio of 2:1 corresponding on one hand-side to the (1/2,0,0) and (0,1/2,0) sites (open symbols) and on the other hand-side to the (0,0,1/2) site (solid symbols). Taken from Ref. [69].*

5.6. Depolarization created by nuclear moments

5.6.1. Classical calculation

We have already few times mentioned that the small field created by the nuclear moments around the muon will create a broadening of the μSR signal in TF and ZF configuration. In the following, we will give a classical calculation of the field width at the muon site created by the nuclear moments. A quantum classical calculation produces the same result.

5.6.1.1. The TF case

We first consider the TF case and define the z-axis as the direction of the applied field. The field created by a single nuclear magnetic moment at the muon site (taken as the origin) is only of dipolar origin as the orbital and contact field vanish. So for the nuclear moment $\mathbf{m}_{N,j}$, we will have a dipolar contribution (see also Eq. 5.9)

$$\mathbf{B}_{\mathrm{dip},N,j}(0) = \frac{\mu_0}{4\pi}\left[\frac{3\mathbf{r}_j(\mathbf{m}_{N,j}\cdot\mathbf{r}_j)}{r_j^5} - \frac{\mathbf{m}_{N,j}}{r_j^3}\right], \qquad (5.88)$$
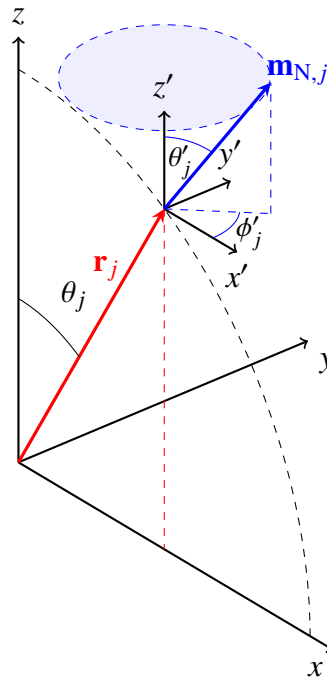
Figure 5.31.: *Sketch of $\mathbf{r}_j$ (vector between the muon located at the origin and a nuclear moment) and $\mathbf{m}_{N,j}$ (nuclear magnetic moment). Without loosing generality, the azimuthal angle of $\mathbf{r}_j$ can be chosen to be zero. In large externally applied field along the z-direction, the nuclear moment will precess around the external field (along the blue circle).*

and of course the total field will be

$$\mathbf{B}_{\text{dip,N}}(0) = \frac{\mu_0}{4\pi} \sum_j \left(\frac{3\mathbf{r}_j(\mathbf{m}_{\text{N},j} \cdot \mathbf{r}_j)}{r_j^5} - \frac{\mathbf{m}_{\text{N},j}}{r_j^3} \right) . \tag{5.89}$$

As discussed in Section 4.2, if the external field is much higher than the internal one then one has solely to consider the field distribution along the applied field *i.e.* the *z*-direction. Expressing the vectors $\mathbf{r}_j$ and $\mathbf{m}_{\text{N},j}$ in the spherical coordinates (see Fig. 5.31), the component z of $\mathbf{B}_{\text{dip,N},j}(0)$ is written as

$$B_{\text{dip,N},j}^z(0) = \frac{\mu_0}{4\pi} \frac{m_{\text{N},j}}{r_j^3} \left[(3\cos^2\theta_j - 1)\cos\theta'_j + 3\sin\theta_j\cos\theta_j\cos\phi'_j\sin\theta'_j \right] . \tag{5.90}$$

In large externally applied field along the *z*-direction, the nuclear moment will precess around the external field and the second term (so-called "non-secular term") on the right hand-side of Eq. 5.90 will average out.

Therefore the depolarization rate in TF is as before given by the second moment of the field distribution along the direction of the external field, that is[20]

$$\begin{aligned} \sigma^2_{\text{TF,N}} &= \gamma_\mu^2 \langle \Delta B_{\text{dip,N}}^z{}^2 \rangle \\ &= \gamma_\mu^2 \left[\langle \left(\sum B_{\text{dip,N},j}^z \right)^2 \rangle - \langle \left(\sum B_{\text{dip,N},j}^z \right) \rangle^2 \right] . \end{aligned} \tag{5.91}$$

The sums are over the nuclear magnetic moments (*i.e.* over *j*) and the average is over all possible orientations of $\mathbf{m}_{\text{N},j}$, that is over all possible θ'_j and ϕ'_j angles.

The second term on the right hand side is zero as the average gives terms of the form

$$\frac{1}{4\pi} \int\limits_0^{2\pi} \int\limits_0^\pi \cos\theta'_j \sin\theta'_j \, d\theta'_j d\phi'_j .$$

On the other side the first term contains only terms of the form

$$\frac{1}{4\pi} \int\limits_0^{2\pi} \int\limits_0^\pi \cos^2\theta'_j \sin\theta'_j \, d\theta'_j d\phi'_j ,$$

which average to 1/3. One therefore gets

$$\sigma^2_{\text{TF,N}} = \frac{1}{3} \left(\frac{\mu_0}{4\pi} \right)^2 \gamma_\mu^2 m_{\text{N}}^2 \sum_j \frac{(3\cos^2\theta_j - 1)^2}{r_j^6} . \tag{5.92}$$

The correct expression is obtained by considering that the expectation value of the angular momentum operator is $\langle \mathbf{I}_{\text{N}}^2 \rangle = \hbar^2 I_{\text{N}}(I_{\text{N}} + 1)$ and we get[21]

$$\boxed{\sigma^2_{\text{TF,N}} = \frac{1}{3} \left(\frac{\mu_0}{4\pi} \right)^2 \hbar^2 \gamma_\mu^2 \gamma_{\text{N}}^2 I_{\text{N}}(I_{\text{N}} + 1) \sum_j \frac{(3\cos^2\theta_j - 1)^2}{r_j^6} .} \tag{5.93}$$

---

[20]Here we use the fact that $\text{Var}(X + a) = \text{Var}(X)$, that is $\text{Var}(B_{\text{ext}}^z + B_{\text{dip,N},j}^z(0)) = \text{Var}(B_{\text{dip,N},j}^z(0))$.

[21]Remember that $\mathbf{m}_{\text{N}} = \gamma_{\text{N}} \mathbf{I}_{\text{N}}$.

This is the situation for single crystals. Therefore, as seen, an indication of the muon site can be obtained by performing angular scans in TF configuration by looking at the Knight-shift (*i.e.* frequency shift), but also by looking at the angular dependence of the depolarization rate obtained in the same measurements.
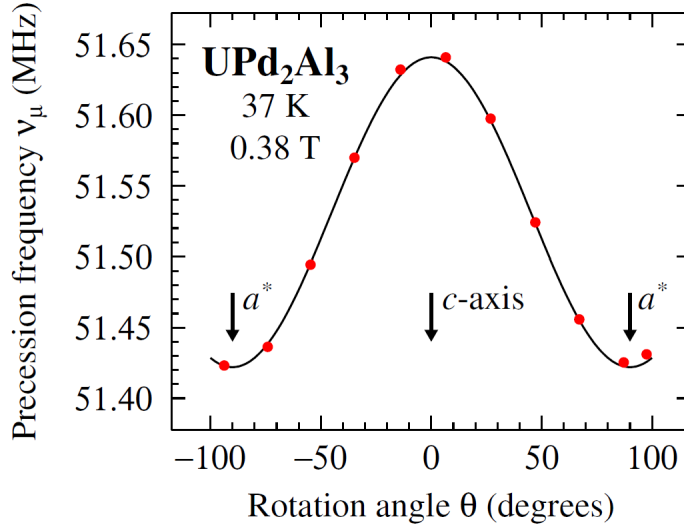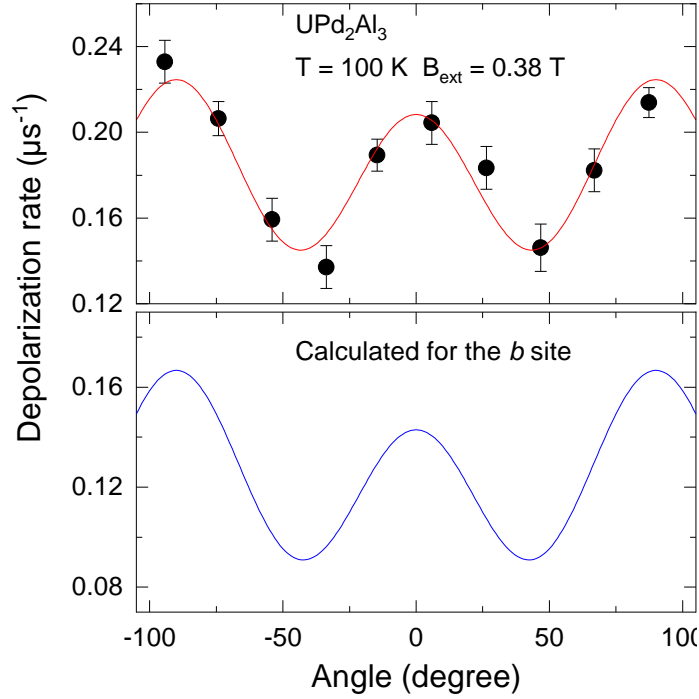

Figure 5.32.: *Angular dependence of the muon depolarization rate measured for a single crystal sample of the hexagonal compound UPd$_2$Al$_3$ in a transverse field of 0.38 T at 37 K (this depolarization correspond to the damping of the µSR signal for which the angular dependence of the frequency is shown on Fig. 5.29. The field is rotated in the $a^* - c$ (or $y - z$) plane and θ denotes the angle between the field and the c axis. Upper part: The solid line is the result of a fit of the function $\sigma_{TF,N}(\theta) = \sigma_0 + aP_2^0(\cos\theta) + aP_4^0(\cos\theta)$ (note that $P_4^0(\cos\theta)$ is the associated Legendre polynomial $P_4^0(\cos\theta) = \frac{1}{8}(35\cos^4\theta - 30\cos^2\theta + 3)$). Lower part: calculated depolarization rate for the b-site. The fitted parameters a and b are very close to the calculated ones. On the other hand the slight deviation between the measured and calculated values of σ_0 can be ascribed to a slight misalignment of the different monocrystalline samples used for the experiment or to lattice imperfections. Adapted from Ref. [69].*

If we deal with a polycrystalline sample, we have to perform the spatial of Eq. 5.93 and we have

$$\frac{1}{4\pi} \int\limits_0^{2\pi} \int\limits_0^{\pi} (3\cos^2\theta'_j - 1)^2 \sin\theta'_j \, d\theta'_j d\phi'_j \ ,$$

which average to 4/5 and we therefore get

$$\sigma^2_{\text{TF,N,poly}} = \frac{4}{15}\left(\frac{\mu_0}{4\pi}\right)^2 \hbar^2 \gamma_\mu^2 \gamma_N^2 I_N(I_N+1)\sum_j \frac{1}{r_j^6} \quad . \tag{5.94}$$

5.6.1.2. The ZF case

In this case the non-secular term cannot be dropped and the muon spin feels the full magnitude of nuclear moment an not solely its projection along the z-direction (here defined by the direction of the initial muon polarization). As explained in page 113, the depolarization rate at short time in ZF will be governed by the second moments for the directions perpendicular to the initial muon polarization (assume to be z). The x and y components of the dipolar fields are

$$B^x_{\text{dip,N},j}(0) = \frac{\mu_0}{4\pi}\frac{m_{\text{N},j}}{r_j^3}\left[(3\sin^2\theta_j-1)\sin\theta'_j\cos\phi' + 3\sin\theta_j\cos\theta_j\cos\theta'_j\right]$$

$$B^y_{\text{dip,N},j}(0) = \frac{\mu_0}{4\pi}\frac{m_{\text{N},j}}{r_j^3}\left[-\sin\theta'_j\sin\phi'\right] \quad . \tag{5.95}$$

We note that in a single crystal the second moments in the x and y directions are a priori not the same and therefore the Kubo-Toyabe function (Eq. 4.20) cannot be used "as is" (see Ref. [71]). However, we can calculate the depolarization at short time σ_{st} which is given by the sum of both moments in the x and y direction (see Page 113) and therefore we have[22]

$$\begin{aligned}
\sigma^2_{\text{st}} &= \gamma_\mu^2\left(\langle B^x_{\text{dip,N},j}(0)^2\rangle + \langle B^y_{\text{dip,N},j}(0)^2\rangle\right)\\
&= \gamma_\mu^2\left(\left[\langle\left(\sum B^x_{\text{dip,N},j}\right)^2\rangle - \langle\left(\sum B^y_{\text{dip,N},j}\right)\rangle^2\right] + \left[\langle\left(\sum B^y_{\text{dip,N},j}\right)^2\rangle - \langle\left(\sum B^y_{\text{dip,N},j}\right)\rangle^2\right]\right) \quad .
\end{aligned} \tag{5.96}$$

As for the TF case, we have to take all possible orientations of the nuclear magnetic moment and we see that the second terms of each moment will average to zero (this just reflects that the average value of each component is zero). The average over the remaining terms will give

$$\sigma^2_{\text{st,ZF,N}} = \frac{1}{3}\left(\frac{\mu_0}{4\pi}\right)^2\hbar^2\gamma_\mu^2\gamma_N^2 I_N(I_N+1)\sum_j\frac{(5-3\cos^2\theta_j)^2}{r_j^6} \quad , \tag{5.97}$$

and the polycrystalline average is

$$\sigma^2_{\text{st,ZF,N,poly}} = \frac{4}{3}\left(\frac{\mu_0}{4\pi}\right)^2\hbar^2\gamma_\mu^2\gamma_N^2 I_N(I_N+1)\sum_j\frac{1}{r_j^6} \quad . \tag{5.98}$$

In the case of a polycrystal, the second moment is isotropic and therefore we have that $\sigma^2_{\text{st,ZF,N,poly}} = 2\sigma^2_{\text{ZF,N,poly}}$, where now $\sigma_{\text{ZF,N,poly}}/\gamma_\mu^2$ is the second moment along one Cartesian direction. In the polycrystalline case the depolarization will therefore be given by the

---

[22]Note that the Covariance between the different $\mathbf{B}_j$ is zero.

Kubo-Toyabe function (Eq. 4.20) with

$$\sigma^2_{\mathrm{ZF,N,poly}} = \frac{1}{2}\sigma^2_{\mathrm{st,ZF,N,poly}} = \frac{2}{3}\left(\frac{\mu_0}{4\pi}\right)^2 \hbar^2 \gamma_\mu^2 \gamma_N^2 I_N(I_N+1) \sum_j \frac{1}{r_j^6} \quad . \tag{5.99}$$

We see that[23]

$$\sigma^2_{\mathrm{ZF,N,poly}} = \frac{5}{2}\sigma^2_{\mathrm{TF,N,poly}} \quad . \tag{5.100}$$

This prediction is confirmed experimentally in different systems as for example ZrH_2. One can compare the depolarization rate obtained in ZF by fitting a Kubo-Toyabe function[24] with the one obtained from the envelope of the oscillation decay of $P_x(t)$ (see Eq. 4.32, here $B_{\mathrm{ext}} = 0.5$ T). ZrH_2 is ideal because there is no electric quadrupole moment, the dipolar field created by the protons (H nuclei) is large and the muon is diffusing very slowly. From the experiment one obtains $\sigma^2_{\mathrm{ZF,N,poly}}/\sigma^2_{\mathrm{TF,N,poly}} = 2.4 \pm 0.1$, which is in good agreement with the prediction.
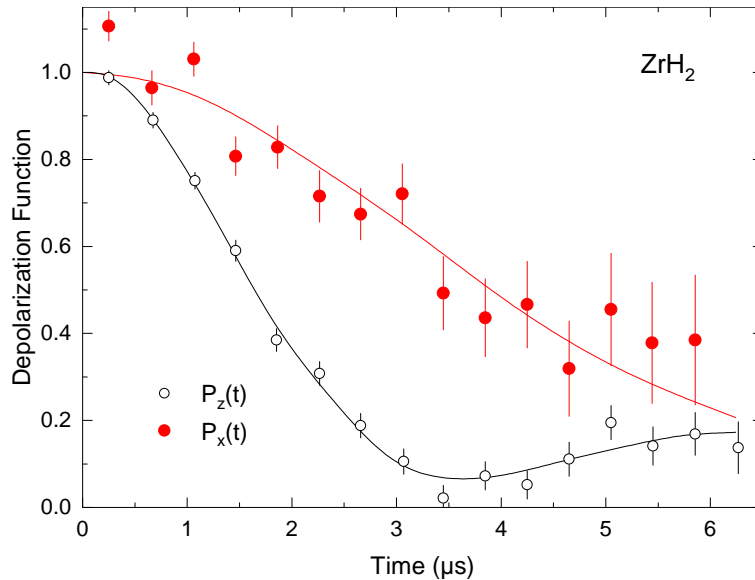
Figure 5.33.: *Observed zero-field depolarization and high-field transverse depolarization in ZrH_2 at room temperature. Taken from Ref. [45].*

5.6.1.3. Comment

Finally we remark here that the situation discussed above corresponds to the so-called Van Vleck limit, *i.e.* where one implies that the axis defined by the applied field in the TF case, or the initial direction of the muon polarization (in the ZF case), provides a natural axis of

---

[23]We note here that the factor is more than 2 (as one could have naively expected) due to the different treatment of the non-secular part in both cases.

[24]It is actually a dynamical Kubo-Toyabe function with slow dynamics (see Eq. 4.48) due to the slow diffusion of the muon.

quantization for the nuclear spin $\mathbf{I}_N$. This is no more valid if the nuclear spin is subject to other interactions which are not negligible compared with the Zeeman interaction. This is the case in presence of a strong electric field gradient for non-vanishing nuclear quadrupole moments (*i.e.* for $I_N > 1/2$). In short, for example in the TF case, the non-secular part cannot be neglected or in other words $\langle I_x \rangle \neq 0$ when the quadrupolar interaction cannot be ignored. The value of $\langle I_x \rangle$ will depend on the strength of the external field and will become negligible for high fields. In the ZF case, the quantization axis is defined by the electric field gradient which extends radially from the muon to a given nuclear moment. The static component of $\mathbf{I}_N$ along this axis has to be considered. More information can be found for example in Ref. [72].

6. Studying the Superconducting State with μSR

"If your interaction has the wrong sign, you can reverse it by making your order parameters have opposite signs. It's a bit mathematical; it's not so physical."

6.1. Introduction

The first material superconductor (SC) was discovered on April 8, 1911 by Heike Kamerlingh Onnes [73]. After having produced liquid helium, he studied the resistance of solid mercury at very low temperatures and observed that at $T_c = 4.2$ K, mercury was loosing its electrical resistance upon cooling.
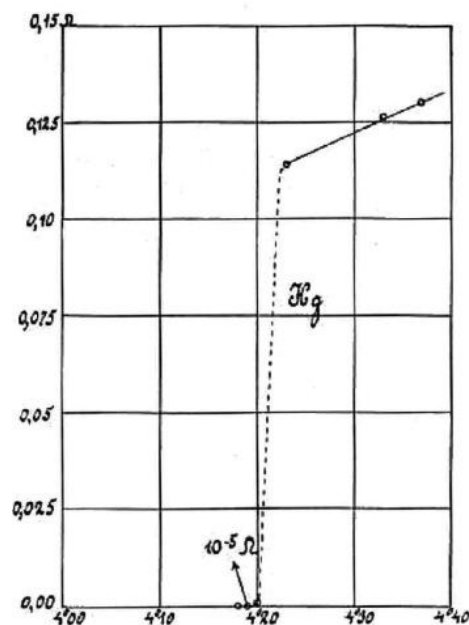
Figure 6.1.: *First measurements of the resistance of a sample of mercury cooled at temperatures around 4.2 K [73].*

Probably most important than the loss of resistivity in the observation that (up to a critical value) the magnetic field is expelled in a SC [74]. This was discovered in 1933 by Meissner

and Ochsenfeld.
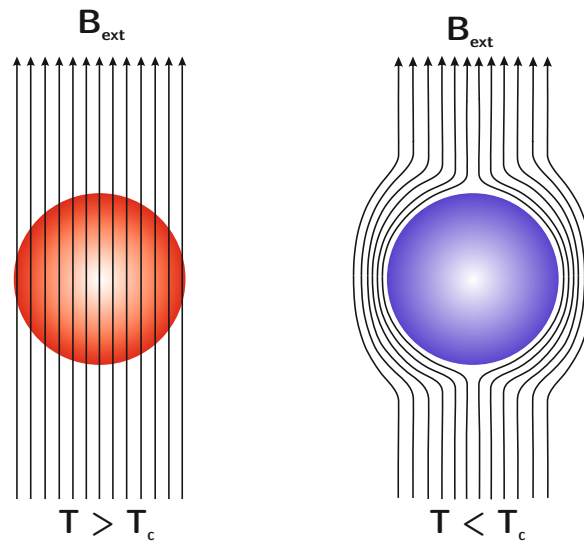
Figure 6.2.: *Schematic view of the Meissner-Ochsenfeld effect.*

The observation of a zero resistivity and of a perfect diamagnetism when applying a field on an already cooled sample could both be the property of a perfect superconductor. On the other side the observation that the diamagnetism occured also when the sample is cooled in field, clearly signified that SC is a new state of matter.
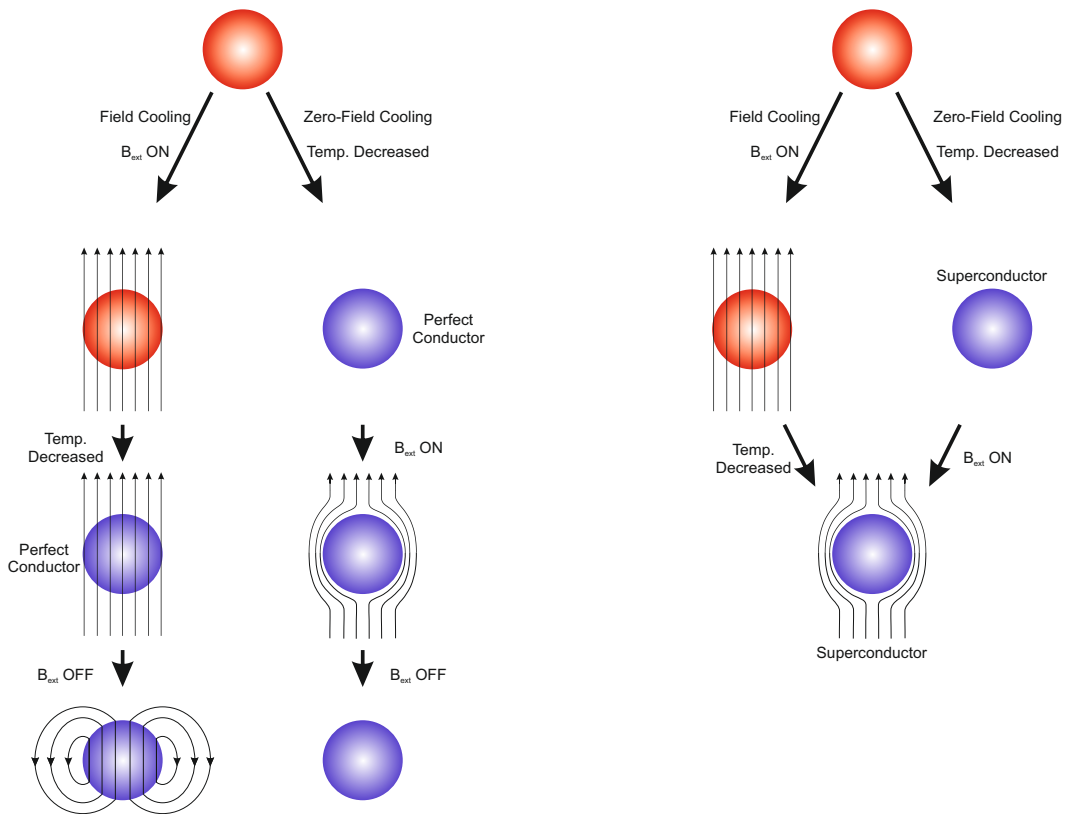
Figure 6.3.: *Comparison between an ideal conductor (left panel) and a superconductor (right panel). Diamagnetism and zero resistivity per se do not mean SC.*

The progresses concerning both the increase of T_c and on the theoretical point of view were rather slow, with a first phenomenological theory put forward by the brothers London in 1935, another phenomenological theory in 1950 By Ginzburg and Landau and finally the microscopic theory (BCS) in 1957 by Bardeen, Cooper and Schrieffer.
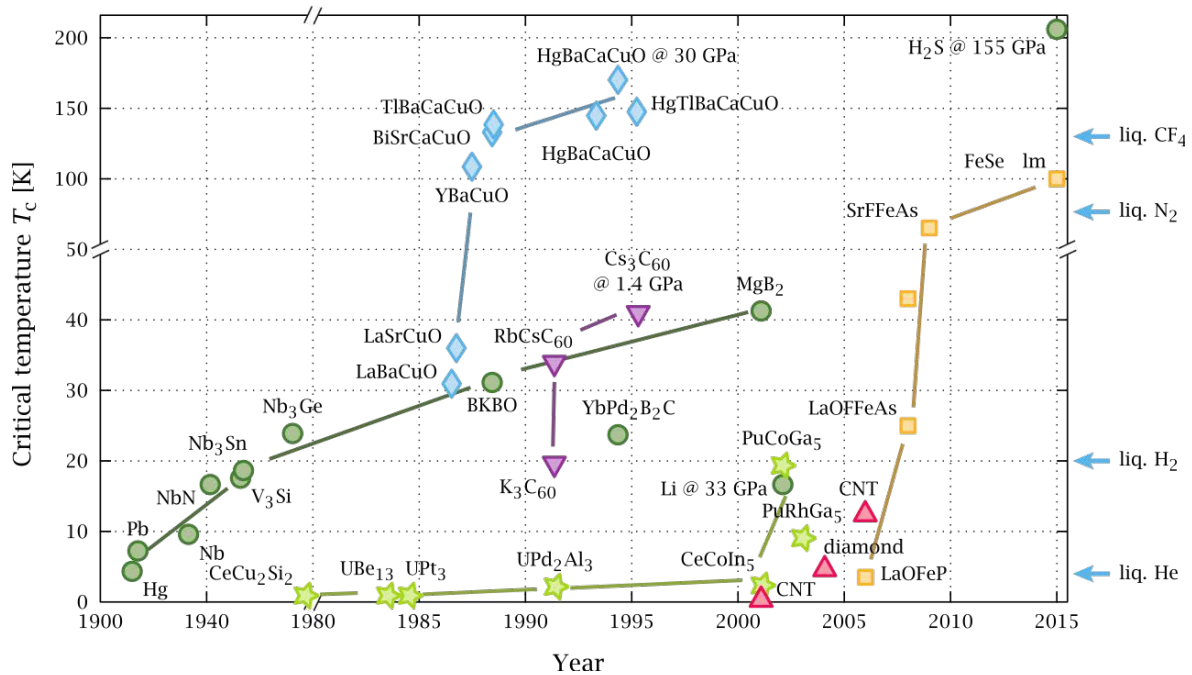
Figure 6.4.: *Timeline of the increase of T_c.*
Taken from https://en.wikipedia.org/wiki/Superconductivity.

6.2. Two characteristic lengths in superconductors

Two parameters play a capital role when describing the superconducting state of a SC.

- The "London penetration depth" characterizes the exponentially decaying magnetic field at the surface of a SC. It is related to the density of superconducting electrons in the material. This length plays a fundamental role in the SC technology.

- Another characteristic length is called the "coherence length". It is related to the Fermi velocity for the material and the energy gap associated with the condensation to the superconducting state. It reflects the fact that the SC electron density cannot change abruptly and that there is a minimum length over which a given change can be made. For example, a transition from the superconducting state to a normal state will have a transition layer of finite thickness which is given by the coherence length.

6.2.1. The magnetic penetration depth

6.2.1.1. The London equations

The equations developed by the brothers London relate the magnetic field and the current in and around a superconductor. Though not providing any explanation about the origin of the SC phenomena, the equations are able to explain the Meissner-Ochensenfeld effect and introduce the notion of penetration depth.

In a sample without resistance, the electrons will feel a force:

$$\mathbf{F} = -e\mathbf{E} = M^* \frac{\partial \langle \mathbf{v} \rangle}{\partial t} \quad, \tag{6.1}$$

where M^* is the effective mass of the electrons.

Recalling that the current density is: $\mathbf{j} = -n_s e \langle \mathbf{v} \rangle$, with n_s beeing the density of the carriers, one obtains the first London equation (*acceleration equation*):

$$\Lambda \frac{\partial \mathbf{j}}{\partial t} = \mathbf{E} \ \text{ with } \ \Lambda = \frac{M^*}{n_s e^2} \tag{6.2}$$

Taking the curl of this equation and using the 3rd Maxwell equation:

$$\nabla \times \mathbf{E} = -\frac{\partial \mathbf{B}}{\partial t} \tag{6.3}$$

one obtains:

$$\nabla \times \frac{\partial \mathbf{j}}{\partial t} = -\frac{1}{\Lambda} \frac{\partial \mathbf{B}}{\partial t} \quad, \tag{6.4}$$

that we can actually write as

$$\frac{\partial}{\partial t} \left(\nabla \times \mathbf{j} + \frac{1}{\Lambda} \mathbf{B} \right) = 0 \quad. \tag{6.5}$$

The quantity in the brackets must be a constant, as the time derivative vanishes. Up to this point the derivation is fully compatible with classical electromagnetism, applied to the frictionless acceleration of electrons in an ideal conductors. The essential new assumption of the London brother is that the bracket is not an arbitrary constant but is actually equal to zero. One therefore gets

$$\nabla \times \mathbf{j} = -\frac{1}{\Lambda} \mathbf{B} = -\frac{1}{\mu_0 \lambda^2} \mathbf{B} \quad. \tag{6.6}$$

This is known as London's second equation, where we have defined

$$\lambda = \sqrt{\frac{M^*}{\mu_0 e^2 n_s}} \quad. \tag{6.7}$$

6.2.1.2. Field and current decay in the Meissner state

Using the London equations and the 4th Maxwell equation:

$$\nabla \times \mathbf{B} = \mu_0 \, \mathbf{j} \quad (\text{assuming } \frac{\partial \mathbf{E}}{\partial t} = 0) \tag{6.8}$$

and taking its curl, one obtains for the Meissner state:

$$\lambda^2 \, \nabla \times \nabla \times \mathbf{B} + \mathbf{B} = 0 \ . \tag{6.9}$$

Taking into account that for a vector $\mathbf{F}$ one always has:

$$\nabla \times (\nabla \times \mathbf{F}) = \nabla(\nabla \cdot \mathbf{F}) - \nabla^2 \mathbf{F} \tag{6.10}$$

and because $\nabla \cdot \mathbf{B} = 0$ (no magnetic monopole), then we finally obtain:

$$\boxed{\mathbf{B} - \lambda^2 \, \Delta \mathbf{B} = 0 \ ,} \tag{6.11}$$

where $\Delta = \nabla^2$ is the Laplacian operator.

Similarly, if we take the curl of Eq. 6.6 and use the 4th Maxwell equation, we obtain

$$\boxed{\mathbf{j} - \lambda^2 \, \Delta \mathbf{j} = 0 \ .} \tag{6.12}$$

Let see the action of a magnetic field on this ideal superconductor. Assuming a field B_0 applied along a long superconducting rod (of diameter R) in the direction $\hat{\mathbf{z}}$, the exact solution of the Eq. 6.11 is:

$$B_z(x) = B_0 \, e^{-x/\lambda} \ , \tag{6.13}$$

where we have taken the limits conditions that $B(x = 0) = B_0$. To cancel the applied field, the superconductor sample will generate supercurrents $\mathbf{j}_s$ near its surface (see London's second equation 6.6) in the y direction which will also decay exponentially as a function of the distance x.

Similarly, if we apply a current I to the superconductor in the z direction, we see from Eq. 6.12 that the current actually only flows in a thin layer at the surface of the superconductor and we have

$$j_z(x) = \frac{I}{2\pi R \lambda} \, e^{-x/\lambda} \ . \tag{6.14}$$

We see that a superconducting wire, in order to transport effectively the current, does not need a large cross-section. This is completely at odd to normal conductors which require a large cross-section to decrease the resistance.
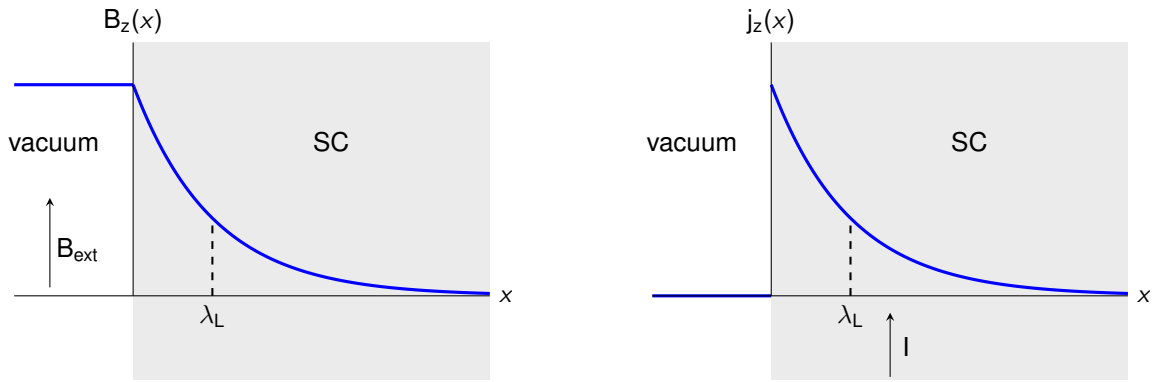
Figure 6.5.: *Left: Decay of the field inside a superconductor over a characteristic length λ. The screening is due to supercurrents flowing around the superconductor. Right: If a current is applied to a superconductor, actually the transport is performed also on a thin layer near the surface.*

We therefore see that the parameter λ defines a **"penetration depth"**, the knowledge of which is mandatory for the SC technology.
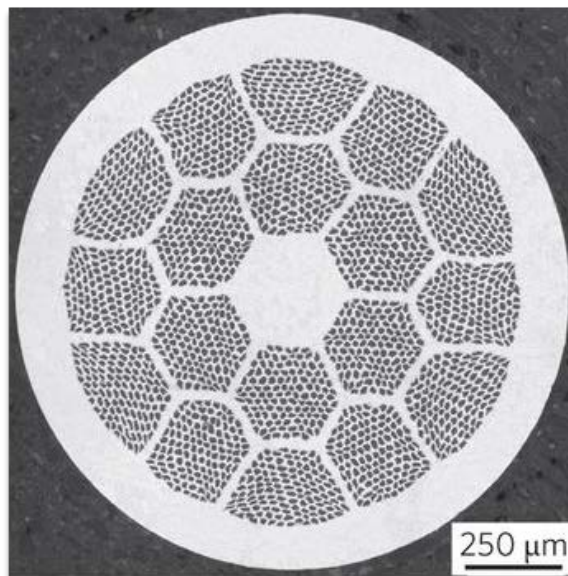
Figure 6.6.: *Cross-section of a superconducting wire made of Bi-2212 material (high-T_c material). The superconducting filaments are the small black dots, which are embedded in a copper matrix (see Ref [75] for details).*

The density of superconducting electrons depends on temperature, and therefore the penetration depth is temperature dependent. For $T \ll T_c$, all of the free electrons are superconducting and the superfluid density is maximum. The density decreases upon increasing temperature until it reaches zero at the critical temperature. Since the penetration depth is proportional to $1/\sqrt{n_s}$ (see Eq. 6.7, the penetration depth increases as the temperature approaches the critical temperature. This reflect the fact that less and less superconducting

currents can screen the applied field. The penetration depth becomes effectively infinite - corresponding to a uniform field in the material - at and above the critical temperature.

Its temperature dependence follows quite well the expression

$$\lambda(T) = \frac{\lambda(T=0)}{\sqrt{1-\left(\dfrac{T}{T_c}\right)^4}} \quad . \tag{6.15}$$
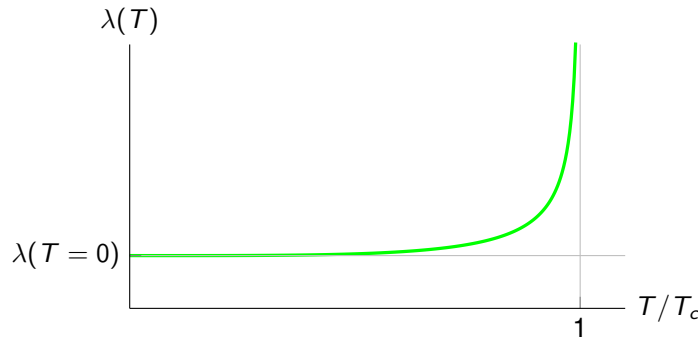
Figure 6.7.: *Temperature dependence of the penetration depth. At low temperature the superfluid density is maximum and the screening of the applied field is the most efficient.*

6.2.2. The coherence length

6.2.2.1. The Ginzburg Landau theory

Following the theory of Landau for second-order phase transitions, Ginzburg and Landau proposed that the free energy density f_s of a SC near the superconducting transition is given as a function of a complex order parameter field ψ, which is nonzero below a phase transition into a superconducting state and is related to the density of the superconducting carriers, *i.e.*[1]

$$n_s = |\psi(\mathbf{r})|^2 \tag{6.16}$$

The free energy density f_s can be expanded in a series:

$$f_s = f_n + \alpha|\psi|^2 + \frac{\beta}{2}|\psi|^4 + \frac{1}{2m}|(-i\hbar\nabla - 2e\mathbf{A})\psi|^2 + \frac{|\mathbf{B}|^2}{2\mu_0} \quad , \tag{6.17}$$

where $\mathbf{A}$ is the magnetic vector potential with $\mathbf{B} = \nabla \times \mathbf{A}$ and f_n is the energy density in the normal state.

---

[1] No interpretation of the parameter ψ was given in the original paper

The order parameter and the vector potential are obtained by minimizing the Ginzburg-Landau formula with respect to ψ and $\mathbf{A}$.

Let assume first a situation where no magnetic field are present and that we are far into the SC sample, where the SC is homogeneous. Then the two last term of Eq. 6.17 cancel and if we derive as function of ψ we get the equation

$$\alpha\psi + \beta|\psi|^2\psi = 0 \ , \tag{6.18}$$

which has a trivial solution, $\psi = 0$ corresponding to the normal state (*i.e.* $T > T_c$) and another one given by

$$|\psi|^2 = -\frac{\alpha}{\beta} \ . \tag{6.19}$$

By assuming a temperature dependence of the parameter α given by

$$\alpha(T) = \alpha_0(T - T_c) \ . \tag{6.20}$$

we get for $T < T_c$ (assuming $\alpha_0/\beta > 0$)[2]

$$|\psi_\infty|^2 = -\frac{\alpha_0(T - T_c)}{\beta} \ . \tag{6.21}$$

ψ has the typical behaviour for a second order phase transition, *i.e.* it approaches zero as $T \to T_c$.

Let assume now that we are near the interface between a superconductor and vacuum. Always assuming no magnetic field, we can remove the term containing $\mathbf{B}$ and $\mathbf{A}$ from Eq. 6.17. If we now derive as a function of ψ to find the minimum, we get the equation

$$\alpha\psi + \beta|\psi|^2\psi - \frac{\hbar^2}{2m}\nabla^2\psi = 0 \ . \tag{6.22}$$

Taking into account that $\psi(0) = 0$ and that $\psi(x \gg 0) = \psi_\infty$, the solution is given by

$$\psi(x) = \psi_\infty \tanh(\frac{x}{\sqrt{2}\,\xi}) \ , \tag{6.23}$$

where we have define the coherence length

$$\xi = \sqrt{\frac{\hbar^2}{2M|\alpha|}} \ . \tag{6.24}$$

We therefore see that the superconducting order parameter varies not abruptly but over a characteristic distance ξ.

The parameter $\beta = -\alpha/\psi_\infty^2 = -\alpha/n_s$ can be obtained by considering the Eq. 6.7 and 6.24 (assuming $M = M^*$):

$$\beta = \frac{\mu_0}{2}\left(\frac{\kappa e \hbar}{m}\right)^2 \tag{6.25}$$

---

[2]We call the solution $|\psi_\infty|$ as it is valid deep into the SC.

In the BCS theory, the coherence length is connected to the superconducting gap Δ and the Fermi velocity v_F with

$$\xi = \frac{\hbar v_F}{\pi \Delta} \quad . \tag{6.26}$$
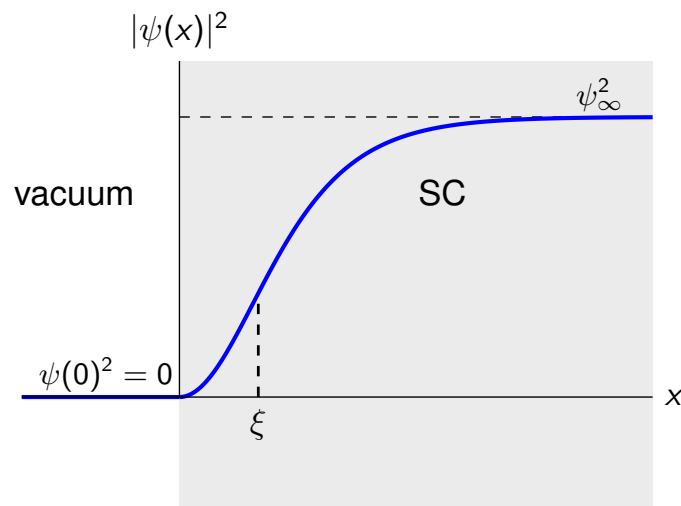
Figure 6.8.: *Evolution of the superconducting order parameter near the interface with vacuum.*

6.3. Two types of superconductor

We have seen that at the interface superconductor/vacuum, the magnetic field decays and the SC order parameter increases over different distances λ and ξ, respectively. We see now that the value of the ratio between these two distances will have an important impact on the type of superconductivity.

But first we have to define the condensation energy of a superconductor.

6.3.1. Condensation energy and energy balance

The condensation energy is the energy gained by the system being in the SC state. To obtain this energy, we consider that the SC state is actually destroyed for an applied field $H \geq H_c$ where H_c is the critical field of the superconductor. So superconductivity is destroyed and the normal state is restored when one has provided the magnetic energy $\mu_0 H_c^2 / 2$. Hence, we can write

$$f_{\text{condens.}} = f_n - f_s = \frac{\mu_0 H_c^2}{2} \ .\tag{6.27}$$

Now assume two superconductors, one characterized with $\xi \gg \lambda$ and the other with $\lambda \gg \xi$. Assume that both superconductor are seeing a field H_c and that they just remain in the SC state before turning normal. We will have the following situations at the interface superconductor/vacuum:

1. For the SC with $\xi \gg \lambda$, the energy penalty for excluding the field will grow quickly (short λ), whereas the energy gain for being in the SC state will grow (negatively) slowly (long ξ). Therefore, near the interface we will have a net energy penalty (see Fig. 6.9, left column).

2. For the SC with $\lambda \gg \xi$ the energy penalty for excluding the field will grow slowly (long λ), whereas the energy gain for being in the SC state will grow (negatively) quickly (short ξ). Therefore, near the interface we will have a net energy gain (see Fig. 6.9, right column).
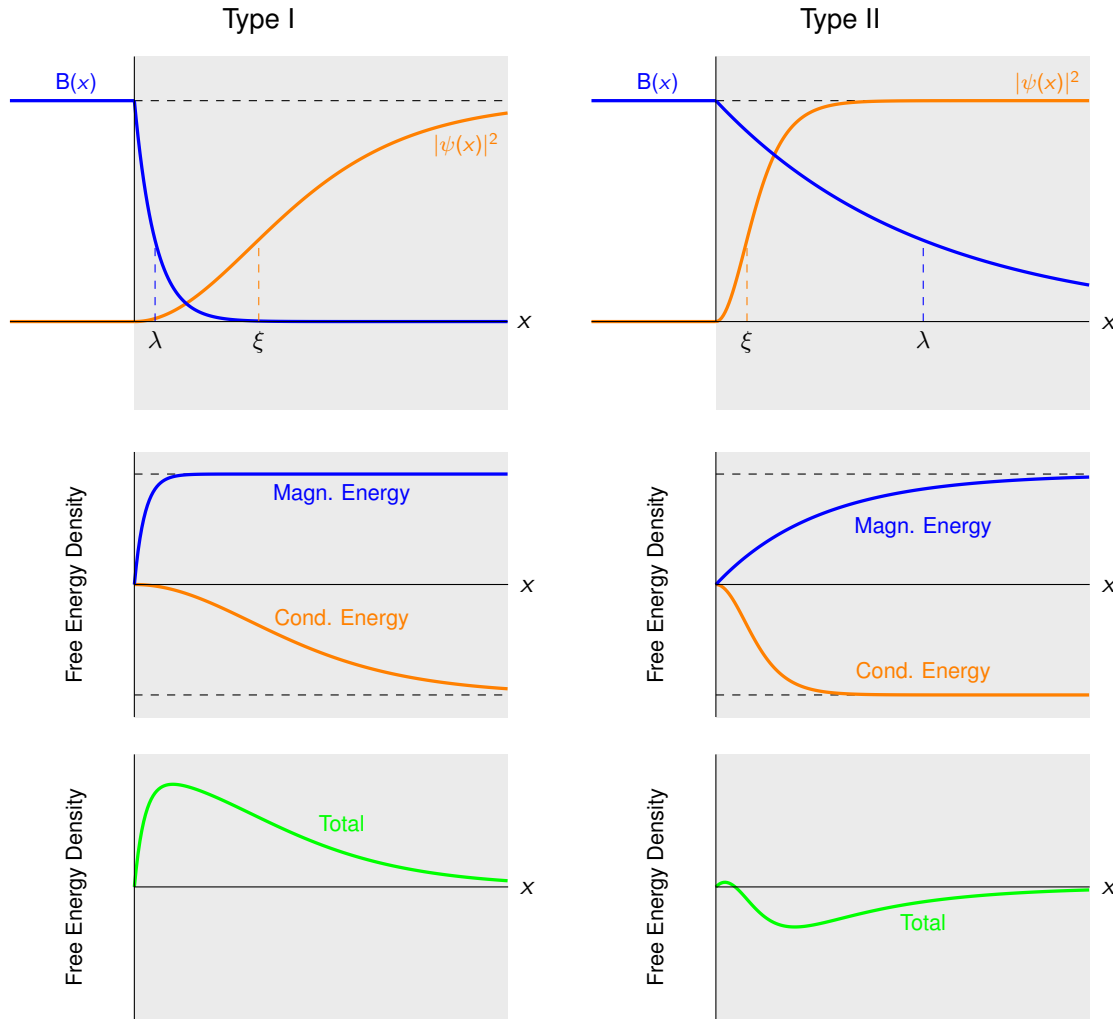
Figure 6.9.: *Left: Situation for $\xi \gg \lambda$. Right: Situation for $\lambda \gg \xi$. For some values of field, a type II superconductor (right column) will actually gain energy by creating interfaces.*

6.3.2. Type I and type II superconductors

The situation described above clearly differentiate between two types of superconductors. For the superconductors where $\xi \gg \lambda$ (type I superconductors), superconductivity is abruptly destroyed when the applied field is above H_c, as it would cost energy to maintain the SC state. In superconductors where $\lambda \gg \xi$ (type II superconductors), a subdivision of the superconductor into an alternating sequence of thin normal and superconducting slices is energetically favorable. Actually, for a type II superconductor above a critical value H_{c1} a mixed state occurs (also known as the vortex state, or Abrikosov state or Shubnikov state) in which an increasing amount of magnetic flux penetrates the material. At a second critical field H_{c2}, superconductivity is destroyed. Note that between H_{c1} and H_{c2}, the system preserves a zero electrical resistivity. Type II superconductors play a fundamental technological role as the value of H_{c2} is much higher than the one of H_{c1} for a type I superconductor. A more stringent

criteria to define to which type a superconductor belongs is given by the Ginzburg-Landau theory. Here one introduces the Ginzburg-Landau parameter

$$\kappa = \frac{\lambda}{\xi} \ .$$ (6.28)

The criterion for type I or II superconductivity is found to be

$$\text{type I}: \quad \kappa < \frac{1}{\sqrt{2}}$$

$$\text{type II}: \quad \kappa > \frac{1}{\sqrt{2}}$$

Table 6.1.: *Typical superconductors.*

Materials	ξ (nm)	λ (nm)	T_c (K)	H_{c2} (T)
Type I				
Al	1600	16	1.2	0.01
Pb	83	37	7.2	0.08
Sn	230	34	3.7	0.03
Type II				
Nb	38	39	9.3	0.4
Nb$_3$Sn	3	80	18	25
YBCO	1.5	150	92	150
MgB$_2$	5	185	37	14
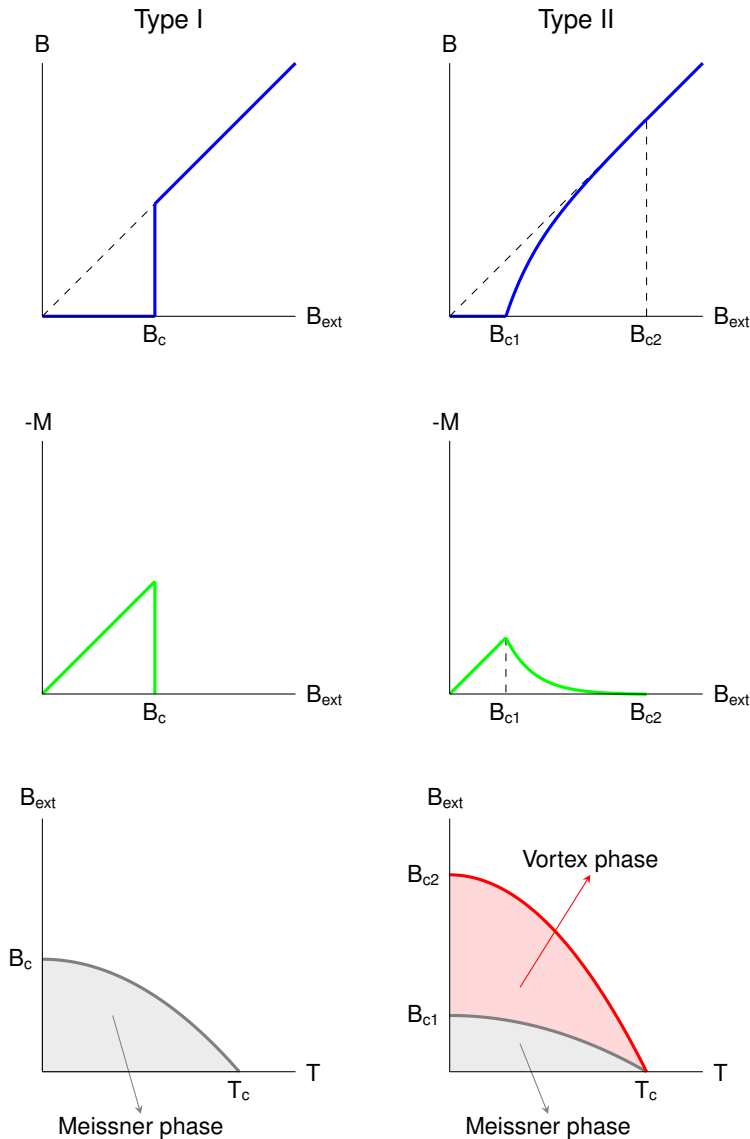
Figure 6.10.: *Comparison between type I (left column) and type II (right column) superconductors. For a type II superconductor, for an applied field above H_{c1} the field begins to penetrate the sample in form of vortices, as the interface energy is favorable (see Fig. 6.9). The internal field B is no more equal to zero. For the type II superconductors, above H_{c2} the superconducting state is destroyed. In the Meissner state of both kind of superconductors, the field is expelled from a superconductor at the exception of a fine layer determined by the penetration depth.*
The field H_c for a type II superconductor, correspond to the field for which the area between H_{c1} and H_c admitting still $M = -H$ is equal to the one between H_{c1} and H_{c2} for the real M curve.

Actually almost all the elements which are superconductors are of type I. Niobium is a type II conductor but close to the border to type I. The coherence length ξ is related to the mean free path ℓ of the conduction electrons in the normal state of the metal, which is usually large

for very pure elemental crystals but normally strongly reduced in alloys. Alloys are almost exclusively of the type II.

6.4. Abrikosov state of a type II superconductor

In reality a type II superconductor is not subdivided into thin slices but the field penetrates the sample in the form of flux tubes (vortices) which arrange themselves usually in a triangular pattern forming a so-called "Flux Line Lattice" (FLL).[3]
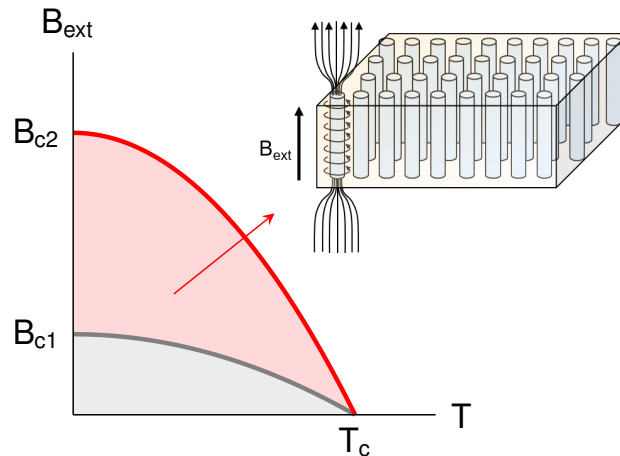
Figure 6.11.: *For a type II superconductor, between H_{c1} and H_{c2}, the field penetrate in the form of vortices forming (in the ideal case) a regular lattice.*
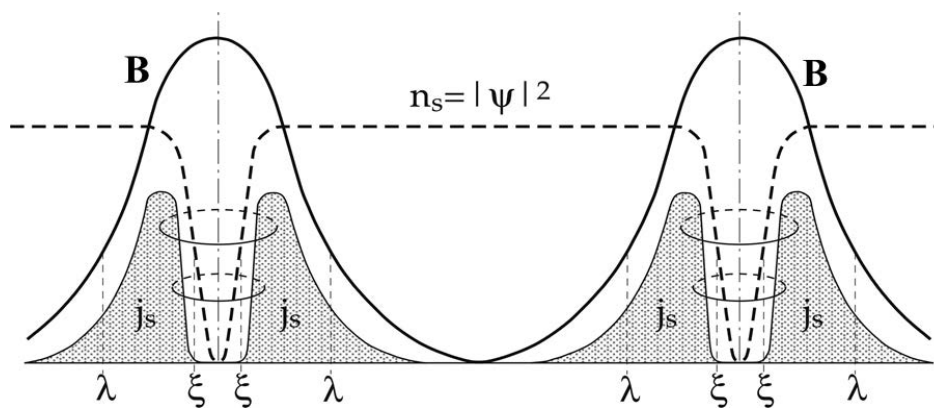
Figure 6.12.: *Evolution of the field and superconducting order parameter between vortices. Around a vortex, superconducting currents $\mathbf{j}_s$ will flow in order to screen the field (analog to the situation of the Meissner state at the interface SC/vacuum). The distance between the vortices is governed by the value of the applied field.*

---

[3]Note that the energy configuration between triangular and quadratic lattice is very small and subtle effects can favorize configurations other than triangular.

The core of a flux tube is normal and the magnetic flux is quantified and equal to

$$\Phi_0 = \frac{h}{2e} = 2.067 \times 10^{-15} \text{ Wb} \ .$$ (6.29)

The vortex diameter correspond to $2 \times \xi$ and outside the vortex, the field decrease will be directly related to the penetration depth.

6.4.1. Field in the Abrikosov state

As seen in Section 4.2, the μSR signal will reflect the internal field distribution when measuring with an applied internal field (see Equation 4.28). Therefore, one can expect that the μSR signal recorded in the superconductor for a field between H_{c1} and H_{c2} will provide information on the characteristic lengths of a superconductor, *i.e.* λ and ξ.
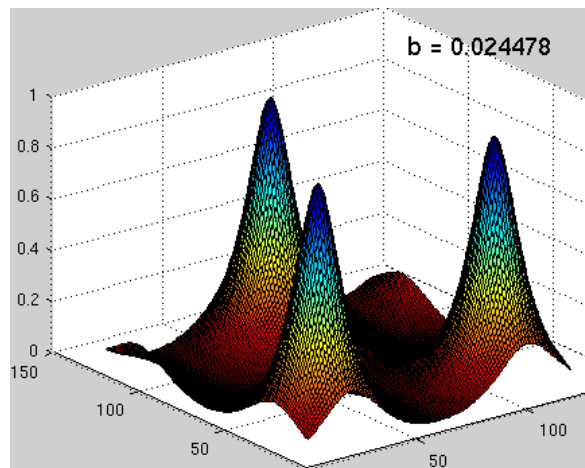
Figure 6.13.: *Field inside a type II superconductor for an applied field corresponding to about 2.5% of the upper critical field H_{c2}. The field maxima are of course located at the vortices positions.*

What is important to recognize is that the position of the vortices is not related to the underlaying crystallographic structure and that the spacing between the vortices is just given by the value of the applied field (see below Eq 6.34). Therefore, the muon, which are stopping at a well defined crystallographic site, will sample randomly the field distribution created by the FLL.

Qualitatively, we expect to see the following picture when applying a field above H_{c1} to a superconductor:
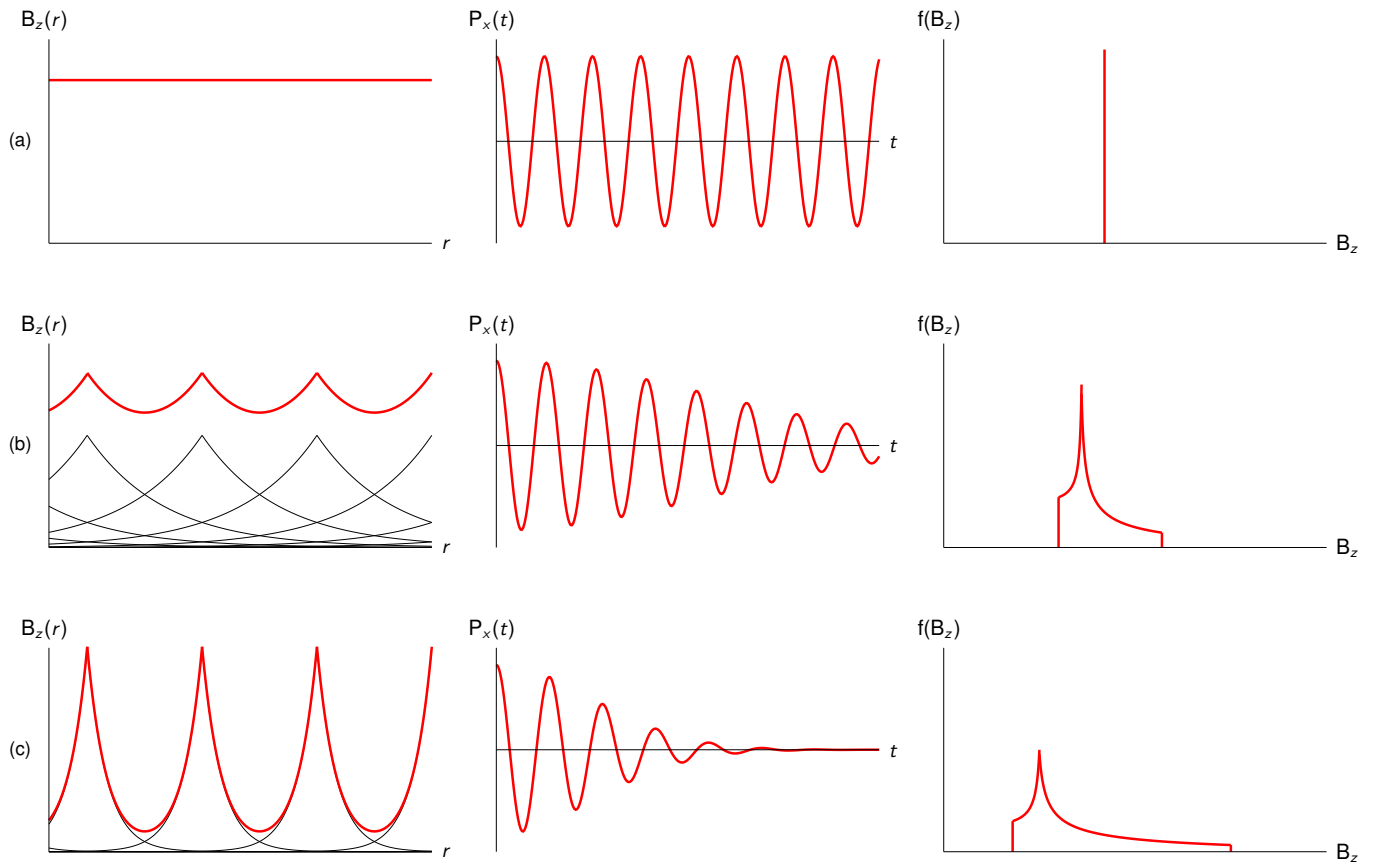
Figure 6.14.: *First row (a): In the normal state the field distribution will be extremely narrow and the μSR signal [here marked as $G(t)$] will basically not decay. Middle row (b): just below T_c, the penetration depth is long (as the superfluid density is small). The maxima of $B(r)$ are located at the vortices. The μSR signal begins to show a depolarization. Lower row (c): For $T \ll T_c$, the penetration depth is short (high superfluid density) create a rapid depolarization of the μSR signal.*

Figure 6.15.: *Example of a spatial distribution of the magnetic field $B_z(r)$ and the corresponding local magnetic field distribution $f(B)$ for an ideal hexagonal FLL determined by the numerical Ginzburg-Landau method. The parameters used for the calculations are $\lambda = 50$ nm, $\xi = 20$ nm, and $\langle B \rangle = 0.3 \times \mu_0 H_{c2} \simeq 246.8$ mT, and intervortex distance $d = 69.5$ nm. Adapted from Ref. [76].*

The ideal FLL has three characteristic fields: (i) the maximal field B_{max} corresponds to the field in the vortex core, (ii) the field at the peak of $f(B)$ is the saddle point field B_{sad} (located in the middle between neighboring vortices), and (iii) the minimal field B_{min} is in the center of the triangle of vortices forming the hexagonal FLL.

6.4.1.1. Field due to one vortex

Let first calculate the field around a single vortex.
Taking into account the presence of one vortex, the second London equation becomes:

$$\mu_0 \lambda^2 \, \nabla \times \mathbf{j} + \mathbf{B} = \hat{\mathbf{z}} \, \Phi_0 \, \delta(x) \ . \tag{6.30}$$

and Eq. 6.11 is now given by

$$\mathbf{B} - \lambda^2 \, \Delta \mathbf{B} = \hat{\mathbf{z}} \, \Phi_0 \, \delta(x) \ \ . \tag{6.31}$$

The exact solution of the Eq. 6.31 is:

$$B_v(r) = \frac{\Phi_0}{2\pi\lambda^2} K_0\!\left(\frac{r}{\lambda}\right) \tag{6.32}$$

Here, K_0 is the modified Bessel-function of the second kind (0-th order). This solution is valid assuming that the coherence length (radius of the vortex) ξ is basically zero.[4]

The Equation 6.32 can be approximated for different limits:

$$B_v(r) \sim \ln\left(\frac{\lambda}{r}\right) + 0.12 \qquad\qquad \xi \ll r \ll \lambda$$

$$B_v(r) \sim \sqrt{\frac{\pi\lambda}{2r}} e^{-\frac{r}{\lambda}} \qquad\qquad r \gg \lambda \qquad\qquad (6.33)$$

6.4.1.2. Field distribution of an extreme type II superconductor

We assume here that the Ginzburg-Landau parameter $\kappa \gg 1$, *i.e.* we neglect the vortex core. The London model is valid (up to $\sim B_{c2}/4$). The vortex cores are separated and non-interacting and then we have a linear superposition of the vortex fields
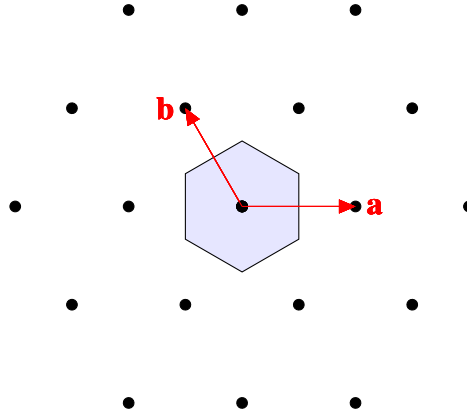
The vortex lattice is hexagonal and specified by the vectors **a** and **b**. As seen, each vortex carries a flux Φ_0. The blue area S has the value

$$S = d^2 \frac{\sqrt{3}}{2} \ ,$$

where d is the spacing between the vortices, and the flux of one vortex is

$$\Phi_0 = S \cdot \langle B_z \rangle$$

and therefore

$$d = \sqrt{\frac{2\Phi_0}{\langle B_z \rangle \sqrt{3}}} \ . \qquad\qquad (6.34)$$

The special field distribution $\mathbf{B}(\mathbf{r})$ must fulfill the modified London equation

$$\mathbf{B}(\mathbf{r}) - \lambda^2 \Delta\mathbf{B}(\mathbf{r}) = \phi_0 \sum_n \delta(\mathbf{r} - \mathbf{r}_n)\hat{z} \qquad\qquad (6.35)$$

---

[4]The solution diverges for $r \to 0$, but this is an unphysical solution as ξ is always finite.

We expect a periodic magnetic field and therefore we can work in the **k** space (Fourier space).

We have the reciprocal vectors

$$\mathbf{a}^* = 2\pi \frac{\mathbf{b} \times \mathbf{c}}{\mathbf{a} \cdot (\mathbf{b} \times \mathbf{c})}$$

$$|\mathbf{a}^*| = |\mathbf{b}^*| = \frac{4\pi}{\sqrt{3}} \frac{1}{d}$$

and a point of the reciprocal space is defined by

$$\mathbf{k}_{m,n} = m \cdot \mathbf{a}^* + n \cdot \mathbf{b}^*$$
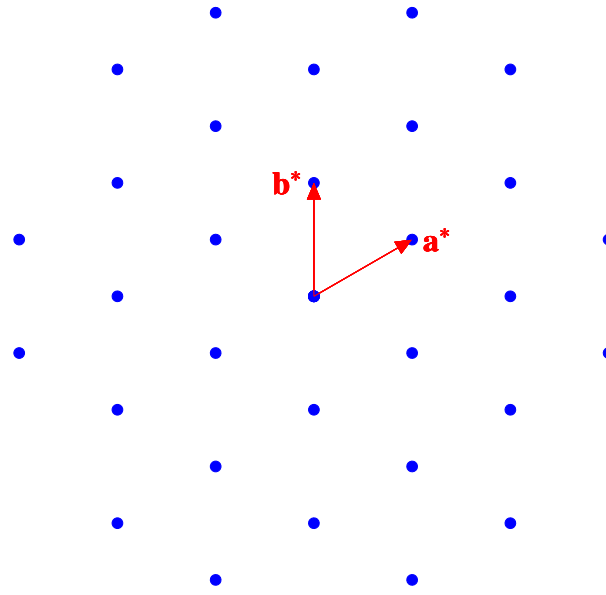
We can write

$$\mathbf{B}(\mathbf{r}) = \sum_{\mathbf{K}} \mathbf{b_k} \exp(i\mathbf{k}\mathbf{r}) \tag{6.36}$$

with Fourier components

$$\mathbf{b_k} = \frac{1}{S} \int \mathbf{B}(\mathbf{r}) \exp(-i\mathbf{k}\mathbf{r}) d^2\mathbf{r} \tag{6.37}$$

The modified London equation becomes (field only along $\hat{z}$):

$$\sum_{\mathbf{k}} (\mathbf{b_k} + \lambda^2 k^2 \mathbf{b_k}) \exp(i\mathbf{k}\mathbf{r}) = \hat{\mathbf{z}} \, N\Phi_0 \sum_{\mathbf{k}} \exp(i\mathbf{k}\mathbf{r}) \tag{6.38}$$

where $N = 1/S$ is the vortex density.

One finds:

$$\mathbf{b_k} = \frac{\langle B_z \rangle}{1 + \lambda^2 k^2} \hat{\mathbf{z}} \tag{6.39}$$

and therefore

$$B_z(\mathbf{r}) = \sum_{\mathbf{k}} \frac{\langle B_z \rangle}{1 + \lambda^2 k^2} \exp(i\mathbf{k}\mathbf{r}) \tag{6.40}$$

With $b_{\mathbf{k}=0} = \langle B_z \rangle$, the second moment $\langle \Delta B_z^2 \rangle = \langle B_z^2 \rangle - \langle B_z \rangle^2$ of the field distribution is given by (see Parseval theorem):

$$\langle \Delta B_z^2 \rangle = \sum_{\mathbf{k} \neq 0} |\mathbf{b_k}|^2 \tag{6.41}$$

Taking into account the perfect triangular lattice where:

$$k^2 = k_{m,n}^2 = \frac{16\pi^2}{3d^2}(m^2 - mn + n^2) \text{ and that } k^2\lambda^2 \gg 1 \tag{6.42}$$

we write

$$\langle \Delta B_z^2 \rangle = \frac{3\Phi_0^2}{64\pi^4\lambda^4} \sum_{\mathbf{k} \neq 0} \frac{1}{(m^2 - mn + n^2)^2} \tag{6.43}$$

and finally

$$\boxed{\langle \Delta B_z^2 \rangle = 0.00371 \frac{\Phi_0^2}{\lambda^4}} \ . \tag{6.44}$$

The quantity $\langle \Delta B^2 \rangle$ is directly related to the magnetic penetration depth λ.

The most important point here is that if we can measure the second moment of the field distribution, we can determine the London penetration depth.

Note that Eq. 6.44 predicts a field width independent of the external field. This arise from the the assumption that $k^2\lambda^2 \gg 1$ that is that the unity in the denominator of Eq. 6.40 may be discarded and thus $\langle B_z \rangle$ drops out [remember that $k \propto 1/d \propto \sqrt{\langle B_z \rangle}$].

It holds also [5]:

$$B_{\text{min}} - \langle B \rangle \propto \frac{1}{\lambda^2}$$

$$B_{\text{max}} - \langle B \rangle \propto \frac{1}{\lambda^2}$$

$$B_{\text{saddle}} - \langle B \rangle \propto \frac{1}{\lambda^2} \tag{6.47}$$

---

[5] About the demagnetization in the vortex state. The quantities H, magnetization M, demagnetization factor N ($0 \leq N \leq 1$) and mean magnetic flux $\langle \Delta B \rangle$ (*i.e.* the observed mean internal field) are related to each other by:

$$H = \frac{\langle \Delta B \rangle}{\mu_0} - M = H_{\text{ext}} - NM \ . \tag{6.45}$$

Since the μ^+ Knight shift in high-T_c materials is negligible, the muon spin precession shift is given by:

$$\langle \Delta B \rangle - \mu_0 H_{\text{ext}} = (1 - N)\mu_0 M \quad (M < 0) \ . \tag{6.46}$$
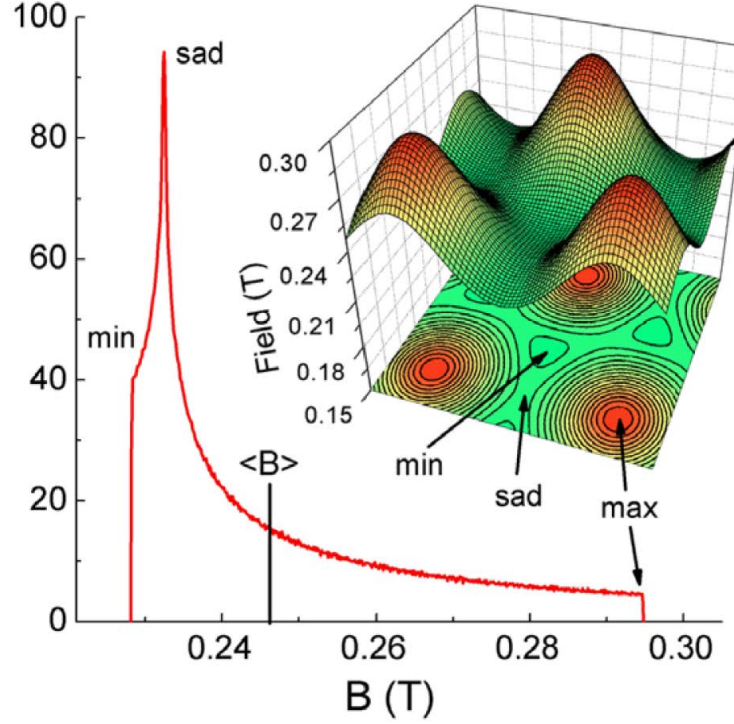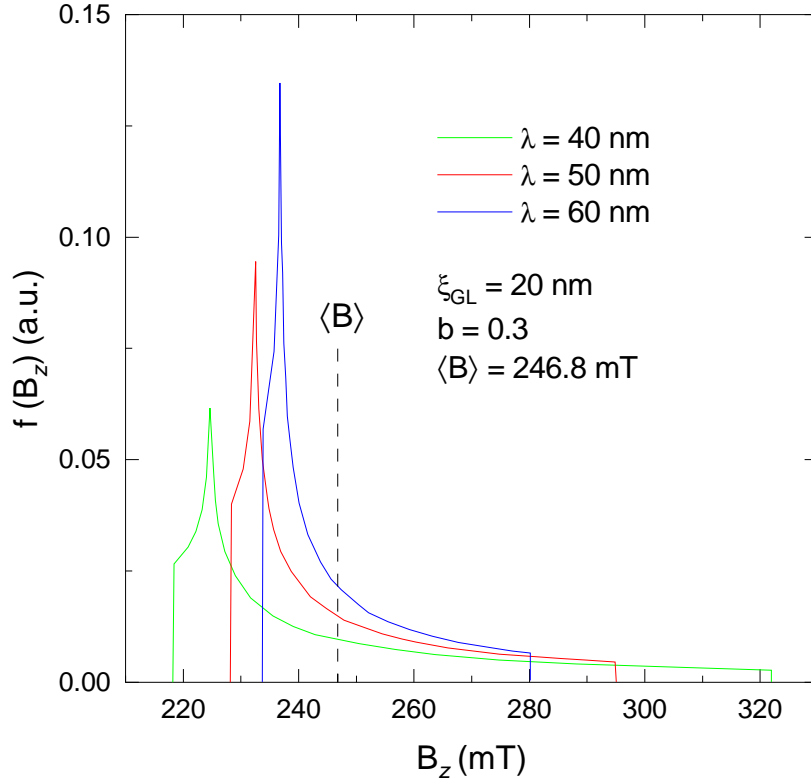
Figure 6.16.: *Example of a spatial distribution of the magnetic field $B_z(r)$ and the corresponding local magnetic field distribution $f(B)$ for an ideal hexagonal FLL determined by the numerical Ginzburg-Landau method. The parameters used are the same as in Fig. 6.15, but with different values of the penetration depth.*
Adapted from Maisuradze et al. [76].

The above relation between the second moment $\langle \Delta B_z^2 \rangle$ and penetration depth holds when $H_{\text{ext}} \ll H_{c2}$ and in such a case the second moment is constant.

6.4.1.3. Corrections due to the coherence length and the magnetic field

In the above calculation of the second moment of the field distribution, we have neglected the size of the magnetic vortices (*i.e.* we have assumed $\xi = 0$). This is valid for strongly type II superconductors, that is for very high values of κ. As the coherence length is connected to the value of the second critical field H_{c2} by[6]

$$\mu_0 H_{c2} = \frac{\Phi_0}{2\pi\xi^2} \ , \tag{6.48}$$

when one neglects ξ one assumes $H_{c2} \rightarrow \infty$ and therefore an applied field H_{ext} always smaller than H_{c2}. This is equivalent of writing Eq. 6.43, where we have removed the field dependence of the second moment of the field distribution.

---

[6]Obtained from the Ginzburg-Landau theory.

B(r)   **FFT**

$2\xi_1$

$2\xi_2$
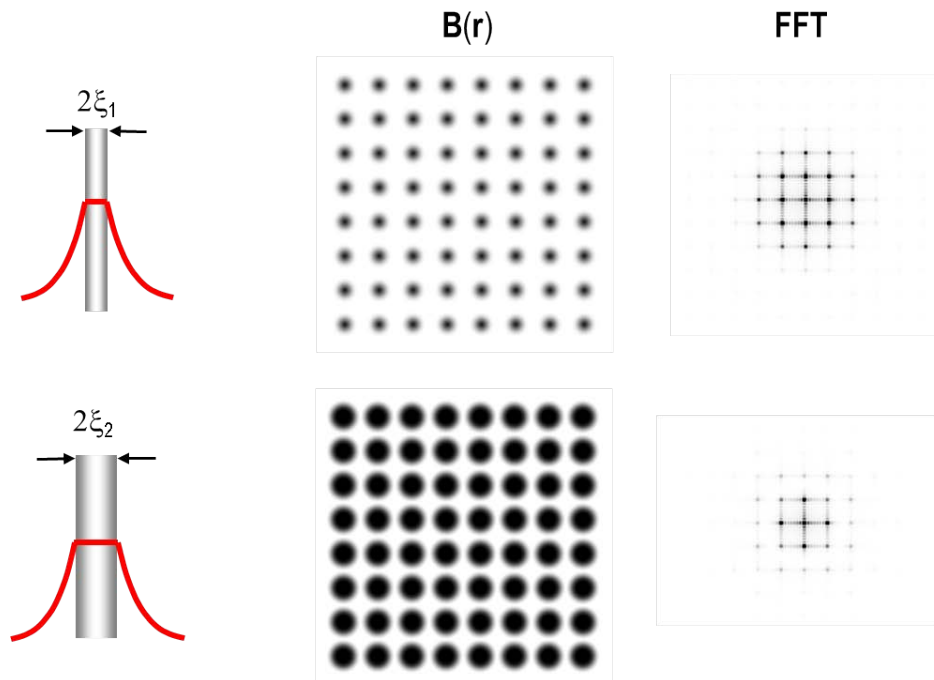
Figure 6.17.: *Effect of the coherence length with a fixed value of the external field and of the penetration depth. Example of simple Fourier Transforms for two cases where the penetration depth λ and the applied field are the same, but where the coherence length are different. Note that the squared geometry is taken as a simplification. The upper row exhibits a situation with a short ξ (radius of the vortices), whereas the lower row is a situation with a longer ξ. Note the FFT picture, where the intensities of the $\mathbf{b_k}$ components with $\mathbf{k} \gg 1$ are decreased.*
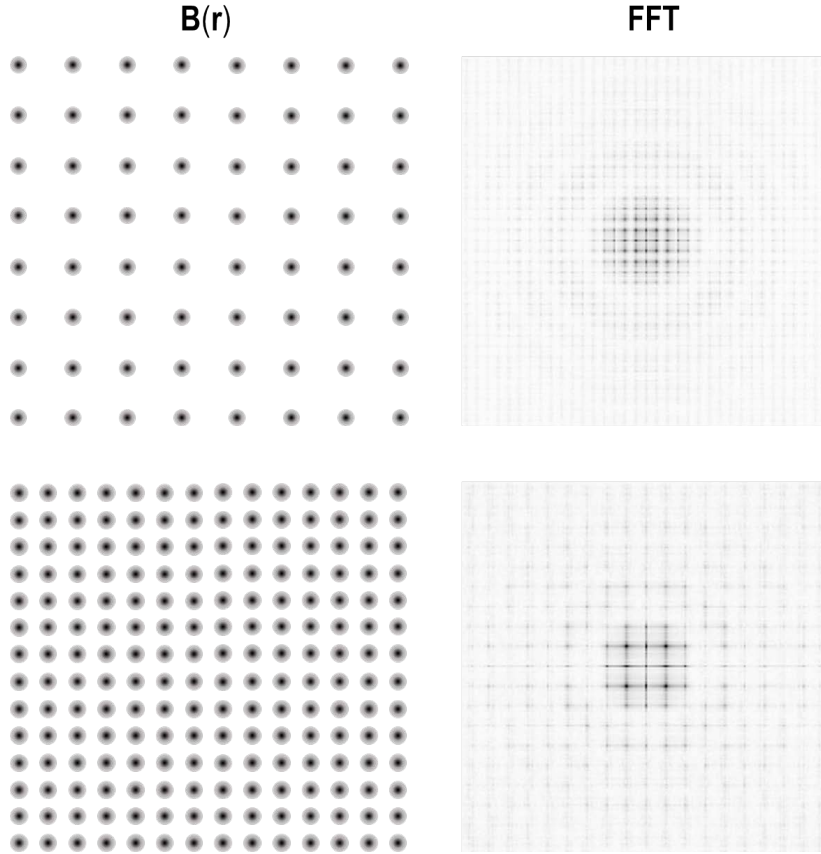
Figure 6.18.: *Effect of the magnitude of the external field with a fixed value of the coherence length (vortex radius) and of the penetration depth. Remember (Eq 6.34) that the spacing between vortices reflects the strength of the applied field (smaller spacing → stronger field) and that in the reciprocal space (Eq 6.42) the spacing will increase for increasing fields. Example of simple Fourier Transforms for two cases representing low fields (upper row) and high fields (lower row). Note that the squared geometry is taken as a simplification. Note the FFT picture, where the intensities of the $\mathbf{b_k}$ components with $\mathbf{k} \gg 1$ are decreased more strongly for high fields.*

If the value of the coherence length is no more negligible, then corrections are needed. Different models have dealt with this situation:

- The first model is the so-called London model with Gaussian cut-off where the Fourier components are decreased for large $\mathbf{k}$ [77].

$$\mathbf{b_k} = \frac{\langle B_z \rangle}{1 + k^2 \lambda^2} \hat{\mathbf{z}} \quad \Rightarrow \quad \mathbf{b_k} = \frac{\langle B_z \rangle \, e^{-k^2 \xi^2 / 2}}{1 + k^2 \lambda^2} \, \hat{\mathbf{z}} \qquad (6.49)$$

- The so-called "Modified London Model" [78] where an additional term is introduced in the cut-off

$$\mathbf{b_k} = \frac{\langle B_z \rangle}{1 + k^2 \lambda^2} \hat{\mathbf{z}} \quad \Rightarrow \quad \mathbf{b_k} = \frac{\langle B_z \rangle \, e^{-k^2 \xi^2 / [2(1-b)]}}{1 + k^2 \lambda^2 / (1 - b)} \, \hat{\mathbf{z}} \; , \qquad (6.50)$$

where $b = H_{\text{ext}}/H_{c2}$.

- The so-called "Analytical Ginzburg-Landau Model" (see Ref. [79] for details).

When $B_{\text{ext}} \ll B_{\text{c2}}$ does not hold anymore, then a field dependence (*i.e.* a decrease) of the second moment $\langle \Delta B^2 \rangle$ occurs.
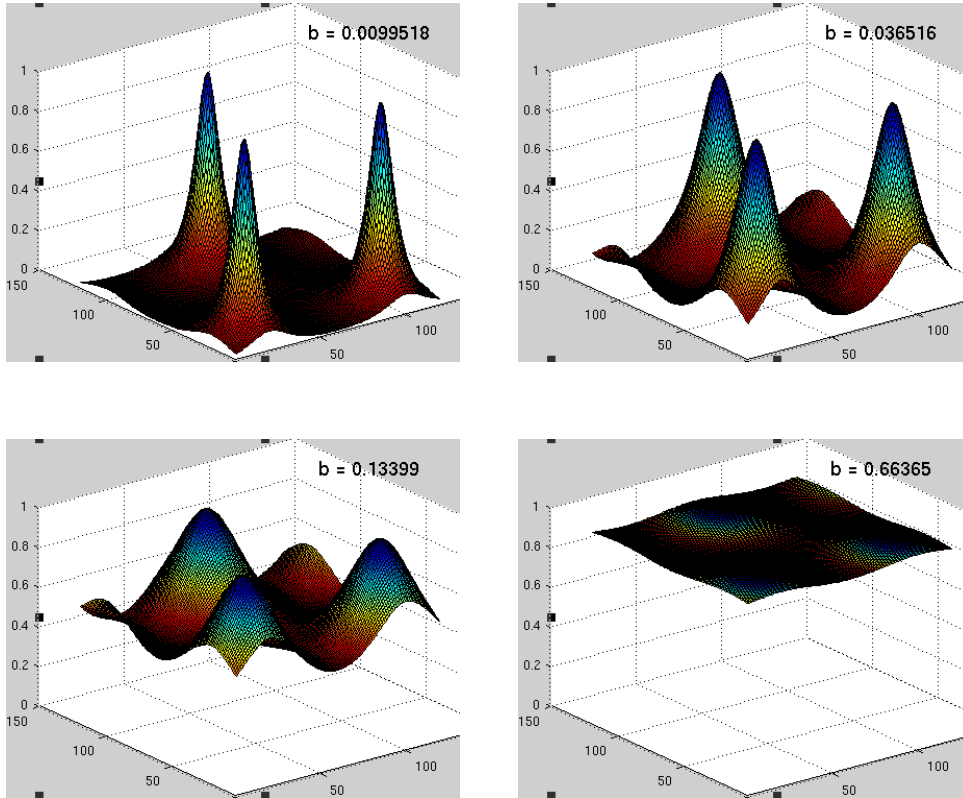
Figure 6.19.: *Numerical calculation of the field profile in the Abrikosov state of a type II superconductor. The parameter b represents the ratio H_{ext}/H_{c2}. The parameters used for the calculations are $\lambda = 50$ nm, $\xi = 20$ nm. Note that the distance between the vortices is dependent of the applied field (see Eq.6.34). On the figures, the distance between the vortices is normalized.*

A good analytical approximation of the field dependence is furnished by the model of Brandt [80] which allows one to calculate the second moment of the field distribution.

$$\langle \Delta B_z^2 \rangle = 7.523 \cdot 10^{-4} \left(1 - \frac{H_{\text{ext}}}{H_{\text{c2}}}\right)^2 \left[1 + 1.21\left(1 - \sqrt{\frac{H_{\text{ext}}}{H_{\text{c2}}}}\right)^3\right]^2 \frac{\Phi_0^2}{\lambda^4} \qquad (6.51)$$

In the case of low external magnetic field compared to upper critical field, that is when $H_{\text{ext}}/H_{c2} \to 0$, then Eq. 6.51 converges to Eq. 6.44.

Hence, if the field dependence of the second moment is obtained, the parameters λ and ξ (through H_{c2}, see Eq. 6.48) can be determined.
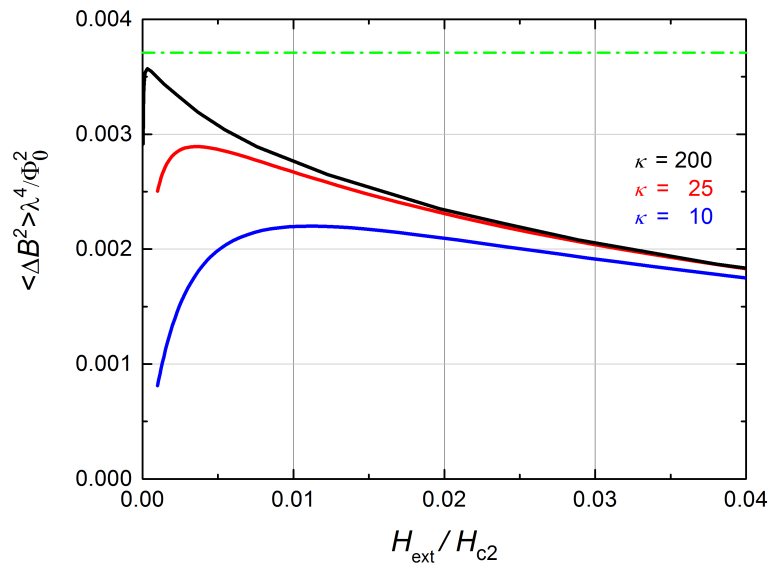
Figure 6.20.: *Effect of the magnitude of the external field on the value of the second moment of the FLL field distribution. The green line represents the ideal case where $H_{c2} \to \infty$.*

6.5. Obtaining the characteristic lengths from μSR

The muon-spin rotation technique is one of the most powerful and unique tools for studying the internal magnetic field distribution $f(B)$ associated with the FLL in type-II superconductors. From TF μSR experiments, $f(B)$ profiles can be directly obtained by performing a Fourier transformation of the μSR signal in the time domain.

The problem is to extract the values of λ and ξ from these profiles.

6.5.1. Obtaining the penetration depth

Generally, the magnetic field penetration depth λ is determined from the second moment $\langle \Delta B_z^2 \rangle$ of the internal field distribution $f(B)$. As discussed, for an isotropic extreme type-II superconductor where $(\lambda \gg \xi)$ one can use Eq. 6.44. Traditionally, many studies reported in the literature, just assume that the second moment given by Eq. 6.44 is actually produced by a Gaussian field distribution due to the FLL. This is of course incorrect for perfect crystals (the actual field distribution is the one shown on Fig 6.15). However, in a real material, there are perturbations of the periodic vortex lattice caused by random pinning of the vortices and fluctuations in temperature or applied magnetic field, which lead to an almost Gaussian field distribution.
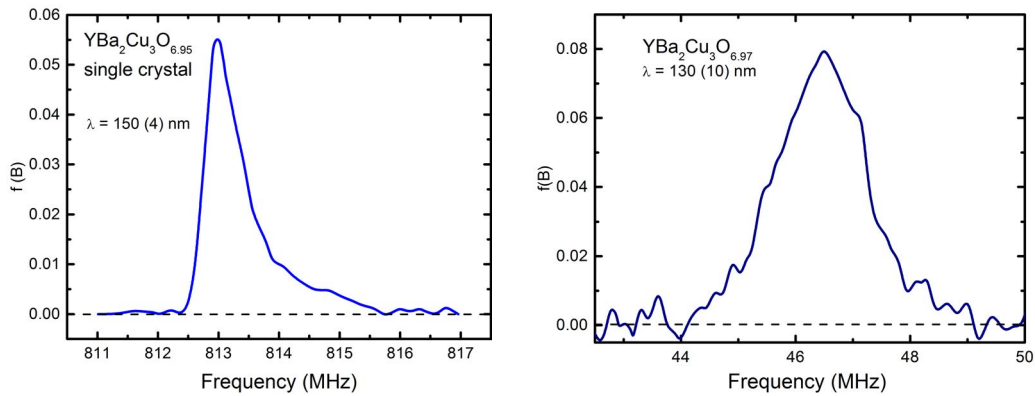
Figure 6.21.: *Comparison of $f(B)$ for a single crystal of YBCO [81] and in a polycrystalline sample [82].*

By using what we have seen in Section 4.2 (see Eq. 4.32), we see that if we assumed a Gaussian field distribution, then a measure of the μSR TF depolarization rate in the superconducting state σ_{sc} is a direct determination of the second moment $\langle \Delta B_z^2 \rangle$, with the relation

$$\sigma_{\text{sc}}^2 = \gamma_\mu^2 \langle \Delta B_z^2 \rangle = \gamma_\mu^2 (\langle B_z^2 \rangle - \langle B_z \rangle^2) \tag{6.52}$$

Assuming Eq. 6.44 and Eq. 6.52, there is a simple numerical relationship between the muon

depolarisation rate σ and the superconducting penetration depth λ namely

$$\lambda = \frac{327.5}{\sqrt{\sigma_{\mathrm{sc}}}} \quad , \tag{6.53}$$

where σ_{sc} is in $\mu\mathrm{s}^{-1}$ and λ in nm.

To determine the magnetic penetration depth the magnetic field is applied above T_c. Then the temperature is gradually lowered below T_c (field cooling). This way one obtains a regular flux line lattice below T_c ($H_{c1} < H_{\mathrm{ext}} < H_{c2}$). Above T_c, the depolarization of the μSR signal will reflect the narrow field distribution created by the nuclear moments (leading to a weak depolarization) and below T_c, the broad field distribution created by the FLL will depolarize the muon ensemble rapidly.

The total depolarization rate obtained below T_c contains a part due to the field distribution created by the FLL (σ_{sc}) but also the weak broadening due to the nuclear moments (say σ_{n}) which is also present above T_c. As this later contribution is temperature independent, the temperature dependence of σ_{sc} is obtained with

$$\sigma_{\mathrm{sc}}(T) = \sqrt{\sigma(T)^2 - \sigma_n^2} \quad , \tag{6.54}$$

where σ_n is determined above T_c and assumed temperature independent for lower temperatures.
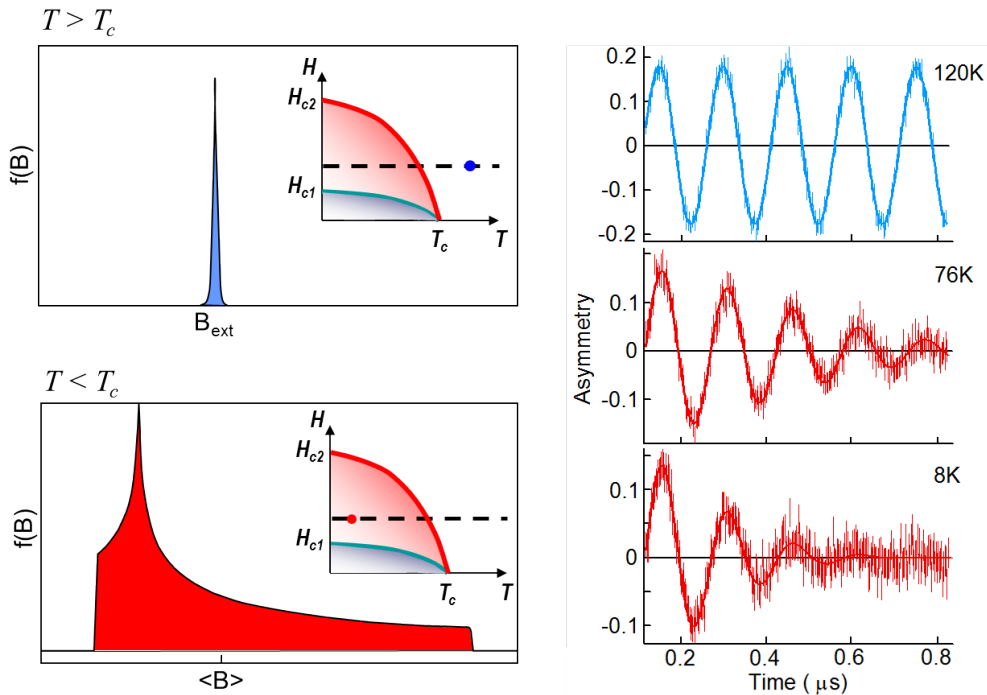
Figure 6.22.: *Schematics of the effect of the FLL field distribution on the μSR signal. The situation above T_c shows a very weak depolarization (only due to the nuclear moments, blue curve). Below T_c a stronger depolarization reflects the broad field distribution from the FLL. Data taken on a YBCO sample (see Ref. [82]).*
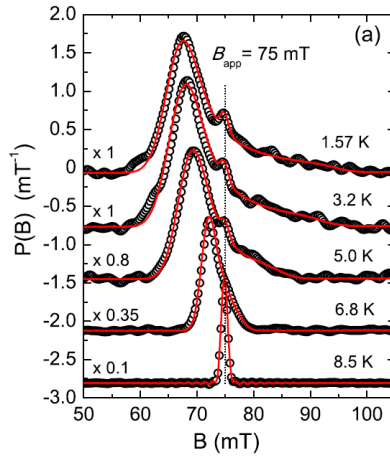
Figure 6.23.: *Temperature dependence of the measured field distribution obtained by Fourier transforming the µSR signal. Note the very sharp signal for $T > T_c$. The measurements were performed in the $LaPt_4Ge_{12}$ system (see Ref. [83]). Upon cooling the field distribution becomes broader, reflecting the decrease of the penetration depth (see Fig. 6.7).*
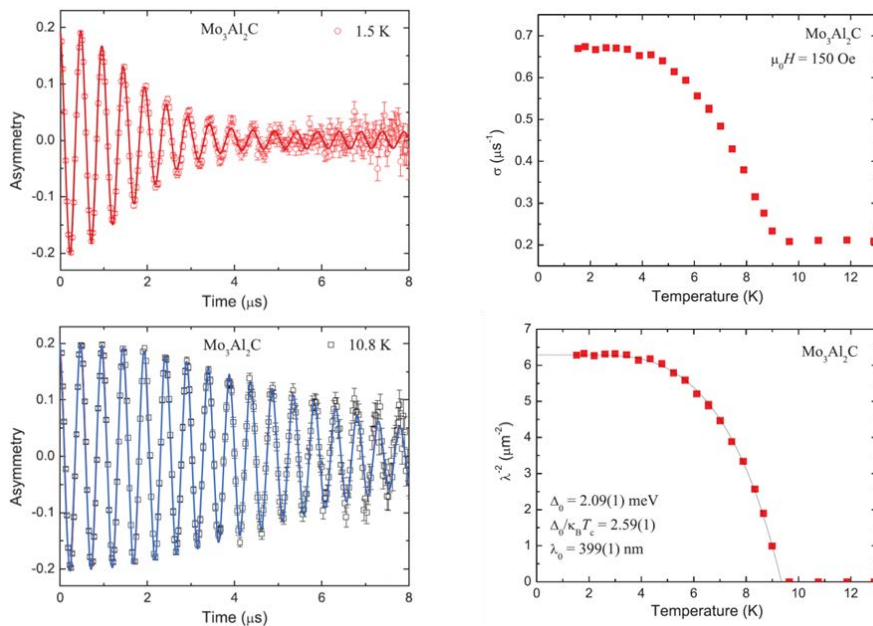
Figure 6.24.: *Example of penetration depth determination by µSR in the compound Mo_3Al_2C. Mo_3Al_2C is a nonmagnetic compound whose superconductivity was discovered in the 1960's. Because of its lack of inversion symmetry, this compound has regained interest and its superconducting properties have recently been revisited. The two figures on left-hand side show the difference of the depolarazation above and below T_c. Note the non-negligible depolarization above T_c due to the nuclear moments. The additional depolarization below T_c arises from the FLL. On the right-hand side the raw temperature of the depolarization is shown, as well as the temperature dependence of $\lambda^{-2} \propto n_s$ obtained from the data using the Eqs. 6.54 and 6.52.*
Adapted from Ref. [84].

(a) *BaPt$_{4-x}$Au$_x$Ge$_{12}$ from Ref. [85]*

(b) *Ba$_{0.65}$Rb$_{0.35}$Fe$_2$As$_2$ from Ref. [86]*

(c) *Ca$_3$Ir$_4$Sn$_{13}$ from Ref. [87]*

(d) *Nb$_2$PdSn$_5$ from Ref. [88]*

(e) *FeS from Ref. [89]*

(f) *(La$_{0.84}$Fe$_{0.16}$)OHFe$_{0.98}$Se from Ref. [90]*
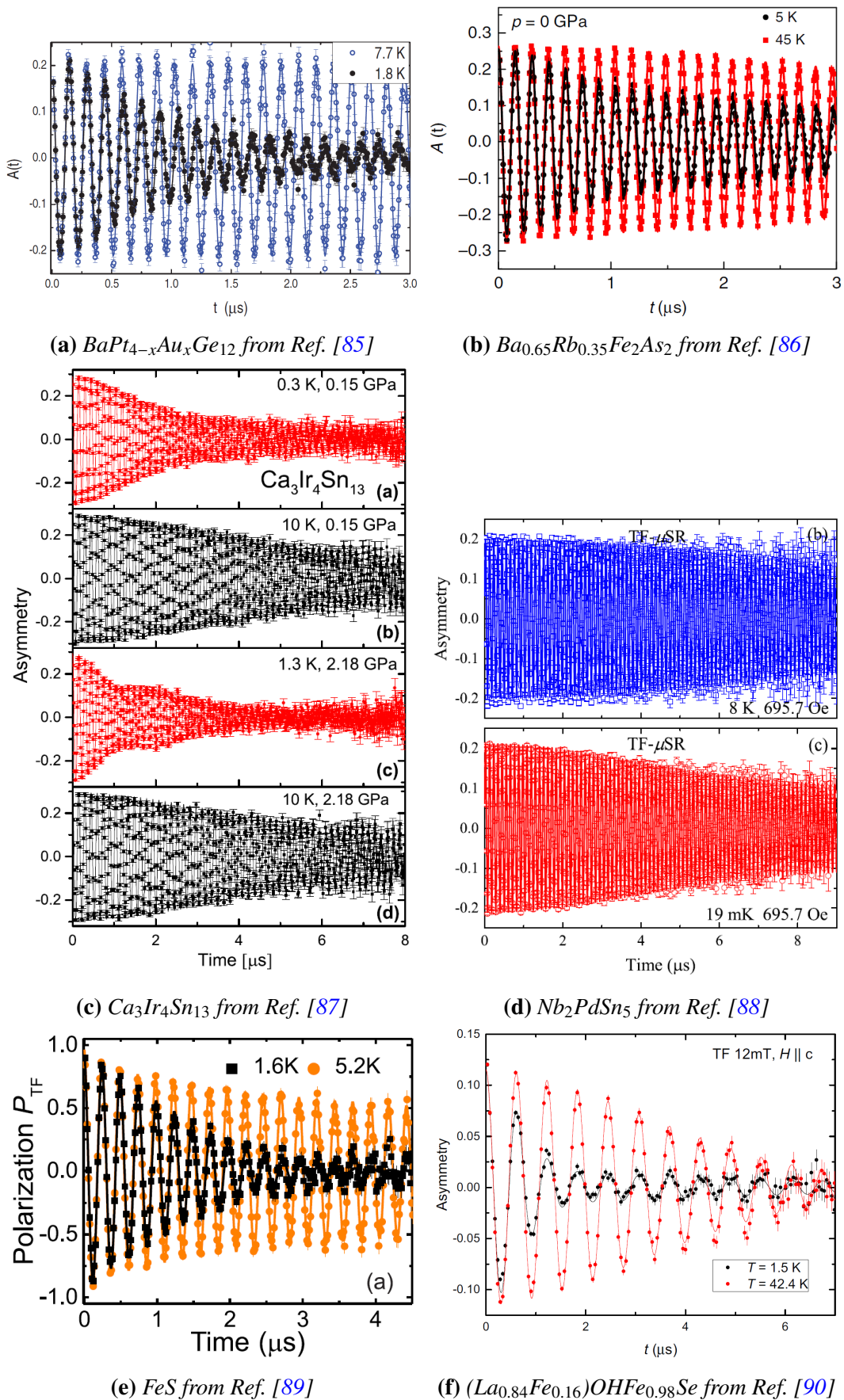
Figure 6.25.: *Examples of μSR signals measured above and below T$_c$.*

6.5.1.1. Multi-Gaussian approach

For very pure crystals, a simple Gaussian approach to model the FLL field distribution is far from an ideal situation to reproduce the long tail in the high-field region.
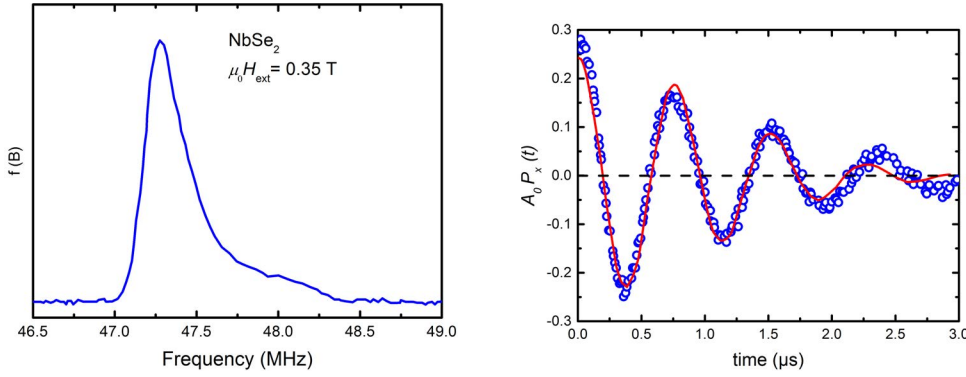
Figure 6.26.: *Left: field distribution of the FLL measured by μSR in a pure crystal of NbSe₂. Right: best fit obtained using a Gussian to model the field distribution. This kind of fits are useful during the experiment, since this often yields a fair qualitative picture of the variation of μSR with temperature, but the fits are generally not good for pure crystals.*
Adapted from Ref. [91].

Different fitting models are used to obtain an asymmetric field distribution. In order to estimate $\langle \Delta B^2 \rangle$, one often assumes that $f(B)$ is a sum of N Gaussian distributions (generally two or three). One gets:

$$f(B) = \frac{1}{\sqrt{2\pi}} \sum_{i=1}^{N} \frac{\varepsilon_i}{\sqrt{\langle \Delta B^2 \rangle_i}} \exp[(B - \langle B \rangle_i)^2 / (2\langle \Delta B^2 \rangle_i)] \ , \qquad (6.55)$$

where ε_i represents the weight of the i-th Gaussian with $\sum \varepsilon_i = 1$.

The first and second moment are then (see Exercices)

$$\langle B \rangle = \sum_{i=1}^{N} \varepsilon_i \langle B \rangle_i \ \text{ and} \qquad (6.56)$$

$$\langle \Delta B^2 \rangle = \sum_{i=1}^{N} \varepsilon_i \left[\langle \Delta B^2 \rangle_i + (\langle B \rangle_i - \langle B \rangle)^2 \right] \ . \qquad (6.57)$$
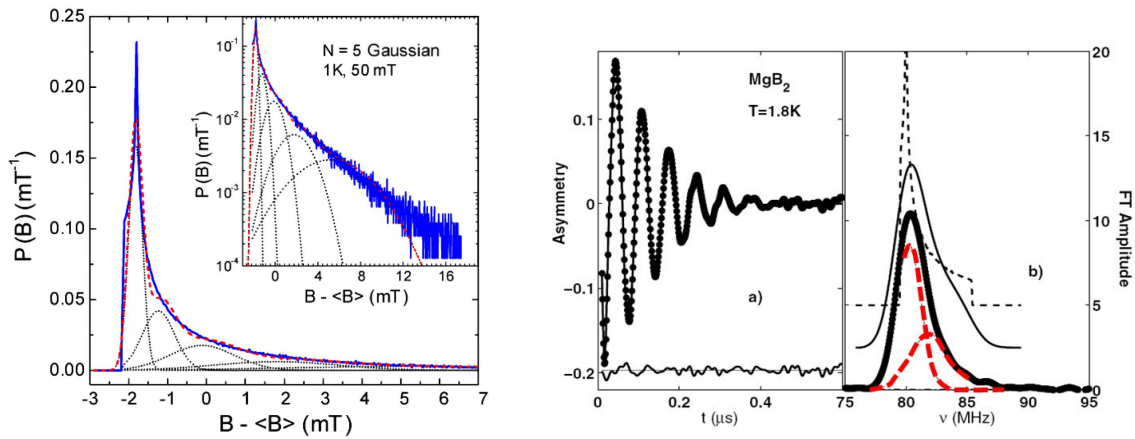
Figure 6.27.: *Left: Comparison of a simulated ideal field distribution* $f(B)$ *with the one obtained using a multi-Gaussian fit with* $N = 5$ *(red dashed line). The five individual Gaussian components used for the fit are also shown (black dotted lines). The inset shows the same plot but on a semi-logarithmic scale (from Ref. [76]). Right: TF μSR data recorded with* $\mu_0 H_{ext} = 0.6$. *The left part of the plot represents the data in a rotating reference frame and the right part of the plot shows the FFT of the muon asymmetry (symbols) and of the two-Gaussian fit (red curves); The black dashed curved shows the ideal FLL distribution with* $\lambda = 52$ *nm and* $\xi = 23$ *nm, whereas the black solid line represents the same distribution with some broadening due to disorder (from Ref. [92]).*

6.5.2. Obtaining the coherence length

As said, the coherence length can be obtained by studying the field dependence of the penetration depth (*i.e.* of the μSR depolarization rate). Equation 6.51 is usually used and the two parameter λ and ξ (related to H_{c2} through Eq. 6.48) can be determined.

An example is given by the iron pnictide superconductor RbFe$_2$As$_2$ [93].
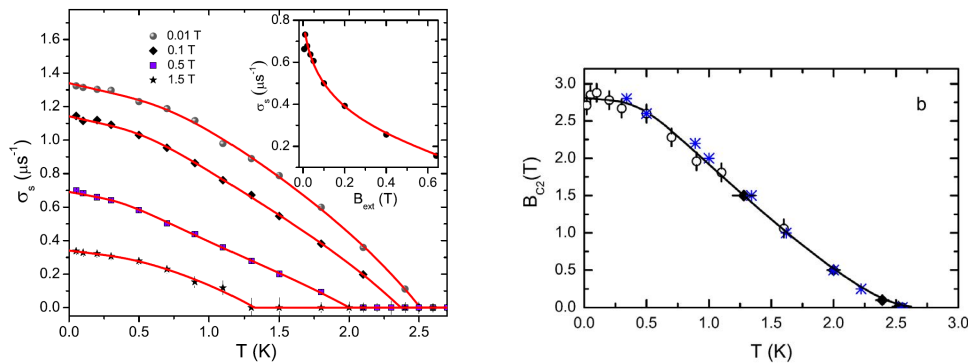
Figure 6.28.: *Left: Temperature dependence of the μSR depolarization rate (Gaussian fit) for different applied fields (lines are guides to the eyes). Inset: field dependence of the depolarization rate obtained at 1.6 K and analyzed using the Eq. 6.51. Right (from Ref. [93]). Right: Upper critical field for RbFe$_2$As$_2$. The open circles are obtained by analyzing the field dependence of the depolarization rate using Eq. 6.51. The diamonds are the value obtained by analyzing the temperature dependence of the depolarization rate. The stars correspond to the complete disappearance of the resistivity in field. The line is a guide to the eyes.*
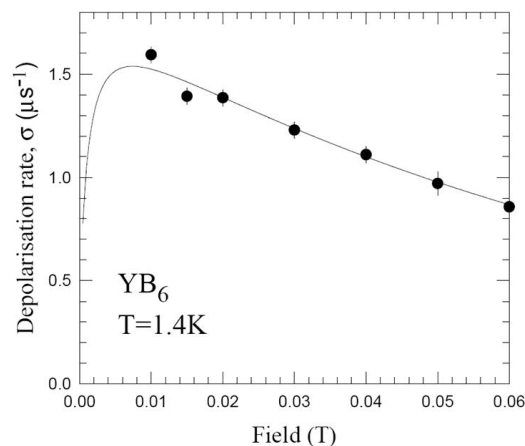
Figure 6.29.: *Another example obtained on the system YB$_6$, from which a penetration depth, λ of 192 nm and a coherence length, ξ, of 33 nm is obtained. (see Ref. [94]).*

6.6. Testing the superconducting gap symmetry

From a μSR measurement we obtain $\sigma \propto 1/\lambda^2 \propto n_s/M^*$. The temperature dependence of n_s contains information on the superconducting gap $\Delta(T)$ Therefore, the temperature dependence of λ provides information on the superconducting gap function.

The wave function of the two paired electrons can be written as the product of a space and a spin part:

$$\Psi(\mathbf{r_1}, S_1, \mathbf{r_2}, S_2) = \phi(\mathbf{r_1}, \mathbf{r_2})\chi(S_1, S_2) \tag{6.58}$$

The wave function must be antisymmetric with respect to particle exchange. If the spin state is a singlet $S = 0$, *i.e.*

$$\chi = \frac{1}{\sqrt{2}}(|\downarrow\uparrow\rangle - |\uparrow\downarrow\rangle), \tag{6.59}$$

the space part must be even, *i.e.* *s*-wave ($\ell = 0$), *d*-wave ($\ell = 2$), etc. *s*-wave superconductor are conventional BCS superconductors, whereas high-T_c cuprate superconductors have *d*-wave symmetry. This is observable in a measurement of the temperature dependence of the magnetic penetration depth.

By taking into account the thermal population of the quasiparticle excitations of the Cooper pairs (Bogoliubov quasiparticles) the generalized BCS theory predicts (*i.e.* not assuming a gap symmetry):

$$n_s(T) = n_s(0)\left(1 - \frac{1}{\pi k_{\mathrm{B}}T}\int\limits_0^{2\pi}\int\limits_0^\infty f(\varepsilon, T)[1 - f(\varepsilon, T)]d\varphi d\varepsilon\right) \tag{6.60}$$

where the Fermi function is:

$$f(\varepsilon, T) = \frac{1}{1 + e^{\sqrt{\varepsilon^2 + \Delta^2(\varphi, T)}/k_{\mathrm{B}}T}} \ . \tag{6.61}$$

ε is the energy of the normal state electrons measured from the Fermi level ($E = \sqrt{\varepsilon^2 + \Delta^2(\varphi, T)}$ is the energy of the quasiparticles measured from the Fermi level).

For the isotropic *s*-wave pairing the superconducting gap $\Delta(\varphi) = \Delta(0)$ is spherically isotropic, and the solution of Eq. (6.60) when $T \ll T_c$ [95] gives:

$$n_s(T) = n_s(0)\left(1 - \sqrt{\frac{2\pi\Delta(0)}{k_{\mathrm{B}}T}}e^{-\frac{\Delta(0)}{k_{\mathrm{B}}T}}\right) \tag{6.62}$$

and the penetration depth is:

$$\lambda(T) = \lambda(0)\left(1 + \sqrt{\frac{\pi\Delta(0)}{2k_{\mathrm{B}}T}}e^{-\frac{\Delta(0)}{k_{\mathrm{B}}T}}\right) \tag{6.63}$$
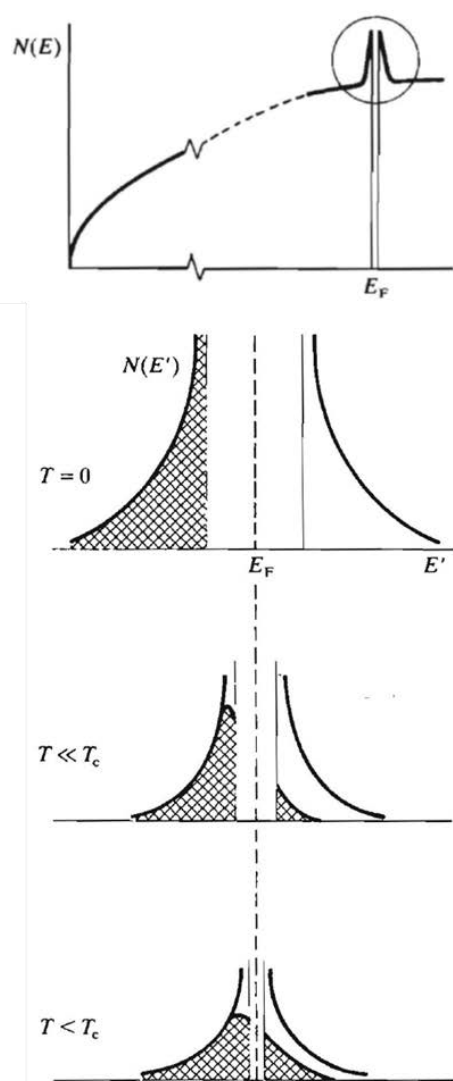
Figure 6.30.: *Density of states and state population at different temperatures in an s-wave superconductor, showing the opening of the superconducting gap with temperature.*

We have seen that by measuring the depolarization rate, we have access to the superfluid density and the penetration depth as

$$\sigma_{\mathrm{sc}} \propto \sqrt{\langle \Delta B^2 \rangle} \propto \frac{1}{\lambda^2(T)} \propto n_s(T) \ , \tag{6.64}$$

and we can therefore determine the value of the superconducting gap and test its topology.
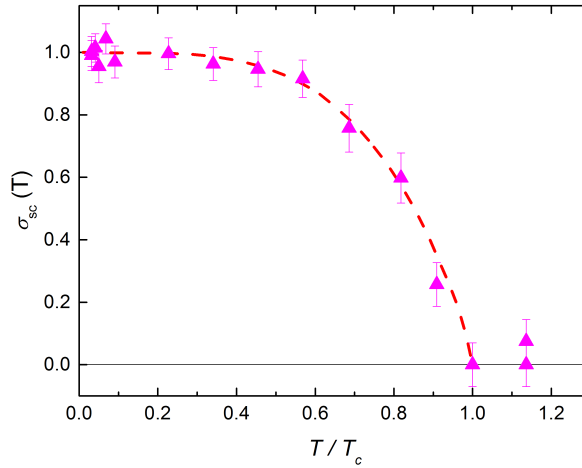
Figure 6.31.: *Temperature dependence of the μSR depolarization rate measured in the system Mo_3Sb_7. As $\sigma_{sc} \propto 1/\lambda^2(T) \propto n_s(T)$ we can test Eq. 6.60. The red line is a fit assuming a s-wave gap. The plateau at low temperatures, shows that we have to introduce some thermal energy to the system in order to decrease the superfluid density (i.e. break Cooper pairs). The value of the gap is found to be $\Delta(0) = 0.39(1)$ meV. Adapted from [96].*

Instead, if we have for a *d*-wave superconductor, the gap function is given by:

$$\Delta(T, \varphi) = \Delta(T) \cos(2\varphi) \qquad (6.65)$$
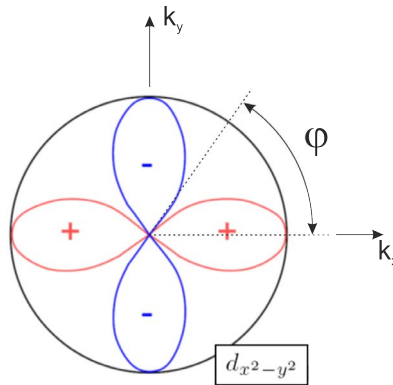
Figure 6.32.: *Schematics of a gap with d symmetry. It has a lower symmetry that the Fermi surface.*

As the gap disappears along some directions of the Fermi surface ("nodes"), extremely-low energy quasiparticles excitations (and therefore significant pair-breaking) may occur at very low temperature, reducing quite effectively the superfluid density.

This is reflected in a different T dependence of λ than the situation above for *s*-wave pairing.
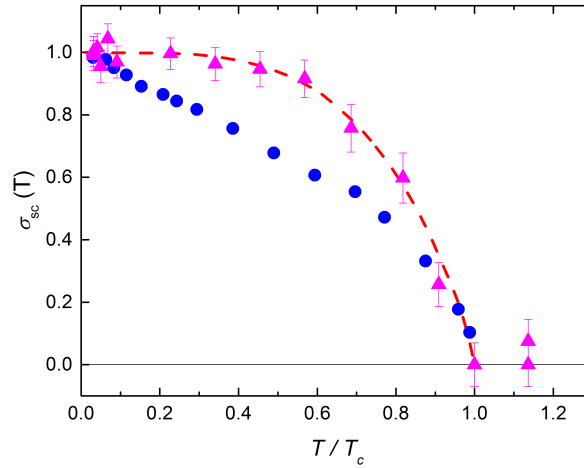
Figure 6.33.: *Comparison between the temperature dependence of the µSR depolarization rate measured in the systems Mo$_3$Sb$_7$ (magenta) and YBa$_2$Cu$_3$O$_{7-\delta}$. As before, the red line represents what is expected for a s-wave gap. Note the different temperature dependence for the YBa$_2$Cu$_3$O$_{7-\delta}$ system reflecting a d-wave gap topology. Adapted from [96] and [81].*

Remembering that:

$$\lambda = \sqrt{\frac{M^*}{\mu_0 e^2 n_s}} \, ,$$

one gets [97]: (for $T \ll T_c$)

$$\lambda(T) \propto \lambda(0)\left(1 + C\frac{T}{\Delta(0)}\right) \, . \tag{6.66}$$
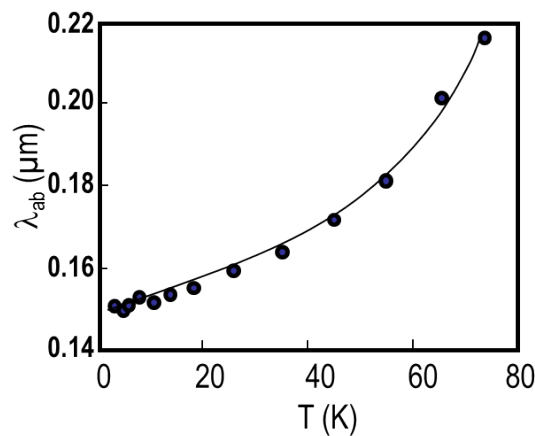
Figure 6.34.: *$\lambda_{ab}(T)$ for YBa$_2$Cu$_3$O$_{7-\delta}$ showing the linear dependence at low temperatures. The line represents $\Delta\lambda_{ab}(T)$ obtained with microwave absorption. Adapted from [81].*

6.7. Determining the anisotropy of the magnetic penetration depth

In Fig. 6.34, we have displayed the penetration depth in the *ab*-plane. The reason arises from the strong anisotropy in the high-T_c system YBa$_2$Cu$_3$O$_{7-\delta}$. In this system, the superconductivity can be considered almost 2-dimensional, with a strongly anisotropic penetrations depth. Along the tetragonal *c*-axis, λ_c will be much longer than the value measured in the plane (λ_{ab}). By performing measurements as a function of the angle (say θ) on single crystals, one can determine the anisotropy. The theory predicts:

$$\sigma_{sc}(\theta) = \frac{\text{Cst}}{\lambda_{ab}\lambda_c} \sqrt{\sin^2(\theta) + \frac{\lambda_c^2}{\lambda_{ab}^2} \cos^2(\theta)} \quad . \tag{6.67}$$

In this equation, λ_{ab} and λ_c are the principal values of the London penetration depth for a superconductor with uniaxial asymmetry. λ_{ab} and λ_c are controlled by superconducting screening currents flowing respectively parallel and perpendicular to the CuO$_2$ planes. $\lambda_c^2/\lambda_{ab}^2$ is the ratio of the principal values of the effective mass. θ is the angle between the external field and the *c*-axis. The expression may be shown to arise from an anisotropic London equation approach, so long as the flux lattice structure is qualitatively the same at all angles.
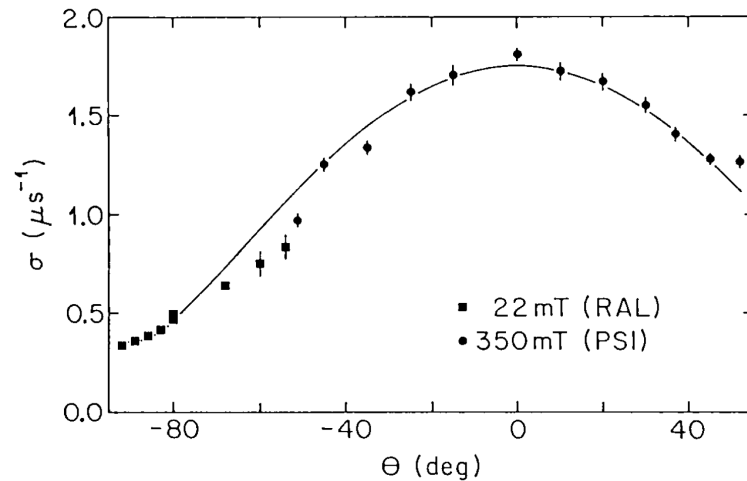
Figure 6.35.: *Angular dependence of the µSR depolarization rate. The line is a fit using Eq. 6.67. Taken from [98].*

6.8. Multiple superconducting gaps

6.9. Uemura relation, Uemura plot: Correlation between T_c and σ

Since the discovery of superconductivity in the copper oxide materials there has been a considerable effort to find universal trends and correlations amongst physical quantities to find a clue to the origin of the superconductivity. One of the earliest patterns that emerged was the linear scaling of the Gaussian relaxation rate σ_{sc} with the superconducting transition temperature (T_c). This is referred to as the "Uemura" relation and works reasonably well for the underdoped materials.

The linear relation between T_c and σ_{sc} implies a direct correlation between T_c and the superfluid density divided by the effective mass, *i.e.* n_s/M^*. As seen, the magnetic penetration depth in cuprates is anisotropic and for polycrystalline samples λ is an average of λ_c and λ_{ab} ($ab = CuO_2$ planes). For $\lambda_c \gg \lambda_{ab}$, λ is only sensitive to λ_{ab} (see Eq. 6.67).

Such a correlation is not consistent with conventional BCS theory, where

$$T_c \simeq \frac{2\hbar\omega_D}{k_B} e^{-\frac{2}{VN(E_F)}} , \tag{6.68}$$

where ω_D is the Debye frequency (phonon coupling), $N(E_F)$ is the density of states at the Fermi level and V is the effective attractive pair potential for the Cooper pairs. In Eq. 6.68 T_c is proportional to ω_D and not simply related to n_s. The Uemura relation indicates that these "unconventional" superconductors belong to a different class from the one of the previously known conventional superconductors.
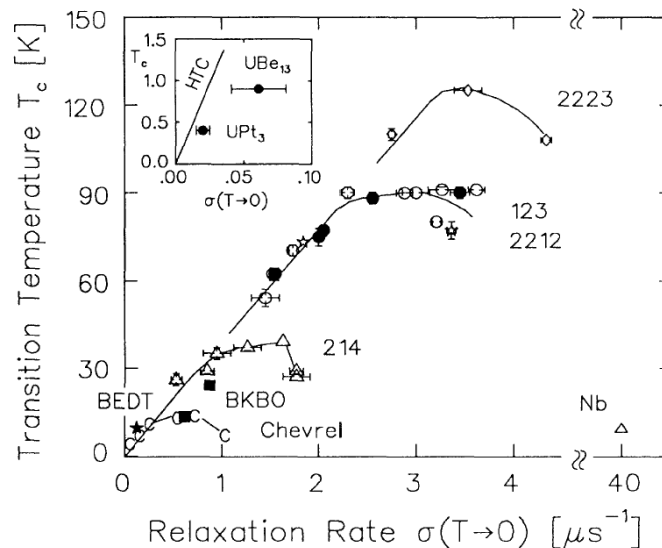
Figure 6.36.: *Plot of T_c vs $\sigma_{sc} \propto n_s/M^*$ for the cuprates. Taken from [99].*

High-T_c superconductors are to large extent two dimensional, since the CuO_2 planes contain

most of the supercarriers. For a 2D electron gas the Fermi energy is given by:

$$E_F = k_B T_F = \frac{\hbar^2 \pi n_{s,2D}}{M^*} \quad . \tag{6.69}$$

$n_{s,2D}$ is the carrier concentration within the superconducting planes calculated from the volume carrier density using $n_s d$, where d is the interplanar spacing. Therefore, for a 2D system one has $T_F \propto \sigma_{sc}$.

On the other side, for a 3D system the Fermi temperature is given by

$$E_F = k_B T_F = \frac{\hbar^2 (3\pi^2)^{2/3} n_s^{2/3}}{M^*} \quad . \tag{6.70}$$

To determine T_F for a 3D system, the measured muon depolarization rate must therefore be coupled with, for example, the Sommerfeld constant, γ,

$$\gamma = k_B T_F = \left(\frac{\pi}{3}\right)^{2/3} \frac{k_B^2 M^* n_e^{1/3}}{\hbar^2} \quad , \tag{6.71}$$

where n_e is the carrier density, assumed to correspond to n_s at $T = 0$ K. Combining Eqs. 6.70 and 6.71 we have for a 3D system $T_F \propto \sigma_{sc}^{3/4} \gamma^{1/4}$

Using this approach, Uemura et al. [99] demonstrated a correlation between T_c and T_F. The cuprate, heavy fermion, organic, fullerene and Chevrel phase superconductors all posses a more or less similar linear trend with $1/100 < T_c/T_F \ll 1/10$. This is not observed in BCS superconductors (Nb, Sn, Al, etc.) for which $T_c/T_F < 1/1000$. The second version of the "Uemura plot" of $\log(T_c)$ plotted vs $\log(T_F)$, shown in Fig. 6.37, appears to differentiate between the "exotic" and "conventional" superconductors. From the Uemura plot it is tempting to place "exotic" superconductors in a class of its own.

The Uemura plot has been taken as an indication that the strongly coupled exotic superconductors may, in a thermodynamic sense, be close to Bose-Einstein condensation. The condensation temperature of an ideal boson gas is defined only by n_s and M^*, and is independent of the scale of the pairing interaction. The Bose-Einstein condensation temperature for an ideal 3D boson gas as

$$k_B T_B \propto \frac{n_B^{2/3}}{M_B} \quad . \tag{6.72}$$

If we assume that the boson is actually the Cooper pair, we have $M_B = 2M^*$ and $n_B = n_s/2$.

All the exotic superconductors are found to have values of T_c/T_B in the range 1/3 to 1/30, emphasizing the proximity of these systems to a Bose-Einstein-like condensation.
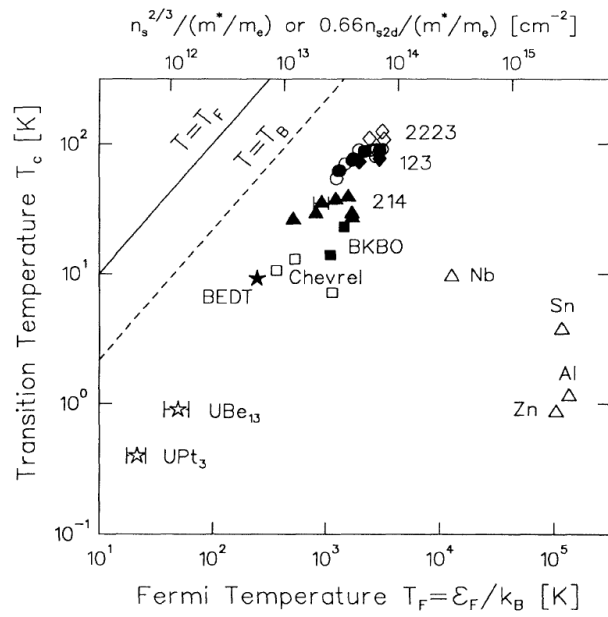
Figure 6.37.: *A log-log plot of T_c, vs the Fermi temperature estimated from the results of σ_{sc} and γ. Taken from [99].*

6.10. Dynamics of the FLL

6.10.1. Melting through temperature

6.10.1.1. Stabilization with defects

6.10.2. Moving the FLL with an applied current

7. Low energy muons: a tool to study thin films and heterostructures

For this Chapter, and as Elvezio Morenzoni can be considered as one of the fathers of the low-energy muon technique, I took the liberty to essentially reproduce the corresponding Chapter of his lecture script (see Ref. [21]). In addition, a good review article about the technique is provided by the Ref. [100].

7.1. Introduction

Experiments making use of surface muons can not provide depth selective information or study extremely thin samples. With the initial implantation energy of 4.1 MeV typical for surface muons, the stopping range of muons in a solid varies from 0.1 mm to 1 mm with a wide distribution of about 20% of the mean value. Therefore, using surface muons, only μSR measurements of the bulk properties can be performed.
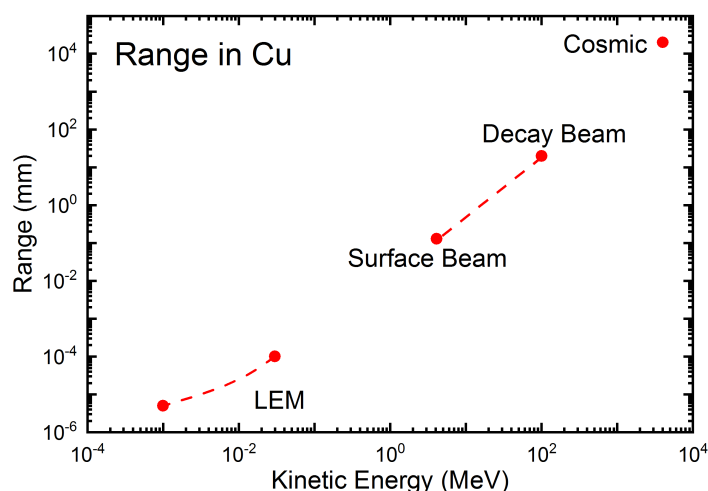
Figure 7.1.: *Mean range of positive muons implanted in a typical material (in this case copper) as a function of their kinetic energy. Whereas surface or decay muon beams are used to investigate bulk properties of matter, low energy muons (LEM) extend the applications of μSR techniques to the study of thin films, multilayers and depth dependent investigation on nanometer scale.*

To extend the scope of the μSR technique to materials which are of interest in the newly

developing technologies of nanomaterials, multilayered thin films, etc., spin-polarized muon beams with tunable energies from several eV to several keV and narrow energy distribution are required. By changing their kinetic energy, these positive muons can be implanted at well-defined depths ranging from just fractions of a nanometer to a few hundred nanometers.

Muons with kinetic energies typically below 0.1 MeV are called "Low Energy Muons" (LEM) or "Slow Muons". A complete review about the generation and application of low energy muons is provide in Ref. [100].

7.2. Generation of low energy muons

Conventional methods to reduce the phase-space volume (*i.e.* the spread of the momentum around its average value times the spatial spread) of a charged particle beam include electron or stochastic cooling.

- Electron cooling realized by merging a dense monoenergetic electron beam with the beam to be cooled. Prior merging, the velocity of the electrons is made equal to the average velocity of the beam to be cooled. The particle of the beam to be cooled undergo Coulomb scattering in the electron gas and therefore exchange momentum with the electrons. Thermodynamic equilibrium is reached when all the particles have the same momentum, which requires that the much lighter electrons have higher velocities. Thus, kinetic energy is transferred from the charged particles of the beam to the electrons. The electron beam is finally bent away from the ion beam.

- Stochastic cooling makes use of the electrical signals that the individual charged particles generate in a feedback loop to reduce the tendency of individual particles to move away from the other particles in the beam and therefore reducing the entropy.

However these processes are too slow for unstable particles, where rapid action is required within the particle lifetime. In clear, other methods had to be found to cool the positive muons.

7.2.1. Moderation in thin layers of cryosolids

A simple way to act on charged particles is to slow them down in matter (see Section 2). However, when a high-energy beam traverses a thin metallic foil a few hundred micrometers thick, the energy spectrum of the particles exiting the foil is very broad. Fortunately, the interactions of particles implanted in some well-selected materials (called moderators) lead to a preferential emission at energies of a few electronvolts. One can make use of this specific property to produce low energy muons.

The most successful method of generating muons with energies of the order of 15 eV is the muon moderation technique in condensed van der Waals gases. Very preliminary results

were first obtained at the TRIUMF facility in Canada[101], but the subsequent decisive developments were performed at the Paul Scherrer Institute (PSI) in Switzerland. Nowadays, LEM experiments at PSI are routinely performed for nanoscale investigations.
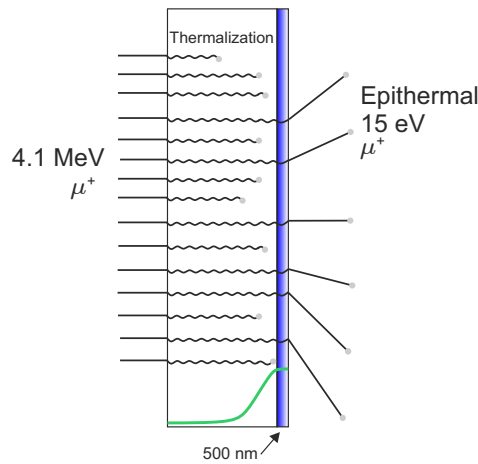
Figure 7.2.: *Schematics of the LEM production. Surface muons are sent to a thin silver foil having a thickness of 100 μm and cooled at about 6 K. The muons loose a large fraction of their kinetic energy in the foil. Some muons will be stopped in the foil (stopping profile roughly represented by the green curve) but some will pass through the thin layer of cryosolid (blue layer), where their energy will decrease down to a value given by the energy band gap of the cryosolid. The emitted epithermal muons have an energy of the order of 15 eV.*

The various moderation steps can be summarized as follows.

1. Surface muons (4.1 MeV) are sent to a thin-foil substrate. They rapidly loose energy in the thin-foil (thickness of about 100 μm) by Coulomb collisions with electrons and by ionizing and exciting the target atom. This process represents the $1/\beta^2$ region of the Bethe formula (see Section 2.1.2).

2. When a muon has lost most of its kinetic energy, at energies below about 10 keV, charge-exchanging cycles, involving muonium formation in one collision (where the positive muon captures an electron) and muonium break-up in one of the subsequent collisions, also acquire importance as energy-dissipating mechanisms. This corresponds to the region on the left-hand side of the maximum on Fig. 2.4. The width of the thin-foil substrate is so chosen that the muons traversing it and entering the cryosolid have an energy for which these capture and loss of electrons are important.

3. In wide-band-gap perfect insulators, such as the cryosolids krypton, argon, nitrogen, and neon (band-gap energy between 11 and 22 eV), these electronic processes have high threshold energies. That is, the muon must at least possess a kinetic energy comparable to the band-gap in order to ionized an atom. Therefore, once the muon has reached a kinetic energy of the order of the band-gap, the energy loss mechanisms are strongly suppressed or even become energetically impossible. As a consequence, the energy loss rate becomes considerably lower, since only the inefficient elastic scatter-

ing and phonon excitation processes remain as energy loss mechanisms.

4. This results in a large escape depth L for epithermal muons (about 100 nm for Ar and 50 nm for Kr). That is, the muons can basically move unperturbed once they reach a low energy. This gives rise to a particularly efficient moderation to epithermal energies in these materials. Once going through the thin cryosolid overlayer, the epithermal muons are ejected. The mechanism is hot emission: the observed muons exiting the cryosolid are particles that have not completely thermalized in the thin cryosolid layer, and therefore they are termed "epithermal" (*i.e.* above thermal) muons.
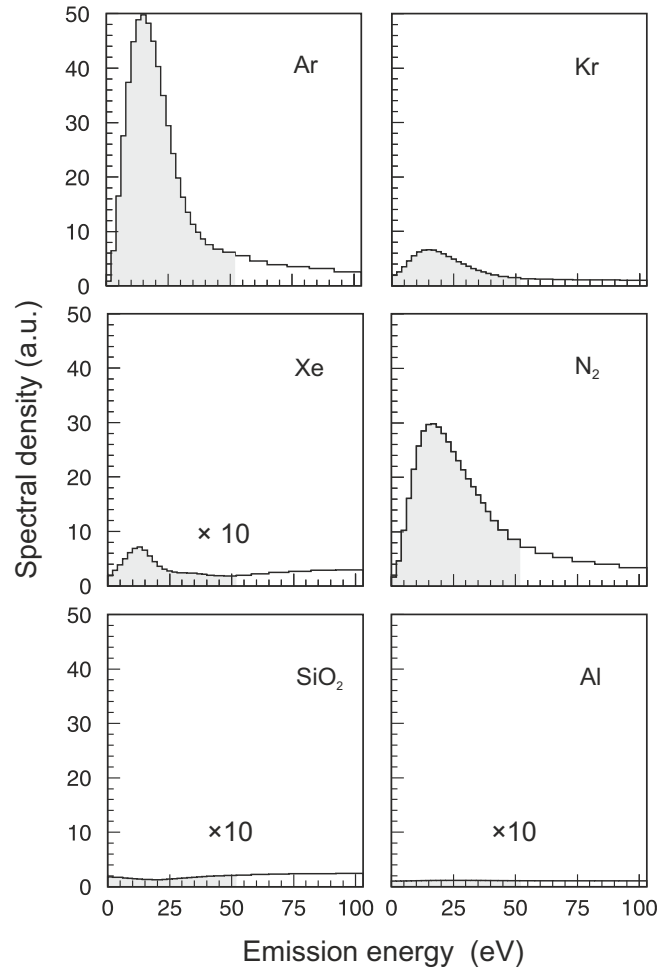
Figure 7.3.: *Energy spectral density of the muons escaping different types of cryosolids (see also Fig. 7.2).*

Epithermal muon emission conserves the initial polarization (practically 100%) since, as already discussed, depolarization via electron and Coulomb scattering is negligible and the overall time for slowing down to about 10 eV is very short (of the order of 10 ps). The moderation efficiency to obtain epithermal muons from surface muons is given by

$$\varepsilon_\mu = \frac{N_{\text{epith}}}{N_{\text{surf}}} = \frac{\Delta\Omega(1 - f_{\text{Mu}})L}{\Delta R} \ , \tag{7.1}$$

where $\Delta\Omega$ is the probability to escape into vacuum (*i.e.* 50% for isotropic angular distribution), f_{Mu} is the muonium formation probability [meaning that $(1 - f_{Mu})$ is the muon fraction remaining "free"] and ΔR is the straggling (spread of the range values) of the surface muons. As the escape depth value L is much shorter than the straggling, the moderation efficiency is very low. It is between 1.5×10^{-4} for solid neon and about 5×10^{-5} for solid nitrogen or argon. Therefore, to obtain a decent LEM beam, the availability of high luminosity for the primary muon beam is essential.
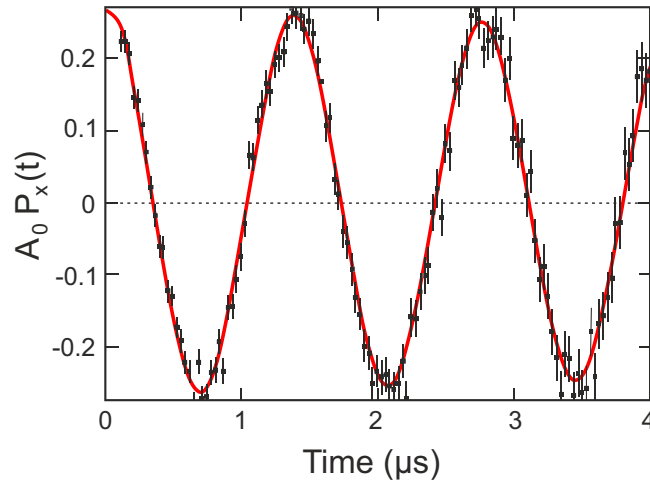
Figure 7.4.: *TF μSR signal recorded in a silver sample for very slow muons emitted from a solid argon layer. The muon spins were precessing in a 5 mT transverse magnetic field. The amplitude corresponds to essentially 100% polarization. Adapted from Ref. [102]*
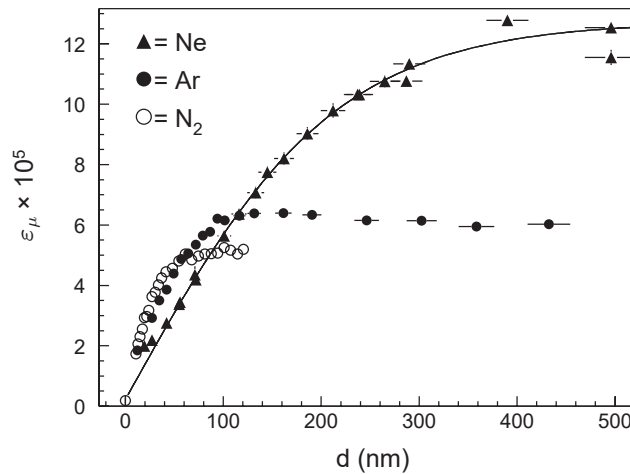
Figure 7.5.: *Moderation efficiency ε_μ , defined as the number of epithermal muons divided by the number of incoming surface muons , for various moderating materials as a function of the thickness of the solid van der Waals layer condensed onto a patterned Ag substrate, which was held at a temperature of 6 K. From Refs. [103] and [104].*

7.2.2. Laser resonant ionization of muonium

An alternative idea to obtain an ultraslow muon source is to start with thermal muonium having a kinetic energy of only 0.2 eV. This kind of muonium states are produced with a surprisingly high efficiency of several percent by simply stopping the surface muon beam in a hot tungsten foil located in vacuum. The thermal muonium atoms can be subsequently ionized by a suitable laser radiation to finally obtain bare ultraslow muons. The wavelengths of the lasers are chosen in such a way that the combined energy of the photons absorbed by the muonium atom equals the binding energy of muon and electron and the muons are released without any increase in the kinetic energy [105]. In theory, the laser ionization efficiency depends only on the incident laser intensity and could be as high as 100%. However, the laser system cannot work continuously at high intensity. Therefore, this method is well-suited for pulsed muon beams with the use of the laser illumination frequency matching the one of the accelerator beam. Also, it appears difficult to cover the entire volume of the produced muonium cloud with the laser. The laser ionization frequency is thus considerably reduced.

This method has been tested at the ISIS (UK) pulsed muon source producing about 10-20 slow muons per seconds. Since few years, efforts are underway to implement this LEM production technique at the μSR facility at J-PARC (Japan) where higher intensities are expected [106]. However, as said, the huge technical challenge is the reliable availability of a suited laser system with sufficient power.

Whereas the production of slow muons with a moderation in cryosolids produces a beam which is still 100% polarized, low energy muons produced by muonium ionization have a polarization of 50% (see Section 8.3; the muonium state $|\uparrow_\mu\downarrow_e\rangle$ is not an eigenstate of the system as seen in Eq. 8.9) which represents an additional drawback, as the maximum asymmetry observed in a μSR spectra will be reduced by a factor two.
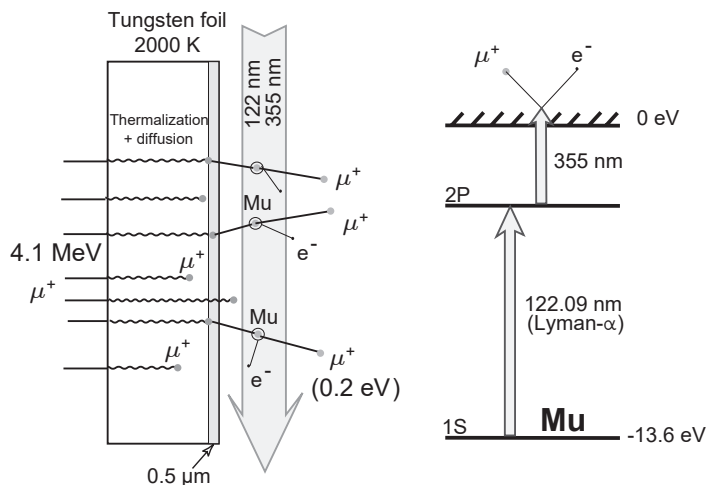
Figure 7.6.: *Principle of thermal muonium (Mu) generation from tungsten foil and 2-photon resonant ionization of muonium resulting in the production of low energy positive muons. From Ref. [100].*

7.3. The Low-Energy Muon (LEM) instrument at PSI

Epithermal muons emitted from a moderator represent the source of the low energy beam of polarized positive muons with tunable energy in the desired range. The practical realization of this scheme, developed and in use at PSI, is shown in Figs 7.7 and 7.8. This beam is an example of a tertiary beam (the primary being the proton beam generating pions and the secondary is the surface muon beam originating from the decay of the pions).

The detailed operation is as follows. Surface muons with a continuous rate of presently $\sim 2 \times 10^8$ muons/s are sent into the cryogenic moderator held at a positive potential between 12 and 20 kV. Epithermal muons emerging from the moderator are accelerated in this potential, transported and focused by electrostatic lenses and a mirror to the sample, where they arrive at a rate of $\sim 4.5 \times 10^3$ muons/s.
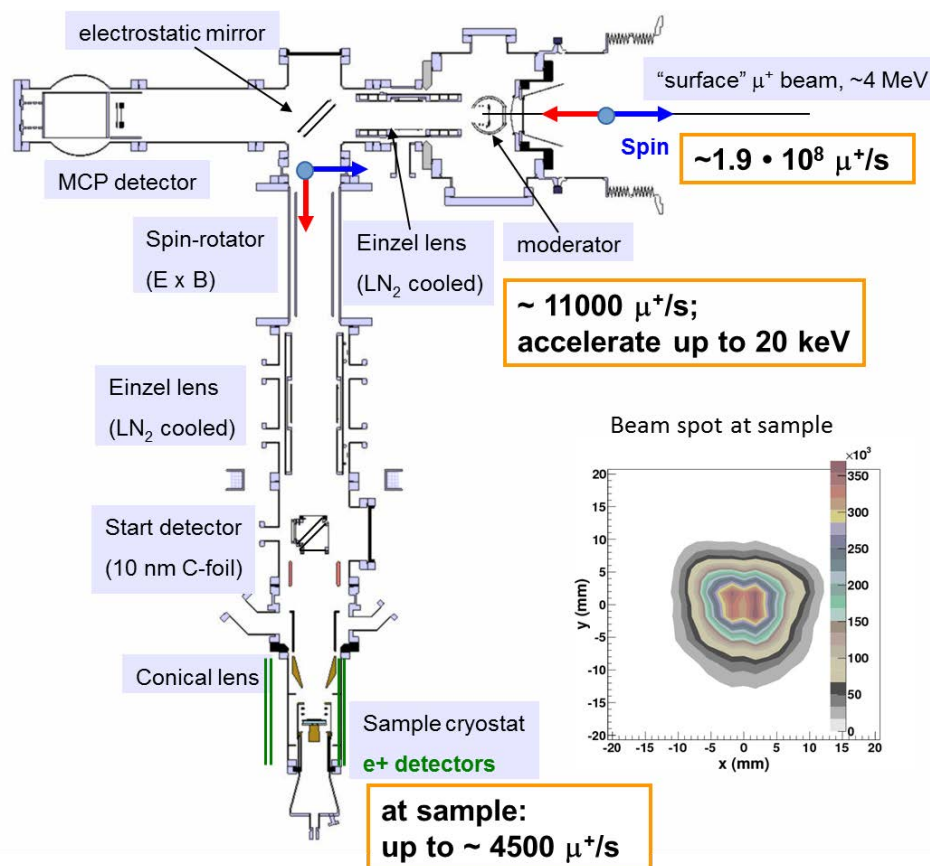
Figure 7.7.: *Low energy polarized muon beam generated via moderation and μSR spectrometer for experiments on thin films, multilayers and near surface regions at the Paul Scherrer Institute.*
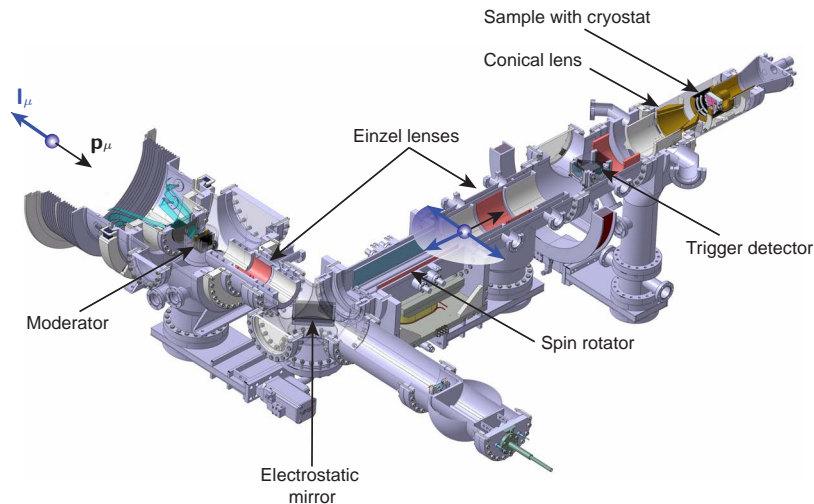
Figure 7.8.: *Details of the main components of the LEM setup.*

The electrostatic mirror is used to separate the low energy muons from any fast muons exiting the moderator. As for a continuous beam the arriving time of the muon is necessary[1], *i.e.* the time t_0, the low energy muons are detected after the mirror when they pass through a 10 nm thick carbon foil (corresponding to only about 50 atomic layers) placed at an intermediate focus of the beam transport system ("trigger detector" in Figs. 7.7 and 7.8). The positive muons traversing the foil eject a few electrons, which are directed by a grid system to a micro-channel plate detector where they are detected and providing the t_0-signal. This scheme keeps the amount of material interacting with the muons and the consequent effects on the trajectory minimal, while allowing for an efficient (>80%) and fast detection.
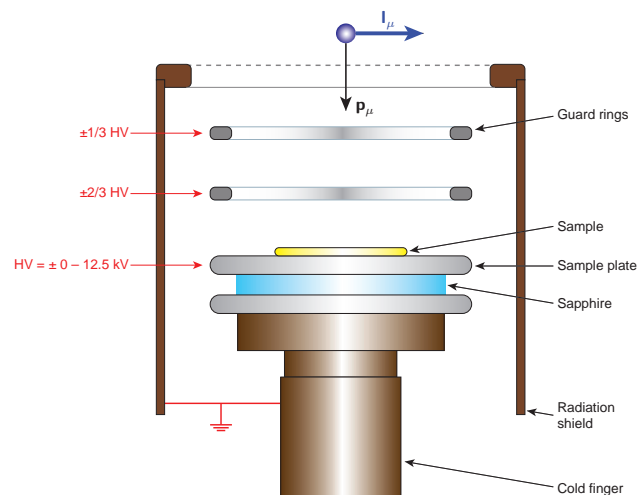
Figure 7.9.: *Scheme of the low energy polarized muon beam when entering into the cryostat holding the sample to be investigated.*

---

[1]Remember: PSI delivers so called continuous beams and only one muon at a time has to be present in the sample, see Section 3

On passing through the carbon foil, the muons lose about 1 keV and acquire an energy spread having a standard deviation of about 0.4 keV. The trigger signal is also used to measure the time-of-flight (TOF) of each low energy muon after it has been detected at a scintillator on entering the apparatus. By analyzing the TOF information, one can discard muons coming from the moderator with energies outside the epithermal region, but with low enough energy to be reflected by the mirror. The final kinetic energy of the muons implanted into the sample may be varied over the range 0 to 30 keV by applying an accelerating or decelerating potential of up to 12 kV to the sample (Fig. 7.9). The sample is thus mounted in good thermal but electrically insulated to the cryostat.
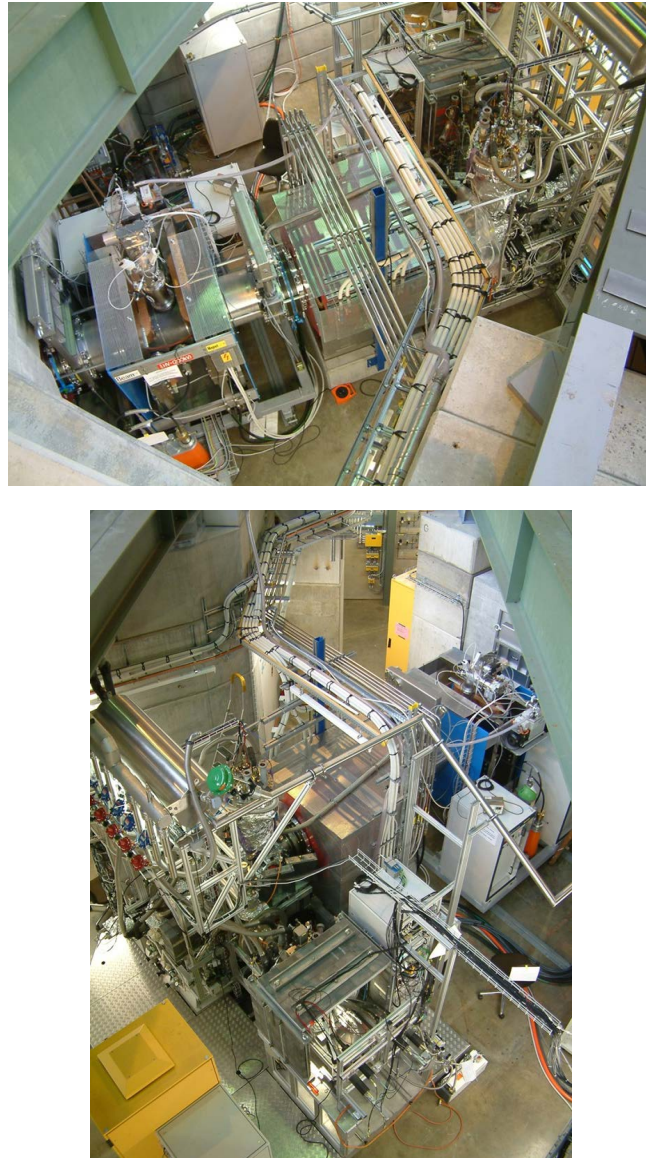
Figure 7.10.: *μSR LEM instrument in the μE4 area at PSI. Left: last section of the high intensity surface muon beam feeding the LEM apparatus. Right: LEM Apparatus. The surface muons are coming from the right. The moderator cryostat with the 90° deflection as well as the μSR spectrometer and sample chamber in the lower part of the picture are visible.*

The 90°deflection at the electrostatic mirror has also the practical effect of transforming the initially longitudinally polarized muon beam into a transversely polarized beam (when the muons arrive at the sample, they are horizontally polarized, transverse to their direction of motion). A small spin rotator can rotate the spin by 90°to have the spin parallel to the momentum [107]. The decay positrons from the muons implanted in the sample are detected by a set of scintillator detectors placed left, right, above and below the beam axis.

7.4. Stopping profiles of Low-Energy Muons in thin films

In μSR experiments making use of surface or decay muon beams the exact muon stopping depth is not known and is also irrelevant, as long as the sample is homogeneous. In these experiments it is sufficient to ensure that the muons stop inside the sample. In contrast, for unrestricted use of muons on the nanometer scale, it is important to understand the muon implantation behavior in detail.

As we have seen in Section 2, when the muon enters into a solid sample the initial kinetic energy is dissipated within a few picoseconds. The muon continuously loses energy predominantly by electronic collisions and changes direction mainly by Coulomb scattering with the target nuclei. For a LEM beam of kinetic energy E_{kin}, a stopping profile $n(\ell, E_{kin})$ is obtained (ℓ depth from the sample surface) which arises from the random nature of the collision process. The mean value of this profile is called the range and is reported in Fig. 7.1 for a typical material. It represents the mean value of the projection along the beam direction of the total distance traveled (projected range, R_p). The corresponding straggling of this range (ΔR_p) arises on one side from the energy spread of the beam (in case of the LEM beam at PSI, this represents about 0.4 keV; see above). On the other side, even for perfectly monoenergetic particles there is an inherent limit to the depth resolution due to the statistical broadening of the implantation profile. This intrinsic broadening is the dominant effect for muon of energy larger than about 2 keV. At low energies the profile width is typically 5-10 nm.

To determine experimentally the stopping depth, one can rely on the difference between the magnetic field response of "free" muons in metals compared to the one of muonium. Because of the coupling of the muon and electron spins in the case of the muonium, the two states (free muon and muonium in the triplet state, $m_F = \pm 1$) have completely different muon spin precession frequencies in a low static magnetic field $\mathbf{B}_{ext}$ transverse to the initial spin direction. Hence, a magnetic field of say $B_{ext} = 3$ mT will produce a frequency of $\nu_\mu = \omega_\mu/(2\pi) = \gamma_\mu \times B_{ext} \simeq 0.407$ MHz for a free muon and $\nu_{Mu\ eff.} = \omega_{Mu\ eff.}/(2\pi) = \gamma_{Mu\ eff.} \times B_{ext} \simeq 41.9$ MHz for a muonium (see Eq. 8.40 in Section 8).

In a sample composed of a thin (thickness d) metallic layer (where solely "free" muon is formed) deposited on an insulator (where muonium is formed), the amplitude of the corresponding frequency in the μSR signal is then directly related to the fraction of muons stopped in the corresponding layer. In the measurement, one determines the partial integral of the stopping distribution in the metallic layer, *i.e.*

$$N(d, \ell, E_{kin}) = \int_0^d n(\ell, E_{kin})d\ell \ . \tag{7.2}$$

The measurement is repeated for different energies, and therefore different ranges. By comparing these fractions with the predictions obtained by Monte Carlo simulations, which calculate step-by-step the trajectory of the particle implanted and simulate their slowing down, scattering and thermalization, we are able to test our understanding of these processes.
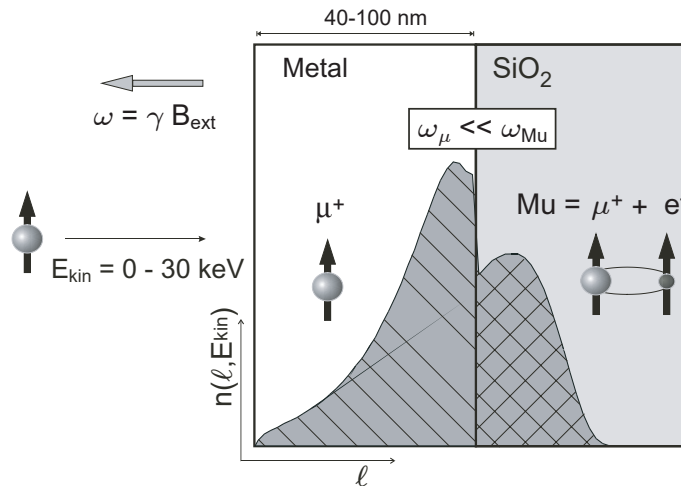
Figure 7.11.: *Principle of the muon depth profile studies in metal-insulator films. The fraction of muons stopping in the metal or in the insulator layer can be distinguished by their different Larmor frequency. The results can be compared with Monte Carlo simulations of the muon stopping profile $n(\ell, E_{kin})$.*

Figure 7.12 shows as an example the "free" muon fraction measured in a bilayer consisting of copper (where "free" muon is formed) deposited on quartz (SiO_2; where muonium is formed). After an increase at low energies, the fraction of muons stopping in the copper saturates, when essentially all the particles thermalize in the copper layer. Increasing further the muon kinetic energy the fraction decreases, indicating that the muons go through the metallic layer and reach the insulating layer, where they predominantly form muonium. Therefore, the decrease of the "free" muon fraction is accompanied by a corresponding increase of the muonium fraction (not shown). The observed initial increase of the "free" muon fraction with energy at a few keV is a consequence of reflection and simultaneous neutralization of muons scattered at the metallic surface or re-emerging from the bulk. This effect is especially pronounced in samples containing heavy elements. The comparison with simulated integrals of implantation profiles and reflection probabilities shows that we are able to correctly predict the behavior of keV muons.
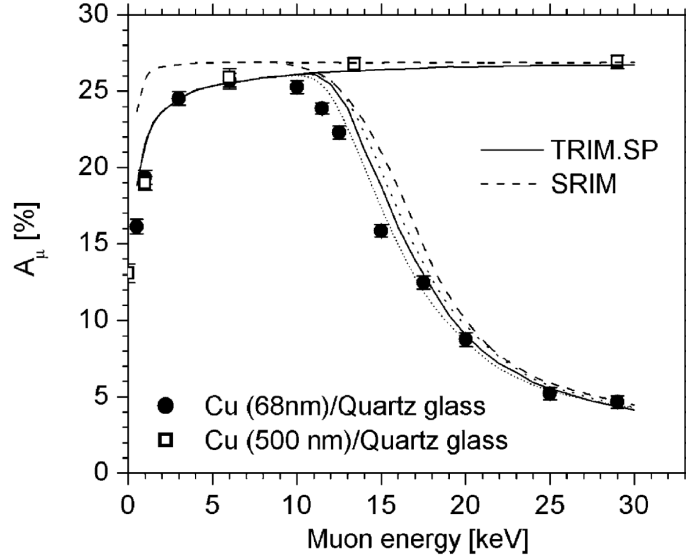
Figure 7.12.: *Energy dependence of the diamagnetic asymmetry in Cu deposited on a quartz glass: closed symbols thin (d = 68 nm), open symbols thick (d = 500 nm) sample. The solid lines are the prediction of a simulation based on the TRIM.SP Monte Carlo program [108]. The dotted line in the intermediate energy region shows upper and lower limits due to the layer thickness uncertainty. The dashed curves are the predictions of the Monte Carlo simulation code SRIM2000 [109]. Taken from Ref. [110].*

The full differential implantation profile can be directly determined in a single implantation and imaging experiment. In analogy with the magnetic resonance imaging technique, the implantation profile can be obtained by applying to the sample an inhomogeneous transverse magnetic field $\mathbf{B}_{ext}(\ell)$ of known gradient. Note that the field is now applied along the surface of the sample and as defined in Section 3.5.2 this direction is called the *z*-direction. The value of the field is dependent from the sample depth ℓ. One studies the spectrum of the Larmor precession frequencies. The different local magnetic field at each stopping site causes a corresponding precession of the muon spin. The time evolution of the polarization $P_x(t)$ measured at a well-defined energy E_{kin} is related to the field profile of $\mathbf{B}_{ext}(\ell)$ and the stopping distribution $n(\ell, E_{kin})$ as follows

$$P_x(t) = \int_0^\infty f(B) \cos(\gamma_\mu B t + \phi) dB \ . \tag{7.3}$$

The phase ϕ is a setup parameter and essentially reflects the rotation of the muon spin prior to enter into the sample (the external field extends outside the sample). The field distribution $f(B)$ is obtained by Fourier transform. The differential muon stopping distribution $n(\ell, E_{kin})$ is connected to the field distribution by the relationship

$$n(\ell, E_{kin})d\ell = f(B, E_{kin})dB \ , \tag{7.4}$$

which states that the probability that a muon will experience a field in the interval $[B, B + dB]$ is given by the probability that it will stop at a depth in the range $[\ell, \ell + d\ell]$.

From the later Equation, we see that if we impose a field gradient, and if we obtain the field distribution seen by the muon ensemble by performing a Fourier transform from the μSR signal, we can determine the differential stopping distribution with

$$n(\ell, E_{kin}) = f(B, E_{kin})\frac{dB}{d\ell} \quad . \tag{7.5}$$

For low-energy muons, the range and straggling are very small and therefore large field gradient are necessary in order to extract the implantation profile. As a test experiment, one can make use of the magnetic field exponentially penetrating the surface of an extreme type-II superconductor in the Meissner state. Just below the surface $B_z(\ell) = B_{ext}\exp(-\ell/\lambda)$ (where λ is the magnetic penetration depth; see Section 6.2). With typical values of $B_{ext} \simeq$ 10 mT and $\lambda \simeq 100$ nm, field gradients of the order of 10^5 T/m can be generated within the range distribution of low energy muons.[2]
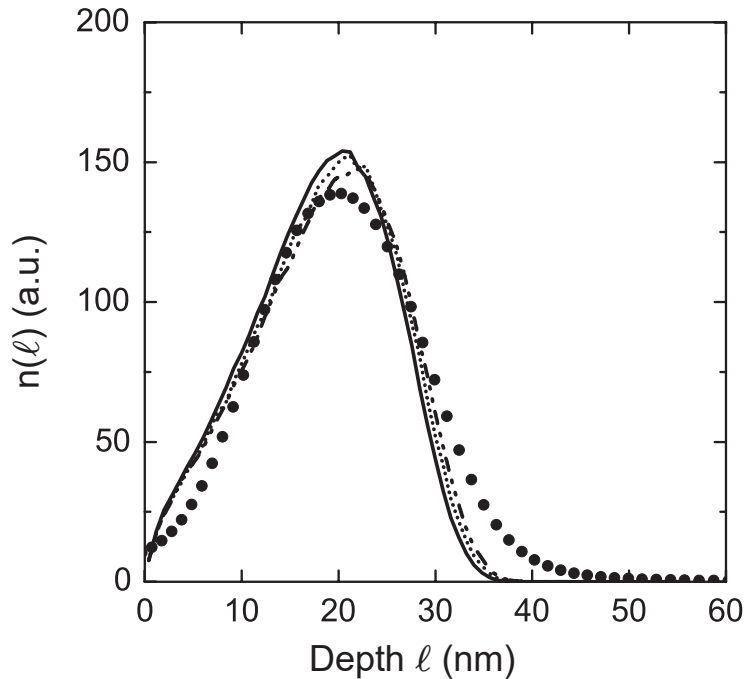
Figure 7.13.: *Implantation profile of 3.4 keV muons in a thin film of YBa$_2$Cu$_3$O$_{7-\delta}$ obtained by the direct imaging technique (circles). The profile is compared with predictions of Monte Carlo calculations using the code TRIM.SP with different assumptions about the scattering potential. From Ref. [103]. The various tests show that muon implantation profiles in thin films and heterostructures can be reliably simulated with a modified version of the Monte Carlo simulation program TRIM.SP.*

---

[2]Note that in the next Section we will assume the knowledge of the implantation profile $n(\ell, E_{kin})$ to microscopically prove that the field is penetrating exponentially a superconductor in the Meissner state and to make an absolute measurement of the London penetration depth and its temperature dependence. Here, by contrast, we assume an exponentially decaying magnetic profile with known penetration depth λ to measure the depth profile. The argument is non-circular since for the present analysis the value of λ was determined by an independent measurement in the vortex state [111].
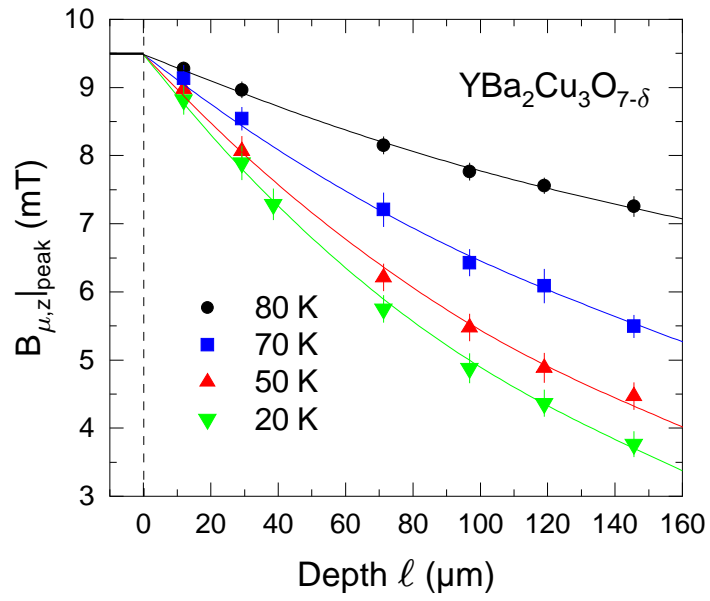
Figure 7.14.: *Monte Carlo simulation of stopping profiles of low energy muons in YBa$_2$Cu$_3$O$_{7-\delta}$, as a function of the implantation energy.*

7.5. Examples of LEM studies

7.5.1. Magnetic field penetration at the surface of superconductors

The depth sensitivity in nanometer range of low energy muons implanted in the surface region and the local character of the muon probe allow to directly measure single values of magnetic fields as a function of depth, thus to image magnetic field profiles beneath the surface of materials on a nanometer length. At the moment, no other technique is able to provide this information.

To illustrate the near surface sensitivity of low energy μSR, we consider here the Meissner effect and a measurement of $B(\ell)$. This yields a direct determination of otherwise not easily accessible quantities such as magnetic penetration depth and coherence length. As we have seen in Section 6.2, for a superconductor in the Meissner state an applied magnetic field is excluded from the bulk and will penetrate only in a near surface region. In the so-called London limit (*i.e.* for a strong type II superconductor with $\lambda \gg \xi$, for a plane superconducting surface, the functional form of the decaying magnetic field $B(\ell)$ is predicted to be exponential (see Eq. 6.13), with the decay length determined by a single parameter, the London penetration depth λ.

It is interesting to note that Eq. 6.13 was predicted already in 1935 by the London brothers [112], but never experimentally tested before at microscopic level. Low energy μSR provided the first experimental proof of it. Differently from a measurement in the vortex state, the measurement in the Meissner state provides an absolute and model independent determination of λ. A determination of λ from the vortex state (see Section 6.5.1) is a very reliable and efficient method but it has to rely on a theory which has to describe the vortex state relating the measured field distribution $f(B)$ (or its moments) with λ. Also, in Section 6.5.2, we have seen a method to obtain the coherence length ξ of the superconducting state by studying the vortex state in a type-II superconductor as a function of field. Now, the question is to know whether these quantities could be obtained from LEM μSR in the Meissner state, which could allow their determination also for type-I superconductors.

7.5.1.1. Strongly type-II superconductors

Investigating the Meissner state of a strongly type by LEM μSR allows one to directly determine the penetration depth. The study is performed by applying a field below H_{c1} and parallel to the surface of a thin superconductor (of say thickness $2d$). If the field decay in the superconductor is exponential and follow Eq. 6.13, one expects a field profile in the superconducting layer given by

$$B(\ell) = B_{\text{ext}} \frac{\cosh(\dfrac{d - \ell}{\lambda})}{\cosh(\dfrac{d}{\lambda})} \quad . \tag{7.6}$$

For a determination of the penetration depth, one performs separated measurements by varying the kinetic energy of the muon (and therefore varying their implantation depth) and by measuring each time the mean field seen by the muon ensemble.[3] Figure 7.15 exhibits the measurements performed on thin film of the high-T_c superconductor $YBa_2Cu_3O_{7-\delta}$ which provided the *first* confirmation of the exponential decay of the applied field below the surface of a superconductor.
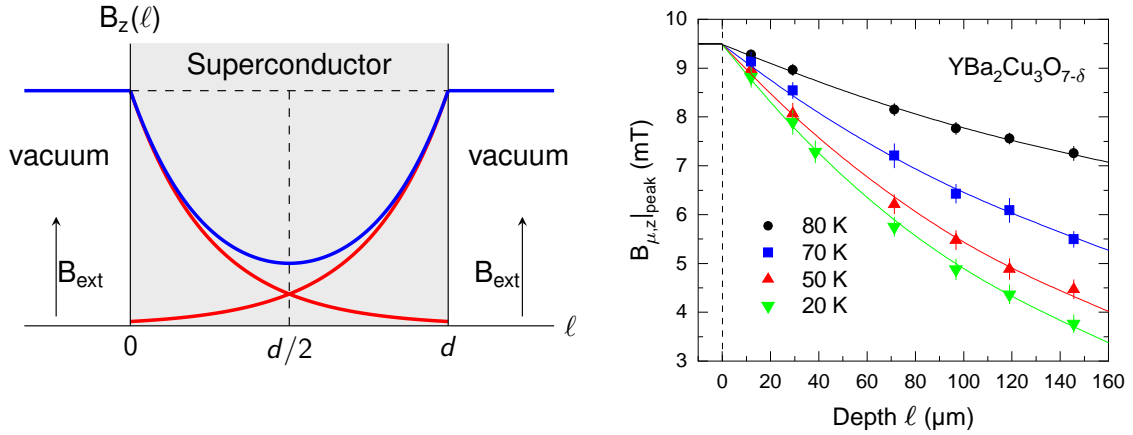
Figure 7.15.: *Left panel: difference between the field profile in a thin super-conductor (thickness 2d) obtained by assuming a field penetration from solely one side (red curve; Eq. 6.13) and the one obtained by assuming correctly that the field penetrates from both sides (blue line; Eq. 7.6). The penetration depth is taken here as $\lambda = d/2$. Right panel: Values of field versus depth extracted from LEM μSR on a thin film of the high-T_c superconductor $YBa_2Cu_3O_{7-\delta}$. Note that here we assume that all the muon stop at the same ℓ, taken as the maximum of the curves shown on Fig. 7.14. The different curves represent various values of sample temperature 20 K, 50 K, 70 K, and 80 K (from bottom to top). The solid lines represent fits of Eq. 7.6 to the data with λ as the free parameter ($d = 350$ nm). The value of ℓ has been corrected by a small quantity ℓ_0, corresponding to a "dead layer". This may partly be due to a thin layer that is non-superconducting, but arises mainly from the surface roughness of the film, which increases the effective penetration depth in the surface layers. From Ref. [113].*

---

[3] Note that if we just consider the mean value, we assume that all the muons stop at the same position [corresponding to $n(\ell, E_{\text{kin}})$ being a delta-function at a given ℓ for a given E_{kin}].

7.5.1.2. Weak type-II superconductors and type-I superconductors

For those superconductors, the coherence length of the Cooper pair cannot be neglected. For those systems, Pippard [114] obtained the penetration depth on the basis of a non-local electromagnetic response of the superconductor. The underlying idea is that the quantum state of the electrons forming the superfluid cannot be arbitrarily localized (the Cooper pair size is actually given by ξ).

The intrinsic non-locality originates in the fact that superconductivity is carried by Cooper pairs formed by two electrons that can be very far apart (up to several hundreds of nanometers), while intuitively the current density $\mathbf{j}(\mathbf{r})$ is better associated with the displacement of their centers of gravity. From the London's second equation (Eq 6.6) and remembering that the magnetic field is given by the vector potential ($\mathbf{B} = \nabla \times \mathbf{A}$), we can write the relation between the current and the field in the London local model as

$$\mathbf{j}(\mathbf{r}) = -\frac{1}{\mu_0 \lambda^2}\mathbf{A}(\mathbf{r}) \ . \tag{7.7}$$

Pippard as shown that for the non-local case, one has to replace this Equation by the non-local one

$$\mathbf{j}(\mathbf{r}) = -\frac{1}{\mu_0}\frac{3}{4\pi\xi\lambda^2}\int\left(\frac{\boldsymbol{\rho}(\boldsymbol{\rho}\cdot\mathbf{A}(\mathbf{r}'))}{\rho^2}\right)\left(\frac{1}{\rho^2}e^{-\rho/\xi}\right)d^3r' \ . \tag{7.8}$$

This Equation reflects the fact that one should use some averaging, taking into account the values of $\mathbf{A}$ where the electrons actually are. The first bracket in the integral expresses the projection of the vector $\mathbf{A}(\mathbf{r}')$ on the direction $\boldsymbol{\rho} = (\mathbf{r}' - \mathbf{r})$, whereas the second bracket represents the weighting of $\mathbf{A}(\mathbf{r}')$ in the integral. This weight decreases exponentially with the distance between $\mathbf{r}$ and $\mathbf{r}'$, with characteristic length ξ. The special form of this equation was motivated by an earlier non-local generalization of Ohm's law.

If $\mathbf{A}$ does not change appreciably on the scale of ξ, the local London equation is recovered[4] On the other side, for conventional type-I superconductors ξ is much larger than λ. Then $\mathbf{A}$ drops to zero on a length scale of $\lambda \ll \xi$. According to Pippard's equation (7.8), the electrons respond to the vector potential averaged over regions of size ξ. This averaged field is much smaller than $\mathbf{A}$ at the surface so that the screening current $\mathbf{j}$ is strongly reduced and the magnetic field penetrates much deeper than predicted by the London theory, *i.e.*[5] $\lambda_{\text{eff}} \gg \lambda$. Also the shape of $B(\ell)$ will be rather different than the exponential behaviour of the local case: initially $B(\ell)$ will decrease slowly and have a negative curvature, *i.e.* a deviation from the exponential behavior. Also one expects to even have a sign reversal of the magnetic field before returning to zero. As said, in the non-local case the Cooper pairs are very extended

---

[4]If $\mathbf{A}$ does not change appreciably, it can extracted from the integral. At this point since $\mathbf{j}$ is a vector depending on a single vector $\mathbf{A}$, both remaining vectors $\boldsymbol{\rho}$ have to be projected to $\mathbf{A}$ and one has to solve an integral

$$\int_0^{2\pi}\int_0^{\pi}\int_0^{\infty}\frac{\rho^2\cos^2\theta}{\rho^4}e^{-\rho/\xi}\sin\theta\,\rho^2 d\rho d\theta d\phi \ .$$

[5]Note that here we assume that λ is the London penetration depth given by Eq. 6.7.

compared to the magnetic penetration profile and the electrons of a Cooper pair do not sense the same field, leading to a screening response which is less effective (the slope is less steep compared to a local response). This has a second effect: since the field penetrates deeper, at some depth enough Cooper pairs will experience it and start to "overcompensate", leading to the negative curvature as well as to the field reversal of $B(\ell)$ before approaching zero.
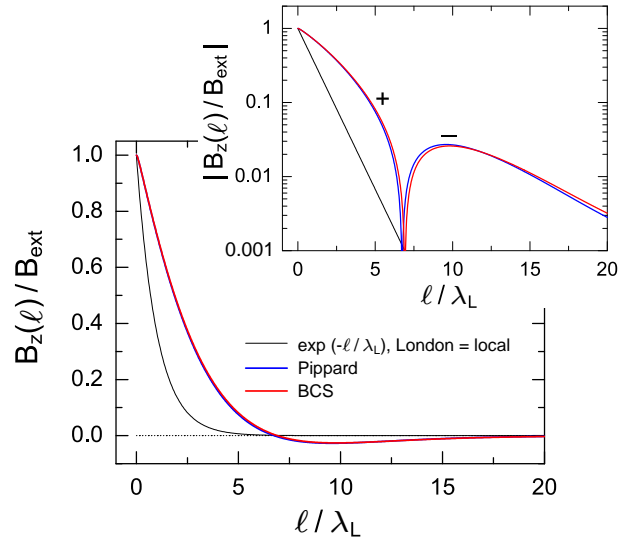
Figure 7.16.: *Magnetic penetration profile in the Meissner state of aluminum according to the usual local model (Equation $B(\ell) = B_{ext}\exp(-\ell/\lambda)$) and the non-local model (Pippard and BCS approach).*
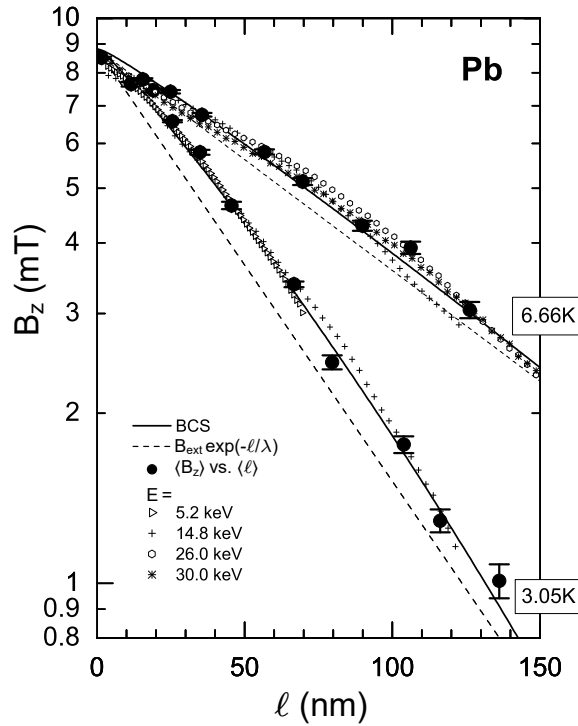
Figure 7.17.: *Magnetic penetration profiles for Pb at various temperatures. The dashed line represents $B(\ell) = B_{ext}$. Taken from Ref. [115].*

7.5.2. Giant proximity effect in cuprate heterostructures

By directly mapping the magnetic field profile in cuprate heterostructures, it is possible to probe the diamagnetic Meissner response of non-superconducting cuprate barrier layers, when they are brought in close contact with superconducting layers. Generally the adjacency of materials with different electronic properties gives rise to reciprocal influence. For instance, if a thin normal metal layer is brought in close contact with a superconducting layer, in the interface region Cooper pair can enter the normal layer. The layer may become superconducting and at the same time superconductivity is weakened in the superconducting layer ("proximity effect").
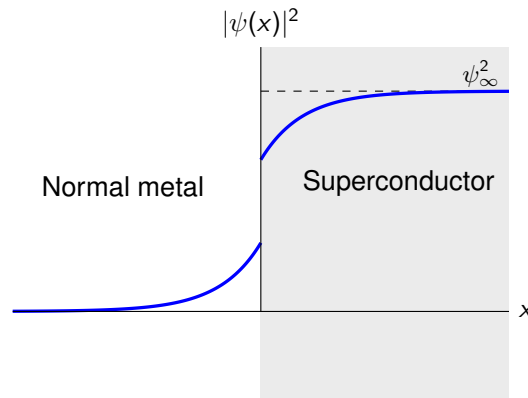
Figure 7.18.: *Normal-superconducting bilayer, showing qualitatively the order parameter and the proximity effect.*

In cuprates the proximity effect is non-conventional due to the anomalous "normal" (metallic) state above the critical temperature T_c of high-temperature-superconducting cuprates which features a pseudogap in the density of states and unexpected charge and spin responses.

The results of $B(\ell)$ are shown on Fig. 7.19 for heterostructures consisting of three layers, each 46 nm thick. Optimally doped $La_{1.84}Sr_{0.16}CuO_4$ ($T_c \simeq 32$ K) was used for the top and the bottom "electrodes", whereas underdoped $La_{1.94}Sr_{0.06}CuO_4$ ($T'_c < 5$ K) served as the "barrier". The barrier with a low T'_c offers a broad temperature interval to search for putative long-range proximity effects. Similar results have been obtained with 32 nm thick barriers. The main result is as follows: At 10 K, 15 K and 17 K - that is, well above T'_c - the local field is lower than the applied field at all depths, meaning that the entire heterostructure excludes the magnetic flux like a conventional superconductor. The profile has the form of an exponential field decay in the Meissner state with the flux penetrating from both sides (Eq. 7.6) and looks like that for two superconductors with different magnetic penetration depths. The observed field profile reflects the shielding supercurrent. This is unexpected when one recalls that in this geometry the supercurrent must pass through the "barrier" $La_{1.94}Sr_{0.06}CuO_4$ region that is 46 nm thick.
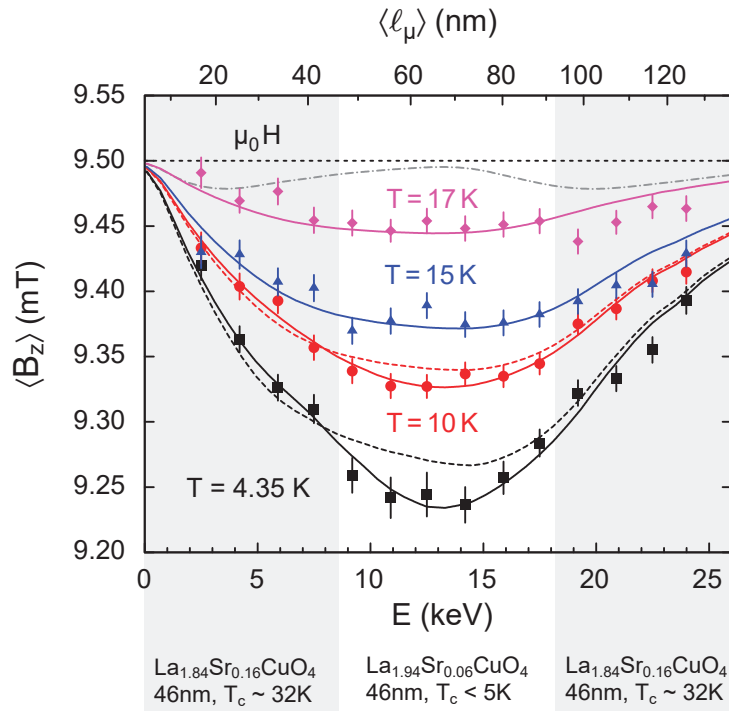
Figure 7.19.: *Depth profile of the local field in a cuprate heterostructure at different temperatures. The vertical lines indicate the position of the interfaces of the $La_{1.84}Sr_{0.16}CuO_4$ (46 nm)/$La_{1.94}Sr_{0.06}CuO_4$ (46 nm)/$La_{1.84}Sr_{0.16}CuO_4$ (46 nm) heterostructure. The horizontal dashed line shows the applied field of 9.5 mT. Points: measured average fields. The entire heterostructure excludes the magnetic flux like a superconductor: it shows the Meissner effect with the central layer active in the screening. This functional form can only be observed if shielding supercurrents flow across the underdoped barrier. The lines are obtained from fits using a London model. The fit takes into account the energy-dependent muon stopping profiles, which are also used to calculate the average stop depth $\langle \ell_\mu \rangle$ (upper scale). From Ref. [116].*
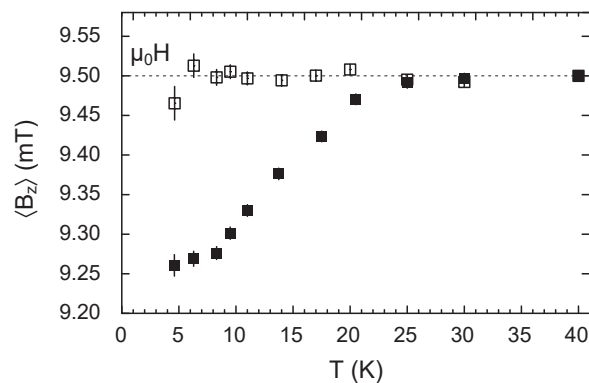
Figure 7.20.: *Temperature dependence of the field measured at the center of the underdoped layer acting as a barrier with thickness of 46 nm in the trilayer (filled symbols). The open symbols are measurements on a single underdoped sample. In the first case the average local field has a diamagnetic shift up to $T_{eff} \simeq 22$ K. Above this temperature its value is within the experimental error equal to the applied field. No shift is observed for a single underdoped layer.*

The conventional proximity theory in which the depth of penetration of Cooper pairs into a normal metal is given by the induced coherence length ξ_N cannot account for this observation. In the usual situation, where the electron-electron interaction goes to zero in the normal state, one has $\xi_N = \hbar v_F/(2\pi k_B T)$ in the clean limit and $\xi_N = [l\hbar v_F/(2\pi k_B T)]^{1/2}$ in the dirty limit, where l is the mean free path and v_F is the Fermi velocity. For $T > 8$ K, this gives a coherence value of the order of 1 nm, *i.e.* much smaller than the barrier thickness of 46 nm. Several models (existence of local superconducting clusters, quenching of phase fluctuations by the presence of adjacent layers with long-range phase order) have been proposed that are able to provide an enhanced length scale of the proximity effect.

7.5.3. Probing the spin injection in an organic spin valve

Recently great efforts have been undertaken to use the spin degree of freedom in electronic devices. The most common method for using the spin in devices is based on the alignment of the electron spin ('up' or 'down') relative to either a reference magnetic field or the magnetization orientation of a ferromagnetic layer. Device operation normally proceeds with measuring a quantity such as the electrical current that depends on how the degree of spin alignment is transferred across the device. The so-called 'spin valve' is a prominent example of such a spin-enabled device.

Lately, the use of organic materials in spintronics has attracted significant interest, primarily due to their ease and small cost of processing as well as electronic and structural flexibility. Spin valves consist essentially of two ferromagnetic layers which can be magnetized parallel or antiparallel to each other and a barrier layer. One of the ferromagnetic layer is considered as fixed ("hard" layer) and the other one is magnetically soft and its magnetization direction can be switched. When the ferromagnetic layers are antiparallel the electrical resistance is higher than when they are aligned due to the "giant magnetoresistive effect".[6] One of the key parameter characterizing a spin-valve is the spin-diffusion length. Its determination is difficult and the only practical way of accessing the spin diffusion in organic spin devices is by measuring the magnetoresistance but the determination of the spin diffusion length is here rather indirect.

An organic spin valve is an example of heterostructure studied with LEM μSR, which is also a prototype device. We describe here a way to determine the spin diffusion length by LEM μSR (see Ref [117] for details).

The principle of the determination of the spin-diffusion length by LEM μSR is as follows:

- As the coercive field is stronger in FeCo than in NiFe, one can prepare with an external field the top and bottom ferromagnetic layer in 4 different states.

- Spins are injected from the top (and bottom) layers into the spin valve by applying a small voltage across the structure. These spins have long spin coherence time of more than 10^{-5} s which is much long than the muon-lifetime.

---

[6] A. Fert and P. Grünberg won the Nobel prize in 2007 for the discovery of this effect.

- These injected spins give rise to a static, at least from the muon point of view, electronic polarization $\langle \mathbf{S}_z(\ell) \rangle$. In the organic material, this will produce a static field $\mathbf{B}_{\mathrm{spin}}(\ell) \propto \langle \mathbf{S}_z(\ell) \rangle$. This local field will add (or substract) to the external field $\mathbf{B}_{\mathrm{ext}}$ used to select the spin valve state.

- The muons will detect the field $B_\mu = B_{\mathrm{ext}} \pm B_{\mathrm{spin}}(\ell)$ at different depths in function of their kinetic energy.

- The field distribution $f(B_\mu)$ is obtained from the Fourier transform of the μSR signal.

- $B_{\mathrm{spin}}(\ell)$ can be determined by switching on/off the injection with current (voltage) and by changing its sign with respect to the external field, *i.e.* by reversing the magnetization of the NiFe electrode.
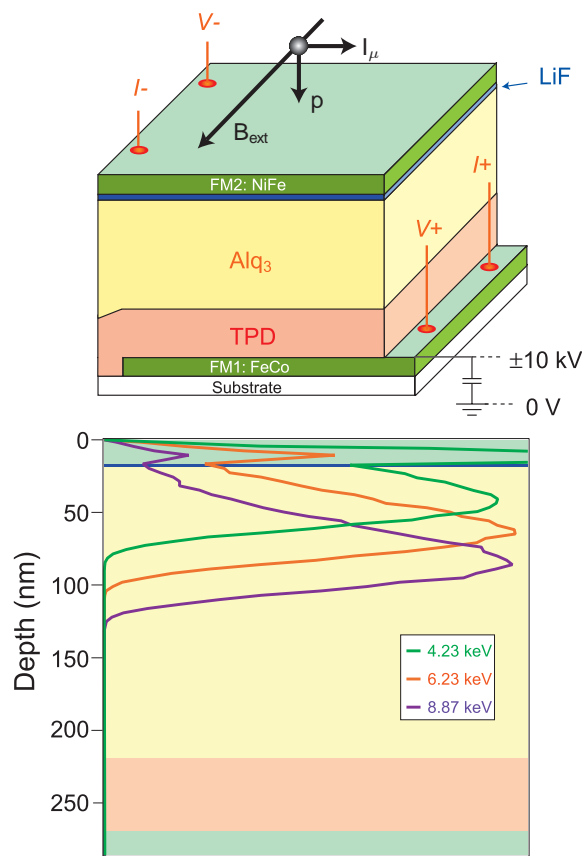
Figure 7.21.: *Top: A schematic diagram showing the structure of our device. The layers FM1 and FM2 and the two ferromagnetic layers. Bottom: Depth profile showing the calculated probability that a positively charged muon with an implantation energy of 4.23, 6.23 or 8.87 keV (green, orange or purple line) comes to rest at a certain depth within the device (so-called stopping or implantation profile). Taken from Ref. [117].*
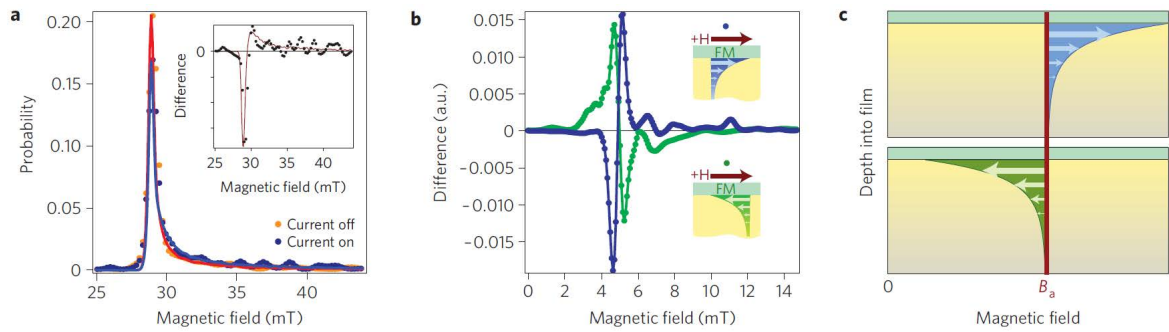
Figure 7.22.: *a) The distribution of magnetic fields for the implantation energy of 6.23 keV and an applied magnetic field of 29 mT. The data with a current density of 0 and 3 mA/cm^2 are shown in red and blue, respectively. The circles show the experimentally measured data that exhibit a small but significant difference between current-on and -off. Inset: The difference between the two data sets. b) The difference between the experimentally measured distribution of magnetic fields with the injection current on and off, for an applied field of 5 mT. The blue and green lines show different configurations, where the direction of the external field with respect to the spin polarization of the injected charge carriers is either parallel or antiparallel. It is clear that when in the parallel configuration, the current-on lineshape is skewed to higher magnetic fields, whereas in the antiparallel configuration, the current-on lineshape is skewed to lower magnetic fields. c) Schematic diagram of the two cases reported in b) showing the expected spatial distributions of local magnetic field in the organic layer for both configurations. When the spins of the injected charge carriers are aligned (anti-aligned) with respect to the applied field, the μSR lineshape is skewed to the higher (lower) fields. Taken from Ref. [117]*
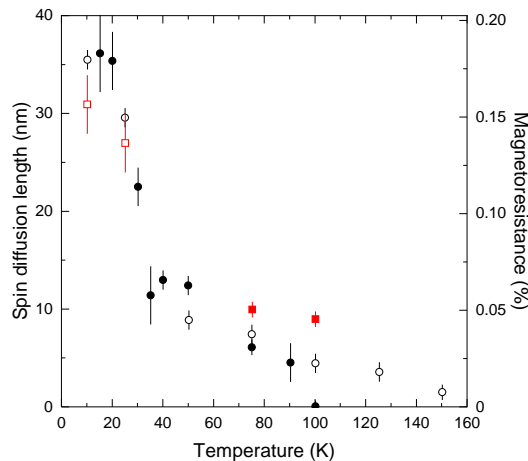
Figure 7.23.: *Temperature dependence of the spin diffusion length extracted from the muon measurements (red, two different samples indicated by the squares and circles) plotted together with the temperature dependence of magnetoresistance (black symbols) for a further two different samples (indicated by the open and filled triangles), where there is clearly a qualitative agreement between the macroscopic and microscopic techniques. Inset: The same magnetoresistance data plotted on a linear scale. Taken from Ref. [117]*

8. Muonium

8.1. Introduction

Muonium is a true light hydrogen isotope made up of an antimuon (*i.e.* μ^+) and an electron, which was discovered in 1960 [118]. It has the chemical symbol Mu. It possesses similar Reduced Mass, Bohr Radius and Ionisation Energy to the hydrogen atom. It is particularly interesting for spectroscopic investigations because:

- It is a simple, pure leptonic system.

- It is only sensitive to weak, electromagnetic interaction, and gravitation.

- The μ^+ is a point like particle (from scattering experiments: dimension $< 10^{-18}$ m $\simeq$ 1/1000 proton radius).

Therefore, it addition to its study in materials, the muonium can be used to test fundamental laws and symmetries and for precision measurements of fundamental parameters.

The main properties of the Muonium are:

Mass: $M_{\mathrm{Mu}} = 0.1131 \times M_{\mathrm{H}} = 207.77 \times M_{\mathrm{e}}$

Reduced Mass: $\bar{M}_{\mathrm{Mu}} = 0.9956 \times \bar{M}_{\mathrm{H}} = \dfrac{M_\mu M_e}{M_\mu + M_e}$

   The reduced mass is the "effective" inertial mass (in our case almost equal to the electron mass) moving in a potential field (see Newtonian mechanics).

Bohr Radius: $a_{\mathrm{Mu}} = 1.0044 \times a_0$

   The classical Bohr radius a_0 is determined by considering in a classical Bohr model (for $n = 1$) that the Coulomb force is the centripetal force *i.e.*
   $$\frac{M_e v^2}{r} = \frac{e^2}{4\pi\epsilon_0 r^2}$$
   and taking into account that the angular momentum is quantized: $L = r M_e v = n\hbar$

Ionisation Energy: $R_{\mathrm{Mu}} = 0.9956 \times Ry = 0.9956 \times \left(-\dfrac{\bar{M}_e\, e^4}{(4\pi\epsilon_0)^2 2\hbar^2} \right) = -13.54$ eV

8.2. Muonium ground state and hyperfine interaction

8.2.1. Ionisation energy

In Section 5.1.1, we have already treated the interaction muon-electron and we will concentrate here on the main points relevant for the muonium.

As in the hydrogen atom, and if we ignore in a first step all spin-coupling interactions, the Hamiltonian of the muonium is the radial kinetic energy operator and Coulomb attraction force between the positive muon and negative electron. The Hamiltonian is in a first step given by the spin-free Hamiltonian $\hat{\mathcal{H}}_0$ of the Eq. 5.3. The Coulomb force is given by $F = -e^2/(4\pi\epsilon_0 r^2)$ and since the attraction is a central force, the potential energy is related to the force by $F = -dV(r)/dr$ and therefore $V(r) = -e^2/(4\pi\epsilon_0 r)$. The Hamiltonian $\hat{\mathcal{H}}_0$ is therefore[1]

$$\hat{\mathcal{H}}_0 = \frac{\mathbf{p}^2}{2\bar{M}_{\mathrm{Mu}}} + V(r)$$
$$= -\frac{\hbar^2}{2\bar{M}_{\mathrm{Mu}}}\nabla^2 - \frac{e^2}{4\pi\epsilon_0 r} \quad , \tag{8.1}$$

where we have written the momentum operator as $\mathbf{p} = -i\hbar\nabla$. Using the time-independent Schrödinger equation , we can therefore write

$$\left(-\frac{\hbar^2}{2\bar{M}_{\mathrm{Mu}}}\nabla^2 - \frac{e^2}{4\pi\epsilon_0 r}\right)\psi(r,\theta,\phi) = E\psi(r,\theta,\phi) \quad . \tag{8.2}$$

The solution is found by expanding the Laplacian in spherical coordinates and the solutions can be expressed with generalized Laguerre polynomials of degree $(n-\ell-1)$, and and with the spherical harmonic functions of degree ℓ and order m_S.

For the ground state level (with main quantum number $n = 1$ and $\ell = 0$) one obtains the following wave function and energy level

$$\psi_{1s}(r) = \frac{1}{\sqrt{\pi a_{\mathrm{Mu}}^3}}\exp\left(-\frac{r}{a_{\mathrm{Mu}}}\right) \tag{8.3}$$

$$E_{1s} = -\frac{\bar{M}_{\mathrm{Mu}}\, e^4}{(4\pi\epsilon_0)^2 2\hbar^2} = -13.54\ \mathrm{eV} \quad . \tag{8.4}$$

This energy level is the energy that one needs to ionize the muonium.

---

[1]The Hamiltonian $\hat{\mathcal{H}}_0$ contains the reduced mass of the system muon-electron (which is almost identical to the electron mass) as it should. In the Eq. 5.3 it was approximated by the electron mass.
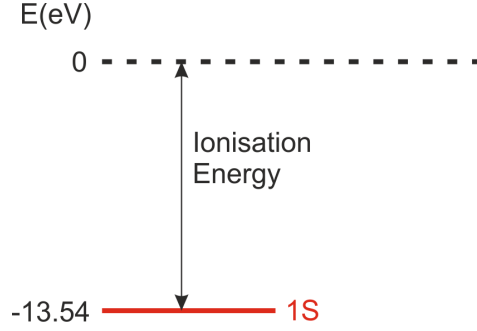
Figure 8.1.: *Schematics of the ionization energy for the electron in the ground state* 1s.

8.2.2. Hyperfine interaction

We have now to introduce the effect of the spins. As before, we have already treated this aspect in Section 5.1.1 and wrote the spin-Hamiltonian in Eq. 5.4. If we consider the electron in the 1s state, having a wave-function given by Eq. 8.3 the probability density of the electron around the muon will be isotropic. Therefore, the averaging of the dipolar part in Eq. 5.4 over the spherical distribution of the electron in the 1s orbital will vanish. The same for the orbital field and the only term to take into account is the contact term as the probability density of the electron at the muon position is finite. Therefore, the spin-part of our Hamiltonian is given by Eqs. 5.15 and 5.16 and is

$$
\begin{aligned}
\hat{\mathcal{H}}' &= \hat{\mathcal{H}}'_{\text{cont}} \\
&= \frac{2\mu_0}{3} g_e \mu_B g_\mu^* \mu_N |\psi_{1s}(0)|^2 \, \mathbf{I}_\mu \cdot \mathbf{S} \\
&= A \, \mathbf{I}_\mu \cdot \mathbf{S} \ .
\end{aligned}
\tag{8.5}
$$

The parameter A is called the "hyperfine interaction constant". Using the wave function for the 1s state (Eq. 8.3) we have

$$
|\psi_{1s}(0)|^2 = \frac{1}{\pi a_{\text{Mu}}^3} \ .
\tag{8.6}
$$

In Eq. 8.5, we have "extracted" the $\hbar$ constants from the spins-operators, so to express A in energy units. We have therefore

$$
\begin{aligned}
A &= \frac{2\mu_0}{3} g_e \mu_B g_\mu^* \mu_N |\psi_{1s}(0)|^2 \\
&= \frac{2\mu_0}{3} \hbar^2 \gamma_e \gamma_\mu \frac{1}{\pi a_{\text{Mu}}^3} \\
&= \hbar \, \omega_0 \ \text{with} \ \omega_0 = 2\pi \times 4463 \ \text{MHz.}
\end{aligned}
\tag{8.7}
$$

We must now find the eigenstates and eigenvalues of the contact Hamiltonian. This is a typical example of system with two identical spins. The correct mathematical way to obtain

them is the usual one leading to calculate the matrix elements of the Hamiltonian in a chosen base (we present this in the next Section 8.2.3 for the case with field). We can here start from a more hand-waiving approach.

By writing the total spin of the muonium as[2] $\mathbf{F} = \mathbf{I}_\mu + \mathbf{S}$, we can see that the states $|\uparrow_\mu\uparrow_e\rangle$, $|\downarrow_\mu\downarrow_e\rangle$, $|\downarrow_\mu\uparrow_e\rangle$ and $|\uparrow_\mu\downarrow_e\rangle$ (that we call the "Zeeman" states) are not eigenstates of $\mathbf{F}^2$, but are eigenstates of F_z, the total z-component of the total spin. We see that the possible eigenvalues of F_z on these states are $+1$, 0 (twice) and -1. Since we have a state with $m_F = +1$ and no state with higher m_F we must have a triplet $F = 1$ and therefore also a singlet with $F = 0$. With this is mind, we have to find the eigenstates which are also appropriate for $\mathbf{F}^2$. We can already deduce that we have for

$$
\begin{aligned}
m_F = 1 \quad &: \text{ one eigenstate:} \qquad\qquad\qquad |\uparrow_\mu\uparrow_e\rangle \\
m_F = 0 \quad &: \text{ two eigenstates composed by: } |\uparrow_\mu\downarrow_e\rangle \text{ and } |\downarrow_\mu\uparrow_e\rangle \\
m_F = -1 &: \text{ one eigenstate:} \qquad\qquad\qquad |\downarrow_\mu\downarrow_e\rangle
\end{aligned}
$$

We can form linear combinations of the states $|\uparrow_\mu\downarrow_e\rangle$ and $|\downarrow_\mu\uparrow_e\rangle$, where we choose the appropriate weights[3] $1/\sqrt{2}$ for normalization, which are eigenstates to the quantum numbers $F = 1$ and $F = 0$

We find a triplet of states $|F, m_F\rangle$, belonging to the spin quantum number $F = 1$, with magnetic spin quantum numbers $m_F = -1, 0, 1$

$$
\begin{aligned}
|1, -1\rangle &= |\downarrow_\mu\downarrow_e\rangle \\
|1, 0\rangle &= \frac{1}{\sqrt{2}}\left(|\uparrow_\mu\downarrow_e\rangle + |\downarrow_\mu\uparrow_e\rangle\right) \\
|1, 1\rangle &= |\uparrow_\mu\uparrow_e\rangle
\end{aligned}
\tag{8.8}
$$

and a singlet with quantum numbers $F = 0$ and $m_F = 0$

$$
|0, 0\rangle = \frac{1}{\sqrt{2}}\left(|\uparrow_\mu\downarrow_e\rangle - |\downarrow_\mu\uparrow_e\rangle\right) \quad . \tag{8.9}
$$

Note that we could have also calculated the state $|1, 0\rangle$ by applying the lowering operator F_- to the $|\uparrow_\mu\uparrow_e\rangle$ state.

We can now calculate the eigenvalues of the Hamiltonian of Eq. 8.5 noting that $\mathbf{F}^2 = \mathbf{I}_\mu^2 + \mathbf{S}^2 + 2\,\mathbf{I}_\mu\cdot\mathbf{S}$ (as $\mathbf{I}_\mu$ and $\mathbf{S}$ commute) and the energy levels are given by

$$
E_F = \frac{A}{2}\left[F(F+1) - I_\mu(I_\mu+1) - S(S+1)\right] \tag{8.10}
$$

---

[2] Of course, the sum of angular momenta is an angular momentum acting in the appropriate complex vector space. Each angular momentum is defined on a different vector space (say V_i), but the sum is defined in the tensor product of the vector spaces $V_1 \otimes V_2$. In other words, one should write $\mathbf{F} = \mathbf{I}_\mu \otimes \mathbb{1}_e + \mathbb{1}_\mu \otimes \mathbf{S}$. This is written, for brievity, as $\mathbf{F} = \mathbf{I}_\mu + \mathbf{S}$. The same is true for the spin states as for example $|\uparrow_\mu\uparrow_e\rangle$, which should actually be written as $|\uparrow_\mu\rangle \otimes |\uparrow_e\rangle$.

[3] They are the Clebsch-Gordon coefficients for the addition of two spin 1/2's.

with $I_\mu = 1/2$, $S = 1/2$ and $F = 0$ or 1, and therefore

$$\text{Triplet}: E_{F=1} = \frac{1}{4}A$$
$$\text{Singlet}: E_{F=0} = -\frac{3}{4}A \quad . \tag{8.11}$$
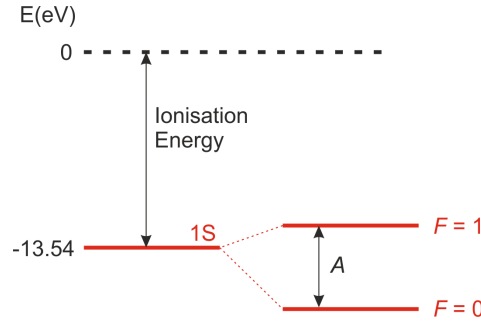
Figure 8.2.: *Schematics of the ionization energy for the electron in the ground state* 1s *with the additional splitting due to the contact interaction. Note that for clarity the splitting is strongly enhanced compared to the ionisation energy* $(A \simeq 18.5 \times 10^{-6} \ eV)$.

Note that the total eigenstates will contain a space contribution (given by Eq. 8.3) and a spin contribution given by the Eqs. 8.8 or 8.9.

8.2.3. Adding an external field

We now look at the muonium response to an externally applied magnetic field. The field will have a Zeeman interaction on both spins and the spin Hamiltonian will acquire two additional terms

$$\hat{\mathcal{H}}'_{\text{tot}} = \hat{\mathcal{H}}' + \hat{\mathcal{H}}'_{\text{Zeeman}}$$
$$= A\, \mathbf{I}_\mu \cdot \mathbf{S} + g_e \mu_{\text{B}}\, \mathbf{S} \cdot \mathbf{B} - g_\mu^* \mu_{\text{N}}\, \mathbf{I}_\mu \cdot \mathbf{B} \quad , \tag{8.12}$$

where the positive sign for the Zeeman interaction on the electron reflects the opposite direction of the spin compared to the one of the magnetic moment. The eigenstates defined by Eqs. 8.8 and 8.9 are no more good eigenstates. To find the eigenvalues of the Hamiltonian, we have first to express its matrix components in a chosen base. The simple choice is to use the "Zeeman" states (see above). We consider that the field is applied along the z-axis and use the fact that we can write

$$\mathbf{I}_\mu \cdot \mathbf{S} = I_{\mu,z} S_z + \frac{1}{2}\left(I_- S_+ + I_+ S_-\right) \quad . \tag{8.13}$$

One obtains the following matrix elements in the Zeeman base

$$\hat{\mathcal{H}}'_{\text{tot},ij} =$$

$$= \begin{pmatrix} \frac{1}{4}\hbar\omega_0 + \frac{1}{2}\hbar\omega_e - \frac{1}{2}\hbar\omega_\mu & 0 & 0 & 0 \\ 0 & -\frac{1}{4}\hbar\omega_0 + \frac{1}{2}\hbar\omega_e + \frac{1}{2}\hbar\omega_\mu & \frac{1}{2}\hbar\omega_0 & 0 \\ 0 & \frac{1}{2}\hbar\omega_0 & -\frac{1}{4}\hbar\omega_0 - \frac{1}{2}\hbar\omega_e - \frac{1}{2}\hbar\omega_\mu & 0 \\ 0 & 0 & 0 & \frac{1}{4}\hbar\omega_0 - \frac{1}{2}\hbar\omega_e + \frac{1}{2}\hbar\omega_\mu \end{pmatrix} , \quad (8.14)$$

where we have taken out $\hbar$ from the spin operators; $\omega_0 = A/\hbar$ as defined in Section 8.2.2; $\omega_e = \gamma_e B_z$ and $\omega_\mu = \gamma_\mu B_z$.

Here again, we have to find the eigenvalues and eigenstates. As shown in your Quantum Mechanics lecture, this is performed using the Equation[4]

$$\sum_j \left(\hat{\mathcal{H}}'_{\text{tot},ij} - E\,\delta_{ij} \right) a_j = 0 \ , \qquad (8.15)$$

where E are the different solutions for the eigenvalues and the a_j describe the development of the spin eigenstates in the base chosen to write $\hat{\mathcal{H}}'_{\text{tot},ij}$ (in this case the Zeeman base). One obtains the following eingenvalues[5]

$$\boxed{\begin{aligned} E_1 &= \frac{1}{4}\hbar\omega_0 + \frac{1}{2}\hbar\omega_e - \frac{1}{2}\hbar\omega_\mu \\ E_2 &= -\frac{1}{4}\hbar\omega_0 + \frac{1}{2}\hbar\left[(\omega_e + \omega_\mu)^2 + \omega_0^2 \right]^{1/2} \\ E_3 &= \frac{1}{4}\hbar\omega_0 - \frac{1}{2}\hbar\omega_e + \frac{1}{2}\hbar\omega_\mu \\ E_4 &= -\frac{1}{4}\hbar\omega_0 - \frac{1}{2}\hbar\left[(\omega_e + \omega_\mu)^2 + \omega_0^2 \right]^{1/2} \end{aligned}}$$

$$(8.16)$$
$$(8.17)$$

We see that if $B_z = 0$, then $\omega_e = \omega_\mu = 0$ and we obtain, as expected, the results found in Section 8.2.2

$$E_1 = E_2 = E_3 = \frac{1}{4}\hbar\omega_0 = E_{F=1}$$

$$E_4 = -\frac{3}{4}\hbar\omega_0 = E_{F=0} \ .$$

We can now use these values and introduce them in Eq. 8.15 to obtain the eigenstates. We have only to concentrate on the 2×2 sublattice of the matrix in Eq. 8.14 and we get the

---

[4]This Equation represents in fact a system of Equations with unknown a_j. This system has a non-trivial solution only when $\text{Det}\left[\hat{\mathcal{H}}'_{\text{tot}} - E\,\mathbb{1}\right] = 0$, which defines the eigenvalues, which are then plugged in Eq. 8.15 to obtain the eigenstates.

[5]Note that we have regrouped the eigenvalues corresponding to the triplet at $B = 0$ (1 to 3) and to the singlet at $B = 0$ (4).

eigenstates[6] (see Exercises)

$$
\begin{aligned}
|\psi_{\text{spin},1}\rangle &= |\uparrow_\mu\uparrow_e\rangle \\
|\psi_{\text{spin},2}\rangle &= \sin\delta|\uparrow_\mu\downarrow_e\rangle + \cos\delta|\downarrow_\mu\uparrow_e\rangle \\
|\psi_{\text{spin},3}\rangle &= |\downarrow_\mu\downarrow_e\rangle \\
|\psi_{\text{spin},4}\rangle &= \cos\delta|\uparrow_\mu\downarrow_e\rangle - \sin\delta|\downarrow_\mu\uparrow_e\rangle \ .
\end{aligned}
\tag{8.18}
$$

where we have defined[7]

$$
\cos\delta = \frac{1}{\sqrt{2}}\left(1 + \frac{\omega_e + \omega_\mu}{\left[\omega_0^2 + (\omega_e + \omega_\mu)^2\right]^{1/2}}\right)^{1/2}
\tag{8.19}
$$

and

$$
\sin\delta = \frac{1}{\sqrt{2}}\left(1 - \frac{\omega_e + \omega_\mu}{\left[\omega_0^2 + (\omega_e + \omega_\mu)^2\right]^{1/2}}\right)^{1/2} \ .
\tag{8.20}
$$

We note that we do note call anymore these state $|F, m_F\rangle$ states as those are good quantum number only in zero field. At zero field $\cos\delta = \sin\delta = 1/\sqrt{2}$, as we expect (see eigenstates defined by Eqs. 8.8 and 8.9), and at high field $\sin\delta \to 0$ and $\cos\delta \to 1$, and we see that at high fields we retrieve the Zeeman states, as the interaction between the spins will be dominated by the field-spins interaction (Paschen-Back limit). Therefore

$$
\begin{aligned}
|\psi_{\text{spin,i}}\rangle \text{ base } &\xrightarrow{B\to 0} |F, m_F\rangle \text{ base} \\
|\psi_{\text{spin,i}}\rangle \text{ base } &\xrightarrow{B\to\infty} \text{Zeeman base}
\end{aligned}
$$

---

[6]Here also we have regrouped the eigenstates for the triplet at $B = 0$ (1 to 3) and for the singlet at $B = 0$ (4). The states 2 and 4 are obtained by diagonalizing the submatrix 2×2.

[7]We have defined here the expansion parameters as a sine and a cosine as for normalization reasons we need $\cos^2\delta + \sin^2\delta = 1$.
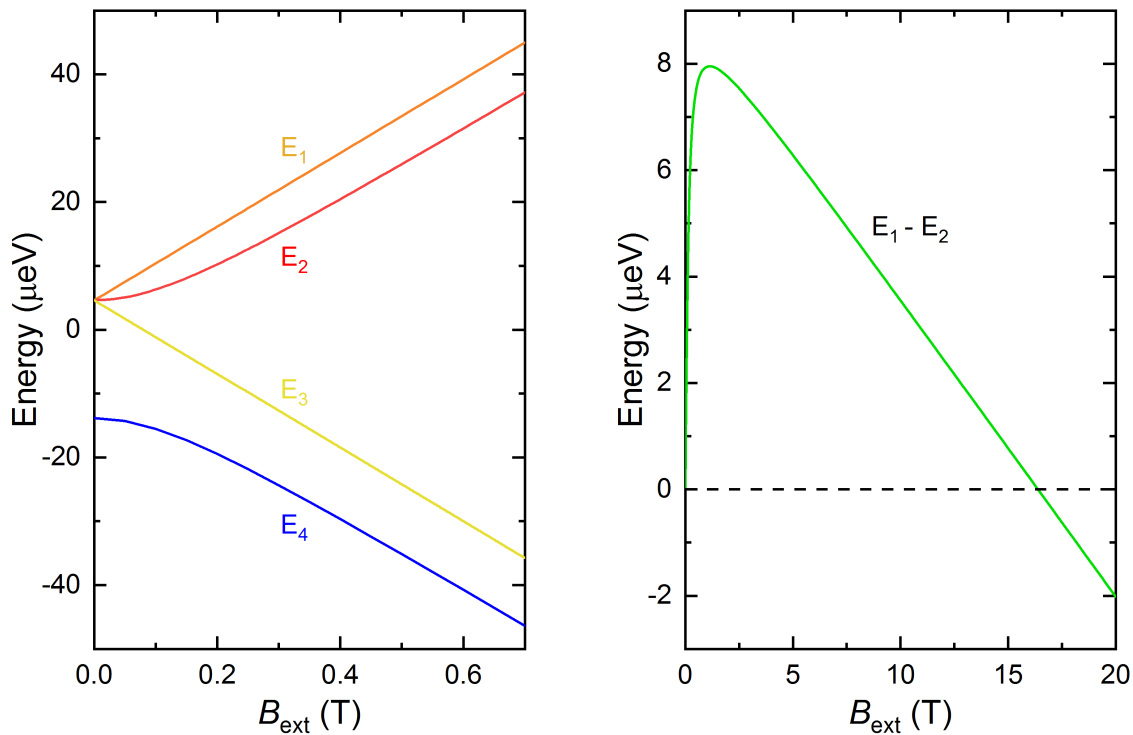
Figure 8.3.: *Left: So-called Breit-Rabi diagram of an isotropic muonium in a magnetic field. In the absence of a magnetic field, the triplet states are degenerate and located at a higher energy than the singlet state. The degeneracy of the triplet states is lifted in the magnetic field. Right: Difference between the energy of the triplet states $m_F = +1$ and $m_F = 0$ is shown. The energy levels E_1 and E_2 cross at about 16.4 T. At very high fields, the most unfavorable state has, as expected, the eigenstate $|\psi_{spin,2}\rangle \rightarrow |\downarrow_\mu\uparrow_e\rangle$, which represents both magnetic moments pointing to the direction opposite to the external field (remember that the spin direction of the electron is opposite to the magnetic moment). Similarly, the most favorable state has the eigenstate $|\psi_{spin,4}\rangle \rightarrow |\uparrow_\mu\downarrow_e\rangle$, which represents both magnetic moments pointing to the direction of the external field.*

8.3. Time evolution of the muon polarization in the muonium state

8.3.1. Introduction

Our task in this Section is to understand the time evolution of the muon polarization in the muonium state.

We start first with the situation at time $t = 0$. We have as before a muon beam which is 100% polarized (say the z-direction) and therefore 100% of the muons are in the state $| \uparrow_\mu \rangle$. The muon is implanted into the sample, where it will pickup an electron to form the muonium. The electron is not polarized and therefore along our quantization z-axis, we have 50% of the electrons in the state $| \uparrow_e \rangle$ and 50% in the state $| \downarrow_e \rangle$. Therefore, we have the following probability to observe these initial states of the muonium:

$$\text{Probability and states:} \quad \begin{cases} 50\% & | \uparrow_\mu \uparrow_e \rangle \\ 50\% & | \uparrow_\mu \downarrow_e \rangle \end{cases} \tag{8.21}$$

In the zero and longitudinal field configuration, the state $| \uparrow_\mu \uparrow_e \rangle$ is eigenstate of the Hamiltonians 8.5 and 8.12 [see the muonium spin eigenstates without field (Eqs. 8.8 and 8.9) and with field applied in this case longitudinally (Eq. 8.18)], and therefore this state will not show any time dependence even when the external field is applied the muon polarization (LF mode). On the other hand the state $| \uparrow_\mu \downarrow_e \rangle$ is not an eigenstate and therefore a time dependence will occur for this state. Intuitively, it is clear that this state will fluctuate between the mixed states $|\psi_{\text{spin},2}\rangle$ and $|\psi_{\text{spin},4}\rangle$ (see Eq. 8.18). The Section 8.3.2 presents the result for the longitudinally applied field.

In the transverse field configuration, both states above (that we call now $| \uparrow_\mu \uparrow_e \rangle_\perp$ and $| \uparrow_\mu \downarrow_e \rangle_\perp$) are not eigenstate as the field defines a quantization axis different from the one of the initial polarization. In this case, we expect that the full polarization will oscillates. The Section 8.3.3 presents the result for the transverse applied field.

Following Annex A.5.1, one can write within the Heisenberg view the time evolution of the muon polarization as

$$\begin{aligned} \mathbf{P}(t) &= \langle \boldsymbol{\sigma} \rangle(t) \\ &= \text{Tr}\left[\rho(0)\boldsymbol{\sigma}(t)\right] \quad . \end{aligned} \tag{8.22}$$

The task is now to find out the representation of the density operator which is a 4×4 matrix in the Hilbert space of the muon and electron spin. If we first concentrate to the muon spin (*i.e.* working in 2 dimensions), we know from Annex A.5.2 that we can write the density matrix for the muon as

$$\begin{aligned} \rho_\mu(0) &= a_0 \cdot \mathbb{1}_\mu + \mathbf{a} \cdot \boldsymbol{\sigma}_\mu \\ &= \frac{1}{2} \cdot \mathbb{1}_\mu + \frac{1}{2} P_{\mu,x}(0)\sigma_{\mu,x} + \frac{1}{2} P_{\mu,y}(0)\sigma_{\mu,x} + \frac{1}{2} P_{\mu,y}(0)\sigma_{\mu,z} \\ &= \frac{1}{2}\left[\mathbb{1}_\mu + \mathbf{P}_\mu(0) \cdot \boldsymbol{\sigma}_\mu\right] \quad . \end{aligned} \tag{8.23}$$

An equivalent form is obtained for the electron

$$\rho_e(0) = \frac{1}{2} \left[\mathbb{1}_e + \mathbf{P}_e(0) \cdot \boldsymbol{\sigma}_e \right] \quad, \tag{8.24}$$

and the total density matrix is

$$\rho(0) = \rho_\mu(0) \otimes \rho_e(0) \quad. \tag{8.25}$$

If we take into account that $\mathbf{P}_e(0) = 0$, then we obtain

$$\rho(0) = \frac{1}{4} \left[\mathbb{1}_\mu \otimes \mathbb{1}_e + \mathbf{P}_\mu(0) \cdot \boldsymbol{\sigma}_\mu \otimes \mathbb{1}_e \right] \quad, \tag{8.26}$$

that we usually write simply as

$$\rho(0) = \frac{1}{4} \left[1 + \mathbf{P}_\mu(0) \cdot \boldsymbol{\sigma}_\mu \right] \quad. \tag{8.27}$$

We know introduce this result in our Eq. 8.22 and we obtain

$$\begin{aligned} \mathbf{P}(t) &= \frac{1}{4} \sum_k \langle k | (1 + \mathbf{P}_\mu(0) \cdot \boldsymbol{\sigma}_\mu) \, \boldsymbol{\sigma}_\mu(t) | k \rangle \\ &= \frac{1}{4} \sum_{k,n} \langle k | 1 + \mathbf{P}_\mu(0) \cdot \boldsymbol{\sigma}_\mu) | n \rangle \, \langle n | \boldsymbol{\sigma}_\mu(t) | k \rangle \quad, \end{aligned} \tag{8.28}$$

where the $|k\rangle$ and the $|n\rangle$ represent the different eigenstates defined in Eq. 8.18. We have now finally to find the matrix elements $\langle n | \boldsymbol{\sigma}(t) | k \rangle$ and we use for that the Heisenberg Equation so that

$$-i\hbar \frac{\mathrm{d}}{\mathrm{d}t} \boldsymbol{\sigma}_\mu(t) = \left[\hat{\mathcal{H}}', \boldsymbol{\sigma}_\mu(t) \right] \quad. \tag{8.29}$$

The solution is

$$\boldsymbol{\sigma}_\mu(t) = \exp(i\hat{\mathcal{H}}'t/\hbar) \, \boldsymbol{\sigma}_\mu \, \exp(-i\hat{\mathcal{H}}'t/\hbar) \quad, \tag{8.30}$$

and therefore we have

$$\langle n | \boldsymbol{\sigma}_\mu(t) | k \rangle = \langle n | \boldsymbol{\sigma}_\mu | k \rangle \, \exp(i\omega_{nk}t) \quad, \tag{8.31}$$

where we have defined

$$\omega_{nk} = \frac{E_n - E_k}{\hbar} \quad. \tag{8.32}$$

We can now calculate the time dependence of the polarization. We use the completeness relation and take into account that $\langle k | 1 | n \rangle = \delta_{kn}$ and that $\sum_{k,n} \delta_{kn} \langle n | \sigma_{\mu,i} | k \rangle = 0$ for $i = x, y, z$. We get

$$\mathbf{P}(t) = \frac{1}{4} \sum_{k,n} \langle k | \mathbf{P}_\mu(0) \cdot \boldsymbol{\sigma}_\mu | n \rangle \, \langle n | \boldsymbol{\sigma}_\mu | k \rangle \cdot \exp(i\omega_{nk}t) \tag{8.33}$$

8.3.2. Longitudinal (and zero) field case

Here we admit that both the field and the initial muon polarization are along the z-direction. We have that $\mathbf{P}_\mu(0) = P_\mu(0)\,\hat{\mathbf{z}}$ (with $P_\mu(0) = 1$) and also $\mathbf{B} = B\,\hat{\mathbf{z}}$. Therefore, $\mathbf{P}_\mu(0)\cdot\boldsymbol{\sigma}_\mu = \sigma_{\mu,z}$. We solve Eq. 8.33 using this and the eigenstates defined in Eq. 8.18 and we find (see Exercices)

$$
\begin{aligned}
P_\mu^z(t) &= \frac{1}{4}\left\{2 + 2\left(\cos^2\delta - \sin^2\delta\right)^2 + 4\cos^2\delta\sin^2\delta\left(e^{i\omega_{24}t} + e^{-i\omega_{24}t}\right)\right\} \\
&= \frac{1}{2}\left\{1 + \left(\cos^2\delta - \sin^2\delta\right)^2 + 4\cos^2\delta\sin^2\delta\cos(\omega_{24}t)\right\} \ ,
\end{aligned}
\tag{8.34}
$$

where we used the definition given by Eqs. 8.19 and 8.20 and

$$
\begin{aligned}
\omega_{24} &= \frac{E_2 - E_4}{\hbar} \\
&= \sqrt{(\omega_e + \omega_\mu)^2 + \omega_0^2} \ .
\end{aligned}
\tag{8.35}
$$

We see that even for a field $B = 0$ we have an oscillating muon polarization. As $\omega_{24,B=0} = \omega_0$ and $\cos\delta \to 1/\sqrt{2}$ and $\sin\delta \to 1/\sqrt{2}$ we can write

$$
P_\mu^z(t, B=0) = \frac{1}{2}\left\{1 + \cos(\omega_0 t)\right\} \ .
\tag{8.36}
$$
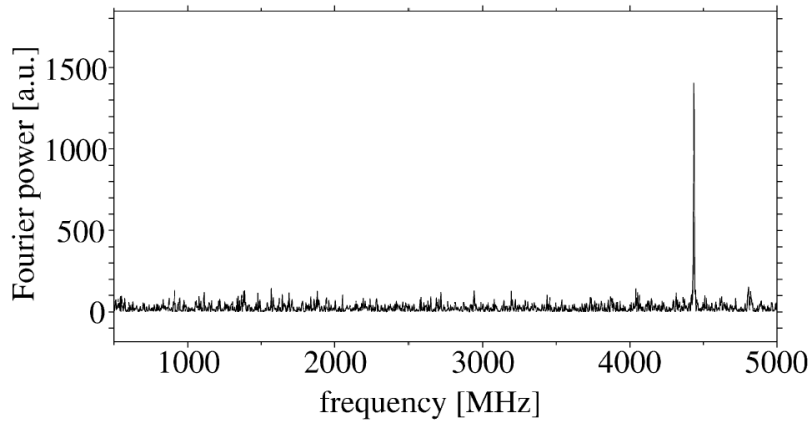
Figure 8.4.: *A zero-field μSR spectrum of quartz at room temperature. The muonium contact field frequency (4.49 GHz) is close to the vacuum value (4.463 GHz). The FWHM time resolution of this experiment is 150 ps. Taken from [119].*

This oscillation is due to the contact field in the muonium state. The angular velocity of the oscillation $\omega_0 = 2\pi \times 4463$ MHz is extremely high and usual μSR instrument cannot detect it. Special instruments, with for example detectors based on SiPMs, can possibly achieve a good enough time resolution (see Fig. 8.4), but conventional instrument cannot. Therefore,

usually, the observable μSR signal for muonium is solely given by the non-oscillatory part, *i.e.*

$$P^z_{\mu,\text{non-osc}}(t, B = 0) = \frac{1}{2} \; . \tag{8.37}$$

This non-oscillatory part will increase, following Eq. 8.34, when a field is applied longitudinally. This reflects that the external field will surpass the internal field due to the contact interaction. Even though one cannot determine directly the hyperfine splitting A between the triplet and the singlet states (*i.e.* corresponding to the angular velocity $\omega_0 = A/\hbar$), we can deduce it from the field at which half of the polarization is recovered [or better, by fitting the whole curve $P^z_{\mu,\text{non-osc}}(t, B)$]. For this field (that we call $B_{1/2}$) we have

$$\left(\cos^2 \delta - \sin^2 \delta \right)^2 = 1/2 \; \text{ and therefore}$$

$$\omega_0 = \omega_e + \omega_\mu = (\gamma_e + \gamma_\mu) B_{1/2} \; . \tag{8.38}$$

It is important to note that the muon polarization is not actually lost in muonium. It can be considered as shared with the electron to an extent that depends on the applied external field. If quantum irreversible processes cause relaxation of the electron spin by interaction with the medium, all the polarization will eventually disappear, but in the simple case described here where the muonium is in vacuum, the muon polarization always returns periodically to its full value.
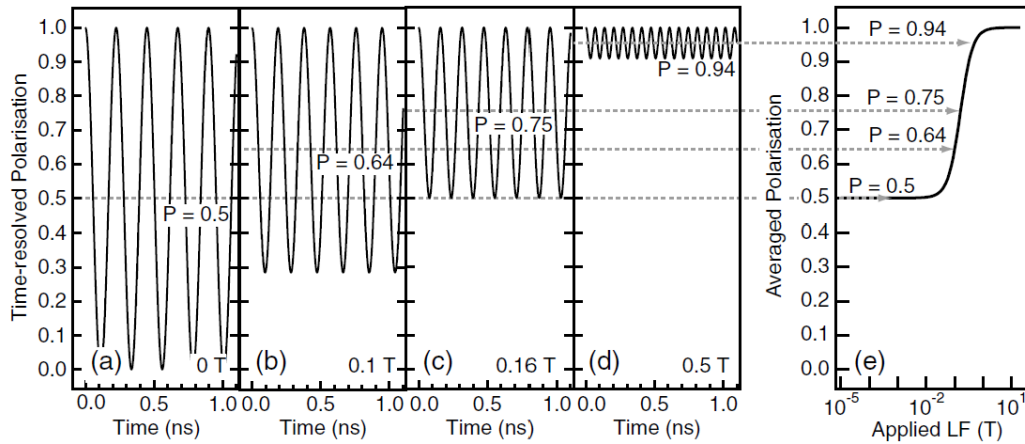
Figure 8.5.: *(a) to (d) μSR signal expected for isotropic vacuum muonium in zero-field and longitudinally applied fields. Note the very short oscillation periods. (e) Corresponding repolarization curve. Taken from Ref. [120].*

8.3.3. Transverse field case

We can now play the same game when we apply a field transverse to the initial muon polarization. That is we admit that, as usual, the field is along the z-direction and that the initial muon polarization is along the x-direction. We have that $\mathbf{P}_\mu(0) = P_\mu(0)\,\hat{\mathbf{x}}$ (with $P_\mu(0) = 1$) and $\mathbf{B} = B\,\hat{\mathbf{z}}$. Therefore, $\mathbf{P}_\mu(0) \cdot \boldsymbol{\sigma}_\mu = \sigma_{\mu,x}$. We again solve Eq. 8.33 using this and the eigenstates defined in Eq. 8.18 and we find

$$P_\mu^x(t) = \frac{1}{2}\left\{\cos^2\delta\left[\cos(\omega_{12}t) + \cos(\omega_{34}t)\right] + \sin^2\delta\left[\cos(\omega_{14}t) + \cos(\omega_{23}t)\right]\right\} \quad . \quad (8.39)$$

Here again, by looking at Fig. 8.3, we see that we cannot detect all the frequencies with the limited time resolution of an usual μSR instrument. We can differentiate few ranges:

- *For very low fields:*
  The frequencies (or better said angular velocities) ω_{14} and ω_{34} are to high to be observed and therefore only the frequencies ω_{12} and ω_{23} are measurable. We have that

$$\omega_{12} \simeq \omega_{23} \equiv \omega_{\text{Mu eff.}} = \frac{1}{2}(\omega_e - \omega_\mu) = \frac{1}{2}(\gamma_e - \gamma_\mu)B \qquad (8.40)$$

  and $\sin\delta = \cos\delta = 1/\sqrt{2}$. The polarization detected in the μSR signal can therefore be written as

$$P_\mu^x(t, B \ll 1) = \frac{1}{2}\cos(\omega_{\text{Mu eff.}}t) \quad . \qquad (8.41)$$

  This means that in very small TF fields (< 0.5 mT), muonium shows only half of the polarization amplitude (corresponding to the precession of the $m_F = \pm 1$ components in the triplet state at $B = 0$). As the gyromagnetic ratio is inversely proportional to the mass and as $M_\mu \simeq 206.77 \times M_e$ (see Table 1.2), the muon spin polarization in this state precesses with a Larmor frequency $\omega_{\text{Mu eff.}} \simeq -103.38 \times \omega_\mu$ (with opposite sense of the precession compare to the one of a "free" muon). As shown in Section 7.4, this allows one to distinguish the charged (μ^+) from the uncharged state (Mu).

  The polarization function $P_\mu^x(t, B \ll 1)$ does not provide any information on the muonium state since $\omega_{\text{Mu eff.}}$ does not depend on a muonium parameter. However, the detection of an oscillation with a precession about two orders of magnitude faster than expected for "free" muon together with a fifty per cent missing fraction is a clear signature of muonium formation.

- *Small fields:*
  Here also, ω_{14} and ω_{34} are to high to be observed and therefore only the frequencies ω_{12} and ω_{23} are measurable. However, we can no more write that $\omega_{12} \simeq \omega_{23}$ and we have

$$P_\mu^x(t, B < 1) = \frac{1}{2}\left\{\cos^2\delta\cos(\omega_{12}t) + \sin^2\delta\cos(\omega_{23}t)\right\} \quad . \qquad (8.42)$$

  Using the beat frequency formula

$$\begin{aligned}
y(t) &= a\cos(\omega_a t) + b\cos(\omega_b t) \\
&= (a+b)\cos\left(\tfrac{\omega_b - \omega_a}{2}t\right)\cos\left(\tfrac{\omega_b + \omega_a}{2}t\right) + (a-b)\sin\left(\tfrac{\omega_b - \omega_a}{2}t\right)\sin\left(\tfrac{\omega_b + \omega_a}{2}t\right) \quad ,
\end{aligned}$$
$$(8.43)$$

we can rewrite

$$P_\mu^x(t, B < 1) = \tfrac{1}{2}\cos\left(\tfrac{\omega_{23}-\omega_{12}}{2}t\right)\cos\left(\tfrac{\omega_{23}+\omega_{12}}{2}t\right) +$$
$$+ \tfrac{1}{2}(\cos^2\delta - \sin^2\delta)\sin\left(\tfrac{\omega_{23}-\omega_{12}}{2}t\right)\sin\left(\tfrac{\omega_{23}+\omega_{12}}{2}t\right) \ , \qquad (8.44)$$

where $(\omega_{23} - \omega_{12})/2$ represents a characteristic beating formula.

As said in the previous Section, if the field is small enough, the eigenstates tend to the $|F, m_F\rangle$ states and the possible transitions correspond to the selection rules[8]

$$\Delta F = 0, \pm 1 \qquad \text{and} \qquad \Delta m_F = \pm 1 \ . \qquad (8.45)$$
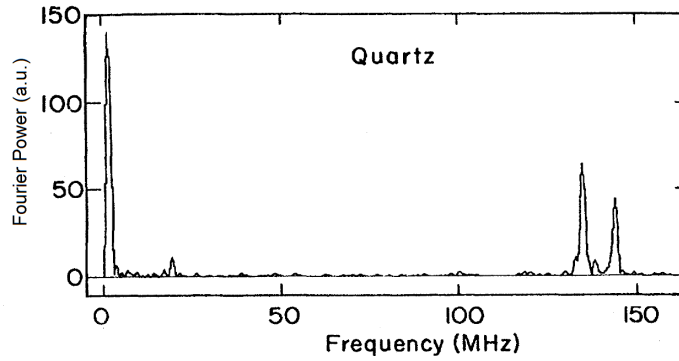
Figure 8.6.: *Transverse-field μSR frequency spectra taken at 10 mT in quartz at room temperature. One can identify the precession components from diamagnetic ("free") muon (at ~ 1.355 MHz) and isotropic muonium (the pair $\nu_{12} = 2\pi \times \omega_{12}$ and $\nu_{23} = 2\pi \times \omega_{23}$ centered on 140 MHz). Taken from Ref. [121].*

- *For high fields:*
  According to Eq. 8.39, only two frequencies can be detected in high field as $\sin\delta \to 0$ and $\cos\delta \to 1$ and we have

$$P_\mu^x(t, B \gg 1) = \frac{1}{2}\left\{\cos(\omega_{12}t) + \cos(\omega_{34}t)\right\} \ . \qquad (8.46)$$

As said in the previous Section, if the field is high enough, the eigenstates tend to the Zeeman states and the possible transitions correspond to the selection rules

$$\Delta m_e = 0, \pm 1 \qquad \text{and} \qquad \Delta m_\mu = 0, \pm 1 \ , \qquad (8.47)$$

which reduces to

$$\Delta m_e = 0 \qquad \text{and} \qquad \Delta m_\mu = \pm 1 \ , \qquad (8.48)$$

if the two high energy transitions (namely between states 1 and 4, and between states 2 and 3) cannot be detected.

---

[8]But usually only the transition with $\Delta F = 0$ are observed corresponding to the frequencies ω_{12} and ω_{23}.
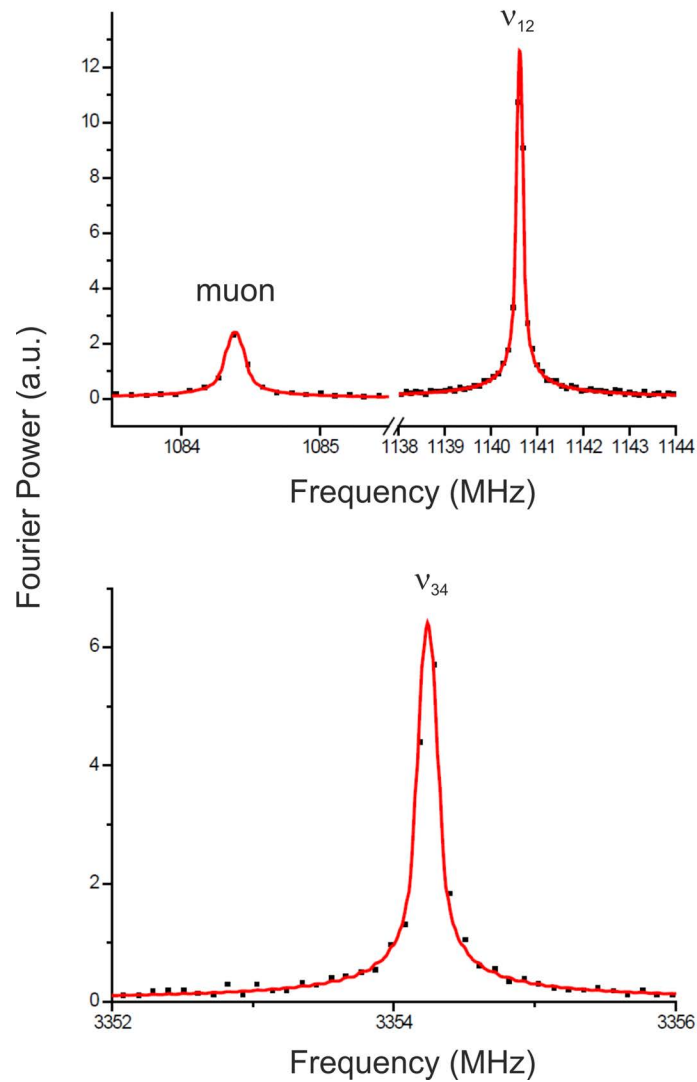
Figure 8.7.: *Breit-Rabi diagram and transitions in a synthetic quartz crystal measured with the HAL-9500 high resolution spectrometer at PSI in a 8 T field. The high-field instrument HAL-9500 uses SiPMs to transform and amplity the scintillator signals. It has a very good time resolution (of the order of 60 ps) allowing one to perform muonium spectroscopy at high field (Robert Scheuermann, private communication).*
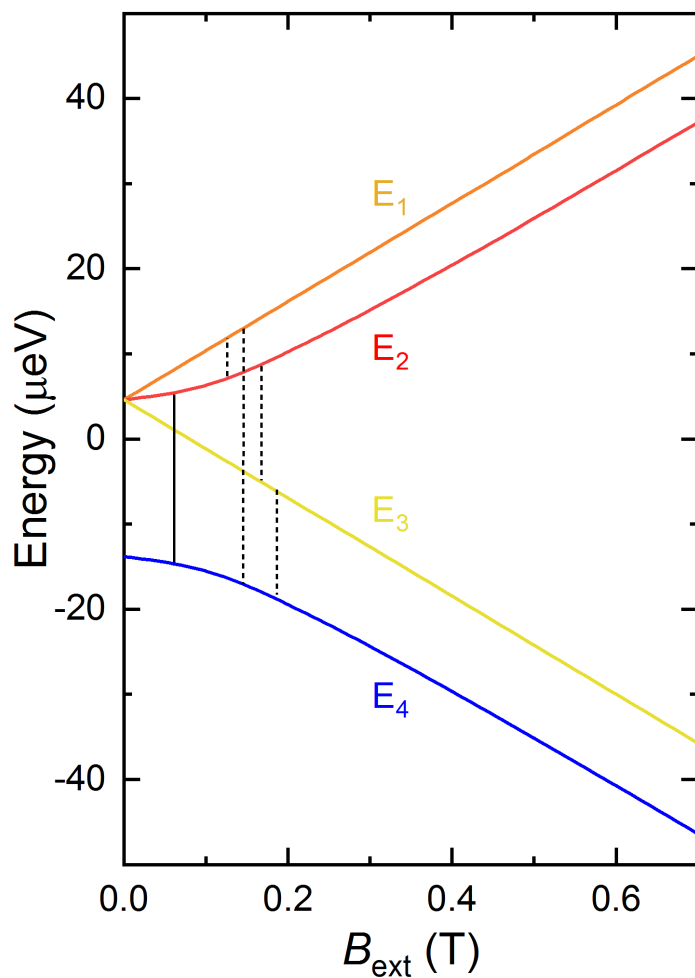
Figure 8.8.: *Breit-Rabi diagram of an isotropic muonium in a magnetic field. The vertical black lines indicate the transitions which are observed in zero- or longitudinal- (full line), and transverse-field (dotted lines) experiments.*

8.4. Few examples of muonium studies

What we have discussed so far is a situation where we have an isotropic muonium state, neglecting its interaction with the environment. Interestingly, this situation is observed not only in vacuum but also in a number of semiconductors, dielectrics and in organic compounds. It is formed when i) the free electron density at the muon site in the material is small enough so that the screening of the Coulomb interaction is weak; and ii) when the point symmetry at the muonium site is high.

In alkali fluorides the hyperfine coupling is slightly higher than in vacuum muonium. This corresponds to a slightly compressed wave function with slightly shorted Bohr radius of the $1s$ state (see Eq 8.6). Generally the hyperfine coupling is smaller. In some semiconductors it is even much smaller than in the free state. For instance in the elementary semiconductors of the group IV the electron spin density at the muon site is only 50% of the value in the free atom.
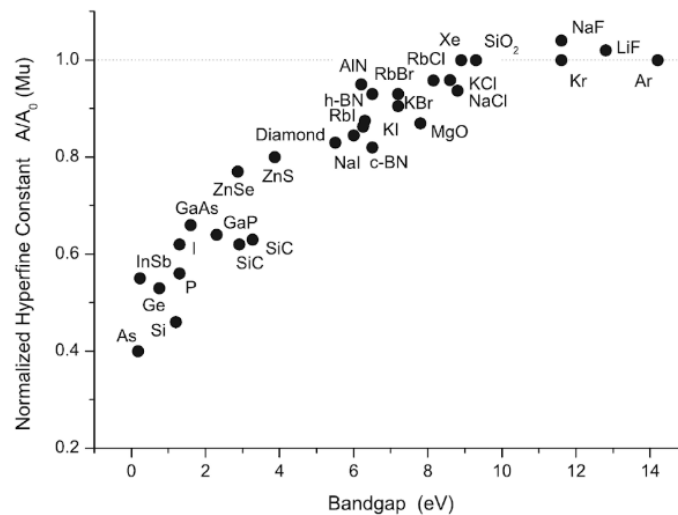
Figure 8.9.: *Hyperfine constant for interstitial muonium in semiconductors and dielectrics. The graph shows the correlation between the hyperfine contact constant normalized to the vacuum value (which represents the spin density at muon site) and the band-gap of host material. Taken from Ref. [122].*

The broad correlation between the hyperfine constant and band-gap value reflects that the muonium retains its atomic character when there is a wide separation between the bonding and anti-bonding orbitals of the host material. When these energy levels are close (narrow gap) this promotes a larger admixture and the atomic character of the muonium is lost.

Hydrogen in the Earth's deep interior is thought to exist in interstitial sites in minerals. For example stishovite is an hard and dense tetragonal form of silicon dioxide. It is very rare on the Earth's surface, but it appears to be a predominant form of silicon dioxide in the Earth, especially in the lower mantle. Positive muon implanted in stishovite was found to capture electron to form muonium. The hyperfine-coupling parameter and the relaxation rate of spin polarization of muonium in stishovite is very large, suggesting that muonium is squeezed

in small interstitial voids without binding to silicon or oxygen. These results imply that hydrogen may also exist in the form of neutral atomic hydrogen in the deep mantle.
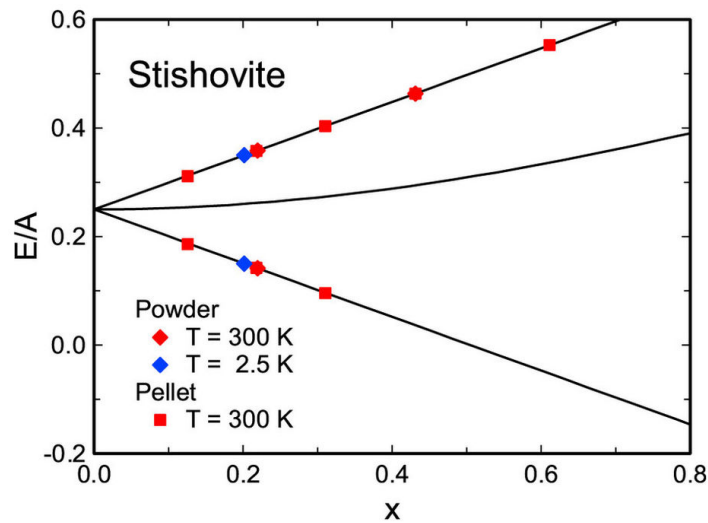
Figure 8.10.: *Energy diagram of muonium in stishovite as a function of applied transverse field. The parameter x denotes the field given as $x = B_{ext}(\gamma_e + \gamma_\mu)/\omega_0$. The three solid lines, in order from top to bottom, represent theoretical values of E_1/A, E_2/A and E_3/A. The data of E_1/A and E_3/A, from left to right, correspond to the measurements at 20, 35, 50, 70, and 100 mT. Taken from Ref. [123].*

A large muonium fraction was found in stishovite as is the case in quartz. Interstitial voids of stishovite, which consists of SiO_6 octahedra, are much smaller than those of quartz, which consists of SiO_4 tetrahedra. Therefore, this suggests that the formation of muonium is not controlled by the size of interstitial voids. The angular velocity ω_0 for muonium in stishovite at 300 K is determined to be 4.67(3) GHz and at 2.5 K it is 5.17(14) GHz. These values are significantly larger than 4.463 GHz for muonium in vacuum and for muonium 4.49(2) GHz in quartz. the hyperfine coupling parameter $A = \hbar\omega_0$ is, as seen in Section 8.2.2, a measure of $1s$ electronic orbital size. Therefore, a very large hyperfine-coupling parameter of muonium in stishovite, which is even larger than that in quartz, suggests that muonium is squeezed in small interstitial voids without binding to silicon or oxygen

8.5. Anomalous muonium and weakly bound muonium

In several semiconductors an additional muonium state has been found with a hyperfine constant which is axially symmetric around the [111] crystal axis. This state is called "anomalous muonium" or "anisotropic muonium" and indicated as Mu*. For this state the Hamiltonian is written as

$$\hat{\mathcal{H}}'_{\text{tot,anom}} = A_{\parallel} I_{\mu,z} S_z + A_{\perp} \frac{1}{2} \left(I_- S_+ + I_+ S_- \right) + g_e \mu_B \, \mathbf{S} \cdot \mathbf{B} - g_{\mu}^* \mu_N \, \mathbf{I}_{\mu} \cdot \mathbf{B} \ , \qquad (8.49)$$

The energy eigenvalues and eigenvectors for Mu* are orientation dependent. However, simple analytical expressions can be obtained in some cases. For example, by applying a field along the [111]-axis (z direction) we have

$$\hat{\mathcal{H}}'_{\text{tot,anom}} = A_{\parallel} I_{\mu,z} S_z + A_{\perp} \frac{1}{2} \left(I_- S_+ + I_+ S_- \right) + g_e \mu_B \, S_z \cdot B_z - g_{\mu}^* \mu_N \, I_{\mu,z} \cdot B_z \ , \qquad (8.50)$$

and the eigenvalues can be calculated as in the isotropic case and one gets

$$E_1 = \frac{1}{4} \hbar \omega_{0,\parallel} + \frac{1}{2} \hbar \omega_e - \frac{1}{2} \hbar \omega_{\mu}$$

$$E_2 = -\frac{1}{4} \hbar \omega_{0,\parallel} + \frac{1}{2} \hbar \left[(\omega_e + \omega_{\mu})^2 + \omega_{0,\perp}^2 \right]^{1/2}$$

$$E_3 = \frac{1}{4} \hbar \omega_{0,\parallel} - \frac{1}{2} \hbar \omega_e + \frac{1}{2} \hbar \omega_{\mu}$$

$$E_4 = -\frac{1}{4} \hbar \omega_{0,\parallel} - \frac{1}{2} \hbar \left[(\omega_e + \omega_{\mu})^2 + \omega_{0,\perp}^2 \right]^{1/2} \qquad (8.51)$$

$$(8.52)$$

where of course $A_{\parallel} = \hbar \omega_{0,\parallel}$ and $A_{\perp} = \hbar \omega_{0,\perp}$.

The hyperfine interaction of Mu* is generally smaller than that of isotropic muonium. For example, in silicon $A_{\perp}(Mu^*)/A(Mu) \simeq 0.05$ and the anisotropy is $A_{\perp}/A_{\parallel} \simeq 0.2$. The precession frequencies depend not only on the magnetic field strength but also on its direction.
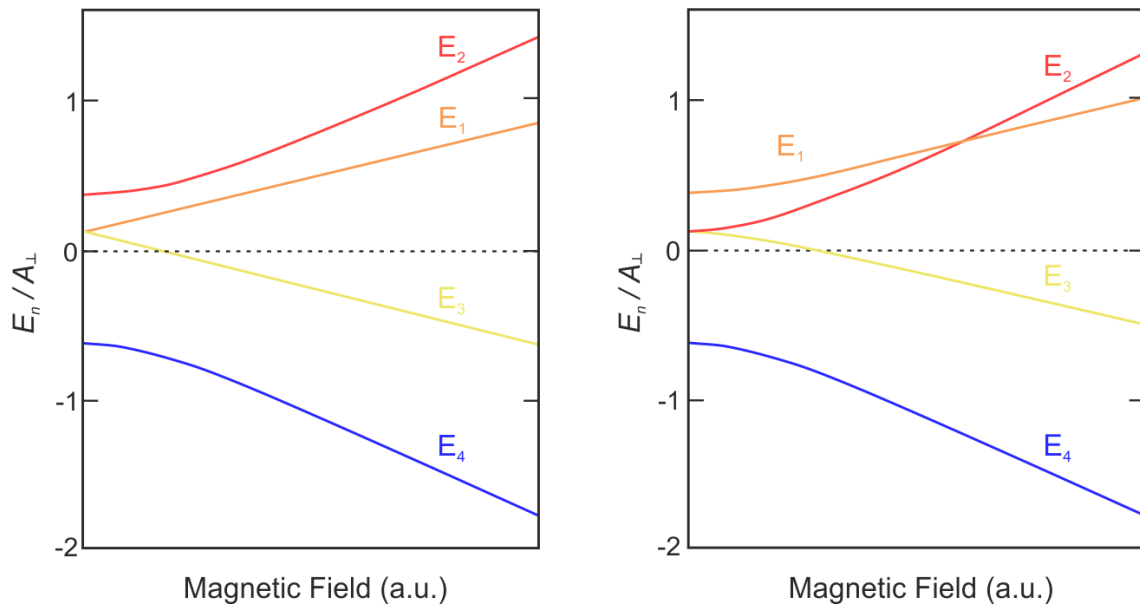
Figure 8.11.: *Schematics of the hyperfine energy-level diagram for anisotropic Mu* for the case where the field is applied along the [111] symmetry axis (left) and perpendicular to it (right panel). Note that fictitious values of the gyromagnetic ratios have been chosen for clarity. In this example $A_\perp / A_\parallel = 2$.*
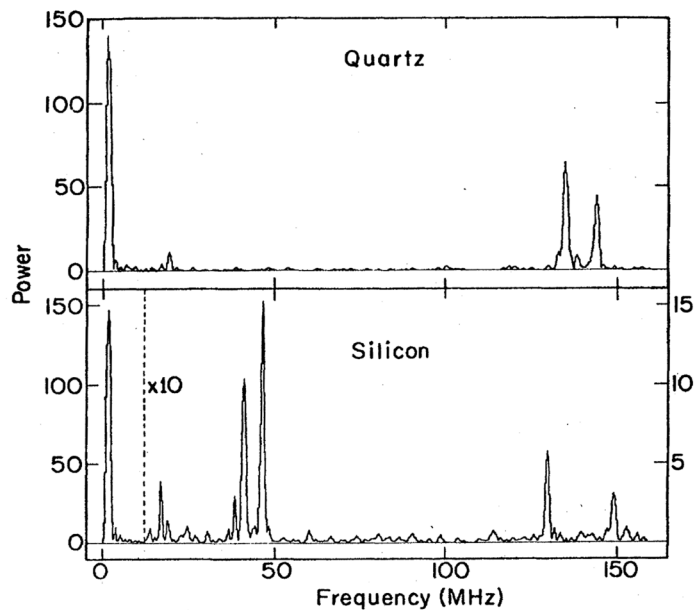
Figure 8.12.: *Fourier transforms of transverse-field µSR spectra taken with an external field of 10 mT in quartz at room temperature (top) in silicon at 77 K (bottom, field along [111]) showing the precession components from "free" muon ($\nu_{\mu^+} \simeq 1.36$ MHz) and isotropic Mu (the pair ν_{12} and ν_{23} centered around 140 MHz). Note the larger Mu splitting in Si, indicating a weaker hyperfine interaction. Note also the presence in Si but not in quartz, of Mu* precession lines (ν_{12} and ν_{34}, with an angle of 70.5° between the direction of the field and the [111] axis) at 41 and 46 MHz. Taken from Ref. [121].*
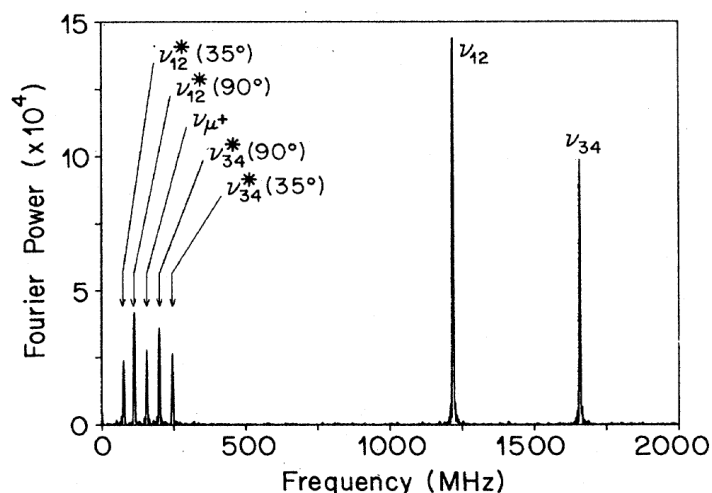
Figure 8.13.: *Fourier transforms of transverse-field μSR spectra taken with a high-field, high-time-resolution apparatus in GaAs at 10 K with a 1.15 Tesla field applied along the [110] axis. Note the two Mu lines ν_{12} and ν_{34} and also the Mu* lines $\nu_{ij}(\theta)$ (where θ is the angle between the [111] Mu* symmetry axis and the applied field). Taken from Ref. [124].*

Muonium states in elemental and III-V compound semiconductors have been found and studied to a great extent. Muonium can either be isotropic, when in a symmetric interstitial site such as the tetrahedral site in diamond (Mu^T), or anisotropic when situated at the bond-center site (Mu^{BC}). In these semiconductors, isolated hydrogen and muonium are known to form deep-level centers.
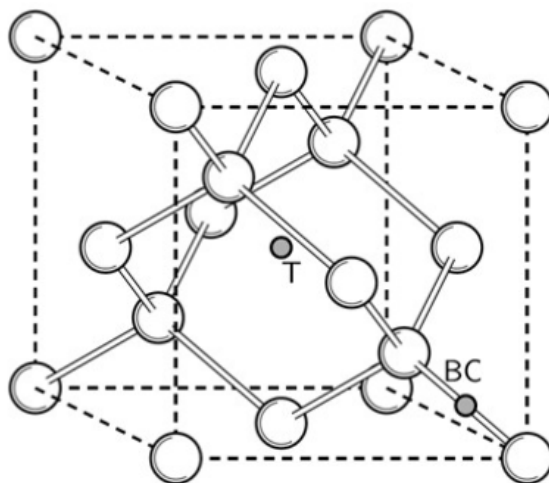
Figure 8.14.: *Two different muonium sites in for example Silicon and Germanium (BC: "Bond Centered Muonium"; T: "Tetrahedral Muonium".*

More recently, studies of muonium in II-VI semiconductors revealed the existence of a third form of neutral anisotropic muonium in CdS, CdSe, CdTe and ZnO. This state has a binding energy characteristic or shallow-level donor centers and is believed to be at the interstitial

site anti-bonding to S (Se, Te, or O). Its hyperfine interaction is very weak, amounting to approximately 10^{-4} of the vacuum value.

Figure 8.15 shows the μSR signal in CdS, taken over a period of eight muon lifetimes. The Fourier transform of the signal shows five distinct frequencies, indicating an extremely shallow muonium state and providing the first information on this hydrogen-like impurity in the compound [125]. In addition to the Larmor precession signal at 1.38 MHz, the Fourier spectrum shows two pairs of lines symmetric around the central line. The outer pair and the inner pair together with their intensity ratios can be assigned to two orientations of the muonium defect center. The shallow muonium state is described by a hyperfine tensor which can be oriented along definite crystallographically equivalent directions (specific bond directions) which have different orientation with respect to the applied magnetic field.

The asymmetry as a function of temperature shows that the "free" muon signal grows at the expense of the muonium signals. This is taken as evidence that the muonium center becomes ionized, *i.e.*, that the electron is no longer bound to the muon. The binding energy of the electron obtained from the activation energy is $E = 18$ meV, *i.e.* much smaller than the band gap of about 2.5 eV. This clearly indicates that muonium forms a shallow level with a widely distributed electron wave function as already suggested by the low hyperfine interaction.
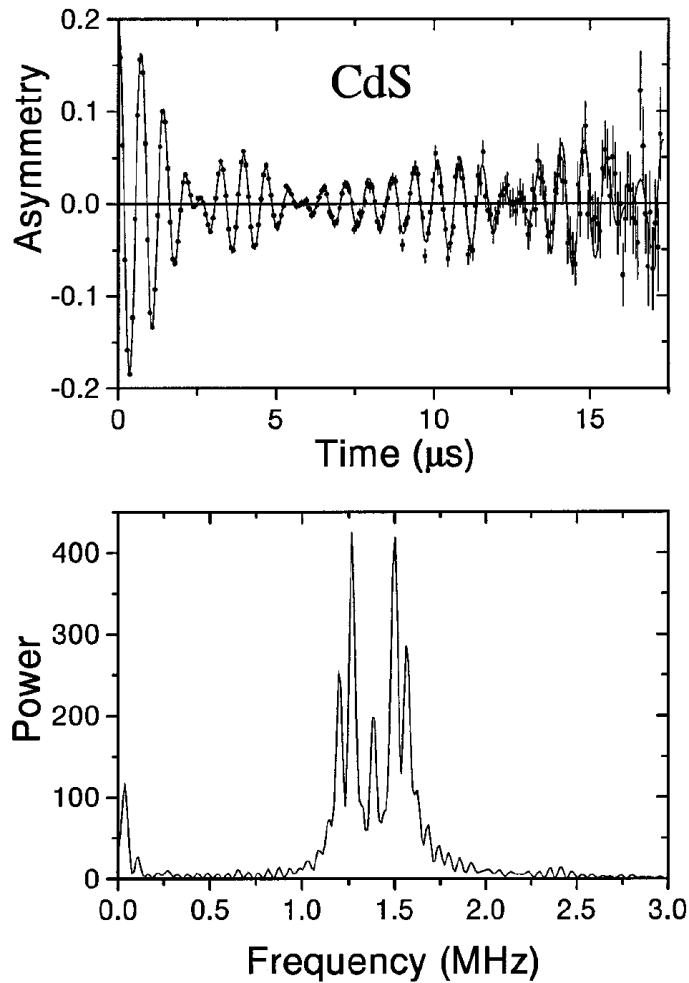
Figure 8.15.: *μSR spectrum and its Fourier transform for undoped CdS at 2.1 K. The magnetic field of 10 mT was parallel to the hexagonal ⟨0001⟩ axis which was also normal to the plane of the disk-like sample. In this geometry, one Cd-S bond direction (suggested to be the symmetry axis of the hyperfine tensor) is at 0° and three are at 70.6° to the field direction. Taken from Ref. [125].*

The question remains to understand which parameter governs the formation of either deep-level muonium of shallow donor muonium. Of all the relevant properties, none of those which are known (*e.g.* bandgap, dielectric constant, bond-length, crystal structure etc.) shows a threshold for the transition from deep to shallow behaviour. There is increasing evidence that it is not the overall width of the conduction-band which plays a role, but rather the depth of its minimum below the vacuum continuum (the "electron affinity").
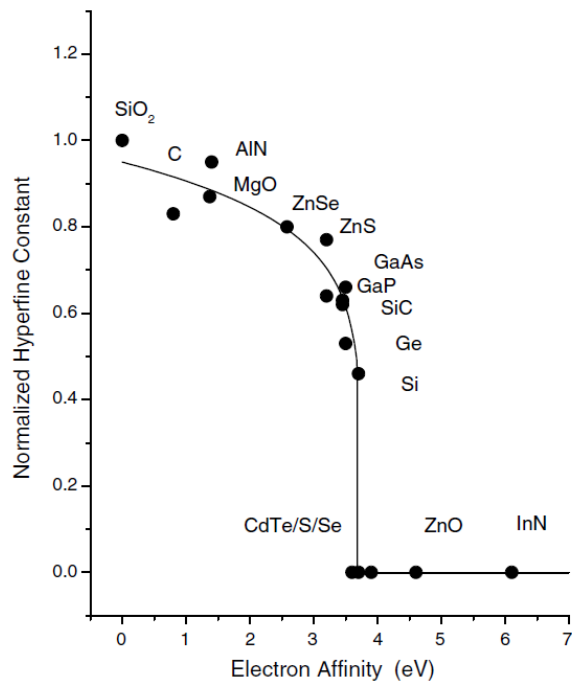
Figure 8.16.: *Correlation of the muonium hyperfine constant (normalized to that of the free atom: values for the shallow-donor states are not zero but rather 10^{-4}) with the electron affinity, i.e. depth of the conduction band minimum. Taken from Ref. [126].*

9. The use of Negative Muons: μ^-SR and Elemental Analysis

Up to now we have discussed how positive muons can be utilized through different techniques to investigate the properties of matter. The specific advantage of the positive charge, leading to a muon localization at an interstitial site, is one of the main reason that at least 95% of all μSR related research makes use of positive muons. An additional reason, as we will discuss below, is the availability of more intense beams compared to negative muons. This being said, negative muons can indeed be employed to perform μ^-SR to extract specific information in some specific materials. Also, the use of negative muons has seen a revival in the last few years due to its rediscovery as a non-destructive tool for depth-resolved elemental analysis. In this Section, we will discussed these different aspects.

9.1. Negative muon beams

Negative muons are produced by the decay of a negative pion. Due to the reduced number of possible reactions leading to the formation of a negative pions in the production target bombarded by protons, the cross section for negative pion production is lower than the one for positive pions. For a proton energy below 600 MeV, basically solely single pion production reactions can be considered. In addition to the reaction processes leading to the creation of a single positive pion (see Eq. 1.1), one reaction leads to a single negative pion creation

$$p + n \rightarrow p + p + \pi^- \ .\tag{9.1}$$

Therefore, in general one can expect that the flux of negative muons, arising from negative pion decay, measured at all energies will be lower than for positive muons.

We have seen in Section 1.8.3.2 that for positive muons an intense mono-energetic beam ($E_{\mathrm{kin}} \simeq 4.1$ MeV) can be obtained by looking only at muons arising from positive pions decaying near the surface of the production target, and it is fair to say that the availability of such beam has boosted the development of the μSR technique. To obtain such a beam, the decay of the positive pion must occur at rest. This is indeed possible since the positive pion, analogue to a positive muon, will stop in the production target at an interstitial site. On the other side, negative pions stopping in the production target will have a very high probability to be captured into Bohr orbits around the nuclei of the target atoms. Being a hadron, the pion feels the strong interaction and will very rapidly be annihilated (already in an extended orbit) at a rate many orders of magnitude greater than its decay rate. Hence, surface muons beam are only possible with positive muons.
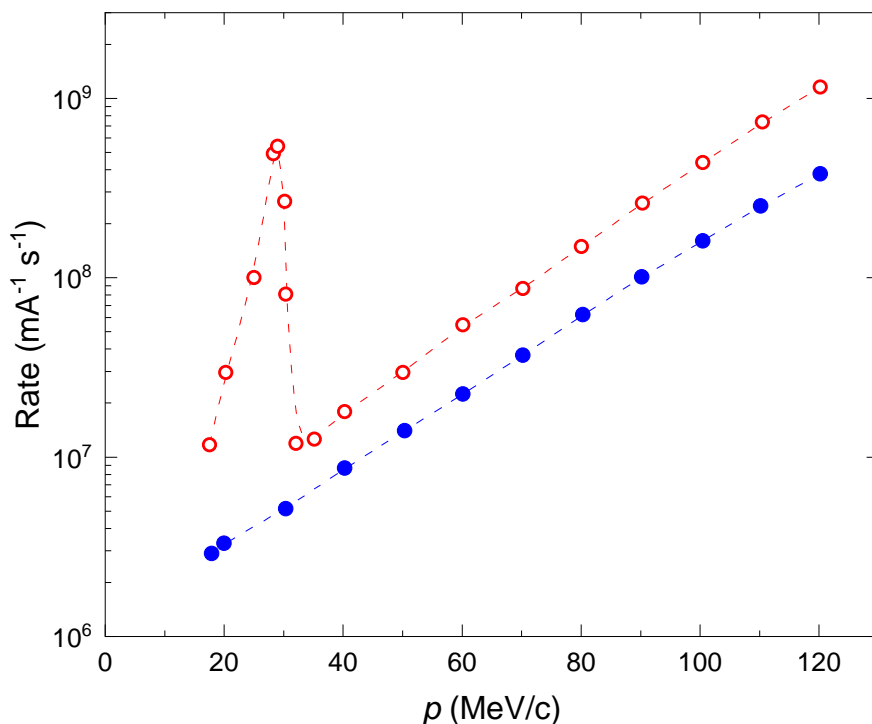
Figure 9.1.: *Intensity difference between positive and negative muon beams reported as a function of the muon momentum. The data were obtained at the πE5 beamline at PSI.*

Negative muon beams are possible with so-called "cloud" muons, i.e. originating from pions having enough energy to escape the production target and which decay in-flight between the target and the first bending magnet. Since the only requirement defined for the muons is their momentum defined by the first bending magnet, these muons can be created in forward or backward decay processes (see also Section 1.8.3.1) from pions with different momenta at decay time. Hence, the polarization of such cloud beams is very low.

Another possibility to obtain a high-energy negative muon beam is from negative pions decaying in flight in a long solenoid after a kinematic selection, in an identical manner as positive pions (see Section 1.8.3.1). By choosing forward or backward processes, these negative muons will have a reasonable polarization.

9.2. Implantation of negative muons in matter

When implanting negative muons in matter, the first deceleration processes taking place will be similar to the one for positive muons, that is an electrostatic interaction with the outer electrons of the target atoms. This leads for a large range of momentum to a similar stopping power $-dE/dx$ as the one for positive muons (see also Figure 2.4). The main difference will occur at low energy, *i.e.* when the velocity of the negative muon becomes similar to the one of the atomic electrons. At this point, the negative muon will strongly feel the Coulomb created by the positive charge of the nearby nucleus and will be captured forming a muonic

atom.

9.2.1. Muonic atoms

In this exotic atom, the muon will very rapidly cascade down to its $1s$ ground state. The muon cascade is characterized by different processes. X-rays[1] are produced corresponding to the energy difference of the muonic states involved in the cascade. Also Auger effect, corresponding to the ejection of electrons from the outer most orbits, comes into play, and in addition, in heavy atoms, the energy of muon transitions between low-lying states can be higher than the binding energy of a neutron leading to a neutron release (nuclear Auger effect).

Since the muon has a mass about 207 times higher that the one of the electron (see Table 1.2), its orbits will be a factor 207 closer to the nucleus than the respective ones of the electron. Following the Bohr theory (see also Section 8.1 on page 277), one can deduce that the radius is proportional to the inverse of the reduced mass

$$r_{n,\mu} = \frac{4\pi\varepsilon_0\hbar^2\,n^2}{\bar{M}_\mu Z e^2} = \frac{\hbar n^2}{\bar{M}_\mu Z c\alpha} \quad . \tag{9.2}$$

Note that we call $r_{n=1,\mu}$ the muonic Bohr radius, which is often written as $r_{n=1,\mu} = a_{0,\mu}$.
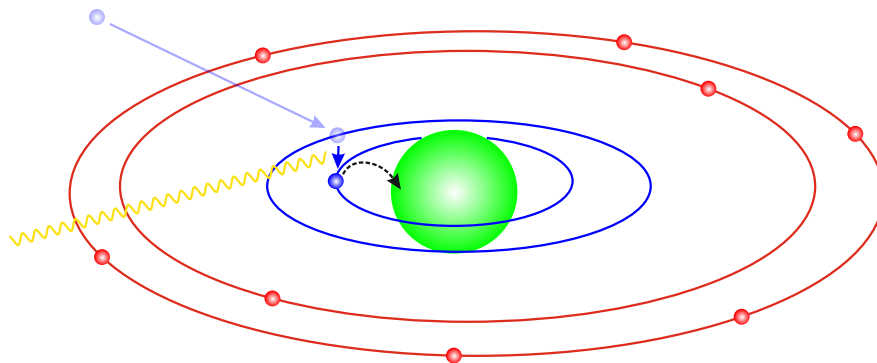
Figure 9.2.: *Sketch of the capture of the muon by an atom of the sample. For simplicity, we have drawn the first capture orbital of the muon rather closed to the nucleus. The negative muon (hell and dark blue) is first captured by the atom and decays down to its $1s$ orbital. During the cascade, characteristic X-rays are emitted. The muon orbitals are much closer to the nucleus than the electronic ones (see Eq. 9.2). For simplicity and clarity, the ratio between the muon and electron orbital radius is chosen here arbitrarily. Also, in reality the muon is first captured at a muon orbital having a radius close to the one of the $1s$ electron orbital (see text). In a second step, the muon in the $1s$ orbital may be captured by the nucleus itself (symbolized by the black arrow; see Section 9.2.3).*

---

[1]In this Chapter, the generic term of X-ray will be employed, even though sometimes the involved energies correspond to gamma rays.

Similarly, and by considering in a first step that the nucleus is a point charge Ze, the binding energies for the different states are increased by the same factor 207. This can be seen by considering again the simple Bohr model where one obtains that

$$E_n = -\frac{\bar{M}_\mu \, Z^2 e^4}{(4\pi\varepsilon_0)^2 2n^2\hbar^2} \quad , \tag{9.3}$$

where $\bar{M}_\mu$ is the reduced mass of the system formed by the muon and the nucleus (with usually $\bar{M}_\mu \simeq M_\mu$). As the same formula (replacing $\bar{M}_\mu$ with $\bar{M}_e$) applies for an electron orbiting around the nucleus, the ratio of the reduced masses provides the ratio of the energies of corresponding states (for same principal quantum number n). The energy is often expressed using the fine structure constant[2]

$$\alpha = \frac{1}{4\pi\varepsilon_0}\frac{e^2}{\hbar c} \quad , \tag{9.4}$$

and therefore we can write

$$E_n = -\frac{1}{2}\frac{(Z\alpha)^2 \bar{M}_\mu c^2}{n^2} \quad . \tag{9.5}$$

Actually, the Bohr model ignores the fine structure of the levels, that is the relativistic effects and the spin-orbit coupling. Hence, all states with same n principal quantum number and different azimuthal quantum number ℓ have the same binding energy in this model. Again considering the nucleus as a point charge, the Dirac equation provides the correct levels with

$$E_n = \bar{M}_\mu c^2 \left[1 + (Z\alpha)^2\left(n - j - \frac{1}{2} + \sqrt{(j+1/2)^2 - (Z\alpha)^2}\right)^{-2}\right]^{-1/2} \tag{9.6}$$

and by performing a limited expansion one obtains[3]

$$E_n = -\frac{1}{2}\frac{(Z\alpha)^2 \bar{M}_\mu c^2}{n^2} - \frac{\bar{M}_\mu c^2}{2n^4}\left(\frac{n}{j+\frac{1}{2}} - \frac{3}{4}\right)(Z\alpha)^4 + ... \quad . \tag{9.7}$$

The first term corresponds to the one found in Eq. 9.5 and the second term gives the first order fine structure correction. Here, j is the total angular momentum quantum number arising from the combination of the spin and angular momentum.

The negative muon will be captured in an excited state with similar energy and size as the $1s$ level of the corresponding normal atom, i.e. with a principal quantum number n satisfying $r_{n,\mu} = r_{1s,e}$ which, by applying Eq. 9.2 leads to $n = 14 \simeq (M_\mu/M_e)^{1/2}$.

As said above, the emission of Auger electrons will also be important during the cascade of the negative muon to its $1s$ state. However, we will focus here the discussion to the X-ray emission as this will play a central role for the elemental analysis. The characteristic energy

---

[2] α can be interpreted as the ratio between the energy necessary to overcome the Coulomb repulsion between two particles with elementary charges of the same sign located at a distance s apart and the energy of a photon with wavelength $\lambda = 2\pi s$.

[3] We omit here the rest mass energy.

of X-rays emitted (or absorbed) by atoms, and corresponding to electron transitions between atomic energy levels, is given by the empirical Moseley's law. In a first approximation[4], the X-ray energy emitted by the transition of an electron between atomic levels with principal quantum numbers n_i (initial) and n_f (final) is given by

$$E_{i \to f,e} = \frac{\bar{M}_e}{M_e} R_y (Z - S_{\text{scr},e})^2 \left(\frac{1}{n_f^2} - \frac{1}{n_i^2} \right) \quad . \tag{9.8}$$

The ratio of the reduced mass to the normal one is very close to 1 and is used as the definition of the Rydberg constant in energy, R_y, is

$$R_y = \frac{M_e e^4}{8 \varepsilon_0^2 h^2} \quad . \tag{9.9}$$

The atomic number Z is here replaced by $Z_{\text{eff}} = (Z - S_{\text{scr},e})$ as the charge of the nucleus seen by the electron involved in the transition is screened by electrons between itself and the nucleus. For K_α transitions, $S_{\text{scr},e} = 1$ as an L electron sees a nuclear charge which is shielded by the electron from the K shell.[5]

The X-rays produced during *muonic* transitions are much more energetic than the ones for electronic transitions as

$$\begin{aligned} E_{i \to f,\mu} &= \frac{\bar{M}_\mu}{M_e} R_y (Z - S_{\text{scr},\mu})^2 \left(\frac{1}{n_f^2} - \frac{1}{n_i^2} \right) \\ &\simeq \frac{\bar{M}_\mu}{\bar{M}_e} \times E_{i \to f,e} \\ &\simeq 207 \times E_{i \to f,e} \quad . \end{aligned} \tag{9.10}$$

The first approximation sign is necessary as the radius of the $1s$ muonic orbital is much smaller that the corresponding electron one (see Eq. 9.2) and therefore the cascading muon does not see any nucleus charge screening, *i.e.* $S_{\text{scr},\mu} = 0$, whereas we had $S_{\text{scr},e} = 1$ for the electron as seen above.

---

[4]The Eq. 9.5 is used here.
[5]To allow a K_α transition a unique electron must occupy the K shell.
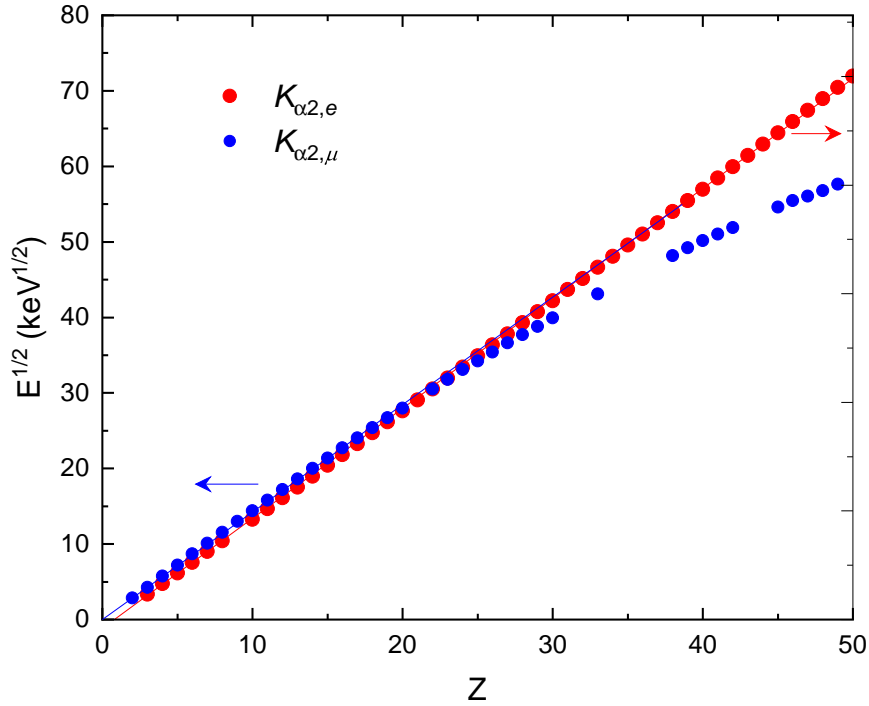
Figure 9.3.: *Comparison between the energy of the photon emitted during a $K_{\alpha 2}$ (or $K - L_2$) transition [red points and right scale for normal atoms (electron transitions); blue points and left scale for muonic atoms (muon transitions)], plotted as a function of the atomic number. The vertical axis report the square root of the energy and are scaled by a factor $\sqrt{M_\mu / M_e}$ (see text). Note that the $x - $ intercept for the electronic transition lies at $Z = 1$ (i.e. corresponding to $S_{scr} = 1$) and for muonic transition at $Z = 0$ (i.e. corresponding to $S_{scr,\mu} = 0$). Note also the linearity [corresponding to $E_{K_{\alpha 2}} \propto (Z - S_{scr,X})^2$] for small Z values (see Eqs. 9.8 and 9.10).*

Equations 9.8 and 9.10 indicate that the square root of the transition energies should scale with the atomic number Z. As shown on Figure 9.3, such a relation is clearly observed for electronic transitions. For large values of Z, the deviation from linearity observed for muonic transitions reflects that the size of the nucleus cannot be neglected anymore with respect to the characteristic radius of the muonic state. Note that such deviation will be less important for large values of n_f, for which the characteristic radius of the final muonic state will be large and therefore the validity of the point charge approximation for the nucleus will hold.

9.2.2. Polarization

Until its capture by an atom, the negative muon retain its full polarization as the positive muon as solely Coulomb interactions have affected its energy loss. When the capture occurs and during the cascade, polarization will be lost due to the spin-orbit coupling and hyperfine interaction with nuclei possessing a finite nuclear spin. This depolarization loss depends on the capture level, the atomic number Z, the effect of radiative transitions or Auger pro-

cesses. Calculations [127] as well as measurements indicates a polarization of about 1/6 of the original polarization.

9.2.3. Lifetime

In vacuum, a negative muon will have the same lifetime as a positive muon, but the picture changes when implanted in matter. As we have seen in the previous Sections, the positive muon will still retain its normal mean lifetime after its implantation. This reflect the fact that the positive muon is located at an interstitial site and therefore cannot be involved in nuclear reactions and its decay will be similar to what happens in vacuum.

The situation is different for negative muons, as the muon is located very close to the nucleus. For increasing values of Z, the radius of the nucleus increases and the probability that the muon is captured by the nucleus is no more negligible (see Fig. 9.2). If such capture takes place a reaction

$$\mu^- + p \to n + \nu_\mu \tag{9.11}$$

will occur hence reducing the lifetime of the muon. This reaction will transform the nucleus having a charge Ze to one having a charge $(Z-1)e$. For example the above reaction taking place in iron will lead to

$$\mu^- + {}^{56}_{26}\text{Fe} \to {}^{56}_{25}\text{Mn}^* + \nu_\mu \quad . \tag{9.12}$$

The Mn isotope is in an excited state and will release energy in the form of an X-ray.[6]

The capture probability of a negative muon by the nucleus depends on the size of the nucleus, whose charge radial density can be expressed as [128]

$$\rho_\text{N}(r) = \frac{\rho_0}{1 + \exp\left(\frac{r-R}{a}\right)} \quad , \tag{9.13}$$

where a represents here the surface thickness with a typical value of $a \simeq 0.5$ fm, R is the nuclear radius with $R = r_0 A^{1/3}$ where one usually assumes $r_0 = 1.25$ fm and where A is the mass number. For a vanishing surface thickness, one obtains over a radius R a homogeneous charge density $\rho_0 = 3Ze/(4\pi R^3)$.

When the muon is on its ground state $1s$, the probability of finding it in a volume element is

$$|\psi_{1s,\mu}(r)|^2 = \frac{1}{\pi a_{0,\mu}^3} \exp\left(-\frac{2r}{a_{0,\mu}}\right) \quad . \tag{9.14}$$

---

[6]Note that the isotope produced is in an excited with an energy of the order of 10 to 20 MeV above its ground state. This is usually more than the binding energy of a neutron. Therefore, neutrons can be emitted in the process and the following reactions, for example in the case of iron, can also take place

$$\mu^- + {}^{56}_{26}\text{Fe} \to {}^{55}_{25}\text{Mn}^* + n + \nu_\mu$$

$$\mu^- + {}^{56}_{26}\text{Fe} \to {}^{54}_{25}\text{Mn}^* + n + n + \nu_\mu \quad .$$
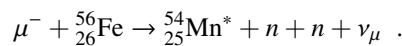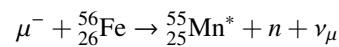
As the muonic Bohr radius $a_{0,\mu}$ is proportional to the inverse of Z (see Eq. 9.2), Eqs. 9.13 and 9.14 tell us that the overlap of these functions increases with Z and therefore also the capture probability of the muon by the nucleus.
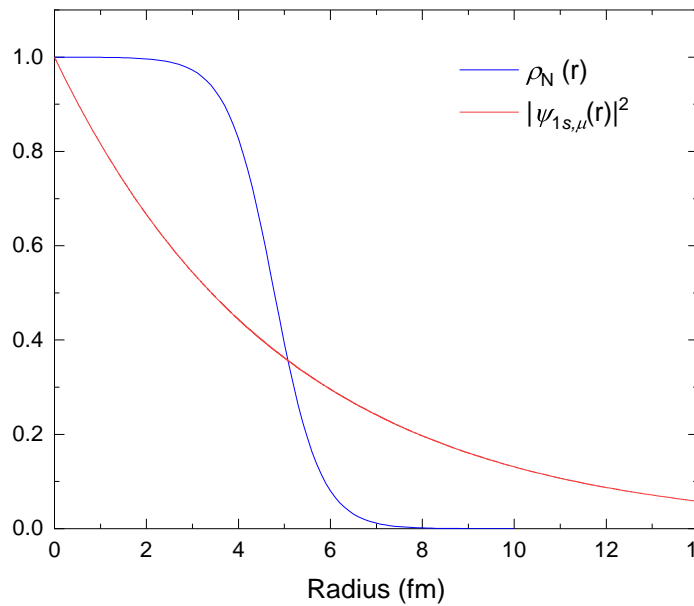
Figure 9.4.: *Example for Iron of the radial dependence of the nucleus charge density and of the probability density of the muon. Note that the later was calculated following the simple Boch formula, i.e. assuming a point charge nucleus.*

The increase of the capture probability upon increasing atomic number leads to a reduction of the bound negative muon lifetime. Whereas for light elements the negative muon lifetime is close to the value observed for the free muon, for heavy elements one observes a drastic decrease with $\tau_\mu(Z) < 100$ ns for $Z \gtrsim 40$. One can write

$$\frac{1}{\tau_\mu(Z)} = \frac{1}{\tau_{\mu,\,\text{free}}} + \frac{1}{\tau_{\mu,\,\text{Nucl. capt}}(Z)} \quad , \tag{9.15}$$

reflecting the sum of different decay probability channels.
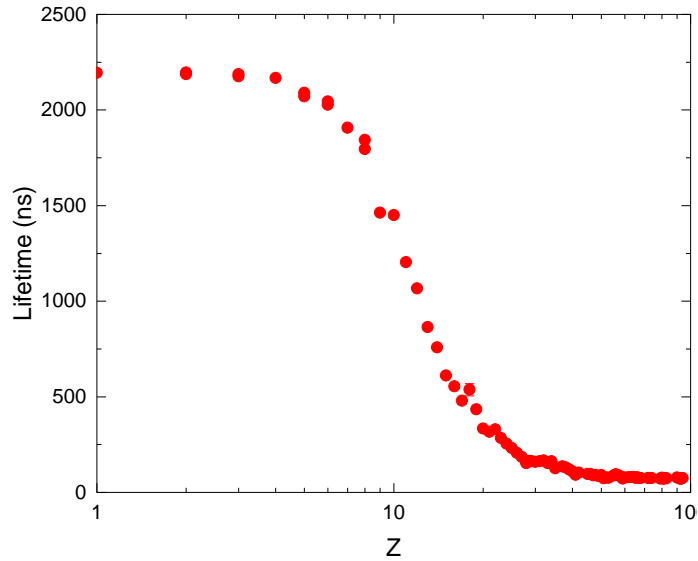
Figure 9.5.: *Evolution of the observed negative muon lifetime as a function of the atom number (note the logarithmic scale).*

9.3. μ^-SR

9.3.1. "Conventional" μ^-SR

Even though the overwhelming majority of the muon-spin spectroscopy measurements are performed with positive muons, experiments with negative muons are possible once the negative muon ends its cascade and is located in its $1s$ state. From the points discussed above, it is actually clear that the μ^-SR technique faces different challenges.

For a muon-spin spectroscopy measurement, one can define a figure of merit which is given by

$$F = A^2 N \ , \tag{9.16}$$

where A is the asymmetry of the recorded μSR signal and N is the muon rate. The asymmetry signal is directly proportional to the initial muon polarization, which, as seen in Section 9.2.2, is strongly reduced for negative muons after the cascade.[7] An additional problem is the beam intensity, at least for some momentum ranges, as solely "cloud" muons are involved (see Fig. 9.1). Even if we assume similar intensities for negative and positive muon beams, μ^-SR measurements require measurement times about a factor 30 longer than standard μSR measurements to reach a similar figure of merit. This was probably the main obstacle to the development of the μ^-SR technique, as the financial and manpower cost to run a simple experiment are prohibitive.

---

[7]Remember also that prior to the cascade, the polarization of the beam is already reduced due to the necessity to use "cloud" muons (see Section 9.1).

But additional difficulties are connected to the technique. In general, interesting materials are alloys composed with different chemical elements. By performing μ^-SR in such material, the negative muons will be attracted by the positive charges of the different nuclei. This will result in different sub-ensembles i of negative muons having different lifetimes $\tau_{\mu,\,i} = \tau_\mu(Z, i)$, as Z is different for the different nuclei. Therefore, Eqs. 1.18 and 3.3 (replacing positrons by electrons) will only be valid for one sub-ensemble with a given lifetime $\tau_{\mu,\,i}$.

When performing μ^-SR measurement on an alloy containing i atomic species, a detector histogram of the number of electrons detected as a function of time is given by

$$N_e(t) = \sum_i B_i + N_{0,\,i}\, e^{-\dfrac{t}{\tau_{\mu,\,i}}} \left[1 + A_{0,\,i}\, \mathbf{P}_i(t) \cdot \hat{\mathbf{n}} \right] . \tag{9.17}$$

Therefore, the extraction of the time evolution of the muon polarization (*i.e.* the μ^-SR signal) can be a very difficult task in view of the large number of parameters, in particular in alloys containing a many different elements.[8] Note that muons captured in different atomic species will usually experience different local fields and therefore present different time evolutions of their spins adding to the complexity of the signal. Also the interpretation of the time-evolution of the muon polarization in the $1s$ state is not straightforward. This time-evolution will be determined by the interaction between the magnetic moment of the negative muon and the ones of the electron shell of the muonic atom (hyperfine interaction) and on the interaction of these moments with the surrounding medium.

As an example, we report on Fig. 9.6 measurements performed on MgH_2 and MgB_2 [129], with the goal to determine the parameters characterizing the hydrogen diffusion. In normal μSR such determination is not trivial, as a motional narrowing of the field seen by the muon (see Section 4.3.2.1) signaling diffusion could arise either from a hydrogen diffusion or from the diffusion of the muon itself (or from both effects). The idea to perform μ^-SR in MgH_2 was to study the time evolution of the spins of the negative muons which are captured by the Magnesium atoms and therefore are not diffusing. The MgB_2 system was taken as a comparison. The fact that about 90% of the Mg nuclei (^{24}Mg isotopes) are lacking a nuclear spin is a key ingredient as the spin of the negative muons captured by the Mg-ions senses a local field mainly caused by the surrounding hydrogen spins. The negative muons captured on the 10% abundant ^{25}Mg ions with $I = 5/2$) will have a completely different time-evolution of their polarization in a magnetic field, *i.e.* the spin will precess at a entirely different frequency. This arises as the muon spin is locked to the spin of the nucleus by hyperfine interaction. As clearly seen on Fig. **??**, the fit of a typical μ^-SR signal is rather complicated with here five muon-lifetimes: for the Mg ions ($\tau_{Mg} = 1.067(2)\ \mu$s), for the carbon and oxygen ions contained in the sample holder made of PET ($\tau_C = 2.0263(15)\ \mu$s and $\tau_O = 1.795(2)\ \mu$s), for the lead of the beam collimator ($\tau_{Pb} = 0.0754(10)\ \mu$s) and finally a very long lifetime of the order of 20 μs for an signal of unknown origin (possibly reflecting a time-dependent background). The asymmetries are very small and at the most of the order of 0.04 of the Mg-signal. The conclusions of this study was that in MgH_2 one could observed in ZF measurements a dynamical Kubo-Toyabe function and a partial decoupling in LF indicating the

---

[8]Not also that the negative muon lifetimes in stable isotopes of a given element (for example ^{63}Cu and ^{65}Cu) is slightly different due to the different nucleus radius and therefore the different negative muon capture probability by the nucleus. Therefore, this could blur the search for subtle effects in the μ^-SR signal.
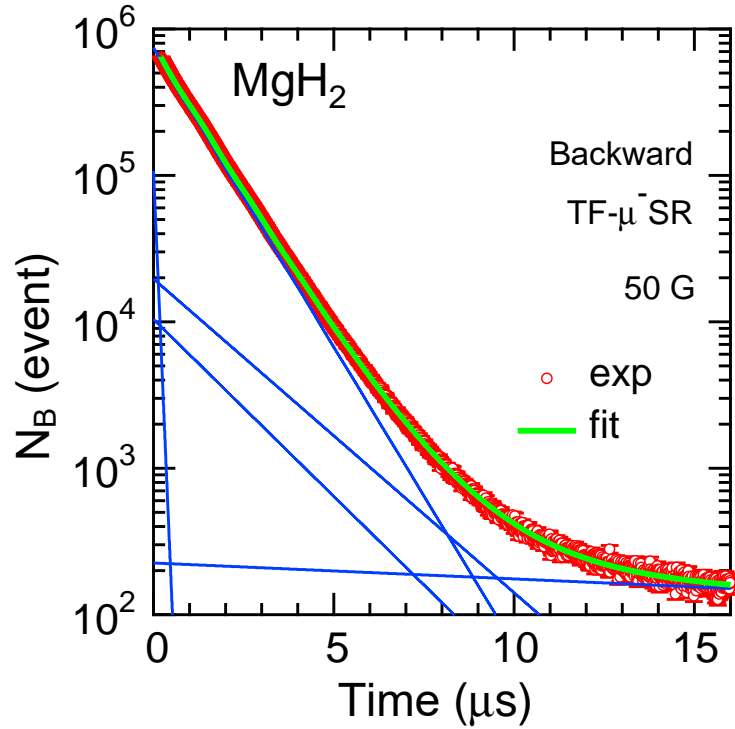
Figure 9.6.: *Backward (with respect to the initial negative muon polarization) histogram recorded in a TF-field of 50 G in MgH$_2$. The red points are the experimental data, the green line is the fit using Eq. 9.17 and five contributions represented by the blue lines (adapted from Ref. [129]).*

occurrence of fluctuations attributed to hydrogen diffusion. However, due to the very long measurement time, no temperature dependence of the diffusion parameters could be determined.

9.3.2. X-ray triggered μ^-SR

At this point, one could ask whether a solution is at hand to disentangle the different elements contributions of the μ^-SR signal. A possible path was first provided by Arlt *et al.* [130], and taken over by different studies in semiconductors (see for example [131, 132]). The idea is to record the energy of characteristic X-rays emitted during the muon transition to its 1*s* ground state after its capture by an atom of the sample. As we have seen above, this cascade is basically in coincidence with the muon arrival (within few picoseconds) and the X-rays energy depend on the atom that has captured the muon (see Eq. 9.10). Therefore, one can tag a muon-electron event with the corresponding transition energy, say for example $K_{\alpha 1}$, and hence route this event to a specific histogram. Each histogram will contain the events that occurred in a specific type of atoms of the sample and therefore the analysis of the μ^-SR signal will be greatly simplified. Even though this technique is particularly elegant, it faces the problem that a typical X-ray detector (for example HPGe) will cover an extremely small portion of the solid angle and therefore many muon-electron event will lack the energy tag. Hence, the already very low count rate will be even further drastically reduced.

9.4. Elemental analysis

If the use of negative muons for muon-spin spectroscopy faces important issues, there is another material research area where they appear to be more and more exploited. Indeed, negative muons offer the very interesting perspective to be used as an non-destructive method to performed depth-dependent elemental analysis in costly and very rare materials.

The use of negative muons for elemental analysis has been recognized rather early and numerous experiments were performed in the 1970's mostly at PSI (for an early review see [133]). However, probably due to the lack on muon rate at that time, the technique was basically abandoned for quite some time. Recently, this technique has been "rediscovered" through efforts made at the pusled muon sources ISIS and J-PARC (see for example [134]). We will call this technique MIXE (for Muon-Induced X-ray Emission).

9.4.1. Principle

The principle of the technique itself is actually simple and already contained in the Equations that we developed so far.

As we have seen in Section 9.2, negative muons implanted in a sample have a similar stopping profile than positive muons with a characteristic Bragg peak (see Section 2.1.2). That is, they stop in the sample at a well defined depth (within an unavoidable straggling) that depends on their momentum. At this sample depth, which can be tuned by tuning the muon momentum, they will be captured by one atom of the sample and characteristic X-rays will be sent during the cascade. As this energy varies as $E_{i \to f, \mu} \propto (Z-1)^2$ (see Eq. 9.10 and Fig. 9.3) the type of atom having captured the muon can be determined by looking at the energy of the emitted X-rays. By recording the time of the muon arrival, we can concentrate with the data-acquisition at X-ray events that are basically in coincidence with the muon event. This allows us to get rid of other delayed X-ray events arising possibly from the relaxation of an excited nucleus after capturing a muon (see Eq. 9.12).

The very important feature is that not only we can implant our muons deep into the sample, but also the X-rays produced during the cascade have most of the time enough energy to escape from the sample itself and can therefore be detected by X-ray detectors as germanium-based HPGe detectors. The attenuation of an X-ray beam in material is dependent upon absorption and scattering effects such as coherent (Rayleigh) and incoherent (Compton) scattering, photoelectric absorption and pair production. The attenuation of this beam is given by the Beer-Lamber-Bouguer law, which can be written (if the attenuation is not varying with the length over which the attenuation takes place ℓ) as

$$I(\ell) = I_0 \, \exp(-\mu\ell) \ . \tag{9.18}$$

Here μ is the linear attenuation coefficient, which is dependent on the beam energy, I_0 is the initial photon beam intensity. Very often, the mass attenuation coefficient μ/ρ is used instead of the linear attenuation coefficient, as μ/ρ is rather similar for different materials in

the energy range of the X-rays. Here, ρ is the mass density of the material. Therefore, we can write

$$I(\ell) = I_0 \, \exp[-(\mu/\rho)\rho\ell] \; . \tag{9.19}$$

Figure 9.7 exhibits the mass attenuation coefficient for iron. The electron binding energy of the $1s$ electron is 7112 eV and it represents the highest possible energy of a photon emitted during the transition of an electron from a higher level to the ground state $1s$, for example in an X-ray fluorescence (XRF) measurement. The sudden increase of the X-ray mass attenuation coefficient, which is called K-edge, clearly visible on Fig. 9.7 corresponds also to the $1s$-electron binding energy. It occurs when the energy of a X-ray beam is just above the binding energy of the ground state, as a photon having an energy above the $1s$-binding energy has more probability to be absorbed than a photon having an energy just below. Taking the energy of a photon beam to correspond to the energy of the electronic $K_{\alpha2,e}$ ($2p_{1/2} \rightarrow 1s$) transition, that is 6392 eV for iron, one obtains $\mu/\rho \simeq 70.71$ cm^2/g and $\mu \simeq 555.8$ cm^{-1}. Therefore, a drop of 50% of a photon beam intensity will occur after only about 12 μm. Similarly, for a photon beam having an energy of the corresponding transition $K_{\alpha2,\mu}$ of a muonic iron atom, that is 1256 keV for iron[9], one obtains $\mu/\rho \simeq 5.21 \times 10^{-2}$ cm^2/g and $\mu \simeq 0.41$ cm^{-1}. Therefore, a drop of 50% of a photon beam intensity will occur after about 17 mm.

Hence we see that photon produced by MIXE will travel a much longer distance into the material than a photon produced by X-ray fluorescence. In other words, it will have a very high probability to escape the material and to be detected by an external X-ray detector.

.

9.4.2. Simple examples

Figure 9.9 shows an example of measurement realized on an iron sample irradiated with a negative muons beam having a momentum of 26.5 MeV/c. This momentum correspond to a penetration depth of the muons into iron of about 200 μm. The characteristic X-rays were collected with a HPGe detector. One clearly observes almost the Lyman, Balmer and Paschen muonic series, *i.e.* corresponding to muons cascades from muonic levels with higher principal quantum numbers to the levels with $n_f = 1$, $n_f = 2$ and $n_f = 3$, respectively.

This simple measurement illustrates one of the main advantage of the MIXE technique, that is the capacity to implant muons deep into the material and still being able to collect X-rays outside of the material to identify the atom having captured the muon.

The next example was obtained from a "sandwich" sample composed by a trilayer of Fe/Ti/Cu, each having 500 μm thickness. By tuning the momentum beam accordingly, one can change the penetration depth of the negative muons and therefore scan the occurence of different elements. The top panel of Figure 9.10 exhibits the results of muon-capture Monte-

---

[9]This energy is slightly below $207 \times K_{\alpha2,e}$ as it can be seen from Fig. 9.3, where the point for the iron $K_{\alpha2,\mu}$ transition ($Z = 26$) is just below the linear extrapolation (see caption of Fig. 9.3).
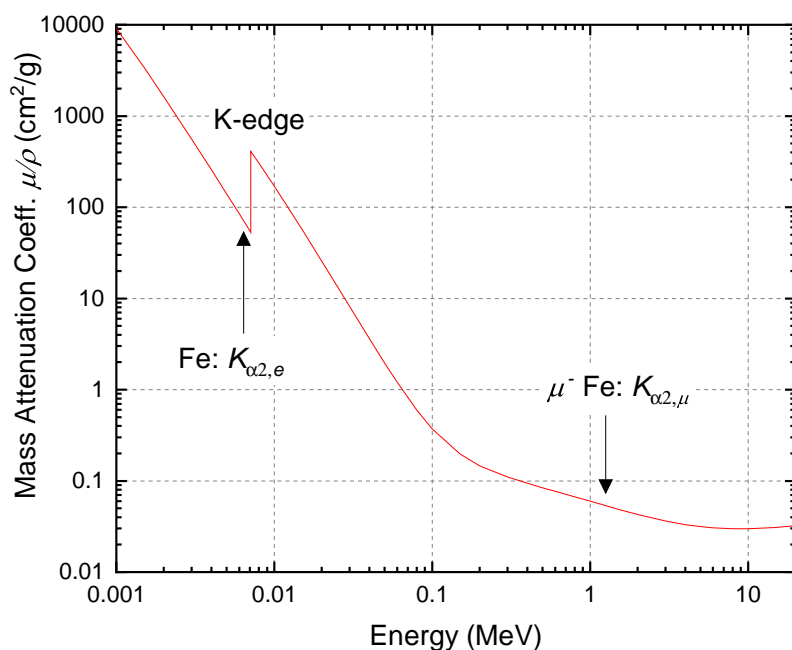
Figure 9.7.: *Mass attenuation coefficient shown for an energy range covering the $K_{\alpha2,e}$ and $K_{\alpha2,\mu}$ transitions (shown by arrows). Note also the K-edge corresponding to the ionization energy of the electronic 1s level.*

Carlo simulations for momenta used during the experiment.[10] From these simulations and the sample geometry, we can compute the expected type of atoms stopping the negative muons and compare these expectations with, for example, the intensity of the different K_α lines for the three different elements. As the efficiency of a HPGe detector is dependent of the X-ray energy, care has to be taken when comparing the K_α lines occurring at different energies (lower panel of Figure 9.10). We see that the MIXE technique provides us with quite accurate even when implanting the muons deep into the material. We have nevertheless to make here clear one important point. In the example shown, the environment of the muon at the end of its trajectory is homogeneous (except at the very exact interface between different layers) and solely one type of atom can absorb the muon. The situation is usually different in many cases, where alloys and compounds are studied. Here at the end of its trajectory, the muon will "see" different types of atoms. The capture probabilities of the negative muon are not the same for different atomes and a quantitative description of those is important for the application of the MIXE technique in nondestructive elemental analysis. In presence of different candidate atoms possibly capturing the muon, the integrated intensities of the $K_{\alpha,\mu}$ lines from the different elements can be utilized as a qualitative measure for its elemental composition. However, these intensities need to be corrected with the respective capture probabilities to obtain atomic abundances. Early experiments indicated that the capture probability $P(Z)$ depends mainly on the electron quantun numbers n and l and the atomic number Z, and on a minor level on the valence of the element and concentration. It was shown that

---

[10]Note that additional material, as entry scintillator and vacuum window, is in the path of the beam prior the sample.
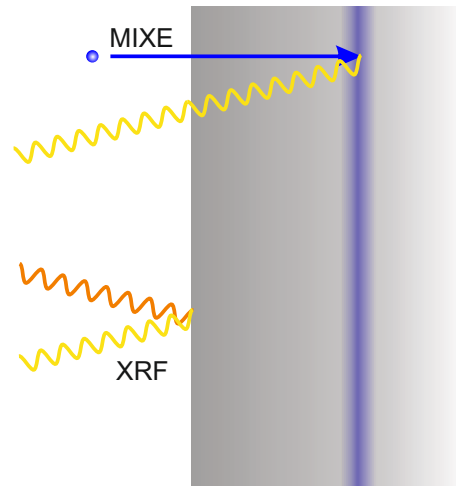
Figure 9.8.: *Sketch of the difference between the MIXE technique and the XRF technique. For XRF, one observes the emission of characteristic "secondary" X-rays (in yellow) from atoms that have been excited by high-energy X-rays (in red). As these secondary X-rays have limited energy, this elemental analysis technique is restricted to surface studies. In the MIXE technique, the characteristic X-rays emitted have much higher energy. Hence, even if muons are implanted deep into the material, the probability to observed the characteristic X-ray is ouside of the material is very high. By changing the momentum of the muon beam, one can hence perform a depth-dependent analysis of the elemental composition of the material.*

for a binary compound $Z_k Z'_{k'}$, formed by two elements Z and Z' having concentrations k and k' respectively, the capture ratio determined by studying the MIXE intensities $R(Z, Z', k, k')$ (taking into account the energy dependent efficiency of the detector) is given by

$$R(Z, Z', k, k') = A(Z, Z')\frac{k}{k'} \quad , \tag{9.20}$$

where $A(Z, Z')$ is the capture ratio. Figure 9.11 exhibits measurements on bronze samples with composition $Cu_{k(Cu)}Sn_{k(Sn)}Pb_{k)Pb)}$. The ratios of the observed MIXE X-ray lines is a measure of the capture ratio $R(Z, Z', k, k')$ between two elements[11] and the measurements clearly indicate that they are proportional to the ratios of the concentrations, *i.e.* in this case $A(Sn,Cu)$ and $A(Pb,Cu)$. This indicates that the capture ratios $A(Z, Z')$ are independent of the concentrations. Also, this Figure demonstrates that Eq. 9.20 is also valid for ternary compound [135].

Remarkably, it is found that $A(Z, Z')$ can be satisfactorily approximated by [136]

$$A(Z, Z') = \frac{P(Z)}{P(Z')} \quad . \tag{9.21}$$

This is quite remarkable, as it indicates that a knowledge of, on one side, the generic $P(Z)$ and $P(Z')$, and of the measured ratio $R(Z, Z', k, k')$, on the other side, allows one to directly access the concentration ratio.[12]

---

[11]To obtain directly $R(Z, Z', k, k')$, one should compare the same lines for different elements. Here different lines are studied providing a ratio which is proportional to $R(Z, Z', k, k')$.

[12]Note that, as said other factor can influence the capture probabilities, as the valence of the elements.
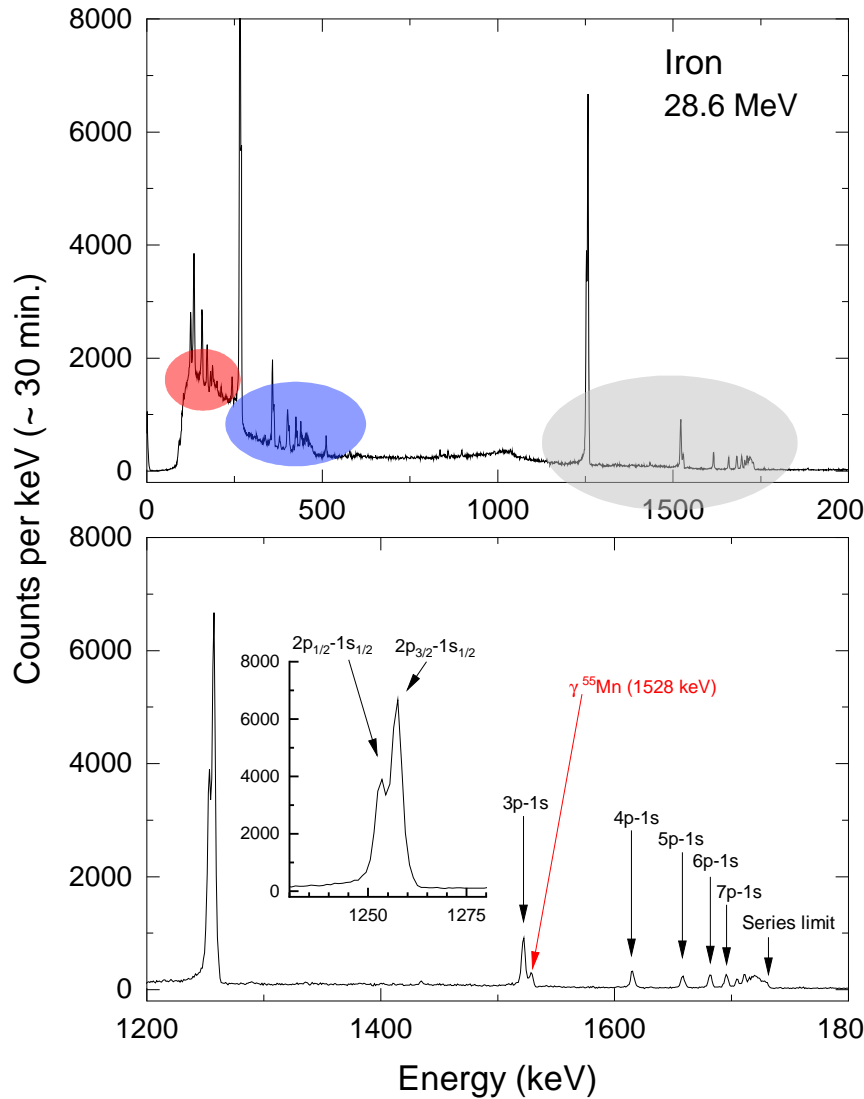
Figure 9.9.: *Upper Panel: Raw X-ray counts obtained during an irradiation of an iron sample with a negative muons beam with momentum 26.5 MeV/c. The typical penetration of the muons is about 200 μm. Clear signals from the muonic Lyman ($n_f = 1$, grey region), Balmer ($n_f = 2$, blue region) and Paschen ($n_f = 3$, red region) series are observable. The data were recorded with one HPGe detector for about 30 minutes. Lower panel: Same Data, but with emphasis to the Lyman series. Note also the signal at 1528 keV, which arises from the release of energy from the $^{55}_{25}Mn^*$ nucleus created after the capture of the negative muons into the iron nucleus and the subsequent neutron emission (see Eq. 9.12 and the footnote on page 307). By decreasing the time window of the data-taking after the muon arrival, this signal can be partially suppressed. The capture rate into the nucleus is about $1/\tau_{\mu, \, Nucl. \, capt}(Fe) \simeq 1/220 \, ns^{-1}$ (see Eq. 9.15). The insert in the lower panel shows details of the $2p \to 1s$ transitions, where the $K_{\alpha 1, \mu}$ and $K_{\alpha 2, \mu}$ are clearly visible. Note the different intensities of these lines (with a ratio close to 2:1) arising mainly from the degeneracies of these levels.*

Figure 9.12 shows the capture probabilities $P(Z)$ determined for different elements. We notice that $P(Z)$ does not smoothly increase as a function of Z, as the electron quantum
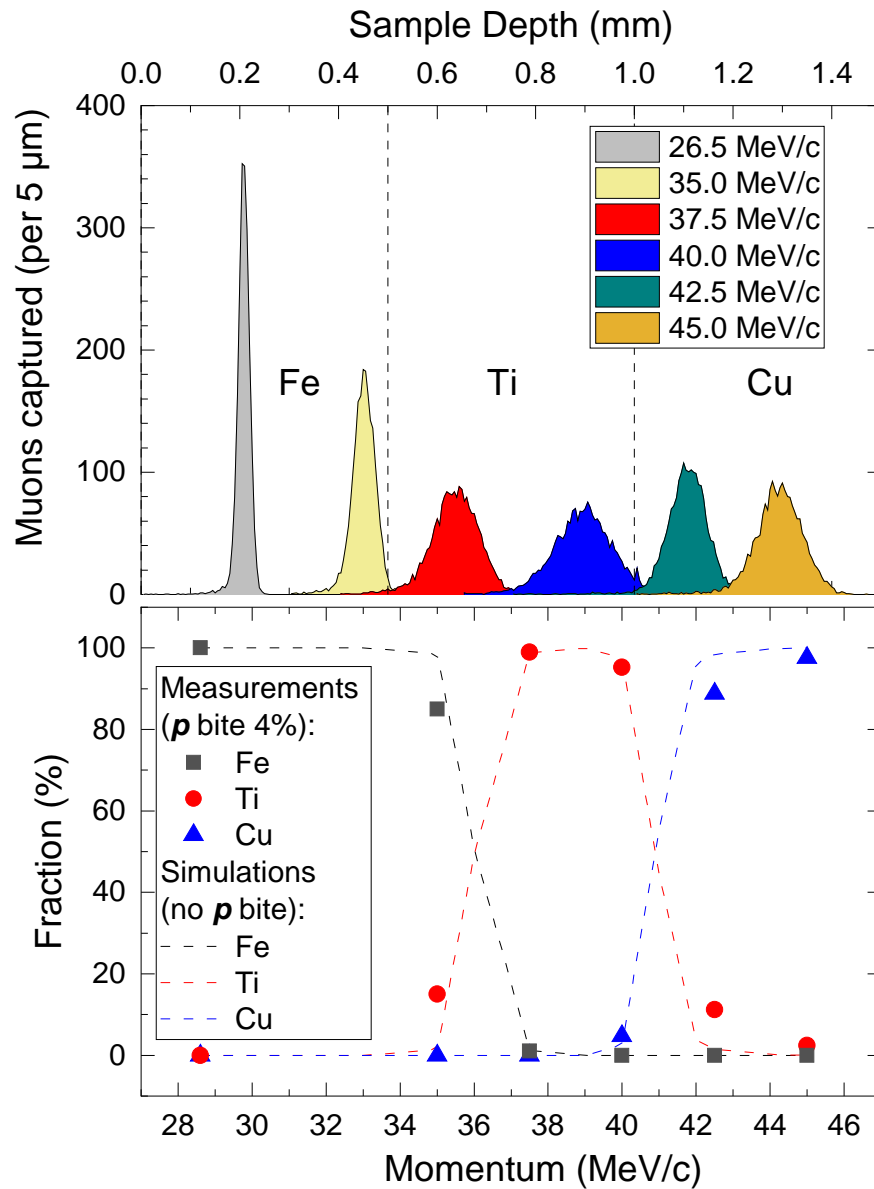
Figure 9.10.: *Top panel: Simulation of the penetration of negative muons into a trilayer sample composed by Fe/Ti/Cu for different beam momenta. Each layer has a thickness of 500 µm. No momentum bite was assumed. Lower panel: Comparison between the detection of elements in the trilayer sample obtained by measuring the MIXE K_α lines (symbols), and the expect results obtained by simulation of the penetration of negative muons (lines, see top panel. Note that here the plot is as function of the nominal beam momentum.*

number n and l of the electron involved in the Auger emission process occurring during the capture of the negative muon have to be considered.
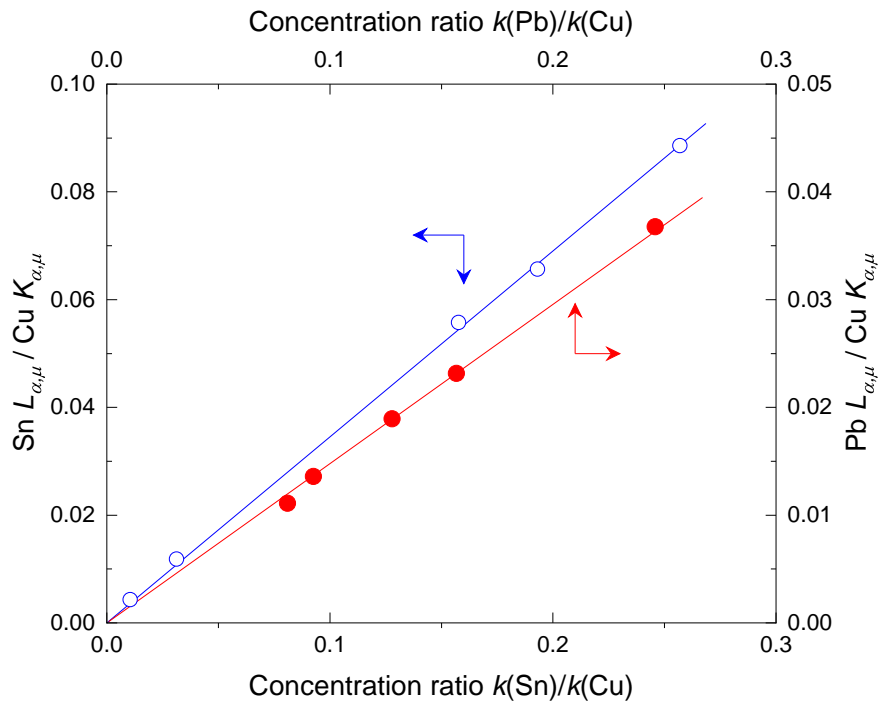
Figure 9.11.: *Measurements in bronze samples $Cu_{k(Cu)}Sn_{k(Sn)}Pb_{k)Pb)}$ of the capture ratio determined by studying MIXE X-ray intensities reported as a function of the ratio of the concentrations (see also Eq. 9.20). Here the $L_{\alpha,\mu}$ lines were used for Sn and Pb and the $K_{\alpha,\mu}$ lines for Cu.*
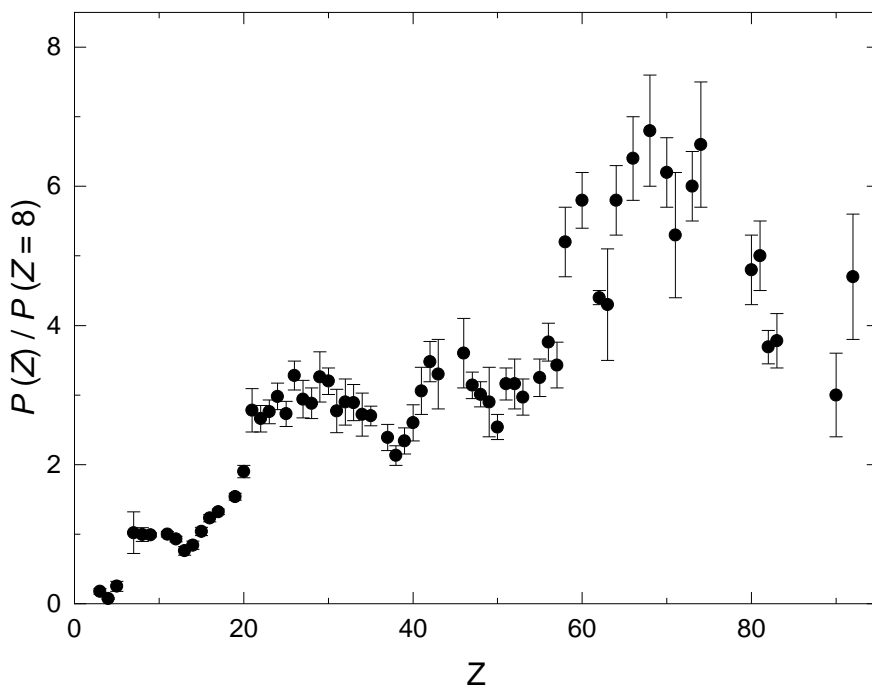
Figure 9.12.: *Capture probabilities $P(Z)$ determined for a series of elements (adapted from Ref. [137]). The values are normalized to the oxygen one, i.e. $P(Z = 8)$.*

9.4.3. Comparison with other techniques

The MIXE technique possesses different characteristics, which can be favorably compared with other elemental analysis methods.

9.4.3.1. Depth-resolution

We have seen that by changing the momentum of the incoming negative muon beam, measurements as a function of the depth can be performed. The penetration can extended to few centimeters.[13] This is of course a fundamental advantage compared to other techniques as XRF and X-ray Photoelectron Spectroscopy (XPS), which use X-rays as primary excitation. Other techniques using different primary excitations as electrons [as Auger Electron Spectroscopy (AES) or Scanning Electron Microscope with Energy Dispersive Spectroscopy (SEM/EDS)] or even protons [as Proton-Induced X-ray Emission (PIXE) or Nuclear Reaction Analysis with Particle-Induced Gamma-ray Emission (NRA/PIGE) have also a very limited depth detection extending to about 10 μm. Other techniques using neutrons as primary excitation [like Prompt Gamma-ray neutron Activation Analysis (PGAA) or Neutron Activation Analysis (NAA)] can indeed detect depth of several centimeters. Nevertheless, here the problem is the neutron absorption, which hugely depends on the type of isotopes in the sample. In addition, the NAA technique requires that the produced radioactive isotopes have a limited lifetime.

9.4.3.2. Non-destructive technique

The MIXE technique is non-destructive.[14] This is not the case with few techniques that we have already mentioned as AES, SEM/ED or Secondary Ion Mass Spectroscopy. Other techniques as Inductive Coupled Plasma Atomic Emission Spectroscopy (ICP-AES) and Inductive Coupled Plasma Mass Spectroscopy (AES-MS), though having a extremely good resolution, will totally destroy (burn) part of the sample.

9.4.3.3. Sensitivity and resolution

The MIXE technique is sensitive to all elements, also the light ones. However here, problems can occur due to the lower capture probability and the rather low energy of the emitted X-

---

[13] We note here that produced X-ray produced during the muon cascade needs also a sufficient energy to escape the material. By taking for example a Lithium-ion battery, the $K_{\alpha,\mu}$ of Lithioum ($Z = 3$) is about 18 keV. This X-ray will have a 50% probability to traverse a 50 μm Aluminum case.

[14] Actually few atoms of the sample will possibly undergo a transmutation due to the capture of the muon into the nucleus (see for example Eq. 9.12). However, with a typical muon rate of about 20 kHz and by assuming a 100% transmutation and a measuring time of typically 30 minutes, one obtain less than 2×10^7 transmutation. This number has to be compared withe the Avogadro number and is therefore totally negligible.

rays. Actually, the problem of the low energy X-rays is even worse for the XRF technique for example.

We note that the capture probability varies by a factor 50 between very light and heavy elements (see Figure 9.12), which is non negligible but still much lower than the variations occurring in the PGAA and NAA techniques.

Also the lateral dimension of a muon beam is rather large compared to a photon beam. Therefore, the use of a collimator (though reducing the beam intensity) or of a suitable muon entry detector (for example a drift chamber or a pixel Silicon detector) should be considered if necessary.

Finally, the detection limit is limited to better than 0.1%, which is usually enough for many application, but cannot be used to look for traces of elements.

This being said, the MIXE technique can be an extremely valuable in situation where the sample is rare and/or costly (for example archaeological findings, cultural heritage objects, meteorites) or when investigating in operando devices (as Lithium-ion batteries for example).

9.4.3.4. Absence of self induced effects

The XRF technique is a powerful technique to determine the elemental composition. Nevertheless, cautions should be taken when determining quantitative information. The main issues are self-produced effects as enhancement and absorption. When studying an alloy (say $A_{k(A)}B_{k(B)}$) by XRF, an enhancement of the intensity of X-rays related to the element A can be observed due to the additional excitation due to the fluorescence radiation produced by the elements present in the sample (assume here B) emitting X-rays with higher energies than the energy of the absorption edge of the element A. In this case, one would extract a value of the concentration higher than the nominal one. Inversely, the absorption effect will consist on the apparent loss of the intensity of the fluorescence radiate due to the partial absorption of it by an element having a lower energy of the absorption edge. For example by using XRF to determine the concentration of iron in alloys (Fe,Ni) and (Fe,Cr), absorption of the Fe fluorescence radiation will occur in the (Fe,Cr) alloys, as $Z(\text{Cr}) < Z(\text{Fe})$, and enhancement occurs in the (Fe,Ni) alloys (as $Z(\text{Ni}) > Z(\text{Fe})$ (see Figure 9.13). The correction of such effects is the biggest difficulty with XRF. As demonstrated with the Figure 9.11, such effects are absent with the MIXE technique, as only one muon is present at a given time in the sample (at least in the continuous beam), and the radiation emitted during the muon cascade cannot be absorbed by another muonic atom.

9.4.4. Continuous vs pulsed-beam

As the HPGe X-ray detectors have a slow response (much longer than the typical time width of a pulse at a pulsed-beam), MIXE only deploys its full capability when used in a continuous beam. Indeed, in a pulsed beam, the probability that a HPGe detector will be hit twice by
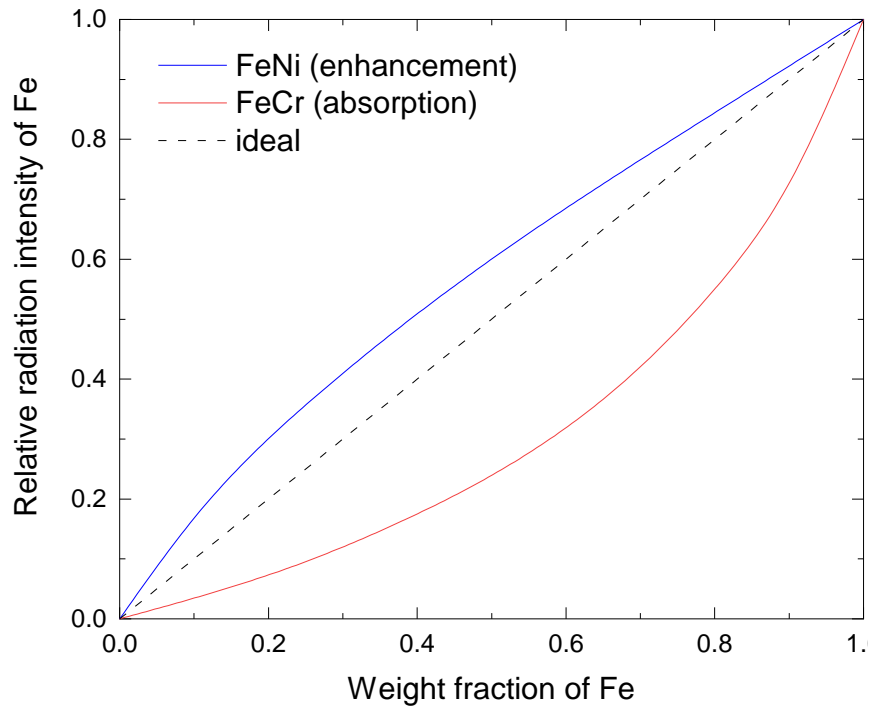
Figure 9.13.: *Absorption and enhancement effects occurring measuring (Fe,Cr) and (Fe,Ni) alloys (see text). Adapted from Ref. [138]).*

X-rays is not negligible, and one should only retain events with a single hit by detector. In a pulsed beam with say 50 Hz repetition rate, this set a limit of 50 events/s per detectors. With a continuous beam, the limit is of sveral thousands events/s per detectors. The reader can convince himself of the difference by looking at Figure 9.14.
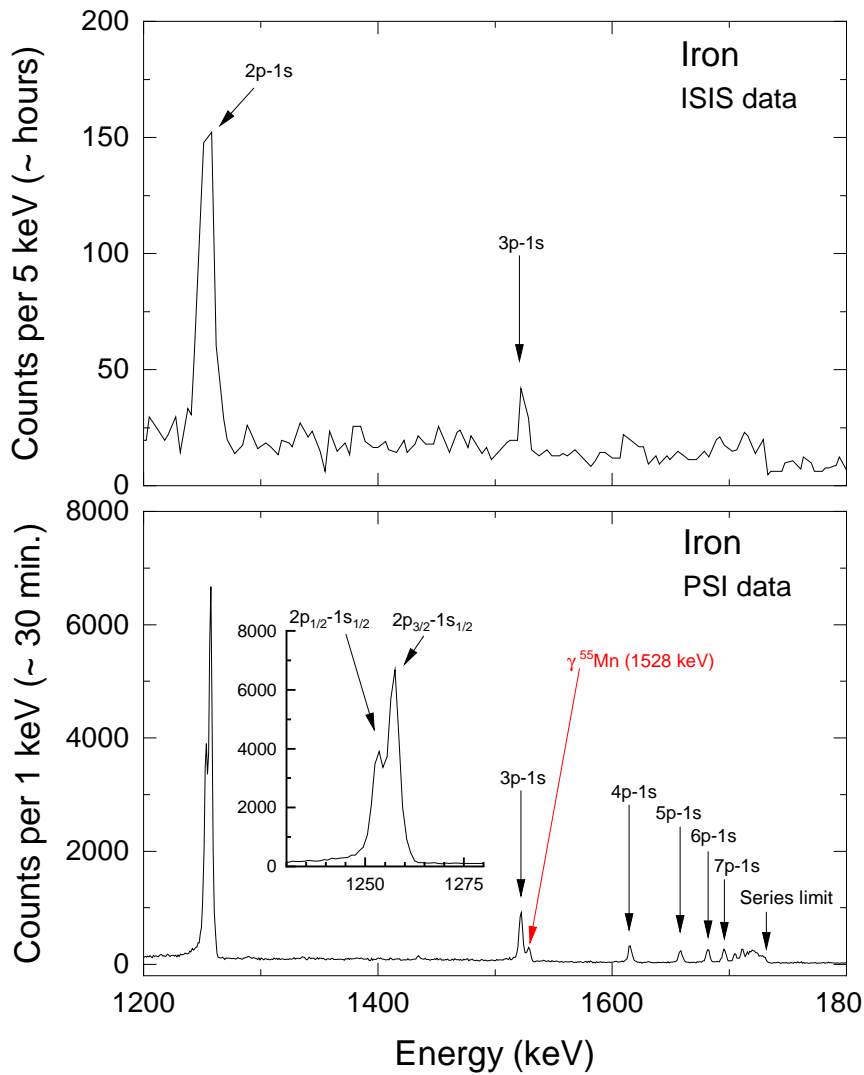
Figure 9.14.: *Comparison between measurements with negative muons performed at ISIS (pulsed-beam) and at PSI (continuous beam). For the measurement performed at ISIS, one can only reliably determine the $K_{\alpha,\mu}$ lines ($2p \to 1s$, not resolved) and the $K_{\beta,\mu}$ ($3p \to 1s$). Note the different binning and the huge difference in counts. Both measurements were taken with similar momentum.*

A. Annex

A.1. Magnetic Moment

A.1.1. Introduction

The magnetic moment plays a fundamental role in magnetism. Classically if an electrical current I forms a loop around an area $|\mathbf{dS}|$ it will create a magnetic moment

$$\mathbf{dm} = I\mathbf{dS} \ ,$$
(A.1)

with units $A \cdot m^2$. The length of $\mathbf{dS}$ is as usual equal to the area of the loop and the vector is normal to the loop and pointing to the direction defined by the current considering the right-hand rule. This object can be considered as a "magnetic dipole" in analogy to the elctrical one where two electric charges (positive and negative) are separated by a small distance along $\mathbf{dS}$. Here, of course, we do not have magnetic monopoles (magnetic charges) but the analogy is very good for long distances.
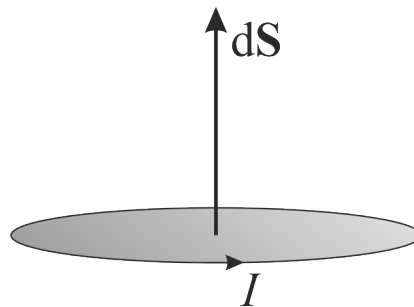
Figure A.1.: *A current forming a loop around an area will create a magnetic moment* **dm**. *The magnetic moment vector will point in the same direction as* **dS**.

For a finite area, we can calculate the magnetic moment $\boldsymbol{\mu}$ by

$$\mathbf{m} = \int \mathbf{dm} = \int I\mathbf{dS} \ .$$
(A.2)

A.1.2. Relation to the angular momentum

When taking a classical object, as the Earth, we see that it can present two types of angular momentum. The orbital angular momentum reflects the rotation of the object about an external point, as the rotation of the Earth around the Sun. On the other hand, the spin angular momentums is due to the rotation of the object itself about an axis going through its center of mass. Similarly, quantum particles possess both orbital angular momentum and spin angular momentum. This is of course a rough analogy, as elementary particles are structureless and the spin angular momentum is an intrinsic property, as mass and charge for example, of the particles.

A.1.2.1. Orbital angular momentum

Let first concentrate on a particle possessing no spin angular momentum. As the charges have a mass (even though very small), the orbital motion of the charges will also be associated to an angular momentum $\mathbf{L} = \mathbf{r} \times \mathbf{p}$. The "gyromagnetic ratio" γ of a system is the ratio of its magnetic moment to its angular momentum, *i.e.*

$$\mathbf{m} = \gamma \mathbf{L} \ . \tag{A.3}$$

If we consider a charged body (charge q) rotating about an axis of symmetry, then (it its charge and mass are both distributed), its gyromagnetic ratio is

$$\gamma = \frac{q}{2M} \ . \tag{A.4}$$

This relation is obtained as follows. Suppose the ring has radius r, area $A = \pi r^2$, mass M, charge q, and angular momentum $L = Mvr$ ($\mathbf{r}$ always perpendicular to the velocity). Then the value of the magnetic dipole moment is (remember that $I = dq/dt$ and we can write $I = q/T$, where T is the rotation period)

$$m = IA = \frac{qv}{2\pi r} \cdot \pi r^2 = \frac{q}{2M} \cdot Mvr = \frac{q}{2M} L \ . \tag{A.5}$$

The Bohr atom model tells us that the angular momentum is quantified in units of $\hbar$ and therefore, if we write for the following equation that $\mathbf{L}$ is given without units (we have therefore to extract $\hbar$ from $\mathbf{L}$) and that the charge orbiting is an electron, it is natural to write

$$\mathbf{m} = -\frac{e\hbar}{2M} \mathbf{L} = -\mu_{\mathrm{B}} \mathbf{L} \ , \tag{A.6}$$

where we have defined the Bohr magneton as

$$\begin{aligned} \mu_{\mathrm{B}} &= \frac{e}{2M_e} \hbar \\ &= 5{,}788\,381\,8012(26) \cdot 10^{-5} \ \mathrm{eV/T} \\ &= 9{,}274\,009\,994(57) \cdot 10^{-24} \ \mathrm{J/T} \ \mathrm{or} \ \mathrm{Am}^2 \end{aligned} \tag{A.7}$$

We see that due to the negative charge of the electron its magnetic moment is always antiparallel to its angular momentum.

An electron with an angular quantum number $\ell = 1$, oriented parallel along the z-axis (magnetic quantum number $m_\ell = +1$), has a magnetic moment of $m_{e,\ell=1} = -\mu_B$.

A.1.2.2. Spin angular momentum

Above, we have omitted the spin angular momentum. Let see now its effect on the moment. The Eq. A.6 suggests that there may be a similar relationship between magnetic moment and spin angular momentum. We can write

$$\mathbf{m}_e = -\frac{g_e\, e\, \hbar}{2M_e}\mathbf{S} = -g_e\, \mu_B\mathbf{S}, \tag{A.8}$$

where g_e is called the *electron g-factor*. Remember that for the above equation the $\hbar$ is extracted from $\mathbf{S}$ and included in the definition of μ_B. Classically, we would expect $g_e = 1$. In fact,

$$g_e = 2\left(1 + \frac{\alpha}{2\pi} + ...\right) = 2.0023192\,, \tag{A.9}$$

where $\alpha = e^2/(2\epsilon_0 hc) \simeq 1/137$ is the so-called *fine-structure constant*. The fact that the electron g_e-factor is (almost) twice that expected from classical physics is only explicable using relativistic quantum mechanics. Furthermore, the small corrections to the relativistic result $g_e = 2$ come from quantum field theory.

The eigenvalue of the z-component of the spin angular momentum are $S_z = \pm 1/2$. Therefore we have a value of the magnetic moment along the quantization axis

$$m_{e,z} = \mp\frac{g_e\, e\, \hbar}{2M_e}\cdot\frac{1}{2} = \mp\mu_B\;. \tag{A.10}$$

and here also the vector $\mathbf{m}$ is always antiparallel to the spin angular momentum.

A.1.2.3. Spin angular momentum of the muon

We have seen that we can write for the muon the relation between the magnetic moment and its spin (see Eq. 1.20)

$$\mathbf{m}_\mu = \gamma_\mu\mathbf{I}_\mu = g_\mu\frac{e}{2M_\mu}\mathbf{I}_\mu \tag{A.11}$$

As already said, we have here the moment and the spin parallel. This relation implies that the $\hbar$ is included in the operator $\mathbf{I}_\mu$. Note that the g-factor for the muon is slightly different from the one of the electron (difference of the order of 0.4%). This is due to QED corrections and possible "Beyond Standard Model" physics. If we extract $\hbar$ from the operator $\mathbf{I}_\mu$, we obtain (similarly to Eq. A.8)

$$\mathbf{m}_\mu = \frac{g_\mu\, e\, \hbar}{2M_\mu}\mathbf{I}_\mu\;. \tag{A.12}$$

Sometimes, one wants to express the muon moment in Bohr magneton $\mu_N = e\hbar/(2M_p)$, where μ_N represents the magnetic moment of a Dirac particle possessing the mass and charge of the proton. Therefore we get

$$\mathbf{m}_\mu = \frac{g_\mu^* e\,\hbar}{2M_p}\mathbf{I}_\mu = g_\mu^* \mu_N \mathbf{I}_\mu \ . \tag{A.13}$$

$$\mathbf{m}_\mu = \frac{g_\mu^* e\,\hbar}{2M_p}\mathbf{I}_\mu = g_\mu^* \mu_N \mathbf{I}_\mu \ .$$

A.2. Spin Angular Momentum

A.2.1. Spin Operators

The spin is an angular momentum, and therefore we can assume that it possesses the same properties as the orbital angular momentum. Therefore, one should be able to define the operators S_x, S_y, and S_z representing the three components of spin angular momentum. We expect also that these operators follow the analogous commutation relations to the ones of the orbital angular momentum operators, L_x, L_y, and L_z. Hence,

$$[S_x, S_y] = i\hbar S_z \,, \tag{A.14}$$
$$[S_y, S_z] = i\hbar S_x \,, \tag{A.15}$$
$$[S_z, S_x] = i\hbar S_y \,. \tag{A.16}$$

Further, we can express the square of the spin angular momentum vector magnitude by the operator

$$S^2 = S_x^2 + S_y^2 + S_z^2 \,. \tag{A.17}$$

One can demonstrate that:

$$[S^2, S_x] = [S^2, S_y] = [S^2, S_z] = 0 \,. \tag{A.18}$$

This indicates that one can simultaneously measure the magnitude squared of the spin angular momentum vector, with one (and only one) of the Cartesian component of the spin. Usually, the z-component, S_z is chosen by convention.

The raising and lowering operators for the spin angular momentum are defined with:

$$S\pm = S_x \pm iS_y \,. \tag{A.19}$$

As the operators S_x, S_y, and S_z are Hermitian, as they represent physical quantities, we have that $S\pm$ are the Hermitian conjugates of one another.

$$(S\pm)^\dagger = S \mp \,. \tag{A.20}$$

Finally, on can show that

$$S_+ S_- = S^2 - S_z^2 + \hbar S_z \,, \tag{A.21}$$
$$S_- S_+ = S^2 - S_z^2 - \hbar S_z \,, \tag{A.22}$$
$$[S_+, S_z] = -\hbar S_+ \,, \tag{A.23}$$
$$[S_-, S_z] = +\hbar S_- \,. \tag{A.24}$$

A.2.2. Spin Space

We now have to discuss the wavefunctions upon which the previously introduced spin operators act. Unlike regular wavefunctions, spin wavefunctions do not exist in real space.

Likewise, the spin angular momentum operators cannot be represented as differential operators in real space. Instead, we need to think of spin wavefunctions as existing in an abstract (complex) vector space. The different members of this space correspond to the different internal configurations of the particle under investigation. Note that only the directions of our vectors have any physical significance (just as only the shape of a regular wavefunction has any physical significance). Thus, if the vector χ corresponds to a particular internal state then $c\chi$ corresponds to the same state, where c is a complex number. Now, we expect the internal states of our particle to be superposable, since the superposability of states is one of the fundamental assumptions of quantum mechanics. It follows that the vectors making up our vector space must also be superposable. Thus, if χ_1 and χ_2 are two vectors corresponding to two different internal states then $c_1\chi_1 + c_2\chi_2$ is another vector corresponding to the state obtained by superposing c_1 times state 1 with c_2 times state 2 (where c_1 and c_2 are complex numbers). Finally, the dimensionality of our vector space is simply the number of linearly independent vectors required to span it (*i.e.*, the number of linearly independent internal states of the particle under investigation).

We now need to define the length of our vectors. We can do this by introducing a second, or *dual*, vector space whose elements are in one to one correspondence with the elements of our first space. Let the element of the second space which corresponds to the element χ of the first space be called $\chi^\dagger$. Moreover, the element of the second space which corresponds to $c\chi$ is $c^*\chi^\dagger$. We shall assume that it is possible to combine χ and $\chi^\dagger$ in a multiplicative fashion to generate a real positive-definite number which we interpret as the length, or *norm*, of χ. Let us denote this number $\chi^\dagger\chi$. Thus, we have

$$\chi^\dagger\chi \geq 0 \tag{A.25}$$

for all χ. We shall also assume that it is possible to combine unlike states in an analogous multiplicative fashion to produce complex numbers. The product of two unlike states χ and χ' is denoted $\chi^\dagger\chi'$. Two states χ and χ' are said to be mutually orthogonal, or independent, if $\chi^\dagger\chi' = 0$.

Now, when a general spin operator, A, operates on a general spin-state, χ, it converts it into a different spin-state which we shall denote $A\chi$. The dual of this state is $(A\chi)^\dagger \equiv \chi^\dagger A^\dagger$, where $A^\dagger$ is the Hermitian conjugate of A (this is the definition of an Hermitian conjugate in spin space). An eigenstate of A corresponding to the eigenvalue a satisfies

$$A\chi_a = a\chi_a . \tag{A.26}$$

If A corresponds to a physical variable then a measurement of A will result in one of its eigenvalues. In order to ensure that these eigenvalues are all real, A must be Hermitian: *i.e.*, $A^\dagger = A$. We expect the χ_a to be mutually orthogonal. We can also normalize them such that they all have unit length. In other words,

$$\chi_a^\dagger\chi_{a'} = \delta_{aa'}. \tag{A.27}$$

Finally, a general spin state can be written as a superposition of the normalized eigenstates of A: *i.e.*,

$$\chi = \sum_a c_a\chi_a . \tag{A.28}$$

A measurement of χ will then yield the result a with probability $|c_a|^2$.

A.2.3. Eigenstates of S_z and S^2

Since the operators S_z and S^2 commute, they must possess simultaneous eigenstate. Let these eigenstates take the form:

$$S_z \chi_{s,m_s} = m_s \hbar \chi_{s,m_s} \,, \tag{A.29}$$

$$S^2 \chi_{s,m_s} = s(s+1) \hbar^2 \chi_{s,m_s} \,. \tag{A.30}$$

Now, it is easily demonstrated, from the commutation relations A.23 and A.24, that

$$S_z (S_+ \chi_{s,m_s}) = (m_s + 1) \hbar (S_+ \chi_{s,m_s}) \,, \tag{A.31}$$

and

$$S_z (S_- \chi_{s,m_s}) = (m_s - 1) \hbar (S_- \chi_{s,m_s}) \,, \tag{A.32}$$

Thus, S_+ and S_- are indeed the raising and lowering operators, respectively, for spin angular momentum. The eigenstates of S_z and S^2 are assumed to be orthonormal: *i.e.*,

$$\chi_{s,m_s}^\dagger \chi_{s',m_s'} = \delta_{ss'} \delta_{m_s m_s'} \tag{A.33}$$

Consider the wavefunction $\chi = S_+ \chi_{s,m_s}$. Since we know, from Eq. A.25, that $\chi^\dagger \chi \geq 0$, it follows that

$$(S_+ \chi_{s,m_s})^\dagger (S_+ \chi_{s,m_s}) = \chi_{s,m_s}^\dagger S_+^\dagger S_+ \chi_{s,m_s} = \chi_{s,m_s}^\dagger S_- S_+ \chi_{s,m_s} = 0 \,, \tag{A.34}$$

where use has been made of Eq. A.20. Equations A.22, A.29, A.30, and A.33 yield

$$s(s+1) \geq m_s(m_s + 1) \,. \tag{A.35}$$

Likewise, if $\chi = S_- \chi_{s,m_s}$ then we obtain

$$s(s+1) \geq m_s(m_s - 1) \,. \tag{A.36}$$

Assuming that $s = 0$, the above two inequalities imply that

$$-s \leq m_s \leq s \,. \tag{A.37}$$

Hence, at fixed s, there is both a maximum and a minimum possible value that m_s can take. Let $m_{s,min}$ be the minimum possible value of m_s. It follows that

$$S_- \chi_{s,m_{s,min}} = 0 \,. \tag{A.38}$$

Now, from Eq. A.21,

$$S^2 = S_+ S_- + S_z^2 - \hbar S_z \,. \tag{A.39}$$

Hence,

$$S^2 \chi_{s,m_{s,min}} = (S_+ S_- + S_z^2 - \hbar S_z) \chi_{s,m_{s,min}} \,, \tag{A.40}$$

giving

$$s(s+1) = m_{s,min}(m_{s,min} - 1) \,. \tag{A.41}$$

Assuming that $m_{s,min} < 0$, this equation yields

$$m_{s,min} = -s \,. \tag{A.42}$$

Likewise, it is easily demonstrated that

$$m_{s,max} = +s \,. \tag{A.43}$$

Moreover,

$$S_- \chi_{s,-s} = S_+ \chi_{s,s} = 0 \,. \tag{A.44}$$

Now, the raising operator S_+, acting upon $\chi_{s,-s}$, converts it into some multiple of $\chi_{s,-s+1}$. Employing the raising operator a second time, we obtain a multiple of $\chi_{s,-s+2}$. However, this process cannot continue indefinitely, since there is a maximum possible value of m_s. Indeed, after acting upon $\chi_{s,-s}$ a sufficient number of times with the raising operator S_+, we must obtain a multiple of $\chi_{s,s}$, so that employing the raising operator one more time leads to the null state (see Eq. A.44). If this is not the case then we will inevitably obtain eigenstates of S_z corresponding to $m_s > s$, which we have already demonstrated is impossible.

It follows, from the above argument, that

$$m_{s,max} - m_{s,min} = 2s = k \,, \tag{A.45}$$

where k is a positive integer. Hence, the quantum number s can either take positive integer or positive half-integer values. Up to now, our analysis has been very similar to that of the orbital angular momentum. Recall, that for orbital angular momentum the quantum number m, which is analogous to m_s, is restricted to take integer values. This implies that the quantum number l, which is analogous to s, is also restricted to take integer values. However, the origin of these restrictions is the representation of the orbital angular momentum operators as differential operators in real space. There is no equivalent representation of the corresponding spin angular momentum operators. Hence, we conclude that there is no reason why the quantum number s cannot take half-integer, as well as integer, values.

In 1940, Wolfgang Pauli proved the so-called *spin-statistics* theorem using relativistic quantum mechanics. According to this theorem, all *fermions* possess *half-integer spin* (*i.e.*, a half-integer value of s), whereas all *bosons* possess *integer spin* (*i.e.*, an integer value of s). In fact, all presently known fermions, including electrons and protons, possess spin *one-half*. In other words, electrons and protons are characterized by $s = 1/2$ and $m_s = \pm 1/2$.

A.2.4. Pauli Representation

Let us denote the two independent spin eigenstates of an electron as

$$\chi_\pm \equiv \chi_{1/2, \pm 1/2} \,. \tag{A.46}$$

It thus follows, from Eqs. A.29 and A.30, that

$$S_z \chi_\pm = \pm \frac{1}{2} \hbar \chi_\pm \,, \tag{A.47}$$

$$S^2 \chi_\pm = \frac{3}{4} \hbar^2 \chi_\pm \,. \tag{A.48}$$

Note that χ_+ corresponds to an electron whose spin angular momentum vector has a positive component along the z-axis. Loosely speaking, we could say that the spin vector points in the $+z$-direction (or its spin is "up"). Likewise, χ_- corresponds to an electron whose spin points in the $-z$-direction (or whose spin is "down"). These two eigenstates satisfy the orthonormality requirements

$$\chi_+^\dagger \chi_+ = \chi_-^\dagger \chi_- = 1 \,, \tag{A.49}$$

and

$$\chi_+^\dagger \chi_- = 0 \,. \tag{A.50}$$

A general spin state can be represented as a linear combination of χ_+ and χ_-: *i.e.*,

$$\chi = c_+ \chi_+ + c_- \chi_-. \tag{A.51}$$

It is thus evident that electron spin space is two-dimensional.

Up to now, we have discussed spin space in rather abstract terms. In the following, we shall describe a particular representation of electron spin space due to Pauli. This so-called *Pauli representation* allows us to visualize spin space, and also facilitates calculations involving spin. Let us attempt to represent a general spin state as a complex *column vector* in some two-dimensional space: *i.e.*,

$$\chi \equiv \begin{pmatrix} c_+ \\ c_- \end{pmatrix} \,. \tag{A.52}$$

The corresponding dual vector is represented as a *row vector*: *i.e.*,

$$\chi^\dagger \equiv \begin{pmatrix} c_+^*, c_-^* \end{pmatrix} \,. \tag{A.53}$$

Furthermore, the product $\chi^\dagger \chi$ is obtained according to the ordinary rules of matrix multiplication: *i.e.*,

$$\chi^\dagger \chi = \begin{pmatrix} c_+^*, c_-^* \end{pmatrix} \begin{pmatrix} c_+ \\ c_- \end{pmatrix} = c_+^* c_+ + c_-^* c_- = |c_+|^2 + |c_-|^2 \geq 0 \,. \tag{A.54}$$

Likewise, the product $\chi^\dagger \chi'$ of two different spin states is also obtained from the rules of matrix multiplication: *i.e.*,

$$\chi^\dagger \chi' = \begin{pmatrix} c_+^*, c_-^* \end{pmatrix} \begin{pmatrix} c_+' \\ c_-' \end{pmatrix} = c_+^* c_+' + c_-^* c_-' \,. \tag{A.55}$$

Note that this particular representation of spin space is in complete accordance with the discussion in Section A.2.2. For obvious reasons, a vector used to represent a spin state is generally known as *spinor*.

A general spin operator A is represented as a 2×2 matrix which operates on a spinor: *i.e.*,

$$A\chi = \begin{pmatrix} A_{11} & A_{12} \\ A_{21} & A_{22} \end{pmatrix} \begin{pmatrix} c_+ \\ c_- \end{pmatrix} \,. \tag{A.56}$$

As is easily demonstrated, the Hermitian conjugate of A is represented by the transposed complex conjugate of the matrix used to represent A: *i.e.*,

$$A^\dagger = \begin{pmatrix} A_{11}^* & A_{21}^* \\ A_{12}^* & A_{22}^* \end{pmatrix} \,. \tag{A.57}$$

Let us represent the spin eigenstates χ_+ and χ_- as

$$\chi_+ \equiv \begin{pmatrix} 1 \\ 0 \end{pmatrix} , \tag{A.58}$$

and

$$\chi_- \equiv \begin{pmatrix} 0 \\ 1 \end{pmatrix} , \tag{A.59}$$

respectively. Note that these forms automatically satisfy the orthonormality constraints A.49 and A.50. It is convenient to write the spin operators S_i (where $i = 1, 2, 3$ corresponds to x, y, z) as

$$S_i = \frac{\hbar}{2}\sigma_i . \tag{A.60}$$

Here, the σ_i are dimensionless 2×2 matrices. According to Eqs. A.14 - A.16, the σ_i satisfy the commutation relations

$$[\sigma_x, \sigma_y] = 2i\sigma_z , \tag{A.61}$$
$$[\sigma_y, \sigma_z] = 2i\sigma_x , \tag{A.62}$$
$$[\sigma_z, \sigma_x] = 2i\sigma_y . \tag{A.63}$$

Furthermore, Eq. A.47 yields

$$\sigma_z \chi_\pm = \pm\chi_\pm . \tag{A.64}$$

It is easily demonstrated, from the above expressions, that the σ_i are represented by the following matrices:

$$\sigma_x \equiv \begin{pmatrix} 0 & 1 \\ 1 & 0 \end{pmatrix} , \tag{A.65}$$

$$\sigma_y \equiv \begin{pmatrix} 0 & -i \\ i & 0 \end{pmatrix} , \tag{A.66}$$

$$\sigma_z \equiv \begin{pmatrix} 1 & 0 \\ 0 & -1 \end{pmatrix} . \tag{A.67}$$

Incidentally, these matrices are generally known as the *Pauli matrices*.

Finally, a general spinor takes the form

$$\chi = c_+\chi_+ + c_-\chi_- = \begin{pmatrix} c_+ \\ c_- \end{pmatrix} . \tag{A.68}$$

If the spinor is properly normalized then

$$\chi^\dagger \chi = |c_+|^2 + |c_-|^2 = 1 . \tag{A.69}$$

In this case, we can interpret $|c_+|^2$ as the probability that an observation of S_z will yield the result $+\hbar/2$, and $|c_-|^2$ as the probability that an observation of S_z will yield the result $-\hbar/2$.

A.2.5. Relating Spinor to Spin Direction

For a general spinor state

$$\chi = \begin{pmatrix} c_+ \\ c_- \end{pmatrix},$$

(A.70)

how do c_+ and c_- relate to the orientation of the spin?

Let us assume that spin is pointing along the unit vector

$$\hat{\mathbf{n}} = (n_x, n_y, n_z) = (\sin\theta\cos\phi, \; \sin\theta\sin\phi, \; \cos\theta)$$

(A.71)

i.e. in direction (θ, ϕ) (θ is the angle with the z-axis and ϕ is the angle with the x-axis).

The spinor must be eigenstate of $\hat{\mathbf{n}} \cdot \boldsymbol{\sigma}$ with eigenvalue unity (actually of $\hat{\mathbf{n}} \cdot \mathbf{S} = \frac{\hbar}{2}\hat{\mathbf{n}} \cdot \boldsymbol{\sigma}$; the axis z is taken as the quantization axis and by doing $\hat{\mathbf{n}} \cdot \boldsymbol{\sigma}$ we write the Pauli matrices along the direction of the spin).

$$\begin{pmatrix} n_z & n_x - in_y \\ n_x + in_y & -n_z \end{pmatrix}\begin{pmatrix} c_+ \\ c_- \end{pmatrix} = \begin{pmatrix} c_+ \\ c_- \end{pmatrix}.$$

(A.72)

Therefore, we find that $c_+/c_- = (n_x - in_y)/(1 - n_z) = e^{-i\phi}\cot(\theta/2)$. Then, making use of the normalisation, $|c_+|^2 + |c_-|^2 = 1$, we obtain (up to an arbitrary phase)

$$\boxed{\begin{pmatrix} c_+ \\ c_- \end{pmatrix} = \begin{pmatrix} e^{-i\phi/2}\cos(\theta/2) \\ e^{+i\phi/2}\sin(\theta/2) \end{pmatrix}}.$$

(A.73)

A.3. The canonical momentum (or generalized momentum)

In an electromagnetic field, a charged particle will feel the Lorentz force

$$\mathbf{F} = q\left[\mathbf{E} + \mathbf{v} \times \mathbf{B}\right] \quad , \tag{A.74}$$

that we can write as (Exercises)

$$M\,\ddot{\mathbf{r}} = q\left[\mathbf{E}(\mathbf{r},t) + \mathbf{v} \times \mathbf{B}(\mathbf{r},t)\right] \quad , \tag{A.75}$$

and for the x coordinate (Exercises)

$$
\begin{aligned}
M\,\ddot{x} &= q\left[\mathbf{E}_x + \dot{y}B_z - \dot{z}B_y\right] \\
&= q\left[-\frac{\partial U}{\partial x} - \frac{\partial A_x}{\partial t} + \dot{y}\left(\frac{\partial A_y}{\partial x} - \frac{\partial A_x}{\partial y}\right) - \dot{z}\left(\frac{\partial A_x}{\partial z} - \frac{\partial A_z}{\partial x}\right)\right] \quad .
\end{aligned} \tag{A.76}
$$

We can show (Exercises) that with the Lagrangian, given in terms of the generalized coordinates $\mathbf{r}$ and generalized velocities $\dot{\mathbf{r}}$ and time,

$$\mathcal{L}(\mathbf{r},\dot{\mathbf{r}},t) = \frac{1}{2}M\,\dot{\mathbf{r}}^2 + q\,\dot{\mathbf{r}} \cdot \mathbf{A}(\mathbf{r},t) - qU(\mathbf{r},t) \tag{A.77}$$

and using the Lagrange's equations of the second kind, *i.e.*

$$\frac{\mathrm{d}}{\mathrm{d}t}\left(\frac{\partial L}{\partial \dot{r}_j}\right) - \frac{\partial L}{\partial r_j} = 0 \tag{A.78}$$

we finally obtain the Eq. A.76.

As $\mathcal{L} = T - U$ and as the potential energy is independent or $\dot{\mathbf{r}}$, then we have that

$$\mathbf{p} = \frac{\partial T}{\partial \dot{\mathbf{r}}} = \frac{\partial \mathcal{L}}{\partial \dot{\mathbf{r}}} \quad , \tag{A.79}$$

and for example

$$p_x = \frac{\partial \mathcal{L}}{\partial \dot{x}} = M\dot{x} + qA_x(\mathbf{r},t) \quad . \tag{A.80}$$

Therefore

$$\mathbf{p} = M\,\dot{\mathbf{r}} + q\mathbf{A}(\mathbf{r},t) \quad , \tag{A.81}$$

which is called the generalized (or canonical) momentum.

The question is to write now the Hamiltonian, and for this we use the Legendre transformation.

A.3.1. Legendre transformation

Consider a function of two independent variables, call it $f(x, y)$. Its differential is

$$df = \left(\frac{\partial f}{\partial x}\right)_y dx + \left(\frac{\partial f}{\partial y}\right)_x dy \tag{A.82}$$

and defining $u \equiv (\partial f / \partial x)_y$ and $w \equiv (\partial f / \partial y)_x$ we can write

$$df = u\, dx + w\, dy \tag{A.83}$$

We call u and x a conjugate pair of variables, and likewise w and y.

We use now the differential

$$d(wy) = y\, dw + w\, dy \tag{A.84}$$

and we subtract Eq. A.83 from this equation and get

$$dg = y\, dw - u\, dx \tag{A.85}$$

where we have introduced the Legendre-transformed function $g \equiv wy - f$. Since we are taking differentials of x and w, we can take those two quantities as the independent variables of the new function $g(x, w)$. Therefore, we have done a Legendre transformation from an original function $f(x, y)$ to a new function $g(x, w)$ by switching from variable y to its conjugate variable w. Of course, one could instead switch x to u or one could switch both independent variables. We see therefore that for two variables, there are 4 possible variants on the function. To make contact with thermodynamics, we might call these various functions the potentials. If instead we have 3 independent variables, there are 8 different potentials, or in general there are 2^n potentials for a function of n independent variables, since each variable can be represented by either member of a conjugate pair.

Let come back to our Lagrangian $\mathcal{L}(\mathbf{r}, \dot{\mathbf{r}}, t)$. We want to transform to a new function (the Hamiltonian) $\mathcal{H}(\mathbf{r}, \mathbf{p}, t)$, where $\mathbf{p}$ is the momentum. Therefore

$$f \equiv \mathcal{L}$$
$$x \equiv \mathbf{r}$$
$$y \equiv \dot{\mathbf{r}}$$
$$w \equiv \left(\frac{\partial f}{\partial y}\right)_x = \left(\frac{\partial \mathcal{L}}{\partial \dot{\mathbf{r}}}\right)_{\mathbf{r}} \equiv \mathbf{p} \quad .$$

So, we finally have

$$g \equiv wy - f = \mathbf{p} \cdot \dot{\mathbf{r}} - \mathcal{L} = \mathcal{H} \tag{A.86}$$

A.3.2. Rewriting the Hamiltonian

We can now write the Hamiltonian So, using Eqs. , we finally have

$$
\begin{aligned}
\mathcal{H}(\mathbf{r}, \mathbf{p}; t) &= \mathbf{p} \cdot \dot{\mathbf{r}} - \mathcal{L} \\
&= \mathbf{p} \cdot \frac{1}{M}(\mathbf{p} - q\mathbf{A}) - \frac{1}{2M}(\mathbf{p} - q\mathbf{A})^2 - \frac{q}{M}(\mathbf{p} - q\mathbf{A}) \cdot \mathbf{A} + qU \\
&= \frac{1}{2M}\left[\mathbf{p} - q\mathbf{A}(\mathbf{r}, t)\right]^2 - qU(\mathbf{r}, t)
\end{aligned}
\tag{A.87}
$$

A.4. The demagnetizing field

Assume a ferromagnetic system with a magnetization $\mathbf{M}$. As the second Maxwell equation (Gauss law) tells us that

$$\nabla \cdot \mathbf{B} = 0 \ , \tag{A.88}$$

and we have

$$\mathbf{B} = \mu_0 \left(\mathbf{M} + \mathbf{H} \right) \ . \tag{A.89}$$

When the magnetization meets the surface of the sample, we will have[1]

$$\nabla \cdot \mathbf{H} = -\nabla \cdot \mathbf{M} \ . \tag{A.90}$$

Therefore (and at the opposite of $\mathbf{B}$) $\mathbf{H}$ is not divergence free and behaves as if magnetic monopoles exist.

Coming back to our ferromagnetic system, the situation shown on Fig. A.2 is as if magnetic monopoles exist at the surface of the sample. The "monopoles" are the caused of the divergence of $\mathbf{H}$.
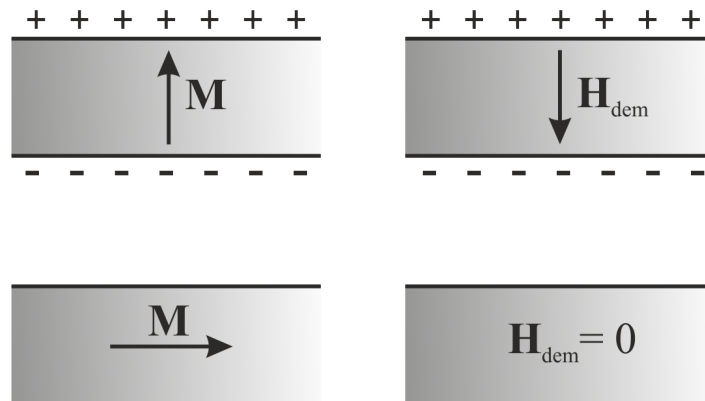
Figure A.2.: *Ferromagnetic infinite flat plate (cross section). The upper row shows the situation when the magnetization perpendicular to the plane of the plate. There is a positive (negative) divergence of the magnetization on the bottom (top) surface. The field $\mathbf{H}_{dem}$ will have opposite divergence. This can be seen as positive and negative poles on the surfaces as shown. If the magnetization is along the plane of the plate (bottom row), the only divergence is at the ends (supposed at an infinite distance). No divergence occurs for the magnetization and no demagnetization field is observed.*

The resulting field is called the "demagnetizing field" and we will write it as $\mathbf{H}_{dem}$, which is strongly dependent on the shape of the sample and the position inside the sample. Taking an ellipsoid sample one can write that

$$\mathbf{H}_{dem} = -\tilde{N} \, \mathbf{M} \ , \tag{A.91}$$

---

[1]Outside the sample we will have $\nabla \cdot \mathbf{H} = 0$.

where $\tilde{N}$ is the demagnetizing tensor. In general, we can write

$$H_{\mathrm{dem},i} = -\sum_j N_{ij} M_j \ .$$

(A.92)

If **M** is defined along the principal direction of the ellipsoid, then one can diagonalize and obtain

$$\tilde{N} = \begin{pmatrix} N_x & 0 & 0 \\ 0 & N_y & 0 \\ 0 & 0 & N_z \end{pmatrix}$$

(A.93)

and the trace is

$$\mathrm{Tr}(\tilde{N}) = N_x + N_y + N_z = 1 \ .$$

(A.94)

A.5. Useful formula from Quantum Mechanics

A.5.1. Time evolution of an operator

With the *Heisenberg* point of view, one can write the time evolution of the expectation value of an observable as

$$
\begin{aligned}
\langle A \rangle(t) &= \langle \psi | A(t) | \psi \rangle \\
&= \sum_{n,p} a_n^* \, a_p \, A_{n,p}(t) \;\; ,
\end{aligned}
\tag{A.95}
$$

where we have expressed ψ as a function of the basis $|\chi_i\rangle$, that is

$$
|\psi\rangle = \sum_i a_i \, |\chi_i\rangle \;\; \text{and}
$$
$$
A_{n,p}(t) = \langle \chi_n | A(t) | \chi_p \rangle \;\; .
\tag{A.96}
$$

The density operator is given as $\rho(0) = |\psi\rangle\langle\psi|$. and one can write the appropriate matrix elements as

$$
\rho_{pn} = \langle \chi_p | \rho(0) | \chi_n \rangle = a_p \, a_n^* \;\; .
\tag{A.97}
$$

Therefore we can rewrite

$$
\langle A \rangle(t) = \sum_{n,p} \langle \chi_p | \rho(0) | \chi_n \rangle \langle \chi_n | A(t) | \chi_p \rangle \;\; ,
\tag{A.98}
$$

and as

$$
\sum_n |\chi_n\rangle\langle\chi_n| = 1 \;\; ,
\tag{A.99}
$$

then

$$
\begin{aligned}
\langle A \rangle(t) &= \sum_p \langle \chi_p | \rho(0) \, A(t) | \chi_p \rangle \\
&= \mathrm{Tr} \left[\rho(0) \, A(t) \right] \;\; .
\end{aligned}
\tag{A.100}
$$

Note that within the *Schrödinger* point of view, where the time dependence if contained in the eigenstates on has

$$
\langle A \rangle(t) = \langle \psi(t) | A | \psi(t) \rangle \;\; ,
\tag{A.101}
$$

and therefore

$$
\langle A \rangle(t) = \mathrm{Tr} \left[\rho(t) \, A \right] \;\; .
\tag{A.102}
$$

A.5.2. 2-D Matrix

A 2×2 matrix (say M) can always be written as a function of the 2×2 unity and Pauli matrices $\mathbb{1}, \sigma_x, \sigma_y$ and σ_z. It is easy to verify that

$$
M = \begin{pmatrix} m_{11} & m_{12} \\ m_{21} & m_{22} \end{pmatrix}
$$
$$
= \frac{m_{11} + m_{22}}{2}\mathbb{1} + \frac{m_{12} + m_{21}}{2}\sigma_x + i\, \frac{m_{12} - m_{21}}{2}\sigma_y + \frac{m_{11} - m_{22}}{2}\sigma_z \ . \qquad \text{(A.103)}
$$

Therefore we can write

$$
M = a_0 \cdot \mathbb{1} + \mathbf{a} \cdot \boldsymbol{\sigma} \ , \qquad \text{(A.104)}
$$

and if M is Hermitian then the a_0, a_x, a_y and a_z coefficients must be real.
Taking into account that $\text{Tr}[\sigma_j] = 0$, $\sigma_x^2 = \sigma_y^2 = \sigma_z^2 = \mathbb{1}$ and that $\sigma_x\sigma_y = -\sigma_y\sigma_x = i\sigma_z$ one shows that

$$
a_0 = \frac{1}{2}\,\text{Tr}[M] \ \ \text{and}
$$
$$
\mathbf{a} = \frac{1}{2}\,\text{Tr}[M\boldsymbol{\sigma}] \ . \qquad \text{(A.105)}
$$

A.6. Useful vector relations

A.6.1. Laplacian

A.6.1.1. Laplacian operator

The Laplace operator is a second order differential operator in the n-dimensional Euclidean space. It is the divergence of the gradient of a function, *i.e.*

$$\Delta \phi = \nabla^2 \phi = \nabla \cdot \nabla \phi \ .$$ (A.106)

In Cartesian coordinates, we can write

$$\nabla^2 \phi = \left(\frac{\partial^2 \phi}{\partial x^2} + \frac{\partial^2 \phi}{\partial y^2} + \frac{\partial^2 \phi}{\partial z^2} \right) \ .$$ (A.107)

A.6.1.2. Vector Laplacian

$$\nabla^2 \mathbf{A} = \nabla(\nabla \cdot \mathbf{A}) - \nabla \times (\nabla \times \mathbf{A})$$ (A.108)

In Cartesian coordinates, we can write

$$\nabla^2 \mathbf{A} = (\nabla^2 A_x, \nabla^2 A_y, \nabla^2 A_z) \ .$$ (A.109)

A.6.2. General identities

$$\mathbf{u} \cdot (\mathbf{v} \times \mathbf{w}) = \mathbf{w} \cdot (\mathbf{u} \times \mathbf{v}) = \mathbf{v} \cdot (\mathbf{w} \times \mathbf{u})$$ (A.110)

$$\mathbf{u} \cdot (\mathbf{v} \times \mathbf{w}) = (\mathbf{u} \cdot \mathbf{w})\mathbf{v} - (\mathbf{u} \cdot \mathbf{v})\mathbf{w}$$ (A.111)

$$\mathbf{u} \cdot (\mathbf{v} \times \mathbf{w}) = -(\mathbf{v} \times \mathbf{w}) \times \mathbf{u}$$ (A.112)

A.6.3. Gradient, divergence and curl

$$\nabla \cdot (\mathbf{A}\phi) = (\mathbf{A} \cdot \nabla\phi) + \phi(\nabla \cdot \mathbf{A}) \tag{A.113}$$

$$\nabla \times (\mathbf{A}\phi) = -(\mathbf{A} \times \nabla\phi) + \phi(\nabla \times \mathbf{A}) \tag{A.114}$$

$$\nabla \cdot (\mathbf{A} \times \mathbf{B}) = \mathbf{B} \cdot (\nabla \times \mathbf{A}) + \mathbf{A} \cdot (\nabla \times \mathbf{B}) \tag{A.115}$$

$$\nabla \times (\mathbf{A} \times \mathbf{B}) = (\mathbf{B} \cdot \nabla)\mathbf{A} - \mathbf{B}(\nabla \cdot \mathbf{A}) - (\mathbf{A} \cdot \nabla)\mathbf{B} + \mathbf{A}(\nabla \cdot \mathbf{B}) \tag{A.116}$$

$$\nabla \cdot (\mathbf{A} \cdot \mathbf{B}) = (\mathbf{B} \cdot \nabla)\mathbf{A} + (\mathbf{A} \cdot \nabla)\mathbf{B} + \mathbf{B} \times (\nabla \times \mathbf{A}) + \mathbf{A} \times (\nabla \times \mathbf{B}) \tag{A.117}$$

$$\nabla \times (\nabla\phi) = 0 \tag{A.118}$$

$$\nabla \cdot (\nabla \times \mathbf{A}) = 0 \tag{A.119}$$

$$\nabla \times (\nabla \times \mathbf{A}) = \nabla(\nabla \cdot \mathbf{A}) - \nabla^2\mathbf{A} \tag{A.120}$$

A.6.4. Some examples

$$\nabla \cdot \mathbf{r} = 3 \tag{A.121}$$

$$\nabla \times \mathbf{r} = 0 \tag{A.122}$$

$$(\mathbf{A} \cdot \nabla)\mathbf{r} = \mathbf{A} \tag{A.123}$$

$$\nabla(\mathbf{r} \cdot \mathbf{A}) = \mathbf{A} + (\mathbf{r} \cdot \nabla)\mathbf{A} + \mathbf{r} \times (\nabla \times \mathbf{A}) \tag{A.124}$$

$$\nabla r^n = nr^{n-1}\frac{\mathbf{r}}{r} = nr^{n-1}\hat{\mathbf{r}} \tag{A.125}$$

Note that the last expression is valid everywhere if $n \leq 0$. On the other side, if $n < 0$ there is a singularity at $r = 0$

Bibliography

[1] A. de Angelis. Domenico Pacini and the discovery of cosmic rays. In *Proceedings of the 32nd International Cosmic Ray Conference*, page 2. The organization, Institute of High Energy Physics, 2011.

[2] R. M. Otis and R. A. Millikan. *Physical Review*, 23:760, 1924.

[3] R. A. Millikan. *Nature (suppl.)*, 121:19, 1928.

[4] V. Hess. *Phys. Z.*, 27:159, 1926.

[5] J. Clay, P. M. van Alphen, and C. G. 'T Hooft. *Physica*, 1:829, 1934.

[6] J. A. Prins. *Nature*, 132(3342):781–781, 1933.

[7] H. Hoerlin, P. Kipfer, and A. Prey. *Naturwissenschaften*, 21(46):822–824, Nov 1933.

[8] H. Bonka. *Physik Journal*, 46(4):126–128, 1990.

[9] P. Kunze. *Z. Phys.*, 1:83, 1933.

[10] S. H. Neddermeyer and C. D. Anderson. *Phys. Rev.*, 51:884, 1937.

[11] H. Yukawa. *Proc. Phys. Math. Soc. Japan*, 17:48, 1935.

[12] B. Rossi and Hall D. B. *Phys. Rev.*, 223:59, 1941.

[13] M. Conversi, E. Pancini, and O. Piccioni. *Phys. Rev.*, 48:71, 1947.

[14] C. M. G. Lattes, H. Muirhead, G. P. S. Occhialini, and C. F. Powell. *Nature*, 159:694–697, 1947.

[15] T. D. Lee and C. N. Yang. *Phys. Rev.*, 104:254, 1956.

[16] C. S. Wu, E. Ambler, R. W. Hayward, D. D. Hoppes, and R. P. Hudson. *Phys. Rev.*, 105:1413–1415, Feb 1957.

[17] J. I. Friedman and V. L. Telegdi. *Phys. Rev.*, 106:1290, 1957.

[18] R. L. Garwin, L. M. Lederman, and M. Weinrich. *Phys. Rev.*, 105:1415–1417, 1957.

[19] G. Jones. *AIP Conference Proceedings*, 79(1):15–36, 1982.

[20] M. Merk, I. van Vulpen, and W. Hulsbergen. Lecture notes for the first year master course on the electroweak part of the standard model. `https://www.nikhef.nl/~wouterh/teaching/PP1/LectureNotes.pdf`. Accessed: 2018.01.31.

[21] E. Morenzoni. Physics with muons: from atomic physics to condensed matter physics. `https://www.psi.ch/lmu/lectures`. Accessed: 2018.01.31.

[22] L. Michel. *Proc. Phys. Soc. (London)*, page 514, 1950.

[23] K. Morishima et al. *Nature*, 2017.

[24] A. E. Pifer, T. Bowen, and K. R. Kendall. *Nuclear Instruments and Methods*, 135:39, 1976.

[25] N. Bohr. *Philosophical Magazine*, 25:10, 1913.

[26] N. Bohr. *Philosophical Magazine*, 30:581, 1915.

[27] H Bethe. *Annalen der Physik*, 5:325, 1930.

[28] C. Patrignani et al. *Chin. Phys. C*, 40:100001, 2017.

[29] Dan. Vid. Sclsk. *Mat. Fys. Medd. Dan. Vid. Selsk.*, 33:1, 1963.

[30] M. Krammer. XII ICFA School on Instrumentation, Bogotá, 2013.

[31] P. Jena et al. *Phys. Rev. B*, 17:301, 1978.

[32] S. K. Estreicher and P. F. Meier. *Phys. Rev. B*, 27:642, 1983.

[33] A. Amato et al. *Review of Scientific Instruments*, 88:093301, 2017.

[34] P. Dalmas de Réotier and A. Yaouanc. *Muon Spin Rotation, Relaxation and Resonance*. Oxford University Press, 2011.

[35] S. Sakarya, P. C. M. Gubbens, A. Yaouanc, P. Dalmas de Réotier, D. Andreica, A. Amato, U. Zimmermann, N. H. van Dijk, E. Brück, Y. Huang, and T. Gortenmulder. *Phys. Rev. B*, 81:024429, 2010.

[36] U. Staub et al. *Physica B.*, 289-290:299, 2000.

[37] R. Khasanov et al. *Journal of Physics: Condensed Matter*, 29:164003, 2017.

[38] Y. Kamihara et al. *Journal of the American Chemical Society*, 130:3296, 2008.

[39] H. Luetkens et al. *Nature Materials*, 8:305, 2009.

[40] R. Kubo and T. Toyabe. A stochastic model for low field resonance and relaxation. In R. Blinc, editor, *Magnetic Resonance and Relaxation*, page 810. North-Holland, 1967.

[41] S.J. Blundell. *Contemporary Physics*, 40:175, 1999.

[42] A. Amato et al. *Phys. Rev. B.*, 52:54, 1995.

[43] L.R. Walker and R.E. Walstedt. *Phys. Rev. B*, 22:3816, 1980.

[44] E. I. Kornilov and V. Y. Pomjakushin. *Physics letters A*, 153:364, 1991.

[45] R. S. Hayano et al. *Phys. Rev. B*, 20:850, 1979.

[46] G. Lamura and other. *Journal of Physics: Condensed Matter*, 26:295701, 2014.

[47] A. Keren. *Physical Review B*, 50:10039, 1994.

[48] C. Balz et al. *Nature Physics*, 12:942, 2016.

[49] Y. Aoki et al. *Physical review Letters*, 91:067003, 2003.

[50] J. Spehling et al. *Physical review B*, 85:140406(R), 2012.

[51] S. J. Blundell. *Applied Magnetic Resonance*, 13(1):155–164, Jul 1997.

[52] L. P. Le et al. *Chemical Physics Letters*, 206(1):405–408, 1993.

[53] Q. Si, R. Yu, and E. Abrahams. *Nature Reviews Materials*, 1:16017, 2016.

[54] A. Amato, R. Feyerherm, F. N. Gygax, A. Schenck, M. Weber, R. Caspary, P. Hellmann, C. Schank, C. Geibel, F. Steglich, D. E. MacLaughlin, E. A. Knetsch, and R. H. Heffner. *EPL (Europhysics Letters)*, 19(2):127, 1992.

[55] R. Joynt and L. Taillefer. *Rev. Mod. Phys.*, 74:235–294, Mar 2002.

[56] G. Aeppli, E. Bucher, C. Broholm, J. K. Kjems, J. Baumann, and J. Hufnagl. *Phys. Rev. Lett.*, 60:615–618, Feb 1988.

[57] R. J. Keizer et al. *Journal of Physics: Condensed Matter*, 11(43):8591, 1999.

[58] A. Schenck, D. Andreica, F. N. Gygax, and H. R. Ott. *Phys. Rev. B*, 65:024444, Dec 2001.

[59] D. Andreica. *Magnetic phase diagram in some Kondo-lattice compounds*. PhD thesis, ETH Zurich, 2001.

[60] A. Amato, P. Dalmas de Réotier, D. Andreica, A. Yaouanc, A. Suter, G. Lapertot, I. M. Pop, E. Morenzoni, P. Bonfà, F. Bernardini, and R. De Renzi. *Phys. Rev. B*, 89:184425, May 2014.

[61] C. Held and M. W. Klein. *Phys. Rev. Lett.*, 35:1783–1785, Dec 1975.

[62] Y. J. Uemura, T. Yamazaki, D. R. Harshman, M. Senba, and E. J. Ansaldo. *Phys. Rev. B*, 31:546–563, Jan 1985.

[63] A. Keren, G. Bazalitsky, I. Campbell, and J. S. Lord. *Phys. Rev. B*, 64:054403, Jun 2001.

[64] I. A. Campbell, A. Amato, F. N. Gygax, D. Herlach, A. Schenck, R. Cywinski, and S. H. Kilcoyne. *Phys. Rev. Lett.*, 72:1291–1294, Feb 1994.

[65] B. A. Frandsen et al. *Nature Communications*, 7:12519, 2016.

[66] S. R. Dunsiger et al. *Nature Materials*, 9:299, 2010.

[67] N. W. Ashcroft and N. D. Mermin. *Solid State Physics*. Saunders College, Philadelphia, USA, 1976.

[68] M. Camani, F. N. Gygax, W. Rüegg, A. Schenck, H. Schilling, E. Klempt, R. Schulze, and H. Wolf. *Phys. Rev. Lett.*, 42:679–682, Mar 1979.

[69] A. Amato, R. Feyerherm, F. N. Gygax, and A. Schenck. *Hyperfine Interactions*, 104(1):115–125, Apr 1997.

[70] R. Feyerherm, A. Amato, F. N. Gygax, A. Schenck, U. Zimmermann, A. Grayevsky, and N. Kaplan. *Hyperfine Interactions*, 85(1):329–335, 1994.

[71] G. Solt. *Hyperfine Interactions*, 96(1):167–175, Dec 1995.

[72] A. Schenck. *Muon Spin Rotation Spectroscopy*. Adam Hilger Ltd., Bristol and Boston, 1985.

[73] H. K. Onnes. *Commun. Phys. Lab. Univ. Leiden*, 12:120, 1911.

[74] W. Meissner and R. Ochsenfeld. *Naturwissenschaften*, 44:787, 1933.

[75] J. V. Minervini. *Nature Materials*, 13:326, 2014.

[76] A. Maisuradze, R. Khasanov, Shengelaya A., and Keller H. *Journal of Physics: Condensed Matter*, 21(7):075701, 2009.

[77] E. H. Brandt. *J. Low Temp. Phys.*, 26:709, 1977.

[78] T. M. Riseman et al. *Phys. Rev. B*, 52:2844, 1995.

[79] A. Yaouanc, P. Dalmas de Réotier, and E. H. Brandt. *Phys. Rev. B*, 55:11107–11110, May 1997.

[80] E. H. Brandt. *Phys. Rev. B*, 68:054506, Aug 2003.

[81] J. E. Sonier, J. H. Brewer, R. F. Kiefl, G. D. Morris, R. I. Miller, D. A. Bonn, J. Chakhalian, R. H. Heffner, W. N. Hardy, and R. Liang. *Phys. Rev. Lett.*, 83:4156–4159, Nov 1999.

[82] B. Pümpin et al. *Phys. Rev. B*, 42:8019, 1990.

[83] A. Maisuradze et al. *Phys. Rev. B*, 92:220503(R), 2015.

[84] E. Bauer et al. *Phys. Rev. B*, 90:054522, 2014.

[85] A. Maisuradze, R. Gumeniuk, W. Schnelle, M. Nicklas, C. Baines, R. Khasanov, A. Amato, and A. Leithe-Jasper. *Phys. Rev. B*, 86:174513, Nov 2012.

[86] Z. Guguchia, R. Khasanov, Z. Bukowski, F. von Rohr, M. Medarde, P. K. Biswas, H. Luetkens, A. Amato, and E. Morenzoni. *Phys. Rev. B*, 93:094513, Mar 2016.

[87] P. K. Biswas et al. *Phys. Rev. B*, 92:195122, 2015.

[88] P. K. Biswas, H. Luetkens, Xiaofeng Xu, J. H. Yang, C. Baines, A. Amato, and E. Morenzoni. *Phys. Rev. B*, 91:100504, Mar 2015.

[89] S. Holenstein, U. Pachmayr, Z. Guguchia, S. Kamusella, R. Khasanov, A. Amato, C. Baines, H. H. Klauss, E. Morenzoni, D. Johrendt, and H. Luetkens. *Phys. Rev. B*, 93:140506, Apr 2016.

[90] R. Khasanov et al. *Phys. Rev. B*, 93:224512, 2016.

[91] J. E. Sonier, J. H. Brewer, and R. F. Kiefl. *Rev. Mod. Phys.*, 72:769–811, Jul 2000.

[92] S. Serventi, G. Allodi, R. De Renzi, G. Guidi, L. Romanò, P. Manfrinetti, A. Palenzona, C. Niedermayer, A. Amato, and C. Baines. *Phys. Rev. Lett.*, 93:217003, Nov 2004.

[93] Z. Shermadini, J. Kanter, C. Baines, M. Bendele, Z. Bukowski, R. Khasanov, H. H. Klauss, H. Luetkens, H. Maeter, G. Pascua, B. Batlogg, and A. Amato. *Phys. Rev. B*, 82:144527, Oct 2010.

[94] A. D. Hillier and R. Cywinski. *Applied Magnetic Resonance*, 13(1):95–109, Jul 1997.

[95] B. Mühlschlegel. *Zeitschrift für Physik*, 155(3):313–327, Jun 1959.

[96] R. Khasanov, P. W. Klamut, A. Shengelaya, Z. Bukowski, I. M. Savić, C. Baines, and H. Keller. *Phys. Rev. B*, 78:014502, Jul 2008.

[97] P. J. Hirschfeld and N. Goldenfeld. *Phys. Rev. B*, 48:4219–4222, Aug 1993.

[98] E. M. Forgan, S. L. Lee, S. Sutton, J. S. Abell, S. F. J. Cox, C. A. Scott, H. Keller, B. Pümpin, J. W. Schneider, H. Simmler, P. Zimmermann, and I. M. Savić. *Hyperfine Interactions*, 63(1):71–72, Feb 1991.

[99] Y. J. Uemura, L. P. Le, G. M. Luke, B. J. Sternlieb, W. D. Wu, J. H. Brewer, T. M. Riseman, C. L. Seaman, M. B. Maple, M. Ishikawa, D. G. Hinks, J. D. Jorgensen, G. Saito, and H. Yamochi. *Phys. Rev. Lett.*, 66:2665–2668, May 1991.

[100] P. Bakule and E. Morenzoni. *Contemporary Physics*, 45(3):203–225, 2004.

[101] D. R. Harshman, A. P. Mills, J. L. Beveridge, K. R. Kendall, G. D. Morris, M. Senba, J. B. Warren, A. S. Rupaal, and J. H. Turner. *Phys. Rev. B*, 36:8850–8853, Dec 1987.

[102] E. Morenzoni, F. Kottmann, D. Maden, B. Matthias, M. Meyberg, T. Prokscha, T. Wutzke, and U. Zimmermann. *Phys. Rev. Lett.*, 72:2793–2796, Apr 1994.

[103] E. Morenzoni, T. Prokscha, A. Suter, H. Luetkens, and R. Khasanov. *Journal of Physics: Condensed Matter*, 16(40):S4583, 2004.

[104] T. Prokscha, E. Morenzoni, C. David, A. Hofer, H. Glückler, and L. L. Scandella. *Applied Surface Science*, 172(3):235–244, 2001.

[105] K. Nagamine, Y. Miyake, K. Shimomura, P. Birrer, J. P. Marangos, M. Iwasaki, P. Strasser, and T. Kuga. *Phys. Rev. Lett.*, 74:4811–4814, Jun 1995.

[106] Y. Miyake et al. *Journal of Physics: Conference Series*, 551(1):012061, 2014.

[107] Z. Salman et al. *Physics Procedia*, 30:55, 2012. 12th International Conference on Muon Spin Rotation, Relaxation and Resonance (μSR2011).

[108] W. Eckstein. *Computer Simulation of Ion-Solid Interactions*. Springer, Berlin, Heidelberg, New York, 1991.

[109] J. F. Ziegler, U. Littmark, and J. P. Biersack. *The stopping and range of ions in solids*. Pergamon, New York, 1985.

[110] E. Morenzoni et al. *Nuclear Instruments and Methods in Physics Research B*, 192:254, 2002.

[111] C. Niedermayer, E. M. Forgan, H. Glückler, A. Hofer, E. Morenzoni, M. Pleines,

T. Prokscha, T. M. Riseman, M. Birke, T. J. Jackson, J. Litterst, M. W. Long, H. Luetkens, A. Schatz, and G. Schatz. *Phys. Rev. Lett.*, 83:3932–3935, Nov 1999.

[112] F. London and H. London. *Proceedings of the Royal Society of London A: Mathematical, Physical and Engineering Sciences*, 149(866):71–88, 1935.

[113] T. J. Jackson, T. M. Riseman, E. M. Forgan, H. Glückler, T. Prokscha, E. Morenzoni, M. Pleines, Ch. Niedermayer, G. Schatz, H. Luetkens, and J. Litterst. *Phys. Rev. Lett.*, 84:4958–4961, May 2000.

[114] A. B. Pippard. *Proceedings of the Royal Society A*, 216:547, 1953.

[115] A. Suter, E. Morenzoni, N. Garifianov, R. Khasanov, E. Kirk, H. Luetkens, T. Prokscha, and M. Horisberger. *Phys. Rev. B*, 72:024506, Jul 2005.

[116] E. Morenzoni et al. *Nature Communications*, 2:272, 2011.

[117] A. J. Drew et al. *Nature Materials*, 8:109, 2009.

[118] V. W. Hughes, D. W. McColm, K. Ziock, and Prepost R. *Phys. Rev. Lett.*, 5:63, 1960.

[119] R. Scheuermann, H. Dilger, E. Roduner, J. Major, M. Schefzik, A. Amato, D. Herlach, A. Raselli, and I. D. Reid. *Physica B Condensed Matter*, 289:698–701, aug 2000.

[120] L. Nuccio, L. Schulz, and A.J. Drew. *Journal of Physics D: Applied Physics*, 47(47):473001, 2014.

[121] J. H. Brewer, K. M. Crowe, F. N. Gygax, R. F. Johnson, B. D. Patterson, D. G. Fleming, and A. Schenck. *Phys. Rev. Lett.*, 31:143–146, Jul 1973.

[122] S. F. J. Cox. *Journal of Physics C Solid State Physics*, 20:3187–3319, aug 1987.

[123] N. Funamori, K. Kojima, D. Wakabayashi, T. Sato, T. Taniguchi, N. Nishiyama, T. Irifune, D. Tomono, T. Matsuzaki, M. Miyazaki, M. Hiraishi, A. Koda, and R. Kadono. *Scientific reports*, 5:8437, 02 2015.

[124] R. F. Kiefl, J. W. Schneider, H. Keller, W. Kündig, W. Odermatt, B. D. Patterson, K. W. Blazey, T. L. Estle, and S. L. Rudaz. *Phys. Rev. B*, 32:530–532, Jul 1985.

[125] J. M. Gil, H. V. Alberto, R. C. Vilão, J. Piroto Duarte, P. J. Mendes, L. P. Ferreira, N. Ayres de Campos, A. Weidinger, J. Krauser, Ch. Niedermayer, and S. F. J. Cox. *Phys. Rev. Lett.*, 83:5294–5297, Dec 1999.

[126] S. F. J. Cox. *J. Phys.: Condens. Matter*, 15:R1727, 2003.

[127] R. A. Mann and M. E. Rose. *Phys. Rev.*, 121:293–301, Jan 1961.

[128] Roger D. Woods and David S. Saxon. *Phys. Rev.*, 95:577–578, Jul 1954.

[129] J. Sugiyama, I. Umegaki, H. Nozaki, W. Higemoto, K. Hamada, S. Takeshita, A. Koda, K. Shimomura, K. Ninomiya, and M. K. Kubo. *Phys. Rev. Lett.*, 121:087202, Aug 2018.

[130] R. Arlt et al. *JINR preprint*, P15-7202, 1973.

[131] M. Koch, K. Maier, J. Major, A. Seeger, W. Sigle, W. Staiger, W. Templ, E. Widmann, R. Abela, V. Claus, M. Hampele, and D. Herlach. *Hyperfine Interactions*, 65(1):1039–1045, Feb 1991.

[132] A. Stoykov, D. Herlach, R. Scheuermann, U. Zimmermann, K. Gritsay, and T. Mamedov. *Physica B: Condensed Matter*, 404:824, 2009.

[133] E. Köhler, R. Bergmann, H. Daniel, P. Ehrhart, and F. J. Hartmann. *Nuclear Instruments and Methods in Physics Research*, 187(2):563 – 568, 1981.

[134] B. V. Hampshire, K. Butcher, K. Ishida, G. Green, D. M. Paul, and A. D. Hillier. *Heritage*, 2(1):400–407, 2019.

[135] R. Bergmann, H. Daniel, T. von Egidy, F. J. Hartmann, J. J. Reidy, and W. Wilhelm. *Phys. Rev. A*, 20:633–638, Sep 1979.

[136] T. von Egidy and F. J. Hartmann. *Phys. Rev. A*, 26:2355–2360, Nov 1982.

[137] T. von Egidy, D. H. Jakubassa-Amundsen, and F. J. Hartmann. *Phys. Rev. A*, 29:455–461, Feb 1984.

[138] R. Sitko and B. Zawisza. Quantification in x-ray fluorescence spectrometry. In Shatendra K. Sharma, editor, *X-Ray Spectroscopy*, chapter 8. IntechOpen, Rijeka, 2012.